PHOTOCATALYTIC REDUCTION OF CARBON DIOXIDE BY ENGINEERED TITANIUM DIOXIDE NANOPARTICLES AND THEIR MODIFIED FORMS

BY

JOSHUA OLUGBENGA OLOWOYO

B.Sc. (Hons) Industrial Chemistry (Ilorin), M.Sc. Physical Chemistry (Ibadan)

MATRIC. NO.: 167067

A Thesis in the Department of Chemistry
Submitted to the Faculty of Science
In Partial Fulfilment of the Requirements for the Degree of

DOCTOR OF PHILOSOPHY

of the

UNIVERSITY OF IBADAN

AUGUST, 2019

ABSTRACT

The continuous burning of fossil fuels has increased the amount of carbon dioxide (CO_2) in the atmosphere, leading to global warming. Photocatalytic reduction of CO_2 to fuels using titanium (IV) oxide nanoparticles (TiO_2-NPs) has been employed to reduce atmospheric CO_2. However, the existing synthetic routes such as sol-gel, microwave, ultrasonic irradiation and spray pyrolysis for TiO_2-NPs were cumbersome. Also nanoparticles produced have some limitations such as low surface area, large band gap, high electron-hole recombination and low photocatalytic efficiency. Hence, the aim of this work was to design simple and energy-saving approaches for the synthesis of improved TiO_2-NPs for photocatalytic reduction of CO_2.

Two kinds of TiO_2-NPs were synthesised separately by Sonothermal (S) and Sonothermal-Hydrothermal (SH) methods to produce TiO_2-S and TiO_2-SH, respectively. The TiO_2-S nanoparticles were doped with varying amount of magnesium to obtain Mg-TiO_2-S. The TiO_2-SH nanoparticles were modified with Reduced Graphene Oxide (RGO) and Carbon Nanotubes (CNTs) to obtain RGO-TiO_2-SH and CNT-TiO_2-SH nanocomposites, respectively. These nanocatalysts were characterised using X-ray diffraction, transmission electron microscopy, X-ray Photoelectron Spectroscopy (XPS), UV-Visible spectroscopy and surface area analysis. Density Functional Theory (DFT) calculations were carried out using Vienna *Ab-initio* Simulation Package to establish the electronic and the structural properties of the reactant molecules deposited on modelled TiO_2-NPs surfaces. Photocatalytic reduction of CO_2 to methanol was performed in acetonitrile-H_2O (9:1, v/v) mixture under ultraviolet and visible light. Data obtained were analysed using descriptive statistics.

The TiO_2-S and TiO_2-SH showed 13.7% and 8.4% rutile phase at phase transition temperature of 450°C, an indication that TiO_2-SH had more anatase phase and higher crystallinity. The crystal size in nm of the predominant anatase phase for TiO_2-S, TiO_2-SH, Mg-TiO_2-S, RGO-TiO_2-SH and CNT-TiO_2-SH were 15.4, 18.1, 15.5, 14.9 and 13.4, respectively. All the nanoparticles were homogenous in nature with the TiO_2-NPs attached to either RGO or CNTs. The XPS revealed Ti2p, O1s, Mg2p, and C1s as the chemical states of the elements present in all the prepared nanoparticles. The calculated band gaps in eV were 3.1, 3.0, 3.1, 2.9 and 2.9 for TiO_2-S, TiO_2-SH, Mg-TiO_2-S, RGO-TiO_2-SH and

CNT-TiO_2-SH, respectively. Their corresponding surface areas were 64.5, 73.1, 121.6, 128.6 and 117.1 m^2g^{-1}, respectively. These indicated the reduction in the band gap and increase in the surface area of nanoparticles when compared with commercial TiO_2-NPs of 3.2 eV and 57.4 m^2g^{-1}. The DFT calculations revealed that the anatase phase of TiO_2-NPs had higher adsorption energy of -0.49 eV for the reactant molecules than the rutile phase of -0.30 eV. Under ultraviolet light, the methanol production rates from the photocatalytic reduction of CO_2 were 1.9, 2.0 and 5.9 $mmolg^{-1}h^{-1}$, using TiO_2-S, TiO_2-SH and Mg-TiO_2-S, respectively; while 2.3 and 1.5 $mmolg^{-1}h^{-1}$ were obtained using RGO-TiO_2-SH and CNT-TiO_2-SH, respectively, under visible light.

The new titanium (IV) oxide nanoparticles and their modified forms were of increased surface area, reduced band gap and lowered electron-hole recombination; thus making the synthetic routes viable and effective.

Keywords: Carbon dioxide reduction, Phase transition temperature, Sonothermal-hydrothermal.

Word count: 480

DEDICATION

This work is dedicated to the Almighty God, who is totally dependable.

ACKNOWLEDGEMENT

I would first appreciate the Almighty God. He is totally dependable. He does not allow His own to be put to shame. He lifted me up and changed my life positively.

I wish to specially acknowledge the past and present Heads of Department of Chemistry, University of Ibadan, Professor A.A. Adesomoju and Professor T. I. Odiaka respectively, and all the members of staff for their contributions in one way or the other, towards the completion of this research.

I wish to express my sincere gratitude to my supervisor Professor J. O. Babalola, for his guidance, encouragement, support and ideas provided during my Ph.D. tenure. Without his contribution, this thesis could not have been completed. I cannot but mention my host supervisors, Dr. Suman L. Jain and Dr. Umesh Kumar, who willingly hosted and supervised my research work at the CSIR-Indian Institute of Petroleum, Dehradun, India. I will be forever grateful to Dr. Umesh Kumar, who against all odds, had faith in me. He trained and molded me into an effective researcher. I greatly appreciate his meaningful advice, mentorship, fatherly care, brotherly support, teacher's patience, tolerance, friendly care, endurance and honesty.

This research work would not have been possible if not for the funding intervention of The World Academy of Science (TWAS) in collaboration with the Council of Scientific and Industrial Research (CSIR). I am grateful for the financial support these bodies provided for me. It gave me a lifetime opportunity.

I also wish to appreciate all the members of the Biophysical Laboratory of the University of Ibadan: Dr (Mrs.) Abimbola Olatunde, Dr. Abraham Oluwole, Mr. Akhigbe, Miss. Vivian, Mr. Koiki Babatunde, Mrs Akin-Ibitayo, Mrs. Opeseitan and others, who in one way or the other contributed to the successful completion of this work. I wish to appreciate the immense contribution of Dr. Martins Omorogie and Dr. Emmanuel Unuabonah towards my research work.

Further, I extend my gratitude to some scientists at CSIR-Indian Institute of Petroleum who helped me in one or other way to complete my Ph.D. First, I am most thankful to Dr. R. R. Bal and Dr. Ankur Bordoloi, who opened the doors of their laboratories for me to access their facilities. I am equally grateful to Dr. Manoj Kumar, Dr. A. K. Sinha, Dr. V. V. D. N. Prasad, Dr. Shubham Paul and Dr. Aarti for helping me

during my research work. I am thankful to the Director of the Institute, Dr. Anjay Ray, who gave me freedom to carry out my research work.

I must also acknowledge the members of my research group at the CSIR-Indian Institute of Petroleum: Dr. Padma Latha, Dr. Aruna Kukrety, Shiv Singh Rawat. Nikita Singhal, Akash Verma, Swatti Saini, Varsha Singh, Asgar Ali, Meenal Kaushal and Upasana Saini. I appreciate their individual contributions and the sharing of research ideas during research meetings and at other times. I cannot but also thank my wonderful friend, Neha Sharma.

Special thanks to members of Analytical Science Division: Mr. Sandeep Saran for XRD, Mr. S. K. Kounathala for scanning electron microscopy, Mr. Raghuvir Singh, Mr. G. M. Bahuguna for FT-IR, Dr. Pankaj Kanaujia, Mr. Deependra Tripathi for GC-MS, Dr. R. K. Chouhan, Mr. Appala Naidu for inductively coupled plasma atomic emission spectroscopy, Mr. Sumit, Mr. Sahil and Dr. Manoj Kumar for transmission electron microscopy analysis. I am indebted to catalytic conversion division for providing their analytical facilities to carry out my research. Special thanks to Nazia Siddqui and Sonu Bhandari for XRD. I am thankful to Mr. Pradeep Tyagi for UV and Kritika Kohli for thermogravimetric analysis.

I wish to specially appreciate Professor Norge Cruz Hernandez, Department of Applied Physics I, University of Seville, Spain and Professor Alexander Voronstov, Altai State University, Russia for their assistance in theoretical calculations in my research work.

I am grateful for a rare assistance given to me by Dr. Oninla of the Department of Chemistry, Obafemi Awolowo University. Despite his busy schedule, he read the first two drafts of my thesis meticulously line by line with dedication.

I am deeply grateful to my biological parents, Elder and Deaconess Stephen Olowoyo, for their moral and financial support. Their sacrifice all these years over me can never be forgotten. They never for once neglect me whether in plenty or in lack. Special thanks to my siblings: Funmi Bewaji, Tobi Olowoyo and Ayo Olowoyo.

I must acknowledge the presence of my spiritual parents; Pastor and Mrs. Adelola, who have been the “behind the scene of everything”. Thanks for your love, unequalled support, advice and encouragement.

Let me use opportunity to thank my wonderful wife, who has been more than a friend. Thanks for the care.

I want to thank and express my apology to all those who were the part of my journey but I am unable to mention name.

CERTIFICATION

I certify that this work wascarried out by Joshua Olugbenga Olowoyo in the Department of Chemistry, University of Ibadan, Nigeria, and the Department of Chemical Science Division, CSIR-Indian Institute of Petroleum, India; and has not been submitted elsewhere for the award of a higher degree.

_____

Supervisor
J. O. Babalola (Ph.D.)
Professor of Physical Chemistry
Department of Chemistry
University of Ibadan,
Ibadan, Nigeria

_____ _____

Host & Co-supervisor I
S. L. Jain (Ph.D.)
Senior Scientist
Chemical Science Division
CSIR-Indian Institute of Petroleum,
Dehradun, India

Host & Co-supervisor II
U.Kumar (Ph.D.)
Scientist
Chemical Science Division
CSIR-Indian Institute of Petroleum,
Dehradun, India

TABLE OF CONTENTS

CHAPTER THREE

LIST OF TABLES

LIST OF FIGURES

LIST OF SCHEMES

LIST OF APPENDICES

LIST OF ABBREVIATIONS

BET	Brunauer–Emmett–Teller
BJH	Barrett–Joyner–Halenda
CB	Conduction Band
CCS	Carbon Capture and Sequestration
Ch	Carboxydothermus Hydrogenoformans
CNTs	Carbon Nanotubes
DFT	Density Functional Theory
DRS	Diffuse Reflectance Spectroscopy
e^-	Electron
E_{bg}	Energy Band Gap
EDX	Energy-Dispersive X-ray Spectroscopy
FID	Flame Ionization Detector
h^+	Hole
HOMO	Highest Occupied Molecular Orbital
GGA-PBE	Generalized Gradient Approximation Perdew–Burke–Ernzerhof
GNS	Graphene Nanosheet
GO	Graphene Oxide
ICP-AES	Inductively Coupled Plasma Atomic Emission Spectroscopy
LHCII	Light-Harvesting Complexes
LUMO	Lowest Unoccupied Molecular Orbital
NHE	Normal Hydrogen Electrode
NPs	Nanoparticles
PAW	Projector Augmented Wave
PZC	Point of Zero Charge

QDs	Quantum Dots
RGO	Reduced Graphene Oxide
RWGS	Reverse Water–Gas Shift
SAED	Selected Area Electron Diffraction
SEM	Scanning Electron Microscope
SOFC	Solid Oxide Fuel Cell
TCD	Thermal Conductivity Detector
TEM	Transmission Electron Microscopy
TGA	Thermogravimetric Analysis
TiNS	Titania nanosheets
UV	Ultraviolet
VB	Valence Band
XPS	X-ray Photoelectron Spectroscopy
XRD	X-ray Diffraction

CHAPTER ONE
INTRODUCTION

The high rate of energy consumption nowadays is of deep concern to humanity, especially in the social-economic-political sphere. The increasing world population has aggravated this concern, therefore could lead to potentially severe consequences on the energy market and trade (Roy *et al.,* 2010; Nam *et al.,* 2011). Researchers are becoming aware and have been taking the necessary steps to meet up with the growing demand for energy. Presently, the sources of energy are insufficient to meet the increasing demand of global energy. It has been estimated that the energy demand will be doubled by the year 2050 and likely to triple by the year 2100 (Cook *et al.,* 2010).

The energy from fossil fuels has contributed to about 80% of world energy supply(Habisreutinger *et al.,* 2013). The burning of fossil fuels is of great importance, because it is known to produce a great quantity of energy per unit weight. These non-renewable fuels take millions of years to be formed; yet they have been continually exhausted than the new ones being produced(Lingampalli *et al.,* 2017; Jaeglé *et al.,* 2005).One major drawback in the use of fossil fuel is the emission of carbon dioxide (CO_2) which is responsible for global warming. To address this issue, the world has taken a huge step to shift its attention towards renewable energy production. Examples of main renewable sources are; nuclear, waves, wind, biomass, geothermal heat, tides and sunlight without the emission of CO_2(Shafiullah *et al.,* 2012). However, the majority of these renewable sources still have their limitations. For example, nuclear energy, which currently provides around 14% of the global electric energy, has some limitations such as the inability to control nuclear chain reaction, difficulty in the safe storing of radioactive wastes and inability to generate liquid fuel for mobility purposes (Dittmar, 2012; Afgan, 2013). With all these challenges of nuclear energy, alternative abundant and sustainable energy sources that will not introduce harmful effect in the environment are required.

Renewable solar energy involves the utilisation of the sun's energy by converting it into useful products. The energy of the sun (1.3×10^5 TW) reaching the surface of the

earth is around 10,000 times greater than the current rate of demand or consumption. The methods that have been adopted to harness the energy from the sun are: solar photovoltaics (Sun *et al.,* 2014), solar heating (Li *et al.,* 2013), solar thermal electricity (Jamel *et al.,* 2013), solar architecture (Lee *et al.,* 2013) and artificial photosynthesis (Habisreutinger *et al.,* 2013). Artificial photosynthesis involves the utilisation of light to produce chemical energy. This makes the process inexpensive, sustainable and pollution free. Furthermore, this can lower the prices of fossil fuels and reduce the costs of alleviating climate change. However, storage of solar energy is a major problem.

Enough physical evidence suggests that CO_2, produced from fossil-fuel burning, is a main contributor to the change in climate (Lacis *et al.,* 2010). The resultant consequences of the change in climate are the rise in global temperature, the melting of glacier and icebergs, increased sea-levels and severe storms (Kenarsari *et al.,* 2013). If not carefully controlled, in the long run, climate change can lead to severe flooding, damage of animal and plant life, consistent famine and droughts in all parts of the world.Despite the significant challenges posed by CO_2, it has been turned into asset by its conversion to fuels by various conversion processes. Such conversion processes are chemical, photochemical, electrochemical, biological, reforming and inorganicprocesses(Das and Daud, 2014). However, the disadvantages associated with these processes are the high operation cost, limitations of raw materials, unsustainability, high electrical voltage and temperature necessities to break down the CO_2 molecules.

Photocatalytic transformation of CO_2 into fuels, for example methane (CH_4), formaldehyde (HCHO), formic acid (HCOOH) and methanol (CH_3OH), is more sustainable and favourable than other technologies. This process can help to reduce the emission of CO_2 from the burning of fossil fuels. Also, it can generate valuable fuels for future energy demands (Yuan and Xu, 2015).Ever since the founding work by Inoue and colleagues in 1979 which demonstrated the conversion of CO_2 to simple, useful C1 chemicals such as CH_3OH, HCHO, CH_4 and HCOOH by using semiconductor photocatalysts for example, GaP, WO_3, TiO_2, SiC, CdS, and ZnO (Inoue *et al.,* 1979). Heterogeneous photocatalytic CO_2 reduction to fuels has received tremendous attention. Heterogeneous photocatalytic CO_2 reduction is the photoconversion of CO_2 to C1–C2 compounds by photon-stimulated reactions over semiconductors.

CO_2, with a linear geometry, is considered as one of the most stable and chemically inert molecules. The dissociation of energy of a C=O bond in CO_2 is known to be around 750 kJ mol^{-1}. This value is higher than other chemical bonds such as C−H (~430 kJ mol^{-1}) and C–C (~336 kJ mol^{-1}) (Xie *et al.,* 2014). The overall effectiveness for the process of the reduction of CO_2 relies critically on the kind of reductants, nature of the semiconductor photocatalysts and their surface area.Several reductants for the photoreduction of CO_2 have been reported. They include H_2O (Kwon *et al.,* 2016), H_2(Kohno *et al.,* 2000a), H_2S (Aliwi and Al-Jubori, 1989) and CH_4(Kohno *et al.,* 2000b). These reductants are regarded as the sacrificial electron donors used for the reduction of CO_2. Among the reductants, H_2O is the most researched because of its low cost and abundance. Moreover, H_2O can serve as the origin of H_2 to generate hydrogenated products such as methanol and methane.

The nature of the semiconductor photocatalysts plays a crucial role in the reduction of CO_2 since photocatalysis processes involve surface-interface and interface-surface reactions. The efficiency of photocatalytic conversion of CO_2 are greatly impacted by a number of characteristic properties of photocatalysts (Tu *et al.,* 2014). Till date, several semiconductor photocatalysts have been explored for the reduction of CO_2. Some examples are SiC, GaP, CdS, ZnO, TiO_2, WO_3, SnO_2, Ta_2O_6, In_2O_3, NiO, CuO, TaON, $SrTiO_3$, CdSe, GaAs and PbS (Liu *et al.,* 2016; Tu *et al.,* 2014).Surface area has been considered to be important in determining the number of active surfaces exposed to the adsorbed reactants during photocatalytic reduction activity. It has been established that high surface area of photocatalysts is favourable for the effective photoconversion of CO_2. In other words, the higher the surface area of photcatalysts, the higher the photocatalytic efficiency. Among the semiconductor photocatalysts, TiO_2 has been the most researched photocatalysts as a result of its unique properties such as high abundance, cost-effectiveness, high crystallinity, suitable optoelectronic property, widely commercial availability and high stability (Liu *et al.,* 2014).

Despite all these qualities, TiO_2 still suffers some challenges such as (i) low surface area (ii) large band gap of 3.0 - 3.2 eV, which falls under the region of ultra-violet (5% of the spectrum of solar light) and (iii) fast recombination of photogenerated charge carriers (Tahir and Amin, 2013). Hence, extensive research works have been made to

suitably increase the surface area, modify the photophysical properties of TiO_2 and prevent these limitations.Several synthetic procedures have been established for the synthesis of TiO_2 nanoparticles (NPs). Some examples are sol-gel, microwave, solvothermal, hydrothermal, ultrasonic irradiation, spray pyrolysis and ultrasound assisted sol-gel technique. Each synthetic route has a different role towards the improvement of the TiO_2 for the proposed applications. The preparatory routes have significant effects on the particle size, particle size distribution, morphology, oxidation state, phase transformation, surface and bulk deposition coverage of TiO_2. Due to the high cost of equipment with the harsh condition involved in most of these synthetic routes, it is still desirable to develop simple approaches,such as sonothermal and sonothrmal-hydrothermal methods, for the synthesis of TiO_2, especially the ones with higher surface area.

Various researchers have adopted several modification techniques for the modification of TiO_2. These modifications have been established and applied for enhanced photocatalytic CO_2 reduction with TiO_2. Examples of such techniques are doping, metal deposition, alkalinemodification, dye sensitisation, carbon-based material loadings and heterojunction construction. These modifications have helped to lower the band gap of TiO_2, reduce the degree of its electron-hole recombinations, thereby extending their lifetime.

1.1 Justification

In this work, two types of mixed-phase TiO_2 were developed using two different synthetic approaches; sonothermal (S) and sonothermal-hydrothermal (SH), providing a much higher surface area in comparison with commercial TiO_2 (P25). These preparatory routes afford the TiO_2 with a phase transition at a lower temperature.

In a way to delay the recombination of TiO_2, TiO_2 doped with magnesium (Mg) was further prepared by a modified sonothermal method. Recently, the doping of TiO_2 with Mg has received considerable attention as a result of the closeness of the ionic radius of Mg to that of Ti. Additional benefits of doping of TiO_2 with Mg have been reported such as (1) the position of energy of the conduction band (CB) minimum of TiO_2 is elevated (Kakiage *et al.,* 2013) and (2) the amount of CO_2 chemisorption on the surface of TiO_2 in the presence of water is increased, leading to the improvement of the efficiency of TiO_2(Teramura *et al.,* 2004; Xie *et al.,* 2014). The difference in the formal charge of Mg^{2+}

and Ti^{4+} encourages the formation of oxygen vacancies. These oxygen vacancies can function as trapping sites on the surface of TiO_2. These sites can trap the photoinduced electrons that have migrated to the surface of TiO_2, leading to the enhancement of photogenerated charge separation (Xie *et al.,* 2014). Majority of the previous researches on Mg-containing TiO_2 were performed as MgO or MgO coated on TiO_2 for the photocatalytic reduction of CO_2(Xie *et al.,* 2014; Kwon *et al.,* 2016). In this work, a barely reported series of Mg-doped TiO_2 have been developed with higher surface area. They were explored for the photocatalytic reduction of CO_2 with H_2O as the reductant.

To reduce the band gap of TiO_2, TiO_2 prepared from sonothermal-hydrothermal route was modified with Reduced Graphene Oxide (RGO) and Carbon Nanotubes (CNTs).Graphene has drawn great attraction within the scientific community since its discovery (Novoselov *et al.,* 2004). RGO, specifically, is an analogue of Graphene Nanosheets (GNS), which is a two-dimensional sp^2-hybridized carbon nanosheet. There are considerable unique properties associated with RGO. These are flexible structure (Lee *et al.,* 2008), relatively good optical transparency (Balandin *et al.,* 2008; Liu *et al.,* 2008b), high chemical stability (Geim and Novoselov, 2007), large surface area (~2600 $m^2\ g^{-1}$) (Wang *et al.,* 2005), excellent mechanical strength (Thostenson *et al.,* 2001), high thermal conductivity (~5000 $W\ m^{-1}\ K^{-1}$) (Ghosh *et al.,* 2008) and excellent mobility of charge carriers (20,000 $cm^2\ V^{-1}\ s^{-1}$) (Bolotin *et al.,* 2008; Allen *et al.,* 2010). The single application of RGO is well known, likewise, the hybridisation of RGO with other semiconductors has been successfully achieved to obtain nanocomposites.

The performance in the photocatalytic activity of TiO_2-NPs could be improved by the coupling of TiO_2-NPs with RGO to obtain RGO-TiO_2 nanocomposites. There have been various synthetic routes for the fabrication of RGO-TiO_2 nanocomposites. Fan and co-workers (2011) prepared RGO-TiO_2 nanocomposites by several techniques using titanium dioxide (P25) and RGO as the starting materials. These techniques are hydrothermal method, hydrazine reduction and UV–assisted photocatalytic reduction. The obtained nanocomposites were applied for the generation of hydrogen from alcohol-water solution under UV-Vis illumination. Among the techniques used, they observed that RGO-P25 obtained from the hydrothermal method had the best performance in the production of hydrogen as a result of the stronger interaction between RGO and P25 (Fan

et al., 2011). Among the several applications of RGO-TiO_2 nanocomposites such as water splitting (Wang *et al.,* 2017a), photocatalytic CO_2 reduction (Tu *et al.,* 2012), dye and organic pollutant degradation (Wang *et al.,* 2016c), lithium-ion batteries (Zhen *et al.,* 2015), and antibacterial activity (Akhavan and Ghaderi, 2009), photocatalytic CO_2 reduction has recently gained attention.Up till now, majority of the studies on the reduction of CO_2 to valuable fuels with RGO-TiO_2 nanocomposites reported methane as the main product (Tan *et al.,* 2015a; Razzaq *et al.,* 2016; Liang *et al.,* 2011; Tan *et al.,* 2015b; Tu *et al.,* 2012; Tu *et al.,* 2013). However, reports on the photocatalytic reduction of CO_2 to methanol are rare.

Ever since the discovery of CNTs by Iijima in 1991 (Iijima, 1991), CNT has drawnsignificant attention from the scientific community with their vast range of applications in photocatalysis, fuel cells andbatteries(Yao *et al.,* 2008; Yu *et al.,* 2005a; Liu *et al.,* 2013). CNTs are known to be favorable candidates as supports and dopants for photocatalysts in place of metal due to their hollow,layered structure, large surface area and high mechanical strength, as well as, unique electron conducting propertiesand charge transfer (Iijima, 1991; An *et al.,* 2012; Yu *et al.,* 2007; Thostenson *et al.,* 2001). CNTs are also known to offer landing sites for coatings with nanoparticles of various sizes (Yu *et al.,* 2007).

The combination of CNTs with TiO_2 can provide an advanced nanocomposite with enhanced quantum efficiency. Three mechanisms have been proposed to explain the improvement of the photocatalytic properties of CNT-TiO_2. Firstly, the formation of heterojunction that delays $e^- - h^+$ pairs recombination (Woan *et al.,* 2009; Yu *et al.,* 2007; Yu *et al.,* 2008a).Secondly, CNTs act as a sensitiser, creating $e^- - h^+$ pairs when excited by light, thereforegenerating additional electrons that are easily transported to the CB of TiO_2 (Vijayan *et al.,* 2012). Thirdly, CNTs act as an impurity by creating Ti−O–C or Ti−C defect sites that allow the absorption of visible light (Vijayan *et al.,* 2012; Pyrgiotakis *et al.,* 2011).Only a few studies have been devoted on the photoreduction of CO_2 with H_2O by the synergistic effect in CNT-TiO_2. Ong and co-workers synthesisedCNT@Ni/TiO_2 nanocomposites by co-precipitation followed by chemical vapourdeposition and found that the nanocomposites were effective for the reduction of CO_2 to methane (CH_4, 0.145 μmol g^{-1} h^{-1}) under visible light(Ong *et al.,* 2013). Gui and colleagues reported the use of

Ag-doped MWCNT@TiO_2 core-shell nanocomposites for continuous CO_2 photoreduction under visible light, in which they obtainedproducts such as methane (0.91 μmol g^{-1} h^{-1}) and ethylene (0.048 μmol g^{-1} h^{-1}) (Gui *et al.,* 2015). Only a few studies related to CNT-TiO_2 composite gave CO, methane and ethylene and CO as products upon photoreduction of CO_2. Nevertheless, all the reported CNT-TiO_2 nanocomposites have a lower rate of product formation and products like methanol are scarce (Ong *et al.,* 2013; Gui *et al.,* 2015).

1.2 Aim and objectives

This research is therefore aimed at engineering different forms of TiO_2 and their modified analogues through simple and easyapproaches and then investigate their photocatalytic potentials for the reduction of CO_2. The above-mentioned aim will be achieved by carrying out the following research objectives. They are to:

- Synthesise two types of the mixed-phase TiO_2 NPs using two novel routes: sonothermal and sonothermal-hydrothermal approaches in order to evaluate their suitability for surface enhancement.
- Characterise the prepared TiO_2 NPs in order to determine various properties of modified forms.
- Perform computational studies on the TiO_2 NPs to check the interaction between the reactants and the products.
- Investigate the photocatalytic potential of the TiO_2 for reduction of CO_2 with H_2O.
- Prepare and modify TiO_2 with carbon-based materials such as (RGO) or CNTs to form heterostructures.
- Characterise the obtained RGO-TiO_2 and CNT-TiO_2 heterostructures.
- Perform computational studies on RGO-TiO_2 and CNT-TiO_2 heterostructures.
- Investigate the photocatalytic potential of RGO-TiO_2 and CNT-TiO_2 heterostructures for the reduction of CO_2 with H_2O.
- Synthesise Mg-doped TiO_2 NPs by a modified sonothermal method.
- Perform various characterisation techniques on the prepared Mg-doped TiO_2 NPs.
- Perform computational studies on the Mg-doped TiO_2 NPs.
- Check the photocatalytic abilities of the Mg-doped TiO_2 NPs for the reduction of CO_2 with H_2O.

CHAPTER TWO
LITERATURE REVIEW

Carbon dioxide, CO_2, is a naturally occurring gas, and its concentration is 0.04% by volume in the atmosphere. Although $CO_2$is considered as a primary cause of global warming, it has many industrial applications in food, oil and chemical industries (Pierantozzi, 1993). CO_2, a greenhouse gas, present in the earth's atmosphere helps to keep the surface of the earth warm by absorbing the outgoing infrared radiation. However, its concentration in the atmosphere has been rising over the last few decades due to natural and human-made activities (Figure 2.1) such as rapid industrialisation, fossil fuel consumption for energy demand, combustion, deforestation and cement manufacturing (Cox *et al.,* 2000; Maginn, 2010; Mikkelsen *et al.,* 2010). According to Keeling's curve, CO_2 concentration reached 410.25 ppm on January 25, 2019, as shown in Figure 2.2.

2.1 Greenhouse effect

The process that keeps earth's surface warm by absorption of outgoing infra-red radiation with the aid of gases present in the atmosphere is called the greenhouse effect. Major greenhouse gases are water vapour (36-70%), CO_2 (9-26%), methane (4-9%) and ozone (3-7%) (Mitchell, 1989; Schneider, 1989; Rosenzweig and Hillel, 1998; Rodhe, 1990). The greenhouse effect is typical of two types: (i) Natural greenhouse effect and (ii) Enhanced greenhouse effect, as shown in Figure 2.3.

2.1.1 Natural greenhouse effect

The Sun is the major source of the temperature of the earth. Approximately, 30 % of the sunlight striking the earth is bounced back / reflected into space by bright surfaces such as the clouds and ice. The land and ocean absorb most of the remaining 70 % of the incoming sunlight. The rest is absorbed by the atmosphere. This absorbed solar energy heats the earth.

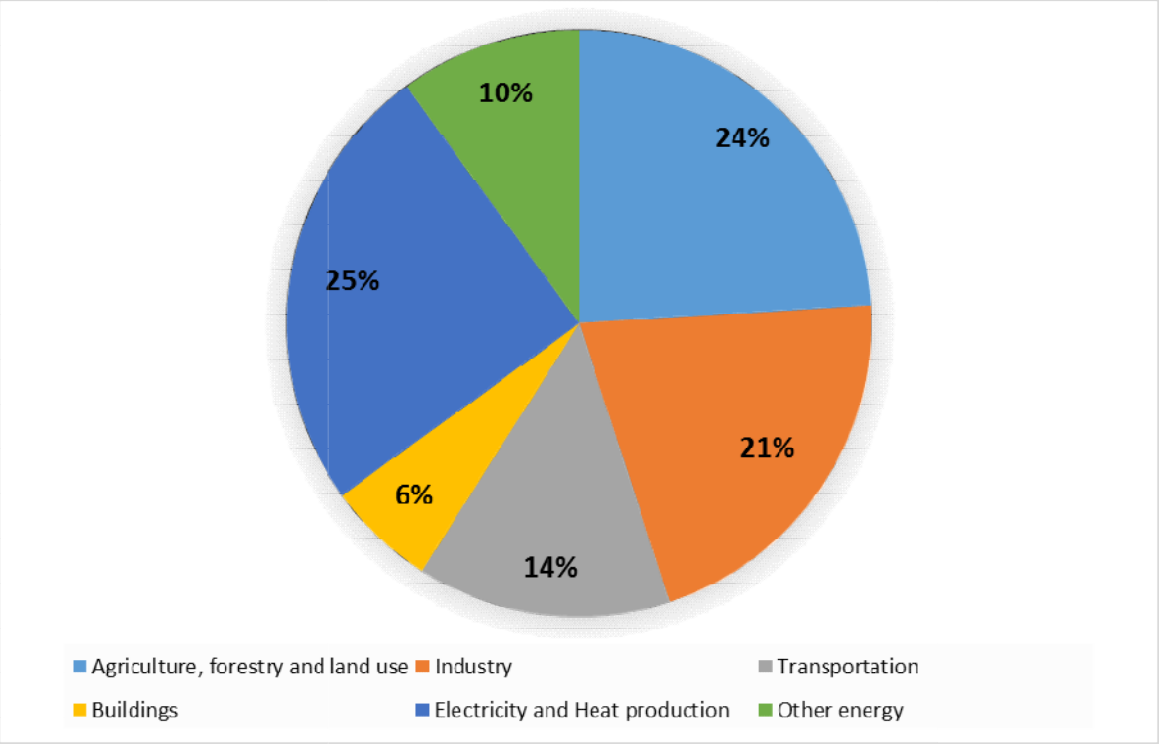

Figure 2.1 Global greenhouse gas emission by economic sector according to the Intergovernmental Panel on Climate Change in the year 2014 (https://www.ipcc.ch/report/ar5/wg3/ retrieved on Oct. 20, 2018).

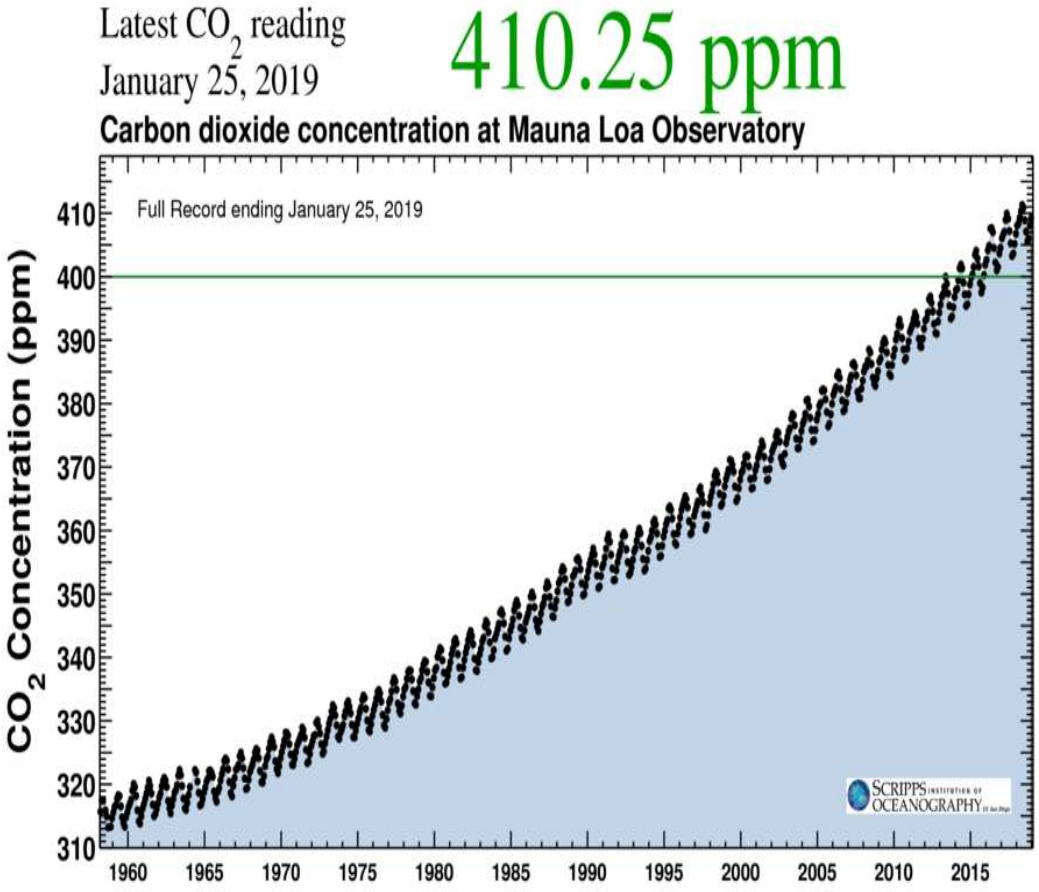

Figure 2.2 Keeling curve for CO_2 concentration. (https://scripps.ucsd.edu/programs/keelingcurve/ retrieved on Jan. 27. 2019).

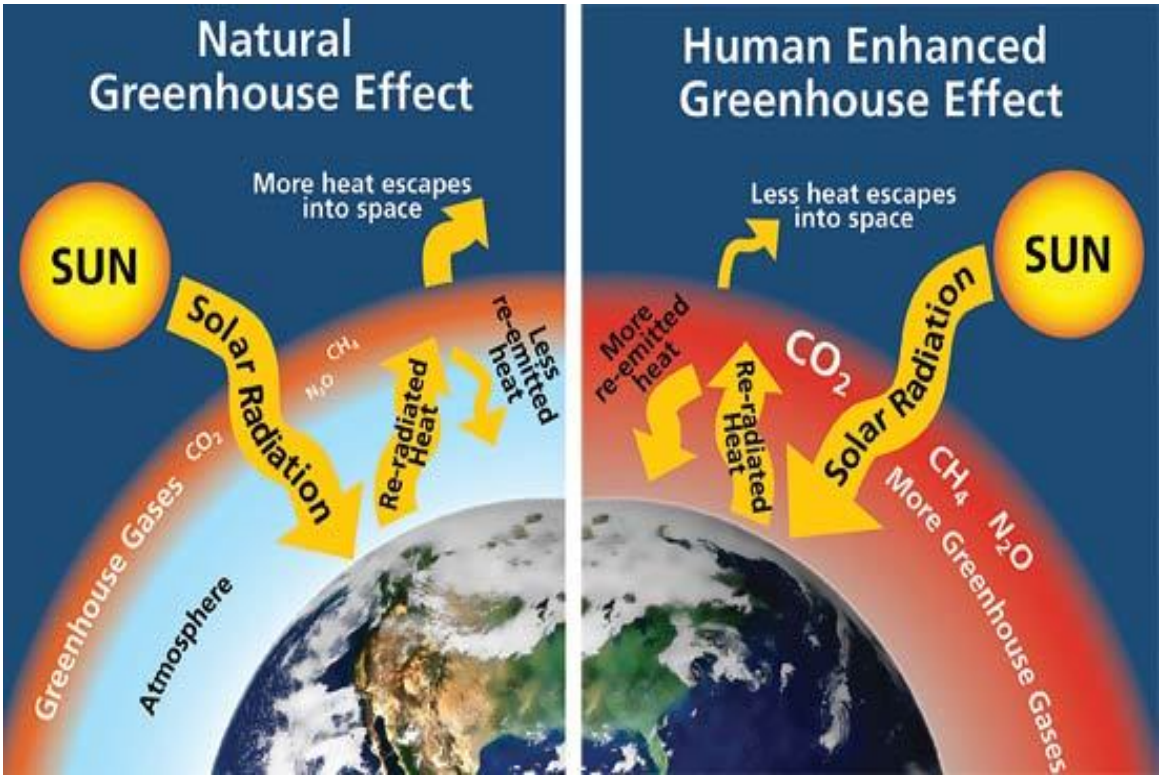

Figure 2.3 Natural and enhanced greenhouse effect. (https://mrgeogwagg.wordpress.com/2015/06/24/greenhouse-effect-and-anthropogenic-warming/ retrieved on Oct. 13, 2018).

As the earth surfaces (rocks, air, and seas) get consequently warmed up, they radiate “heat” energy (thermal infrared radiation). From the surfaces, this energy travels into the atmosphere, where a considerable amount of it is absorbed by long-livedgreenhouse gases (carbon dioxide and methane) and water vapour. When they absorb the energy radiating from Earth’s surface, microscopic water or greenhouse gas molecules turn into tiny heaters. They radiate back in all directions to the earth. The energy that radiates back toward the earth heats both the lower atmosphere and the surface, thereby increasing the heating they acquire from exposed sunlight. This process of absorption-radiation heating by the atmosphere is referred to as the natural greenhouse effect, which is beneficial for life on Earth. Assuming there was no greenhouse effect, the Earth’s average surface temperature would have been very chilly (-18 °C or 0 °F); instead of the comfortable 15 °C (59 °F) that it is today.

2.1.2 Enhanced greenhouse effect

The enhanced greenhouse effect is the process caused by the artificial increment of the concentration of greenhouse gases in the atmosphere. Human activities are mainly responsible for the enhanced greenhouse effect. The effect has led to the issue of global warming.

2.2 Global warming

Global warming is the abnormally rapid increase in Earth’s average surface temperature, and this occurs by the increasing concentration ofmajor contributor to the greenhouse gases, which have drastic consequences for biodiversity. Globally, between the year 1906 and 2005, the global average surface temperature rose from 0.6 to 0.9 °C. The temperature rate has increased almost double in the last half-century as shown in Figure 2.4. Temperatures are certain to go up further, based on a range of probable emission scenarios, average surface temperatures could rise between 2 °C and 6 °C by the end of the 21st century. This rise in temperature would have profound effects across the globe, ranging from the melting of glaciers and icebergs, increased sea-levels and severe storms (Mercer, 1978; Krupa and Kickert, 1989; Mitchell, 1989; Rosenzweig and Hillel, 1998). These changes in nature would in-turn produce distressing results in the form of floods, loss of plant and animal life, frequent droughts and famine in all parts of the world.

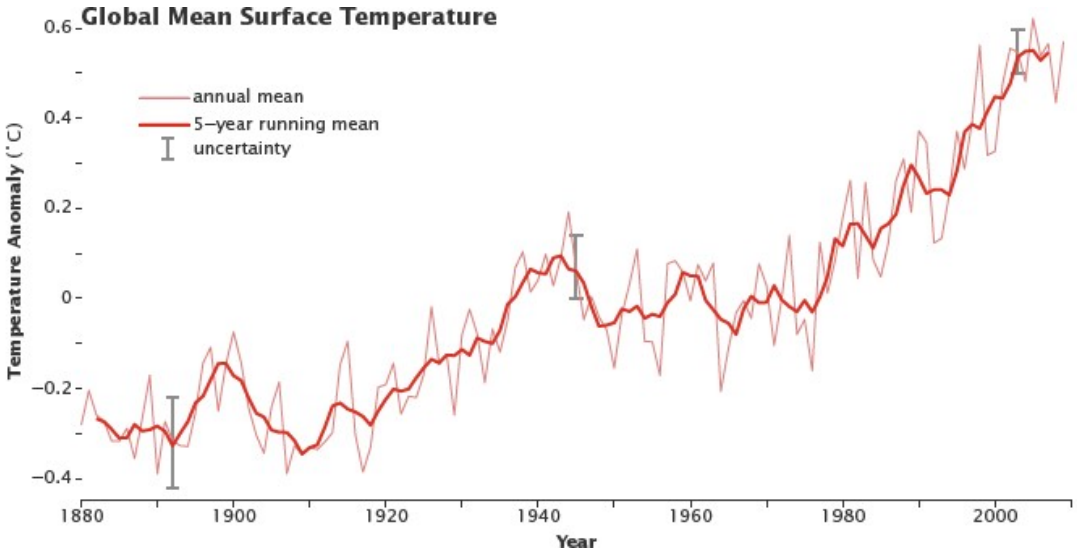

Figure 2.4 The global average temperature from 1800 until the 21st century (https://data.giss.nasa.gov/gistemp/ retrieved on Mar. 9, 2018). The global average surface temperature keeps rising despite the ups and downs. By the beginning of the 21st century, the Earth's temperature was roughly 0.5 °C above the long-term (1952 - 1980) average.

2.3 Need to reduce CO_2

As earlier mentioned, CO_2 is a major greenhouse gas. CO_2 puts us at the extreme risk of irreversible changes if it continues to accumulate unabated in the atmosphere as it has the highest radiative force among all human-influenced climate drivers (Roy *et al.,* 2010; Lingampalli *et al.,* 2017). CO_2 persists in the atmosphere longer than other major heat-trapping gases emitted as a result of human activities.

Therefore, CO_2's long life in the atmosphere delivers the clearest possible rationale for reducing our CO_2 emissions without delay. It is the biggest challenge and needs new ideas and technologies.

2.4 Carbon Capture and Sequestration (CCS)

The process is aimed at preventing excess CO_2 emissions into the atmosphere from power plants (Yu *et al.,* 2008b; Boot-Handford *et al.,* 2014). It involves three steps:

a) CO_2capture from huge location sources such as refineries,power plants, and industries,
b) transportation of captured CO_2 by pipelines or ships, and
c) underground injection and geological sequestration.

The major safety concern about CCS is potential leaks of CO_2. Such leaks can be caused by a successful blowout or pipeline rupture. The captured CO_2 could leak into groundwater aquifers, potentially rendering water undrinkable. These leakages could lead to the death of plants, soil acidification, increased mobility of heavy metals, and possible human fatality.

Except for the risk of lives, high cost (Blomen *et al.,* 2009) and additional energy requirements are also considerable issues to handle in CCS. Therefore, researchers are now paying attention to the utilisation of CO_2 for the syntheses of useful chemicals and fuels.

2.5 Conversion of CO_2 to Value-Added Products

High abundance and low cost are the main advantages of CO_2 as promising feedstock in organic synthesis. CO_2 can be converted into a lot of useful commodities such as urea, carboxylic acids, epoxides, acyclic and cyclic carbonates, polymers and fuels (Sakakura *et al.,* 2007). As well as contributing to the alleviation of inclusive climate changes caused by growing CO_2 emissions, the utilisation of CO_2 for the manufacture of

chemicals also provides an outstanding challenge in exploring new concepts and opportunities for catalytic and industrial development. The important processes for CO_2 conversion to value-added chemicals include thermal, electrochemical, biological and photocatalytic reduction.

2.5.1 Thermal Reduction

CO_2 reduction carried out at elevated temperature and pressure is called thermal reduction. Sophisticated system is required to carry out thermal reduction. The products of thermal reduction are mainly: CO, methanol, and hydrocarbons.

CO can be produced by Reverse Water–Gas Shift (RWGS). RWGS is an endothermic process, which requires high temperatures. At temperature ranging from 200 °C to 500 °C and3:1 H_2: CO_2 ratio at 1 Mpa, the maximum conversion of CO_2 has been reported to be in the range of10% to 50% (Riedel *et al.,* 2001).

The synthesis of methanol from CO_2 and H_2 is an exothermic process. This process has been reported to be kinetically limited at low temperatures and thermodynamically limited at high temperatures resulting in a low theoretical CH_3OH yield of 0.06% at 300 °C and 0.1 MPa (Liu *et al.,* 2003).

Direct hydrogenation of CO_2 can also lead to the production of hydrocarbons such as alkanes and olefins. The CO_2-Fischer–Tropsch process is desirable because it provides a route to produce alkanes and olefins from CO_2 and H_2 directly, but designing catalysts that are water resistant with high olefin selectivity are challenging (Porosoff *et al.,* 2016).

2.5.2 Electrochemical Reduction

CO_2 can be electrochemically converted into various products directly at the surface of solid electrodes. Alternatively, a homogeneous catalyst, which also participates in an electron transfer reaction from solid electrodes, can be additionally incorporated to convert the CO_2. In this context, high-temperature CO_2 conversions are typically carried out using variations of the Solid Oxide Fuel Cell (SOFC), whereas low-temperature systems largelyutilise transition metal electrodes in both aqueous and non-aqueous electrolytes, such as methanol, acetonitrile, propylene carbonate, or dimethyl sulfoxide. The number of products formed at low temperatures is higher than at high temperatures. In other words, the selectivity and performance of SOFC devices often exceed those observed in transition metal electrode systems. Applied potentials of several volts are also

necessary for low temperature aqueous and non-aqueous phase electro-reductions, resulting in large power requirements (Spinner *et al.,* 2012).

2.5.3 Biological Reduction

Eco-friendly and promising ways of CO_2 fixation are provided by microorganisms and enzymes. Enzymes are stereospecific, regiospecific and chemoselective. Inspired by the CO_2 metabolic process in cells, two classes of enzymes (oxidoreductases and lyases) have been successfully utilised for converting CO_2 into different types of fuels/chemicals/materials. Enzymes are generally expensive and environmentally sensitive catalysts. These limitations hinder their industrial applications (Shi *et al.,* 2015).

2.5.4 Photocatalytic Reduction

The reduction of CO_2 by solar light and water in the presence ofcatalysts, which accelerate the reaction in the presence oflight, is termed artificial photosynthesis (Bensaid *et al.,* 2012). Using photocatalysis, solar energy can be converted into chemical energy directly. Among other CO_2 reduction processes, the photocatalytic reduction is beneficial because it uses abundant, renewable sources. Solar energy is the largest exploitable source of energy, and approximately 0.015% of its energy reaching the earth has been estimated to be enough to support life on earth (Lewis and Nocera, 2006).

Photocatalytic reduction of CO_2 to sustainable fuels is a challenging and promising application owing to its many advantages. For instance,

- The reaction can be performed in amoderately mild condition such as room temperature and atmospheric pressure, which results in reduced energy consumption, less catalyst deactivation, safety and stability of the reactor.
- CO_2 reduction process can acquire photocatalytic products of short-chain hydrocarbons, which can overcome the energy crisis to some degree.
- This technology would be favourable for switching the fossil fuel CO_2 as a carbon source in the chemical industry.

Therefore, the photoreduction of atmospheric CO_2 with H_2O to valuable fuel products would save energy supplying as well as protect the environment.

2.6 Fundamentals and Evaluation of CO_2 Photocatalytic Activity

2.6.1 Principle of photocatalysis

Photocatalysis is a phenomenon in which light radiations of energy equal to or greater than the Energy Band Gap (E_{bg}) of a semiconductor strike on its surface and generates Electron (e^-) - Hole (h^+) pairs. This photogenerated e^- and h^+ participate in various oxidation and reduction reactions to generate final products. However, in case the electrons cannot locate any trapped species (CO_2) on the semiconductor surface or their E_{bg} is too small, they recombine immediately and discharge unproductive energy as heat (Kabra *et al.,* 2004).The photo activities of semiconductors depend on some factors such as: (a) composition of the reaction medium, (b) adsorption of reactants (CO_2 and H_2O) on semiconductor surface, (c) type of semiconductor and its crystallographic/morphological properties, and (d) the ability of semiconductor to absorb UV or visible light (Arakawa *et al.,* 2001; de Lasa *et al.,* 2005).

Semiconductors are classified into homogeneous and heterogeneous photocatalysts (Ibhadon and Fitzpatrick, 2013; Centi and van Santen, 2007). The heterogeneous photocatalysts are preferred over homogenous photocatalysts because they can be reused, recycled and regenerated. The heterogeneous photocatalysis phenomenon is presented in Figure 2.5 (Tahir and Amin, 2013).

During the photocatalytic processes, electrons are migrated from the Valence Band (VB) to the Conduction Band (CB), and equal numbers of holes are produced in the CB simultaneously when semiconductor absorbs a flux of photon (Tu *et al.,* 2014). Obtaining the final product in photocatalysis involves many routes due to the complexity of the mechanism. Also, the yield rates of the products are dependent on the lifetime of photogenerated electrons and holes particle. On the other hand, the charge transfer rate depends on the positions of the band edges (CB and VB bands) and redox potentials of adsorbed species. In general, the following paths are possible if the charges have sufficient energy during photocatalysis process (Kabra *et al.,* 2004).

(a) Surface recombination (Path A): - This occurs when electrons and holes recombine on the semiconductor surface.

(b) Volume recombination (Path B): - This occurs when electrons and holes recombine within the volume of the heterogeneous photocatalyst.

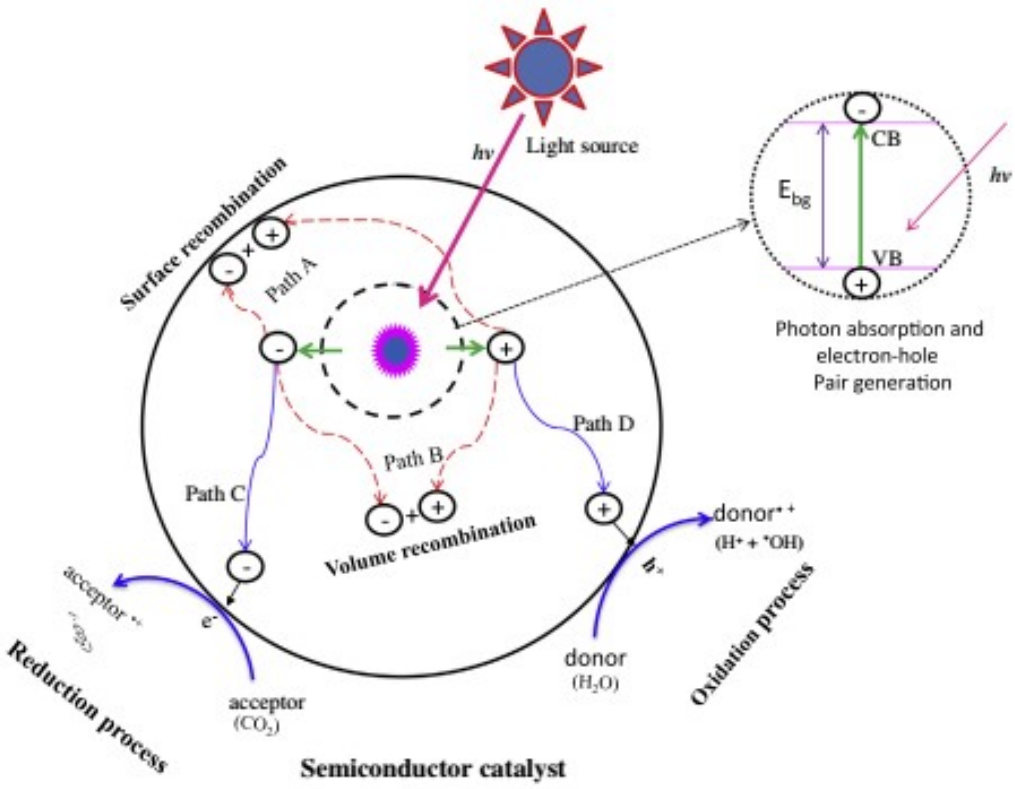

Figure 2.5 Mechanism and pathways for photocatalytic oxidation and reduction processes on the surface of heterogeneous photocatalyst (Tahir and Amin, 2013).

(c) Electron transfer to the outer surface (Path C): - This occurs when the photogenerated electrons move towards the outer surface of the semiconductor and are trapped by the adsorbed species. This electron transfer process will be more efficient if pre-adsorbed species such as CO_2 and H_2O already exist at the catalyst surface. At the surface, the semiconductor can provide an electron to reduce acceptors (CO_2).

(d) Hole transfer to the outer surface (Path D): - This occurs when the corresponding hole are transferred to the surface where an electron from donor species can combine with the surface hole to oxidise donor species (H_2O).

2.6.2 Thermodynamic analysis

Photocatalytic CO_2 reduction is a mimicry of the natural photosynthesis process by converting solar light energy into valuable fuels, without involving other high-energy input (Koci *et al.,* 2008; Yu *et al.,* 2016). Generally, the reaction involved in the photocatalytic reduction of CO_2 can be classified into four main steps (Figure 2.6) which include (1) the adsorption of CO_2, (2) the generation of electron-hole pair as a result of the absorptionof enough incident light energy, (3) the separation of e^--h^+ pairs and their movement to the surface of the photocatalyst and (4) the reduction of CO_2 (Mao *et al.,* 2013; Sarkar *et al.,* 2016; Lan and Shi, 2014). Usually, the photocatalytic reaction is started by the adsorption of CO_2 (Liu *et al.,* 2015). The adsorption capacity of TiO_2 toward CO_2 is considered as one of the major areas that affects its photocatalytic activity.

CO_2 is a thermodynamically stable and chemically inert compound having a closed-shell electronic configuration, linear geometry and $D_{\infty h}$ symmetry, which is difficult to be oxidised or reduced to various chemicals and fuels at a lower temperature (Indrakanti *et al.,* 2009; Freund and Roberts, 1996).

The addition of an electron from an electron donor to CO_2 modifies the symmetry, thereby creating a bending of the molecular structure as a result of repulsion between the newly obtained electron located on the electrophilic carbon atom and the free electron pairs on the oxygen atoms. These changes contribute to the high energy of the Lowest Unoccupied Molecular Orbital (LUMO) of CO_2 and thus the very low electron affinity of the molecule. The reduction of CO_2 by an electron results to the formation of an anion radical $CO_2^{\bullet-}$, which has a strongly negative electrochemical potential of −1.9 V(Equation 2.1) versus the Normal Hydrogen Electrode (NHE) (Koppenol andRush 1987;

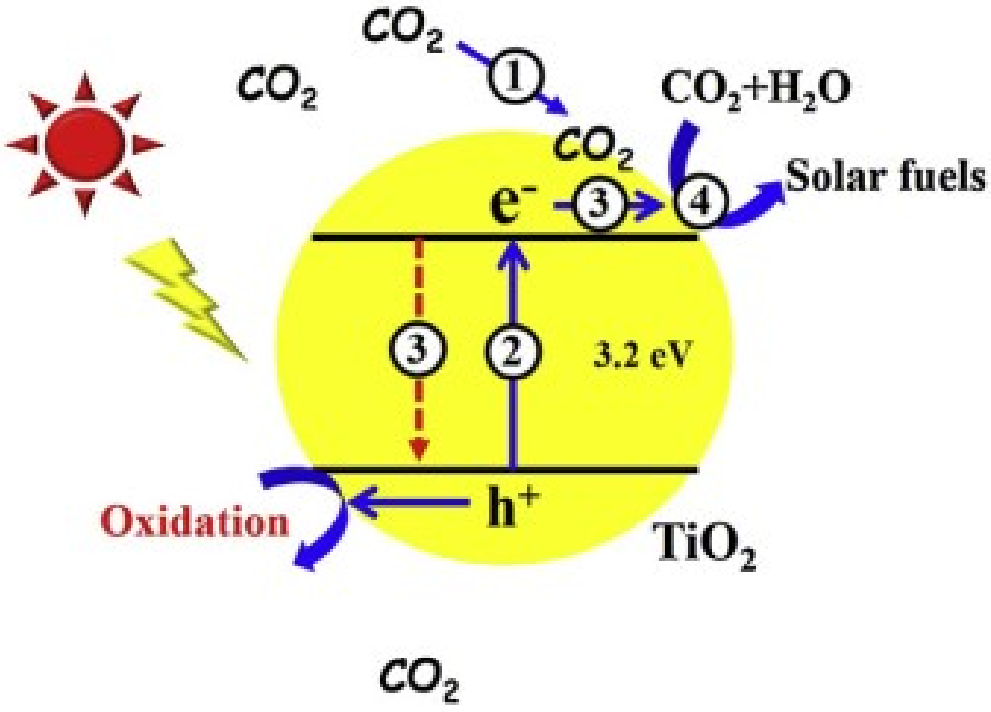

Figure 2.6 Schematic diagram of the mechanism and pathway of photocatalytic CO_2 on the TiO_2 surface. (Low *et al.,* 2017).

Indrakanti *et al.,* 2009).

$$CO_2 + e^- \rightarrow CO_2^{\bullet -} \qquad E^0_{redox} = -1.90\ V \ldots\ldots\ldots\ldots\ldots\ldots (2.1)$$

With this potential value, almost no semiconductor can supply enough potential to transfer a single photogenerated electron to a free CO_2 molecule (Figure 2.7). Therefore, this makes the process highly improbable. Although the transfer of a single electron to CO_2 has a very unfavourable energy balance, the process is better for a proton-assisted transfer of multiple electrons. Table 2.1 shows the list of the electrochemical reduction potentials of CO_2 to various products versus the NHE at pH 7. The reactions require the transfer of required electrons and a corresponding number of protons(Dimitrijevic *et al.,* 2011; Indrakanti *et al.,* 2009). Importantly, the potentials are less negative than the CB of many semiconductors (Figure 2.7), so that it seems that these reactions are feasible. Unfortunately, there is little proof in the literature to provide such concerted multi-electron transfer processes (Kamat, 2012). In other words, the reaction is likely to proceed through a chain of one-electron steps and that the first electron transfer remains a significant obstacle to the photoreduction of CO_2, and likely constitutes a strongly limiting step (Rasko and Solymosi 1994; Gattrell *et al.,* 2006). Hence, it is crucial to understand the initial CO_2 absorption and activation mechanism so that effective semiconductors could be devised to promote CO_2 reduction efficiency (Morris *et al.,* 2009; Tanaka and Ooyama, 2002). This has led to the construction of five models for CO_2 absorption, and these different absorption models determine the different adsorption energy of the system (Figure 2.8) (Liu *et al.,* 2012a).

The first one is that the CO_2 molecule is linearly adsorbed on the surface via the O_a atom as shown in Figure 2.8a. The second is that the CO_2 molecule is adsorbed via the C atom to generate a monodentate carbonate species as shown in Figure 2.8b. The third is the generation of a bidentate carbonate species through the interaction of a CO_2 molecule with the surface via both the O_a and C atom as shown in Figure 2.8c. The fourth is theformation of a bridged carbonate geometry with the C atom of CO_2 pointing downward and two O atoms of CO_2 binding with two metal atoms to form a C···O bond with the O atom on the surface as shown in Figure 2.8d. In the fifth, a bridgingconfiguration with

theC atom of CO_2 pointing upward and two O atoms of CO_2 binding with two metal atoms is

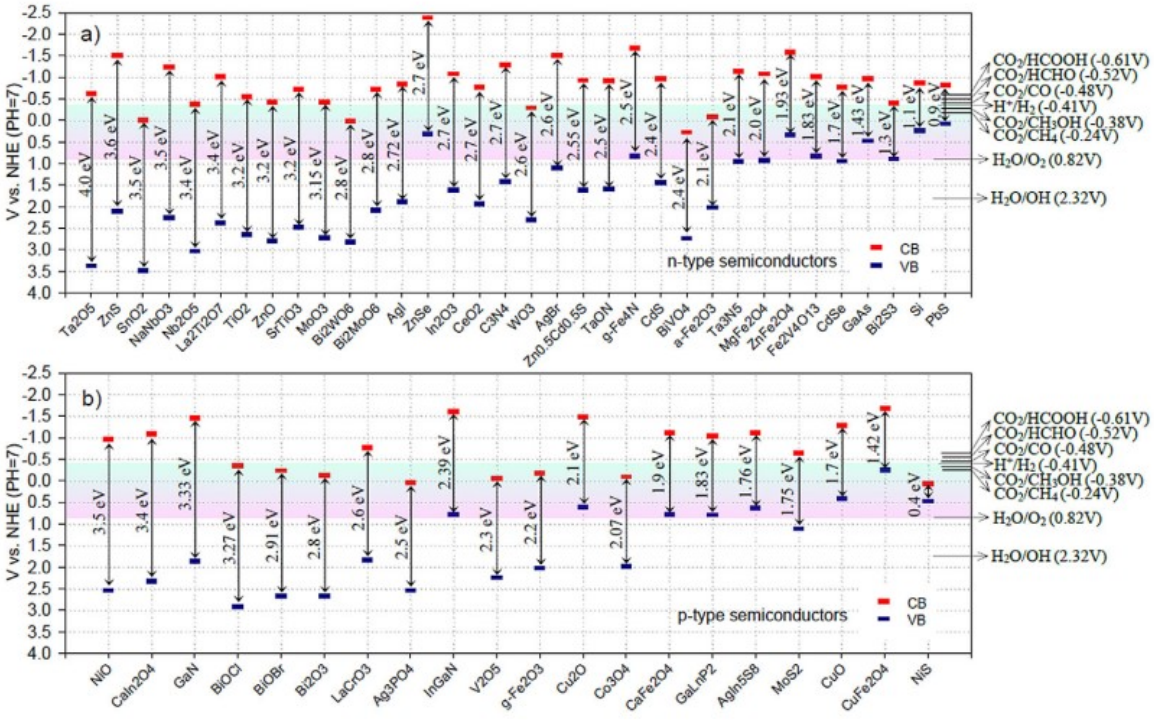

Figure 2.7 Conduction band, valence band potentials, and band gap energies of various semiconductor photocatalysts in relation to the redox potentials of the compound involved in CO_2 reductionat pH 7(Liu *et al.,* 2016).

Table 2.1 The reduction potential (E^0_{redox}) of CO_2 for various products (Liu *et al.,* 2016; Habisreutinger *et al.,* 2013).

Reduction Reaction	E^0_{redox} (V) + NHE
CO_2 (aq) + e^- → $CO_2^{\bullet-}$ (aq)	− 1.9
$CO_2^{\bullet-}$ (aq) + e^- → CO_2^{2-} (aq)	− 1.2
CO_2 (g) + $2H^+$ + $2e^-$ → HCOOH	− 0.52
CO_2 (g) + $2H^+$ + $2e^-$ → HCOOH	− 0.61
CO_2 (g) + $2H^+$ + $2e^-$ → CO + H_2O	− 0.48
CO_2 (g) + H^+ + $2e^-$ → HCO_2^- (aq)	− 0.43
CO_2 (g) + $4H^+$ + $4e^-$ → HCHO (aq) + H_2O	− 0.52
CO_2 (g) + $6H^+$ + $6e^-$ → CH_3OH (g) + H_2O	− 0.38
CO_2 (g) + $8H^+$ + $8e^-$ → CH_4 (g) + $2H_2O$	− 0.24
$2CO_2$ (g) + $8H^+$ + $8e^-$ → CH_3COOH (g) + $2H_2O$	− 0.31
CO_2 (g) + $10H^+$ + $10e^-$ → CH_3CHO (g) + $3H_2O$	− 0.36
$2CO_2$ (g) + $12H^+$ + $12e^-$ → C_2H_5OH (g) + $3H_2O$	− 0.33
$3CO_2$ (g) + $16H^+$ + $16e^-$ → CH_3CH_2CHO (g) + $5H_2O$	− 0.32
$3CO_2$ (g) + $16H^+$ + $16e^-$ → CH_3COCH_3 (g) + $5H_2O$	− 0.31
$3CO_2$ (g) + $18H^+$ + $18e^-$ → C_3H_7OH (g) + $5H_2O$	− 0.31
$3CO_2$ (g) + $18H^+$ + $18e^-$ → $CH_3CH(OH)CH_3$ (g) + $5H_2O$	− 0.30
$2H^+$ + $2e^-$ → H_2	− 0.41

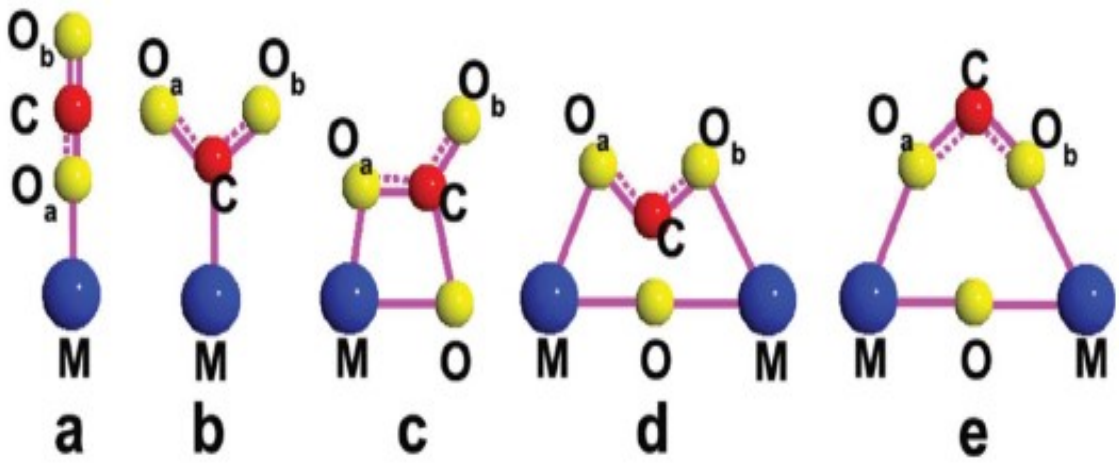

Figure 2.8 Possible configurations of adsorbed CO_2 on the photocatalyst surface (Liu *et al.,* 2012a).

formed (Figure 2.8e). The presence of a M−O−M bond on the surface contributes to the formation of the fourth or the fifth model.

Moreover, the activation or reduction of CO_2 depends on the nature of the reducing agent since CO_2 can only be reduced with the support of reducing agents. H_2O is a preferred reducing agent as compared with other ones such as H_2, S^{2-}, SO_3^{2-}, and amines, due to its richness, availability, non-toxicity, and effectiveness. Photocatalytic reduction of CO_2 with H_2O into hydrocarbon fuels such as CH_4 and CH_3OH is an uphill reaction with a highly positive change in Gibbs free energy: $CO_2 + 2H_2O \rightarrow CH_3OH + 3/2O_2$ ($\Delta G° = 702.2$ kJ mol^{-1}) and $CO_2 + 2H_2O \rightarrow CH_4 + 2O_2$ ($\Delta G° = 818.3$ kJ mol^{-1}). Hence, the input energy is used to overcome these reaction barriers, which is provided by incident light.

Another criterion that affects the activation of CO_2 is the pH of the solution. CO_2 molecule exhibits different geometry at varying pH; the pH also controls the surface charges of semiconductors in solution. The Point of Zero Charge (PZC) of TiO_2 is 6.3. In other words, the TiO_2 surface is more positive when the pH of the solution is below the PZC and more negative when it is above the PZC. The mode of adsorption of CO_2 and the reaction pathway are altered with the change in pH of the solution. For instance, in the alkaline medium, CO_2 exists as HCO_3^- ion, which is adsorbed on the surface of the catalyst to give different adsorption mechanism. At higher pH, CO_3^{2-} is the predominant species at the surface of the semiconductor (Figure 2.9). Since the PZC changes with the semiconductor, the adsorption mode of CO_2 on any particular semiconductor surface also differs. This has led to the formation of different reduction products with an individual semiconductor (Narayanan, 2006).

2.7 TiO_2 and its modification for photocatalytic CO_2 reduction

Among all semiconductors, TiO_2 has been proven as the most suitable, owing to its unique properties, such as high abundance, cost-effectiveness, high crystallinity, suitable optoelectronic property, wide commercial availability and high stability (Kazuhito *et al.,* 2005; Nakata and Fujishima, 2012; Schneider *et al.,* 2014).

In spite of all these qualities, TiO_2 still suffers some challenges such as large band gap and fast recombination of photogenerated charge carriers. The band-gap of TiO_2 (3.0 - 3.2 eV) falls under the UV region, which covers only <5% of the solar spectrum. No absorption is observed in the visible region ($\lambda > 400$ nm) which constitutes the major part

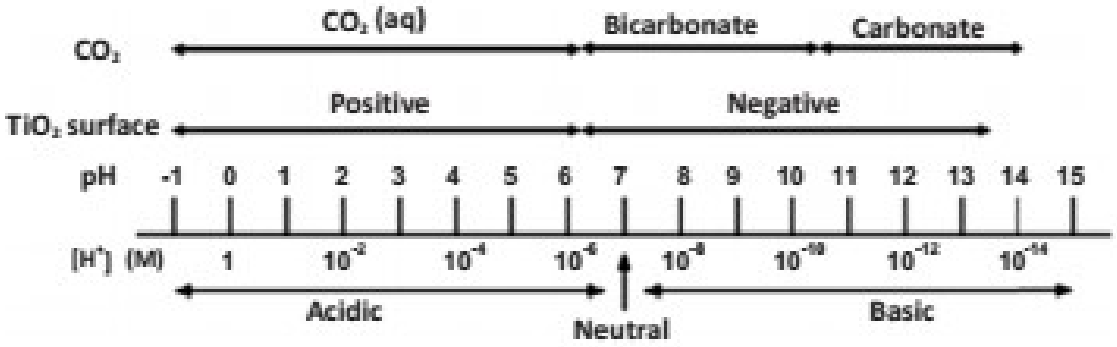

Figure 2.9 CO_2 (speciation) and TiO_2 (surface charge) at different pH.

(43%) of the solar spectrum. The low interfacial charge-transfer rates of photo-generatedcharge carriers and consequently high recombination rate limits TiO_2 efficiency. These challenges directly affect the catalytic efficiency of TiO_2(Tahir and Amin, 2013; Chen *et al.,* 2015; Liu *et al.,* 2012b). Hence, intensive research efforts are being pursued to suitably modify the photophysical properties of TiO_2 and circumvent these shortcomings.

Various researchers have adopted several modification techniques for the modification of TiO_2. These modifications techniques, which include doping, metal deposition, dye sensitisation among others, have been established and applied for the enhancement of the photocatalytic reduction of CO_2 with TiO_2. A schematic diagram of band engineering of $TiO_2$is shown in Figure 2.10.

2.7.1 Doping

As stated earlier, the large band gap (3.2 eV) of TiO_2 has restricted its effective application because only the UV region (5%) of the solar spectrum is required to activate photocatalytic reaction. Therefore, it is crucial to lengthen the absorption range of $TiO_2$from the region of UV to the region of visible light, which accounts for about 43% of sunlight energy (Sher-Shah *et al.,* 2012; Zhang *et al.,* 2016). Doping has been one of the most generally used methods for spreading the light range of TiO_2. Effectively, doping can narrow the band gap of TiO_2 by the introduction ofimpurities into the lattice of TiO_2.The materials that have been studied for the doping of TiO_2 are metals and non-metals (Bou-Orm *et al.,* 2013; Ohno *et al.,* 2004).

2.7.1.1 Metal doping

Over the years, the doping of metal ions into the TiO_2lattice has been demonstrated to be an effective route for hindering e^- - h^+ recombination, thereby enhancing the visible light activity of TiO_2. Several metals such as Ag (Koci *et al.,* 2010), Au (Tahir *et al.,* 2015d), Mg (Bou-Orm *et al.,* 2013), In (Tahir and Amin, 2015a), Ce (Matejova *et al.,* 2014), Cu (Tahir and Amin, 2015b), Sn (Nguyen-Phan *et al.,* 2014) and Co (Sadanandam *et al.,* 2013) have been explored to improve TiO_2 photocatalytic activity and selectivity. The choice of cation or metal ions for doping depends on several criteria (Wonyong *et al.,* 1994; Choi *et al.,* 1994). Such criteria include:

- Ionic radii of dopant should be closer to Ti^{4+}
- Cation should have several oxidation states

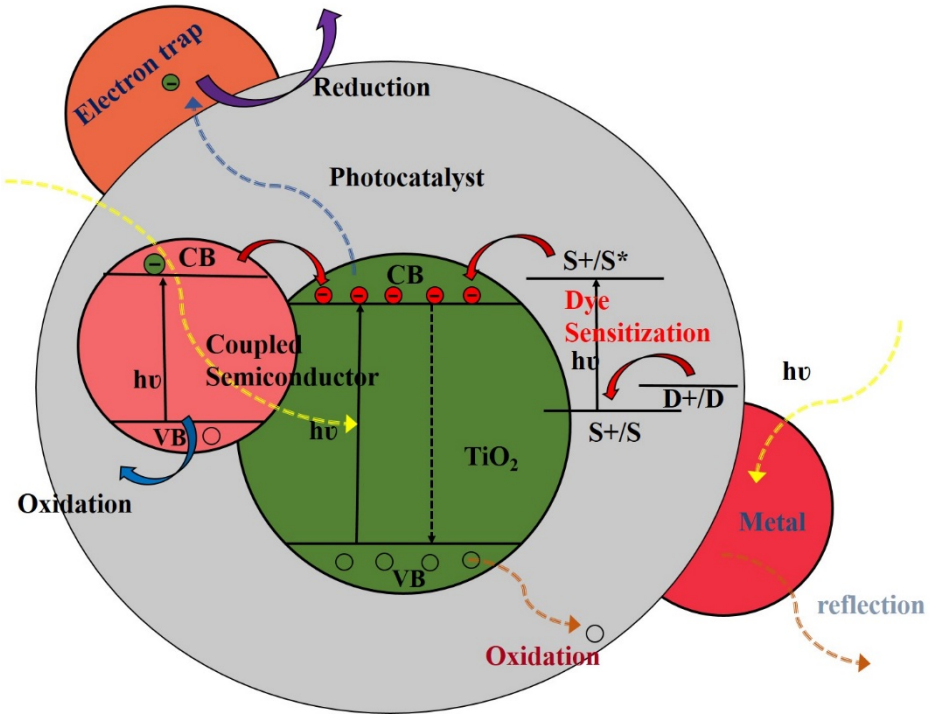

Figure 2.10 Schematic illustration of band engineering of TiO_2. (Liu, Hoivik, *et al.,* 2012).

- Energy levels of $M^{n+}/M^{(n+1)}$ should be nearer to Ti^{3+}/Ti^{4+}
- Electronegativity of dopants should be higher than Ti with incompletely occupied electronic configuration.

According to the structure of the band of TiO_2, the orbitals of O 2p contribute to the filled VB, while the orbitals of Ti 3d, 4s, 4p contribute to the vacant CB. The orbitals of Ti 3d dominate the lower position of CB (Thomas *et al.,* 2007). Upon the doping process, there is introduction of an impurity level in the forbidden band, and this may affect the crystallinity of TiO_2. Doping also results in the production of some defects. For instance, the doping of transition metal can lead to the creation of Ti^{3+} ions, which enhances the photocatalytic activity. The replacement of Ti^{4+} with metal ions in the lattice of TiO_2 introduces an intraband state close to the CB or VB edge.

The significant drawbacks of metal doping are high electron-hole recombination rate due to excessive doping and leaching resulting in photo-corrosion (Litter and Navío, 1996). Overall, these challenges affect the stability and durability of TiO_2.

2.7.1.2 Non-metal doping

Despite the enhancement of photocatalytic activities with the metal doping of TiO_2, the application still suffers some challenges such as photo-corrosion. In recent times, non-metal doping of TiO_2 by substituting the oxygen atoms in the TiO_2 lattice has gained considerable attention. This is because non-metal doped $TiO_2$is more photostablethan metal-doped TiO_2. Non-metal doping regulates the VB structure of the semiconductor, which can enhance the position of VB and lower the band gap of the semiconductor. Theimpurity level created by non-metal dopants may not become the recombination centre of the photogenerated e^-–h^+ pairs (Mao *et al.,* 2013). Some examples of non-metallic elements that have been adopted for the replacement of oxygen in the lattice of TiO_2 are nitrogen (Xu *et al.,* 2007), sulfur (Ohno *et al.,* 2004), fluorine (Di-Valentin and Pacchioni, 2013), iodine (Zhang *et al.,* 2011a) and carbon (Cong *et al.,* 2011).

2.7.1.3 Co-doping

The doping of TiO_2 with metals or non-metals has been approved as an attractive approach to improve the visible light response of TiO_2. On the other hand, TiO_2 response to visible light could be enhanced further using the co-doping approach. Co-doping is

possible with metal/metal, metal/non-metal as well as non-metal/non-metal combinations, which offer a synergistic effect on TiO_2. The coupling of two separate dopants has been adopted to provide a reduced number of carrier recombination centres. It also enhances the visible light absorbance by increasing the solubility limit of dopants (Xu *et al.,* 2008; In *et al.,* 2007; Liu *et al.,* 2008a). Nevertheless, not all dopants are always suitable for this purpose. Therefore, critical factors such as the choice of the pair for co-doping, level of doping and effective method of introducing dopants could affect the photoactivity. Figure 2.11 shows the schematic illustration for the comparison of the band structure of the pure TiO_2, metal-doped TiO_2, and non-metal doped TiO_2.

2.7.2 Metal deposition

An established phenomenon is that the efficiency of TiO_2 for photocatalytic CO_2 reduction is minimal even under the UV–Vis light irradiation (Rankin, 2009; Pathak *et al.,* 2005). The main reason behind this observation is the rapid e^- - h^+ recombination underphotocatalytic CO_2 reduction reaction. Hence, it is crucial to delay this recombination, andthe most widely applied method is the surface modification of TiO_2 via metal loading on its surface (Bazzo and Urakawa 2013; Matejova *et al.,* 2014). So far, several metal Nanoparticles (NPs) have been loaded on the surface of TiO_2. These NPs have been demonstrated to be effective for enhancement of the photocatalytic performance of TiO_2(Koirala *et al.,* 2015; Tseng and Wu, 2004). Some examples of metal nanoparticles used are Au, Pt, Ag and Pd.

The Fermi levels of metal nanoparticles are usuallylower than the TiO_2 conduction band. The loading of these metal nanoparticles on the surface of TiO_2 can lead to the formation of Schottky barrier at the interface between TiO_2 and metal NPs (Figure 2.12) (Rosseler *et al.,* 2010; Chiarello *et al.,* 2010). The photo-induced electrons quickly move from TiO_2 to metal NPs through the Schottky barrier until their Fermi levels are equal (Escobedo *et al.,* 2013; Gallo *et al.,* 2012); whereas, the photogenerated holes remain unaffected on TiO_2. Therefore, the spatial separation of photogenerated electron-hole pairs can be achieved.

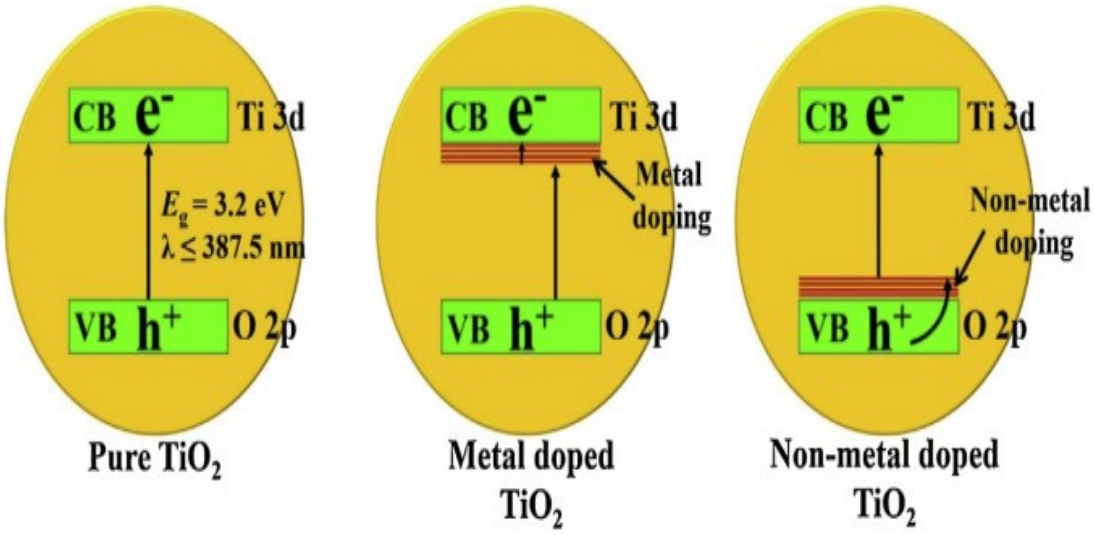

Figure 2.11 Schematic illustration for the comparison of the band structure of the pure TiO_2, metal-doped TiO_2, and non-metal doped TiO_2 (Low *et al.,* 2017).

2.7.3 Alkali modification

Another approach to improving the photocatalytic CO_2 reduction efficiency is by enhanced adsorption of CO_2(Pipornpong *et al.,* 2011). One of the best methods to achieve enhanced adsorption of CO_2 is the formation of chemisorption through alkali sorbents. Adsorption is possible because CO_2 molecule is an acidic oxide. Hence, the modification of TiO_2 with alkali sorbent affords TiO_2 good adsorption capacity towards CO_2 molecule (Lee *et al.,* 2006; Li *et al.,* 2016). CO_2 chemisorption on alkali sorbent involves CO_2 reaction with the reactive groups on the alkali sorbents. This reaction can lead to the formation of intermediate species such as bidentate carbonate species which is beneficial for speeding up the CO_2 reduction reaction. The modification of TiO_2 by alkali does not only enhance the CO_2 adsorption capacity of TiO_2 but also activates the CO_2 molecule for CO_2 reduction reaction. Some of the various alkali sorbents used for the modification of $TiO_2$is NaOH(Meng *et al.,* 2014), MgO (Liu *et al.,* 2013), and amine functional group (Liao *et al.,* 2014).

2.7.4 Dye Sensitisation

Dye sensitisation involves inducement of photo-excited dyes in a way to increase the absorption of TiO_2 in the visible light region (Malato *et al.,* 2009). However, the visible light response of TiO_2 can only be achieved if the dye is adsorbed on its surface. Since the energy level of the dye molecule is more negative than the semiconductor, the electrons are transferred from the dye molecule to the CB of the semiconductor. An ideal dye acting as a photosensitizer must undergo slow backward reactions and fast electron injection to attain high efficiency (Tahir and Amin, 2013; Kumar and Devi, 2011). However, drawbacks such as instability, light and thermal degradation of dye molecules and disposal of undesired intermediates formed during reactions, have been reported (Gupta and Tripathi, 2011). Some of the examples of dyes that have been employed as sensitisers are eosin Y, rhodamine B, porphyrins and phthalocyanine (Yin *et al.,* 2009; Afzal *et al.,* 2013; He *et al.,* 2002; Manbeck and Fujita, 2015).

2.7.5 Carbon-based material loading

As previously mentioned, the loading of metals on TiO_2 has been one of the most commonsynthetic proceduresto improve the performance of photocatalytic reduction of CO_2. However, loading of metals suffer some challenges because they are usually costly

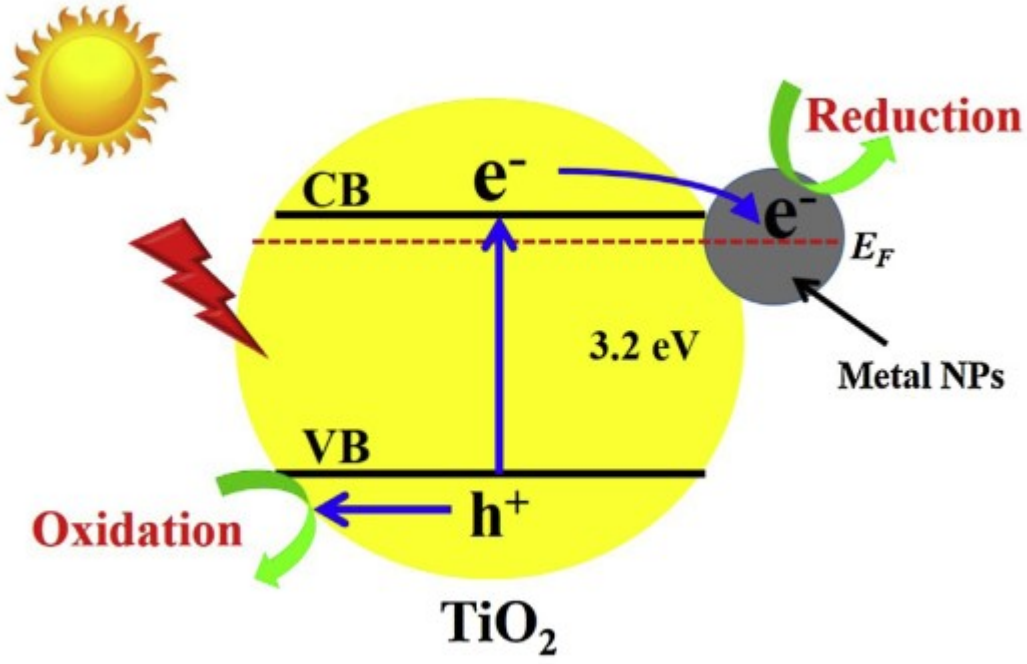

Figure 2.12 Schematic diagramof the mechanism of the photocatalytic reduction of CO_2on metal loading TiO_2 (Low *et al.,* 2017).

and rare, making them unsuitable for wide and large-scale applications (Vasilaki *et al.,* 2015; Qu *et al.,* 2016; Baldissarelli *et al.,* 2015). Therefore, cheaper alternatives to these metals are highly desired. The earth-abundant carbon nanomaterialsare considered to be one of the favorable alternatives for these metal elements due to their unique properties such astunable surface property,high specific surface area and good electron conductivity (Yang *et al.,* 2013; Ran *et al.,* 2014; Leary and Westwood, 2011; Inagaki 2012).Also, these carbon-based materials are abundant, inexpensive and havegood resistance to corrosion for long-term and wide applications (Qi *et al.,* 2016; Lin *et al.,* 2013; Tang *et al.,* 2014). Examples of carbon nanomaterials that have notbeen widely used for enhancement of the photocatalytic CO_2 reduction activity of TiO_2 are Carbon Nanotubes (CNTs) and graphene nanosheets.

2.7.5.1 Carbon nanotubes

Ever since the discovery of CNTs by Iijima in 1991 (Iijima, 1991), CNTs have gainedconsiderable attention from the scientific community with their wide range of applications in areas such asfuel cells,batteries and photocatalysis (Yao *et al.,* 2008; Yu *et al.,* 2005a; Liu *et al.,* 2013). CNTs are known to be favorable candidates as supports and dopants for photocatalysts in place of metal due to their hollow, layered structure, large surface area and high mechanical strength, as well as, unique electron conducting properties and charge transfer (Iijima, 1991; An *et al.,* 2012; Yu *et al.,* 2007; Thostenson *et al.,* 2001).CNTs are also known to offer landing sites for coatings with nanoparticles of various sizes (Yu *et al.,* 2007).

The coupling of CNTs with TiO_2 can provide an advanced nanocomposite with enhanced quantum efficiency. There are three mechanisms that have been proposed to explain the enhancement of the photocatalytic properties of CNT-TiO_2. Firstly, the formation of heterojunction that delays $e^- - h^+$ pairs recombination. Here, under the influence of light, the photogenerated electrons formed on the TiO_2 are transferred from the CB of TiO_2 into the CNTs, and holes remain on the TiO_2 to take part in redox reactions (Woan *et al.,* 2009; Yu *et al.,* 2007; Yu *et al.,* 2008a) A schematic of this mechanism is shown in Figure 2.13a.

Secondly, CNTs act as a sensitiser, creating $e^- - h^+$ pairs when excited by light, therefore generating additional electrons that are easily transported to the CB of

TiO_2(Vijayan *et al.,* 2012). This transfer of electrons allows the formation of superoxide radicals by adsorbed molecular oxygen. As soon as this has occurred, the positively charged nanotubes remove an electron from the VB of the TiO_2 leaving a hole. The present positively charged TiO_2 can then react with adsorbed water to form hydroxyl radicals. The proposed mechanism is provided in Figure 2.13b. Thirdly, CNTs act as impurities by forming Ti−C or Ti−O–Cdefect sites that allow visible light absorption as illustrated in Figure 2.13c (Vijayan *et al.,* 2012; Pyrgiotakis *et al.,* 2011).

2.7.5.2 Reduced graphene oxide

Ever since its discovery (Novoselov *et al.,* 2004), graphene specifically, Reduced Graphene Oxide (RGO), a two-dimensional sp^2-hybridized carbon nanosheet, has attracted immense attention within the scientific community due to its considerable unique properties such as high chemical stability (Geim and Novoselov, 2007), excellent mechanical strength (Thostenson *et al.,* 2001), high thermal conductivity (~5000 W m^{-1} K^{-1}) (Ghosh *et al.,* 2008), theoretically large surface area (~2600 m^2 g^{-1}) (Wang *et al.,* 2005), flexible structure (Lee *et al.,* 2008), tremendous mobility of charge carriers (20,000cm^2 V^{-1} s^{-1}) (Bolotin *et al.,* 2008; Allen *et al.,* 2010), and relatively good optical transparency (Balandin *et al.,* 2008; Liu *et al.,* 2008). These unique properties of RGO make it suitable for application in various fields such as photocatalysis, supercapacitor,solar cell and fuel cell. Aside from the single application of RGO, there have been successful attempts to hybridise RGO with semiconductor nanoparticles such as TiO_2 to form nanocomposites. In particular, the loading of graphene can improve the photocatalytic CO_2 reduction performance of TiO_2 by: (1) promoting the separation of electron-hole pair (2) increasing the specific surface area, (3) improving the adsorption of CO_2via π-π conjugation between CO_2 molecules and graphene, (4) improving the light utilization capacity and (5) activating the CO_2 molecules for reduction reaction (Xiang *et al.,* 2015; Xiong *et al.,* 2016; Cui *et al.,* 2016).

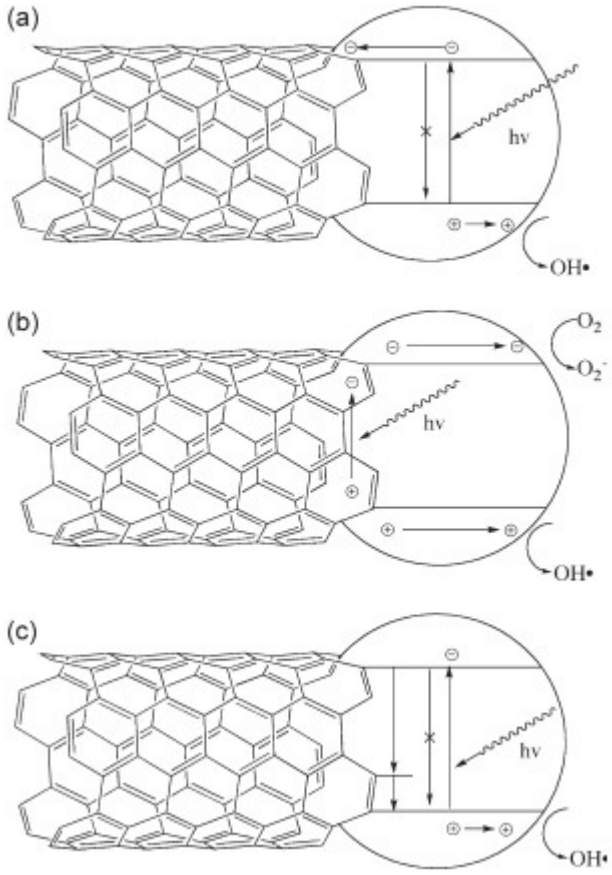

Figure 2.13 The proposed mechanisms for the CNT-mediated enhancement of photocatalysis. (a) CNTs act as an electron sink and scavenge away the electrons hindering recombination. (b) The mechanism proposed by Wang *et al.,*(Wang *et al.,* 2005), where the photon generates an electron-hole pair in the CNT. Based on the relevant positions of the bands, an electron (or the hole) is injected in the titania generatingan O_2^- or an $OH^\bullet$ species. (c) The nanotubes can act as impurity through the Ti–O–C bonds (Woan *et al.,* 2009).

2.8 Review on TiO_2 and Titanium Based Photocatalysts for the reduction of CO_2

The leading approach to photoelectrochemical reduction of CO_2 was reported by Halmann in 1978 over the p-type GaP as a working electrode under a high-pressure Hg lamp. In the experimental setup, $CO_2$was continuously bubbled through a buffer of K_2HPO_4-KH_2PO_4 (aq). The products observed were formic acid, formaldehyde, and methanol after 18 h of illumination (Halmann, 1978). The study was extended by Inoue and co-workers using metal oxide catalysts in CO_2 conversion to carbonaceous fuel. They reduced CO_2 with H_2O to CH_3OH, HCOOH, and HCHO over ZnO, GaP, CdS and SiC semiconductors using Xenon (Xe) and mercury (Hg) lamp (Inoue *et al.,* 1979). Since then, various other photocatalytic systems that employ heterogeneous photocatalysts have been studied. Although there remain many problems, such as the low activity of catalysts and low selectivity of the products, further development of photocatalysts is an essential target.

In 1987, Thampi and co-workers discovered CO_2 hydrogenation to methane (5.18 μmol h^{-1} at 46 °C) over Ru loaded TiO_2 under UV illumination in the gas phase (Thampi *et al.,* 1987). Anpo and coworkers published the first report of a successful reduction of CO_2 at isolated or highly dispersed titania under UV irradiation in 1992.The major products formed under UV irradiation of the anchored catalyst at 275 K are CH_4, CH_3OH, and CO (Anpo and Chiba, 1992).

More recently, Anpo's group reported that higher methane yields couldbe obtained with hydrophilic samples, stating that more open pore structures were beneficial for the photocatalytic CO_2 reduction (Ikeue *et al.,* 2001). Additionally, the selectivity towards the formation of methane was reported to be promoted upon incorporation of noble metal co-catalystssuch as platinum or palladium (Mori *et al.,* 2012). Akhter and co-workerssynthesised TiO_2 nanoparticles and mesoporous TiO_2 using a KIT-6 template and used for CO_2 photoreduction under UV light in the presence of water as the reductant. They observed that TiO_2 nanoparticles produced higher syngas while mesoporous TiO_2 gave more hydrocarbons as well as syngas due to better reaction kinetics, the high surface area, and different morphology. They showed that UV light source, UV intensity, H_2O/CO_2 ratios and catalyst shapes were the main factors that influenced the performance of the catalysts, and these parameters were optimised to increase the fuel products (Akhter

et al., 2015). Li and colleagues synthesised an anatase−rutile nanocomposite using a hydrothermal method followed by calcination at 500 °C. They observed that the prepared mixed-phase nanocomposite had higher photoactivity than Degussa P25 in the reductionof CO_2 to CH_3OH and CH_4 due to the formation of surface phase junction (Li *et al.,* 2008). Besides its role in generating and separating electron-hole pairs during photoexcitation, the anatase (1 0 1) facet played a critical role in adsorbing CO_2 and facilitated the electron transfer from the surface of TiO_2 to CO_2(He *et al.,* 2010). Xu and co-workers synthesised an ultrathin anatase TiO_2 nanosheets of thickness of 2 nm. The prepared nanosheet had 95% of exposed (1 0 0) facet. In comparison with TiO_2 cuboids with 53% of exposed (100) facet, they observed that the nanosheet exhibited about five times higher photocatalytic activity in both H_2 production and CO_2 reduction to CH_4 (Xu *et al.,* 2013). The introduction of defects can provide the adsorptive sites for the activation of CO_2, lowering the barriers for the subsequent reduction reactions and change the product distributions of CO_2 conversion (Kong *et al.,* 2011). The role of oxygen vacancies in promoting CO_2 photoreduction on rutile (1 1 0) and anatase (1 0 1 and 0 0 1) TiO_2 surface was studied using density functional theory calculations (Indrakanti *et al.,* 2011). Li and colleagues reported CO_2 dissociation to CO over Cu(I)/TiO_{2-x} as a result of the availability of oxygen vacancies on the surface of the catalysts (Liu *et al.,* 2012b). Some more recent work on CO_2 reduction is tabulated in Table 2.2.

Several studies have been done to reduce CO_2 over modified TiO_2 by adopting different strategies. Wang and fellow workers synthesised ordered mesoporous silica SBA-15/TiO_2 composites with different proportions of CeO_2 for the photoreduction of CO_2 with H_2O under simulated solar irradiation. The CeO_2 addition influences the light harvesting properties of TiO_2 toward the visible light region. The improved performance was ascribed to the separation of charge carriers induced by the drift of TiO_2 electrons to CeO_2 (Wang *et al.,* 2013b). Recently, 0.1 mol% Ni-TiO_2 yielded 14 μmol g^{-1} methane after 60 min irradiation (Kwak *et al.,* 2015). Wang and co-workers investigated the sensitisation of TiO_2 catalysts using PbS quantum dots, which led to the size-dependent photocatalytic reduction of CO_2 at frequencies varying from the violet to the orange-red edge of the electromagnetic spectrum ($\lambda \sim 420$ to 610 nm). Under broadband illumination

(UV- NIR), the PbS QDs improved CO_2 photoreduction rates with TiO_2 by a factor of 5 in comparison to unsensitized photocatalysts (Wang *et al.,* 2011a).

Under ultraviolet and visible light illumination, Liang and fellow workers synthesised single-walled CNTs-titania nanosheets (TiNS) composites and non-covalently bound solvent exfoliated graphene -TiNS composites, with low carbon defect densities, for the photoreduction of CO_2 to methane in the presence of water (Liang *et al.,* 2012). Hybrid TiO_2/ZnO exhibited high photocatalytic activity of CO_2reduction to methane due to the creation of p-n heterojunctions and high surface area which provided more reaction active sites (Xi *et al.,* 2011). According to Ozcan and co-workers, $[Ru(bpy)_3]^{2+}$ dye-sensitised TiO_2 films showed efficient activity for photoreduction of CO_2 into CH_4 under visible-light illumination, originating from the transfer of catalytically active electrons from organic dye to TiO_2 (Ozcan *et al.,* 2007a,b).

Woolerton and colleaguesreported that TiO_2 nanoparticles (NPs) modified with a photosensitizer and the CO_2-reducing enzyme CODH I from the anaerobic microbe, *Carboxydothermus hydrogenoformans*, provided an extraordinary catalyst for CO_2 photoreduction. The enzyme bypassed the one-electron radical pathway and instead followed a controlled, two-electron reduction pathway, giving CO (E -0.46 V vs SHE at pH 6) as a clean product (Woolerton *et al.,* 2010). Light-harvesting complexes (LHCII) extracted from spinach were attached to the surface of Rh (0.02%)-doped TiO_2 to develop a hybrid catalyst to enhance the visible light absorption. Photocatalysis of CO_2 in an aqueous suspension of Rh−TiO_2 produced CO, acetaldehyde, and methyl formate in moderate yields, although the LHCII-modified catalyst was considerably better at forming acetaldehyde and methyl formate (Lee *et al.,* 2014). Recently, iodine-doped TiO_2nanosheets with exposed (0 0 1) facets yielded 36.36 and 13.71 μmol g^{-1} of CH_4 and CO, respectively, after 4 h under visible light illumination (He *et al.,* 2016). Other modified TiO_2 catalysts for CO_2 reduction are summarised in Table 2.3.

Table 2.2 Recent work on photocatalytic conversion of CO_2 over TiO_2.

Photocatalyst	Light Source	Reaction phase	Conditions	Main products and highest yield	Comments	Reference
Self-standing Ti-containing mesoporous silica thin films (prepared by solvent evaporation method)	100 W high-pressure Hg lamp (UV light)	Gas phase	CO_2 (36 µmol) and gaseous H_2O (180 µmol) 50 °C temp	CH_4 and CH_3OH were the main products	Ti-containing porous silica thin films having small amounts of surface OH groups show the highest selectivity for CH_3OH formation. Films with hexagonal pores show better results than cubic ones.	(Ikeue *et al.,* 2002)
TiO_2 (prepared by sol-gel or precipitation)	8 W Hg Lamp (254 nm) 1.41 mW cm^{-2}	Liquid phase batch reactor	0.2 M NaOH Pressure was 110 kPa	Methane (9.8 µmol g^{-1}) and methanol (1.2 µmol g^{-1}) were major products. The highest yield was obtained with 14 nm TiO_2 crystallites	Effect of particles size was studied. Optimum particle size was a result of competing effects of specific surface area, charge–carrier dynamics and light absorption efficiency	(Kočí *et al.,* 2009)
TiO_2 (prepared by reverse micelle sol-gel route)	250 W Hg Lamp UV-300-700 nm (77 W)	Liquid phase	0.2 N NaOH	Methane and methanol were a major product with little ethanol over TiO_2 and Hombikat	P-25> $RMTiO_2$> Hombikat product selectivity is determined by the coordination environment of surface Ti ions.	(Rajalakshmi *et al.,* 2012)

TiO_2 (prepared by hydrothermal method using titanium oxalate complex) (C and N were doped and confirmed by SIMS and UV)	UV light (2.5 mW cm^{-2}), Visible light (0.12mW cm^{-2}) 500 W high pressure Xe lamp	Aqueous phase (0.08 M $NaHCO_3$)	0.08 M $NaHCO_3$ (30 mL water)	Methanol (max 0.59035 μmol h^{-1} g^{-1} under UV light) (0.478 μmol h^{-1} g^{-1} under visible light) over anatase-brookite	With the increase in pH TiO_2,changes from anatase to rutile to brookite-anatase Visible light absorption is attributed due to C and N doping. Junction effect between two crystallites enhances activity in the anatase-brookite composite.	(Truong *et al.,* 2012)
TiO_2 (anatase A, rutile R and brookite B) (prepared by hydrolysis and hydrothermal route)	150 W solar simulator from Oriel (90 mW cm^{-2}) 200 - 1000 nm	Gas phase (2 ml min^{-1}. flow rate)	CO_2 + water vapor (2.3 v/v%). Samplewas loaded on glass fibre filter	TiB (He) had the highest CO (18.9 μmol g^{-1}) production. TiA (He) had the highest CH_4 (12.89 μmol g^{-1}) production after 6 h illumination.	Oxygen deficiency created by helium pretreatment. Pretreated surfaces were more active than untreated ones. Reaction underwent different reaction pathways on oxygen-deficient anatase and brookite.	(Liu *et al.,* 2012c)
Ti-MCM-41 With varying Si/Ti ratio (hydrothermal method)	UV-254 nm (9 W) (32 μWcm^{-2})	Liquid phase In water, NaOH, and MEA	0.1 g catalyst in 300 mL 0.2 M solution under UV irradiation at 40 °C	CO and Methane. Maximum methane 62.42 μmol g^{-1} over Ti-MCM-41(50)	Ti−MCM-41(50) > Ti−MCM-41(100) > Ti−MCM-41(200). Quantum efficiency = 9.18% over Ti-MCM-41(50)	(Wu *et al.,* 2014)
TiO_2	300 W	Gas phase	$NaHCO_3$ + HCl	Highest CH_4	Surface heterojunction concept	(Yu *et al.,*

(anatase co-exposed 001 and 101 facets)	simulated solar Xe arc lamp	Distance 10 cm		production rate, obtained for HF4.5, is 1.35 μmol$h^{-1}g^{-1}$	was introduced by DFT calculation. (101) facets act as reduction sites, while (001) facets act as oxidation sites on the anatase.	2014)
Montmorillonite modified TiO_2 nanocomposites - MMT/TiO_2 (prepared by sol-gel route and further dip coated over monolith channel)	UV irradiation (200 W high-pressure Hg lamp)	Continuous monolith photoreactor	Gas phase CO_2/CH_4 feed ratio 1.0. (flow 20 mL min^{-1})	Major product CO (237.5 μmol h^{-1} g^{-1}) over 10%MMT loaded TiO_2 at 100 °C. Other products detected at low concentration are C_2H_6, CH_3OH, C_3H_6,andC_3H_8.	Photoactivity was enhanced due to effective CO_2 and CH_4 adsorption and efficient charges transport over highly dispersed MMT/TiO_2 nanocomposites. Products selectivity over 10 wt.% MMT/TiO_2 was in the order of CO (81%) > C_2H_6 (19%) > CH_3OH (0.19%).	(Tahir, *et al.,* 2015c)
Oxygen-rich TiO_2 (catalyst prepared by peroxo-titania route)	Visible light 15 W bulb (8.5 mW cm^{-2})	Gas phase Distance 5 cm	CO_2 + water vapour Continuous gas flow (5 mL min^{-1}) reactor. The catalystwas coated on glass rods	Methane over O_2-TiO_2 (300) 1.03 μmol g^{-1} after 6 h	Visible light absorption and biphasic heterojunction boost the photoactivity.	(Tan *et al.,* 2016)
Mesoporous TiO_2 nanofibres (1D) (Synthesized by	UV light 6 W (λ = 365 nm)	Gas phase Continuous flow mode	CO_2: the H_2O molar ratio of 7.25 Pressure-2 bar	CO and H_2 were major products with minor methane and	Hierarchical mesoporous 1D morphology yields interconnected nanofibres with	(Reñones *et al.,* 2016)

combined electrospinning and sol-gel route)	Temperature-50 °C	methanol. TiO_2-NF-B (under static Ar flow) max CO 203.91 μmol g^{-1} and H_2 394.84 μmol g^{-1} after 20 h irradiation.	large interfaces similar to grain boundaries favours the fast charge transport and a combination of anatase and rutile reduces the recombination rate and improves the photocatalytic activity.

Table 2.3 CO_2 photoreduction over modified TiO_2.

Photocatalyst	Light Source	Reaction phase	Conditions	Main products and highest yield	Comments	Reference
Cu-loaded TiO_2–SiO_2 mesoporous spheres	Xe-lamp (250–400 nm)	Gas phase	20 mg catalyst; $CO_2$and gaseous water vapour	20 CO μmol g^{-1} h^{-1} using Cu–TiO_2–SiO_2	High CO_2 conversion efficiency was as a result of Cu–TiO_2 nanocrystals distributed on theporous matrix of SiO_2.	(Wang *et al.,* 2011b)
C-doped TiO_2	Simulated daylight bulb	Gas phase	CO_2 + gaseous water vapour	2634 μmol g-^{1} HCOOH under the simulated daylight lamp for 6 h	Improved activity was obtainedas a result ofband edge shift to the region of visible light and the enhancement of charge separation efficiency	(Xue *et al.,* 2011)
Alkali modified-TiO_2	300 W Xe lamp UV light 365 nm	Gas phase	CO_2 (80kPa) + 2 mL water	Optimum NaOH-3% Maximum production of CH_4 (52 μmol g^{-1})andH_2 (112 μmol g^{-1})	Surface modification of TiO_2 with NaOH promoted the chemisorption, activation and photocatalytic CO_2 reduction.	(Meng *et al.,* 2014)
CuO-TiO_2 hollow microsphere (template free	Hg UV lamp (40 W; 254 nm; light intensity at the	Gas phase	CO_2 + water vapour 200 μL water + 10 mg catalyst	Methane was major product 2.8, 14.5 and 2.1 μmol g^{-1} h^{-1} for the production of H_2,	The hollow macroporous core-mesoporous shell nanostructure favours multi-light scattering/reflection, resulting in	(Fang *et al.,* 2015)

hydrolysis followed by hydrothermal method)	location of the catalyst: 20 mW cm^{-2})			CO and CH_4 maximum production over 3%CuO-TiO_2 hollow microsphere	the enhanced harvesting of the exciting light. The large surface area provides a significant number of surface active sites for the reactant adsorption and reaction while the hierarchical nanoarchitecture enables fast mass transport of reactant and product molecules within the porous framework. Further CuO improves activity due to improved electron traps, reduced recombination of photogenerated e^- - h^+, and enhanced photoabsorption.	
ZnPy/TiO_2 (solvothermal treatment followed by calcination)	Visible light 300 W Xe-lamp	Gas phase Catalyst amount (60 mg)	CO_2 and H_2O vapourwere produced from the reaction of $NaHCO_3$ (1.00 g, introduced into the reactor before being sealed) and H_2SO_4 solution	Highest yield with 1%ZnPy/TiO_2 producing 8.07 1.01 µmol g^{-1} h^{-1}CO and 1.01 µmol g^{-1} h^{-1} methane	Anatase - brookite mixture. Molecular structural asymmetry and connection of the carboxyl group produce an oriented electron transfer channel of the excited electrons from ZnPy to TiO_2, which make CO_2 conversion possible under visible light irradiation.	(Li, Lin, *et al.,* 2015)

			(5.0 mL, 4.0 M)			
Black TiO_2−coated Cu nanoparticles (Cu@TiO_2)	Visible light 500 W Xe lamp (0.220 W cm^{-2}) 400 - 800 nm	Gas phase	CO_2 (8kPa)+H_2O vapour $CO_2$was produced via $NaHCO_3$ and H_2SO_4	The maximum product obtained with 4%Cu@TiO_2 0.97 µmol of CO and 0.16 µmol of methane, which are 1.7 times higher than bare black TiO_2	Improved photoactivity is due to the embedded metallic Cu, which promotes the formation of oxygen vacancies in TiO_2. Metallic Cu increases the photoinduced charge-separation of TiO_2	(Zhao *et al.,* 2016)
TiO_2-Cu/C (Sol-gel method)	32 W Hg Lamp 253.7 nm	Liquid Phase	CO_2 (0.3 L min^{-1}) + 0.2 N NaOH (125 mL) at temperature 25 - 27 °C	CO and methane product formed. Maximum production 3.789 µmol g^{-1} h^{-1} of methane and 30.123 µmol g^{-1} h^{-1} of CO at TiO_2-Cu/C	Synergistic effect of the energy state of the –O–Cu–O species and carbon could improve the visible light response, promote the separation of photogenerated charge carriers and provide reactive hole sites on the surface.	(Yan *et al.,* 2016)
$SrTiO_3$/TiO_2loaded Au–Cu Alloy Nanoparticles (anodic oxidation followed by hydrothermal,	UV-Vis illumination (Xe lamp)	Liquid phase	Diluted CO_2 in water and hydrazine hydrate. Diluted (33.33% Ar) CO_2	CO (77 µmol g^{-1} h^{-1}) and total HC (725.4 µmol g^{-1} h^{-1}) produced after 6 h. CH_4 is the main product (421.2 µmol g^{-1} h^{-1})	In-situ FTIR was used for the alloy effect. Catalyst stable up to 5 cycles.	(Kang *et al.,* 2015)

Au/Cu were subsequently loaded by MW assisted solvothermal method)						
Au and In modified TiO_2	200 W Hg lamp (150 mW cm^{-2})	Gas phase (catalyst were coated ceramic monoliths) Batch mode	$CO_2 + H_2$ (CO_2/H_2 - 1.5 optimum feed ratio) pressure was 0.40 bar	8,982 µ mol g^{-1} of CO 99% selectivity over 0.2 wt. % Au-3.5 wt. % In/TiO_2	Monolith photoreactor showed efficient CO_2 reduction to CO through RWGS reaction. Higher photoactivity is due to fast electron transfer and the larger illuminated surface area in monolith channels.	(Tahir *et al.,* 2015d)
Zn-Cu promoted TiO_2 (TiO_2 was prepared by hydrolysis, CuO/TiO_2 prepared by impregnation and CZT was prepared by co-	UVC light (254 nm) 18 W	Liquid phase at 25 °C	CO_2 + water	126–184 µmol g^{-1} methane after 24 h	TiO_2 (P-25) ~TiO_2< 2%CuO/TiO_2< 2%CuO–19%ZnO/TiO_2. TiO_2 was present in anatase and brookite phase. strength and amount of CO_2 adsorption sites have influenced the products	(Paulino *et al.,* 2016)

precipitation deposition method)						
MWCNT/TiO_2 core-shell Nanocomposites (core-shell coating of TiO_2 (shell) on MWCNTs surface.)	Visible light irradiation with 15 W energy saving light bulb	Gas phase	CO_2 + water	The highest methane yield of ca. 0.17 µmol g^{-1} $h^{-1}$was recorded at the 6th hour of irradiation time.	The enhanced photoreactivity of this core-shell nanocomposites were achieved via electron transfer between the TiO_2 shell and the MWCNTs, which inhibited the electron-hole pair recombination and improved the overall efficiency of the photocatalysis.	(Gui *et al.,* 2014)
Carbon nanotubes on Ni/TiO_2 (co-precipitation method)	75 W lamp	Gas phase	CO_2 + water vapour	Maximum CH_4 yield of 0.145 mmol g^{-1} h^{-1} using CNT@Ni/TiO_2 nanocomposites	The high catalytic performance of CNT@Ni/$TiO_2$is attributed to the synergistic combination of CNTs and TiO_2 and improved migration of e^- - h^+ pairs.	(Ong *et al.,* 2013)
Ag-MWCNT@TiO_2core-shell nanocomposites	Visible light Irradiation	Gas phase	CO_2 + water	2 wt% of Ag was found to be the most suitable loading, giving the highest total methane and ethylene	With the presence of MWCNTs and Ag dopants in the Ag MWCNT@TiO_2 nanocomposites, the photoexcited electrons are believed to be transported in a	(Gui *et al.,* 2015)

				formation of ca. 6.34 μmol g^{-1} and 0.68 μmol g^{-1}, respectively	few possible pathways: (i) consumed by the electron scavengers, resulting in photoreduction of CO_2 and reaction intermediates; (ii) transported to the neighbouring MWCNT core and Ag dopants; and (iii) unreacted electrons recombined with the holes in the VB.	
Graphene oxide-doped-oxygen-rich TiO_2 (GO–$OTiO_2$) hybrid heterostructure (wet chemical impregnation technique)	Visible light irradiation (15 W) using energy-saving daylight bulbs	Gas phase	CO_2 + water vapour	A total CH_4 yield of 1.718 μmol g^{-1} after 6 h of reaction	The high photocatalytic performance of 5GO–$OTiO_2$was ascribed to the synergistic effect of (i) the visible-light-responsiveness of O_2–TiO_2 (from oxygen excess defects) and (ii) an improved separation and transfer of photogenerated charge carriers at the intimate interface of GO–$OTiO_2$ heterojunctions.	(Tan *et al.,* 2015b)
Noble metal modified RGO/TiO_2	Visible light irradiation with a	Gas phase	CO_2 + water vapour	A total CH_4 yield of 1.70 μmol g^{-1} was achieved after	The ternary nanostructures exhibited enhanced photocatalytic activities as a	(Tan, *et al.,*2015a)

ternary Nanostructures (solvothermal method)	maximum light intensity of 15 W using an energy-saving daylight bulb			6 h of light irradiation	result of improved utilisation of visible light and efficient electron mobility.transfer in the noble metal-doped GT nanojunctions and interfacial electron transfer in the RGO sheets.	
Boron-doped Graphene (B-GR) Nanosheets coupled with TiO_2 Nanoparticles (vacuum activation and ultrasonic method)	300 W The light source to simulate the solar light was Xe lamp.	Gas phase	CO_2 + water vapour	The P25/B-GR shows the highest photogeneration of CH_4 (2.50 mmol g^{-1})	The photo-excited electrons on CB of TiO_2 are injecting into the B-GR, and the photoexcited holes located on B-GR transfer into the VB of TiO_2 through the Ti-O-C bonds, owing to the p-type property of B-GR. This will ensure the separation of the photoproduced electrons and holes.	(Xing *et al.,* 2014)

2.9 Various methods for the synthesis of TiO_2

Several synthetic procedures have been established for the preparation of TiO_2 nanoparticles. They include hydrothermal, microwave, sonochemical and sol-gel. These methods have brought a different perspective towards the enhancement of TiO_2 for the intended applications.

2.9.1 Sol-gel method

The sol-gel method is a widely and commonly used method for the preparation of ceramic nanomaterial such as metal oxides, nitrides, and carbides (Brinker and Scherer, 1990; Macwan *et al.,* 2011). The method involves the transformation of a sol into a gel. The gel is then subsequently thermally treated to remove the solvents used. Sols are solutions of organic and inorganic precursors (such as metal chloride, metal alkoxides or nitrate) and may also contain dense oxide particles or polymeric substances. The sol of TiO_2 is typically transparent. A sol is defined as a colloidal suspension of solid particles in a liquid. In sol-gel method, the precursor (source or starting material) for preparation of a colloid consists of a metal or metalloid element enclosed by several ligands. In the case of TiO_2, the common precursors are methyl alkoxides (such asas titanium alkoxides), which are members of the family of metal-organic compounds. These precursors giveexcellent, morphological andcompositional control over the product properties, such as nanoparticle size,specific surface area and degree of aggregation. (Gopal *et al.,* 1997; Ramimoghadam *et al.,* 2014; Tian *et al.,* 2002).

2.9.2 Hydrothermal method

Hydrothermal method is an interesting approach to prepare micro- and nanometer-sized crystalline TiO_2 powders. The synthesis, in aqueous solvent usually without surfactants/protecting agents, is typically performed in a steel autoclave vessel under relatively high temperatures and saturated vapour pressure (Laudise, 1970; Albrecht, 1985). These conditions then lead to the agglomeration of TiO_2 crystals.

Most hydrothermal processes are similar to the sol-gel method, in that they do not afford materials with tailored properties such as solubility, uniformity, and processability. Nonetheless, the crystallinity of the particles is usually much improved compared to sol-gel methods. Various factors, such as temperature, pH, presence of “mineralizers” (typically, inorganic compounds), stirring and reaction time are pivotal in controlling not

only the morphology of the crystallites but also the phase (Cheng *et al.,* 1995; Aruna 2000; Cargnello *et al.,* 2014).

2.9.3 Solvothermal method

Solvothermal methods are closely related to hydrothermal except that the primary solvent used is not water, although water is sometimes added to promote hydrolysis. Unlike hydrothermal, a larger variety of surfactants or structure directing agents can be employed in solvothermal methods to drive the shape and morphology of the crystallites. One factor that dramatically influences the shape and size of the formed crystallite is the choice of the solvent. For example, Du and co-workers showed that octahedral titania particles could be obtained in toluene whereas spheres were obtained in ethanol following a solvothermal treatment of titanium butoxide in the presence of cetrimonium bromide (Du *et al.,* 2011).

An advantage of the solvothermal over the hydrothermal process is that organic surfactants can be employed, which solubilise the nanocrystals in nonpolar solvents through the formation of inverse micelles (Kim *et al.,* 2003). Surfactants, in combination with other additives, can also help to control the formation of specific facets in titania (Chen *et al.,* 2011).

2.9.4 Microwave processing

The microwave oven has been a commonly used appliance in most kitchens for the past decades. Its advantages over the traditional method of food preparation are time and energy saving. Though the extensive use of microwaves has been for the preparation of meals, yet it has been employed for the processing of material. The microwave radiation range is found between infrared radiation and radio wavesin the electromagnetic spectrum. The wavelength of the microwave is between 1 mm to 1 m, which is equivalent to frequencies between 0.3 and 300 GHz. Within this range of frequency, there are frequencies used for cellular phones,television satellite andradar. The microwaves used in homes, research and medicines, usually come with two frequencies of 0.915 and 2.45 GHz. Recently, microwave furnaces that allow processing at variable frequencies from 0.9 to 18 GHz have been developed for processing of new material (Thostenson and Chou, 1999; Clark *et al.,* 2000; Haque, 1999).

In recent years, microwave-assisted hydrothermal approaches have received a lot of attention for the synthesis of TiO_2 nanomaterial. This is because of several advantages, such as volumetric heating capability, transferring of energy instead of heat, shorter reaction times and heating of the selective material. The heating starts from the interior of the material body, leading to the formation of small particle-sized TiO_2 of high purity. The sol-gel method has also been combined with microwave treatment for the preparation of TiO_2 nanoparticles of smaller particle sizes and high specific surface area (Froschl *et al.,* 2012; Clark *et al.,* 2000).

2.9.5 Sonochemical processing

Sonochemical or sonochemistry, popularly known for its acoustic cavitation, is an approach which involves the production, growth, and collapse of bubbles in a liquid. The sonochemical approachinvolves the application of powerful ultrasound radiation (20 kHz - 10 MHz) in the synthesis procedure. Over the years, the use of sonochemical process has been adopted for the synthesis of nanophase, crystalline TiO_2 and the research is still ongoing. The sonochemicalprocess offers some advantages such as better dispersion of the nanoparticles, a marginally higher surface area, better thermal stability and phase purity. Additional advantages of the use of the sonochemical approach are: control of mineral growth, influence on minerals size distribution, assist for morphological control, elimination of impurities in the mineral, improvement in solid-liquid separation performance, and elimination of the need to add seed minerals (Froschl *et al.,* 2012; Gedanken, 2004; Suslick *et al.,* 1995; Mason, 2007).

CHAPTER THREE
MATERIALS AND METHODS

This chapter describes the materials, characterisation and experimental procedures used in this work.

3.1 Materials

3.1.1 Chemicals used

Titaniumbutoxide ($Ti(OBu)_4$, 97%), graphite powder, sodium nitrate ($NaNO_3$, ≥99%) and potassium permanganate ($KMnO_4$, 98.5%) from Aldrich; methanol (CH_3OH, 99.8%), triethanolamine (TEOA, 97%), hydrochloric acid (HCl, 37%) and N,N-dimethyl formamide (DMF, 99.5%) from Merck; ethanol (C_2H_5OH, 99.99%), hydrogen peroxide (H_2O_2, 50%) and HPLC grade water (H_2O) from Fischer Chemicals; nitric acid (HNO_3, 72.0%) from Ranbaxy Fine Chemical Limited; acetonitrile (ACN, 99.9%) for HPLC spectroscopy from Sd fine-chemical limited; dimethyl sulphoxide (DMSO, 99%) from BDH laboratory;toluene (C_7H_8, 92.14%), sulfuric acid (H_2SO_4, 98%) and hydrazine monohydrate ($H_4N_2.H_2O$, ≥99%) from Loba Chemie; magnesium nitrate hexahydrate ($Mg(NO_3)_2.6H_2O$) and Carbon Nanotubes (CNTs), with thelength of 10 – 30 μm and the diameter of 8 − 15 nm, from Sisco Laboratories Ltd; and CO_2 (99.9995%) from Sigma were used as chemicals. All chemicals were of analytical grade and used without further purification.

3.1.2 Equipment used forsynthesis

Ultrasonicator, air oven, muffle furnace, ball-milling machine, weighing balance, Teflon-lined stainless steel autoclave, ice water bath, centrifuge machine and distillation assembly.

3.1.3 Equipment used for characterisation

UV–Vis. diffuse reflectance spectrophotometer, X-ray diffractometer, surface area analyser, scanning electron microscope, transmission electron microscope, X-ray photoelectron spectrometer, Raman spectrophotometer, thermal gravimetric analyser and inductively coupled plasma atomic emission spectrometer.

3.1.4 Equipment used for photocatalytic activity

Quartz tube reactor, glass tube reactor, gas chromatograph, UVA pen-ray lamps, visible light lamps, septa, magnetic beads and mechanical stirrer. The schematic diagram of the experimental set up is shown in Figure 3.1.

3.2 Synthesis of mixed phase TiO_2 nanoparticles

3.2.1 Preparation of mixed-phase TiO_2

Titanium dioxide nanoparticles (TiO_2) were prepared via two approaches; sonothermal (S) and sonothermal-hydrothermal (SH) methods. In a typical synthesis procedure, 7.33 g of $Ti(OBu)_4$ was dissolved in 20 mL C_2H_5OH and was slowly added to 30 mL H_2O-C_2H_5OH (2:1 v/v) mixture already placed in anultrasonicator. The temperature of the ultrasonicator was set to 70 °C. The resulting mixture was further allowed to ultrasonicate for 1 h at 70 °C to ensure the complete formation of the gel. The obtained precipitate was separated by centrifugation, washed with H_2O, dried in an oven at 80 °C and then calcined under air at 450 °C for 3 h with a heating rate of 5 °C min^{-1} to obtain TiO_2-S. In the SH method, 7.33 g of $Ti(OBu)_4$ in 20 mL C_2H_5OH was added drop wise under ultrasonication to 60 mL of H_2O-C_2H_5OH mixture (2:1 v/v) at temperature of 70 °C. The mixture was allowed to ultrasonicate for 1 h and was transferred into a 100 mL autoclave, which was made up of Teflon-lined stainless steel. The autoclave was put in a muffle furnace and heated for 12 h at temperature of 180 °C with a ramp rate of 1 °C min^{-1}. After heating, the furnace was slowly cooled down to room temperature. A white precipitate was obtained and the solid part was separated by centrifugation (6000 rpm),washed with water and dried in air oven at 80 °C, followed by calcination under air for 3 h at a temperature of 450 °C with a ramp rate of 5 °C min^{-1} to get the TiO_2-SH.

3.2.2 Characterisation of the mixed-phase TiO_2 nanoparticles

The phase transformation and crystalline structure of TiO_2 nanoparticles were identified by the use of X-ray Diffraction (XRD). The instrument used was Bruker D8 Advance X-ray diffractometer. It was equipped with monochromatic Cu Kα, which irradiated X-ray at a wavelength of 1.5418 Å. The range of irradiation, in the angle of 2θ, was from 20° to 80° with a step size of 0.02° s^{-1}. By applying the Scherrer's equation, the crystalline size of the nanoparticles was estimated. The size was obtained from the full width at half-maximum (FWHM) of the (1 0 1) peak of anatase (Ramacharyulu *et al.,*

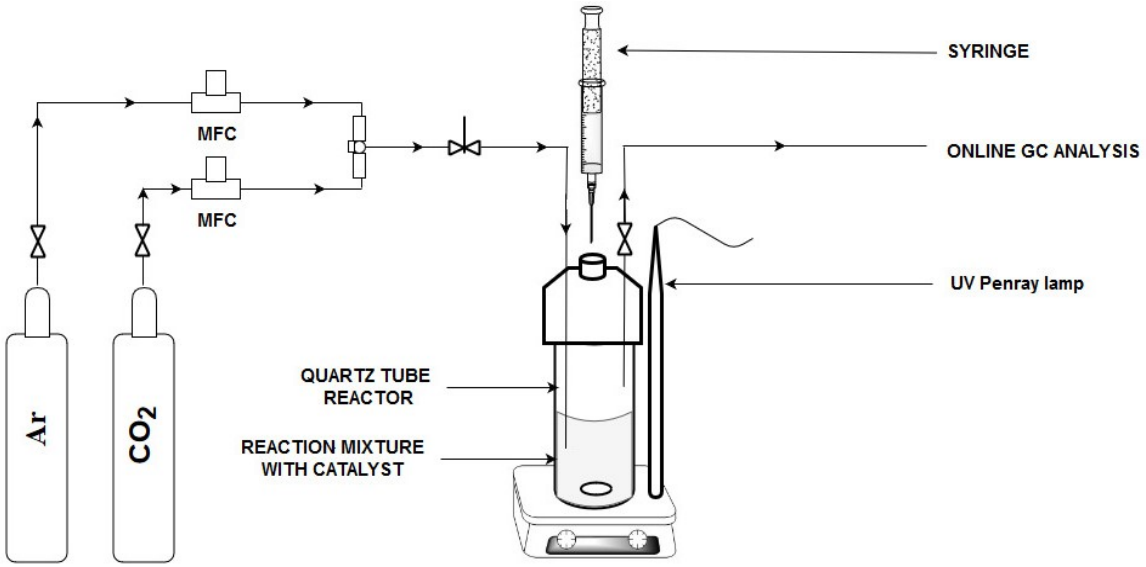

Figure 3.1 Schematic diagram of the experimental setup used for the photocatalytic activity measurements

2014).

$$D = \frac{K\lambda}{\beta \cos\theta} \quad \text{.....3.1}$$

Where λ is the incident radiation wavelength (λ = 1.54056 Å), β is the line width at half-maximum heightand θ is half of the diffraction angle (rad).

Textural characterisation of the nanoparticles was performed using Micromeritics ASAP 2010. The specific surface area of monolayer coverage on the nanoparticles was obtained using the Brunauer–Emmett–Teller (BET) method. The N_2adsorption-desorption properties were examined at -196 °C. The pore size distribution was obtained from the desorption branch of the isotherm using the Barrett–Joyner–Halenda (BJH) method. The total pore volume was taken at the saturation of pores around $P/P_0 = 0.99$.

The UV-Vis. diffuse reflectance spectra were acquired from UV-Vis. spectrophotometer. The spectrophotometer was a product of Shimadzu 2600, which was fitted with an integrated sphere. The range of wavelength is from 200 nm to 800 nm. Barium sulphate was used as the reflecting standard. Values from both absorbance and reflectance were obtained. Values from reflectance were converted into absorbance using the Schuster–Kubelka–Munk equation, $F(R_\infty) = (1 - R_\infty)^2/2R_\infty$, where R_∞ is the diffuse reflectance from a semi-infinite layer. With the assumption of an indirect optical transition, Tauc plot was used to transform the obtained spectra by using the relation $(F(R_\infty)h)^{1/2} \approx (h - \varepsilon_0)$. Where F is the frequency, h is the Planck's constant and ε_0 is the absorption edge energy. Absorption edge and energies of band gap were estimated by extrapolating the decreasing portion of the spectrum to the abscissa at zero absorption (Park *et al.,* 2016; Matejova *et al.,* 2014).

Morphological information on the catalyst particles was investigated by Scanning Electron Microscopy (SEM) and Transmission Electron Microscopy (TEM). The SEM analyses were done on FEI Quanta 200F. It was equipped with Energy-Dispersive X-ray (EDX) spectroscopy. Both TEM and High Resolution (HR)-TEM analyses were performed on JEM-2100 instrument (JEOL, Japan). The resolution was 1.4 Å and the accelerating voltage was 200 kV. The catalyst particles were loaded on the carbon coated copper grid via dispersion in ethyl alcohol using an ultrasonic processor. The elemental mapping in HR-TEM was obtained by the EDX produced by Phoenix using Si (Li) detector with an energetic resolution of 130 eV.

The chemical and elemental composition of the nanoparticles were obtained from X-ray Photoelectron Spectroscopy (XPS). The instrument used was Omicron nanotechnology, Oxford Instrument. It was equipped with a monochromator Aluminum Source (Al kα radiation hν =1486.7 eV).

3.2.3 Density Functional Theory Calculations of mixed-phase TiO_2

This section was performed by a collaborator, Professor Norge Cruz Hernandez of the Department of Applied Physics I, Higher Politics School, University of Seville, Seville, Spain.

The Density Functional Theory (DFT) calculations were performed by using the Vienna *Ab-initio* Simulation Package (VASP) in a periodic framework. These calculations were utilised to establish the electronic and the structural properties of H_2O, CO_2 and CH_3OH deposited on both TiO_2: anatase (1 0 1) and rutile (1 1 0) surfaces(Kresse and Furthmüller, 1996a, b; Kresse and Hafner, 1993, 1994; Kresse and Joubert, 1999; Blöchl, 1994). Projector Augmented Wave (PAW) method (Kresse and Joubert, 1999; Blöchl, 1994) was used to describe the frozen core electrons and their interaction with the valence electrons. The electronic wave function was expanded in-plane waves up to a cut offenergy of 500 eV. A Γ-centred grid of k-points was used for integrations in the reciprocal space, where the smallest allowed spacing between k-points was set at 0.5 $Å^{-1}$ in the Brillouin zone corresponding to the primitive cell. To describe the electron interactions, potentials with the Generalised Gradient Approximation of the Perdew–Burke–Ernzerhof parametrisation form (GGA-PBE) were used (Perdew *et al.,* 1996, 1997). These potentials were corrected by including dispersion interactions proposed by Tkatchenko and Scheffler (Tkatchenko and Scheffler, 2009) as implemented in VASP (Al-Saidi *et al.,* 2012), which is known as PBE-TS. During relaxation, forces on atoms were minimised until they were all smaller than 0.025 eV $Å^{-1}$.

Initially, bulk full geometry optimisationwas performed, including both atom positions and lattice parameters, for anatase and rutile. Both materials were characterised by a tetragonal space group *I4(1)/amd* (Linsebigler *et al.,* 1995) and *P4(2)/mnm* (Meagher and Lager, 1979) for anatase and rutile, respectively. The bulk lattice parameters were *a = 3.786 Å*, c = *9.554 Å*, within 0.4 % of the experimental values (*a = 3.785 Å*, c = *9.514 Å*) (Wyckoff, 1964); and *a = 4.615 Å*, c = *2.950 Å*, within 0.5 % of the experimental values

(*a = 4.593 Å*, c = *2.959 Å*) (Meagher and Lager, 1979) for anatase and rutile, respectively. The surfaces were modeled as a periodically repeated slab inside a supercell, in a similar way used in previous work for anatase (Ortega *et al.,* 2011) and rutile (Sanz *et al.,* 2000; Calzado *et al.,* 2008).

3.2.4 Quantum efficiency calculations

The quantum efficiency of the nanoparticles was obtained by the use of an intensity meter. The intensity meter used was UVP 97-0015-02/UVX digital Ultraviolet radiometer. The radiometer sensor was placed inside the reactor. The intensity of UV light reaching the inside of the reactor was measured to be 0.7 mW cm^{-2}. The measured intensity was used to calculate the quantum efficiency.

3.3 Synthesis of Visible light active RGO-TiO_2 composite

3.3.1 Preparation of Graphene Oxide (GO)

Graphene Oxide (GO) was prepared from graphite powder using a modified Hummer's method (Kumar *et al.,* 2014; Hummers and Offeman, 1958). A beaker of 2000 mL capacity was placed in an ice water bath. The ice water bath was placed on a magnetic stirrer and 450 mL H_2SO_4,12.0 g $NaNO_3$and 10.0 g graphite powder were added in succession, under continuous stirring. The mixture was allowed to stir for 30 min, after which 50.0 g $KMnO_4$ was gently added. Stirring was sustained for further 3 h, followed by gentle addition of 700 mL distilled water. The mixture was then vigorouslystirredovernight at room temperature. This was followed by the addition of 40 mL H_2O_2 (50 wt%). The mixture was stirred for an additional 4 h. A yellow-brown suspension was then obtained. The obtained suspension was washed and centrifuged with 500 mL of 10% HCl. Additional washing was performed by dispersing the suspension in 1000 mL H_2O under vigorous stirring with bath sonication to obtain a single layer sheet of GO. To remove the unexfoliated precipitation, the obtained GO was centrifuged. Finally, a brown dispersion of exfoliated GO was obtained. The dispersion was dried at 80 °C in an oven to obtain solid GO.

3.3.2 Preparation of Reduced Graphene Oxide (RGO)

Reduced Graphene Oxide (RGO) was prepared as follows: 2.0 g of GO was placed in a round bottom flask containing 30 mL C_7H_8. This was followed by the addition of 2 mL H_6N_2O and refluxingfor 12 h at 80 °C. The mixture was allowed to cool to room temperature, centrifuged and dried in the oven at 80 °C. A black RGO powder was obtained.

3.3.3 Preparation of RGO-TiO_2nanocomposites

The RGO-TiO_2 nanocomposites were synthesised by sonothermal-hydrothermal method. A 100 mL beaker containing 30 mL H_2O: C_2H_5OH solution (2:1 v/v) was placed in a sonicator. A 10.0 mg sample of the obtained RGO was added and the mixture was sonicated at 70 °C for 15 min to obtain a homogenised suspension.A solution of 10.0 g Ti $(OBu)_4$ dissolved in 30 mL C_2H_5OH was preparedand added dropwise to the RGO suspension. This was followed by the addition of few drops of HNO_3. The sonication of the mixture was continued for additional 45 min at 70 °C. The sonicated mixture was later transferred into a 100 mL autoclave. The autoclave was sealed and heated for 12 hat a temperature of 180 °C, and then cooled down to room temperature. After hydrothermal treatment, a dark-grey precipitate was obtained and the solid part was separated by centrifugation at 6000 rpm. The solid precipitate was then dried in an air oven for 12 h at80 °C. To finally get 1%RGO-TiO_2 (w/w ratio), code-named 1.0RGO-TiO_2, the collected sample was ground, transferred into an alumina crucible and then calcined in a furnace at 400 °C for 2 h, with a heating rate of 5 °C min^{-1}. Other mass ratios including 2, 5 and 10 wt% were synthesised to obtain 2.0RGO-TiO_2, 5.0RGO-TiO_2 and 10.0RGO-TiO_2, respectively.Same procedure was used for the synthesis of TiO_2 as a reference except the addition of RGO.

3.3.4 Characterisation of RGO-TiO_2 nanocomposites

The RGO-TiO_2 nanocomposites were characterised by different analytical and spectroscopic techniques as described in section 3.2.2. In addition, the thermal strength of the RGO-TiO_2 nanocomposites was done by thermogravimetric analysis (Perkin Elmer TGA4000):a 10.0 mg sample was positioned in a platinum crucible and heated from

ambient temperature to 450 °C at a rate of 10 °C min^{-1} under air atmosphere. Raman analyses of the nanoparticles was performed on STR 500 Airix.

3.3.5 Density Functional Theory Calculationsof RGO-TiO_2 nanocomposites

This section was performed by a collaborator, Professor Alexander V. Voronstov of the Altai State University, Russia.

Graphene infinite nanosheet was shown by a rectangular Graphene Nanosheet (GNS), which is an analogue of RGO having hydrogen passivated zigzag and armchair edges. This GNS had 10 benzene rings along the zigzagedges and six benzene rings in the outer armchair edge. Atomic structure of this $C_{252}H_{44}$ graphene quantum dot after full geometry relaxation is shown in Figure 3.1.

Anatase titanium dioxide nanoparticleswere represented by one of the most stable isomers of anatase decahedral cluster models denoted Ti44r1. This nanoparticle with the molecular formula $(TiO_2)_{121}(H_2O)_6$, contained (0 0 1) and (1 0 1) facets. However, the hydroxyl groups considered were those at the (0 0 1)/ (1 0 1) edges (Vorontsov and Tsybulya 2018c, Vorontsov and Smirniotis 2018a, Vorontsov 2017).

Quantum chemical treatment of the models included complete geometry optimisation of the GNS and GNS-Ti44r1 conjugate. It has been found that interaction of a carbon nanoribbon with the Ti44r1 nanoparticle is much more strong on (1 0 1) facet compared to (0 0 1) facet of the TiO_2 anatase nanoparticle. Due to the structural analogy of CNTs and graphene nanosheets, it was reasonable to suppose much stronger interaction of GNS with (1 0 1) facet compared to the (0 0 1) facet. Hence, the only interaction of GNS with a (1 0 1) facet was considered. Dftb+ program was used for all computations (Aradi *et al.,*2007). The scc-dftb method was utilised for obtaining energy (Elstner *et al.,* 1998) with Slater-Koster files tiorg-0-1 (Dolgonos *et al.,* 2010), and mio-1-1 (Elstner *et al.,* 1998). Geometry optimisationwas performeduntil the maximal force component became smaller than 0.05 kcal $(mol\ Å)^{-1}$. Molecular orbitals were plotted using the 0.0005 isovaluesurface of charge density.

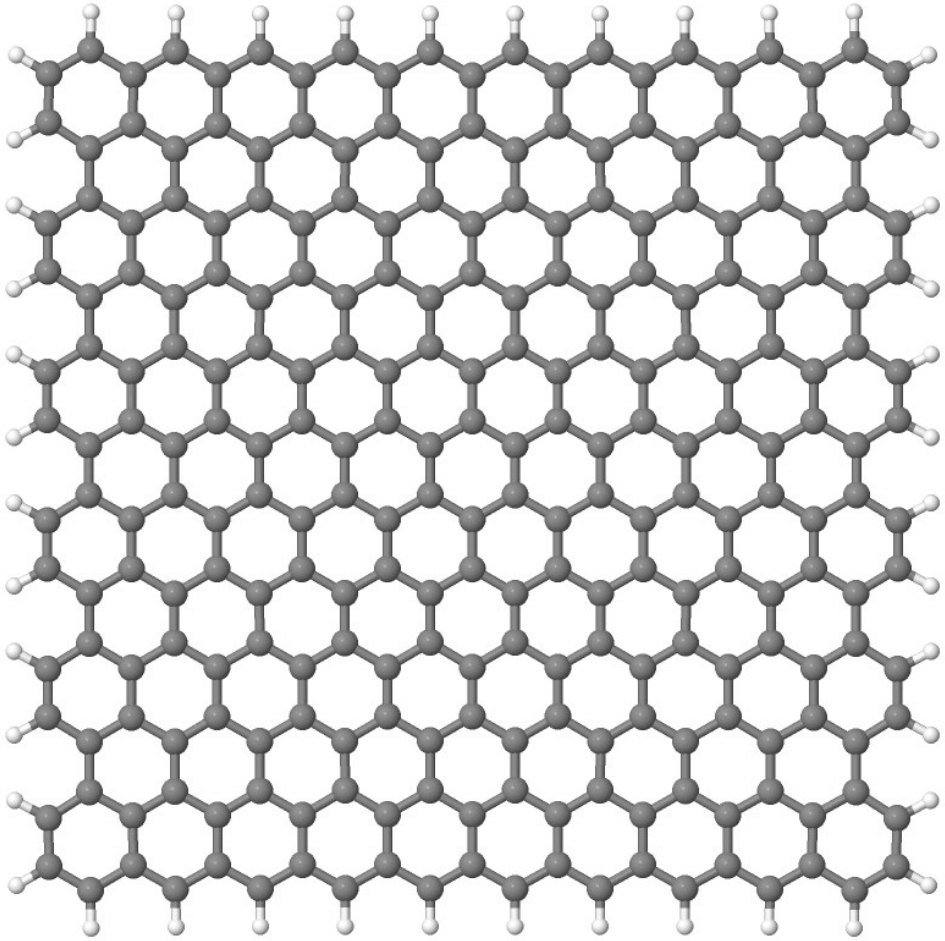

Figure 3.2 Rectangular graphene nanosheet with hydrogen passivated edges used as a graphene model in the present study.

3.4 Synthesis of visible light active carbon nanotubes-TiO_2 composite

3.4.1 Preparation of the CNT-TiO_2 photocatalysts

The CNT-TiO_2nanocomposites were prepared by sonothermal-hydrothermal method. In a typical experiment, 10.0 mg of multi-walled CNTs was added to 30 mL H_2O: C_2H_5OH solution (2:1 v/v) in a 100 mL beaker. A few drops of $HNO_3$was added to the solution and sonicated for 15 min at 70 °C to obtain a homogenised suspension.The addition of HNO_3 helped to activate the CNTs surface by introducing carboxyl (-COOH) and hydroxyl (-OH) groups onit,therebyproviding an improved dispersion of CNTs in the mixture (Omidvar *et al.,* 2012). A solution of 10.0 g Ti $(OBu)_4$ dissolved in 30 mL C_2H_5OH was preparedand added dropwise to the CNTs suspension. This was followed by the addition of few drops of HNO_3. The sonication of the mixture was continued for additional 45 min at 70 °C. The sonicated mixture was later transferred into a 100 mL autoclave. The autoclave was sealed and heated for 12 h at a temperature of 180 °C, and then cooled down to room temperature. After hydrothermal treatment, a dark-grey precipitate was obatined and the solid part was separated by centrifugation at 6000 rpm. The solid precipitate was then dried in an air oven for 12 h at 80 °C. The resulting solid was well ground and calcined at 400 °C for 2 h (with the heating rate of 2 °C min^{-1}) to obtain 1%CNT-TiO_2 (w/w ratio), code-named 1.0CNT-TiO_2. Other mass ratios including 2, 5 and 10 wt% were synthesised to obtain 2.0CNT-TiO_2, 5.0CNT-TiO_2 and 10.0CNT-TiO_2, respectively. A similar procedure was used for the synthesis of pure TiO_2 as a reference except the addition of CNTs.

3.4.2 Characterisation of CNT-TiO_2 nanocomposites

All characterisation procedures are the same as those described in section 3.2.2 and 3.3.4.

3.4.3 Density Functional Theory Calculationsof CNT-TiO_2 nanocomposites

This section was performed by a collaborator, Professor Alexander V. Voronstov of the Altai State University, Russia.

Construction of TiO_2 anatase cluster with their properties, representing a complete anatase nanoparticle, was performed according to an earlier described method (Vorontsov, 2017). In brief, the most stable isomers of anatase decahedral cluster models denoted Ti44r1. The dimensions of the elementary cells of Ti44r1 were 4 x 4 x 1.5in directions a, b

and c, respectively. 12 hydroxyl groups were attached at the four edges between facets (0 0 1) and (1 0 1) of the Ti44r1 cluster in order to ensure the zero charge of the cluster.

A carbon nanotube model, simulating larger multi-walled CNT, was formed by folding a graphene nanosheet containing 308 carbon atoms, which resulted into an object of length about 2.34 nm anddiameter of 0.95 nm. The carbon atoms located at the ends of the carbon nanotube formed armchair edges, which were then passivated by the attachment of hydrogen atoms. All computations were carried out using dftb+ (Aradi *et al.,* 2007) and Gamess(Schmidt *et al.,* 1993) software using tiorg-0-1 (Dolgonos *et al.,* 2010) and mio-1-1 (Elstner *et al.,* 1998) Slater-Koster parameters files.

3.5 Synthesis of Magnesium-doped TiO_2 nanocatalysts

3.5.1 Preparation of the Mg-doped TiO_2photocatalysts

The series of Mg-doped TiO_2 catalysts were synthesised using a modified sonothermal method. Briefly, 8.76 g and 0.11 g of $Ti(OBu)_4$ and $Mg(NO_3)_2.6H_2O$, respectively, were separately dissolved in 50 mL ethanolic solution and then mixed together. The resulting mixture was added dropwise under ultrasonication to 200 mL of ethanol-water (150:50 v/v) mixture at 70 °C. Mg-doped TiO_2 nanoparticles immediately formed from the dropping solution and the resulting reaction mixture was further ultrasonicated at same temperature for 1 h to get Mg-TiO_2-1. A similar method was applied by using 0.21 and 0.42 g of $Mg(NO_3)_3.6H_2O$ to get Mg-TiO_2-2, and Mg-TiO_2-3, respectively. The Mg-TiO_2 catalysts were separated by centrifugation, washed thoroughly with water and calcined under air for 4 hat a temperatureof 400 °C, with a heating ramp rate of 1 °C min^{-1}. Pure TiO_2 sample was also prepared for catalytic comparison using the same procedure without the addition of $Mg(NO_3)_3.6H_2O$.

3.5.2 Characterisation of Mg-doped TiO_2photocatalysts

The actual amount of Mg-doped in Mg-TiO_2 samples was analysed by inductively coupled plasma atomic emission spectroscopy from M/s Leeman Labs Inc, USA equipped with DRE PS 3000UV (simultaneous plus sequential system) Echelle spectrometer. The various samples were mixed with HNO_3 for the digestion of Mg followed by the addition of deionised HPLC grade water. All other characterisation procedures were the same as those mentioned in section 3.2.2.

3.5.3 Computational modelling details of Mg-TiO_2 nanocatalysts

This section was performed by a collaborator, Professor Alexander V. Voronstov of the Altai State University, Russia.

Quantum chemical computations were carried out using the Molecular Orbital Package (MOPAC2016) software. Methods pm6-d3 and pm6 (Stewart, 2007) were used for obtaining enthalpy of formation of Mg-doped TiO_2 nanoparticles while method pm6-d3 which implement Grimme dispersion correction (Grimme *et al.,* 2010) was used to investigate the interaction of the CO_2 with photocatalyst nanoparticles. Decahedral TiO_2 anatase nanoparticle, designated as Ti44r1, was used for doping and CO_2 interaction studies. Using scc-dftb method, it was found that photogenerated holes were located on oxygen atoms at the corners between four adjacent (1 0 1) facets, while photogenerated electrons were distributed among Ti atoms around edges between adjacent (1 0 1) facets away from (0 0 1) facets.

Doping of the Ti44r1 nanoparticle was performed by substitution of a surface Ti atom with the Mg atom and removal of an adjacent oxygen atom to preserve charge neutrality according to the following equation.

$(TiO_2)_{121}(H_2O)_6 + Mg = (MgO)(TiO_2)_{120}(H_2O)_6 + TiO$…….3.2.

Interaction of CO_2 molecule with doped Ti44r1 cluster was studied by placing CO_2 molecule at the oxygen vacancy formed during doping and full optimisation of the structure. The heat of adsorption was calculated by subtracting the enthalpy of formation of CO_2 and Mg/Ti44r1 from the enthalpy of formation of CO_2-Mg/Ti44r1 adsorption complex.

3.6 Photocatalytic CO_2 reduction

The photocatalytic reduction of CO_2 was performed in a closed gas-recirculation reaction setup. The reaction setup was equipped with a 50 cm^3 quartz reactor,gas sampling port,gas inlet, gas outlet andliquid sampling facility. A 5 mg catalyst was addedto 20 mL solution of ACN: water: TEOA (16: 2: 2 v/v), in the photoreduction of the mixed phase TiO_2, RGO-TiO_2 and CNT-TiO_2 catalysts; and ACN: water (16: 4 v/v) in the photoreduction of Mg-TiO_2 nanocatalysts. Each mixture was placed in the ultrasonicator for 10 min to obtain a homogeneous dispersion. The vacuum pump was used to evacuate dissolved gases in the reaction mixture. The mixture was then purged with nitrogen to

remove the remaining dissolved gases. This was followed by the purging of the mixture with CO_2 purging for 30 min to obtain CO_2saturated reaction mixture. The photocatalytic system was irradiated by UVA lamp (Cole-Parmer,PEN-RAY lamp, 8 W,350 nm, 2.13",and 120 μW cm^{-2}) or visible light lamp (20 W white cold LED lamp, 400 - 800 nm Siska LED, 20 mW cm^{-2})to drive the reaction. Small aliquots of liquid/gas sample were withdrawn at a regular time interval.The progress of the reaction was analysed by gas chromatograph(Perkin Elmer Clarus 680) equipped with Flame Ionization Detector (FID) and Thermal Conductivity Detector (TCD) detector, plot-Q and shincarbon columns. Quantification of the production yield was based on calibration curves. The experimentswere performed three times, and a maximum of ca. ±5 % error was observed. The error bars were included in the experimental results.

CHAPTER FOUR

RESULTS AND DISCUSSION

4.1 Synthesis of mixed phase TiO_2 for the photoreduction of CO_2

The mixed phase TiO_2 nanoparticles (NPs), which are TiO_2-S and TiO_2-SH, were prepared according to the method described in Section 3.2.2. Both obtained nanoparticles were white in colour. TiO_2-S and TiO_2-SH were characterisedusing techniques such as X-ray Diffraction (XRD), surface area, Ultraviolet-Visible Diffuse Reflectance Spectroscopy (UV-Vis. DRS), Scanning Electron Microscopy (SEM), Transmission Electron Microscope (TEM) and X-ray Photoelectron Spectroscopy (XPS).

4.1.1 X-ray diffraction characterisation of the mixed-phase TiO_2 nanoparticles

The XRD peaks show that both TiO_2-S and TiO_2-SH photocatalysts are crystalline in nature as shown in Figure 4.1. They both have predominant anatase phase as against rutile – TiO_2-S has 13.7 % rutile, and TiO_2-SH has 8.4 % rutile. The peaks noticed at 25.2°, 37.9°, 47.8°, 54.3°, 55.1° and 62.7° in all the samples were consistent with (1 0 1), (0 0 4), (2 0 0), (1 0 5), (2 1 1) and (2 0 4) planes of tetragonal anatase TiO_2 (Joint Committee on Powder Diffraction Standards (JCPDS) 21-1272). A weak diffraction peak (2θ =27.4°) in both TiO_2 corresponds to the rutile phase (JCPDS 76-1940). It is worthy to note that these synthetic methods afforded the co-existence of anatase-rutile phases below the most reported phase transition temperature (Farhadian and Bagheri-Mohagheghi, 2013). The calculated average crystal size of the predominant anatase phase (1 0 1) from XRD for TiO_2-S and TiO_2-SH are 15.4 and 18.1 nm, respectively, as shown in Table 4.1.

4.1.2 Surface area and UV-Vis. diffuse reflectance spectroscopy characterisation of the mixed-phase TiO_2 nanoparticles

The nitrogen adsorption-desorption isotherms of TiO_2-S and TiO_2-SH catalysts, as shown in Figure 4.2, are of type IV, according to the IUPAC classification, and indicate

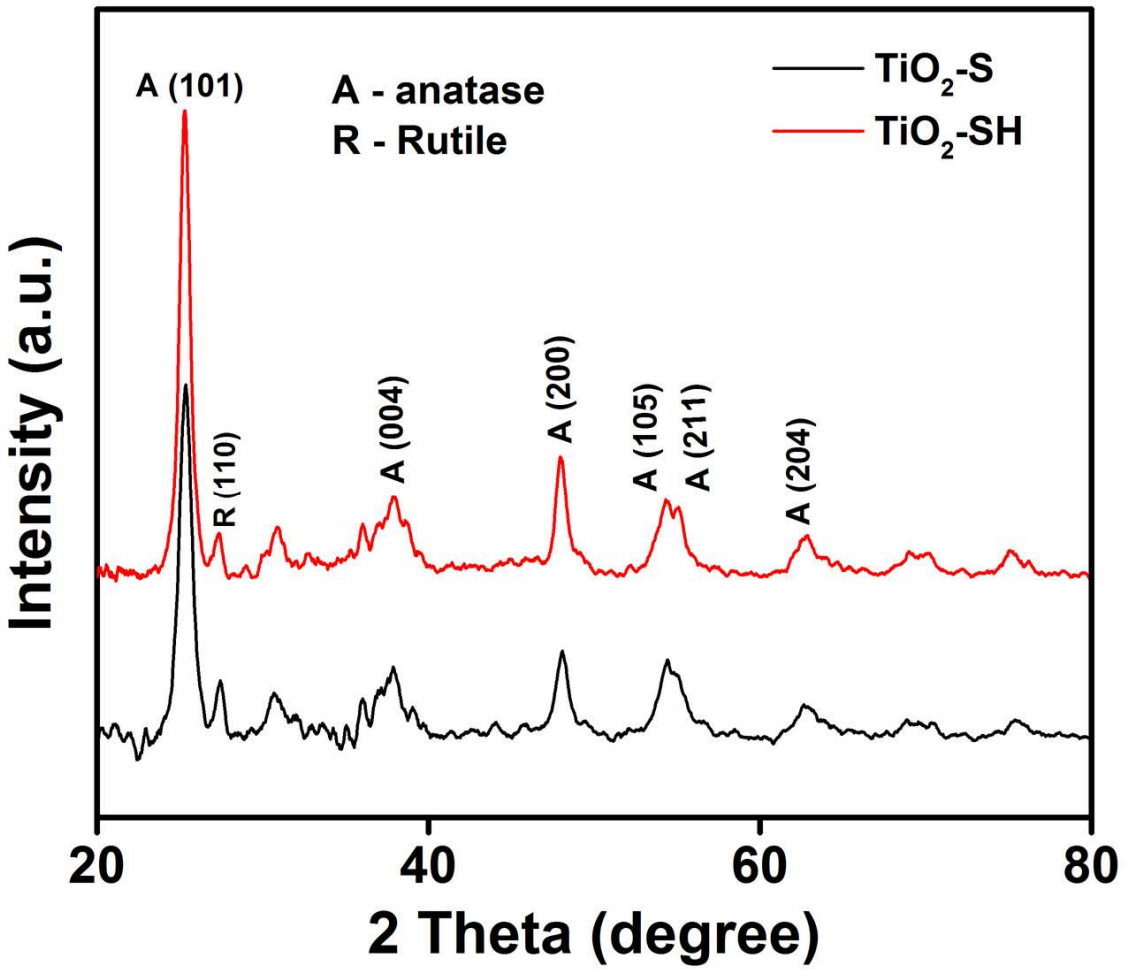

Figure 4.1 X-ray diffraction patterns of the prepared TiO_2-S and TiO_2-SH nanoparticles.

Table 4.1 Phase composition and optical properties of TiO_2-S and TiO_2-SH samples.

Type of catalyst	Crystalline size [nm][a]	Anatase: Rutile	Band gap [eV]
TiO_2-S	15.4	86.27: 13.73	3.05
TiO_2-SH	18.1	91.58: 8.42	3.09

[a]Calculated from XRD and the Debye–Scherrer equation

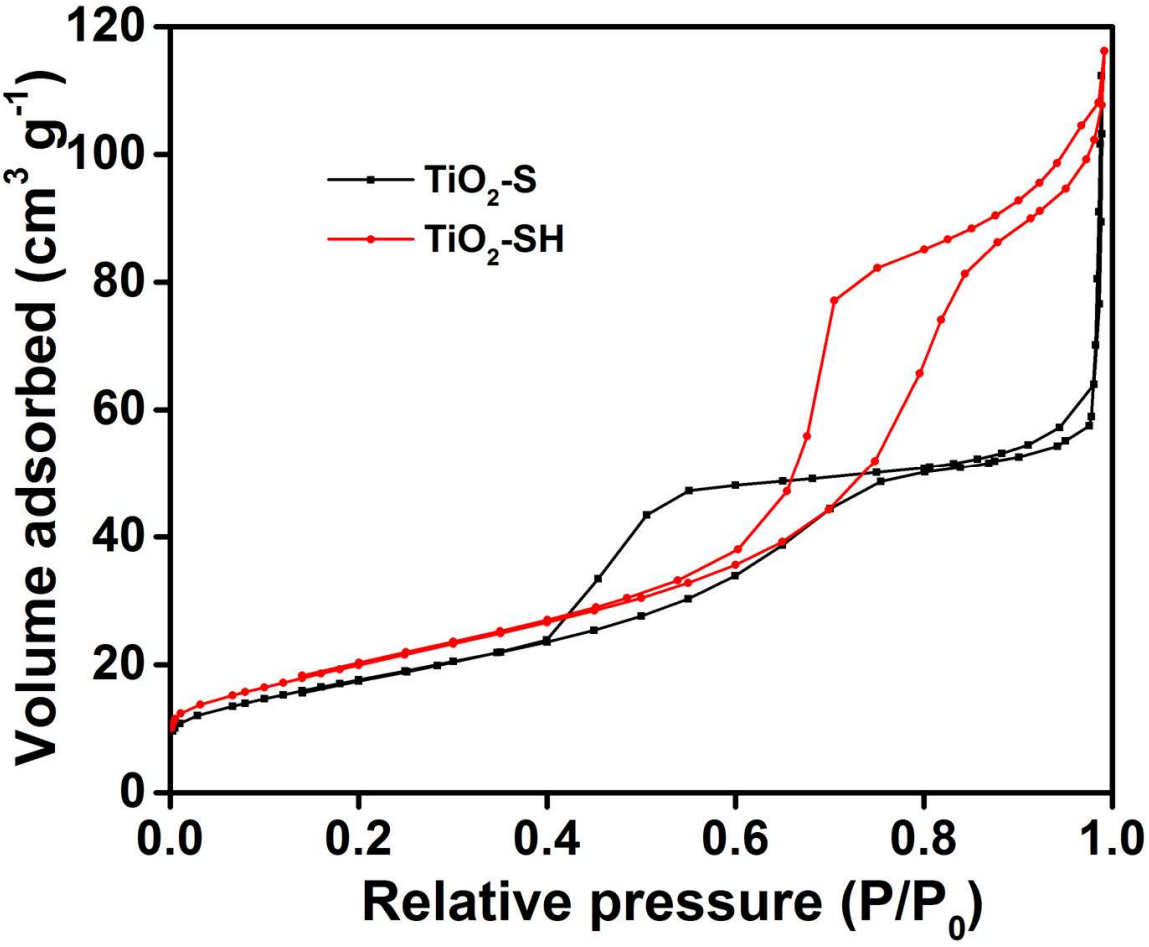

Figure 4.2 N_2adsorption-desorption isotherms of TiO_2-S and TiO_2-SH samples.

the presence of mesopores (Allen, 1997). The isotherms confirmed a bimodal pore size typeof distribution by exhibiting two different hysteresis loops at different P/P_0 range. A steep increasing hysteresis loop at P/P_0 0.99,for TiO_2-S,indicates the presence of macropores. As observed, the hysteresis loop of TiO_2-SH occurred at higher P/P_0 value in comparison with TiO_2-S. This suggests the presence of wider mesopores and fewer macropores in TiO_2-SH. These observations were confirmed by the pore size distribution (PSD) curve and Barrett–Joyner–Halenda (BJH) desorption cumulative pore volume as shown in Figure 4.3 and 4.4, respectively. The PSD curve shows that TiO_2-SH is more homogenous, of higher pore maxima (6.1 nm), contains more mesopores and fewer macropores; while TiO_2-S is less homogenous, of lower pore maxima (3.3 nm) and has slightly fewer mesopores and more macropores. The surface area and pore volume of TiO_2-S and TiO_2-SH are shown in Table 4.2. TiO_2-S has a surface area and pore volume of 64.5 m^2 g^{-1} and 0.17 cm^3 g^{-1} respectively, while TiO_2-SH has 73.1 m^2 g^{-1} and 0.18 cm^3 g^{-1} respectively; indicating that TiO_2-SH has a higher surface area and higher pore volume compared to TiO_2-S. It is worthy to note that broader mesopores and higher surface area are among the factors that determine higher activities towards photocatalytic applications due to easy access of reactant molecules to the active sites in pores (Lowell and Shields, 1991).

The UV–Vis. DRS revealed that TiO_2-S and TiO_2-SH have absorption band edge at 412 and 407 nm respectively, as shown in Figure 4.5. The TiO_2-SH showed a slight blue shift due to less rutile phase and the hyperchromic shift, probably due to the higher surface area. As shown in Figure 4.6, the calculated band gaps of TiO_2-S and TiO_2-SH samples were found to be 3.05 and 3.09 eV respectively, which is typical of the presence of the rutile phase (Wang *et al.,* 2016b).

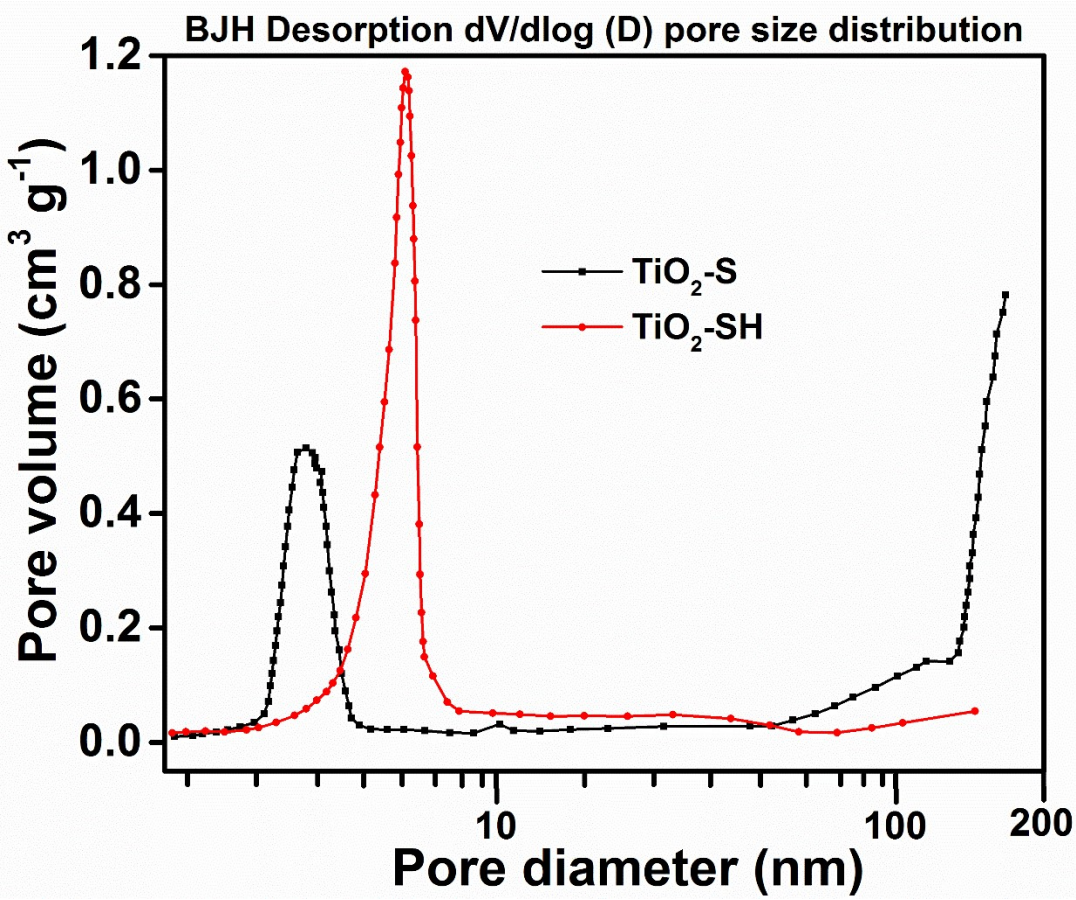

Figure 4.3 Pore size distribution curve of TiO_2-S and TiO_2-SH samples.

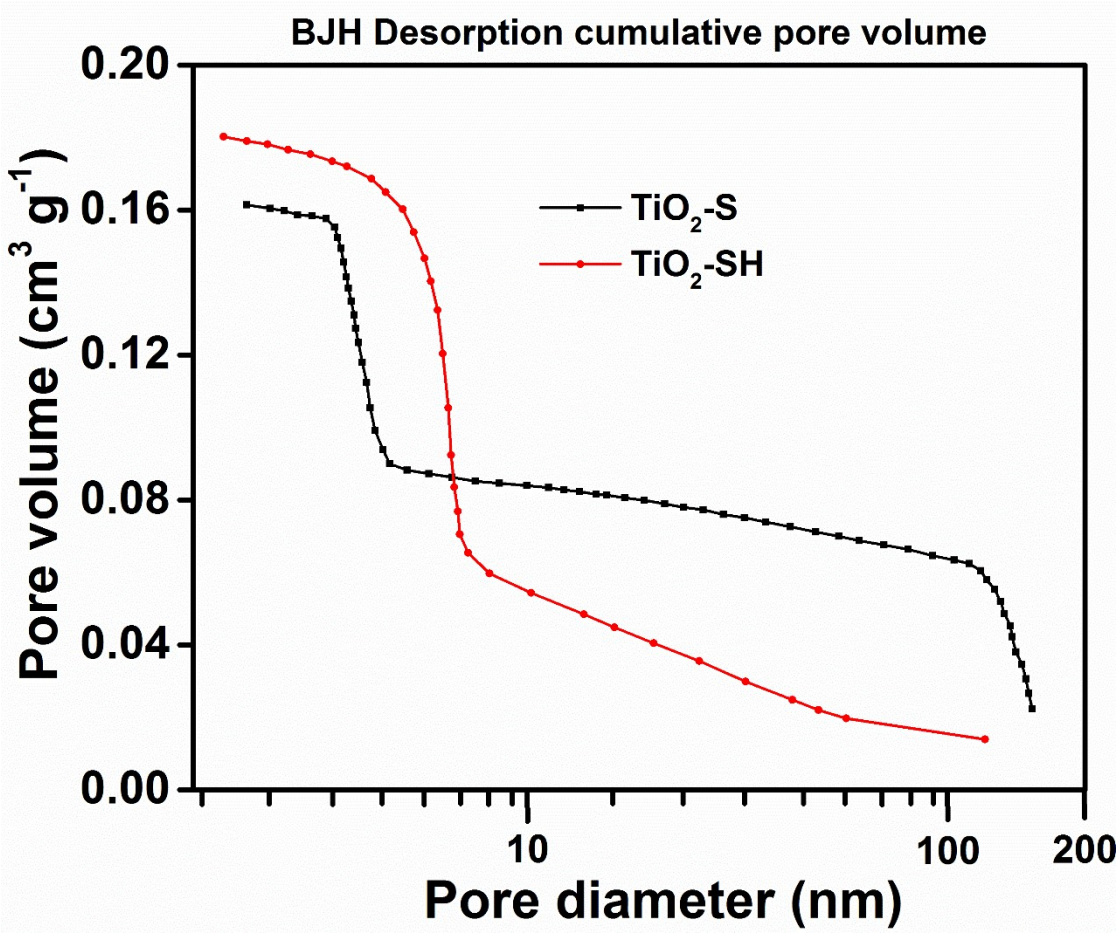

Figure 4.4 Desorption cumulative pore volume curve of TiO_2-S and TiO_2-SH samples.

Table 4.2 Textural properties of TiO_2-S and TiO_2-SH samples.

Type of catalyst	BET Surface area [$m^2\ g^{-1}$]	Pore volume [$cm^3\ g^{-1}$][a]	Average Pore width [nm][a]	Pore Maxima [nm][a]
TiO_2-S	64.5	0.17	6.8	3.3
TiO_2-SH	73.1	0.18	7.4	6.1

[a]Values are taken from BJH desorption branch.

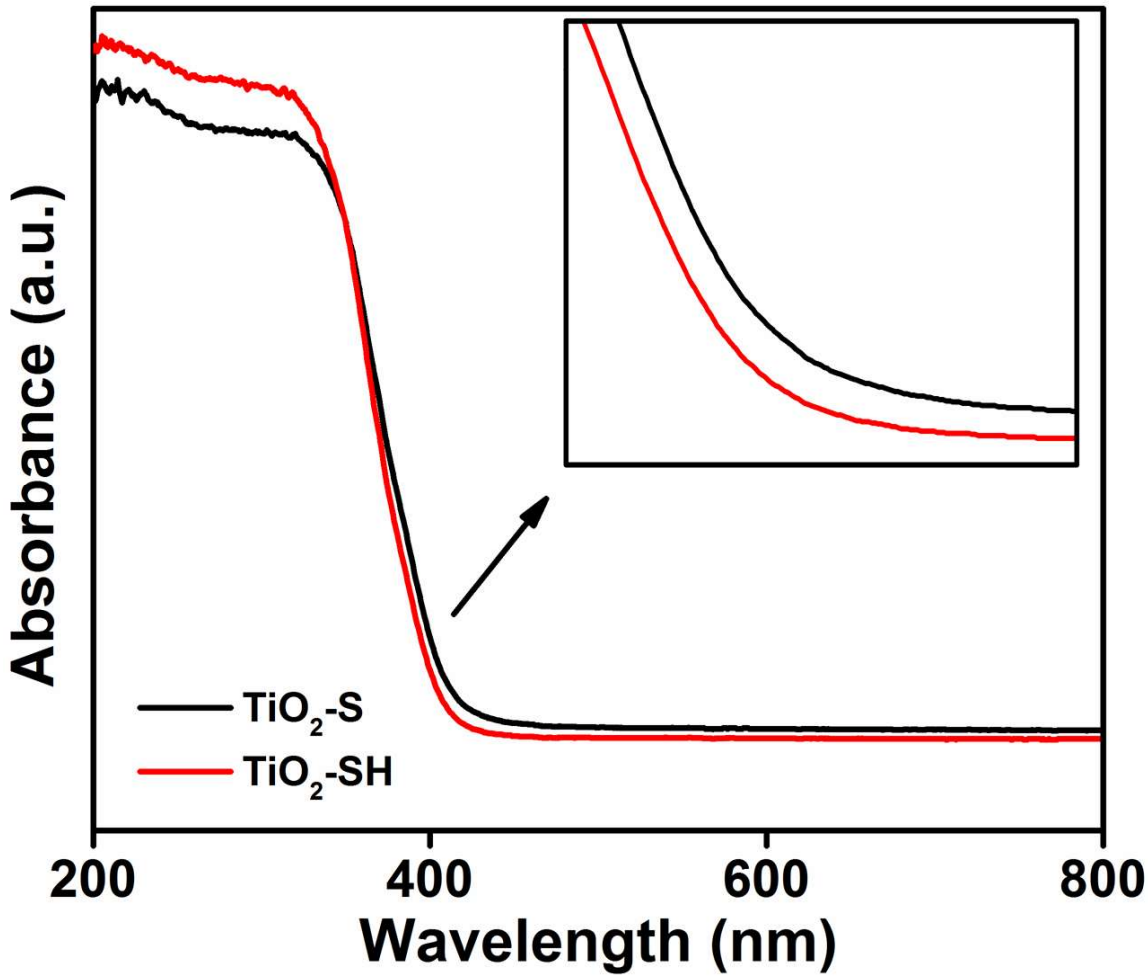

Figure 4.5 UV-Vis. spectra of TiO_2-S and TiO_2-SH samples.

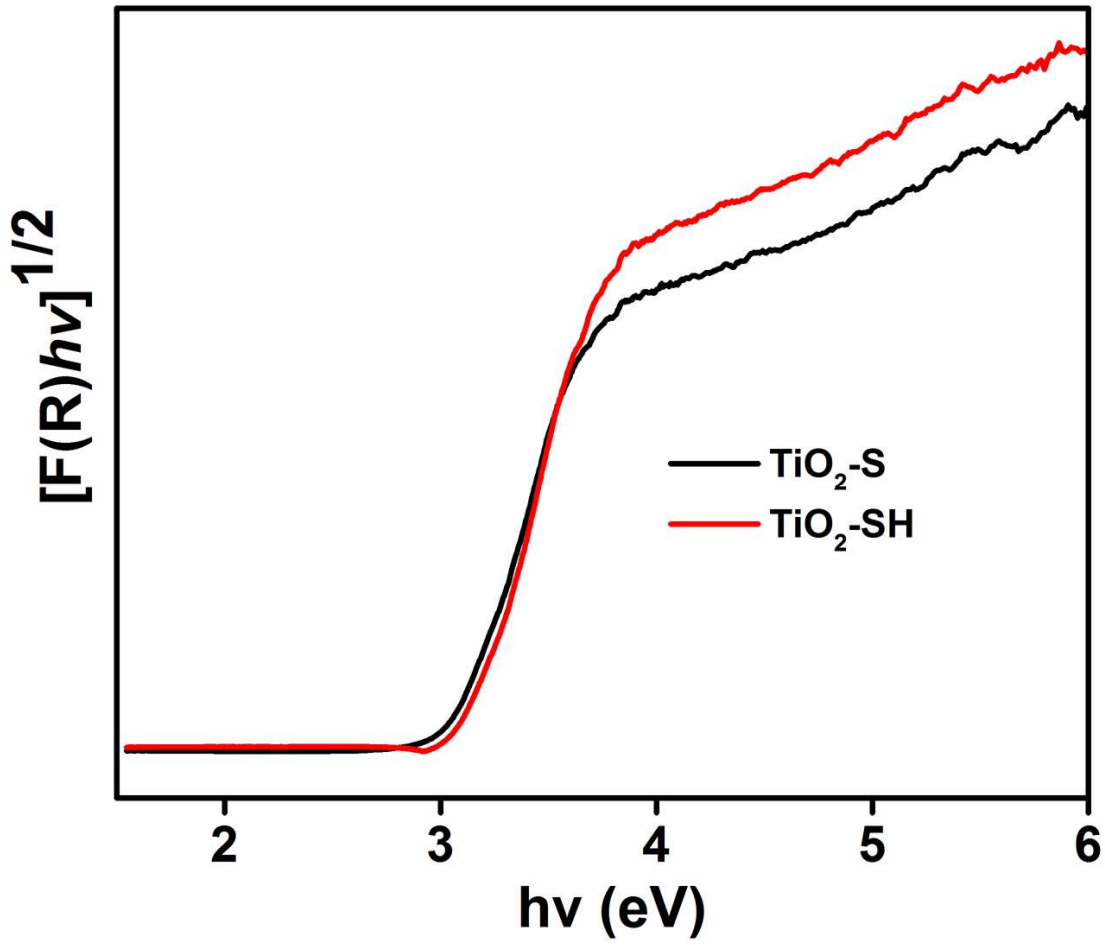

Figure 4.6 Tauc plot of TiO_2-S and TiO_2-SH samples.

4.1.3 Scanning electron microscopy and transmission electron microscopy characterisation of the mixed-phase TiO_2 nanoparticles

The morphologies of the prepared catalysts were revealed by Scanning electron Microscopy (SEM) and Transmission Electron Microscopy (TEM) analyses. As shown in Figure 4.7 and 4.8,no significant difference was observed in the morphologies of the obtained catalysts, as revealed by SEM images. SEM- energy-dispersive X-ray (EDX) analyses of both TiO_2-S and TiO_2-SH confirmed the presence of Ti and O, as shown in Figure 4.9 and 4.10. TEM images revealed that TiO_2-SH sample is more homogenous in size than TiO_2-S; suggesting that agglomeration is reduced in the former as compared to the latter. Moreover, as shown in Figure 4.11 and 4.12, the TEM images of prepared TiO_2revealed that the average particle size of nanoparticles is ca. 15 nm. High resolution (HR) TEM images (Figure 4.13 and 4.14) confirmed the presence of both anatase and rutile phases, which agrees well with the XRD results. The Selected Area Electron Diffraction (SAED) patterns (Figure 4.15 and 4.16) showedseries of spots with both samples as a result of their crystallinity. The series of spots are more prominent in TiO_2-SH, which indicated that TiO_2-SH is more crystalline than TiO_2-S. It was also noticed that TiO_2-SH particles are widely dispersed than TiO_2-S particles as evident from elemental mapping (Figure 4.17 and 4.18).

4.1.4 X-ray photoelectron spectroscopy characterisation of the mixed-phase TiO_2 nanoparticles

XPS measurements were doneto understand the chemical state and composition of Ti and O in both TiO_2-S and TiO_2-SH nanoparticles. The XPS survey spectra of TiO_2-S and TiO_2-SH, shown in Figure 4.19 and 4.20, confirmed the presence of Ti and O in the prepared mixed-phase TiO_2. The C1s observed in the spectra was as a result of the impurity of XPS instrument itself. High-resolution XPS spectrum of TiO_2-S (Figure 4.21) showed Ti^{4+} peaks at 458.3 and 464.1 eV, which are assigned to $Ti2p_{3/2}$ and $Ti2p_{1/2}$ of Ti^{4+} state, respectively (Niu *et al.,* 2013).For TiO_2-SH catalyst, Ti^{4+} peaks shifted to 459.1 and 464.9 eV (Figure 4.22), which are also assigned to $Ti2p_{3/2}$ and $Ti2p_{1/2}$ of Ti^{4+} state, respectively. This shift might be due to the hydrothermal treatment during the synthesis of TiO_2-SH.

The high-resolution spectrum of O1s of the TiO_2-S catalyst (Figure 4.23) was

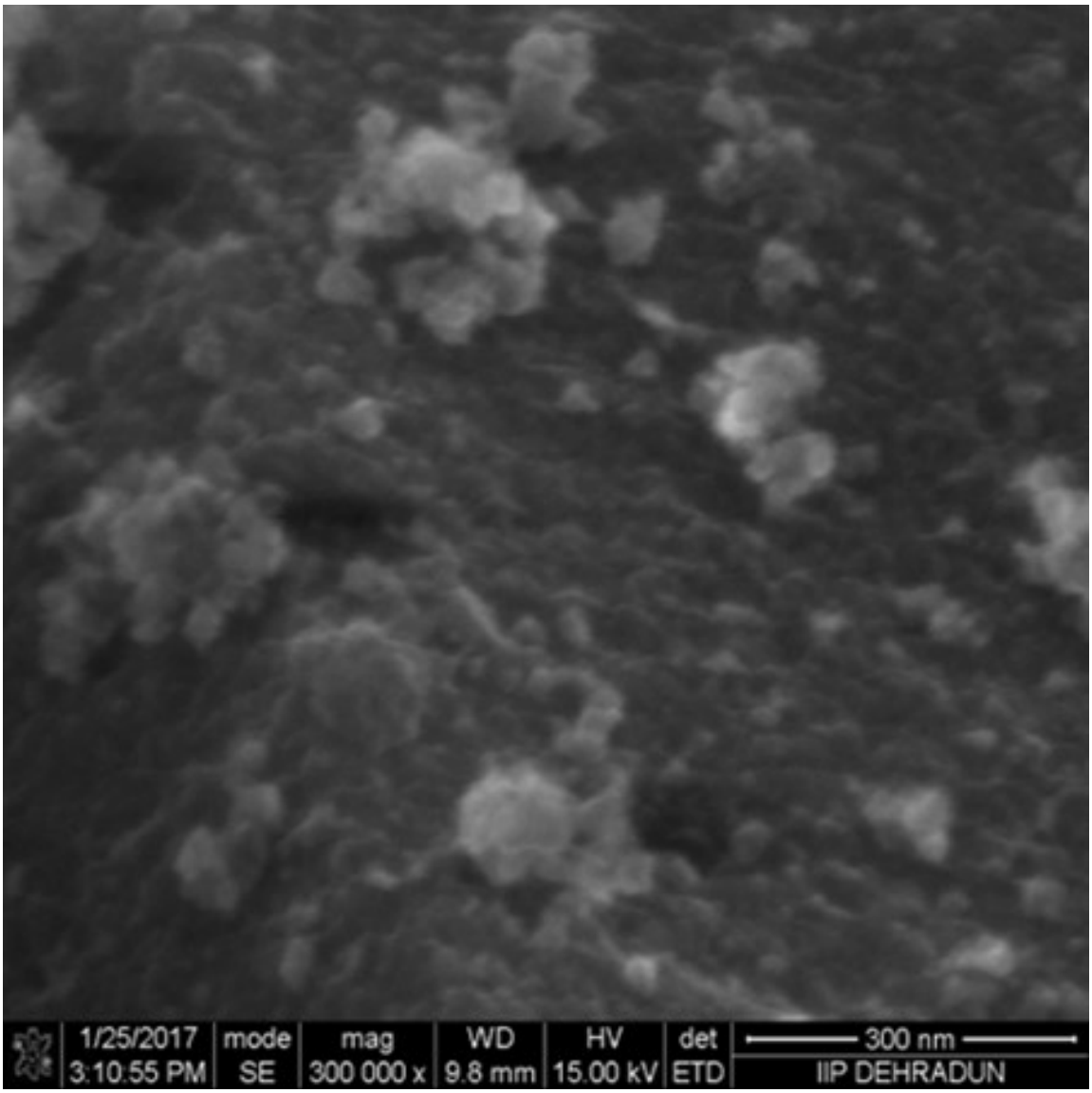

Figure 4.7 Scanning electron microscopy images of TiO_2-S photocatalyst.

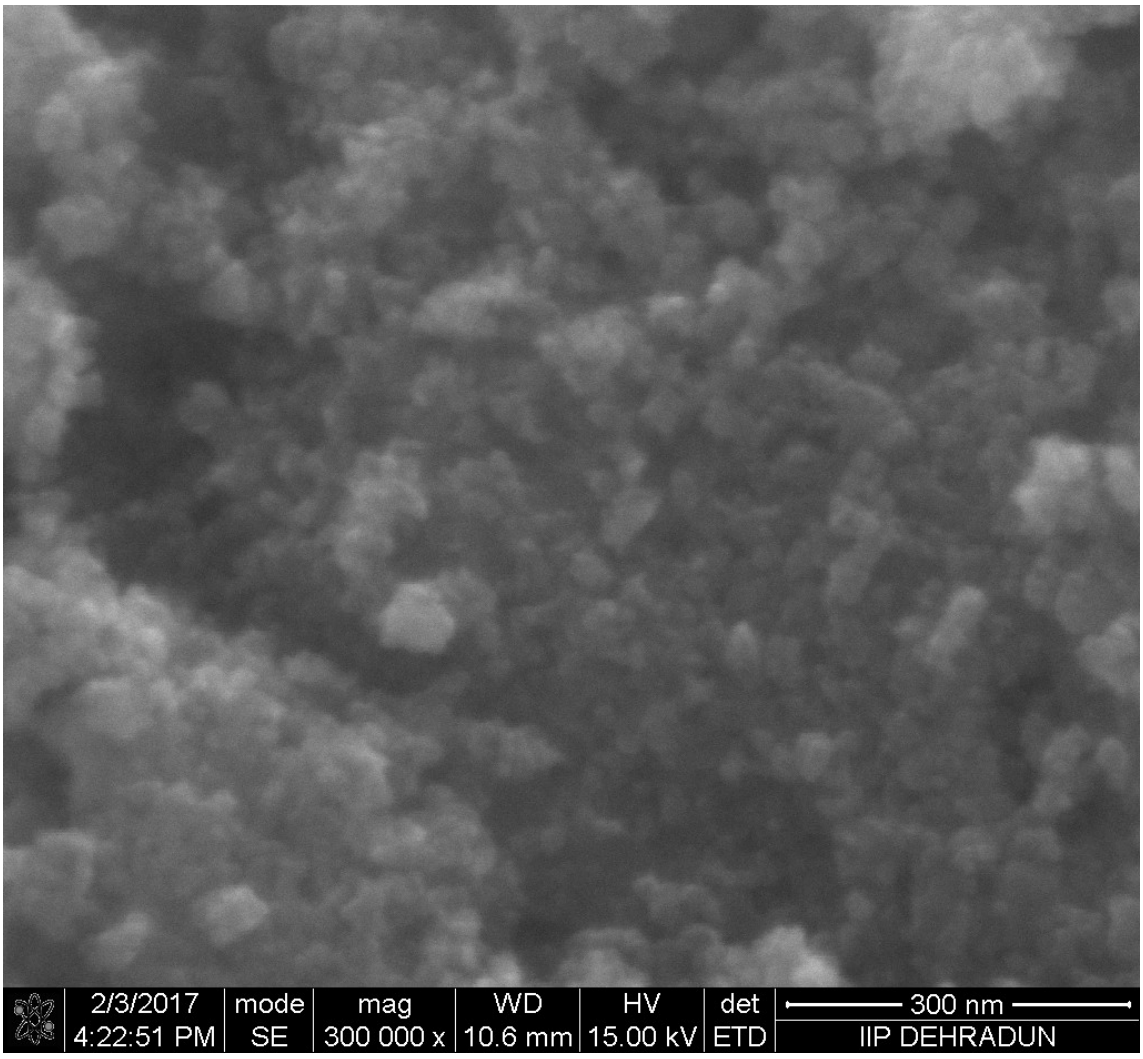

Figure 4.8 Scanning electron microscopy images of TiO_2-SH photocatalyst.

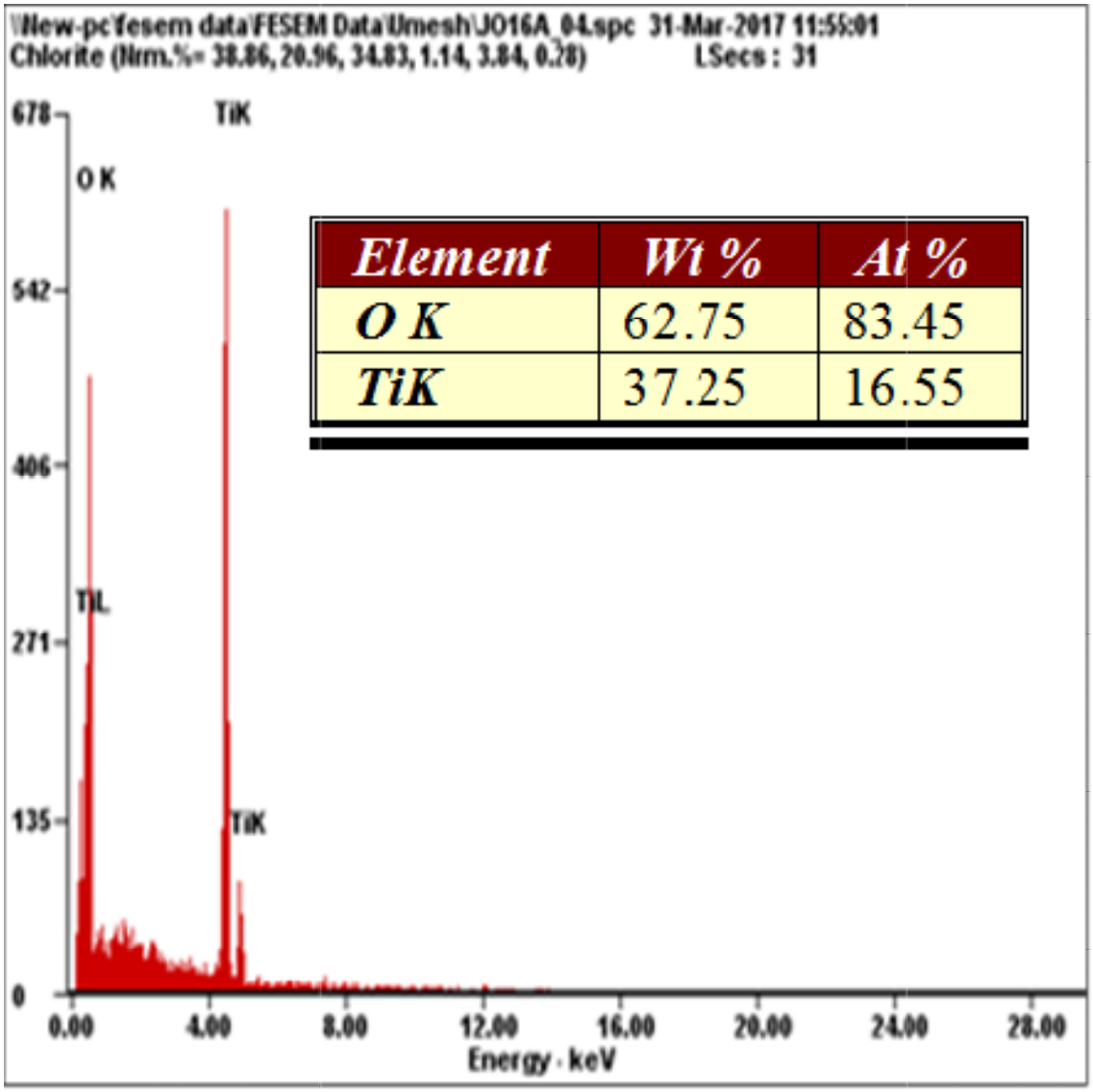

Figure 4.9 Energy-dispersive X-ray spectroscopy image of TiO_2-S photocatalyst.

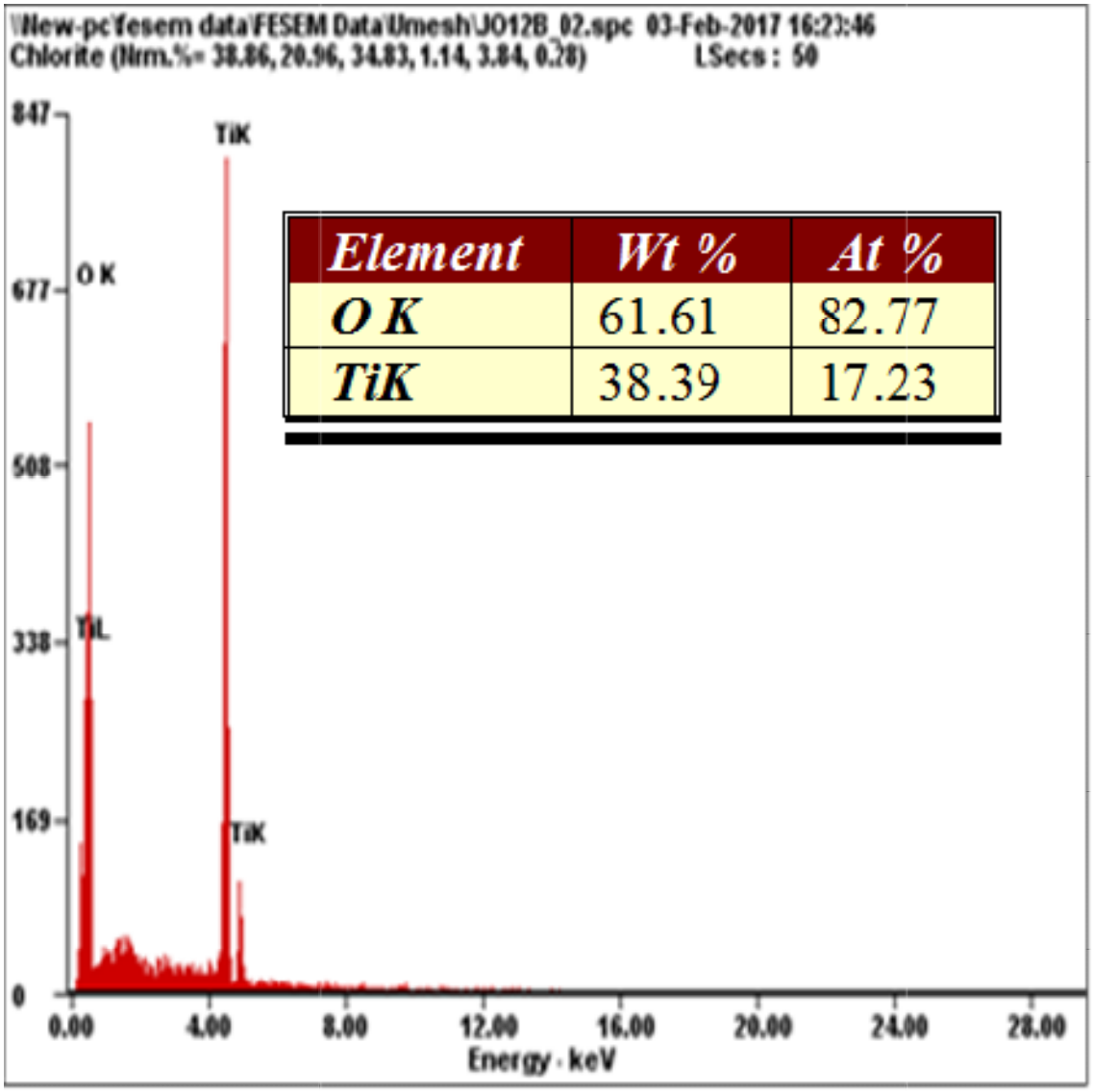

Figure 4.10 Energy-dispersive X-ray spectroscopy image of TiO_2-SH photocatalyst.

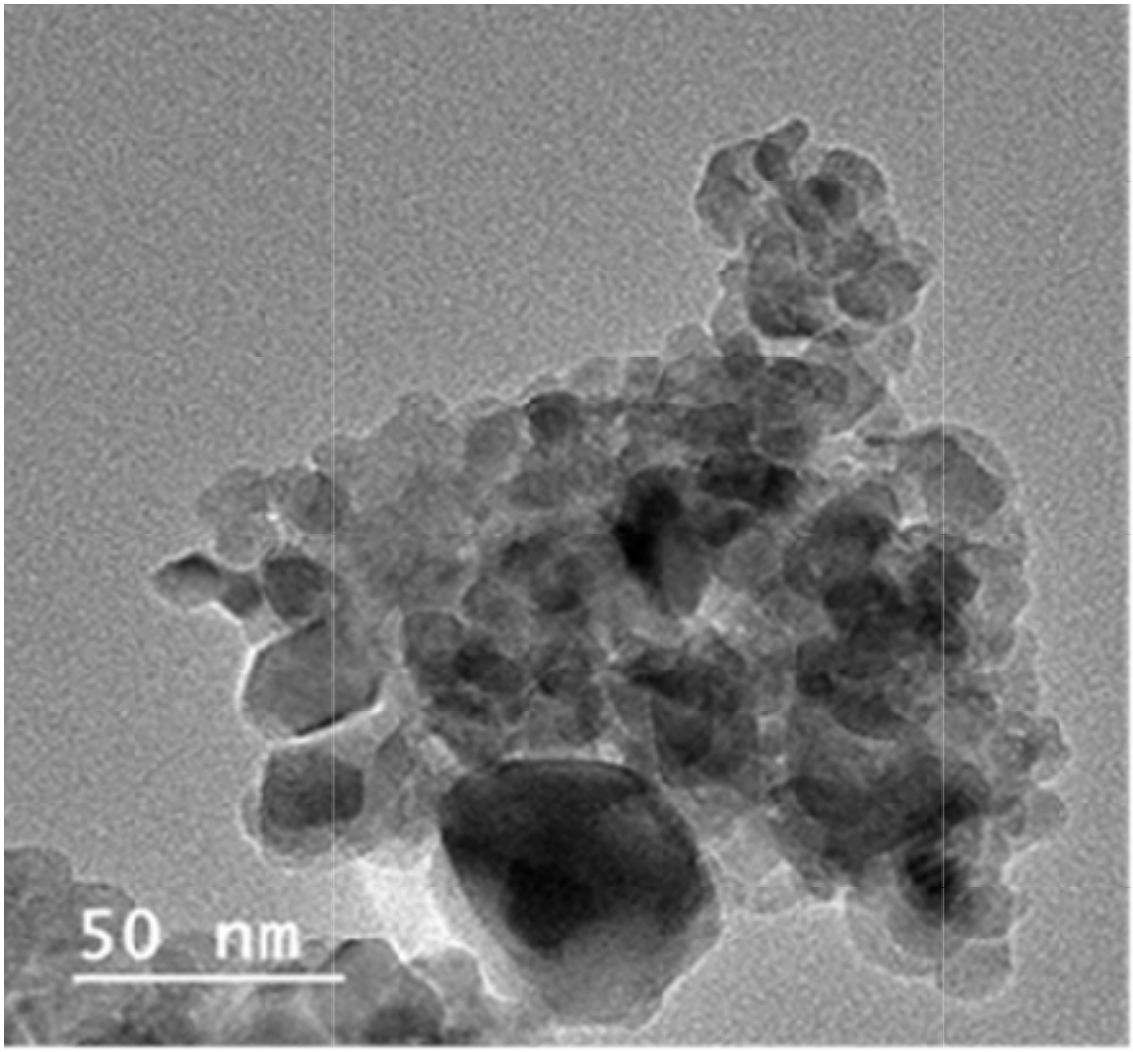

Figure 4.11 Transmission electron microscopy image of TiO_2-S.

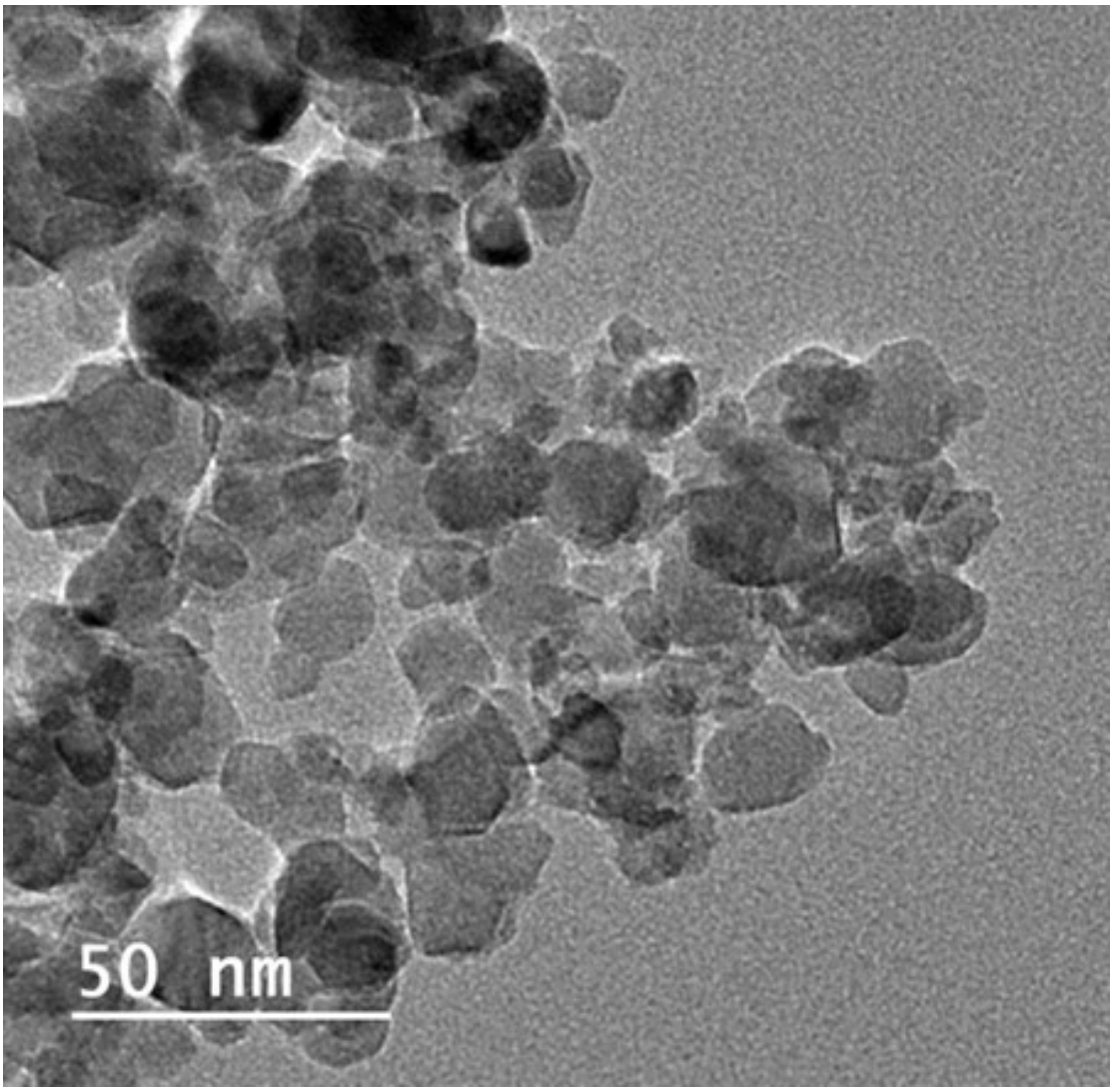

Figure 4.12 Transmission electron microscopy image of TiO_2-SH.

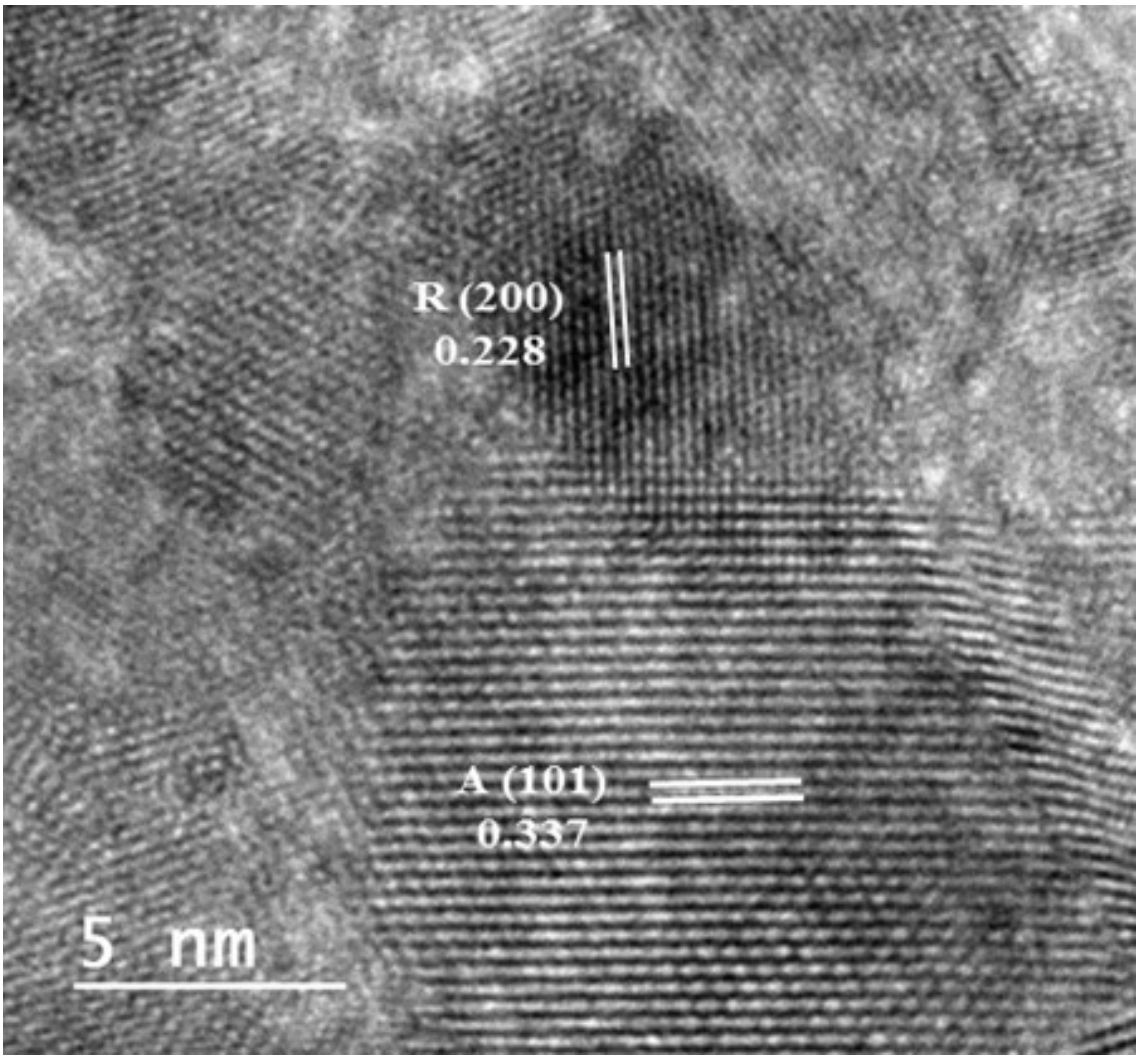

Figure 4.13 High resolution transmission electron microscopy image of TiO_2-S.

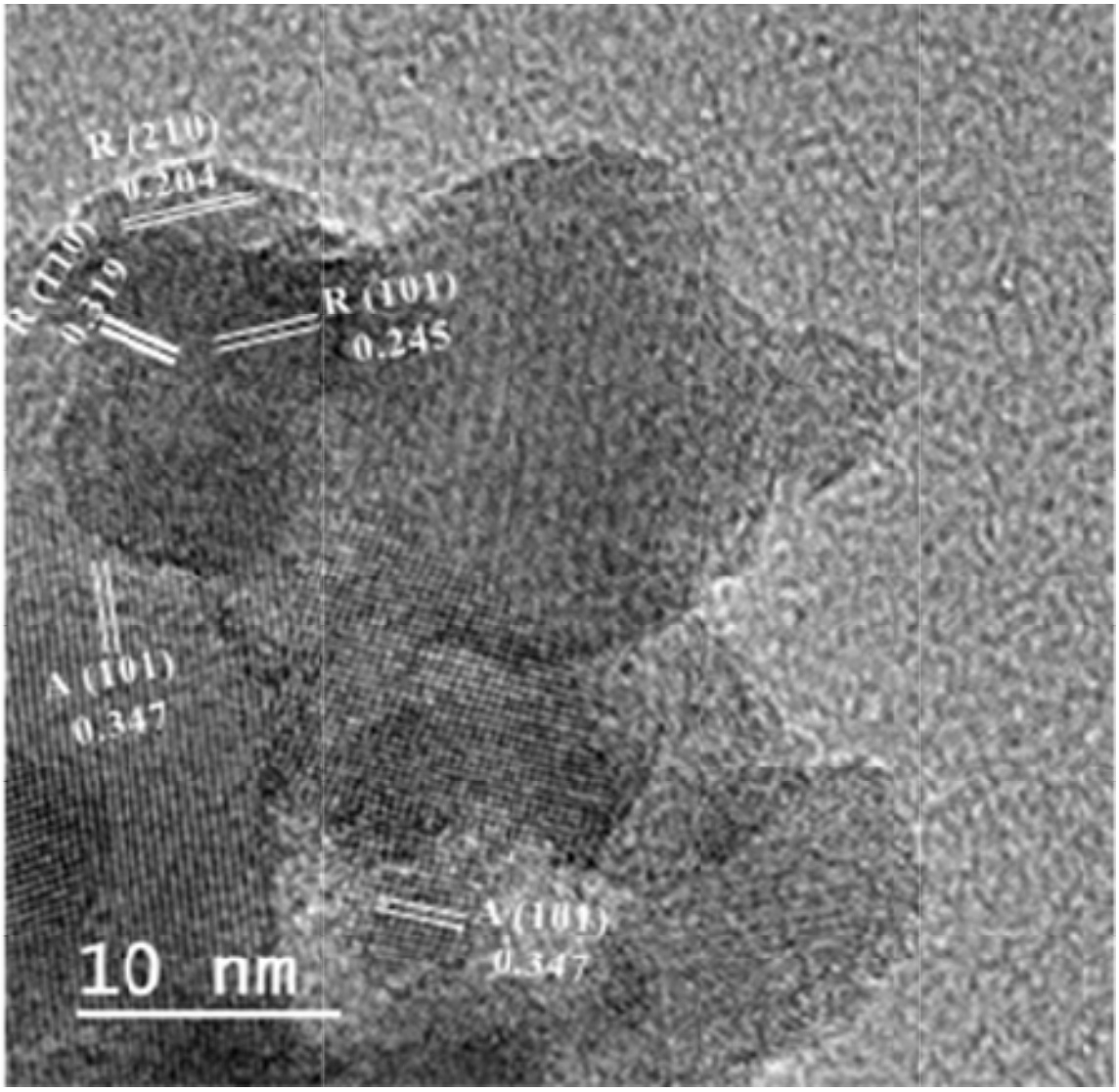

Figure 4.14 High resolution transmission electron microscopy image of TiO_2-SH.

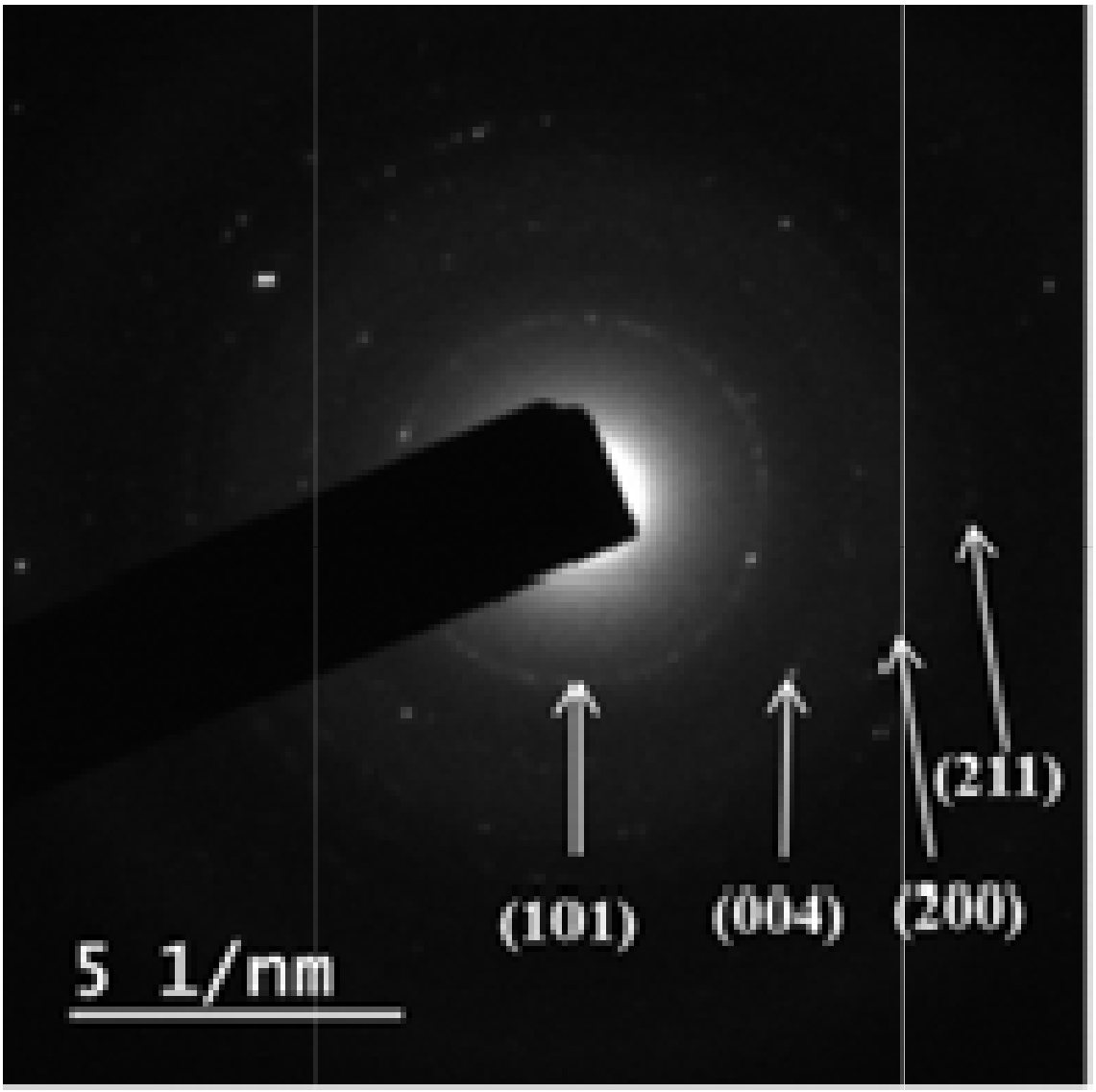

Figure 4.15 Selected area diffraction pattern of TiO_2-S.

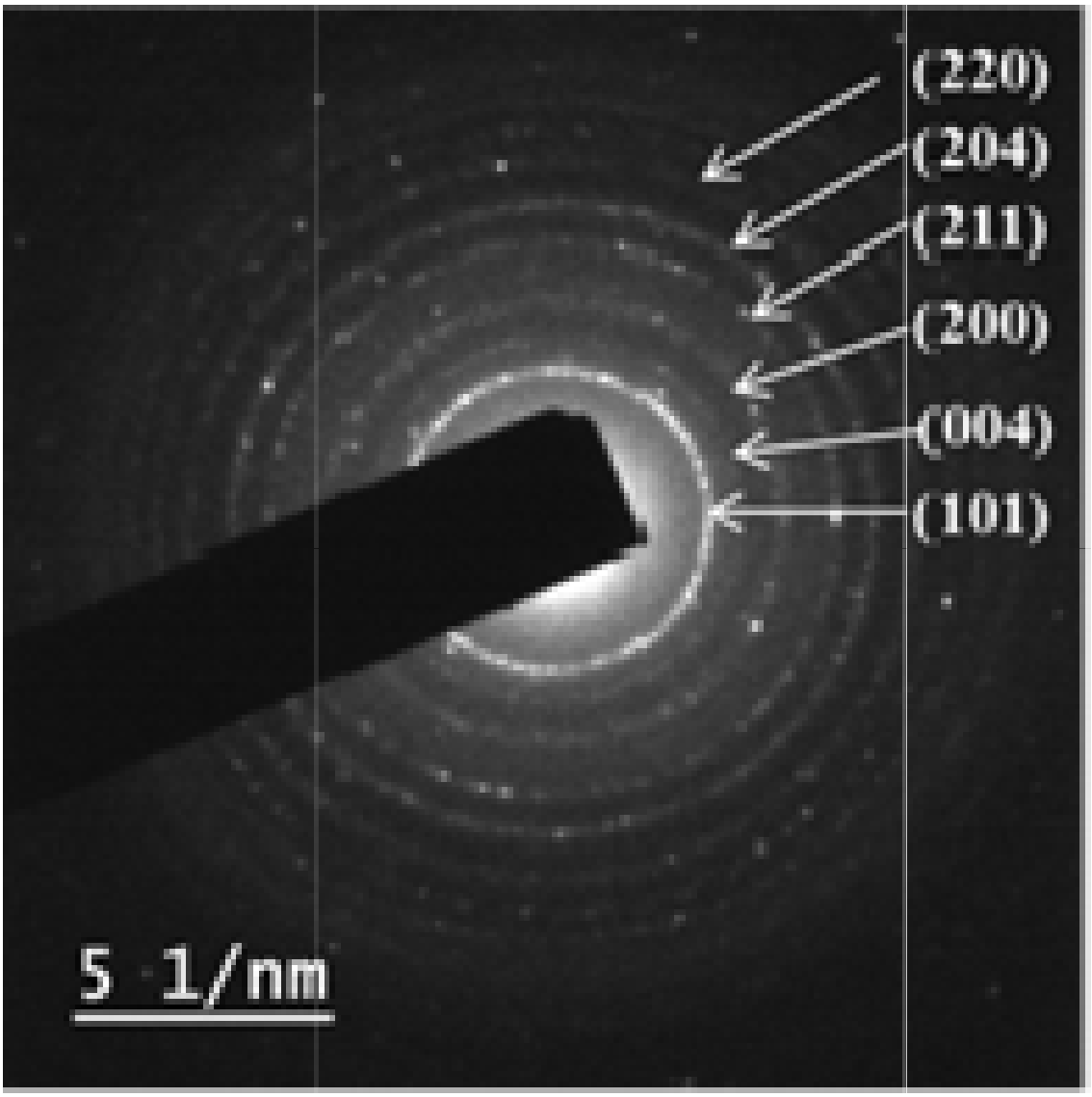

Figure 4.16 Selected area diffraction pattern of TiO_2-SH.

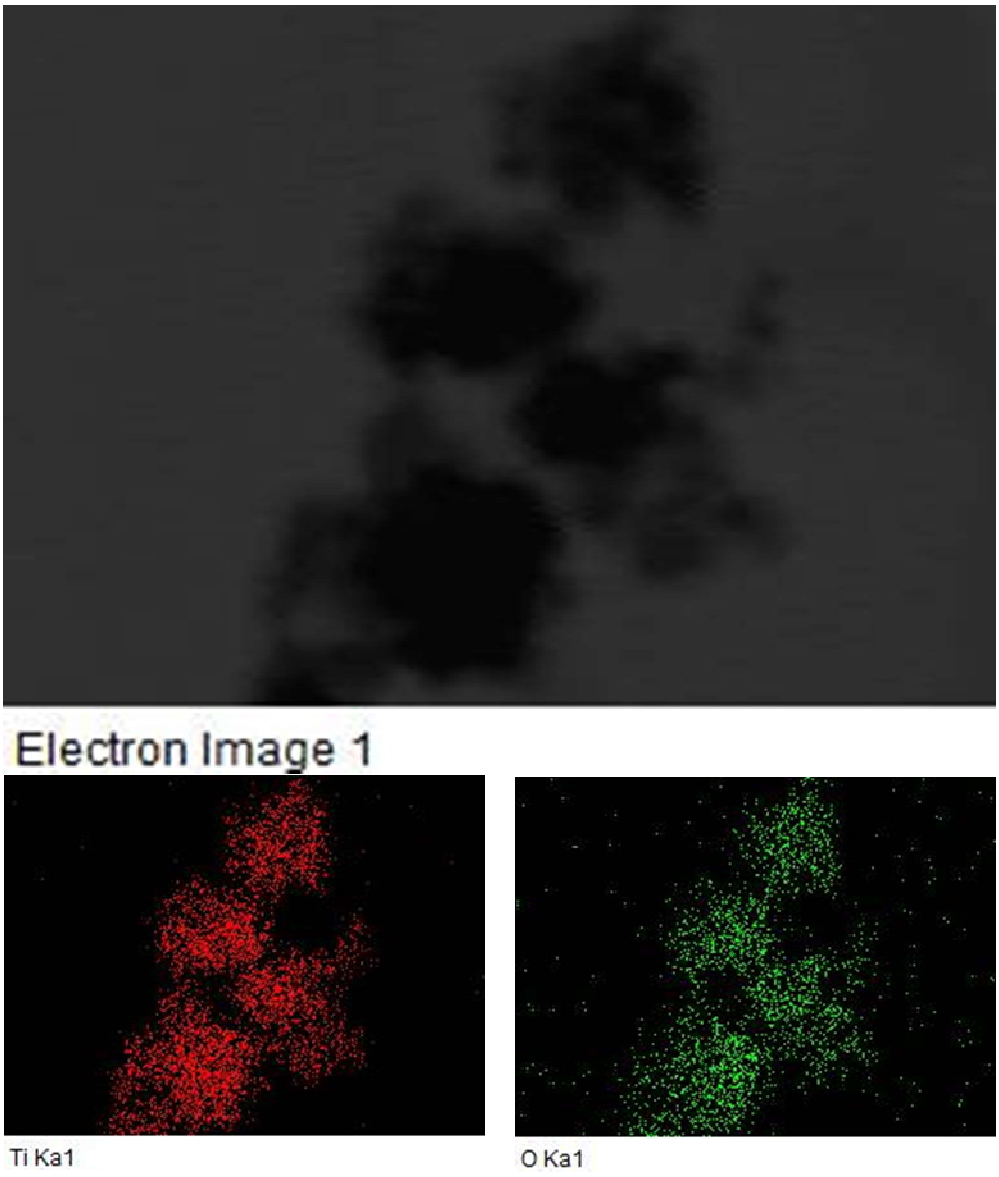

Figure 4.17 Elemental mapping of TiO_2-S.

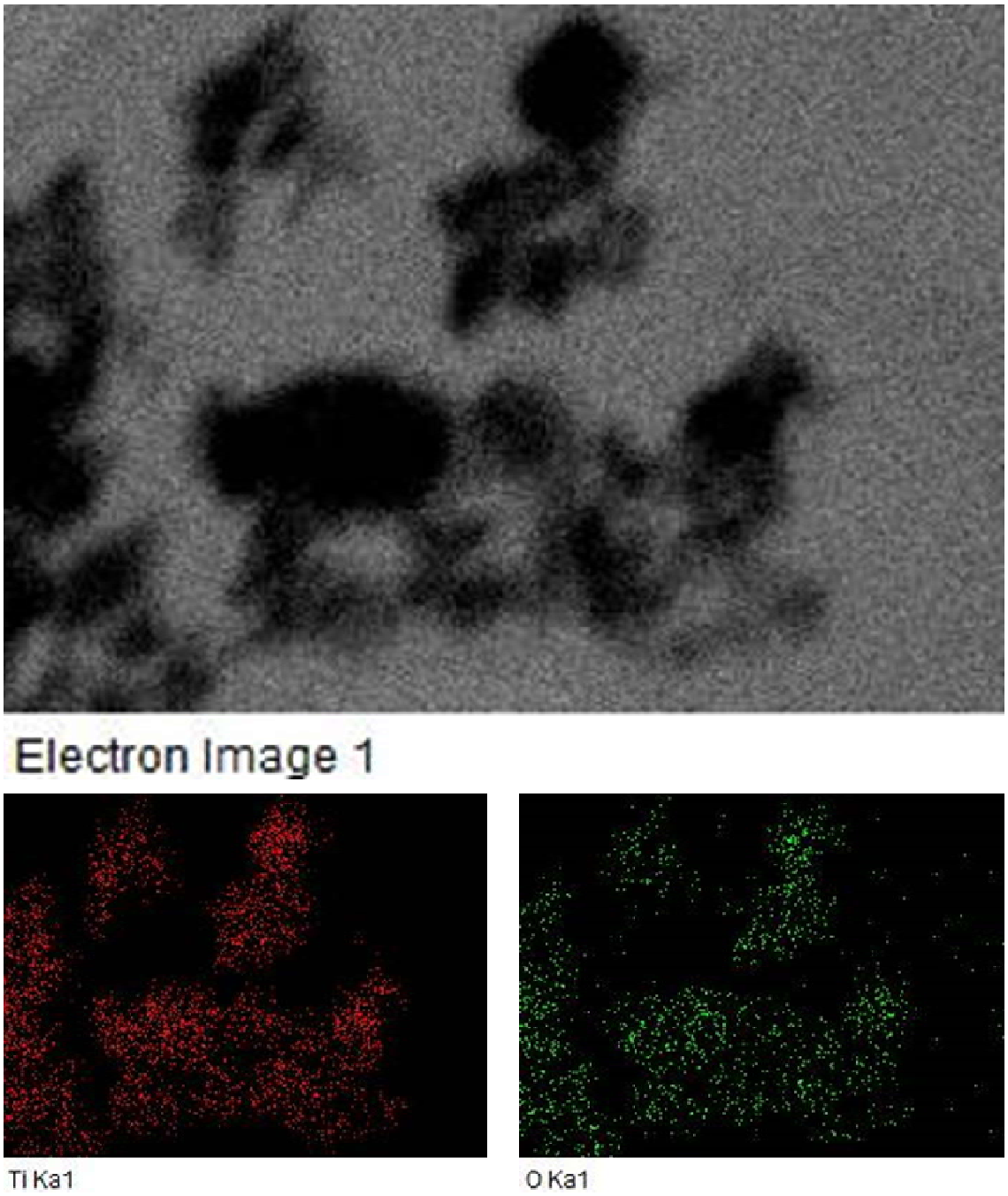

Figure 4.18 Elemental mapping of TiO_2-SH.

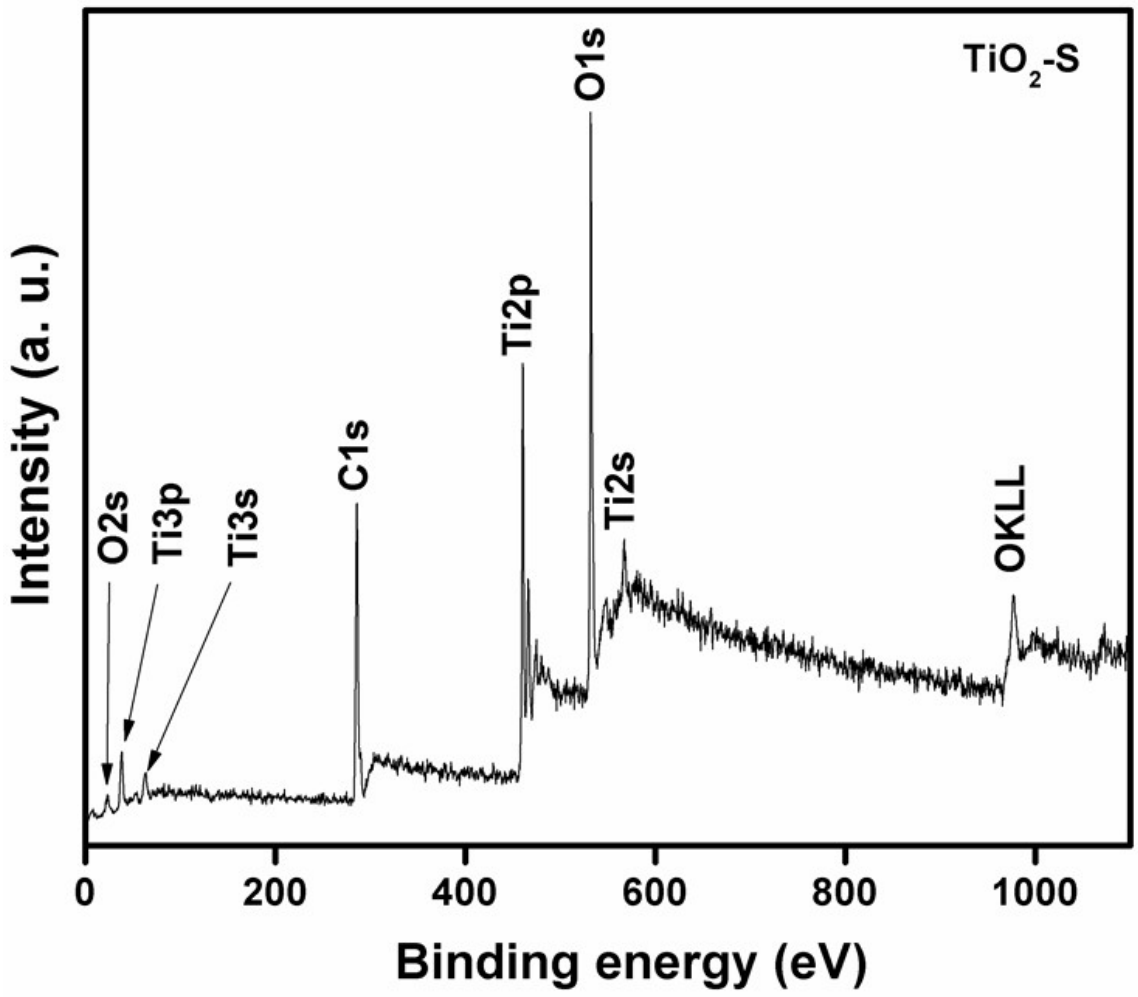

Figure 4.19 X-ray photoelectron spectroscopy survey spectrum of TiO_2-S.

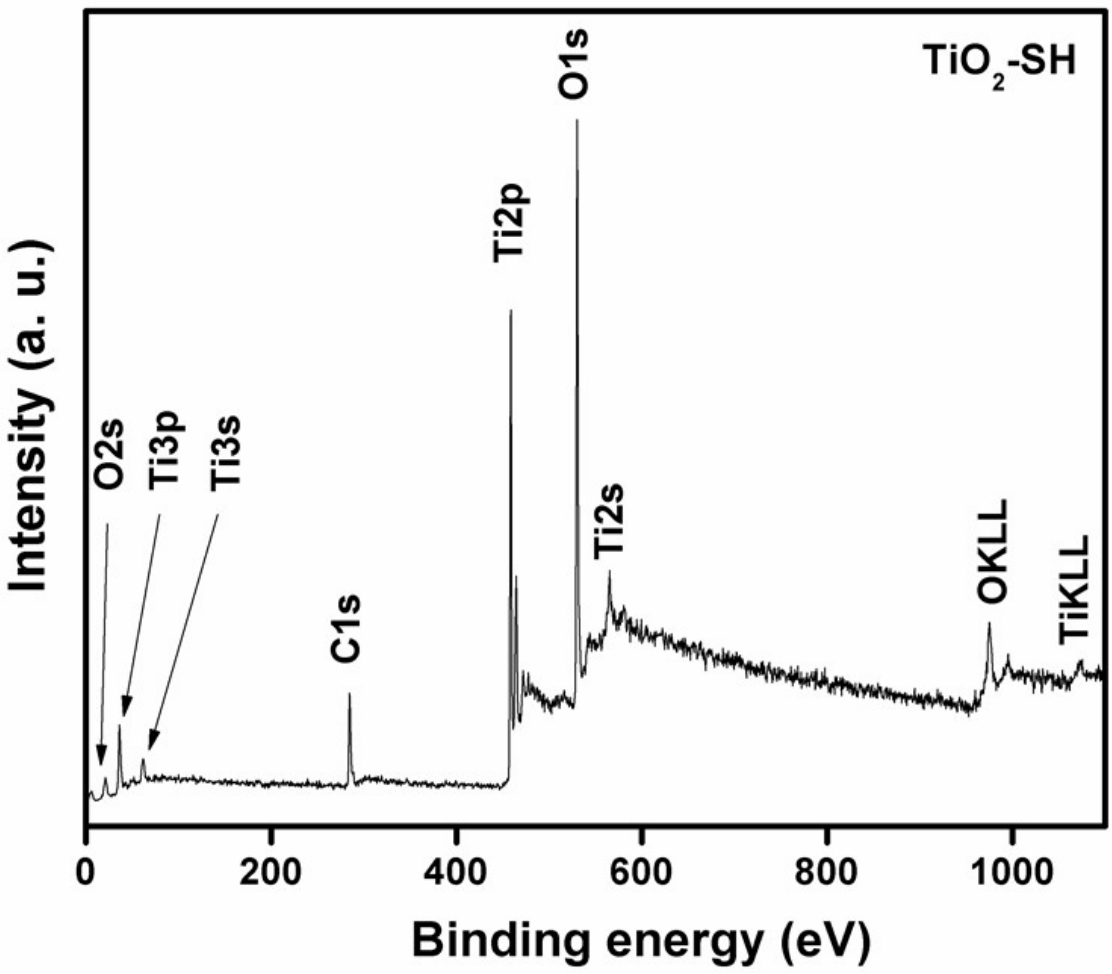

Figure 4.20 X-ray photoelectron spectroscopy survey spectrum of TiO_2-SH.

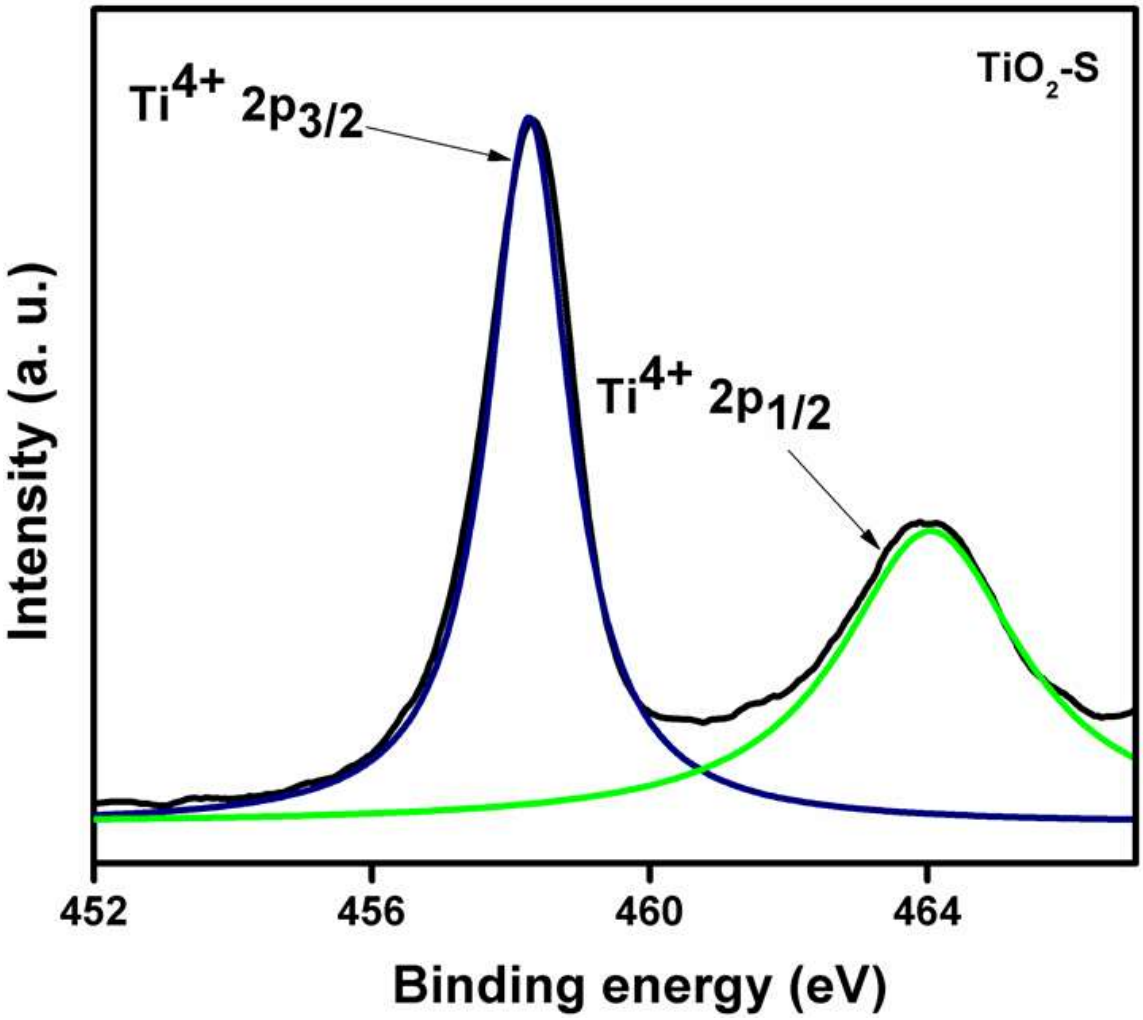

Figure 4.21 High-resolution X-ray photoelectron spectroscopy spectrum of Ti2p of TiO_2-S.

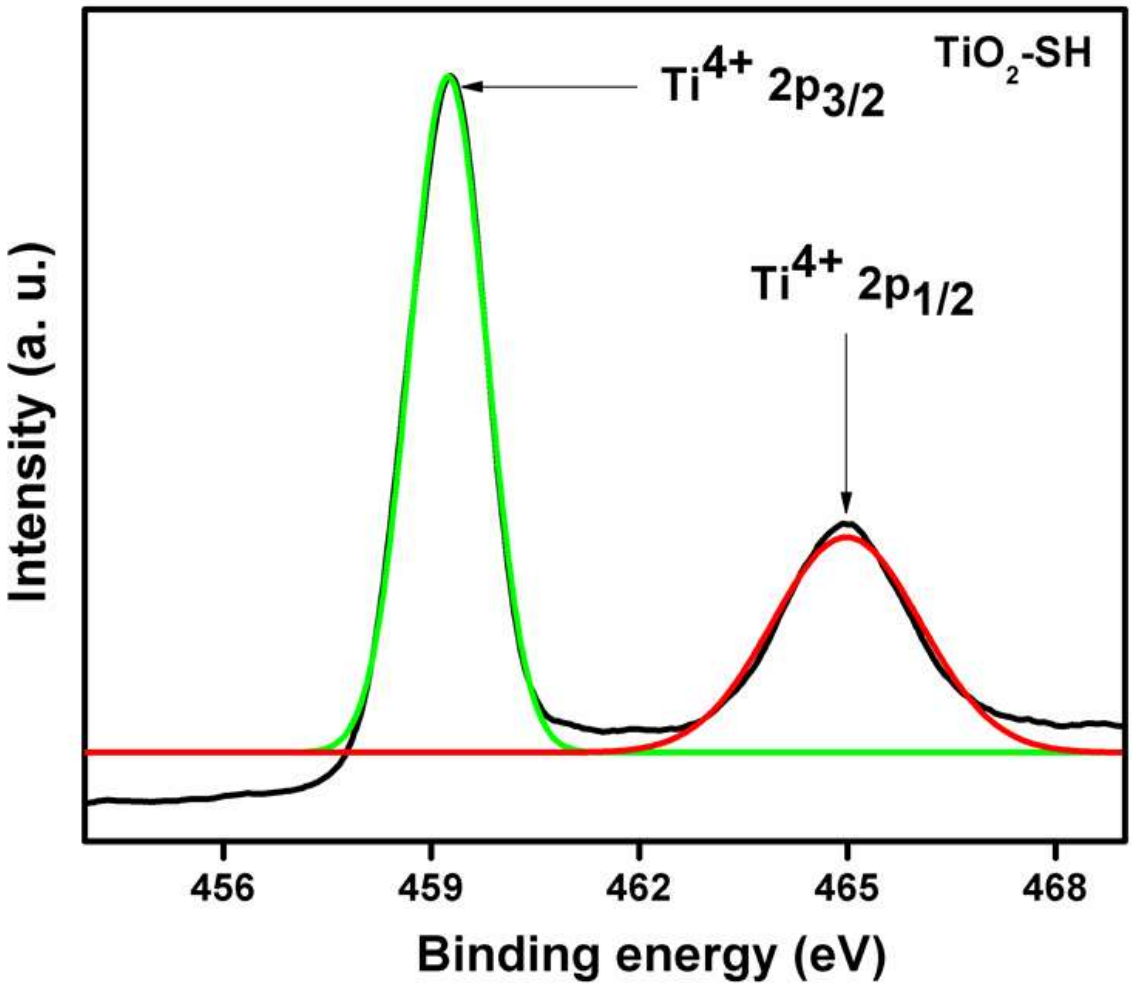

Figure 4.22 High-resolution X-ray photoelectron spectroscopy spectrum of Ti2p of TiO_2-SH.

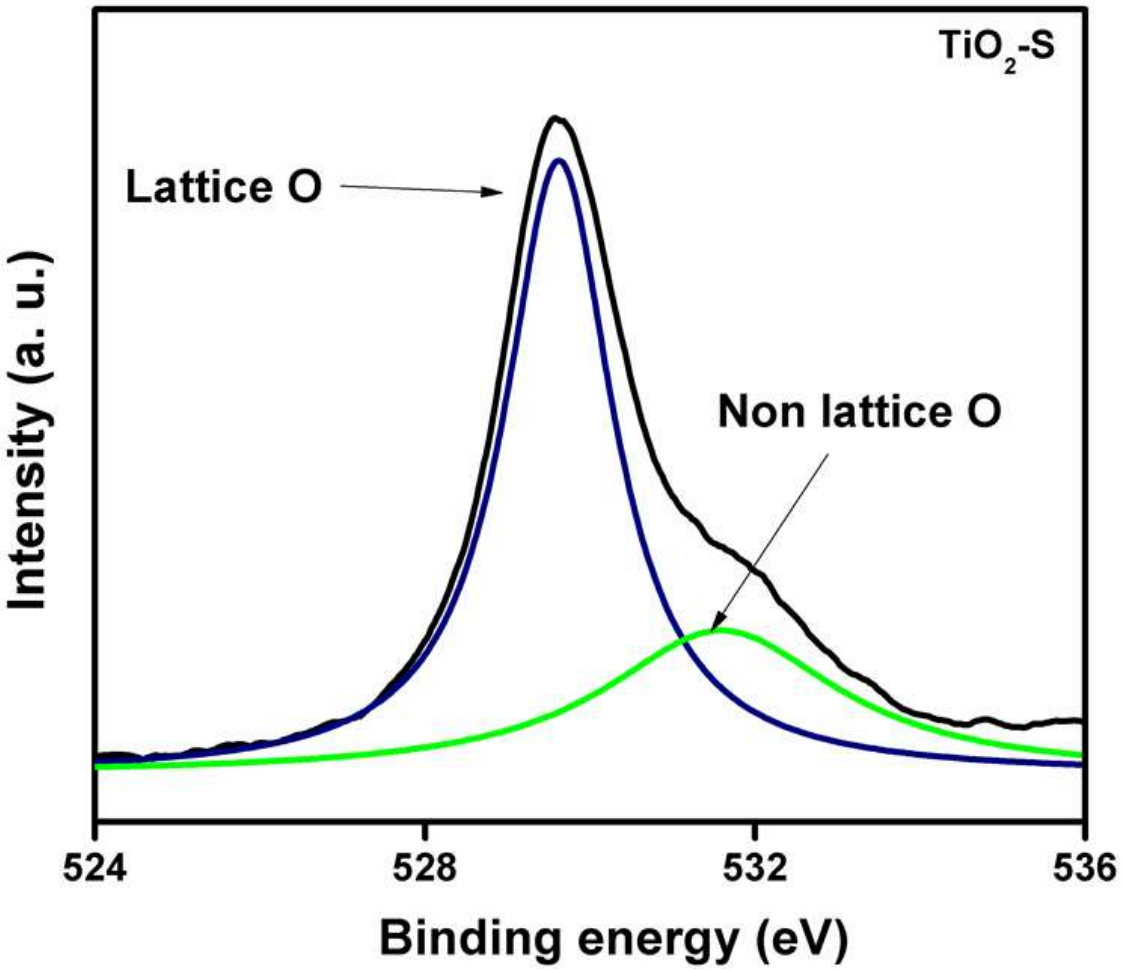

Figure 4.23 High-resolution X-ray photoelectron spectroscopy spectrum of O1s of TiO_2-S.

resolved into two peaks. The two peaks were noticed at 529.6 and 531.6 eV, and have been ascribed to lattice oxygen and non-lattice oxygen (adsorbed OH groups), respectively (Bayati *et al.,* 2010). Similar peaks were observed in the high-resolution spectrum of O1s of the TiO_2-SH catalyst (Figure 4.24). However, the observed peaks for TiO_2-SH catalyst were slightly shifted to 530.5 and 532.4 eV, respectively.

4.1.5 Computational studies of the mixed-phase TiO_2 nanoparticles

The supercell of anatase contains 18 atoms (6 Ti and 12 O), and its dimensions are 1 x 1. In the direction [1 0 1], the slab has three Ti_2O_4 layers and a vacuum of more than 20 Å. The coordinates of the atoms in the bottom atomic layer (1 layer of Ti_2O_4) were kept fixed while the remaining atoms were allowed to relax as shown in Figure 4.25. Eight sites were considered from the side and top view of the 1 x 1 three-layer cell to describe the anatase (1 0 1) surface as depicted in Figure 4.25 and 4.26 respectively. Positions O_1, $O_2$and O_3, correspond to sites on top of the surface oxygens, Ti_1, and Ti_2 correspond to sites on top Ti, while H, H_1, and H_2 correspond to hollow sites.

On the other hand, the supercell of rutile contains 30 atoms (10 Ti and 20 O), and its dimensions are also 1 x 1 as shown in Figure 4.27. Therefore, the systems were described by five-layer-think slabs (Ti_2O_4) separated by a vacuum of more than 20 Å in the [1 1 0] direction. The coordinates of the atoms in the bottom atomic layer (2 layers of Ti_2O_4) were kept fixed while the rest of the atoms were allowed to relax. Four sites were considered as depicted in Figure 4.27. Position Ti_1 corresponds to bridging protruding oxygen adsorption, position Ti_2 on top of Ti, position O on top of basal oxygen, and position H represent the hollow site between two basal oxygens, protruding oxygen, and Ti atom.

As shown in Table 4.3 and 4.4, the adsorption energies were calculated by the expression:

$$E_{ads} = E\ (molecule/surface) - E\ (surface) - E\ (molecule) \quad \text{.....4.1}$$

Where the *molecule* variable can take the values of H_2O, CO_2 and MeOH; and the *surface* would be anatase (1 0 1) and rutile (1 1 0). For the system *molecule/surface*, different orientations of the molecules were tested to calculate the minimum energy. The values of *E (molecule)*were obtained by performing a full geometry optimization of isolated molecules in a 10Å x 10Å x 10Å supercell.

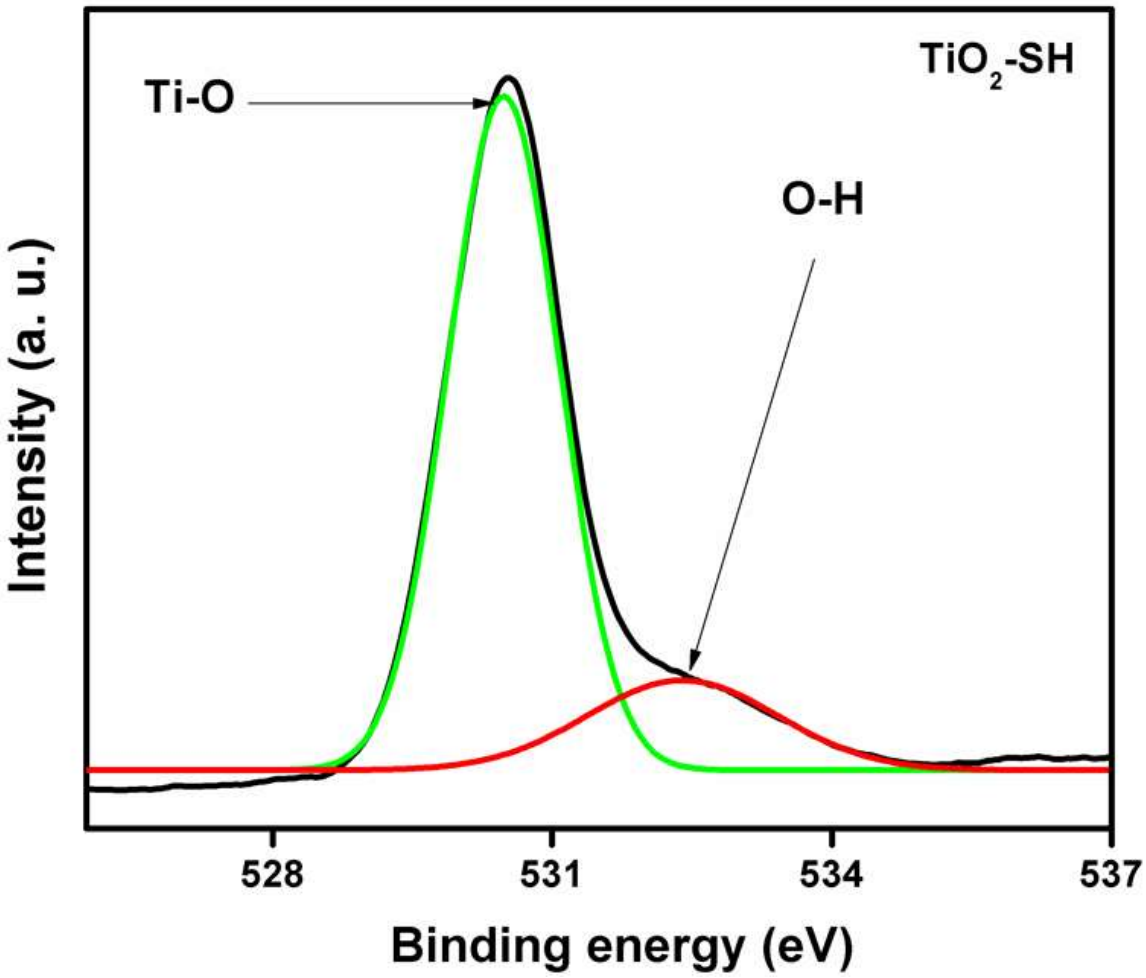

Figure 4.24 High-resolution X-ray photoelectron spectroscopy spectrum of O1s of TiO_2-S.

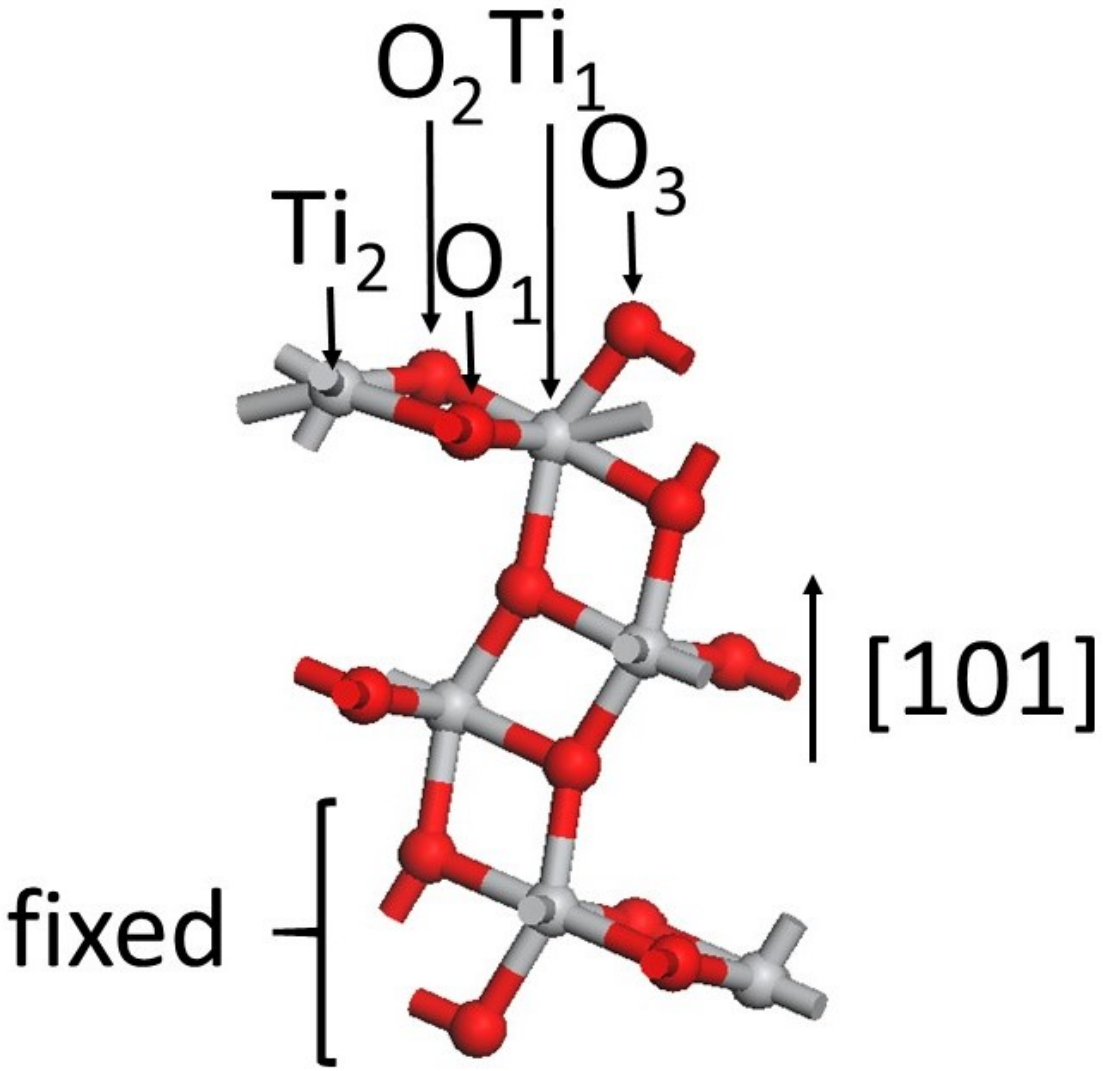

Figure 4.25 Left and right show the side of the 1 x 1 three-layer cell to describe the anatase (1 0 1) surface.

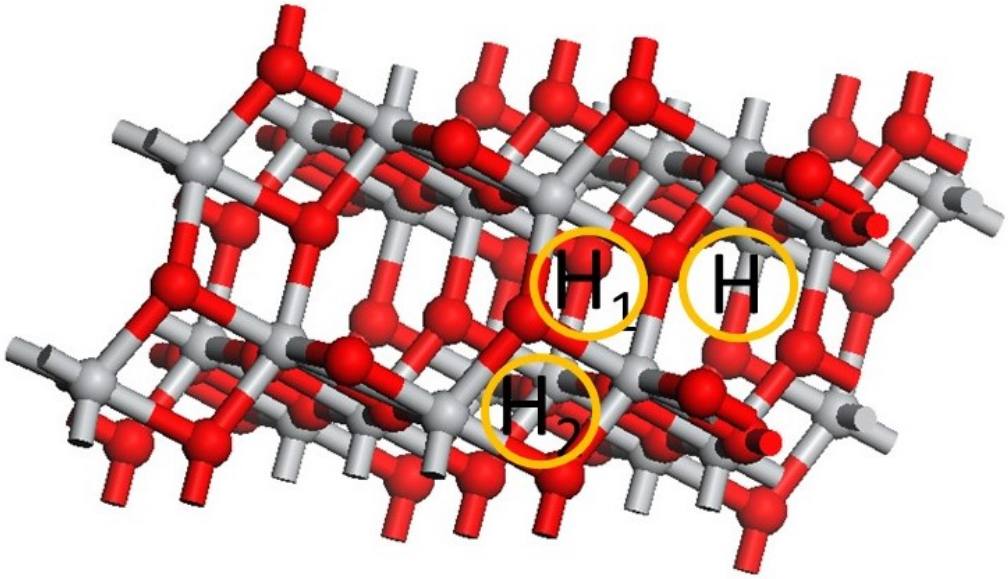

Figure 4.26 Top view of the 1 x 1 three-layer cell to describe the anatase (1 0 1) surface.

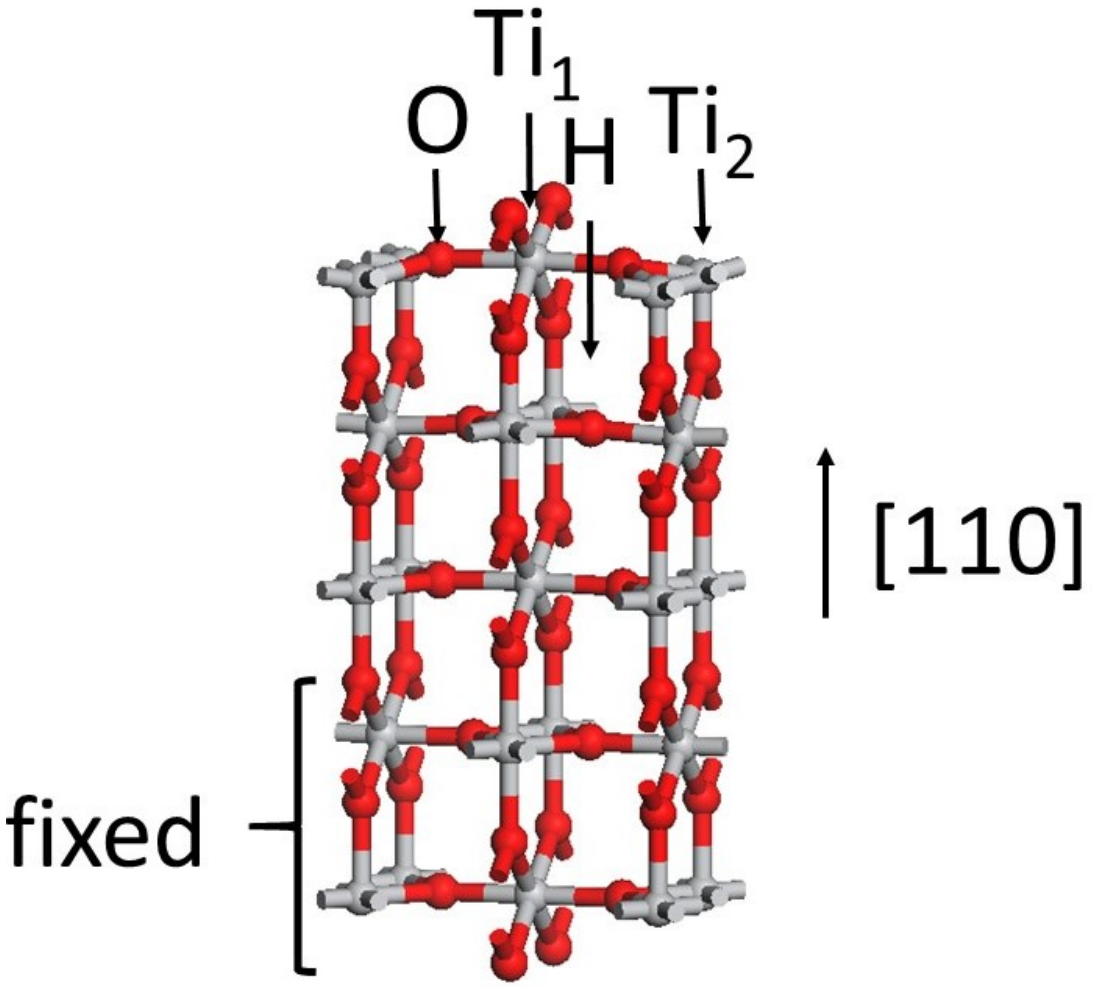

Figure 4.27 Side view of the 1 × 1 five-layer cell to describe the rutile (1 1 0) surface.

Table 4.3 Adsorption energy (eV) of molecule deposited on surface anatase (1 0 1). Only the most stable case for each molecule, after deposited on the surface, are presented here.

Anatase (1 0 1)								
Molecule	O_1	O_2	O_3	Ti_1	Ti_2	H	H_1	H_2
H_2O	-0.92	-0.92	-0.79	-0.91	-0.91	-0.91	-0.39	-0.39
CO_2	-0.49	-0.16	-0.31	-0.37	-0.16	-0.35	-0.34	-0.35
MeOH	-0.94	-0.94	-0.89	-1.01	-0.94	-0.93	-1.02	-0.48

Table 4.4 Adsorption energy (eV) of molecule deposited on surface rutile (1 1 0). Only the most stable case for each molecule, after deposited on the surface, are presented here.

Rutile (1 1 0)				
Molecule	Ti_1	Ti_2	O	H
H_2O	-0.38	-0.69	-0.53	-1.10
CO_2	-0.12	-0.15	-0.20	-0.30
MeOH	-0.35	-0.83	-0.83	-0.84

4.1.6 Photocatalytic CO_2 reduction by the mixed-phase TiO_2 nanoparticles

The photocatalytic reduction of $CO_2$was tested in acetonitrile (ACN), H_2O and triethanolamine (TEOA) mixture under UVA for a period of 24 h as described in section 3.1.5. As shown in Figure 4.28, photocatalytic reduction of $CO_2$was selective towards methanol formation. The methanol production rate of TiO_2-S was found to be 1.87 mmol g^{-1} h^{-1},and rate was slightly increased with TiO_2-SH, which yield 1.97 mmol g^{-1} h^{-1}. The slight increase in the performance of TiO_2-SH over its counterpart could be explained in three ways. Firstly, the adsorption energies of CO_2 were higher for most sites on anatase (1 0 1) surface than rutile as shown in Table 4.3 and 4.4. As previously explained, XRD results showed that the composition of anatase (1 0 1) is higher with TiO_2-SH than TiO_2-S, whereas, rutile phase is less with TiO_2-SH than TiO_2-S. This, therefore, implies that CO_2 had a better interaction with anatase (1 0 1) which subsequently led to higher activity of TiO_2-SH than TiO_2-S. Secondly, the increased performance by TiO_2-SH can be attributed to the higher adsorption energies of H_2O on its surface in comparison to TiO_2-S as shown in Table 4.3 and 4.4. Thirdly, TiO_2-SH showed a higher surface area than TiO_2-S, which indicates that there are more active sites on the surface of TiO_2-SH for the reduction of CO_2.

Based on the higher adsorption energies of TiO_2-SH upon its interaction with CO_2 and H_2O in comparison with TiO_2-S, a significant difference in the methanol production rate would have been expected. However, a small difference (0.1 mmol g^{-1} h^{-1}) in the methanol production rate was observed,which could be explained from the calculated adsorption energies of MeOH on the surface of the anatase and rutile phases (Table 4.3 and 4.4). The adsorption energies for MeOH were observed to be higher in anatase surface than rutile; suggesting that MeOH would leave the rutile surface faster than the anatase. In other words, the methanol will be more retained on the surface of the TiO_2-SH than TiO_2-S. This could be thereason why both TiO_2-S and TiO_2-SH catalysts were equally competent in the production of methanol from the reduction of CO_2. A possible reaction pathway for the formation of methanol from CO_2(Habisreutinger *et al.,* 2013)is shown below:

$$CO_2 + 6H^+ + 6e^- \rightarrow CH_3OH + H_2O \quad \text{.....4.2}$$

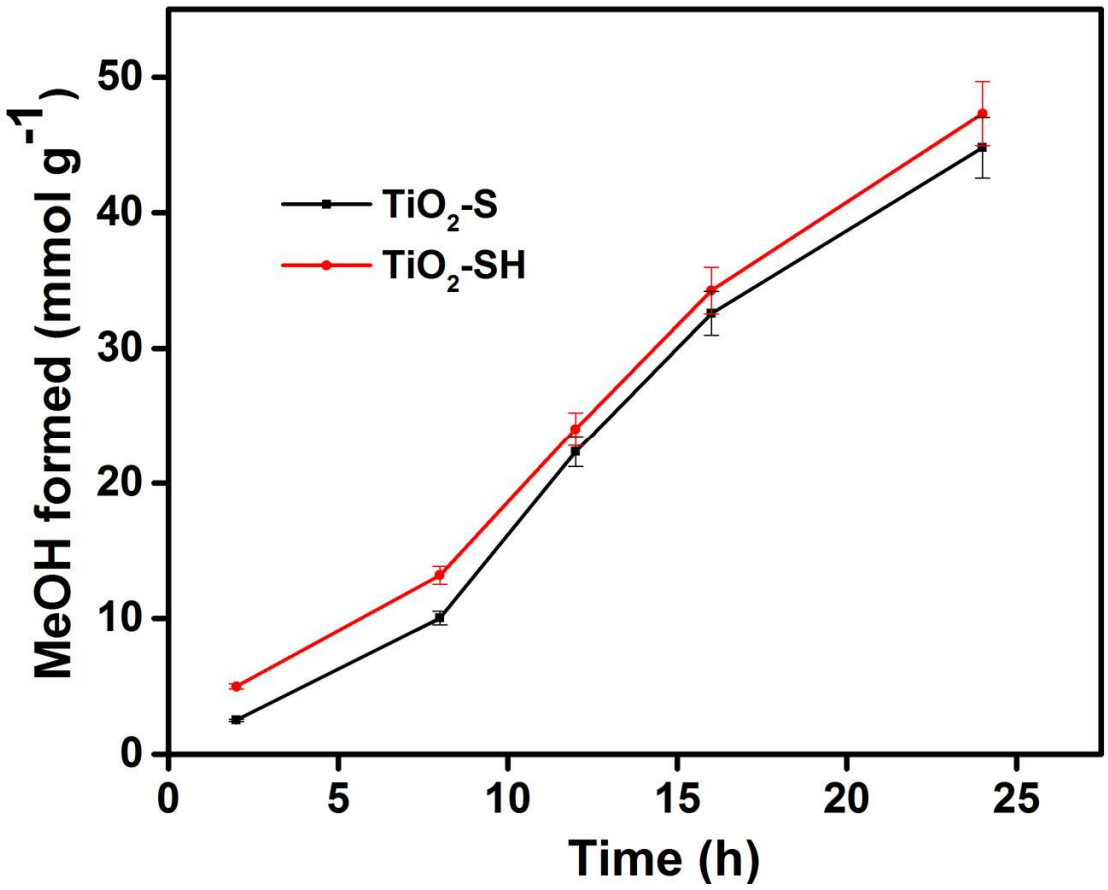

Figure 4.28 Rate of methanol formation from the photoreduction of CO_2 with H_2O in the presence of TEOA under UVA light.

In general, the concept of adsorption energies of particular reactants and products on the different phases of TiO_2 is very crucial in predicting a more favourable phase for photocatalytic activities besides the known synergistic effects (Kho *et al.,* 2010) and the built-in electric field (Xia *et al.,* 2013; Zhang *et al.,* 2011b) at the interface of the mixed-phase junction between anatase and rutile phases. From the calculated energies and experimental results, it can be seen that the catalyst with more anatase phase appeared to be more favourable towards catalytic activities. Hence TiO_2-SH was observed to be more catalytically favourable than TiO_2-S. Moreover, as depicted in Figure 4.14, Table 4.1 and Table 4.2, the hydrothermal treatment involved in the synthesis of TiO_2-SH ensured better separation of various nanoparticles, facilitated homogeneity, higher crystallinity and improved surface area.

The catalytic mechanism for product formation is presented in Scheme 4.1. The band gap of rutile phase is around 3.0 eV, and with the interaction of incident photon, the electron jumps to the conduction band. The conduction band edge potential is higher than anatase. Therefore, the photogenerated electron can easily move to the conduction band of anatase. This process will help to delay the recombination of the photoinducede$^-$ - h^+ pair. Hence the excess of electrons will be available for the photocatalytic reaction at the surface of anatase.

4.1.7 Quantum efficiency calculations

Photocatalytic experiments were performed under batch conditions. Typically, 5.0 mg of catalyst was weighed and loaded into a 50 mL cylindrical quartz reactor of 2.4 cm diameter and length 10 cm. UV-A lamp (UVP -UK of maximum wavelength emission at ~365 nm of power range 8 W) was placed side by side with the reactor. By the use of intensity meter (UVP 97-0015-02/UVX digital Ultraviolet Meter/Radiometer), the light intensity reaching the inside of the reactor (by placing the sensor in the reactor) was measured to be ca. 0.7 mW cm^{-2}. It was assumed that one-sixth of the catalyst surface was under direct irradiation at any reaction time. Since the surface area of the better performing catalyst (TiO_2-SH) was 73.1 m^2 g^{-1}; the total exposed surface of the 5.0 mg used was calculated to be 609.167 cm^2, then it was approximated that the average incident radiation power on the TiO_2-2 was 426.42 mW.

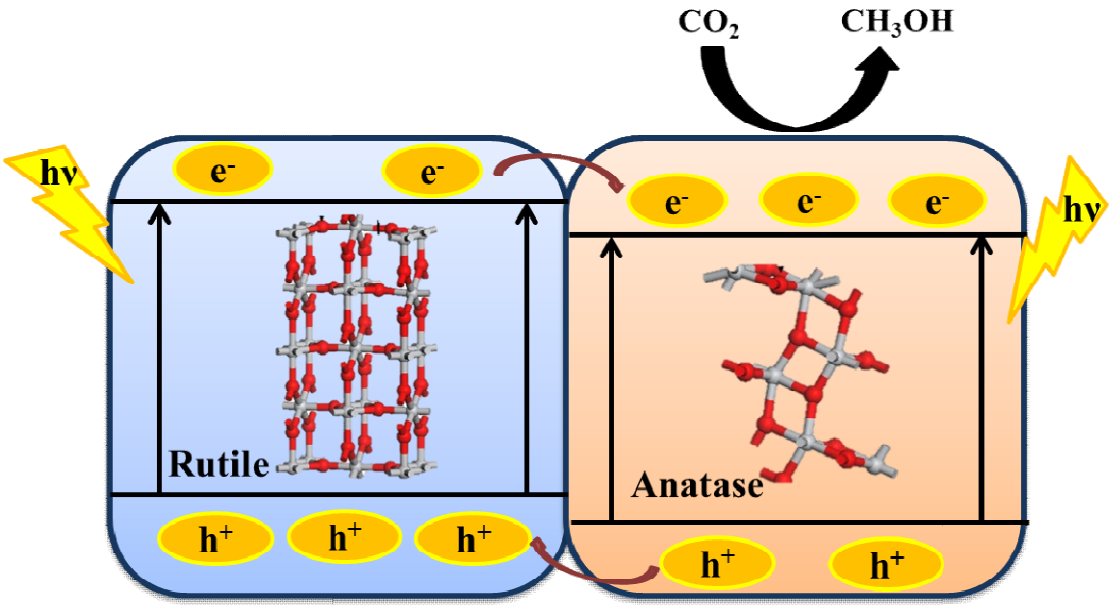

Scheme 4.1. Schematic presentation of activation of small molecules and products formation at the surface of TiO_2-S and TiO_2-SH catalysts.

The methanol production rate revealed that TiO_2-SH was more efficient for the photoreduction of CO_2 (Figure 4.28). In particular, the maximum rate of methanol production observed with TiO_2-SH was 1.97 mmol g^{-1} h^{-1} (26.95 μmol m^{-2} h^{-1}). The rough estimation of the quantum efficiency (QE) was calculated by the equation below:

$$\mathrm{QE}(\Phi) = \frac{\text{Total number of methanol molecules produced in a unit of time}(n_e)}{\text{Total number of photons incident on the catalyst }(n_p)}\ x\ 100 \ldots\ldots\ldots 4.3$$

It should be noted that 6 electrons are required for the production of one methanol molecule. Hence, at the rate of 26.95 μmol m^{-2} h^{-1}, the total number of effective electrons involved per unit time was calculated as:

$$n_e = \frac{6 \times 26.95 \times 10^{-6} \times N}{60 \times 60}\ (electrons\ per\ sec) \ldots\ldots\ldots\ldots 4.4$$

Where N is the Avogrados number. Therefore n_e = 0.2705 × 10^{17} electrons/s. Since the average incident power on the catalyst was 426.42 mW (0.42642 W), the number of incident photons per unit time was $n_p = 0.42642\lambda/hc$. Whereλ is the wavelength (around 365 nm); h is the Planck's constant and c is the speed of light. The value of n_p was therefore calculated as 7.825 x 10^{17} photons. Thus, the corresponding QE of methanol production was found to be 3.46%.

4.2 Synthesis of RGO-TiO_2 composites for the photoreduction of CO_2

TiO_2 Nanoparticles (TiO_2 NPs) and Reduced Graphene Oxide-TiO_2 (RGO-TiO_2) composites, code-named as TiO_2, 1.0RGO-TiO_2, 2.0RGO-TiO_2, 5.0RGO-TiO_2 and 10.0RGO-TiO_2,were prepared according to the method described in Section 3.3.1. The pure TiO_2 was white in colour while all RGO-TiO_2 samples were grey in colour. In addition to the physical techniques used for the characterisation of the mixed-phase TiO_2 (section 3.2.2), Thermal Gravimetric Analysis (TGA) and Raman spectroscopy were employed for the characterisation of TiO_2 NPs and RGO-TiO_2 nanocomposites.

4.2.1 X-ray diffraction characterisation of TiO_2 NPs and RGO-TiO_2 nanocomposites

The XRD images of the prepared pure TiO_2 and RGO-TiO_2 catalysts are depicted in Figure 4.29. For comparison, the XRD pattern of RGO was also shown.The XRD patternof pure RGO showed peaks at 2θ = 25.9° and 43.2°, corresponding to planes (0 0

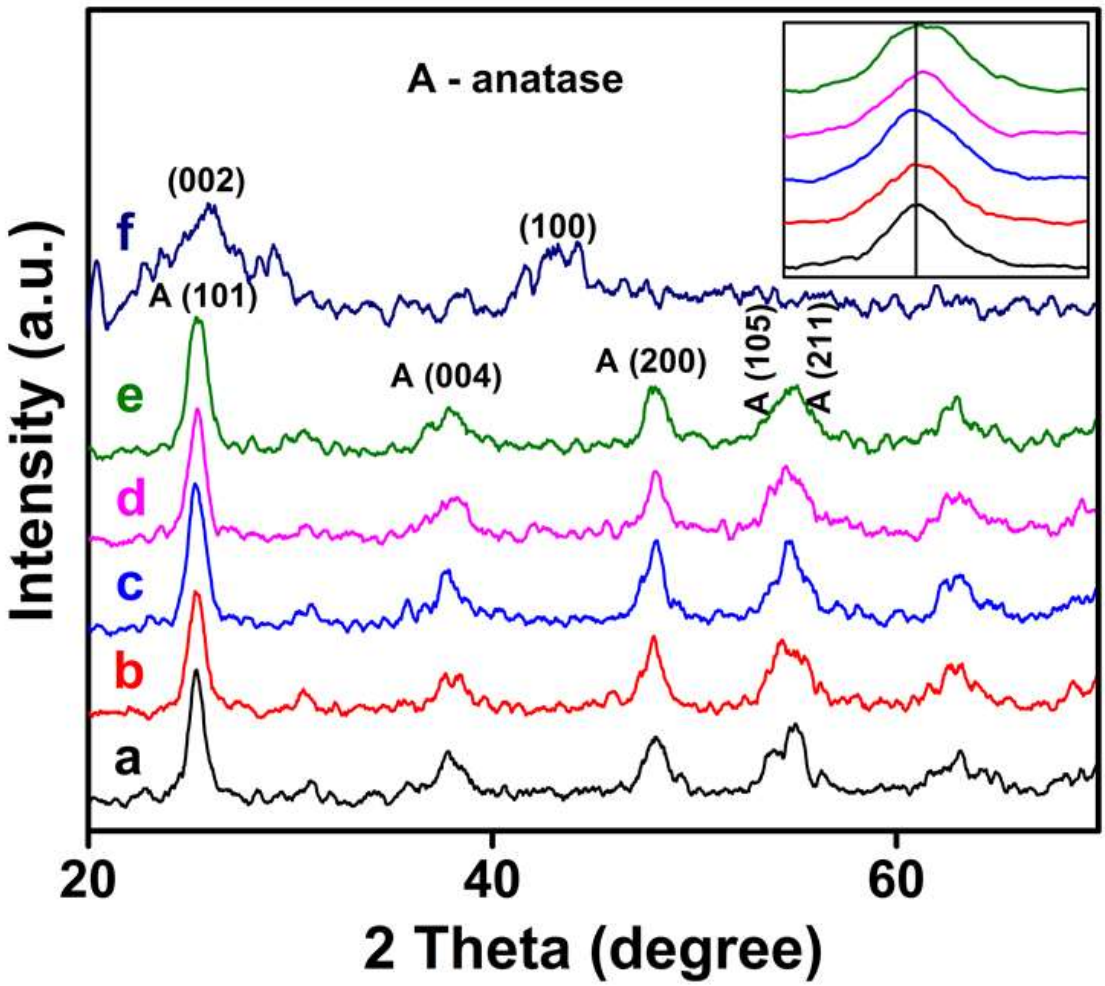

Figure 4.29 X-ray diffraction peaks of (a) pure TiO_2 (b) 1.0RGO-TiO_2 (c) 2.0RGO-TiO_2 (d) 5.0RGO-TiO_2 (e) 10.0RGO-TiO_2 and (f) RGO.

2) and (10 0). Peaks of the XRD patterns of TiO_2 and all RGO-TiO_2 catalysts were in good agreement with the tetragonal anatase TiO_2 (JCPDS 21-1272). No characteristic peaks of RGO were observed in all RGO containing TiO_2 catalysts, signifying that peaks in TiO_2 have overlapped the peaks in RGO. Notably, from Figure 4.29 (inset), the width of the significant anatase peak in TiO_2 became slightly broadened as the amount of RGO increased in RGO-TiO_2 composite. This broadening suggests that the crystalline size of TiO_2 changed with the introduction of RGO. The crystalline sizes of TiO_2 and RGO-TiO_2 nanocomposites were calculated from the half-width of the peak (1 0 1) using the Scherrer's formula as shown in Table 4.5. The crystalline size of the pure TiO_2 was found to be 16 nm; however, the crystalline sizes of TiO_2 in the nanocomposites decreased gradually from 14 nm to 12 nm.

4.2.2 Surface area and UV-Vis. diffuse reflectance spectroscopy characterisation of TiO_2 NPs and RGO-TiO_2 nanocomposites

The BET surface area of the prepared TiO_2 and all RGO-containing samples are shown in Table 4.5. The surface area of pure TiO_2 was found to be 108.3 $m^2 g^{-1}$; however, an increase in surface area was observed for all samples with RGO. In comparison with pure TiO_2, increasing and widening of the hysteresis loop was observed with an increased amount of RGO in the nanocomposites as shown by the N_2 adsorption-desorption isotherm(Figure 4.30). Sample with maximum RGO content showed the presence of macropores as revealed by a steep rise in hysteresis at $P/P_0 = 0.99$. The mesopore-size maxima shifted from 7.5 nm to 6.7 nm except for 5.0RGO-TiO_2, as shown by the pore size distribution curve in Figure 4.31. This showed that the pores were distributed in a narrow range of mesopores at higher RGO content. Both Figure 4.30 (hysteresis loop) and Figure 4.31 (pore size distribution curve) confirmed that the pore-size range had increased after the incorporation of RGO. This observation may help in the smooth diffusion of molecules. Cumulative pore volume also showed the higher volume of pores for thehigher RGO content in the nanocomposites, in comparison with nanocomposites with lower RGO content (Figure 4.32).

To investigate the change in absorption properties of the prepared catalysts, the UV–Vis. DRS spectra of TiO_2 and RGO-TiO_2were obtained as shown in Figure 4.33. The absorption edge of TiO_2, which was determined by the extrapolation of the linear part of

Table 4.5 Physico-chemical properties of the pure TiO_2 and RGO-TiO_2 samples.

Type of catalyst	Crystalline size (nm)	Surface area (m^2/g)	Pore volume (cm^3/g)	Pore Maxima (nm)
TiO_2	16.0	108.3	0.25	7.5
1.0RGO-TiO_2	14.3	111.2	0.25	6.9
2.0RGO-TiO_2	14.1	119.9	0.28	7.0
5.0RGO-TiO_2	14.9	115.2	0.25	7.5
10.0RGO-TiO_2	11.9	128.62	0.27	6.7

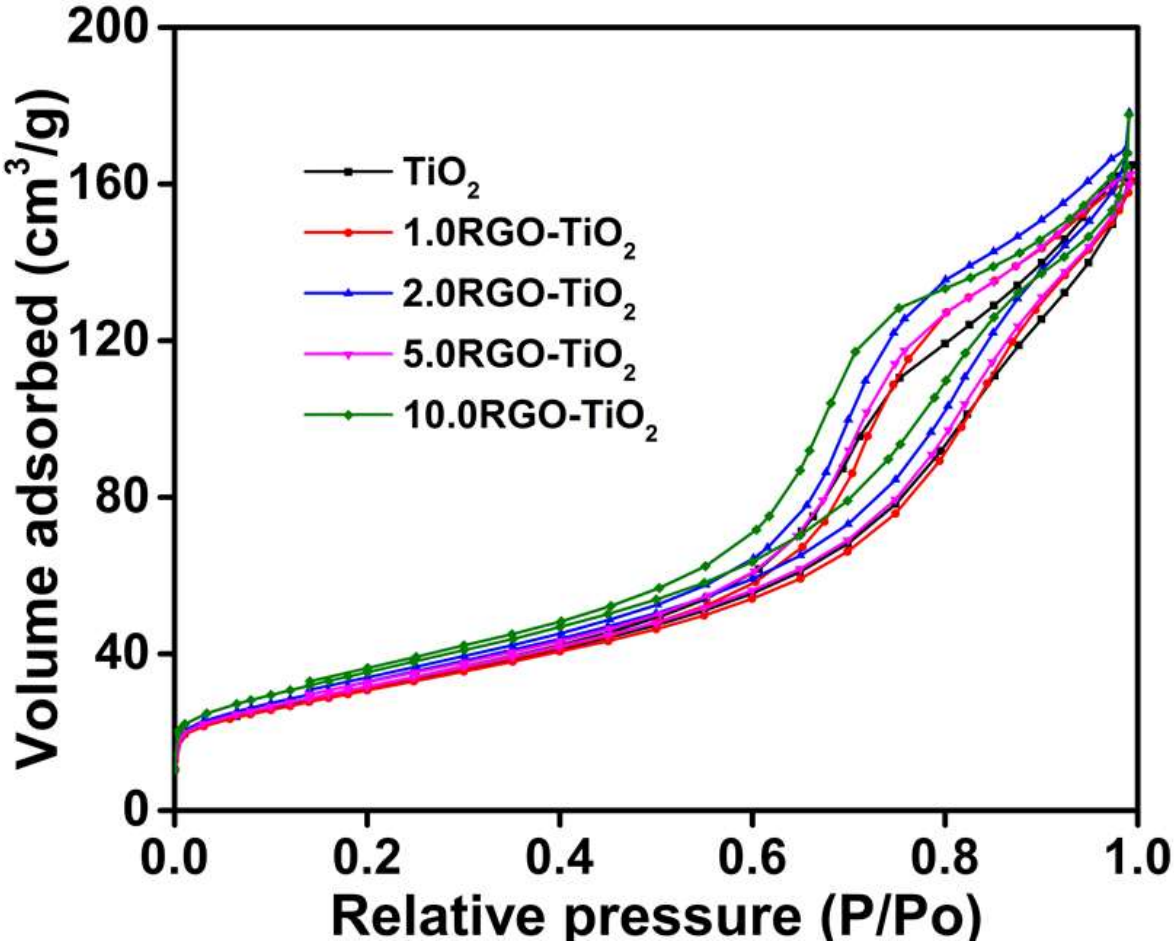

Figure 4.30 N_2 adsorption-desorption isotherms of pure TiO_2 and RGO-TiO_2 samples.

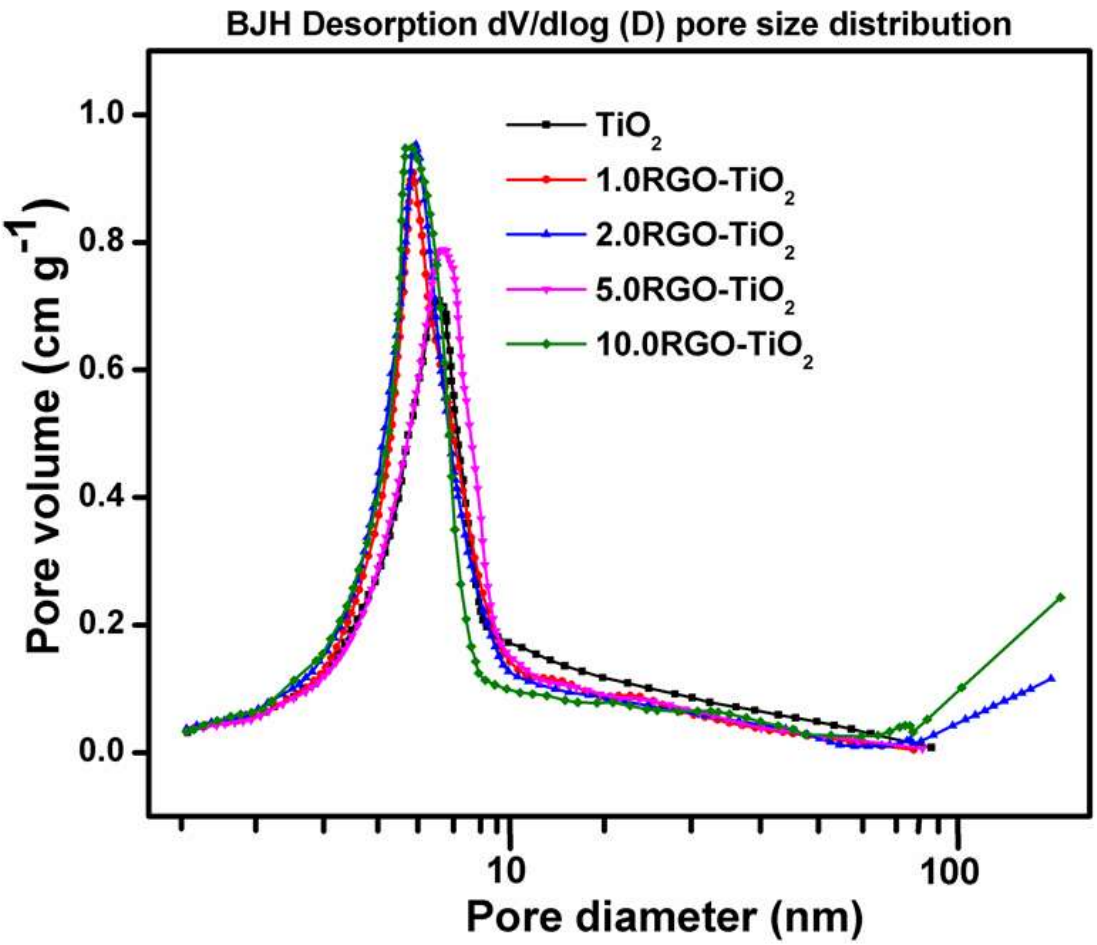

Figure 4.31 Pore size distribution curve of pure TiO_2 and RGO-TiO_2 samples.

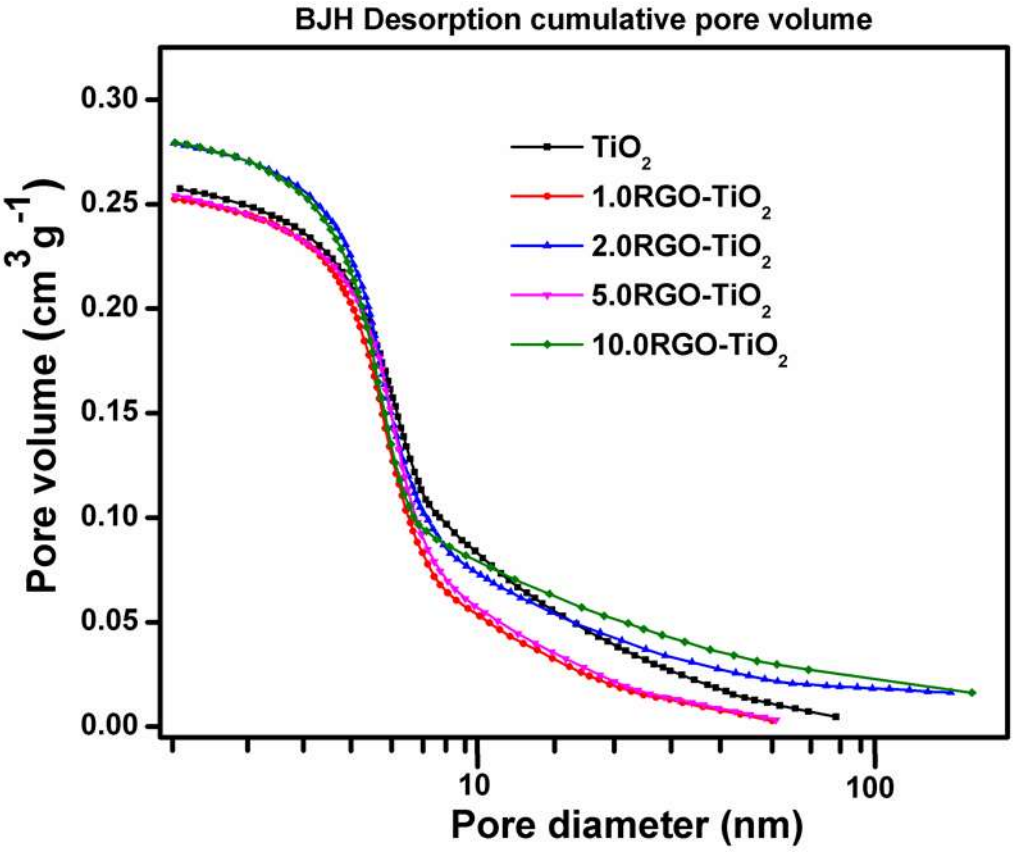

Figure 4.32 Desorption cumulative pore volume curve of pure TiO_2 and RGO-TiO_2 samples.

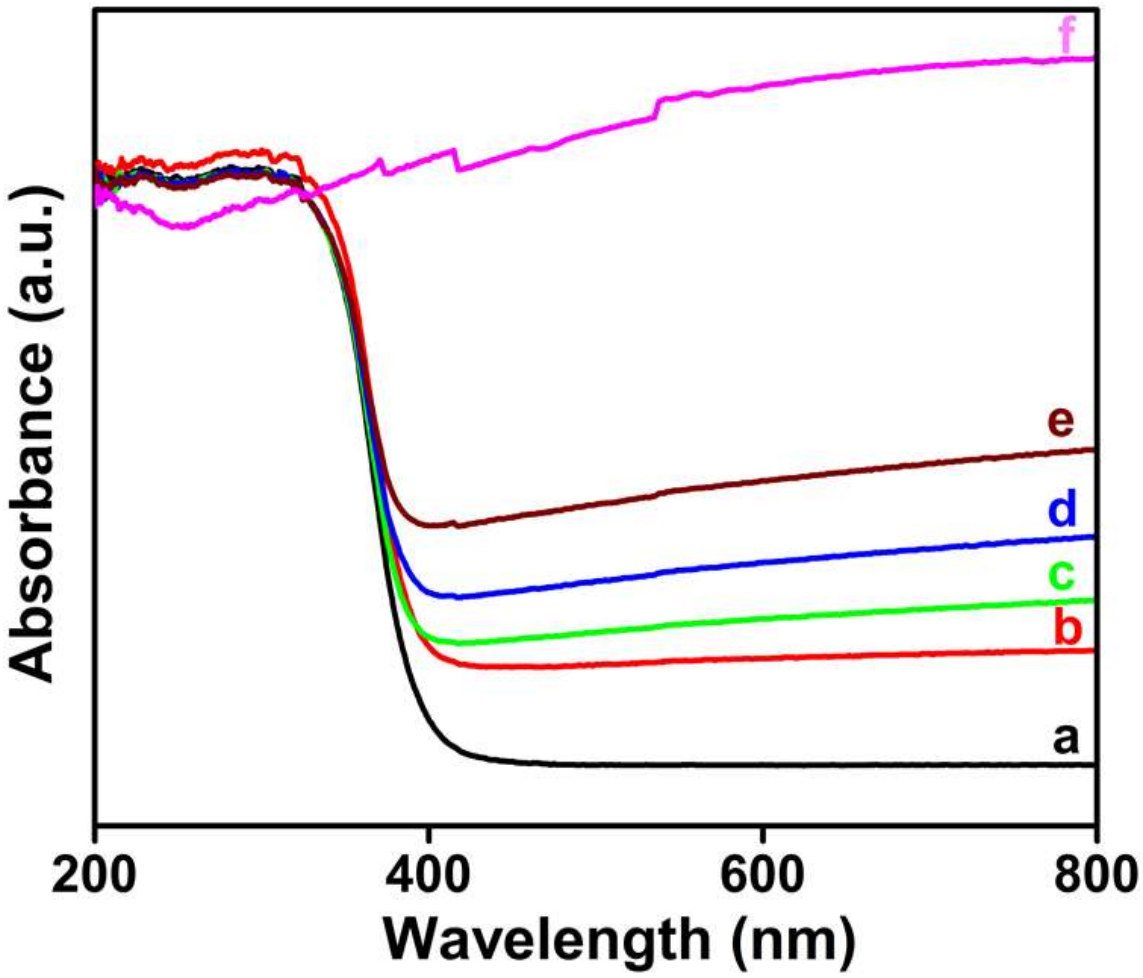

Figure 4.33 UV-Vis spectra of (a) pure TiO_2 (b) 1.0RGO-TiO_2 (c) 2.0RGO-TiO_2 (d) 5.0RGO-TiO_2 (e) 10.0RGO-TiO_2 and (f) RGO samples.

the plot to the horizontal axis, was found to be 392 nm. It was observed that the introduction of RGO into TiO_2 caused a red shift to a longer wavelength in the absorption edge of TiO_2. The intensity of light absorption in the UV region decreased with increasing amount of RGO in the RGO-TiO_2 composites. This trend has been attributed to the reduction in the energy of excited photons, charge-transfer transitions, band gap narrowing, the formation of Ti–O–C bonds and the direct interaction between TiO_2 and RGO (Wang *et al.,* 2015; Wang *et al.,* 2013a; Nguyen-Phan *et al.,* 2014; Sher-Shah *et al.,* 2012). The optical band gap energies of the prepared catalysts were determined from the Tauc plot of $[F(R)hv]^{1/2}$ versus the photon energy via the intercept of the tangent to the x-axis (Jaiswal *et al.,* 2015). As shown in Figure 4.34, the band gap of TiO_2 was calculated to be 3.2 eV while energies of 1.0RGO-TiO_2, 2.0RGO-TiO_2, 5.0RGO-TiO_2 and 10.0RGO-TiO_2 were found to be 3.0, 3.0, 2.9, and 2.9 eV respectively.

4.2.3 Scanning electron microscopy and transmission electron microscopy characterisation of TiO_2 NPs and RGO-TiO_2 nanocomposites

The SEM images of the prepared TiO_2, 1.0RGO-TiO_2, 2.0RGO-TiO_2, 5.0RGO-TiO_2 and 10.0RGO-TiO_2 are shown in Figure 4.35 – 4.39. Agglomerations were observed with all samples as a result of the interaction of small particles. These agglomerations became lessened with an increase in the amount of RGO in TiO_2. The SEM-EDX images revealed the presence of Ti and O elements in pure TiO_2 as shown in Figure 4.40. In addition to Ti and O, SEM-EDX images of 1.0RGO-TiO_2, 2.0RGO-TiO_2, 5.0RGO-TiO_2 and 10.0RGO-TiO_2 catalysts revealed the presence of C (Figure 4.41 – 4.44).

To further understand the morphologies and crystal characteristics of the prepared TiO_2 NPs and all RGO-containing TiO_2, TEM analyses were performed. As shown in Figure 4.45, the TiO_2 catalyst was spherical in shape while the pure RGO had a sheet-like shape (Figure 4.46). Figure 4.47 – 4.50 showed the wrapping of the RGO sheet with theTiO_2 NPs in the nanocomposites. These wrappings became enhanced as the amount of RGO increased with TiO_2. The HRTEM images of all the samples are shown in Figure 4.51 – 4.56. The d-spacing of 0.342 nm was observed with TiO_2 and RGO-containing samples, which is consistent with anatase (1 0 1) plane of TiO_2 (Figure 4.52 – 4.56). The unchanged d-spacing suggests that RGO had little influence on the crystal phase of TiO_2, affirming that the RGO sheets were successfully wrapped over the TiO_2 NPs. The

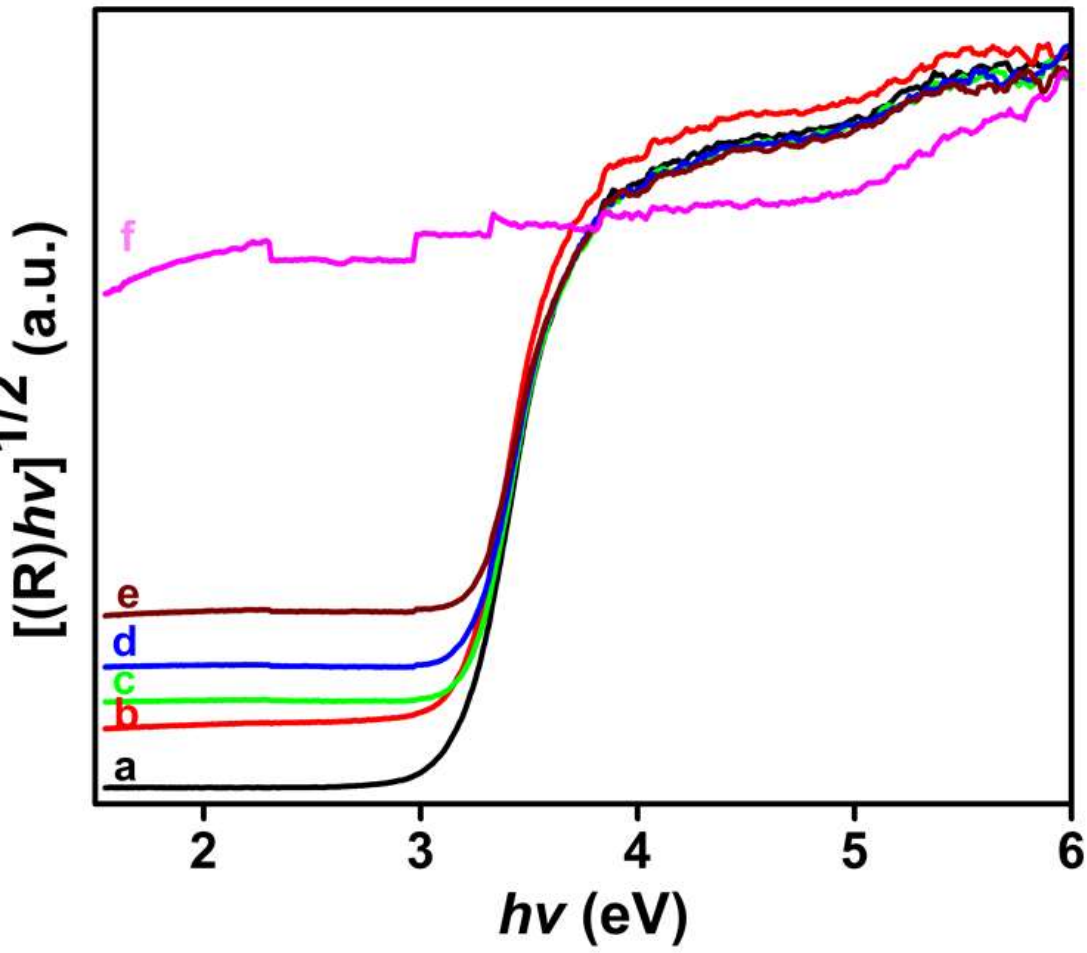

Figure 4.34 Tauc plot of (a) pure TiO_2 (b) 1.0RGO-TiO_2 (c) 2.0RGO-TiO_2 (d) 5.0RGO-TiO_2 (e) 10.0RGO-TiO_2 and (f) RGO samples.

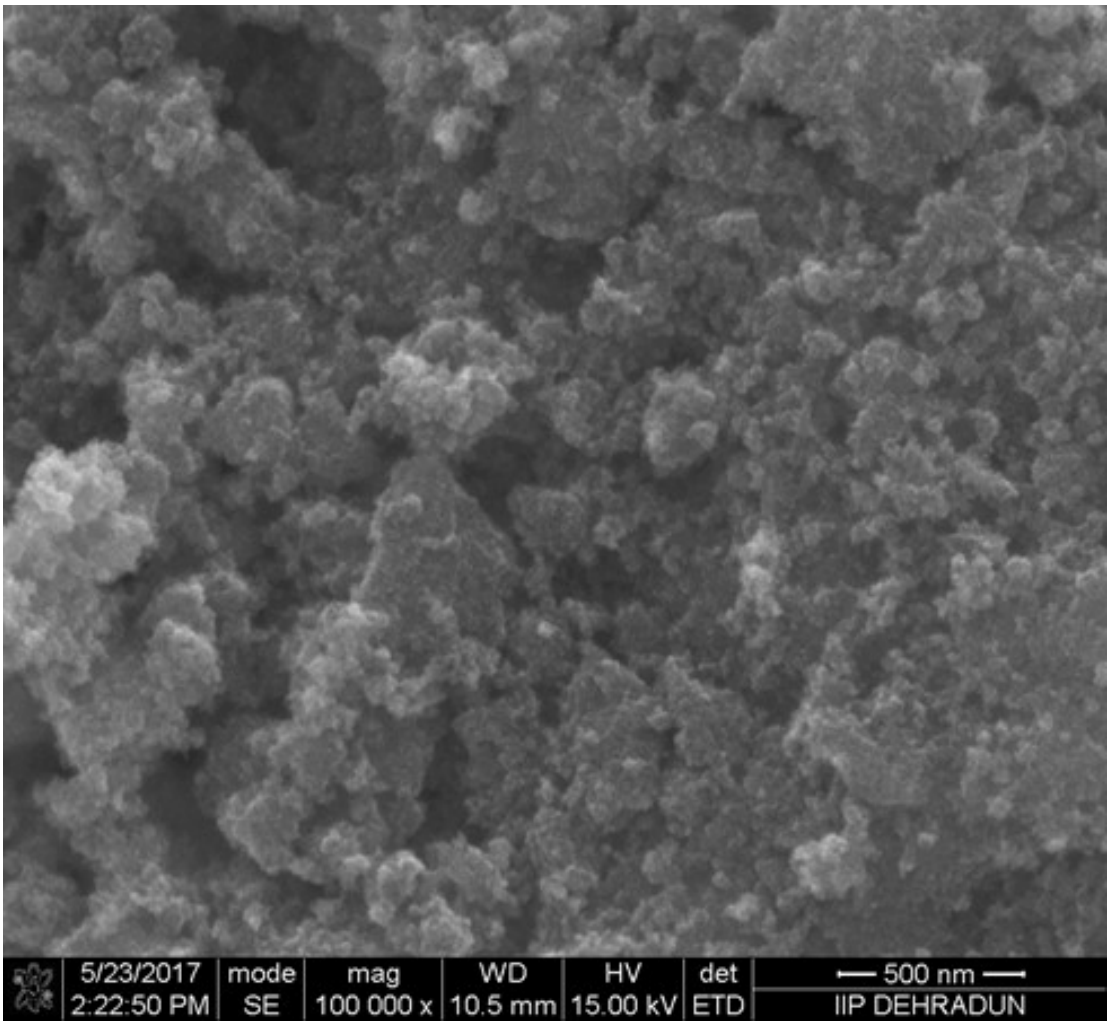

Figure 4.35 Scanning electron microscopy images of TiO_2 photocatalyst.

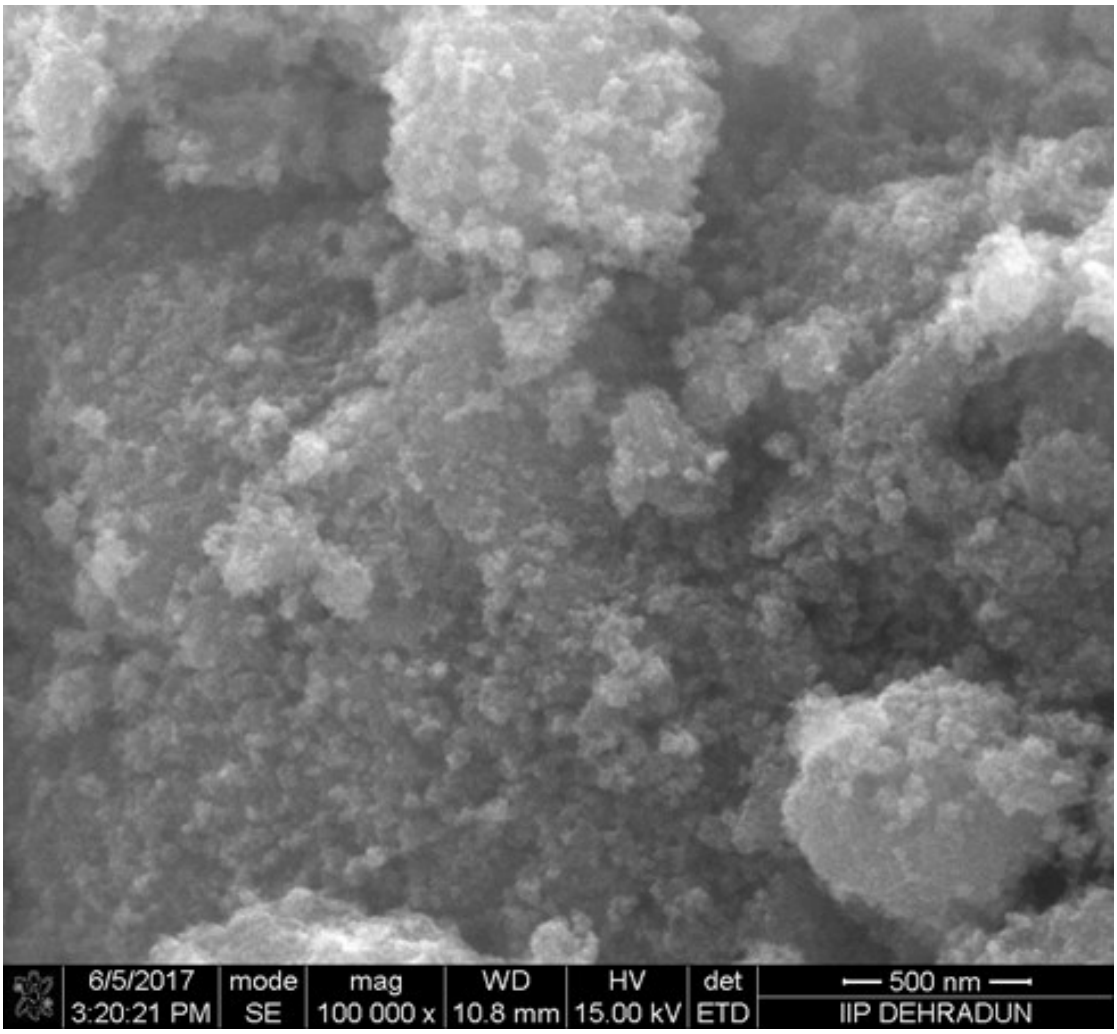

Figure 4.36 Scanning electron microscopy images of 1.0RGO-TiO_2 photocatalyst.

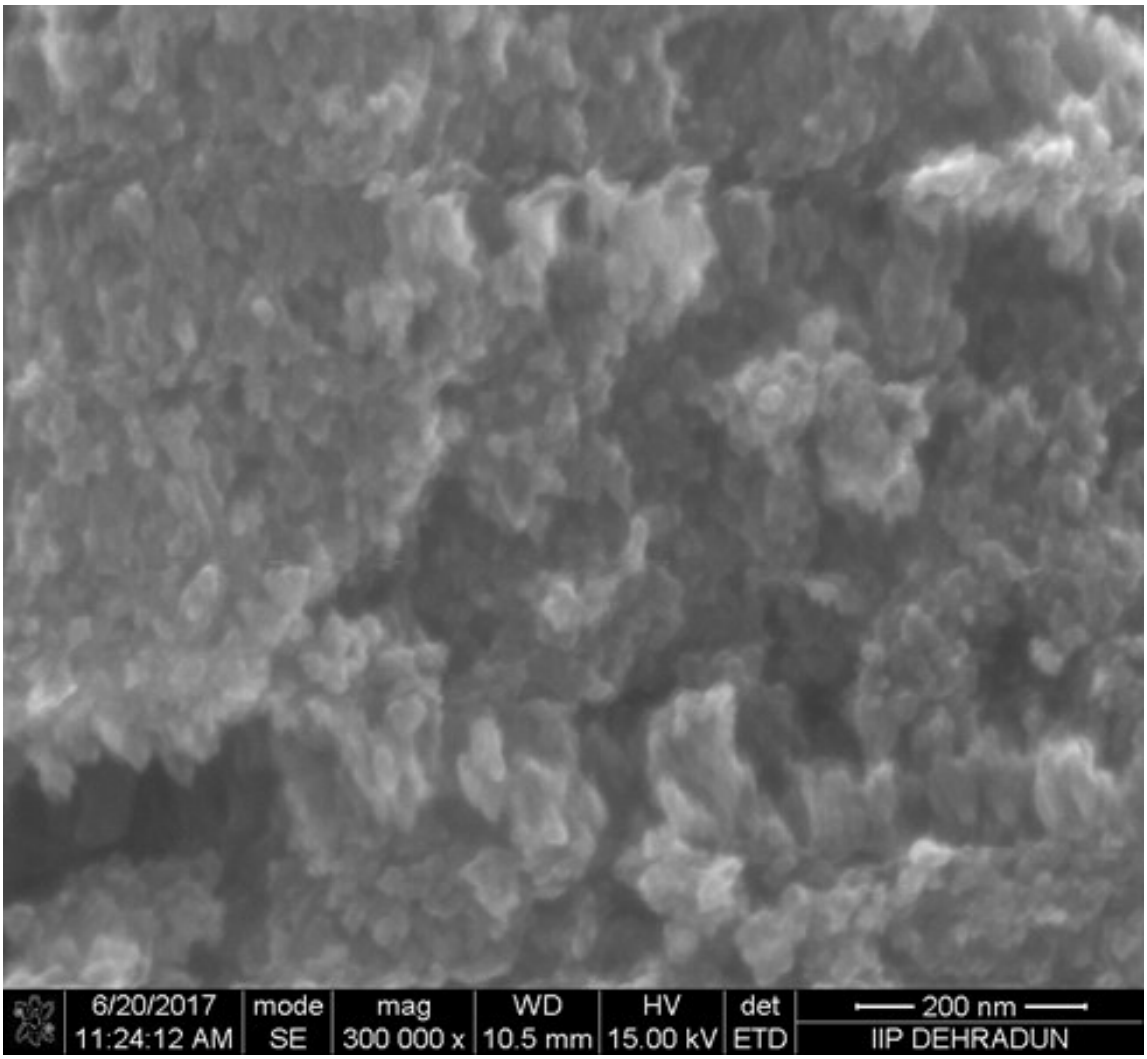

Figure 4.37 Scanning electron microscopy images of 2.0RGO-TiO_2 photocatalyst.

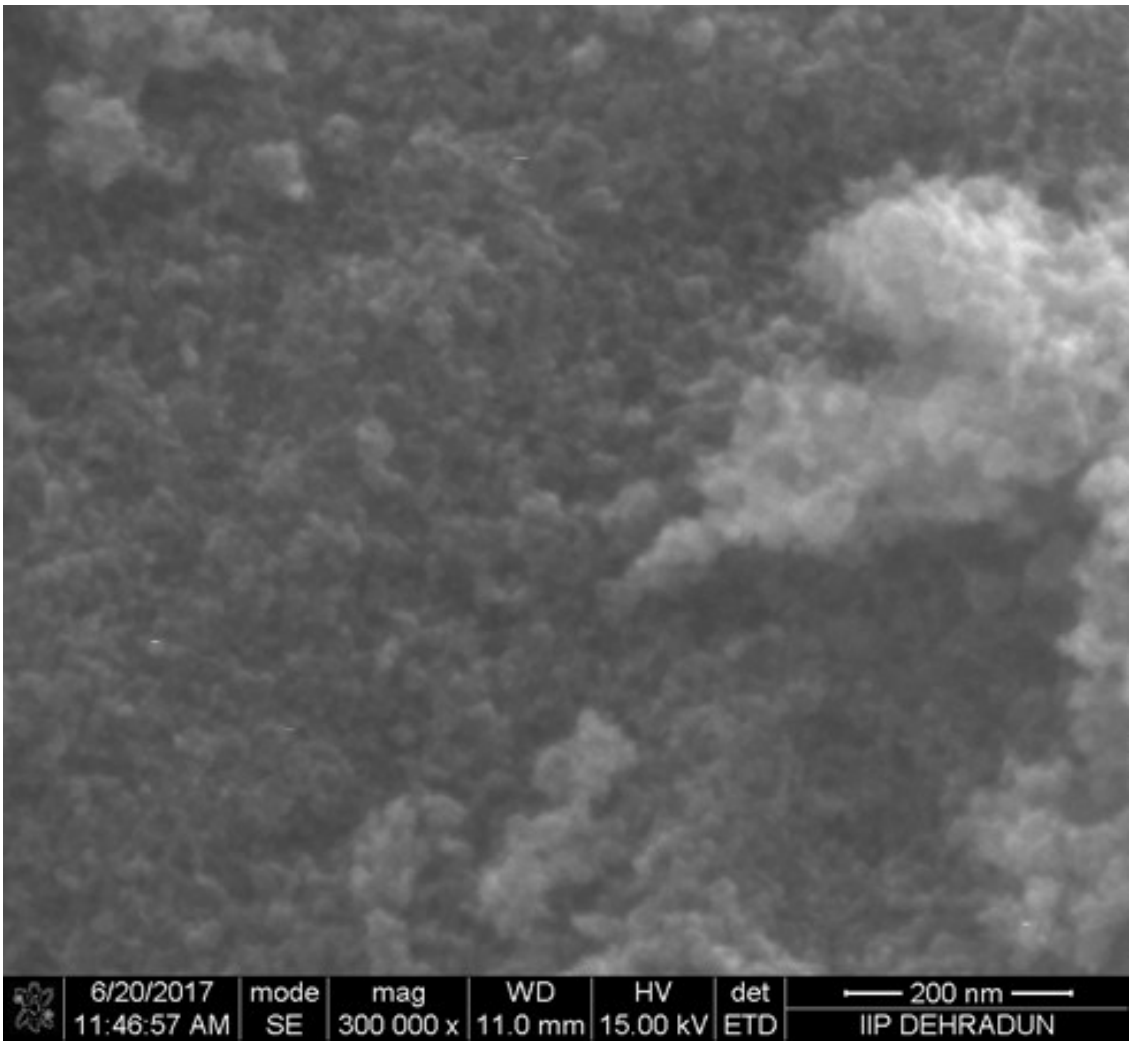

Figure 4.38 Scanning electron microscopy images of 5.0RGO-TiO_2 photocatalyst.

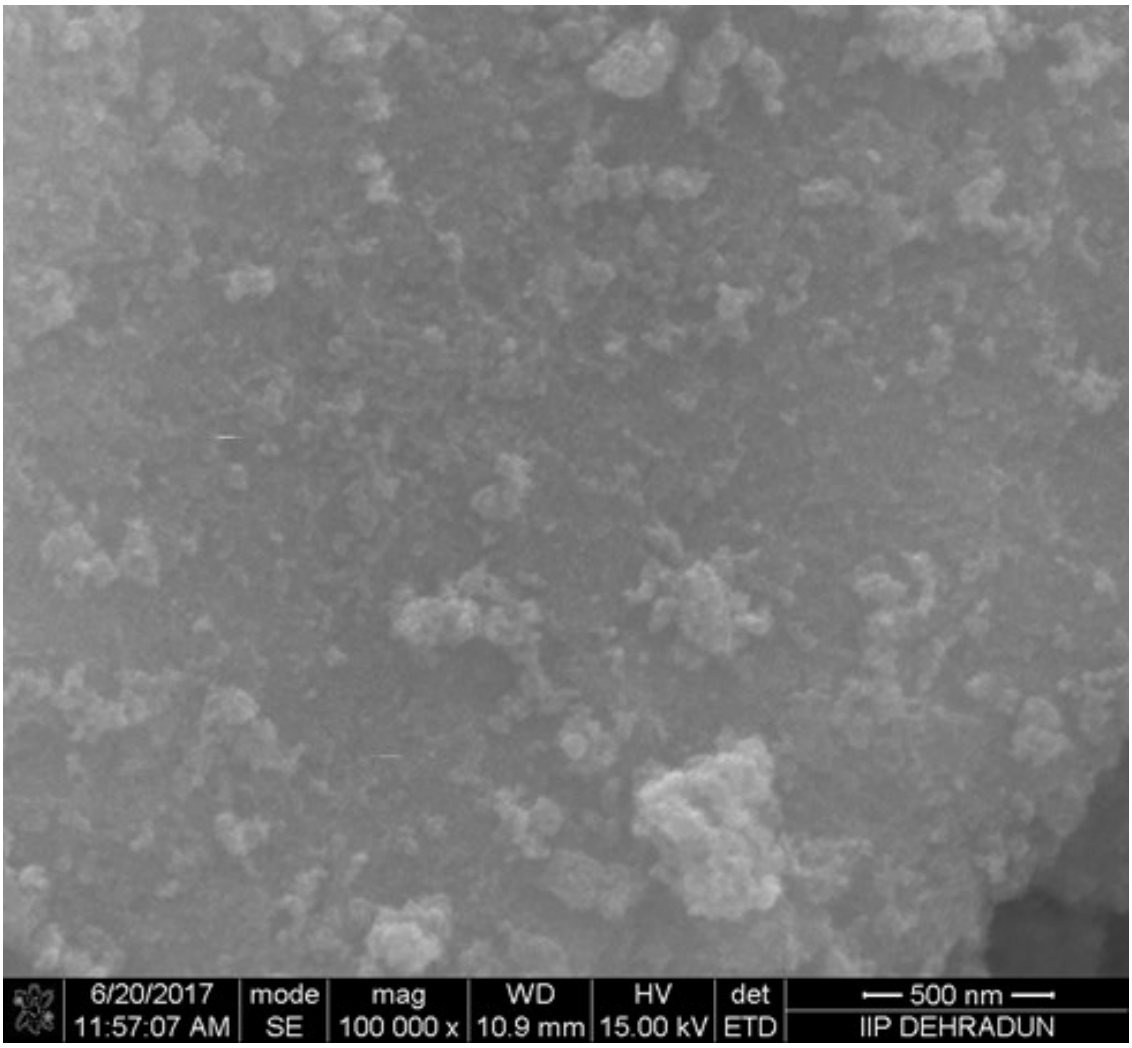

Figure 4.39 Scanning electron microscopy images of 10.0RGO-TiO_2 photocatalyst.

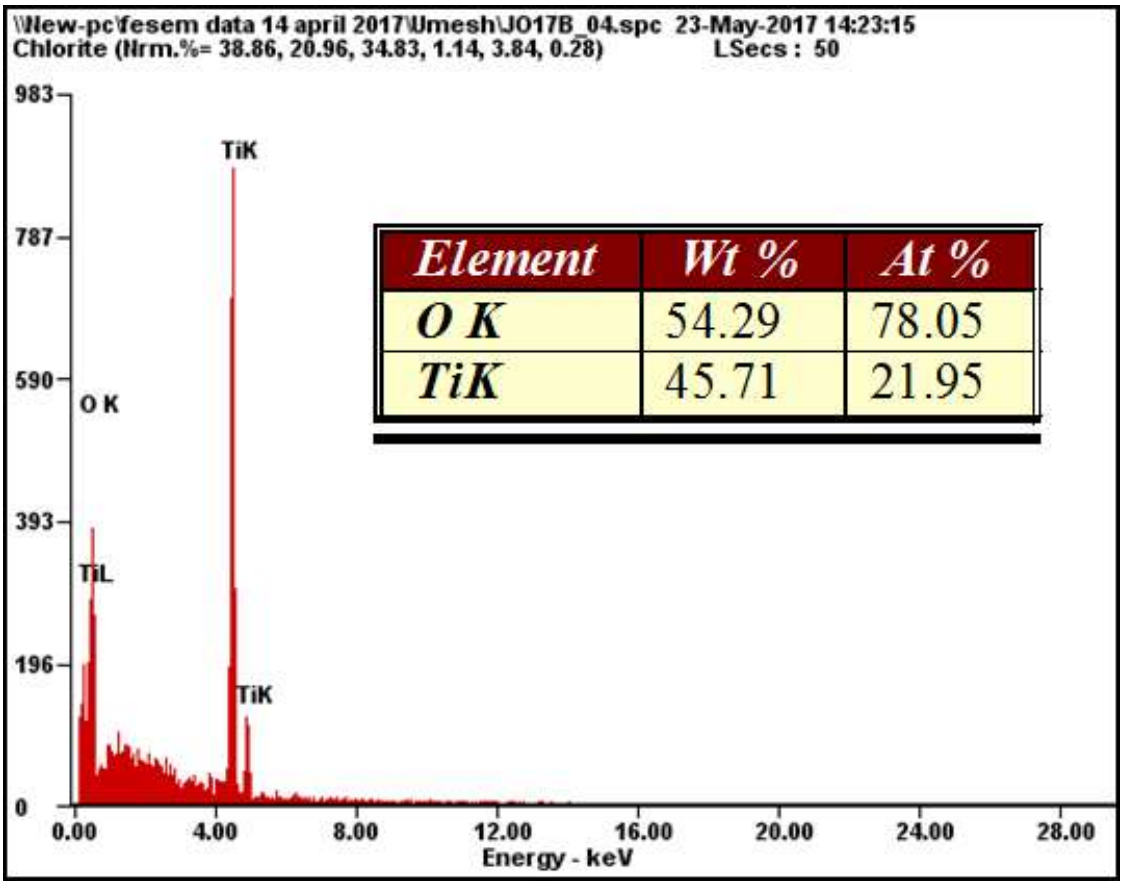

Figure 4.40 Energy-dispersive X-ray spectroscopy image of TiO_2 photocatalyst.

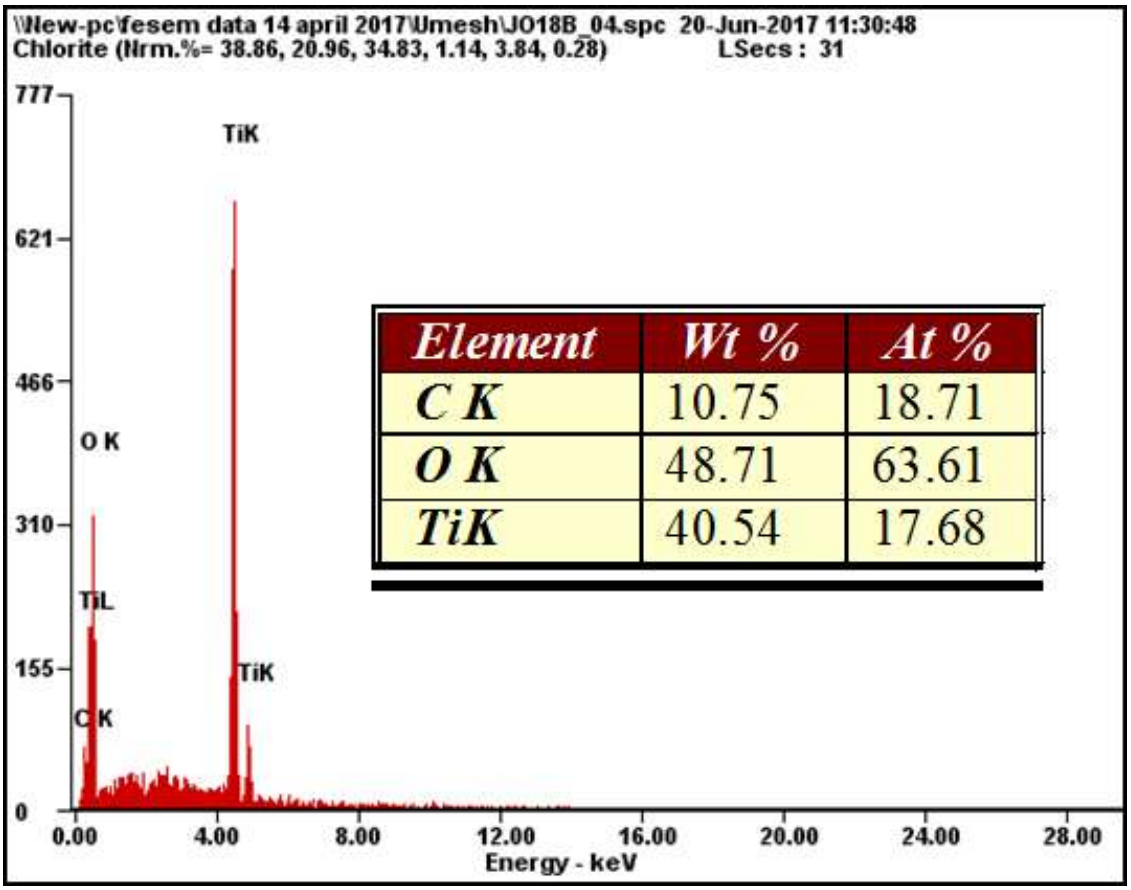

Figure 4.42 Energy-dispersive X-ray spectroscopy image of 1.0RGO-TiO_2 photocatalyst.

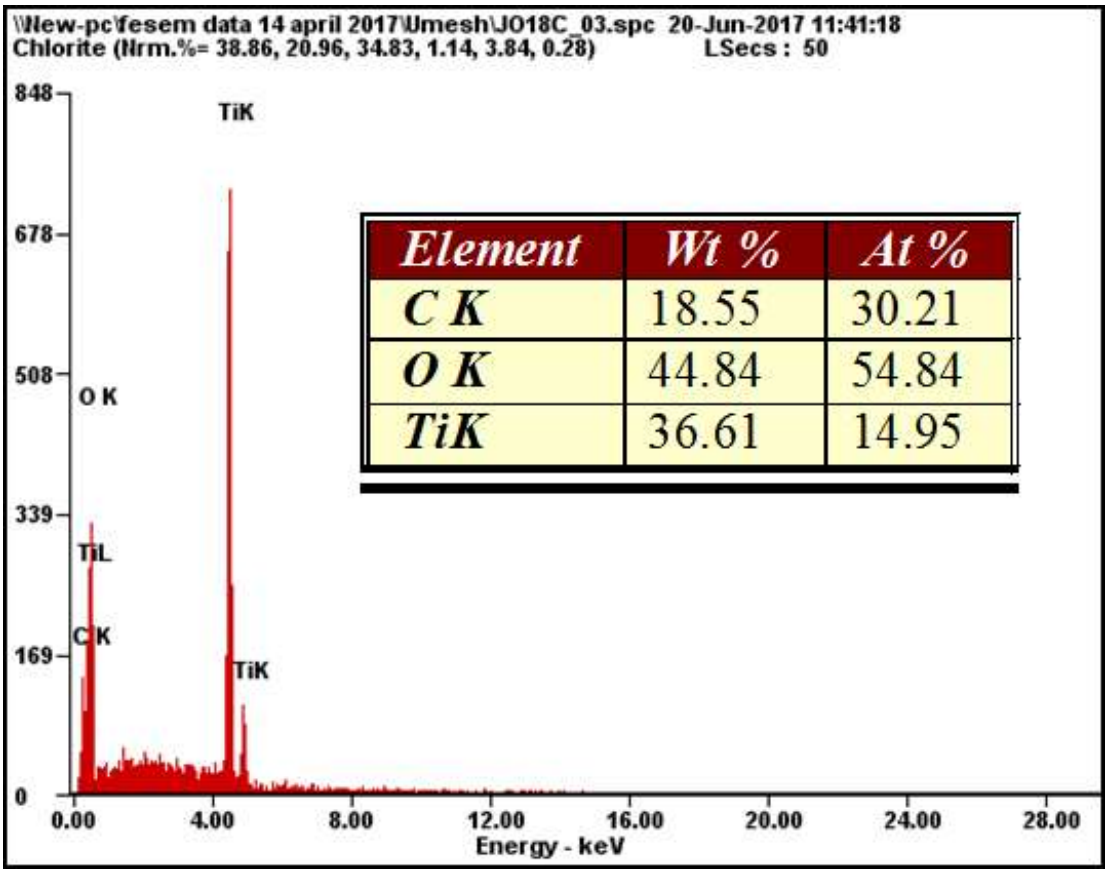

Figure 4.43 Energy-dispersive X-ray spectroscopy image of 2.0RGO-TiO_2 photocatalyst.

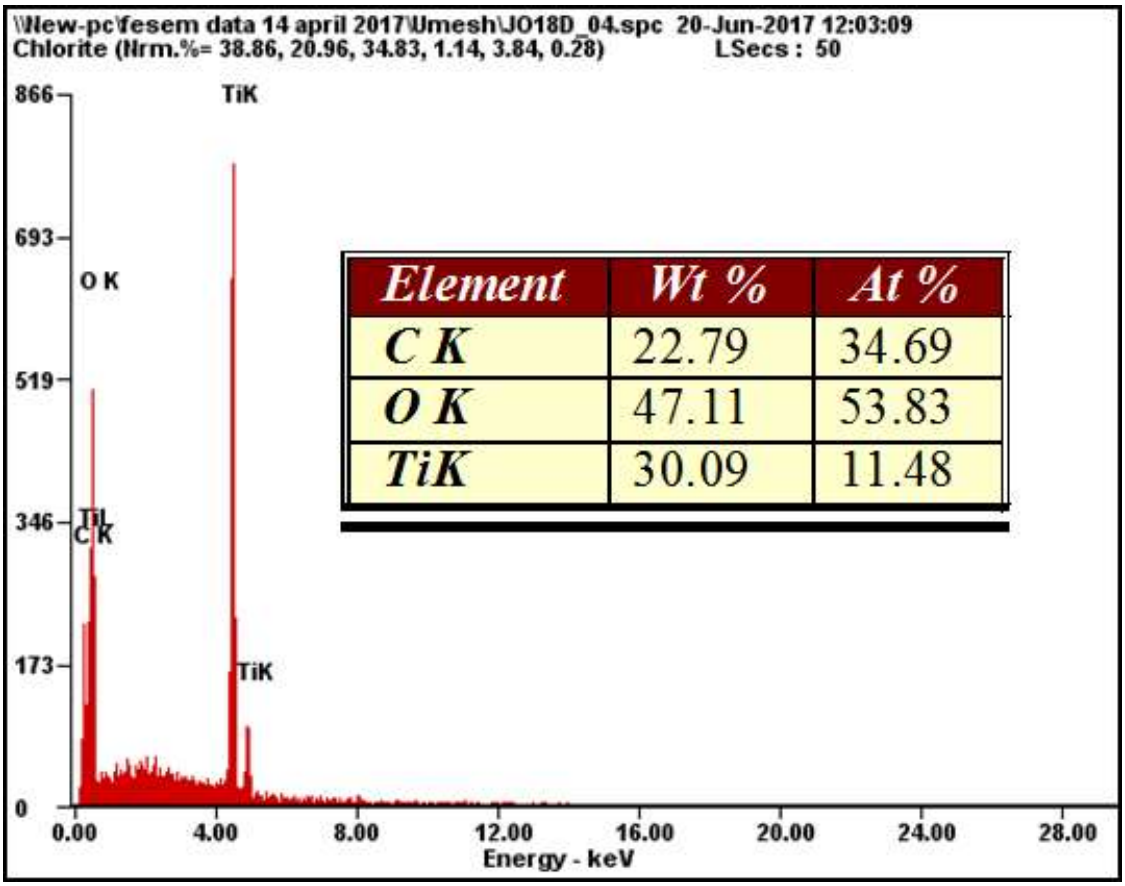

Figure 4.44 Energy-dispersive X-ray spectroscopy image of 5.0RGO-TiO_2 photocatalyst.

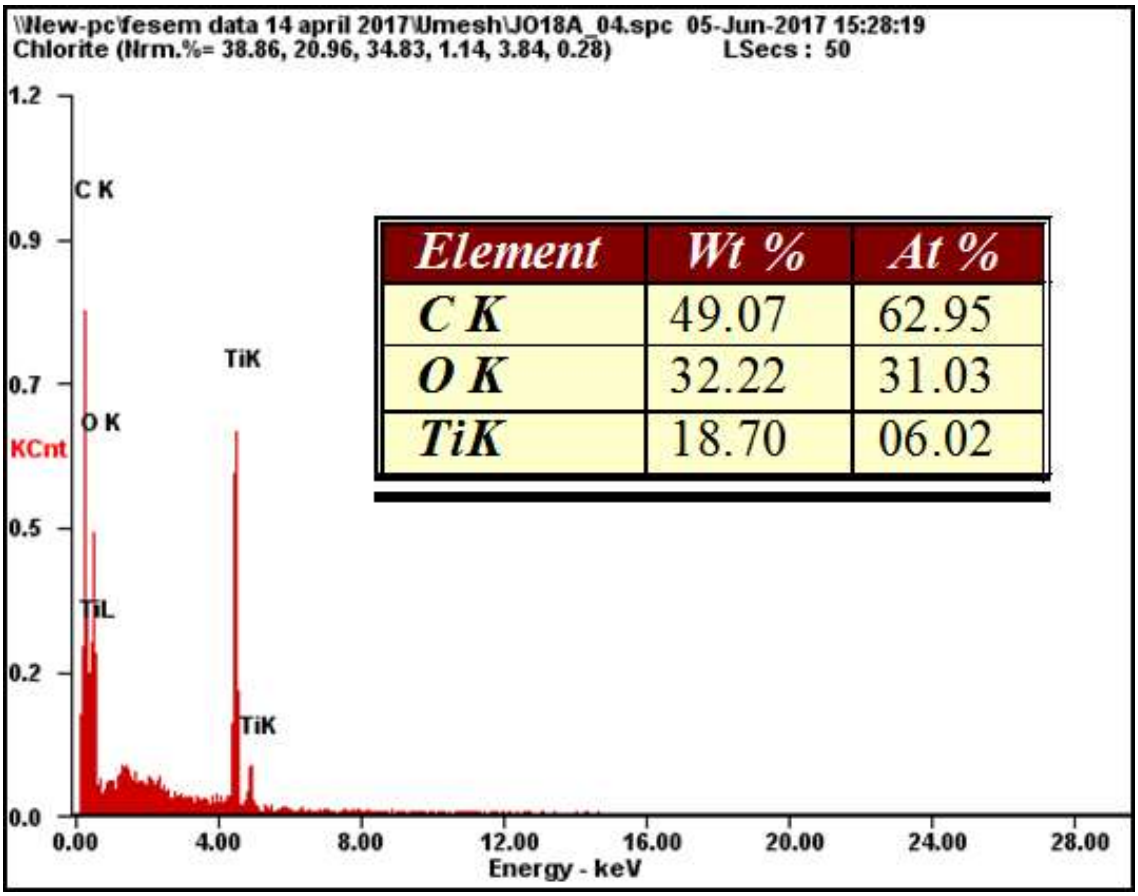

Figure 4.41 Energy-dispersive X-ray spectroscopy image of 10.0RGO-TiO_2 photocatalyst.

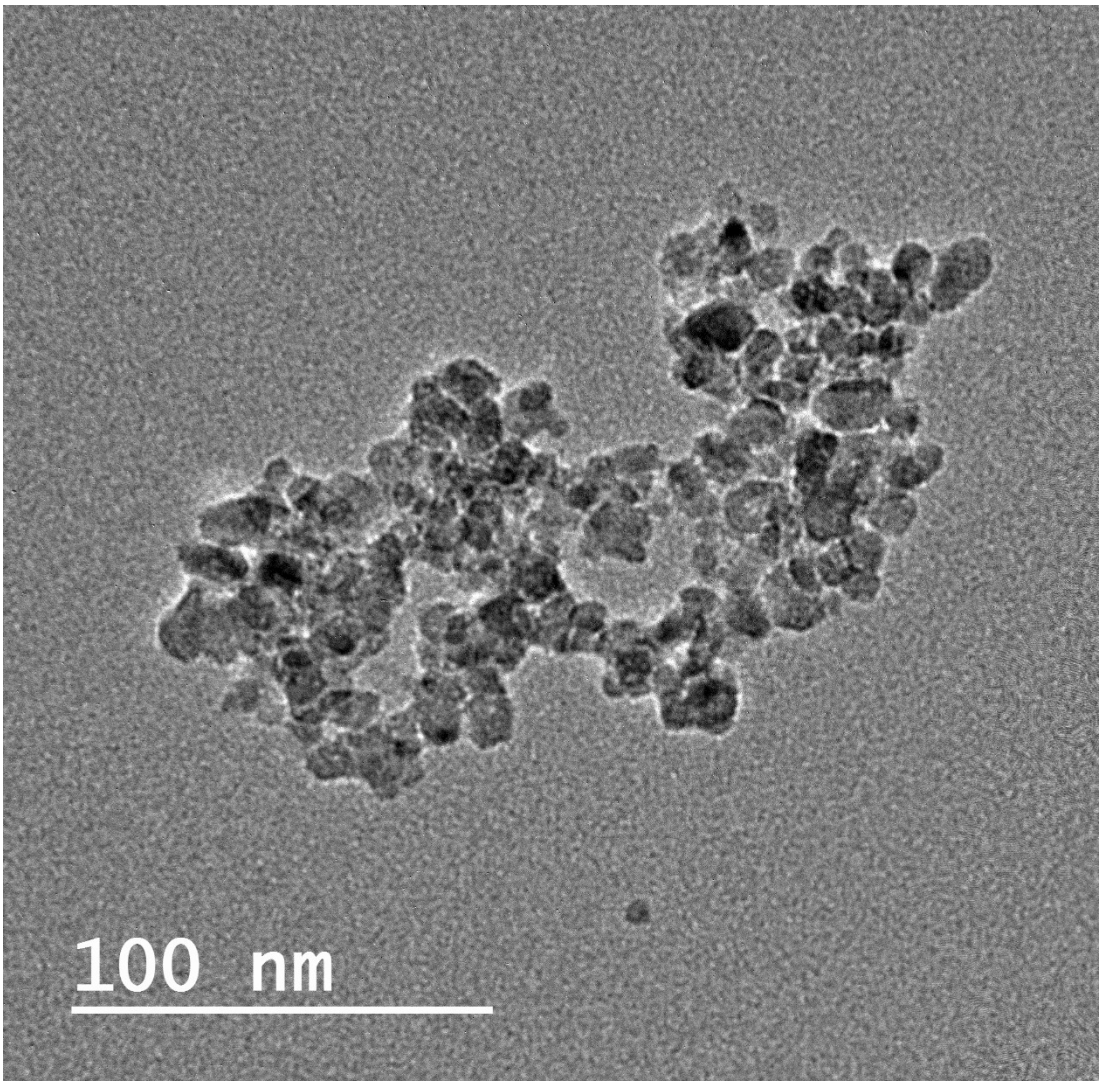

Figure 4.45 Transmission electron microscopy image of TiO_2 photocatalyst.

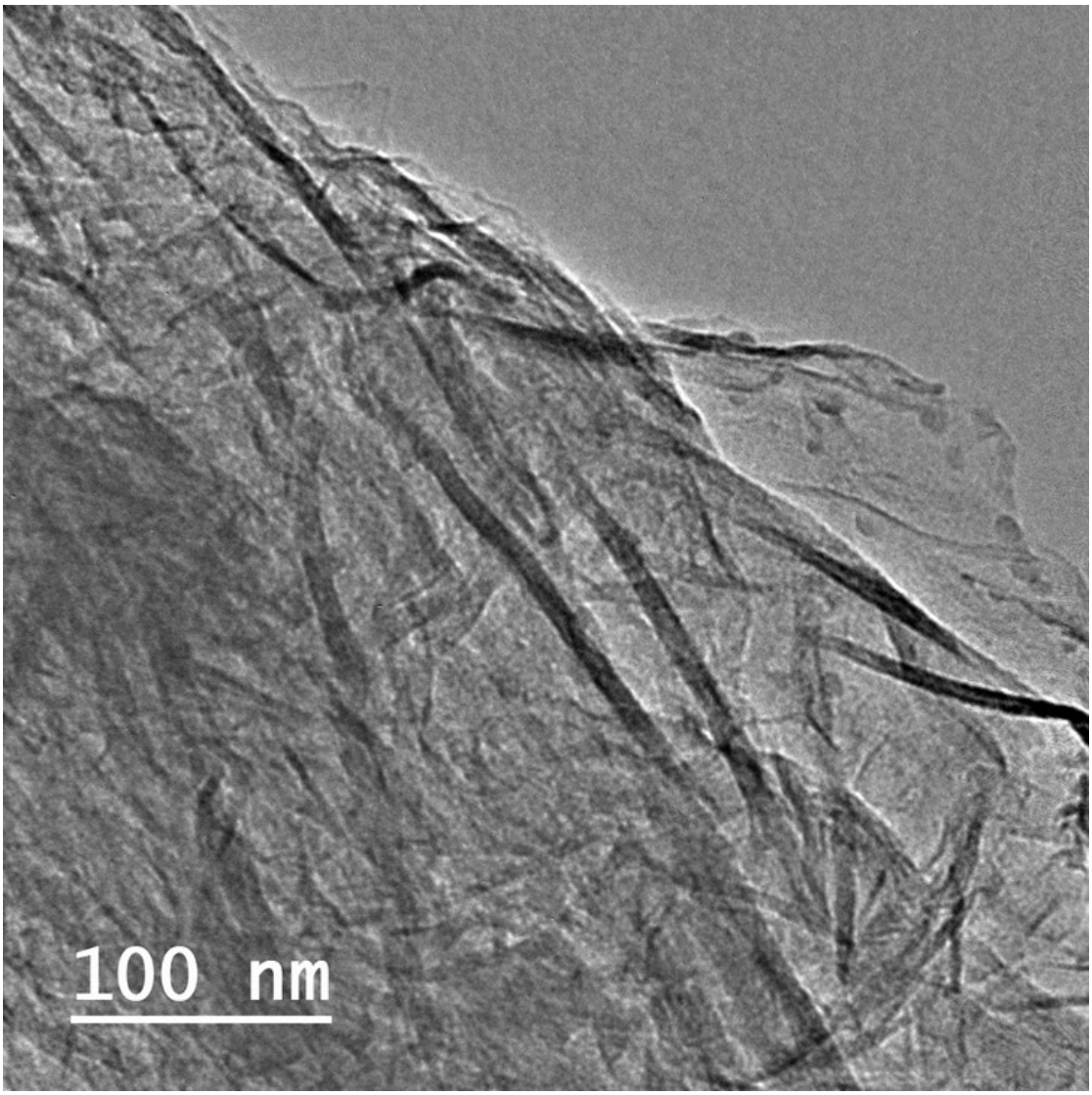

Figure 4.46 Transmission electron microscopy image of RGO sample.

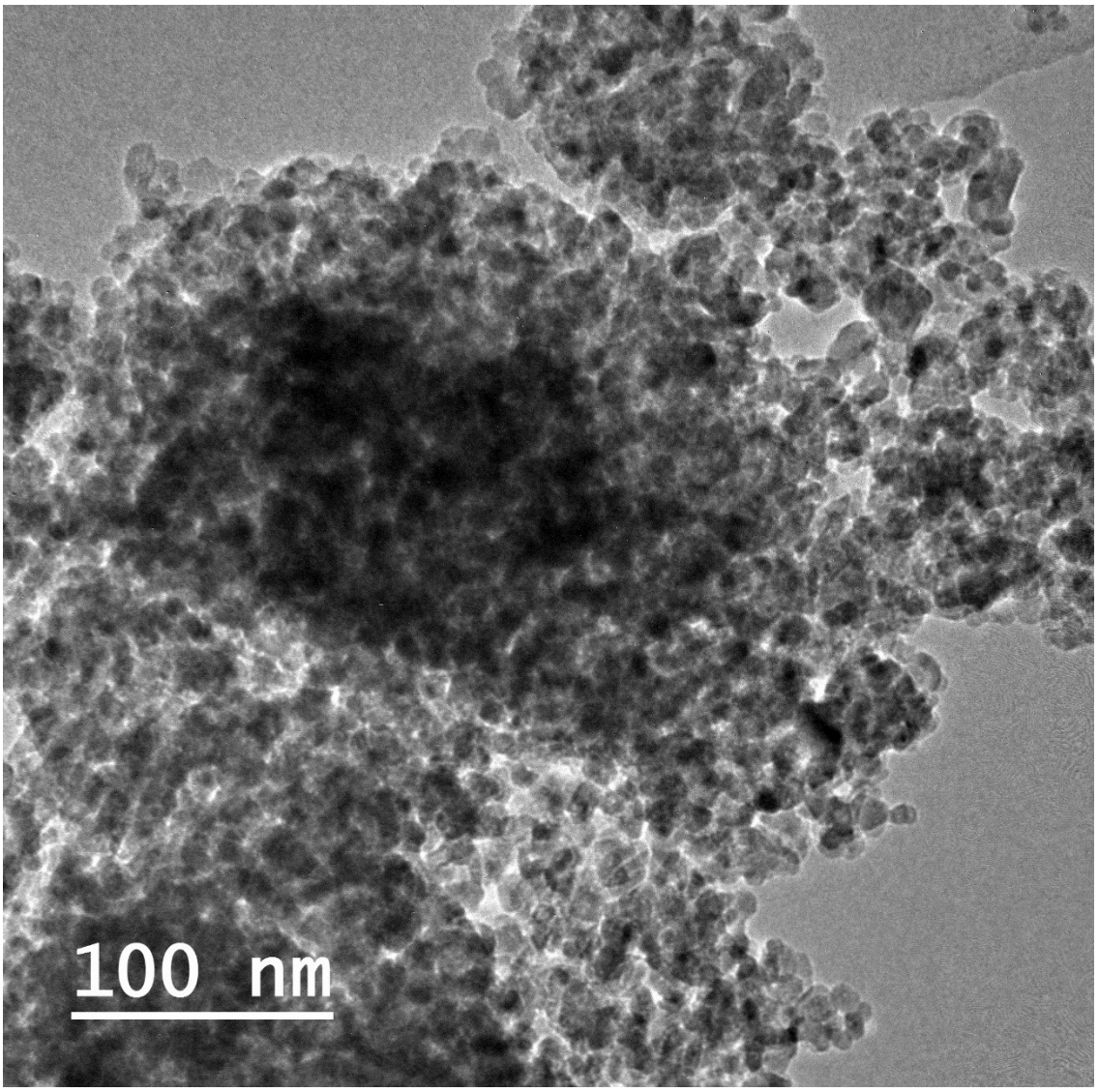

Figure 4.47 Transmission electron microscopy image of 1.0-RGO-TiO_2 photocatalyst.

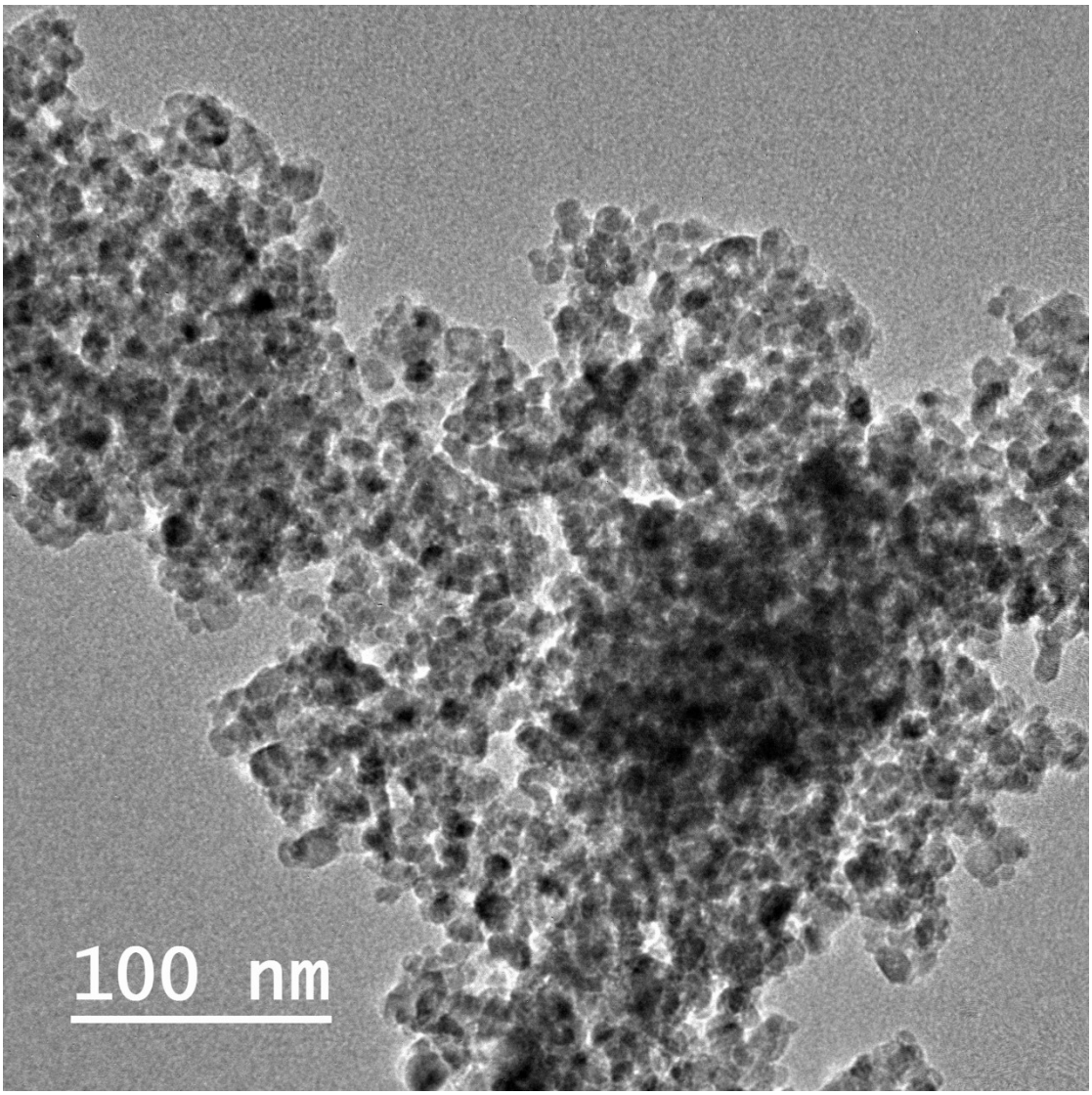

Figure 4.48 Transmission electron microscopy image of 2.0-RGO-TiO_2 photocatalyst.

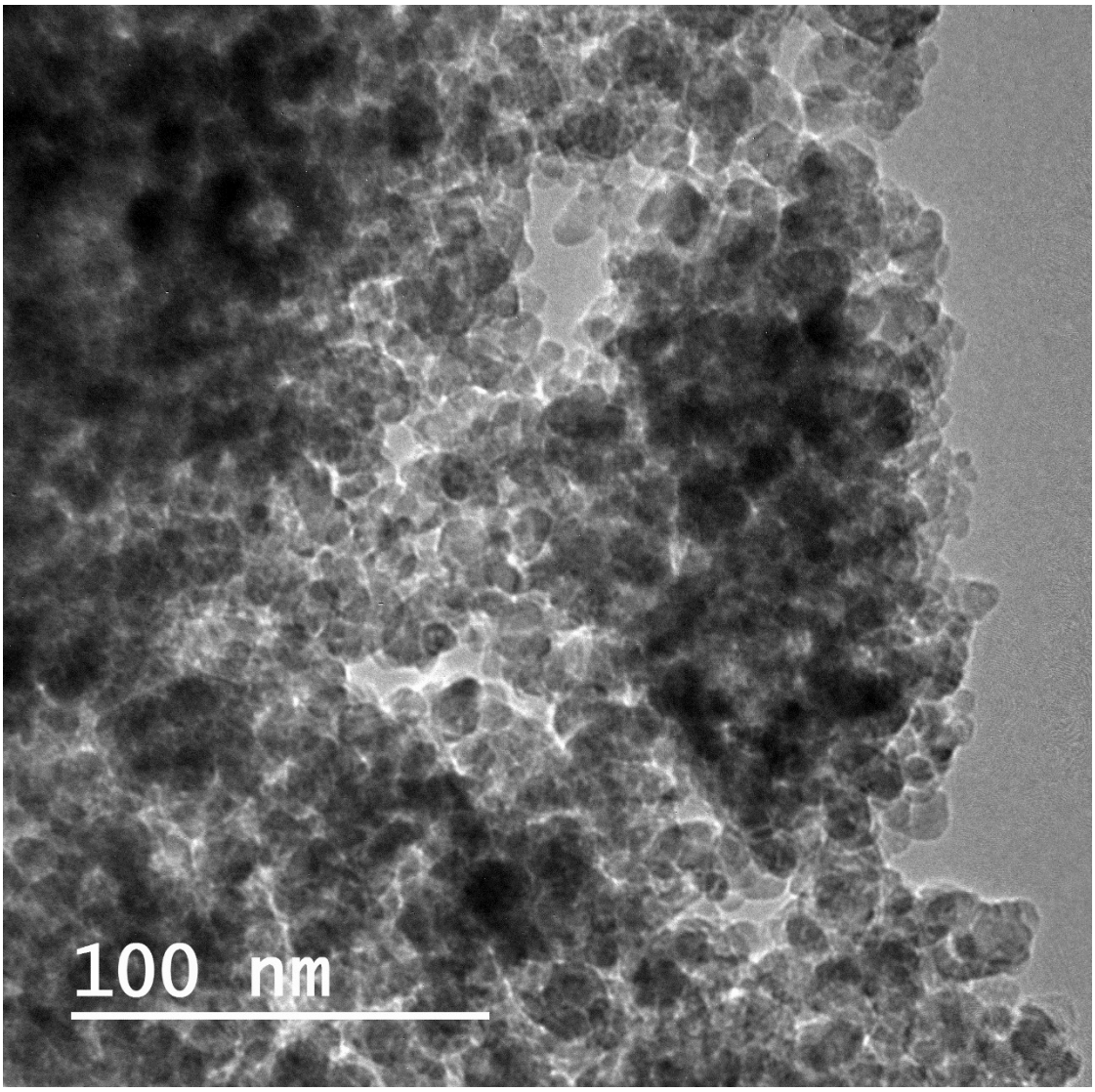

Figure 4.49 Transmission electron microscopy image of 5.0-RGO-TiO_2 photocatalyst.

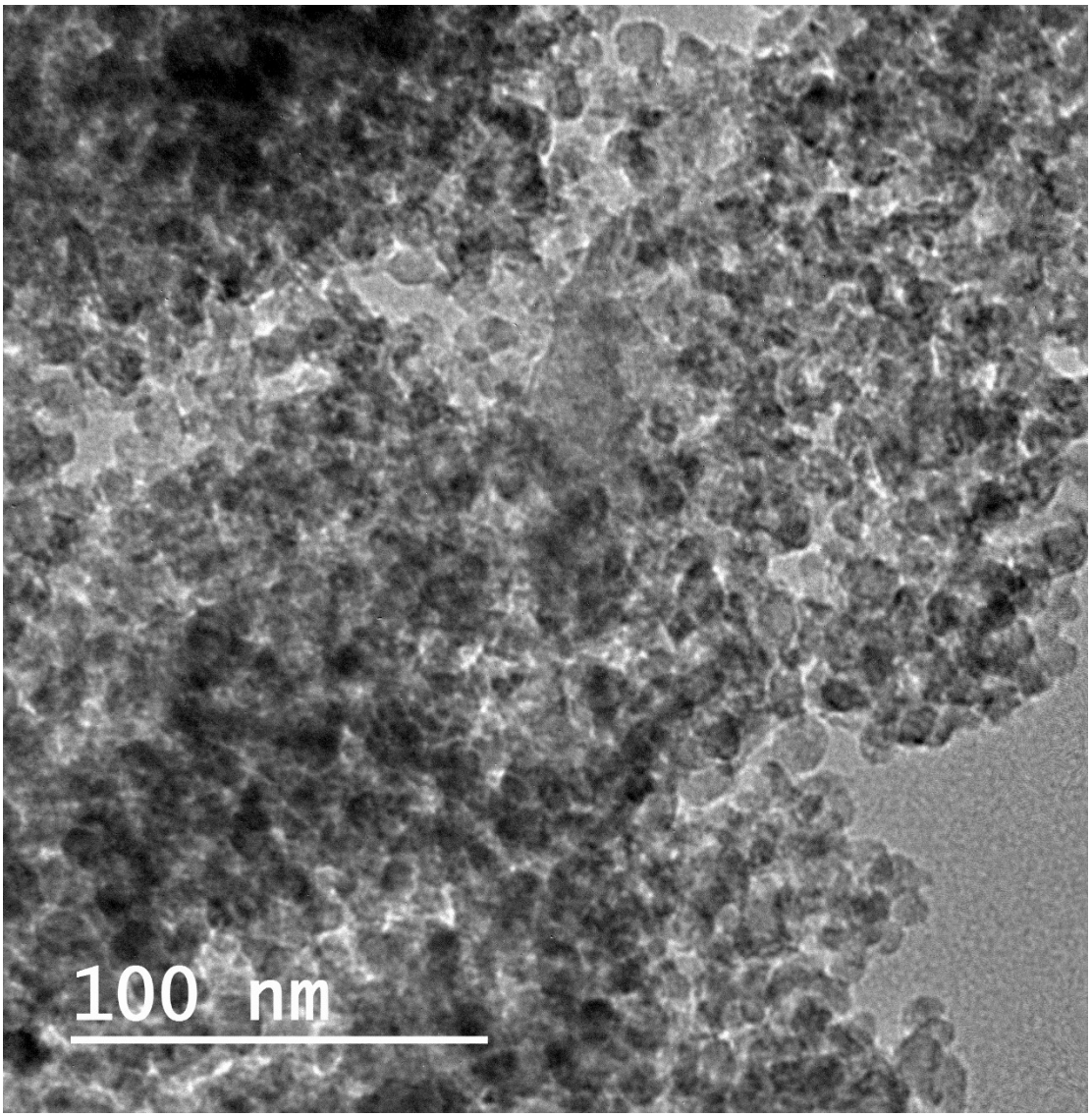

Figure 4.50 Transmission electron microscopy image of 10.0-RGO-TiO_2 photocatalyst.

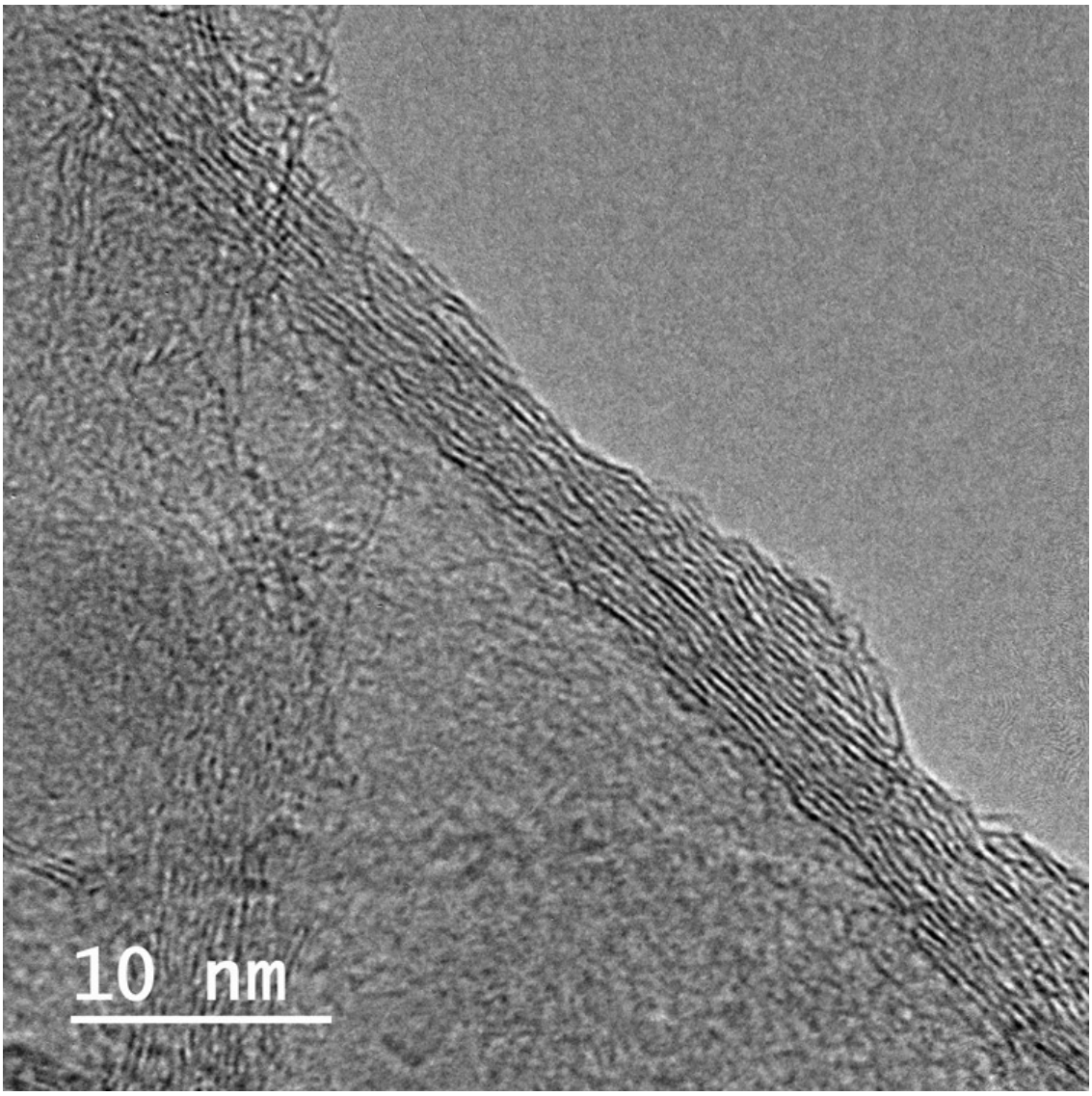

Figure 4.51 High resolution transmission electron microscopy image of RGO

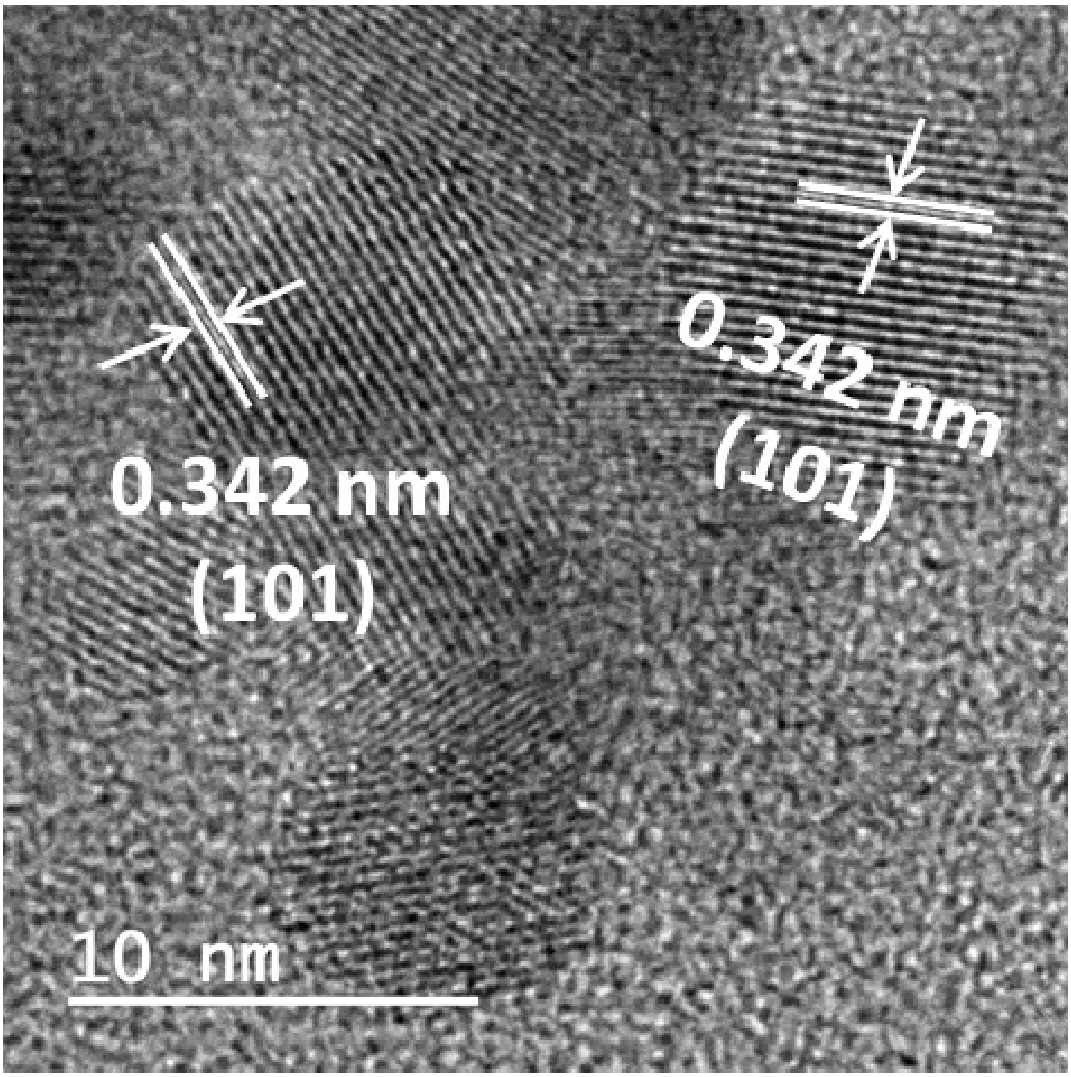

Figure 4.52 High resolution transmission electron microscopy image of TiO_2 photocatalyst.

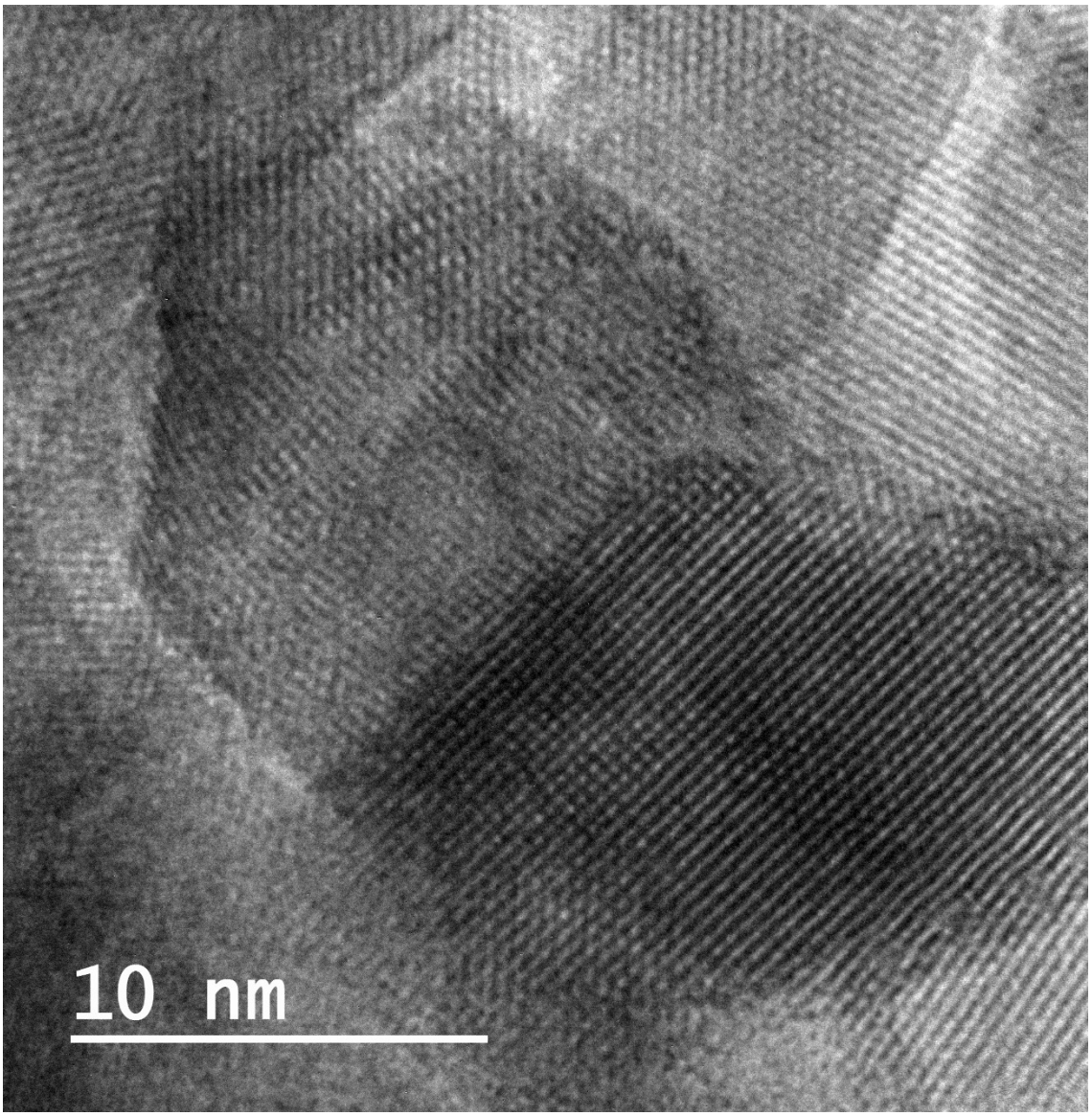

Figure 4.53 High resolution transmission electron microscopy image of 1.0RGO-TiO_2 photocatalyst.

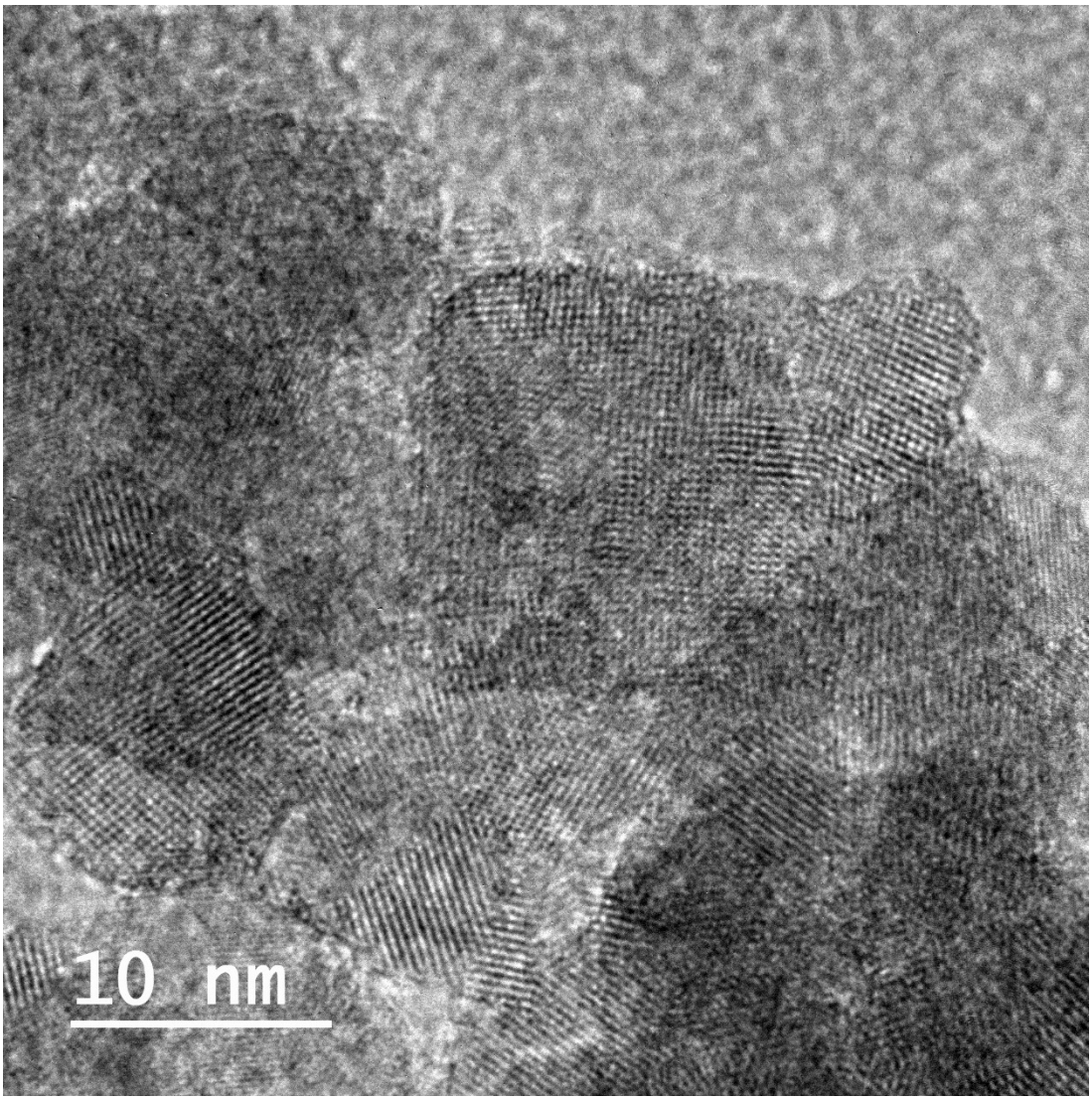

Figure 4.54 High resolution transmission electron microscopy image of 2.0RGO-TiO_2 photocatalyst.

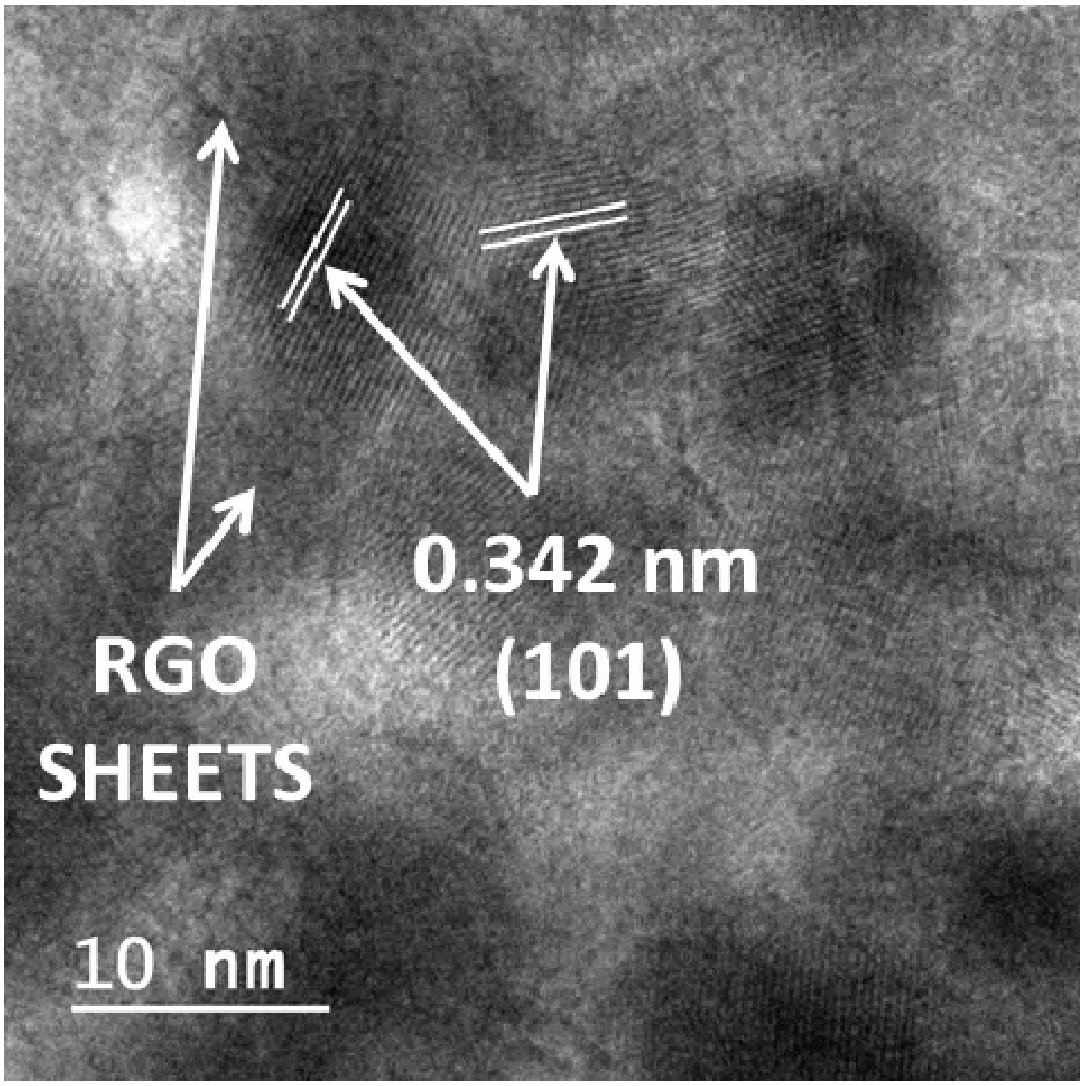

Figure 4.55 High resolution transmission electron microscopy image of 5.0RGO-TiO_2 photocatalyst.

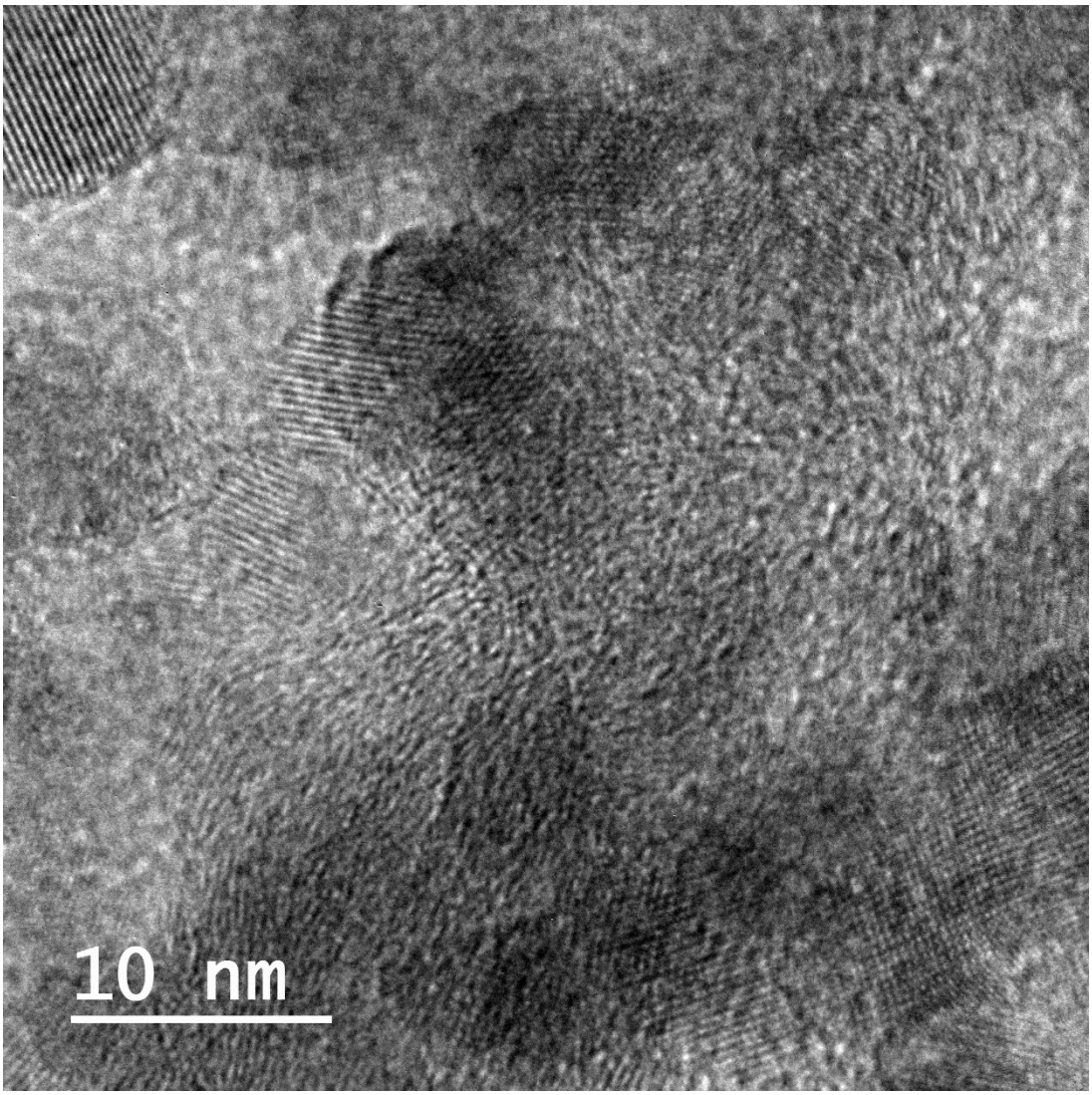

Figure 4.56 High resolution transmission electron microscopy image of 10.0RGO-TiO_2 photocatalyst.

calculated average particle decreased from ca 11.0 nm on TiO_2 to ca 8.0 nm on RGO-TiO_2 composites. The addition of RGO, which served as the support, ensured more dispersion and suppressed the crystal growth of TiO_2 nanoparticles (Gu *et al.,* 2013). The elemental mapping confirmed the presence of Ti and O elements in the ordinary TiO_2 catalyst, as shown in Figure 4.57, while RGO was found to contain C and O only (Figure 4.58). The presence of Ti, O and C in all RGO-TiO_2 samples was also confirmed by the elemental mapping as shown in Figure 4.59 – 4.62.

4.2.4 Thermogravimetric analyses and Raman spectroscopy characterisation of TiO_2 NPs and RGO-TiO_2 nanocomposites

The thermal behaviour of TiO_2, 5.0RGO-TiO_2 and pure RGO were examined by TGA analysis. Two obvious losses were noticed with pure RGO as shown in Figure 4.63. The first loss (ca. 10%) observed in the range of ca. 30 – 125 °C was as a result of the evaporation of the adsorbed moisture. The second loss (15%) observed in the range 125 - 330 °C was due to the burning of remaining organic solvents and oxygen-containing functional groups of RGO (Shen *et al.,* 2011; Chen *et al.,* 2016). The gradual reduction in weight was observed beyond 330 °C. The total weight loss at 900 °C was ca. 50%, which was from the burning of the carbon skeleton (Shen *et al.,* 2011). However, the curve for 5.0RGO-TiO_2 nanocomposite did not reveal the two significant mass losses, indicating the strong wrapping of RGO sheets with TiO_2 (Figure 4.63). The total weight loss (ca. 20%) observed for the nanocomposite at 900 °C indicates the strong interaction between the RGO and TiO_2-NPs, leading to reduced weight loss of RGO. In addition, the weight loss (ca. 10%) experienced by the nanocomposite at the calcination temperature (400 °C) shows that there was no significant weight loss of RGO in the nanocomposites, thereby confirming the stability of the nanocomposite at 400 °C. As shown in Figure 4.64, the spent RGO-TiO_2 catalyst showed a total weight loss of 30% at 900 °C. The further weightloss (10%) with spent RGO-TiO_2 was as a result of the burning out of settled products formed from the reduction of CO_2 on the surface of the nanocomposites.

The Raman spectra of TiO_2, 5.0RGO-TiO_2, and pure RGO samples were obtainedto evaluate the interaction between RGO and TiO_2 (Figure 4.65). For the RGO sample, two characteristic peaks were observed at 1340.8 and 1580.3 cm^{-1}, and the peaks have

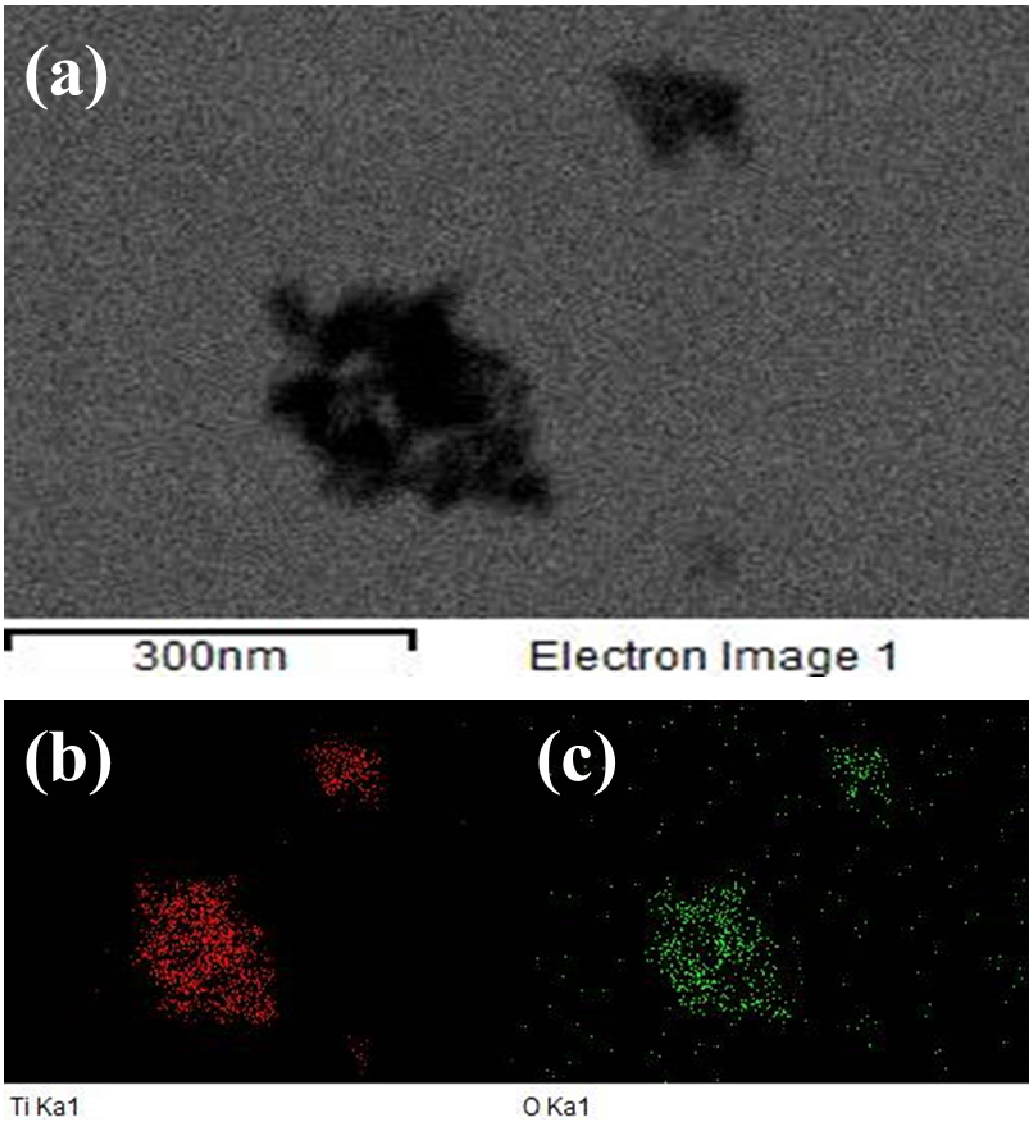

Figure 4.57 Elemental mapping of TiO_2 photocatalyst.

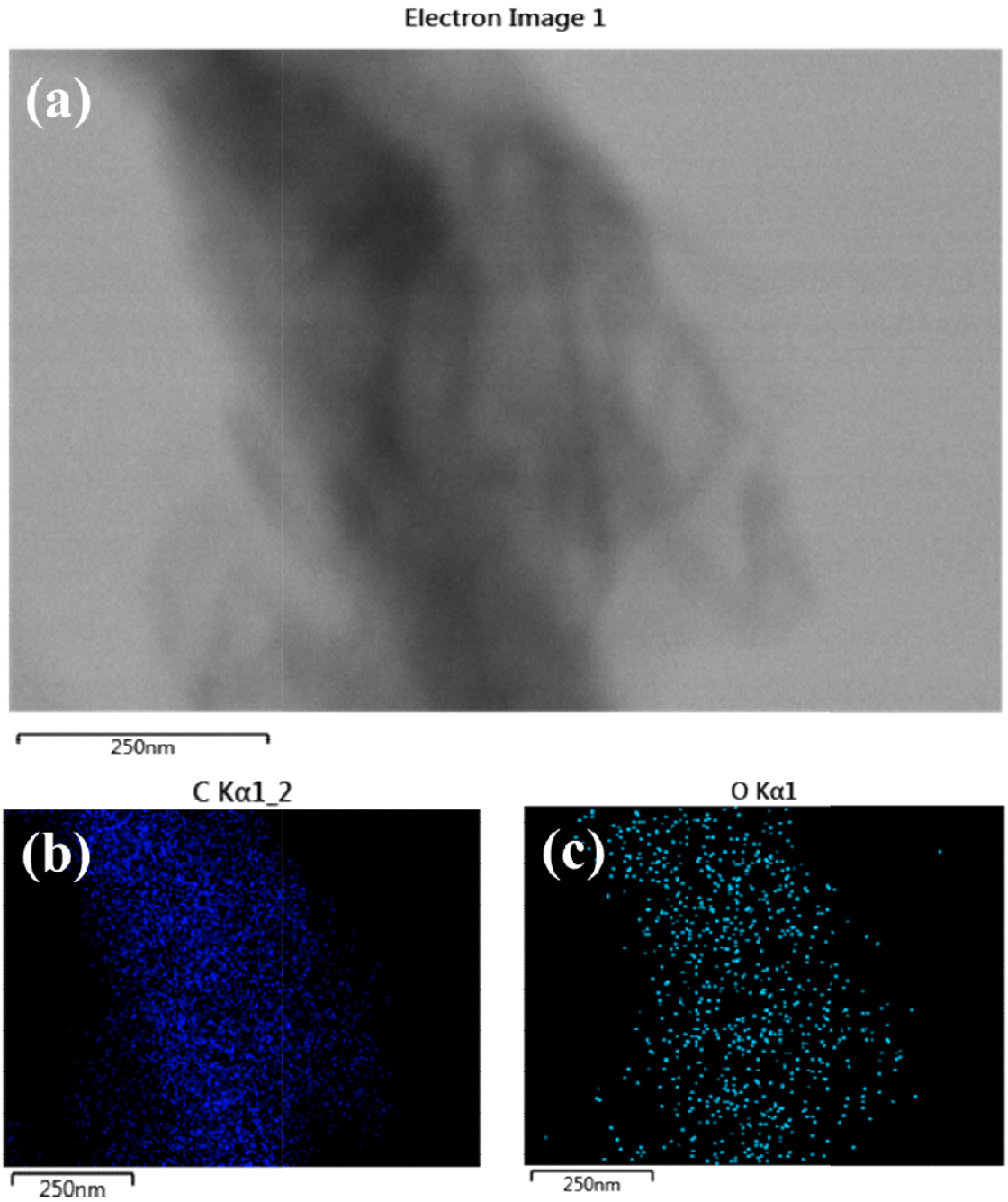

Figure 4.58 Elemental mapping of RGO sample.

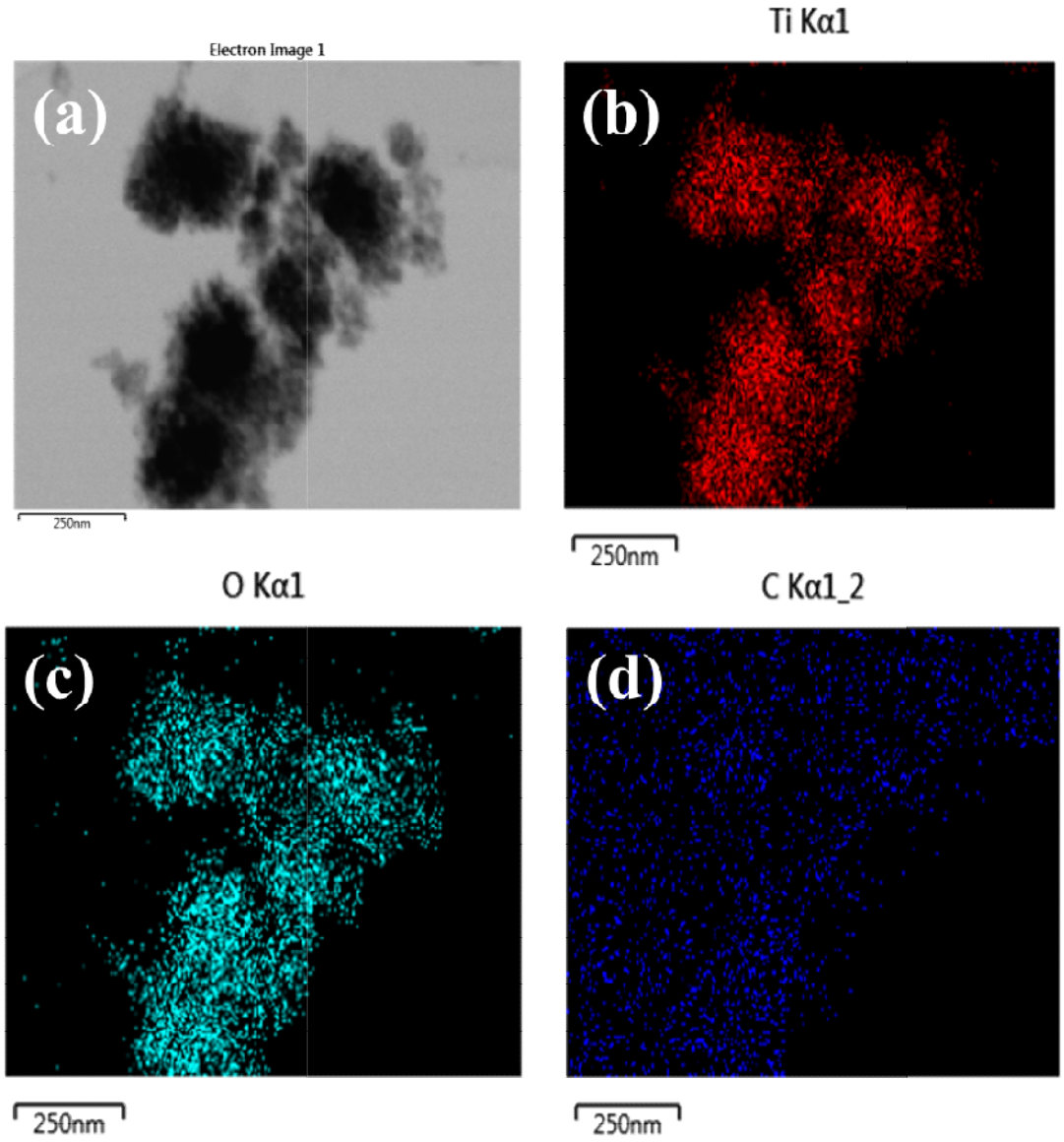

Figure 4.59 Elemental mapping of 1.0RGO-TiO_2 sample.

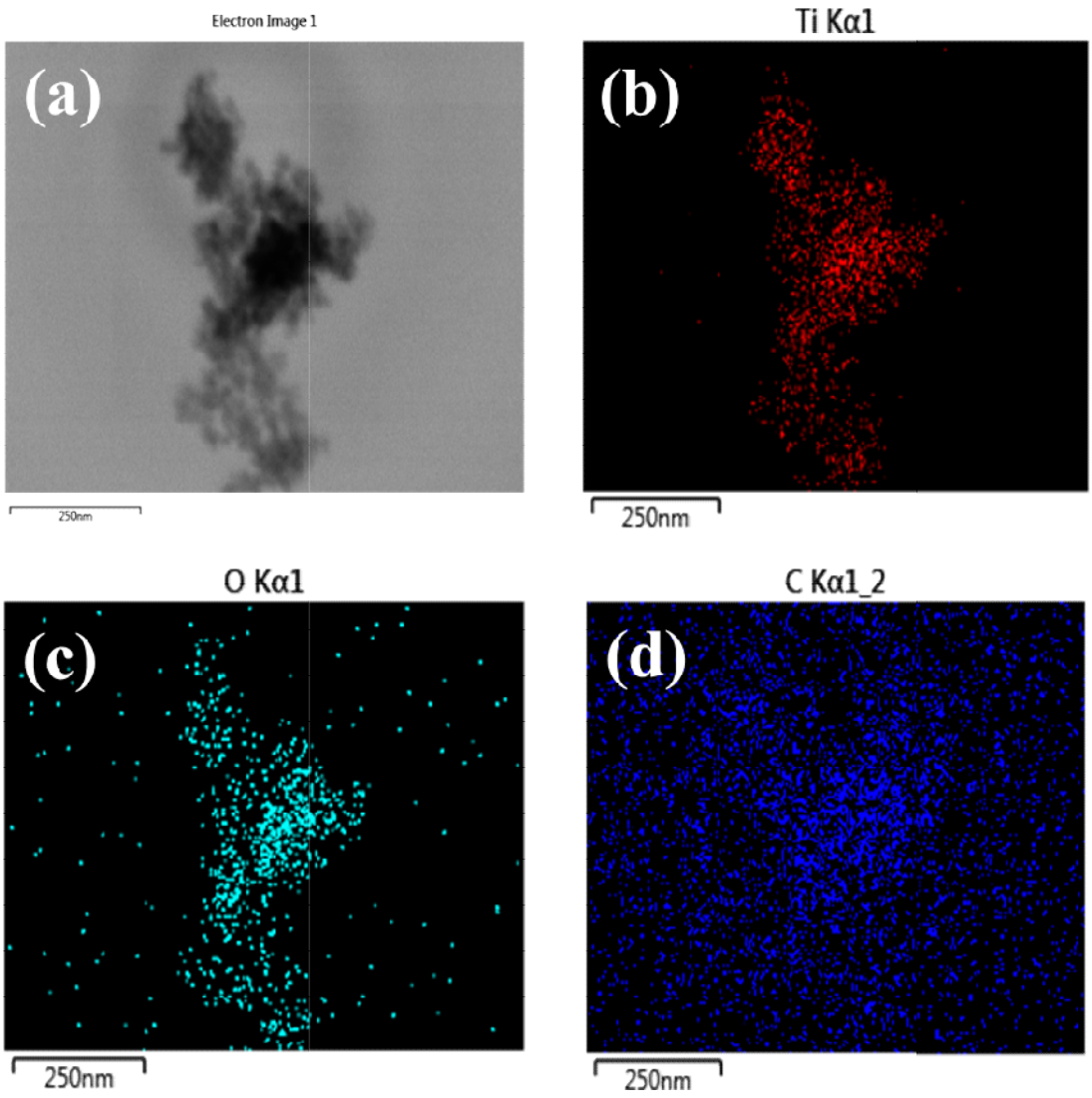

Figure 4.60 Elemental mapping of 2.0RGO-TiO_2 sample.

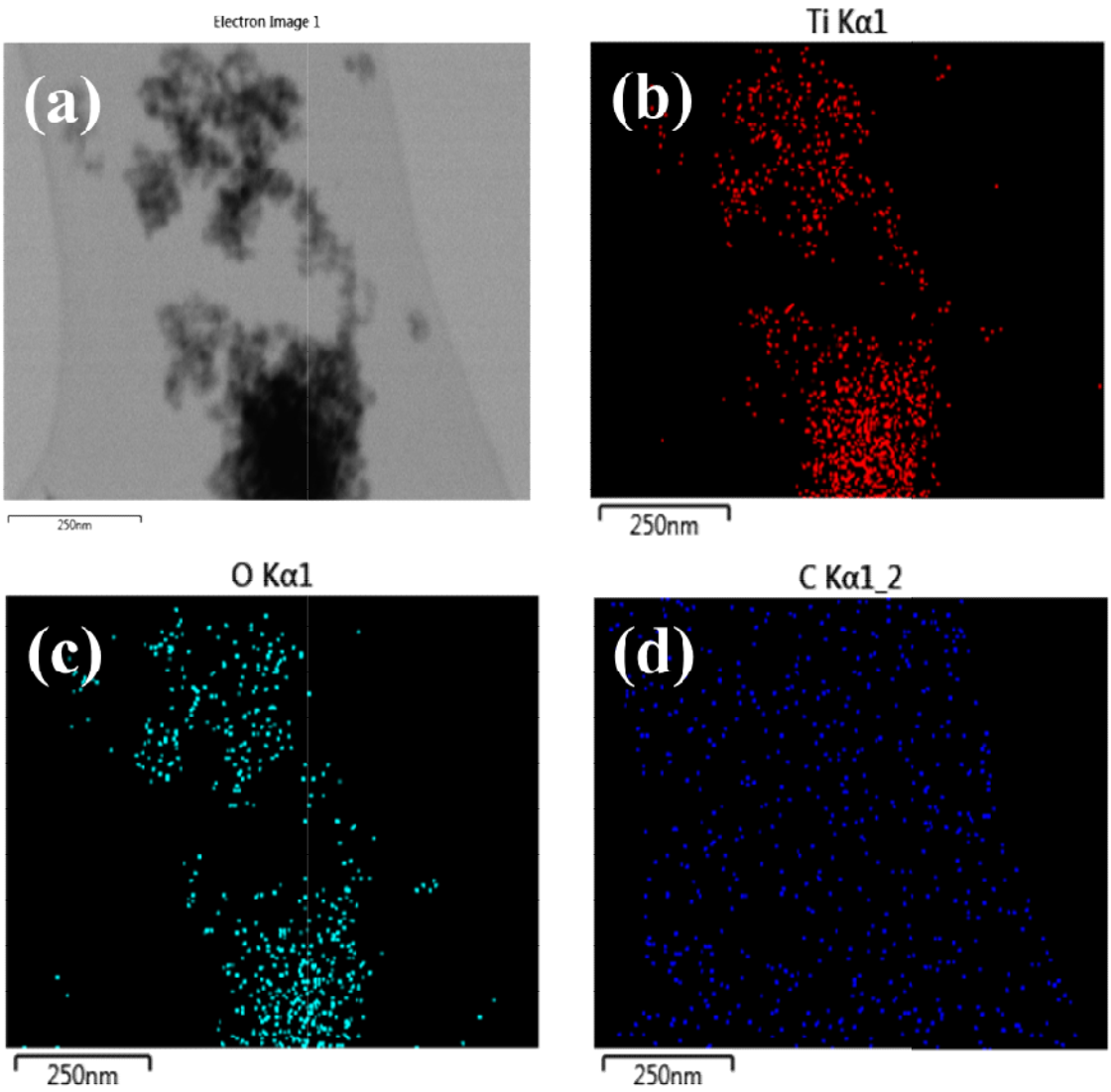

Figure 4.61 Elemental mapping of 5.0RGO-TiO_2 sample.

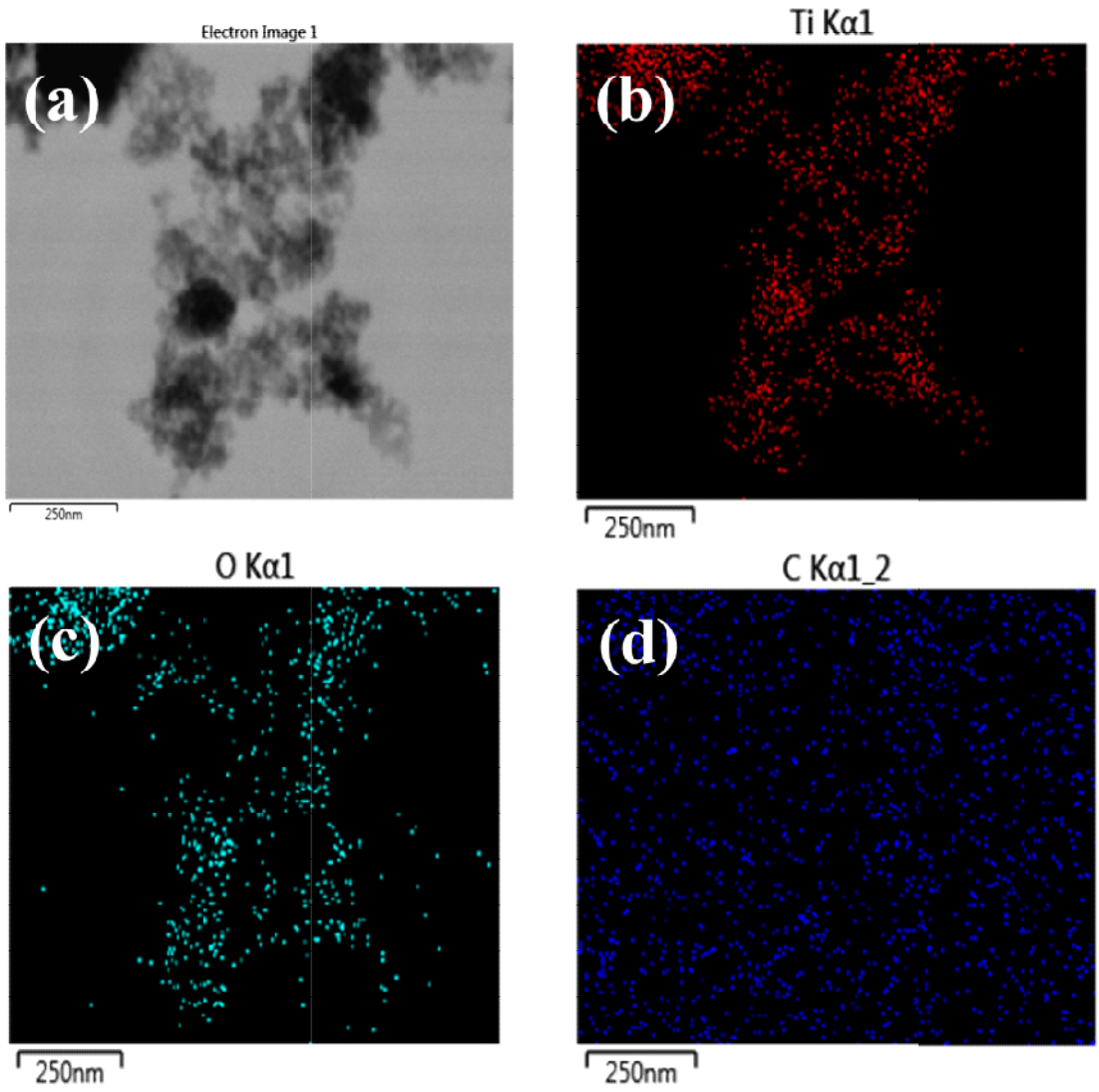

Figure 4.62 Elemental mapping of 10.0RGO-TiO_2 sample.

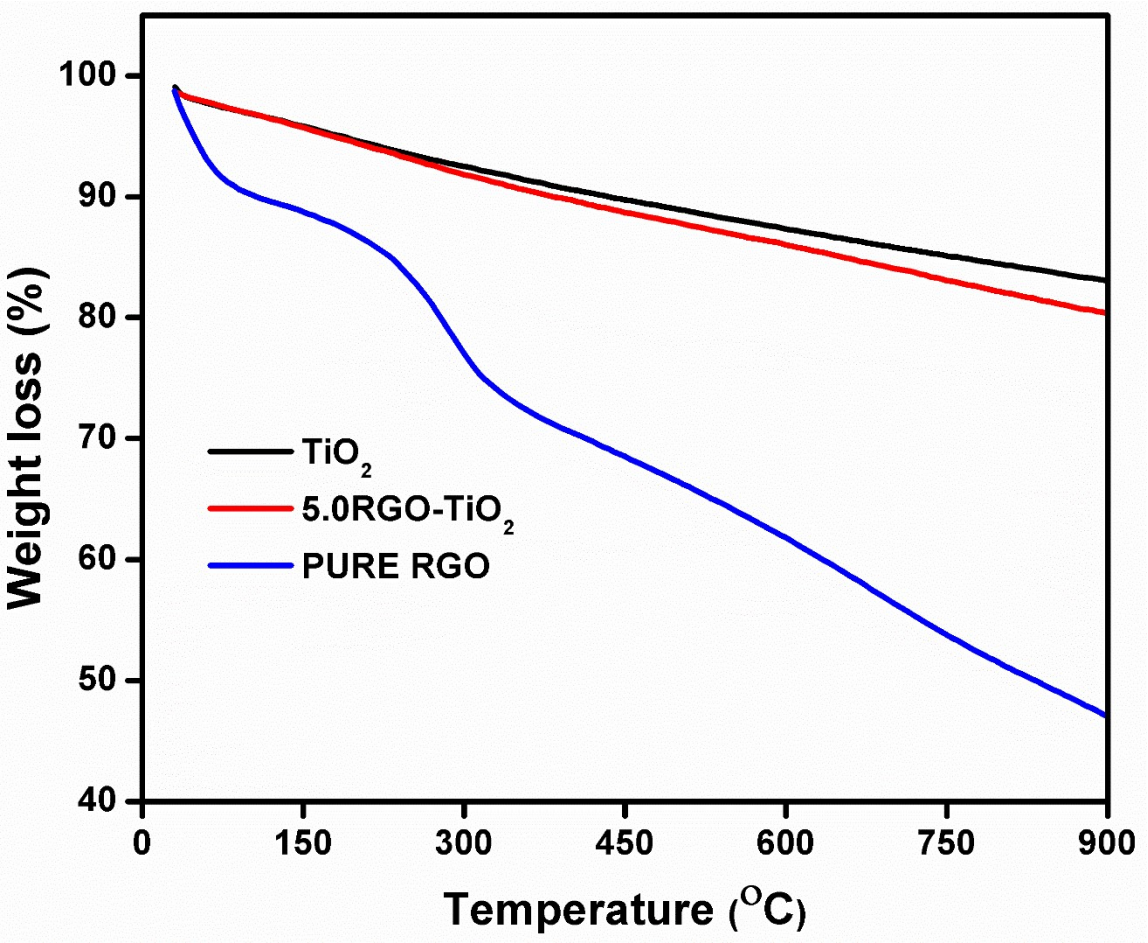

Figure 4.63 Thermogravimetric analyses curves of the prepared TiO_2, 5.0RGO-TiO_2 and pure RGO samples.

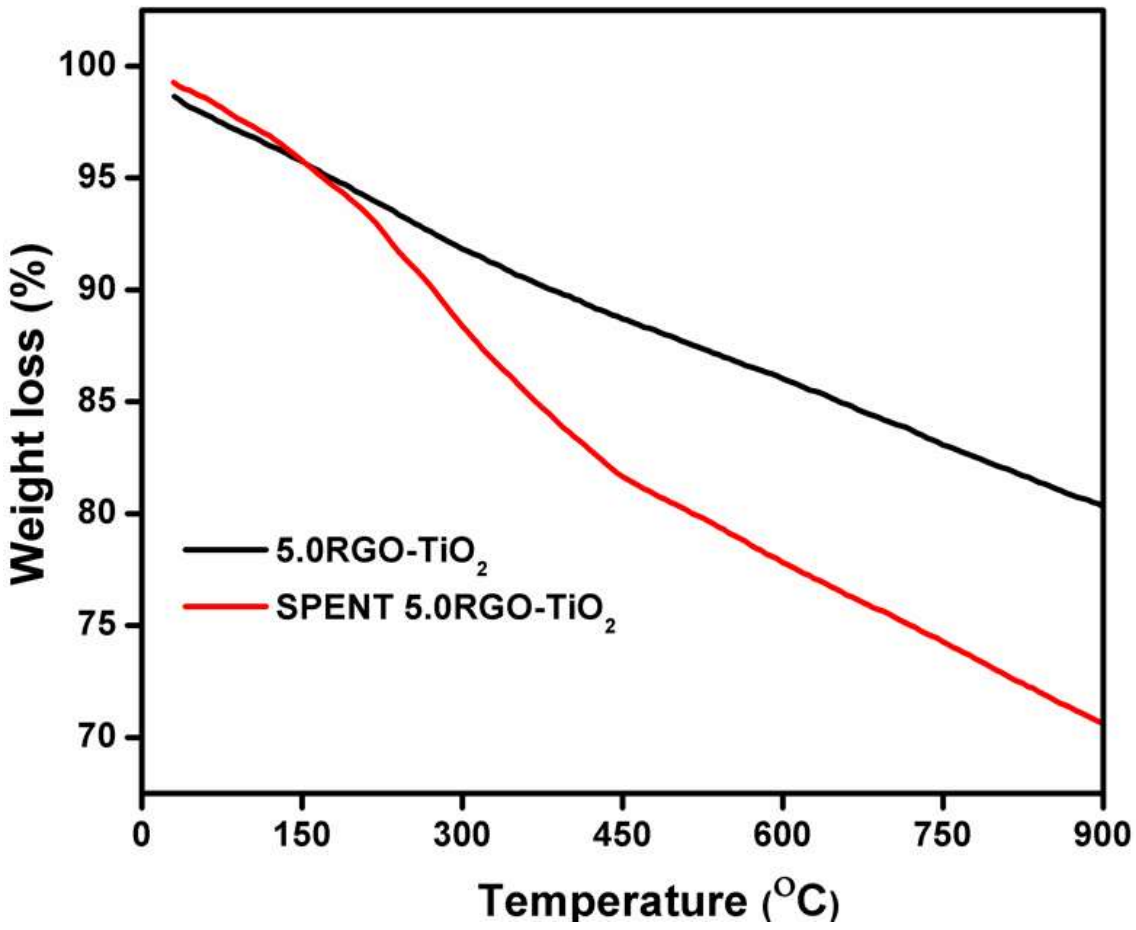

Figure 4.64 Comparison of thermogravimetric analyses curves of 5.0RGO-TiO_2 and spent 5.0RGO-TiO_2 samples.

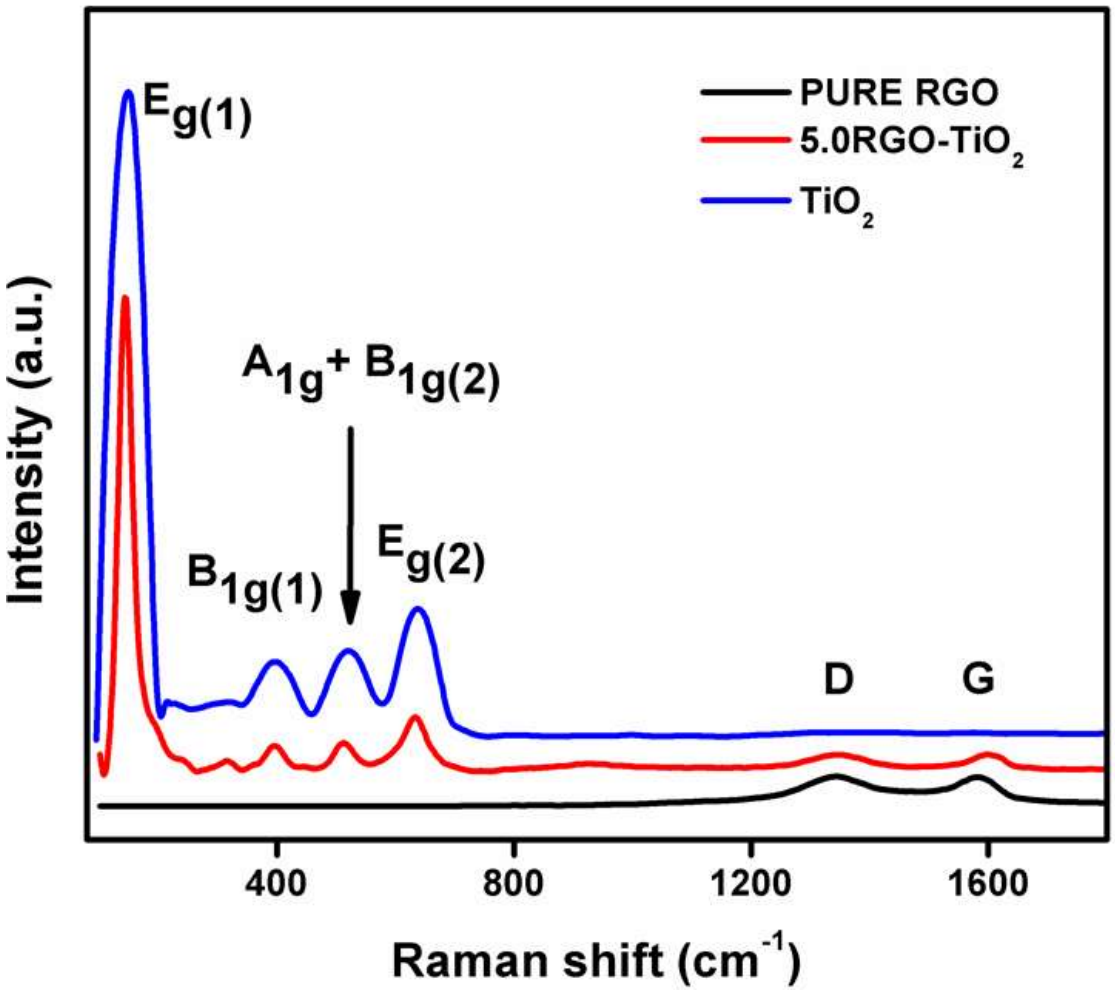

Figure 4.65 Raman spectra of the prepared TiO_2, 5.0RGO-TiO_2 and pure RGO samples.

been assigned to D and G bands, respectively. These bands correspond to the first-order scattering of the E_2g mode observed for sp^2 carbon domain as well as the structuraldefects, amorphous carbon, or edges that break the symmetry and selection rule (Nguyen-Phan *et al.,* 2014; Wang *et al.,* 2013a). The bare TiO_2 showed strong peaks at 149.2, 397.4, 516.8 and 639.5 cm^{-1}, which are typical of Eg(1), B1g(1), A1g + B1g(2) and Eg(2) vibration modes of anatase TiO_2, respectively. The characteristic peaks for both RGO and TiO_2were retained in the spectra of the 5.0RGO-TiO_2 nanocomposite. In comparison, the G band was shifted to 1598.8 cm^{-1} in the composite, confirming the formation of the nanocomposite. However, no shift was observed with the D-band (Shah *et al.,* 2012).

4.2.5 X-ray photoelectron spectroscopy characterisation of TiO_2 NPs and RGO-TiO_2 nanocomposites

To study the surface state and the interaction of the prepared TiO_2 with RGO, XPS technique was employed. The full-scale spectra of pure RGO,TiO_2 and 5.0RGO-$TiO_2$are shown in Figure 4.66 – 4.68. The spectrum of 5.0RGO-TiO_2 (Figure 4.67) shows the presence of Ti, O and C peaks. Nevertheless, C and O peaks are consistent with pure RGO (Figure 4.66). The C peak observed in the spectrum of TiO_2 was due to the instrument reference standard, and this peak was lower in intensity, in comparison with 5.0RGO-TiO_2 (Figure 4.68). The high-resolution XPS spectrum of Ti2p for $TiO_2$is depicted in Figure 4.69. The peaks centred at 458.3 and 464.1 eV have been ascribed to Ti2p3/2 and Ti2p1/2 respectively, which are in good agreement with the binding energy values of Ti^{4+} in pure anatase.For 5.0RGO-TiO_2 composite, these two peaks shifted to 459.7 and 465.5 eV as shown in Figure 4.70. This shift was most possibly as a result of the successful wrapping of RGO with TiO_2 and probably the presence of highly electronegative O, which withdraws the electron density from Ti of 5.0TiO_2-RGO nanocomposite (Sher-Shah *et al.,* 2012).

The high-resolution XPS spectra of C1s from pure RGO and 5.0RGO-TiO_2nanocomposite are shown in Figure 4.71 and 4.72. For pure RGO, the core-level spectrum was fitted into three parts. The main part, centred at about 284.3 eV, has been attributed to the non-oxygenated ring C including C-C, C=C and C-H bonds. The other two parts, centred at 284.9 and 287.4 eV, have been assigned to carbon atoms connecting with

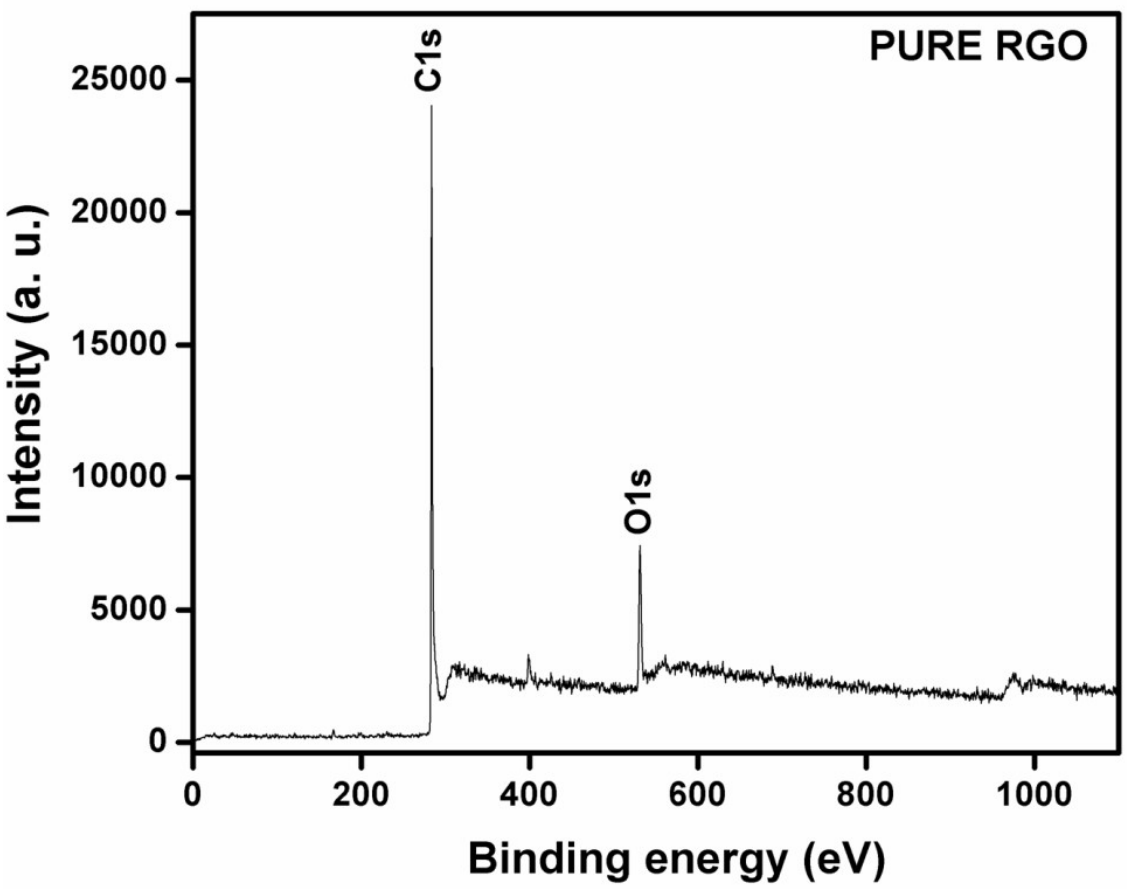

Figure 4.66 X-ray photoelectron spectroscopy survey spectrum of pure RGO.

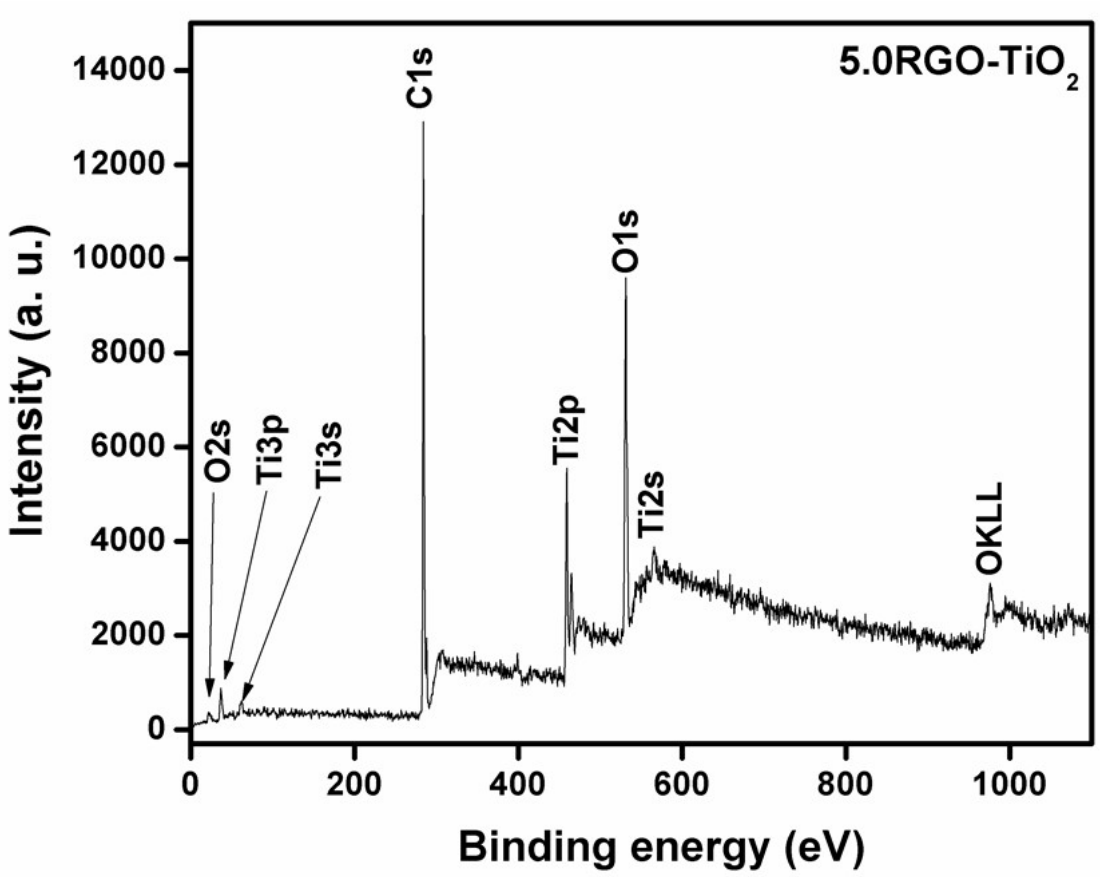

Figure 4.67 X-ray photoelectron spectroscopy survey spectrum of 5.0RGO-TiO_2.

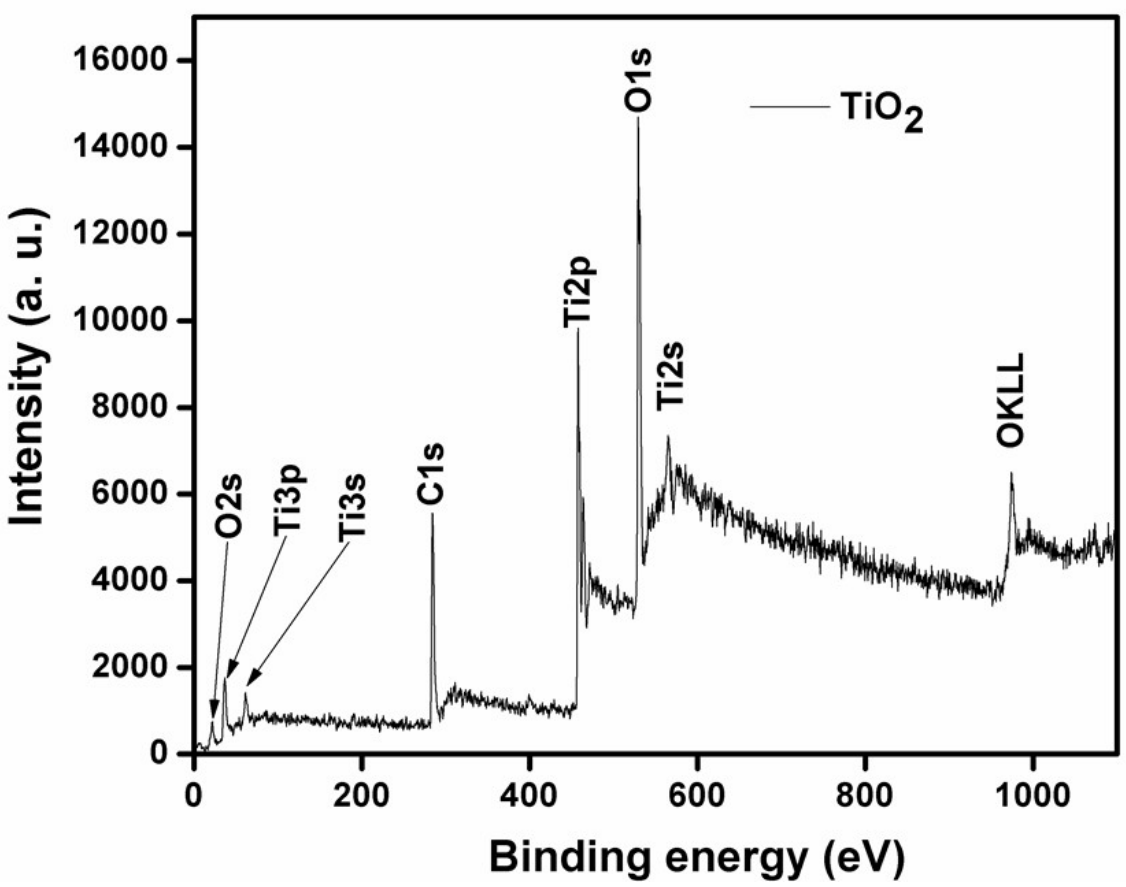

Figure 4.68 X-ray photoelectron spectroscopy survey spectrum of TiO_2.

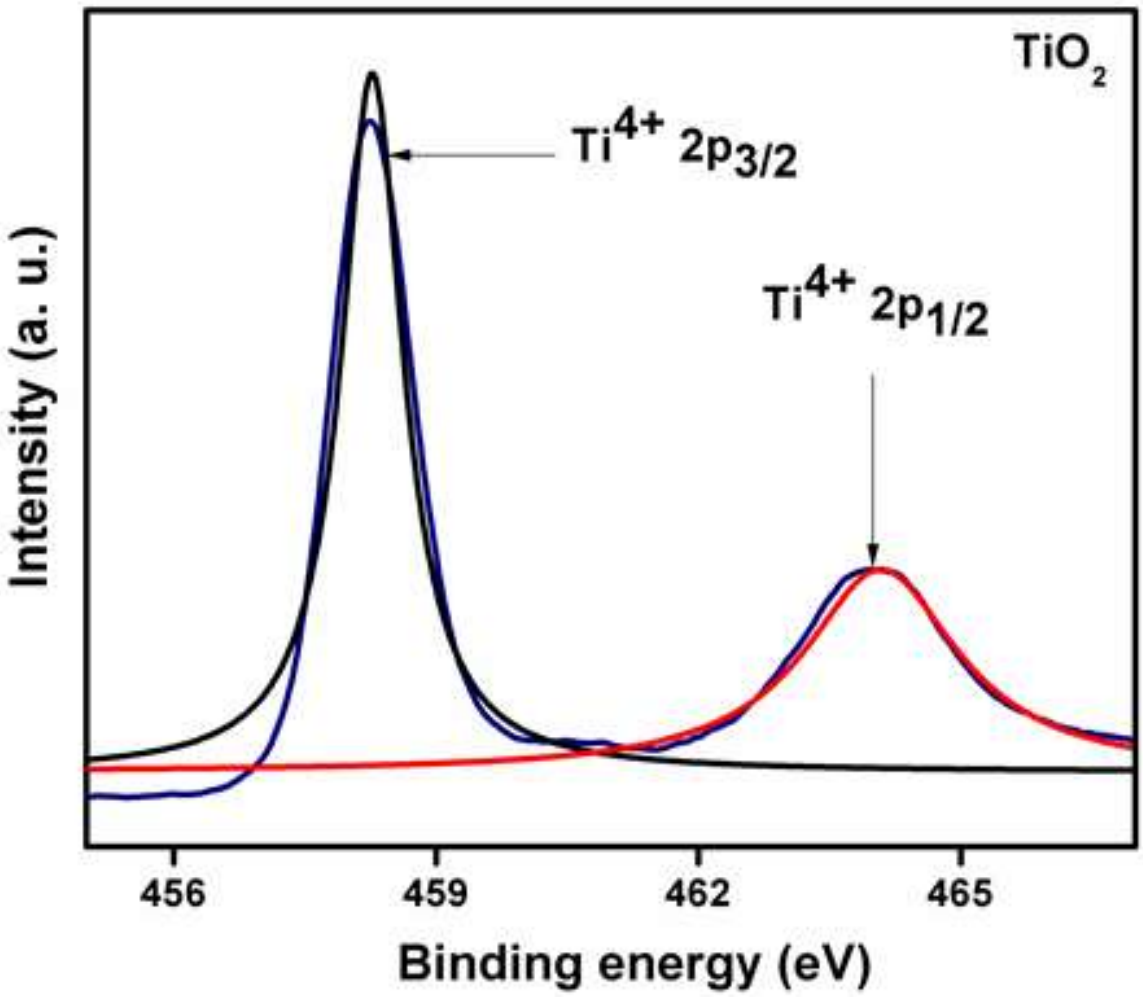

Figure 4.69 High-resolution X-ray photoelectron spectroscopy spectrum of Ti2p of bare TiO_2.

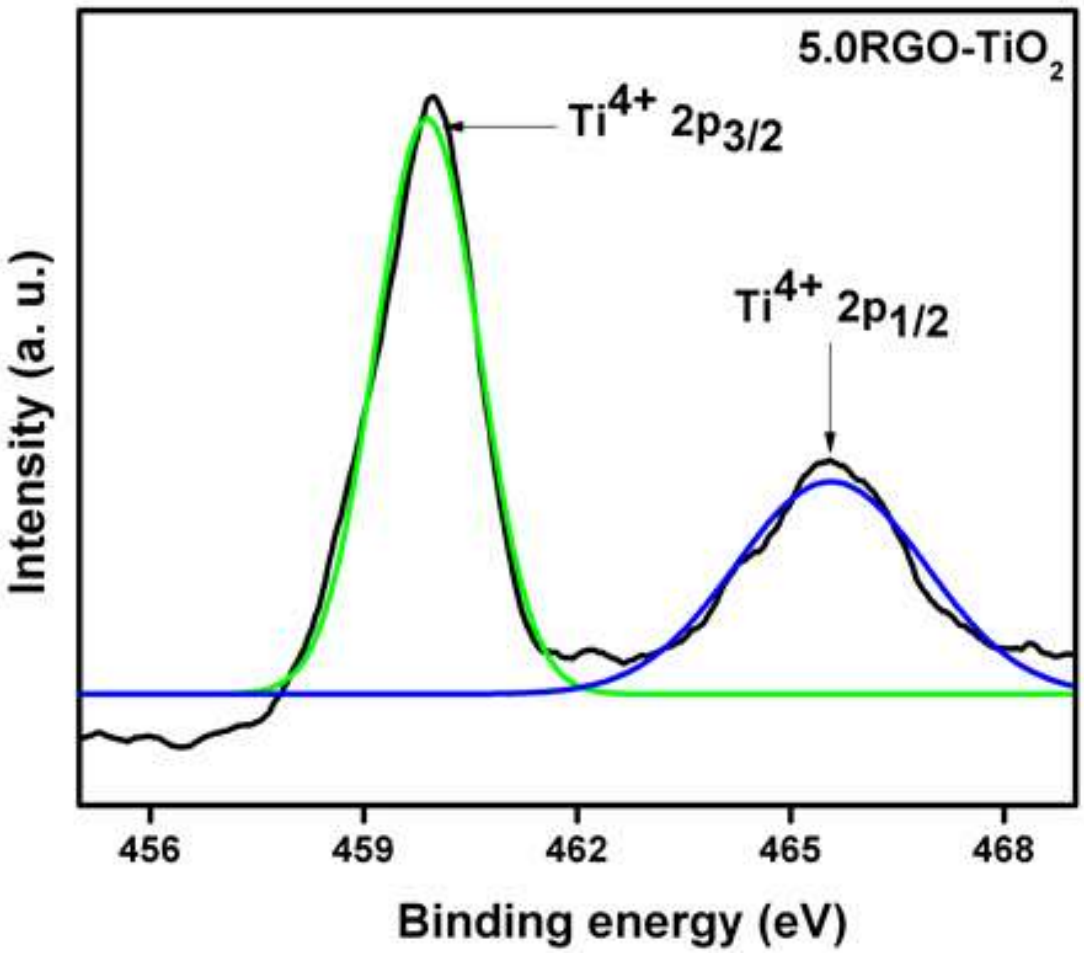

Figure 4.70 High-resolution X-ray photoelectron spectroscopy spectrum of Ti2p of 5.0RGO-TiO_2.

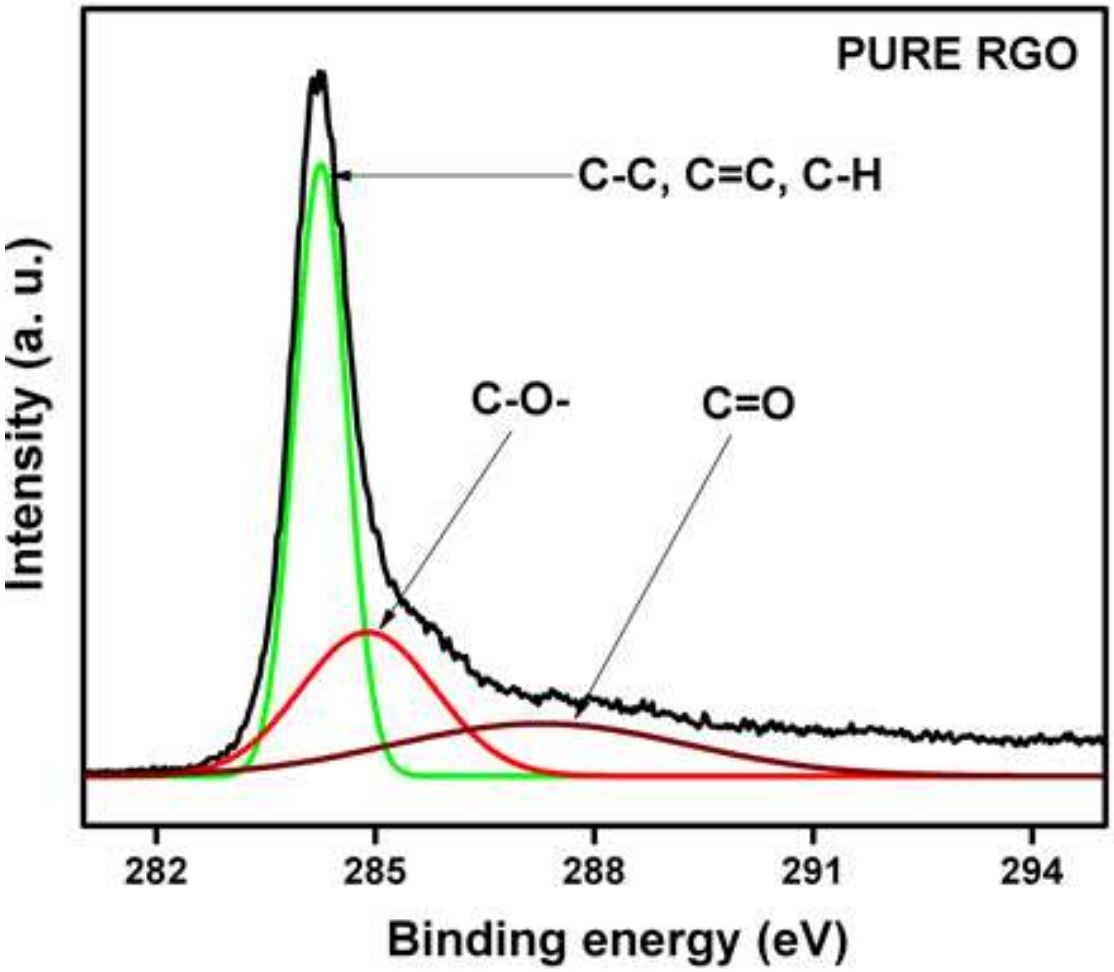

Figure 4.71 High-resolution XPS spectrum of C1s of pure RGO.

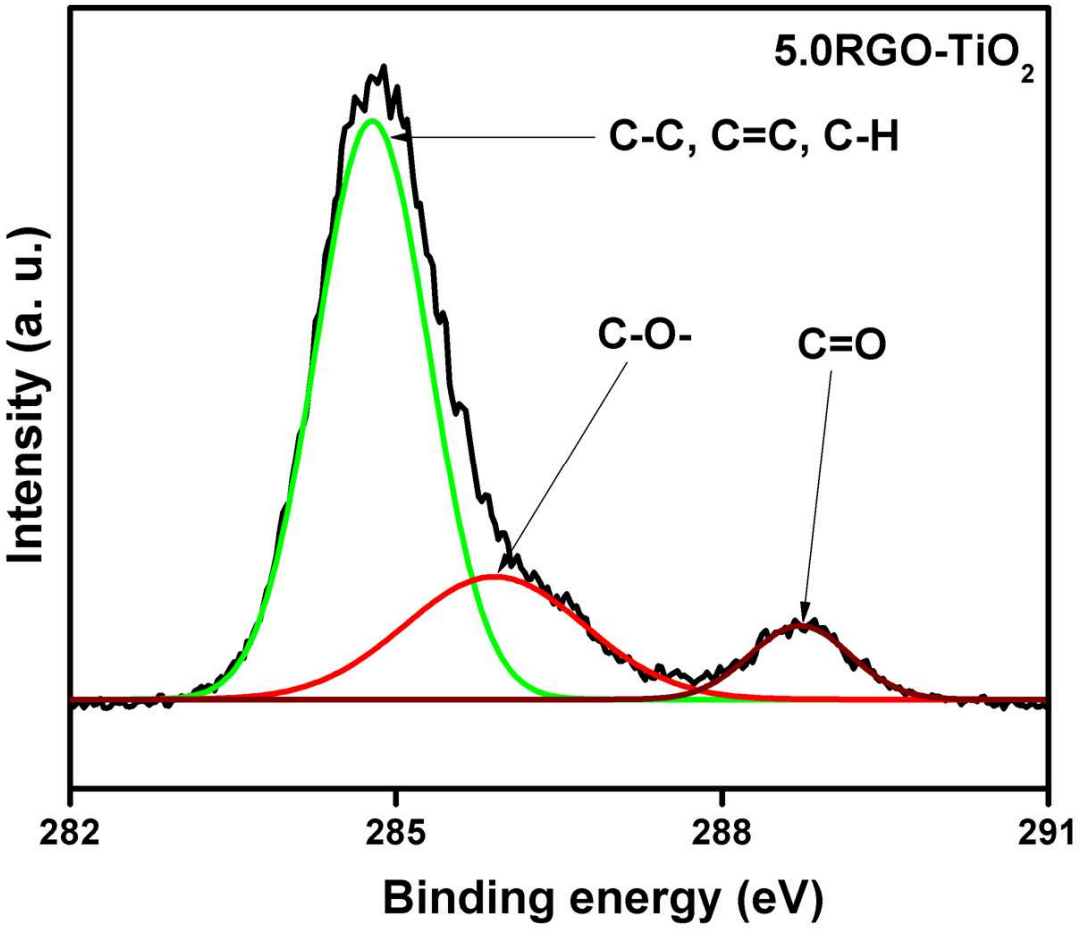

Figure 4.72 High-resolution X-ray photoelectron spectroscopy spectrum of C1s of 5.0RGO-TiO_2.

oxygenate groups, C-O and C=O bonds respectively (Ismail *et al.,* 2013; Wang *et al.,* 2013a). Similar peaks were also observed to be present in 5.0RGO-TiO_2 nanocomposites,but with slight shifts to 284.7, 285.9 and 288.7 eV. The areas of the peaks assigned to C-O and C=O bonds, for 5.0RGO-TiO_2 nanocomposites, were significantly reduced by 61.5 and 83.8 % respectively (Table 4.6), suggesting the elimination of considerable oxygen-containing groups during the hydrothermal process. The observed peak shifts and a decrease in the peaks areas, with 5.0RGO-TiO_2 nanocomposite, indicate the interaction of RGO and TiO_2 in the composite (Leong *et al.,* 2015).

The spectra of O1s for the pure RGO, 5.0RGO-TiO_2 and TiO_2 samples are shown in Figure 4.73 – 4.75. The fitting of the spectrum, into three parts, for the pure RGO, showed two main peaks centred at 531.0 and 532.7 eV, which have been ascribed to carbonyl oxygen from O=C-OH / C=O and hydroxyl oxygen from C-O / C-OH (Figure 4.73). The third peak centred at 535.7 eV is the O from tiny absorbed water (Zhou *et al.,* 2015; Oh *et al.,* 2014). A new peak centred at 530.7 eV was observed with 5.0RGO-TiO_2 (Figure 4.74), which was assigned to intrinsic O atoms that are bound to Ti (Ti-O-Ti) (Luo *et al.,* 2015; Bellamkonda *et al.,* 2017). The new observed peak indicates that there was an interaction between RGO and TiO_2. The peak from C-O / C-OH observed earlier with pure RGO has overshadowed the tiny peak from absorbed water in 5.0RGO-TiO_2sample. As expected for the pure TiO_2, the peaks noticed at 529.5 and 531.7 eV have been assigned to lattice oxygen and non-lattice oxygen (adsorbed OH group) respectively (Figure 4.75).

The XPS survey spectrum of spent 5.0RGO-$TiO_2$is shown in Figure 4.76. Ti, O and C elements were observed with the spent 5.0RGO-TiO_2, thus indicating that the elemental composition of nanocomposite remained unchanged after being used for photocatalytic CO_2 reduction. However, from the high-resolution spectra of the spent 5.0RGO-TiO_2(Figure 4.77 – 4.79),the peak areas of Ti^{4+}, C-C, C=C and C-H were reduced while the peak areas of Ti-O-Ti, O=C-OH, C=O, C-O, C-OH and H_2O were increased in comparison with the unspent 5.0RGO-TiO_2. These increase and decrease in the peak areas were as a result of the settling of oxygenated species from both the reactants and products on the surface of the 5.0RGO-TiO_2.

Table 4.6 X-ray photoelectron spectroscopy data of C1s chemical state of pure RGO and 5.0RGO-TiO_2 samples.

Bonds	Peak Area		Peak Centre	
	Pure RGO	5.0RGO-TiO_2	Pure RGO	5.0RGO-TiO_2
C-C, C=C, C-H	9013.1	6276.3	284.3	284.7
C-O-	5447.5	2100.1	284.9	285.9
C=O	4334.4	703.2	287.3	288.7

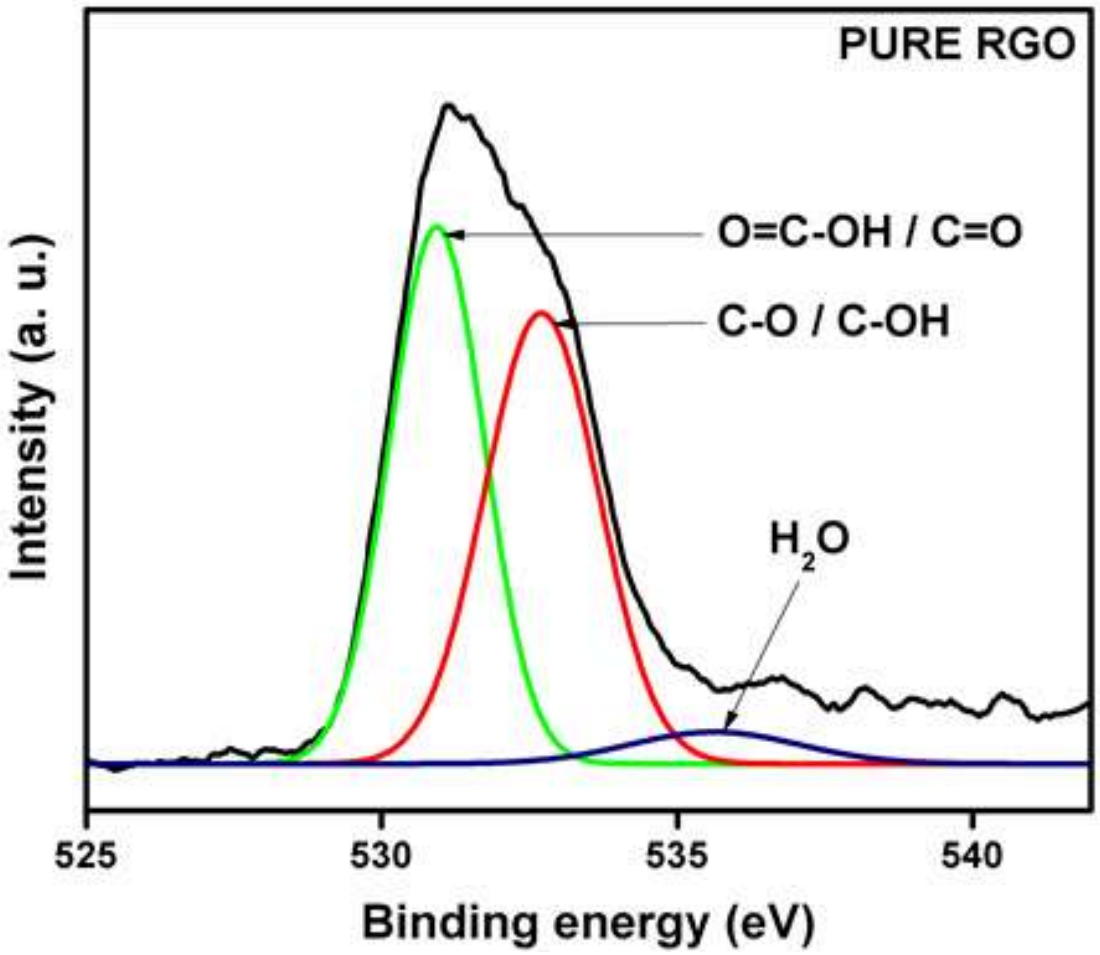

Figure 4.73 High-resolution X-ray photoelectron spectroscopy spectrum of O1s of pure RGO.

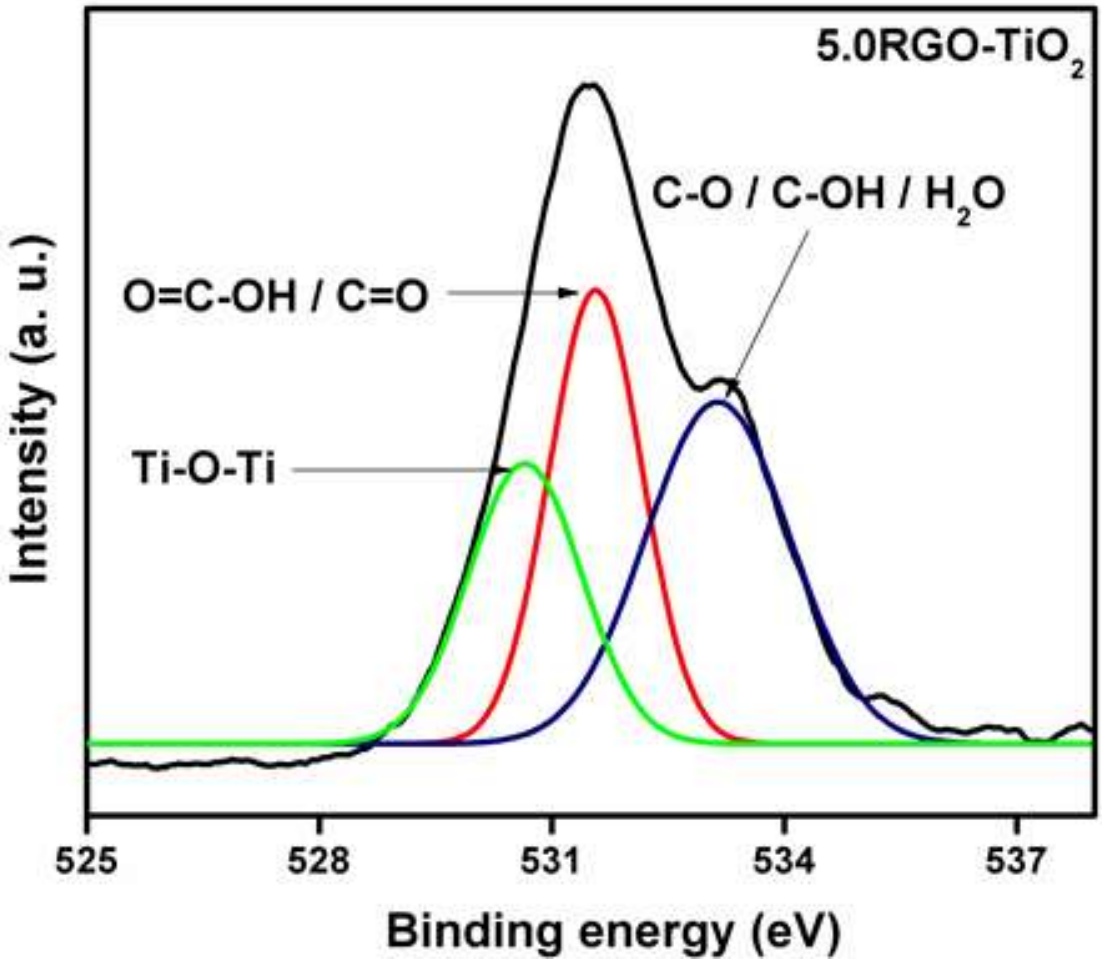

Figure 4.74 High-resolution X-ray photoelectron spectroscopy spectrum of O1s of 5.0RGO-TiO_2.

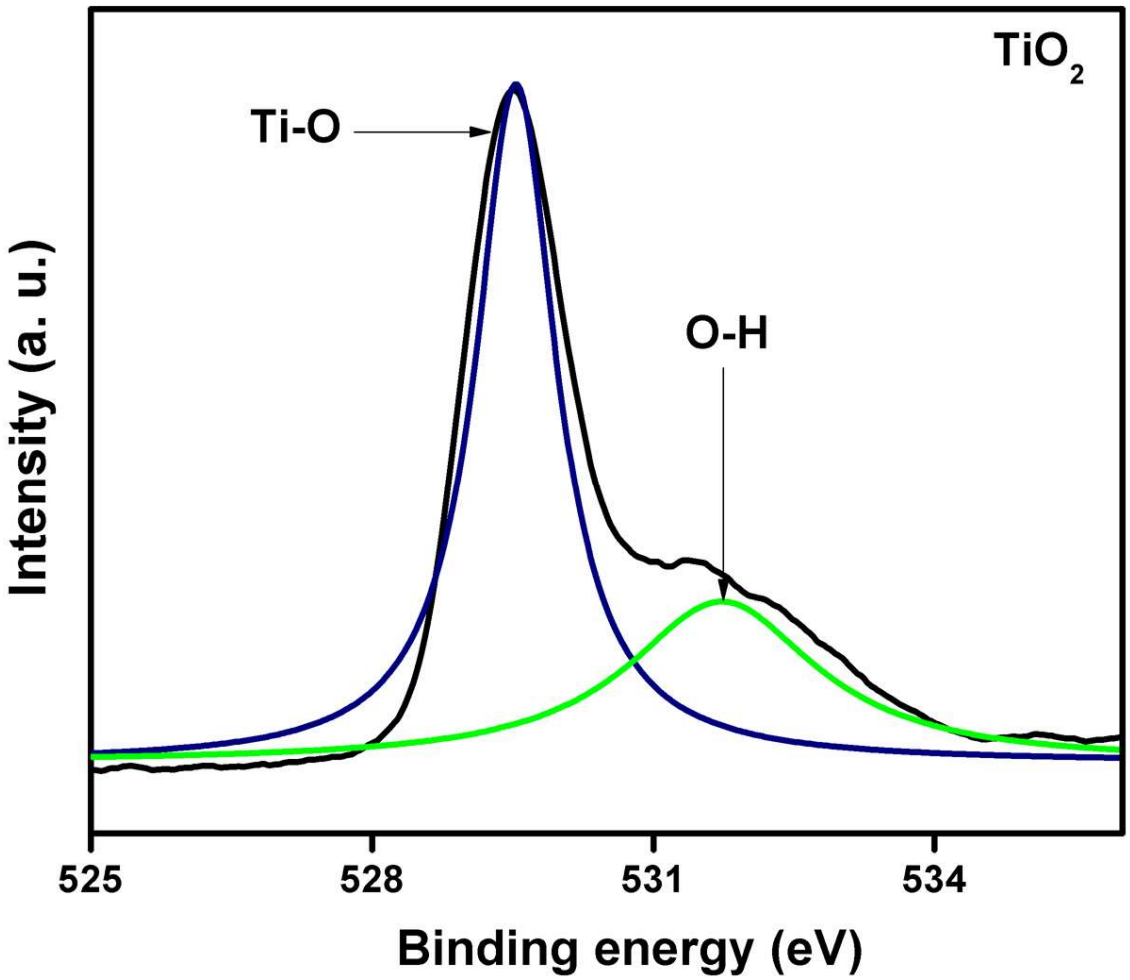

Figure 4.75 High-resolution X-ray photoelectron spectroscopy spectrum of O1s of TiO_2.

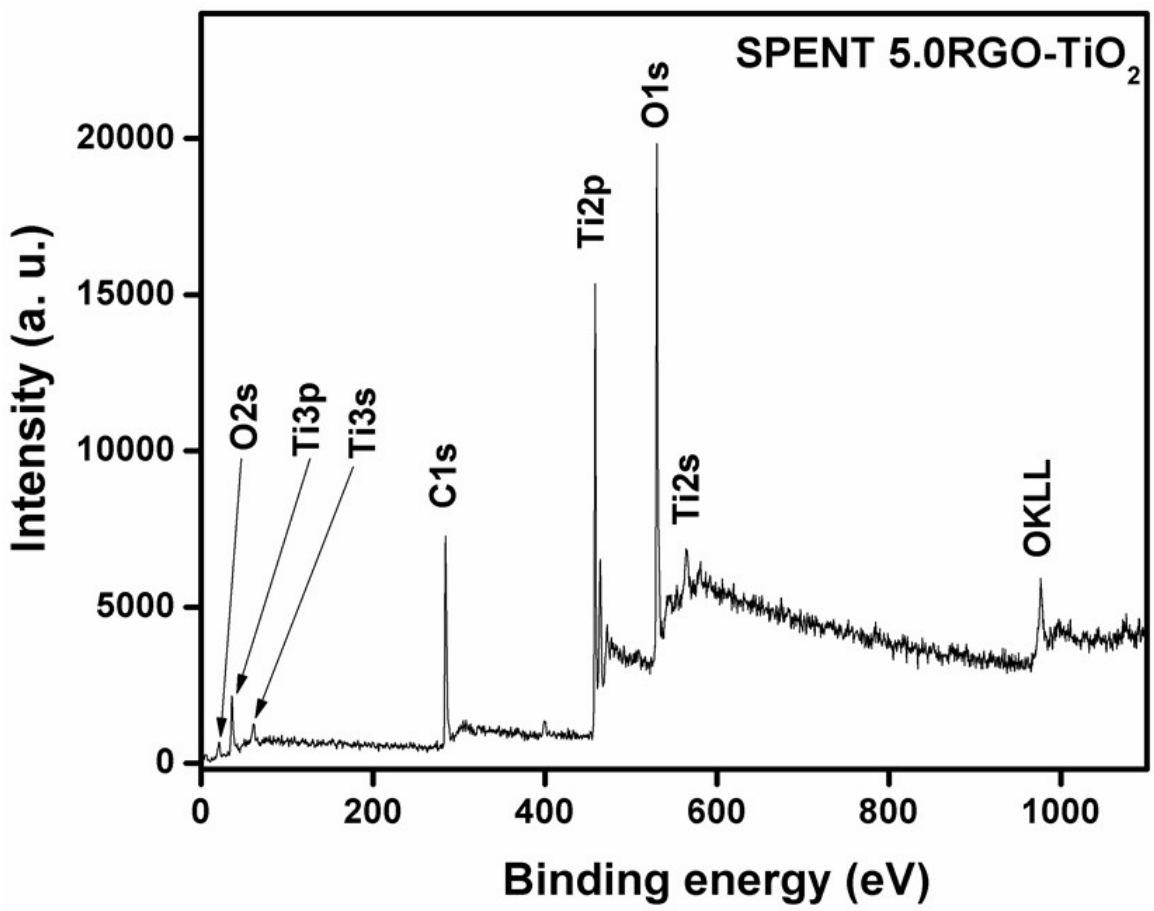

Figure 4.76 X-ray photoelectron spectroscopy survey spectrum of spent 5.0RGO-TiO_2.

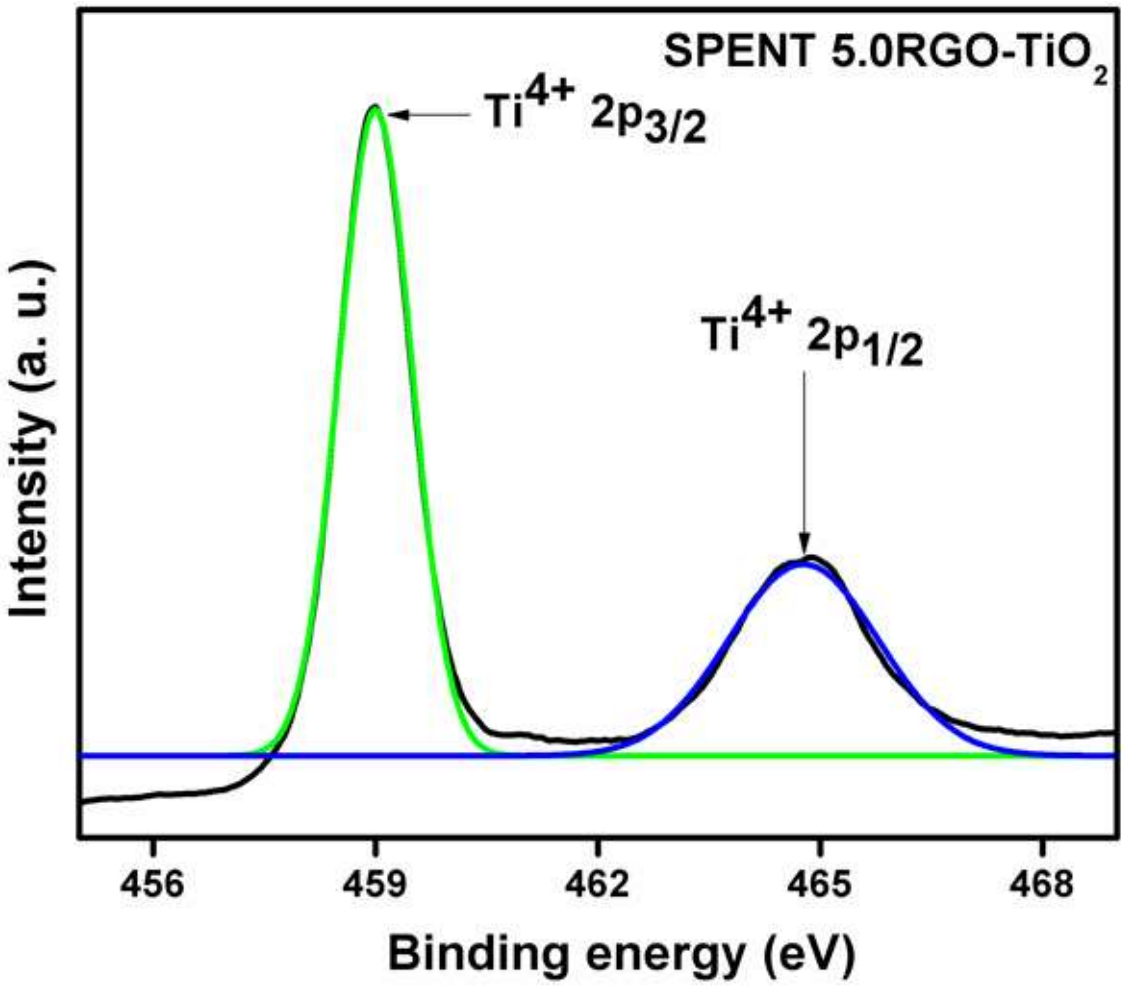

Figure 4.77 High-resolution X-ray photoelectron spectroscopy spectrum of Ti2p of spent 5.0RGO-TiO_2.

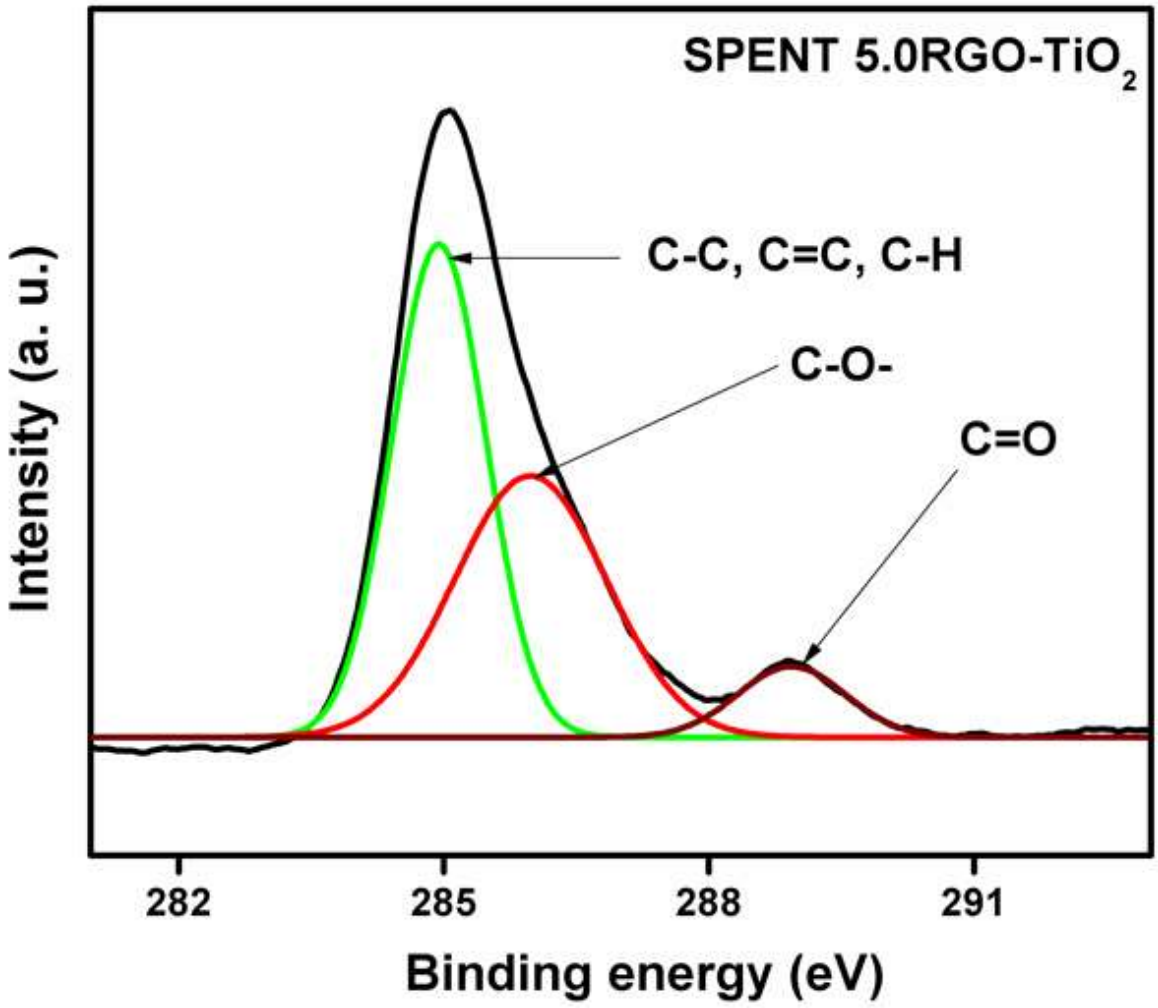

Figure 4.78 High-resolution X-ray photoelectron spectroscopy spectrum of C1s of spent 5.0RGO-TiO_2.

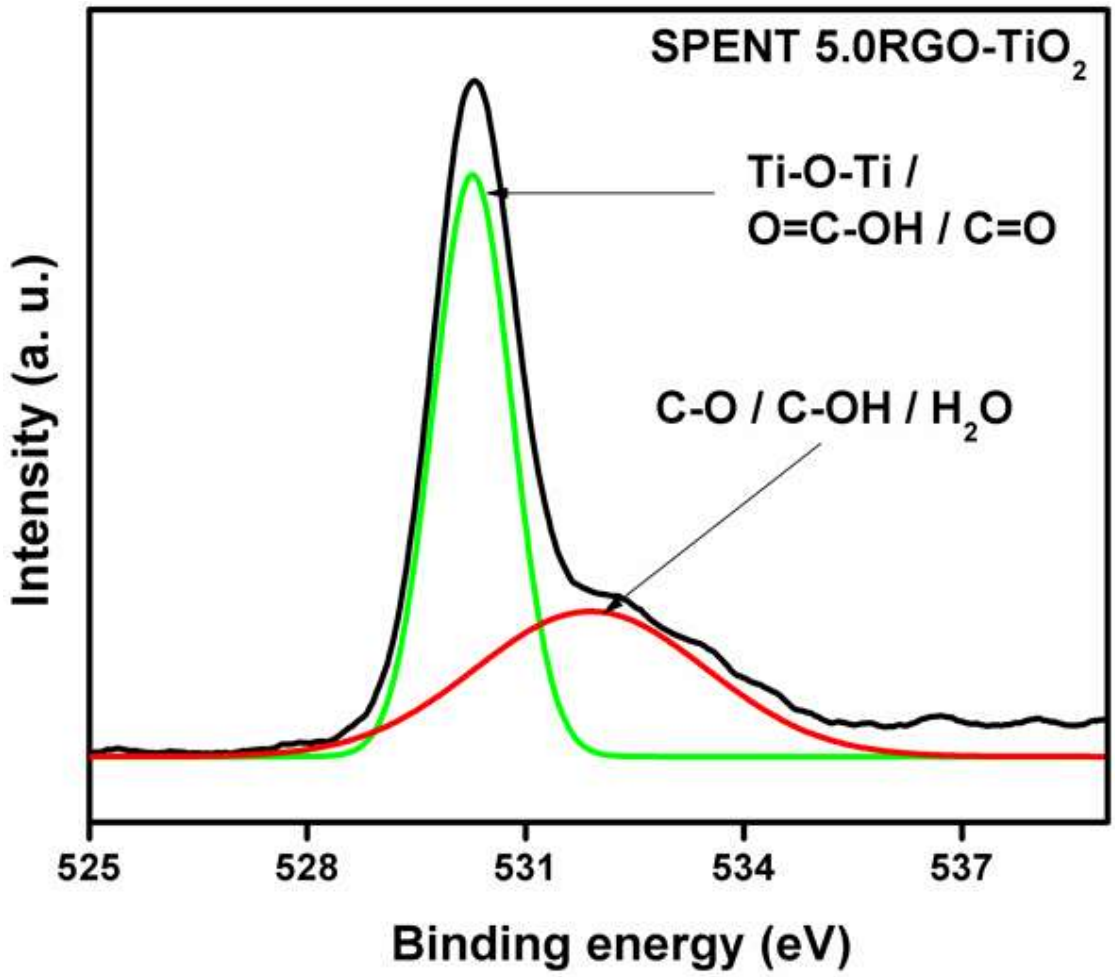

Figure 4.79 High-resolution X-ray photoelectron spectroscopy spectrum of O1s of spent 5.0RGO-TiO_2.

4.2.6 Computational studies of TiO_2 NPs and RGO-TiO_2 nanocomposites

The computational studies of TiO_2 NPs and RGO-TiO_2 nanocomposites were performed by initially placing the graphene nanosheet (GNS) and TiO_2 nanoparticle in a direction such that a (1 0 1) facet of the nanoparticle was located approximately in the centre of GNS. The benefit of using finite size cluster graphene models, as opposed to infinite periodic boundary condition models,is the full presence of rotational degrees of freedom in geometry relaxation of conjugates. Thus, not only the distance between GNS and TiO_2 but also tilting angles can be adjusted. Figure 4.80 and 4.81 show the atomic structure of the conjugate after the full geometry relaxation, using a conjugate gradient method. It was observed that the atoms of carbon of GNS and atoms of (1 0 1) facet moved to a distance closer than the sum of the van der Waals radii (Figure 4.80). The optimisation of the geometry resulted in some rotation of the GNS relative to the initial configuration with the armchair edge parallel to the (0 0 1) surface as shown in Figure 4.81.

Based on the computational results, the adsorption energy of GNS over (1 0 1) facet of the TiO_2 nanoparticle Ti44r1 was -27.38 kcal mol^{-1}. Approximately 63 carbon atoms of the GNS took part in the GNS-Ti44r1 van der Waals complex, and the interaction energy was calculated as 0.43 kcal mol^{-1} of carbon atoms. The value is about twice lower than the average reported in the literature, in which the interaction energy between graphene sheets was 0.804 kcal mol^{-1} C (Vorontsov and Tretyakov, 2018b). The difference may be partially ascribed to the non-flat character of the (1 0 1) surface so that many atoms are not close enough.

The density of states of the separate Ti44r1, GNS, and the GNS-Ti44r1 complex in the range of energy eigenvalues of -10 to 0 eV are shown in Figure 4.82. The Fermi level energy of these nano-objects at 298.15 K is -4.00, -4.48, and -4.49 eV, respectively. Therefore, GNS determines the Fermi level position in the composite. Ti44r1 showed the band gap typical for anatase as shown in Figure 4.82a, while GNS did not show any band gap with a smearing of orbitals population among eigenvalues of -4.55 to -4.37 eV as shown in Figure 4.82b. GNS possessed a significant number of states equal to 20 inside the band gap of Ti44r1 from -5.47 to -2.52 eV. As shown in Figure 4.82c, the formation ofthe GNS-Ti44r1 complex resulted in a significant change in DOS distribution and

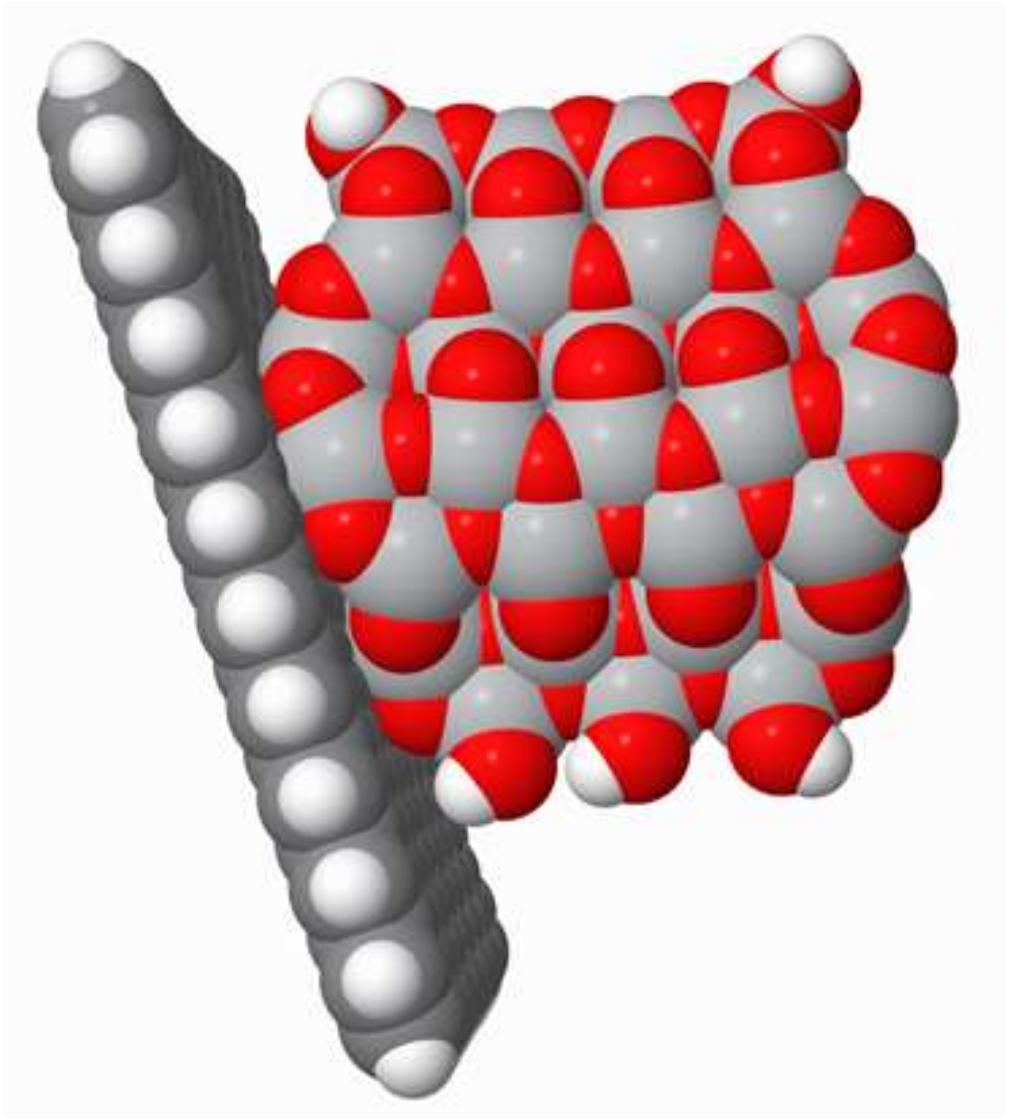

Figure 4.80 Structure of the fully optimised GNS-Ti44r1 conjugate in van der Waals spheres. Atom designations: H - white, C – dark grey, O – red, Ti – grey balls.

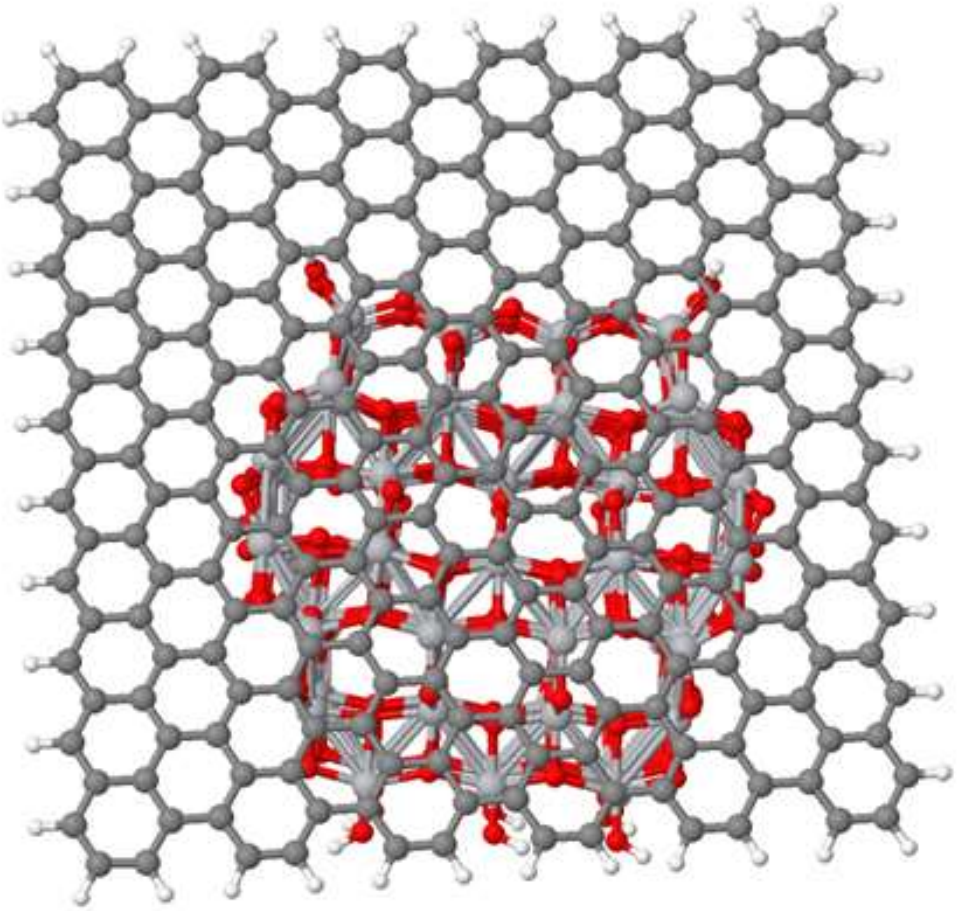

Figure 4.81 Structure of the fully optimised GNS-Ti44r1 conjugate in ball-and-stick representations. Atom designations: H - white, C – dark grey, O – red, Ti – grey balls.

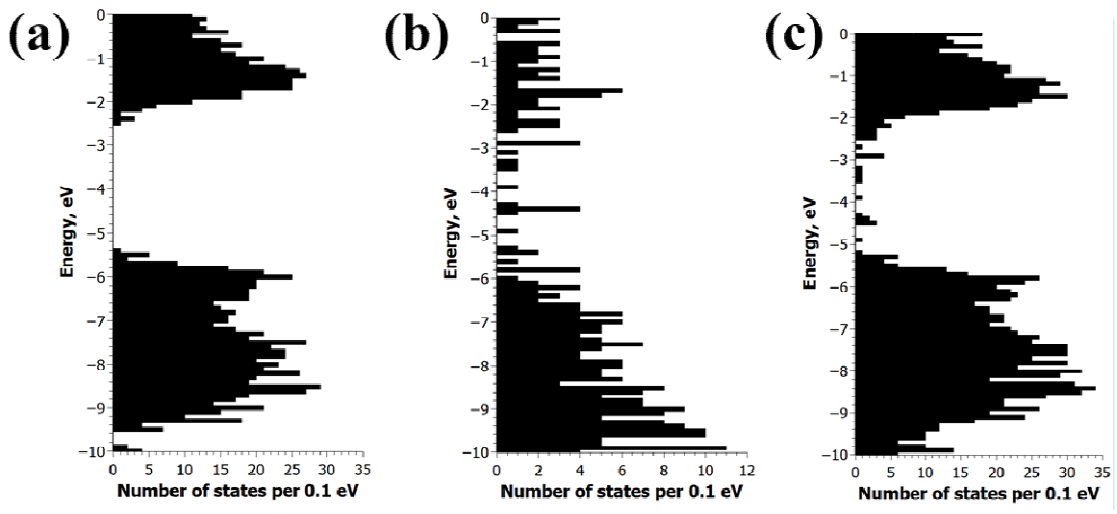

Figure 4.82 Density of states for the (a) optimised TiO_2 nanoparticle, (b) graphene quantum dot and (c) GNS-Ti44r1 conjugate.

appearance of new energy levels inside the Ti44r1 band gap. The number of states inside the band gap became 28.

The presence of states in the band gap for the GNS-Ti44r1 composite means that this composite can be excited under visible light irradiation. However, possibility of a real advantage of the composite in comparison to separate components can be obtained if photoexcitation (1) proceeds under visible light, (2) creates electrons and holes with energy enough to drive the reactions, and (3) produces photogenerated charges with a lifetime long enough for their reaction to complete. There are three different possibilities of photoexcitation with visible light: (1) photoexcitation of graphene component with the creation of electron and hole in graphene; (2) excitation with charge transfer from TiO_2 to graphene; and (3) excitation with charge transfer from graphene to TiO_2. The advantage of the composite is realised if the charge is transferred as a result of photoexcitation. It is often suggested that photogenerated charges are quickly thermalised before taking part in electron transfer reactions (Vorontsov and Tretyakov, 2018b). For graphene, this means recombination of photogenerated charges or a photogenerated electron with energy similar to Fermi energy. Taking the TiO_2 conduction band edge potential as -0.1 V, graphene Fermi level potential is about +2.0 V which is too much positive for the electron to drive any reaction of reduction of interest. Therefore, without external electron donors, only possibility of photogenerated thermalized electron in TiO_2 conduction band provides reactivity enough to carry out the reactions of hydrogen production (E^0 = 0 V at pH 0) or CO_2 reduction (E^0 = -0.24 V for methane product, -0.38 V for methanol, and -0.53 V for CO at pH 7). Another interesting possibility is realised if there is an overlap of orbitals of graphene and TiO_2. If such combined orbitals are within the TiO_2 band gap, they can actively participate in the visible light photoexcitation.

Furthermore, we consider molecular orbitals (MO) of the GNS-Ti44r1 conjugate. Figure 4.83 shows some characteristic examples of MO around the Ti44r1 band gap. Theinvestigation spanned the orbitals range from #1478 (-5.75 eV) to #1559 (-1.98 eV). MO 1478 – 1490 were formed exclusively by oxygen p-orbitals of Ti44r1. MO 1492 (-5.65 eV) shown in Figure 4.83a includes atomic orbitals (AO) of oxygen in Ti44r1 and carbon in GNS. Orbitals 1493 – 1501 are formed by p AO of oxygen and traces of d AO

of titanium across the Ti44r1 nanoparticle. MO 1502 (-5.55 eV) was formed by p oxygen AO

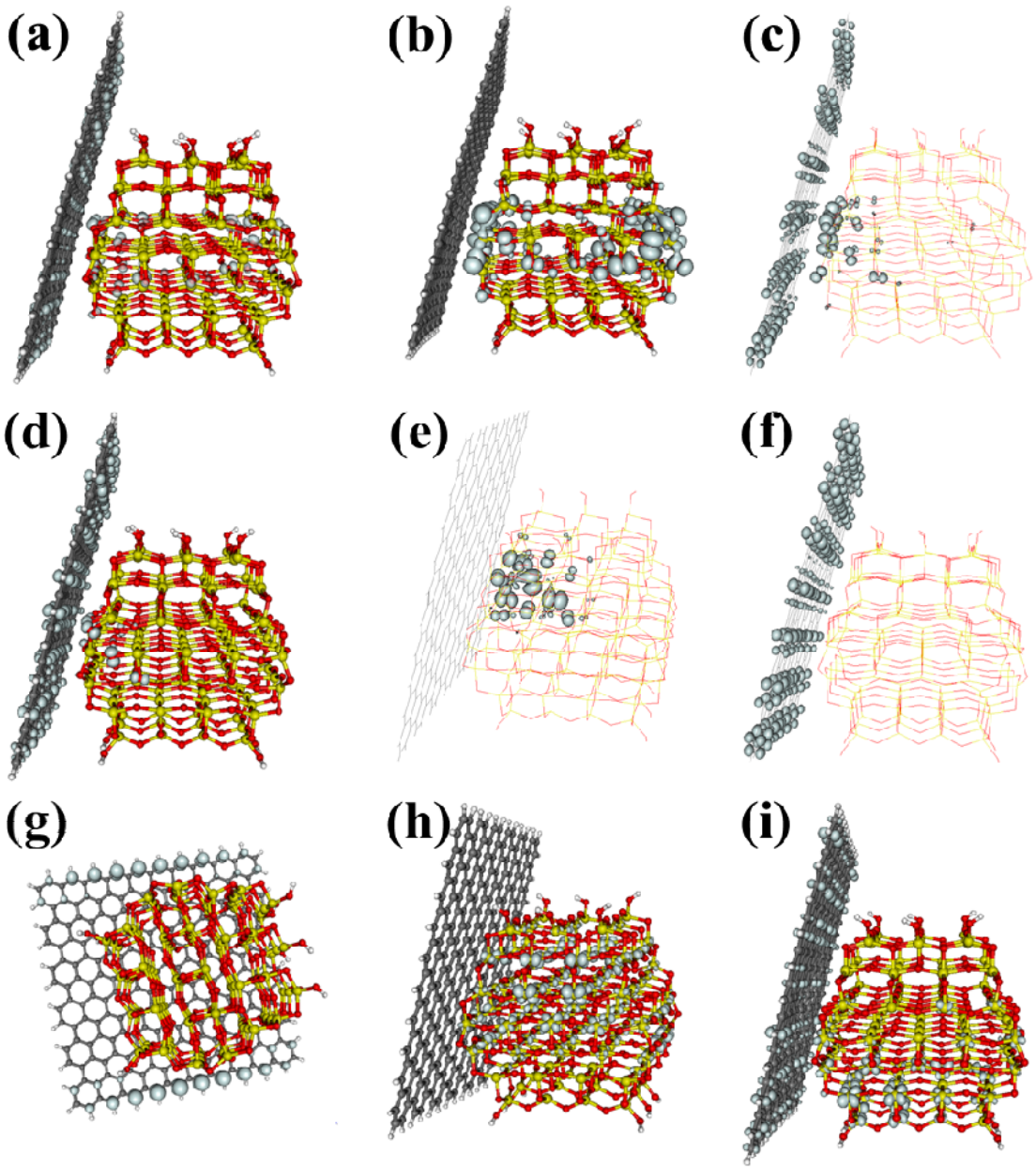

Figure 4.83 Selected molecular orbitals in the GNS-TiO_2 composite: (a) 1492, (b) 1505-1509 except 1507, (c) 1507, (d) 1513, (e) 1514, (f) 1515, (g) 1517, (h) 1538, (i) 1552-1553.

at corners formed by four (1 0 1) adjacent facets and traces of d AO of Ti there. This is characteristic for MO of decahedral anatase nanoparticles at the ceiling of the valence band. Orbitals 1503 (-5.52 eV) and 1504 (-5.48 eV) contain AO of oxygen and carbon. It was supposed that these orbitals correspond to the edge of the valence band since their energy is equal to the HOMO energy of the Ti44r1 nanoparticle (Vorontsov and Smirniotis, 2018a). However, detailed consideration of the upper lying MO led to a different conclusion. Figure 4.83b shows MO 1505 – 1509 (-5.45 to -5.38 eV). These orbitals corresponded to the type of orbitals at the upper part of the valence band of decahedral anatase nanoparticles as well, while MO 1507 shown in Figure 4.83c is a linear combination of GNS and Ti44r1 AO. Further orbitals 1510 – 1512 (-5.36 to -5.32 eV) also contained oxygen AO and traces of Ti AO at the (1 0 1)/(1 0 1)/(1 0 1)/(1 0 1) vertices. MO 1513 (-5.32 eV) shown in Figure 4.83d contains AO of both GNS and Ti44r1. The last orbital corresponding to the HOMO of Ti44r1 is #1514 shown in Figure 4.83e with energy -5.27 eV. Hence, the interaction of Ti44r1 with GNS resulted in a shift of HOMO of Ti44r1 from -5.47 to -5.27 eV, that is by +0.2 eV. The energy gap from -5.27 to -4.95 eV did not have any states.

Molecular orbitals #1515 to 1537 with energy range -4.95 to -2.43 eV were formed exclusively by p_z AO of carbon atoms in GNS. Figure 4.83f shows the first of these MO. The limited size of the GNS caused the appearance of MO with a high contribution from edge carbon atoms. This was the case for MO #1517 that was formed almost exclusively by p_z AO of carbon atoms residing in the zigzag edge of rectangular graphene nanosheet. MO # 1518 (E = -4.50 eV) corresponded to HOMO of the GNS-Ti44r1 conjugate at 0 K. Energy levels 1516 to 1521 were partially filled with electrons. A large number of gaps were noticed in the energy spectrum of GNS-Ti44r1 composite (Figure 4.82c), i. e. -4.95 to -4.56, -3.22 to -3.00, -2.92 to -2.71 to – 2.56 eV with width above 0.2 eV that resulted from the limited size of the graphene nanoribbon used in the modelling.

Contribution from AO of the Ti44r1 nanoparticle towards the conjugate started with the MO #1538 having energy -2.38 eV (Figure 4.83h). The energy of the Ti44r1 LUMO was shifted by +0.15 eV as a result of interaction with GNS. The shift of the HOMO and LUMO energy of Ti44r1 after its interaction with GNS was a consequence of charge injection from electron-rich GNS into TiO_2. No molecular orbital within the Ti44r1

band gap that contained AO of Ti44r1 was observed in the conjugate with GNS as suggested above. The energy range of - 2.38 to -1.98 eV was densely packed with orbitals that belong to Ti44r1, GNS or both components. Figure 4.83i shows two of the four MO formed by both Ti44r1 and GNS in the stated energy range. MO 1552 (-2.06 eV) and 1553 (-2.05 eV) contained d AO of Ti and p_z AO of carbon.

4.2.7 Photocatalytic reduction of CO_2 on TiO_2 NPs and RGO-TiO_2 nanocomposites

The photocatalytic reduction of CO_2 was tested in acetonitrile (ACN), H_2O and triethanolamine (TEOA) mixture (16:2:2 v/v in mL) under UVA for a period of 16 h as described in section 3.1.5 and 3.2.7. The photocatalytic activity of the prepared catalysts; TiO_2, 1.0RGO–TiO_2, 2.0RGO–TiO_2, 5.0RGO–TiO_2 and 10.0RGO–TiO_2, was performed for the reduction of CO_2 under UVA light for 16 h using 5 mg of all the samples. The prepared catalysts showed substantial activity and selectivity in the photocatalytic CO_2 reduction to methanol. Measurements were done initially for 8 h at 4 h intervals for the first day; then the reaction was paused, stored in the dark for few hours and resumed almost midnight and allowed to run overnight for the next 8 h till 16 h (next day). The production of methanol increases with time for all the catalysts. Ordinary TiO_2 exhibited methanol production rate of ca. 1.95 mmol g^{-1} h^{-1}; which is lower than all RGO-containing samples (Figure 4.84). The possibility of this observation could be the large band gap and fast recombination of e^- -h^+ pair in TiO_2 (Wang *et al.,* 2017a; Chen *et al.,* 2016). The wrapping of RGO on TiO_2 showed a significant influence on the photocatalytic activity. Factors including (1) synergistic effect between TiO_2 and RGO as a result of hydrothermal reaction, which allow the formation of chemical bond (Zhang *et al.,* 2017; Fan *et al.,* 2011), (2) reduced recombination of e^- -h^+ pair (Wang *et al.,* 2017b), and (3) higher surface area which provides more active adsorption sites and photocatalytic reaction centers (Chen *et al.,* 2016), could be responsible for the increased activity. Increasein photocatalytic activity was noticed with a higher amount of RGO from 1% to 5% weight ratio in the RGO–TiO_2 composites; however, a decreasing trend was observed with the further addition of RGO. This downward trend suggests that (1) excess RGO, as a competitor with TiO_2, can increase the scattering of light in the photocatalytic system, thus shielding the light reaching the surface of the TiO_2 photocatalysts (Zhang *et al.,* 2017);

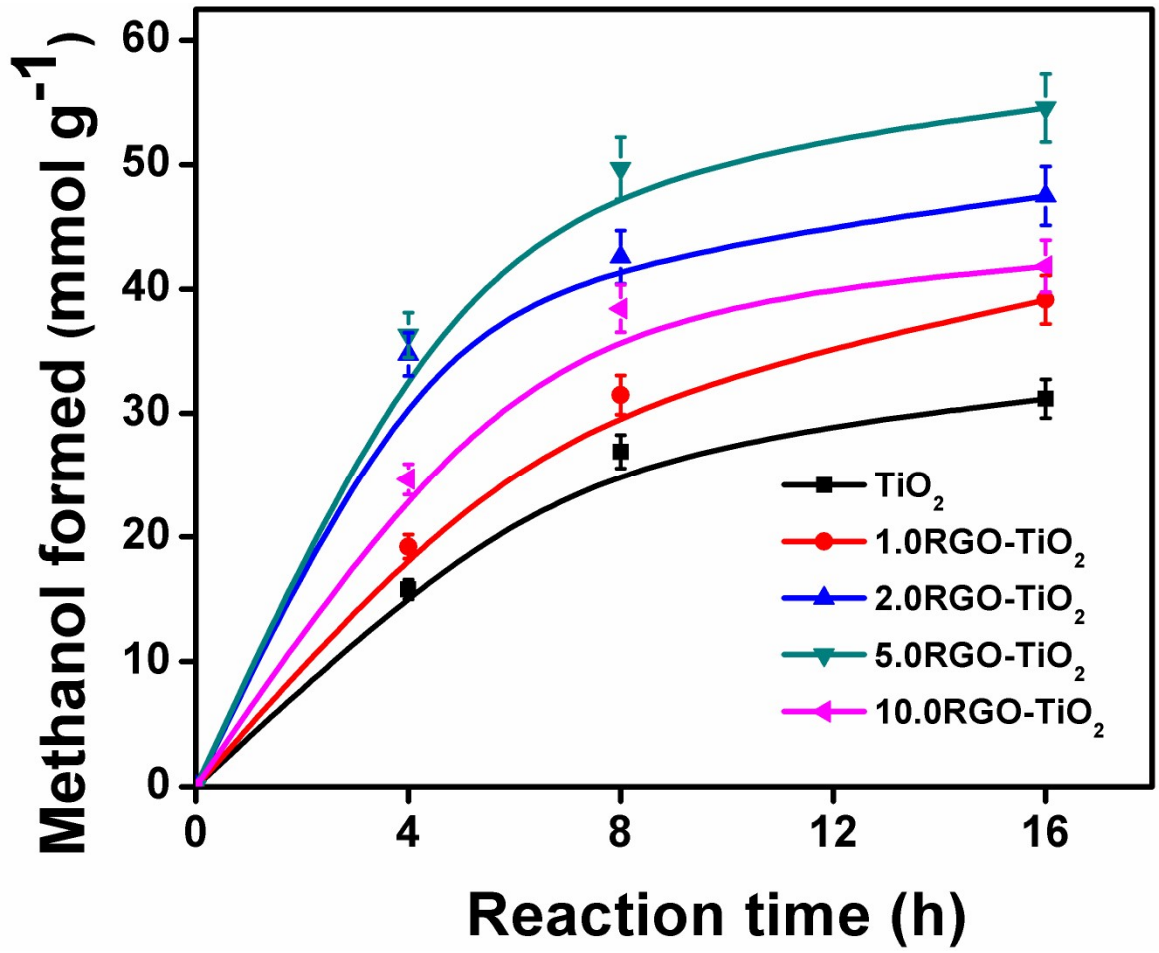

Figure 4.84 Rate of the formation of methanol from the reduction of CO_2 under UVA light irradiation of pure TiO_2 and all RGO-TiO_2 samples.

and (2) RGO can act as a charge–carrier recombination center (Wang *et al.,* 2012). Hence, it is crucial to get the optimum loading amount of RGO in the RGO–TiO_2 composites. Here, the optimum RGO was observed with 5.0RGO–TiO_2 with methanol production rate of 3.41 mmol g^{-1} h^{-1}, almost double the pure TiO_2.

To compare and to further probe the effect of optical properties, photocatalytic reduction of CO_2 to methanol was performed under visible light (from 420 nm to 700 nm) by maintaining the above experimental conditions. Figure 4.85 reveals that all the composites were photocatalytically active under visible light, with 2.0RGO-TiO_2 and 5.0RGO-TiO_2 performing almost equally. These results suggest that RGO narrowed the band gap of TiO_2 in a way to enhance its visible light activity. It is noteworthy that 5.0RGO–TiO_2 under visible light exhibited lower photocatalytic activities when compared in the presence of UVA light. This may be due to the higher amount of TiO_2 in comparison with RGO, which made it difficult for TiO_2 to catalyze the reaction under visible light effectively. Hence, the reaction rate was mainly determined by the amount of TiO_2 catalyst present (Wang *et al.,* 2017b; Li *et al.,* 2012).

The effect of reaction medium on the photocatalytic reduction of CO_2 was performed with 5.0RGO–TiO_2 in the presence of DMF, ACN, and DMSO by keeping other parameters constant under the visible light as shown in Figure 4.86. The trend in the photoreduction activity was found to be ACN < DMSO < DMF yielding 2.32, 0.95 and 0.74 mmol g^{-1} h^{-1} respectively, suggesting that CO_2 had higher solubility in ACN medium, which was crucial in product formation.

4.2.8 Mechanism of photocatalytic reduction of CO_2 on TiO_2 NPs and RGO-TiO_2 nanocomposites

According to the results of the experimental and the theoretical studies, the mechanism of CO_2 photoreduction was suggested as demonstrated in Scheme 4.2. The positive effect of the presence of graphene on the reduction of CO_2 is explained by its induced shift of TiO_2 conduction band (CB) towards more reductive potential and consequent increased rate of electron transfer to adsorbed CO_2 or carbonate species on the photocatalyst surface. Under UV irradiation, photoexcitation of anatase nanoparticles can proceed, and the resulting electrons and holes drive the CO_2 reduction and water oxidation. Excitation also proceeds in graphene. However, its direct contribution to the

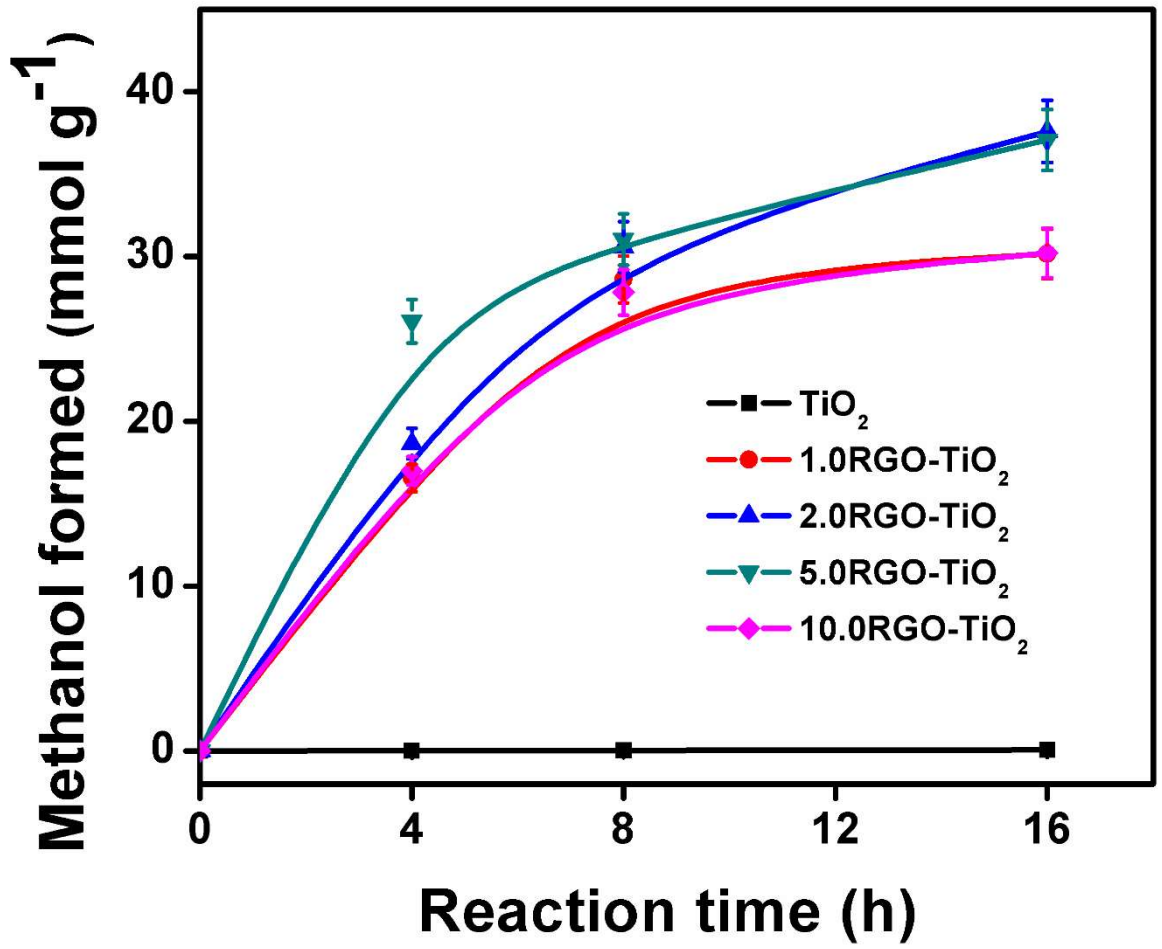

Figure 4.85 Rate of the production of methanol from the reduction of CO_2 under visible light irradiation by all RGO-TiO_2 composites.

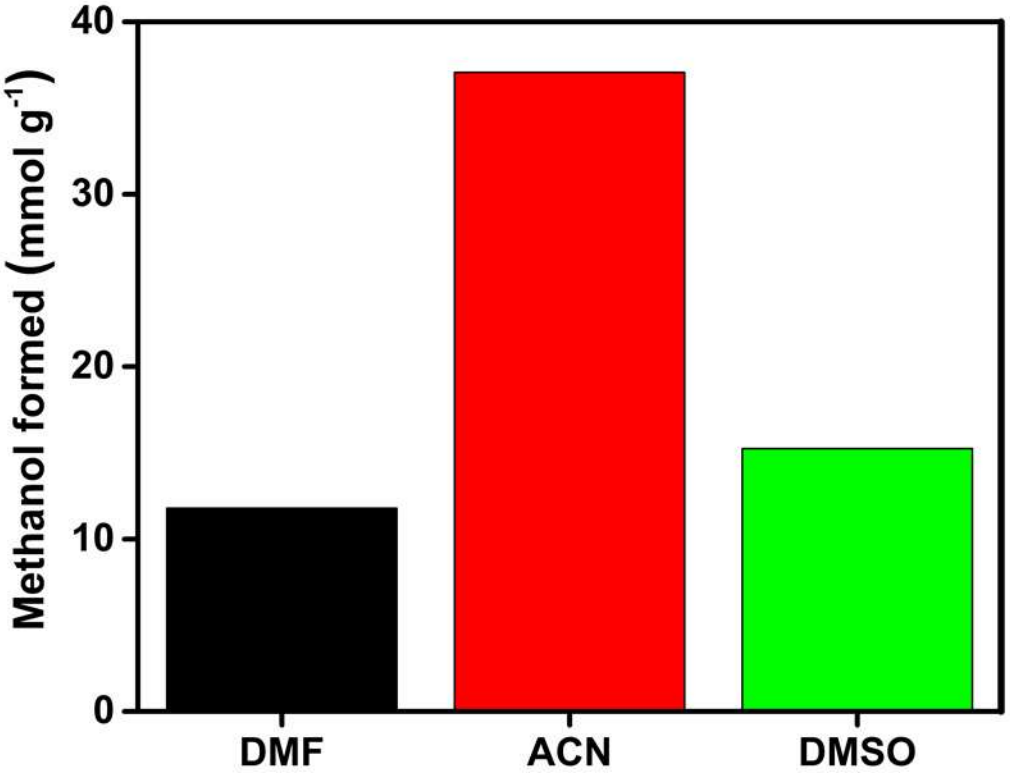

Figure 4.86 Influence of the reaction medium for the production of methanol from CO_2 reduction under visible light by 5.0RGO-TiO_2.

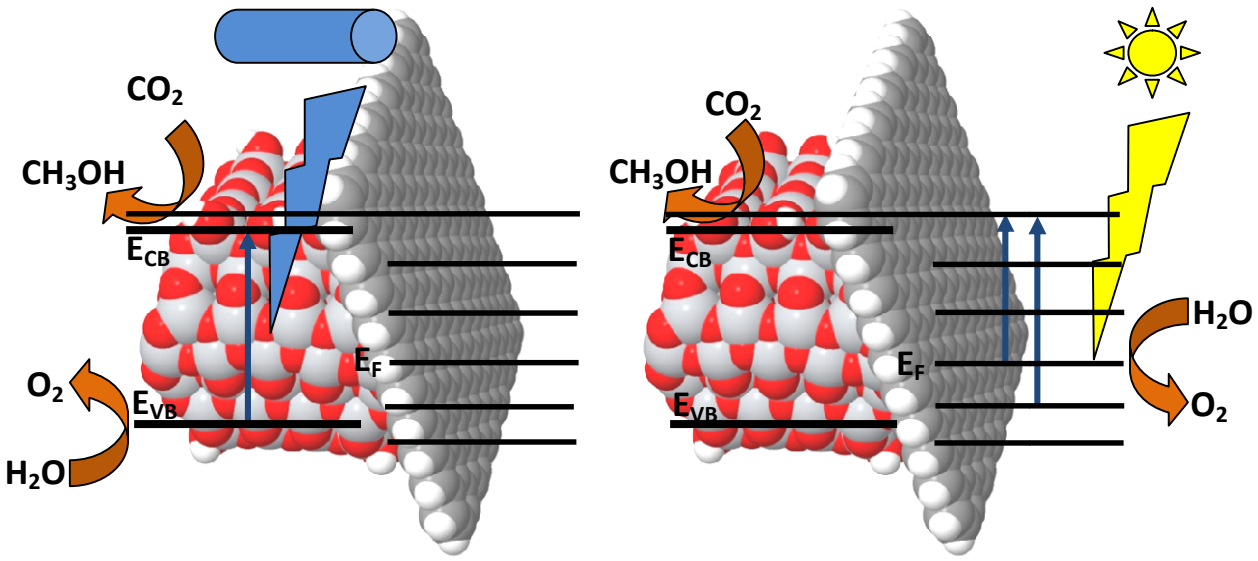

Scheme 4.2 Scheme of electronic excitations and electron transfer processes in the graphene-anatase composite according to the results of computational studies: (a) under UV light irradiation; (b) with visible light photoexcitation.

photoreaction is lower than that of TiO_2 because only moderate amounts of graphene (5 %) were beneficial for the photoreduction.

Under visible light photoexcitation, only graphene could absorb light. Generally, photoreactions should involve electron excitation from energy levels below the Fermi energy to levels with energy large enough for the CO_2 reduction to proceed. TiO_2 nanoparticles are the hosts for the long-lived thermalised charge carriers. Thus, the CO_2 reduction proceeded over TiO_2 nanoparticles surface. The key role of TiO_2 was again confirmed by the best moderate contents of graphene in the composite for the visible-light CO_2 photoreduction. As there were common energy levels for both graphene and TiO_2 component (Figure 4.83), electron photoproduced in graphene freely moved to TiO_2 where it was thermalised into the conduction band bottom level and took part in the CO_2 reduction.

4.3 Synthesis of visible light active CNT-TiO_2 composites

The TiO_2 nanoparticles and CNT-TiO_2 composites, which were code-named as TiO_2, 1.0CNT-TiO_2, 2.0CNT-TiO_2 and 5.0CNT-TiO_2, were prepared according to Section 3.4.1. The bare TiO_2 nanoparticles used for comparison with the obtained CNT-TiO_2 nanocomposites were the same as the ones presented in section 4.2. Therefore, some of TiO_2 nanoparticles characterisation were excluded in section 4.3 to avoid repetition. The pure TiO_2 was white in colour while all CNT-TiO_2 samples were dark grey in colour. All the prepared catalysts were characterisedusing techniques as described in Section 3.2.2 and 3.3.4.

4.3.1 X-ray diffraction characterisation of the TiO_2 NPs and CNT-TiO_2 composites

The XRD images of CNT, TiO_2 and CNT-TiO_2samples are depicted in Figure 4.87. The two peaks positioned at 25.9° and 43.5° have been assigned to (0 0 2) and (1 0 0) planes of the CNT. All diffraction peaks noticed in pure TiO_2 and CNT-TiO_2 were consistent with tetragonal anatase TiO_2 (JCPDS 21-1272). However, no major peak of the CNT at 2θ = 25.9° was noticed in all CNT-TiO_2 samples. The non-appearance of CNT indicates that the peak of CNT at 2θ = 25.9° had been dominated by the significant peak of TiO_2 at 2θ = 25.3°. In Figure 4.87 (inset), an increase in the broadening of the significant peak of TiO_2 at 2θ = 25.3° was observed as the amount of CNT in CNT-TiO_2 composite was increased, suggesting that the addition of CNT decreased the crystal size of TiO_2. With the use of Scherrer's formula, the crystalline size of TiO_2 was calculated to be 16.0 nm and reduced to around 13.2 nm in the composites (Table 4.7). This indicates that CNT reduced the growth of TiO_2 during the calcination stage (Chuan-Yu *et al.,* 2008).

4.3.2 Surface area and UV-Vis. diffuse reflectance spectroscopy characterisation of TiO_2 NPs and CNT-TiO_2 composites

The adsorption-desorption isotherms of TiO_2 and CNT-TiO_2 samples are revealed in Figure 4.88. The isotherms exhibited by all samples are known as type IV isotherm, which is typical of a mesoporous material. The type IV isotherm is further categorized as type H3 hysteresis loop, which is as a result of slit-shaped pores formed from the agglomeration of small particles (Leofanti *et al.,* 1998). The pore size distribution curve of TiO_2 and CNT-TiO_2 samples are shown in Figure 4.89. It was noticed that the pore

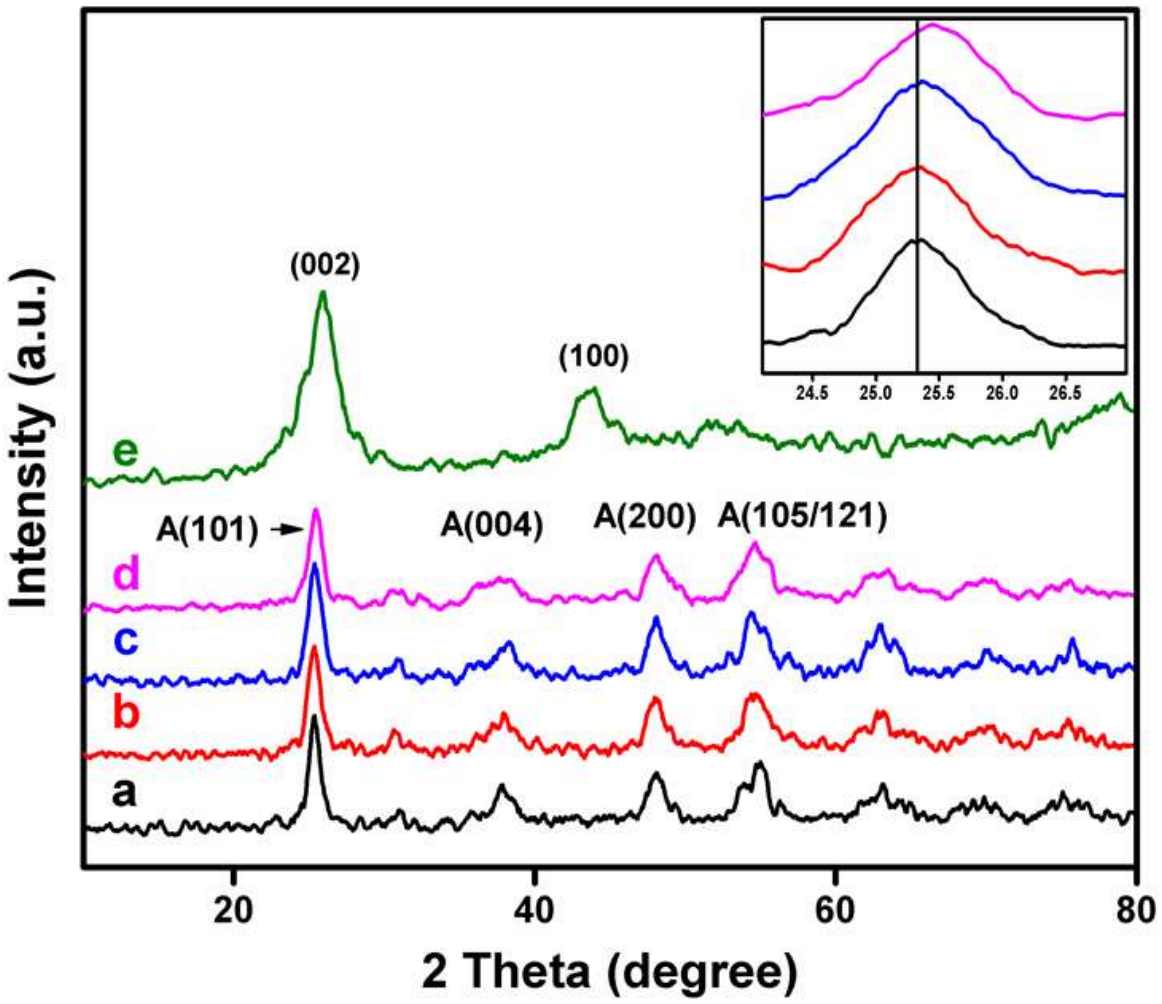

Figure 4.87 X-ray diffraction peaks of (a) pure TiO_2 (b) 1.0CNT-TiO_2 (c) 2.0CNT-TiO_2, (d) 5.0CNT-TiO_2 and (e) CNT.

Table 4.7 Physico-chemical properties of the pure TiO_2 and CNT-TiO_2 samples.

Type of catalyst	Crystalline size (nm)	Surface area (m^2/g)	Pore volume (cm^3/g)	Average Pore width (nm)
TiO_2	16.0	108.3	0.25	7.0
1.0CNT-TiO_2	14.4	110.3	0.26	7.5
2.0CNT-TiO_2	13.4	113.5	0.26	7.4
5.0CNT-TiO_2	13.2	117.1	0.25	6.8

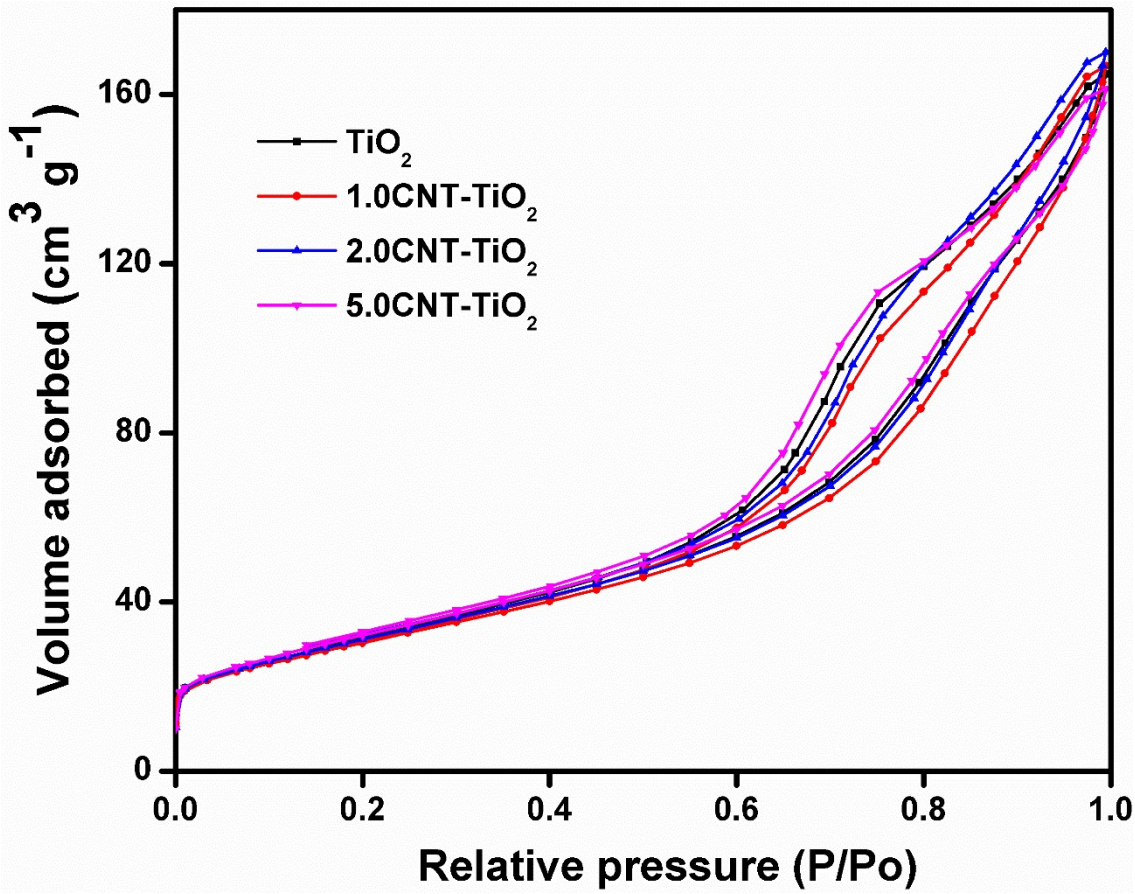

Figure 4.88 N_2 adsorption-desorption isotherms of pure TiO_2 and CNT-TiO_2 samples.

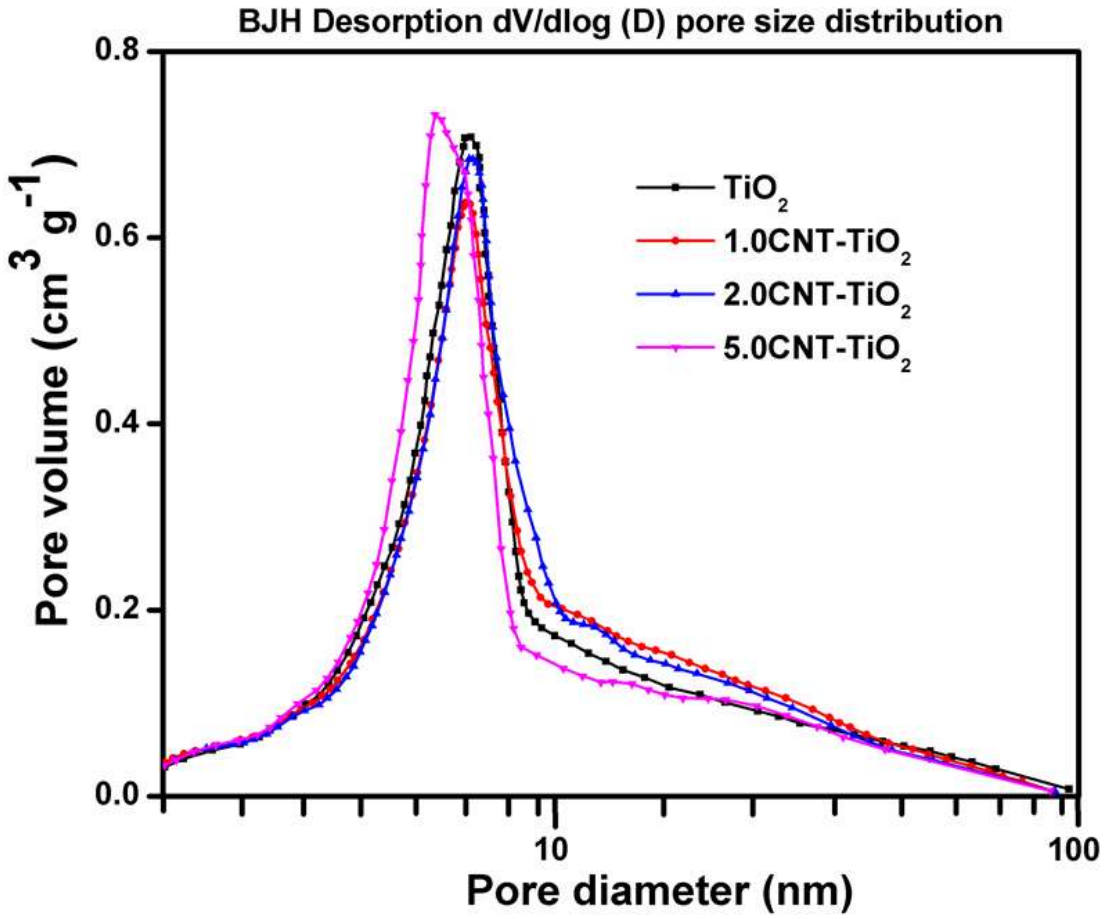

Figure 4.89 Pore size distribution curve of pure TiO_2 and CNT-TiO_2 samples.

maxima were shifted to the lower side as the percentage of CNT in the composite was increased.This suggests that the size of pores decreased with increasing CNT content in titania, while total pore volume remained almost the same for both TiO_2 and CNT-TiO_2 samples (Table 4.7 and Figure 4.90). According to Wheeler's equation (1) shown below.

$$\text{Surface Area} = \frac{4*\text{Pore Volume}}{\text{Pore width (size)}} \quad \ldots\ldots 4.5$$

According to equation 4.5 above, surface area is inversely proportional to pore width. Therefore, the reducing pore size at constant total pore volume observed as the amount of CNTs increased in $TiO_2$was most possibly responsible for higher surface area in all CNT-TiO_2 nanocomposites in comparison with pure TiO_2. The surface areas of TiO_2, 1.0CNT-TiO_2, 2.0CNT-TiO_2 and 5.0CNT-TiO_2 were found to be 108.3, 110.3, 113.5 and 117.1 $m^2 g^{-1}$, respectively (Table 4.7).

The UV−Vis. DRS of CNT, TiO_2 and CNT-TiO_2 composites are depicted in Figure 4.91. The characteristic absorption edge of pure TiO_2 catalyst was found to be 392 nm. This indicates the absorption of TiO_2in the UV region. The addition of CNT extended the light absorption of ordinary TiO_2 into the visible light region. The absorption in the visible light region increased with an increase in the amount of CNT in the CNT-TiO_2 nanocomposites. This red shift to higher wavelength by the CNT-TiO_2nanocomposites was as a result of the electronic interaction between CNT and TiO_2 (Yang *et al.,* 2013; An *et al.,* 2012). However, excessive addition of CNT can impede the illumination intensity of TiO_2 as a result of the shielding effect of the black colouration of CNT(Yu *et al.,* 2005b; Yao *et al.,* 2008; Li *et al.,* 2012). The Tauc plot of the pure TiO_2 and CNT-TiO_2 is shown in Figure 4.92. The energy of the band gap of the pure TiO_2 was calculated to be 3.2 eV; while energies of 1.0CNT-TiO_2, 2.0CNT-TiO_2 and 5.0CNT-TiO_2 were calculated to be 3.0, 2.9 and 2.8 eV, respectively. It could be observed that the band gap of TiO_2 decreased with increasing CNT content, indicating that CNT-TiO_2 composites could effectively absorb visible light (Akhavan *et al.,* 2010; Taleshi, 2015; Nourbakhsh *et al.,* 2016).

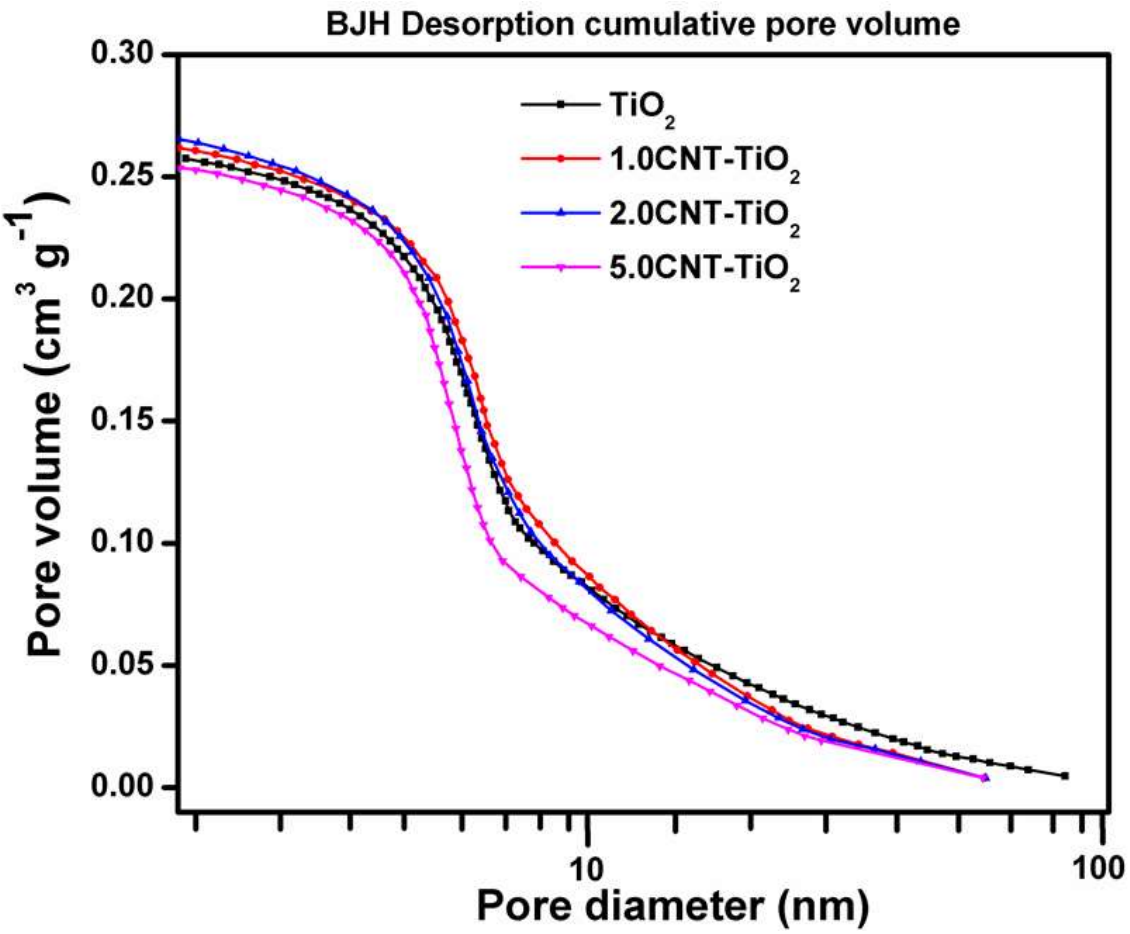

Figure 4.90 Desorption cumulative pore volume curve of pure TiO_2 and CNT-TiO_2 samples.

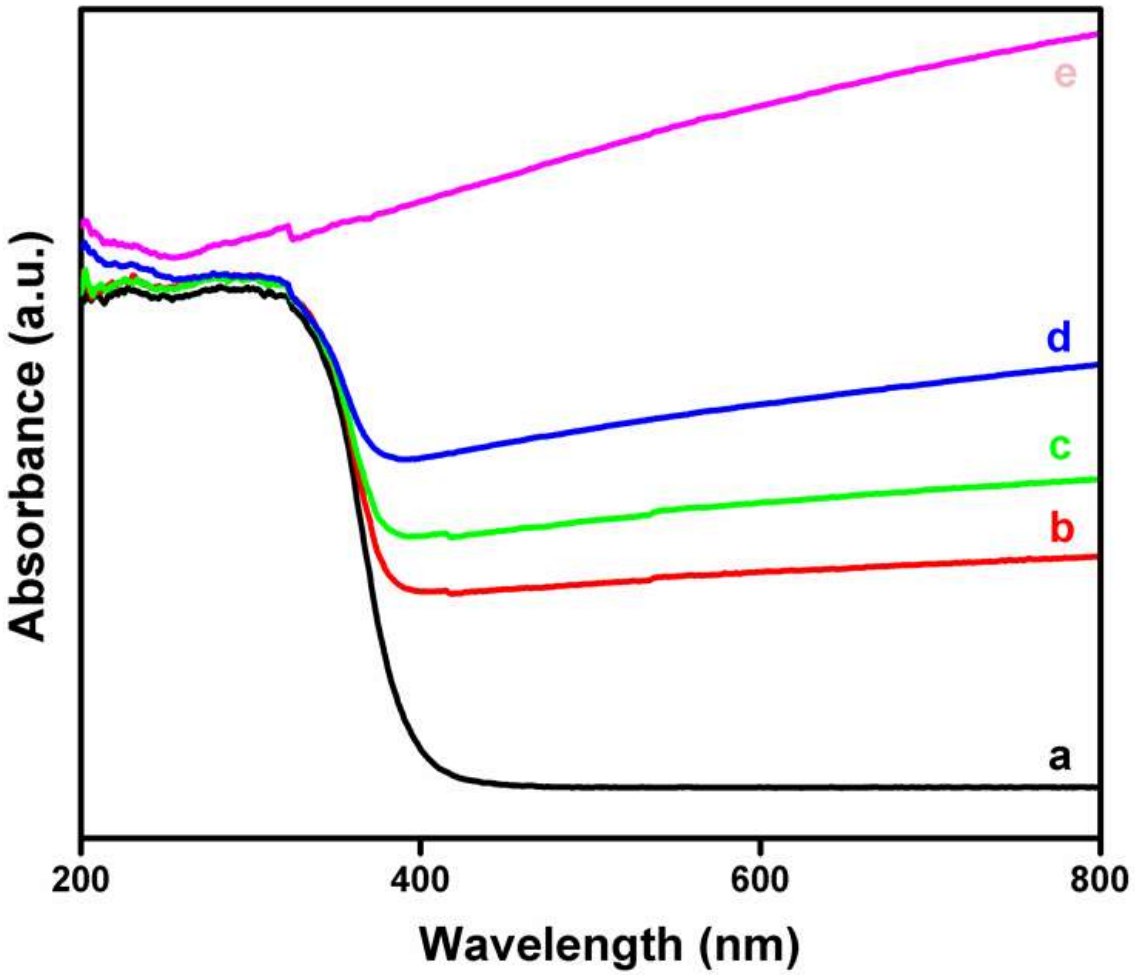

Figure 4.91 UV-Vis spectra of (a) pure TiO_2 (b) 1.0CNT-TiO_2 (c) 2.0CNT-TiO_2 (d) 5.0CNT-TiO_2 and (e) CNT samples.

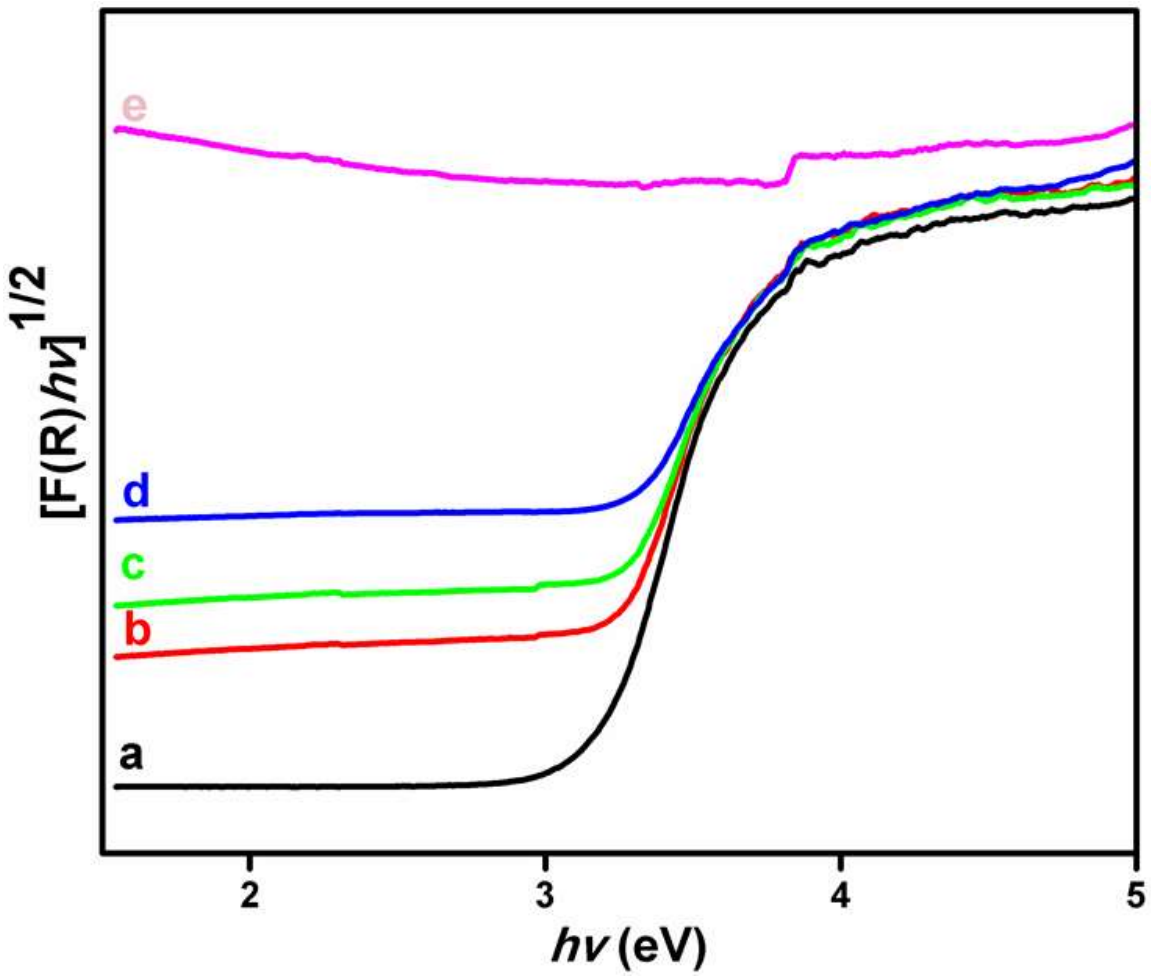

Figure 4.92. Tauc plot of (a) pure TiO_2 (b) 1.0CNT-TiO_2 (c) 2.0CNT-TiO_2 (d) 5.0CNT-TiO_2 and (e) CNT samples.

4.3.3 Scanning electron microscopy and transmission electron microscopy characterisation of TiO_2 NPs and CNT-TiO_2 nanocomposites

The morphologies of pure TiO_2 and CNT-TiO_2 composites with varying amount of CNT are shown by SEM images in Figure 4.93 – 4.95. Agglomeration was observed with TiO_2 as a result of the interaction of smaller size particles. However, with the introduction of CNT, the agglomeration tends to decrease with increasing amount of CNT in the composites. As obvious with the lower content of CNT, larger amount of TiO_2 nanoparticles were wrapped around the CNT. As the amount of CNT increased, more TiO_2 nanoparticles were attached to the wall of the tubes, leading to decrease in agglomeration of TiO_2 (An *et al.,* 2012; Yu *et al.,* 2005b). The presence of Ti, O and C in all the CNT containing samples was confirmed by SEM-EDX as shown in Figure 4.96 – 4.98.

Futhermore, in order to understand the microstructure of the prepared catalysts and to explore the effect of CNT on TiO_2 morphology,TEM images of CNT, TiO_2 and CNT-TiO_2catalysts were obtained.. As depicted in Figure 4.99 – 4.102, the addition of CNT to TiO_2 did not have any significant impact on the morphology of TiO_2. As the amount of CNT increases, more chances were available forTiO_2nanoparticles to be attached onto the wall of CNT (Figure 4.102). The appearance of the composites suggests that the physical and chemical interactions between TiO_2 and varying amount of CNT improved the electron and ion transport properties at the interfaces (Jing *et al.,* 2017). The shape of TiO_2 nanoparticles were spherical with their average particle size of around 12 nm. The size of TiO_2 decreased steadily to 7 nm as the amount of CNT increased in the composites. This suggest thatthe growth of TiO_2 particles was inhibited after the addition of CNT (An *et al.,* 2012). This trend was in agreement with the XRD results. The lattice fringes spacing of 0.342 nm was assigned to (1 0 1) plane of anatase TiO_2 as confirmed by HRTEM images (Figure 4.104). Elementary mapping confirmed the presence of C and O in pure CNT (Figure 4.106), and Ti, O, and C in the CNT-TiO_2 samples (Figure 4.107 - 109).

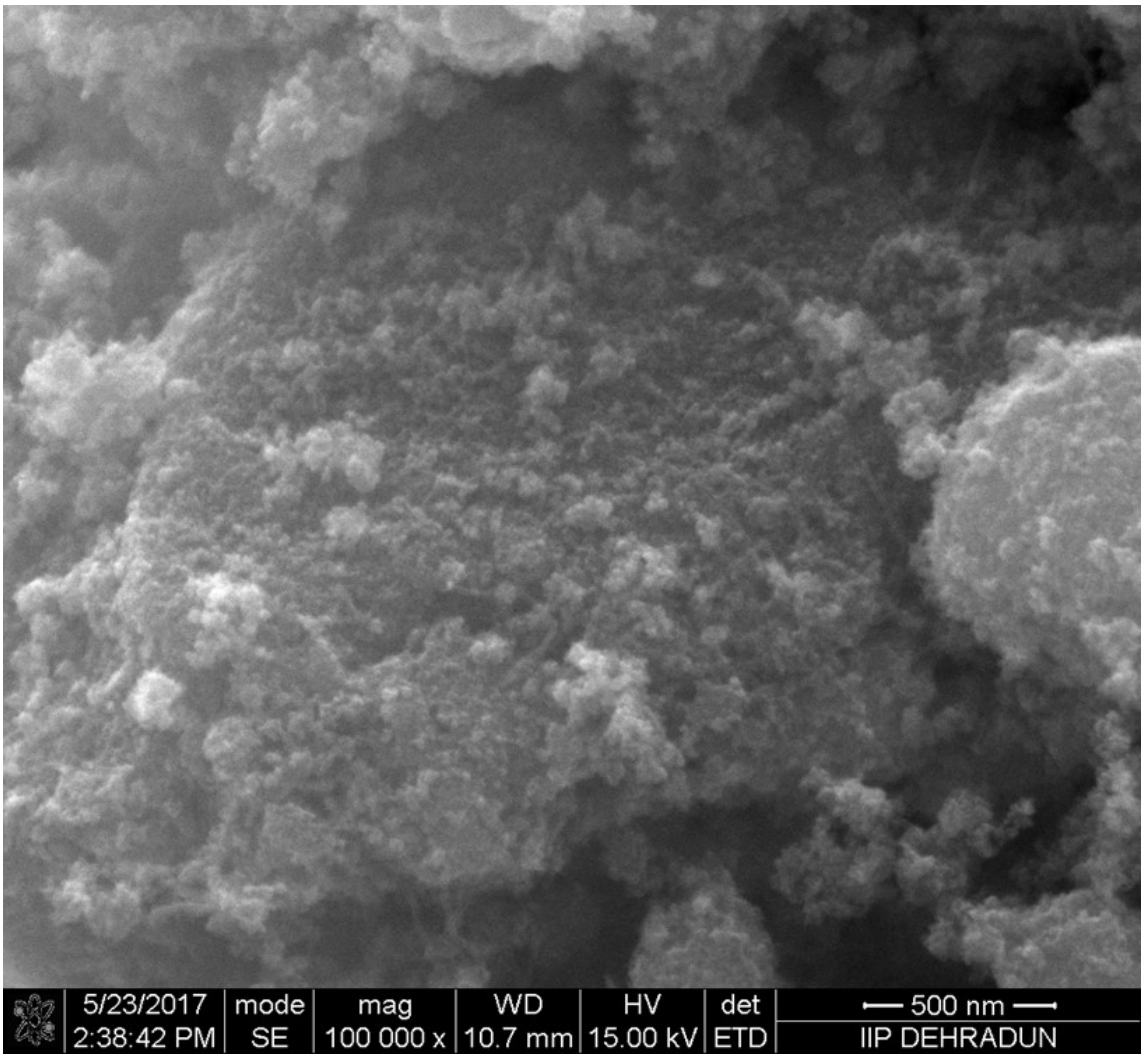

Figure 4.93 Scanning electron microscopy image of 1.0CNT-TiO_2 photocatalyst.

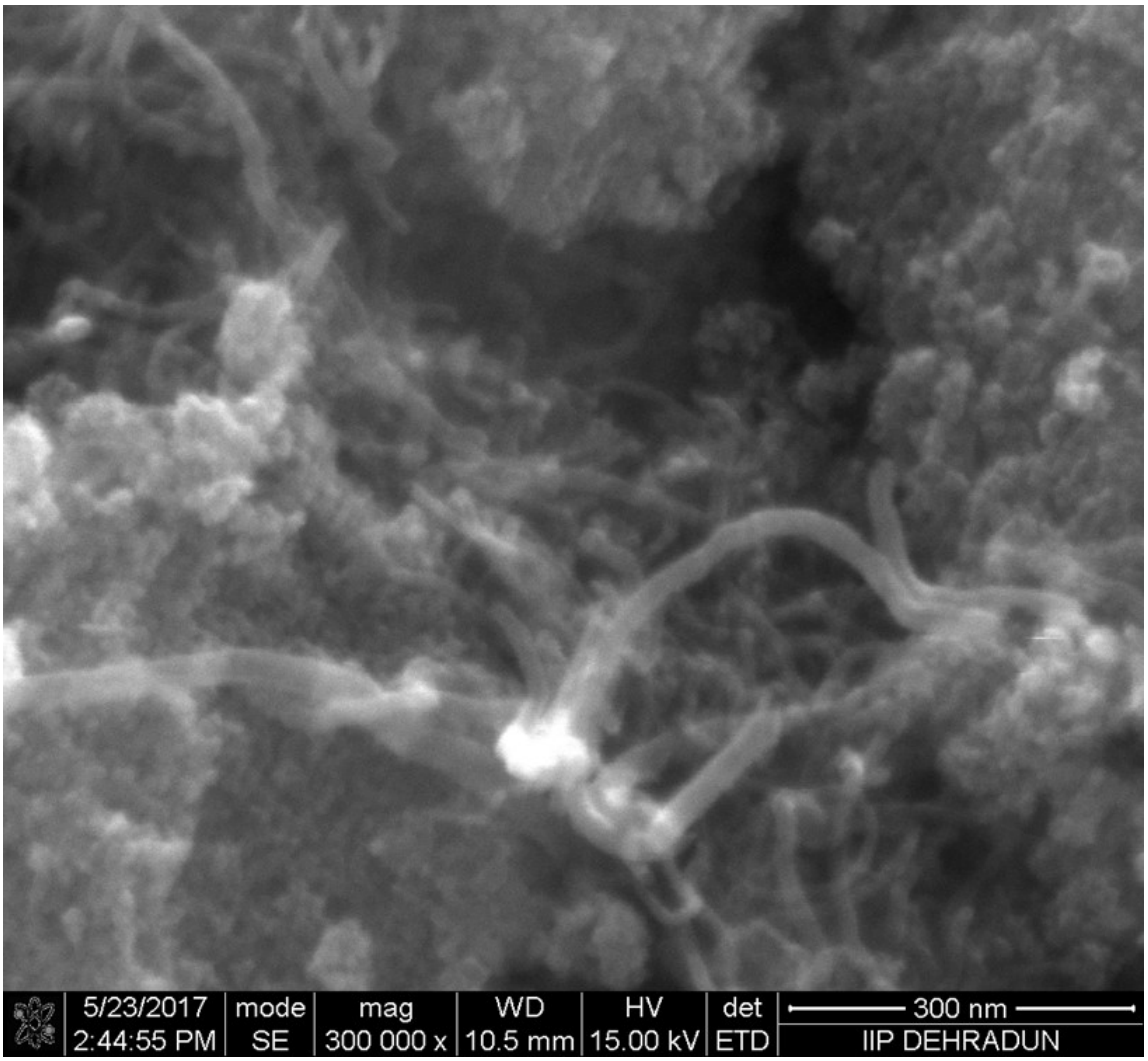

Figure 4.94 Scanning electron microscopy image of 2.0CNT-TiO_2 photocatalyst.

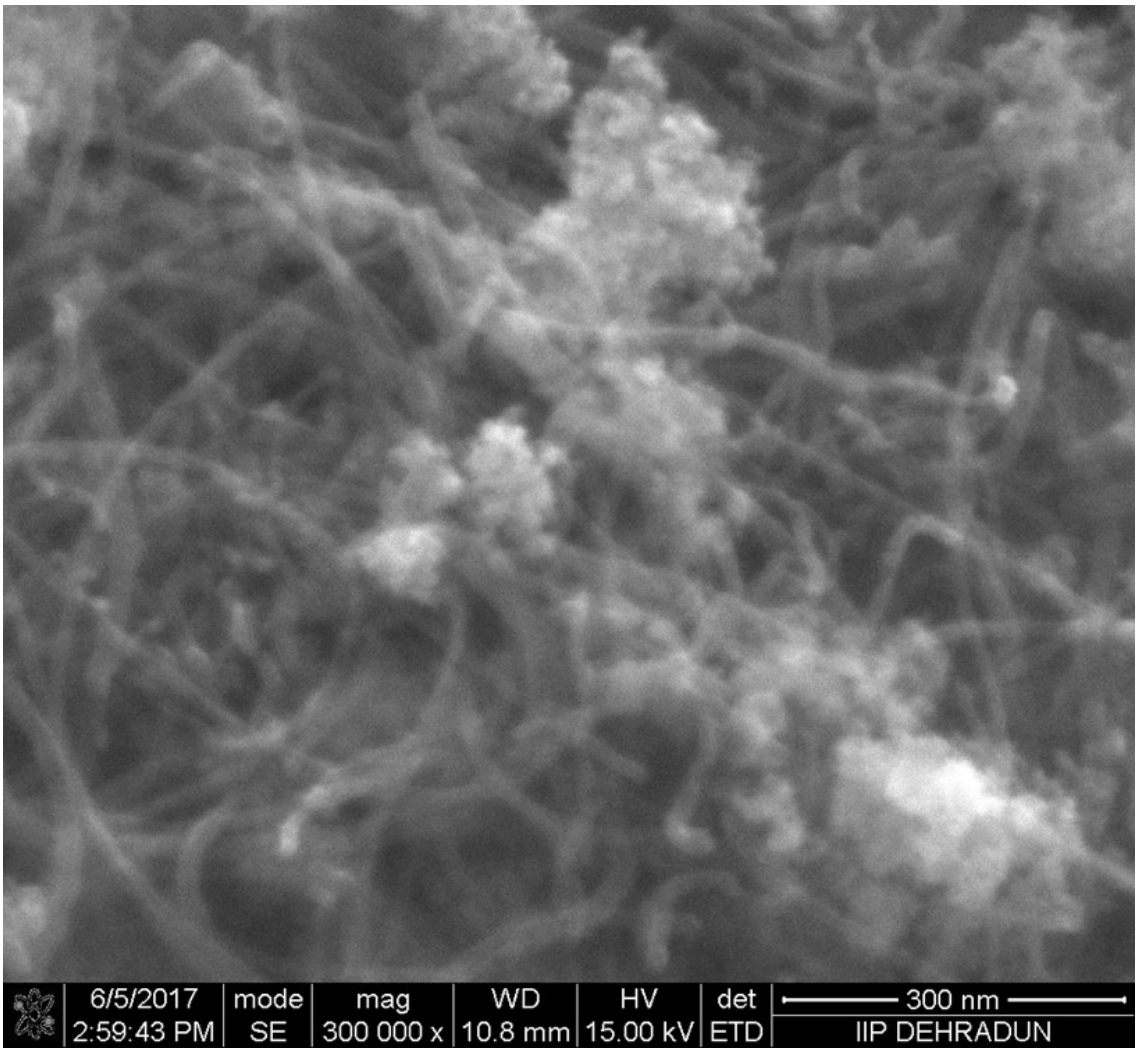

Figure 4.95 Scanning electron microscopy image of 5.0CNT-TiO_2 photocatalyst.

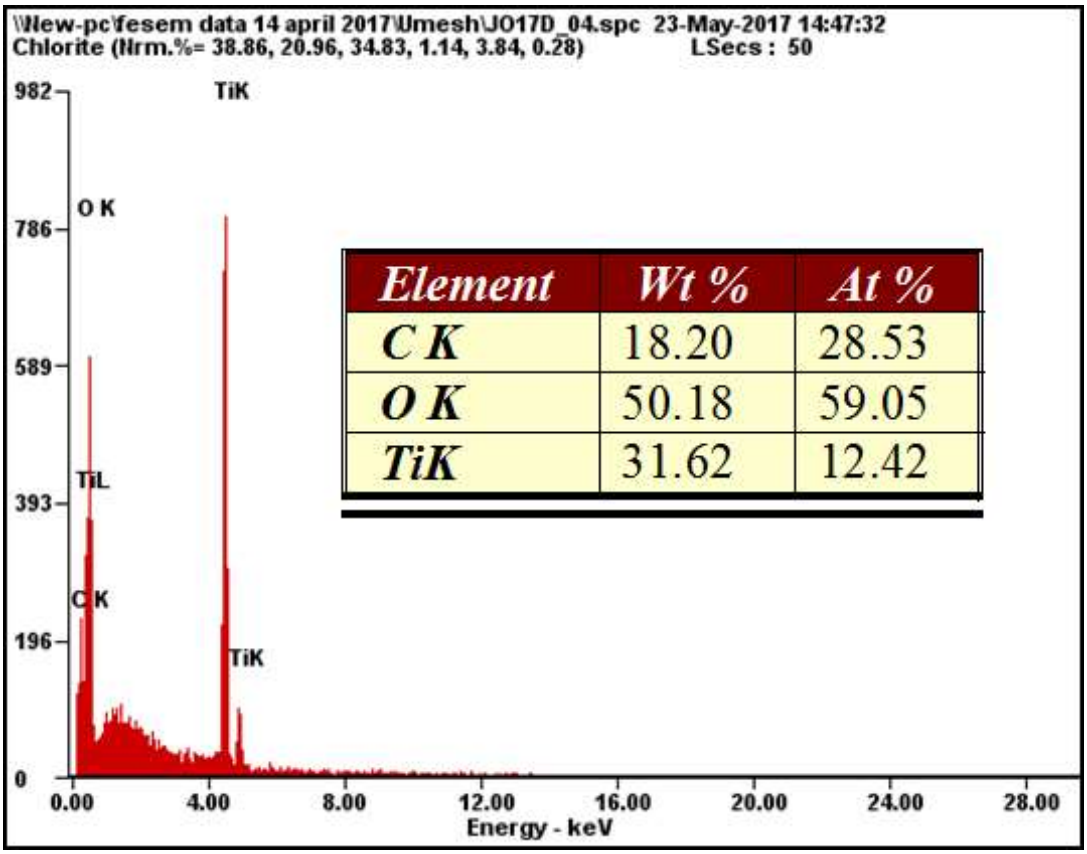

Figure 4.96 Energy-dispersive X-ray spectroscopy image of 1.0CNT-TiO_2 photocatalyst.

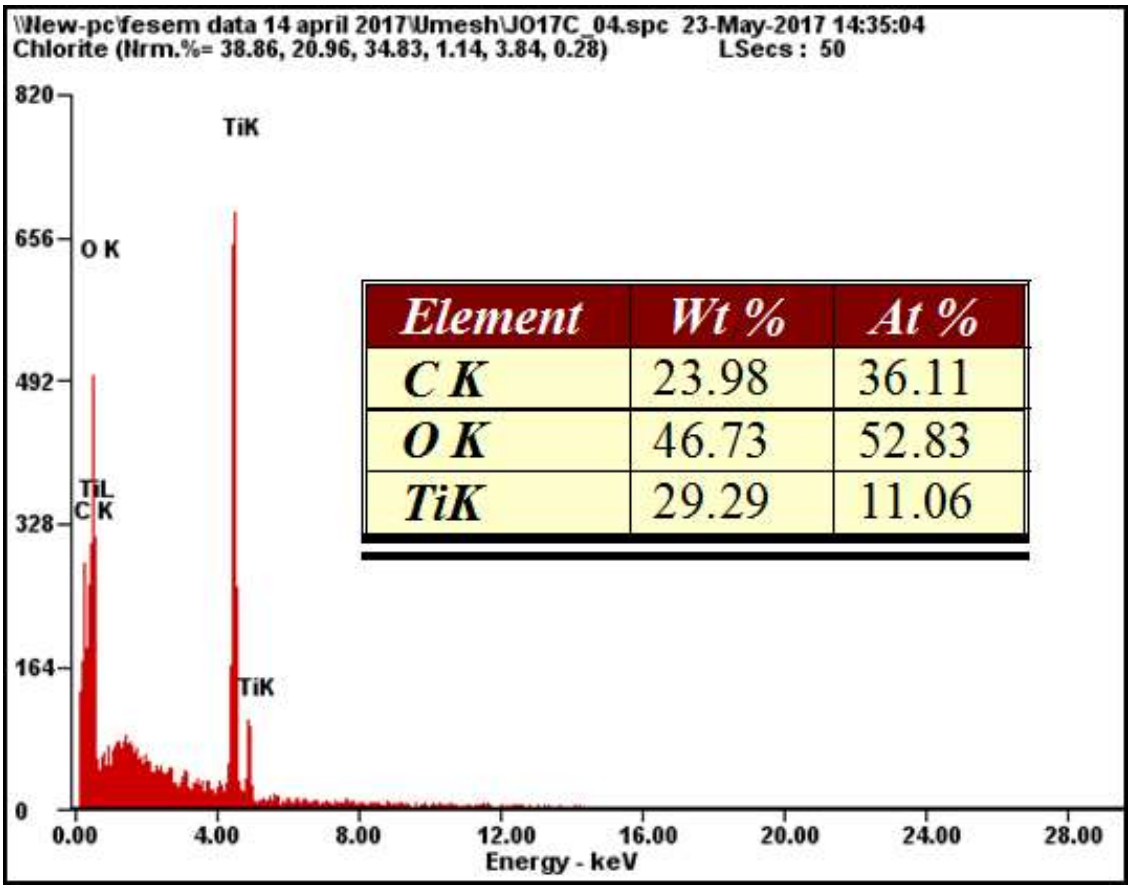

Figure 4.97 Energy-dispersive X-ray spectroscopy image of 2.0CNT-TiO_2 photocatalyst.

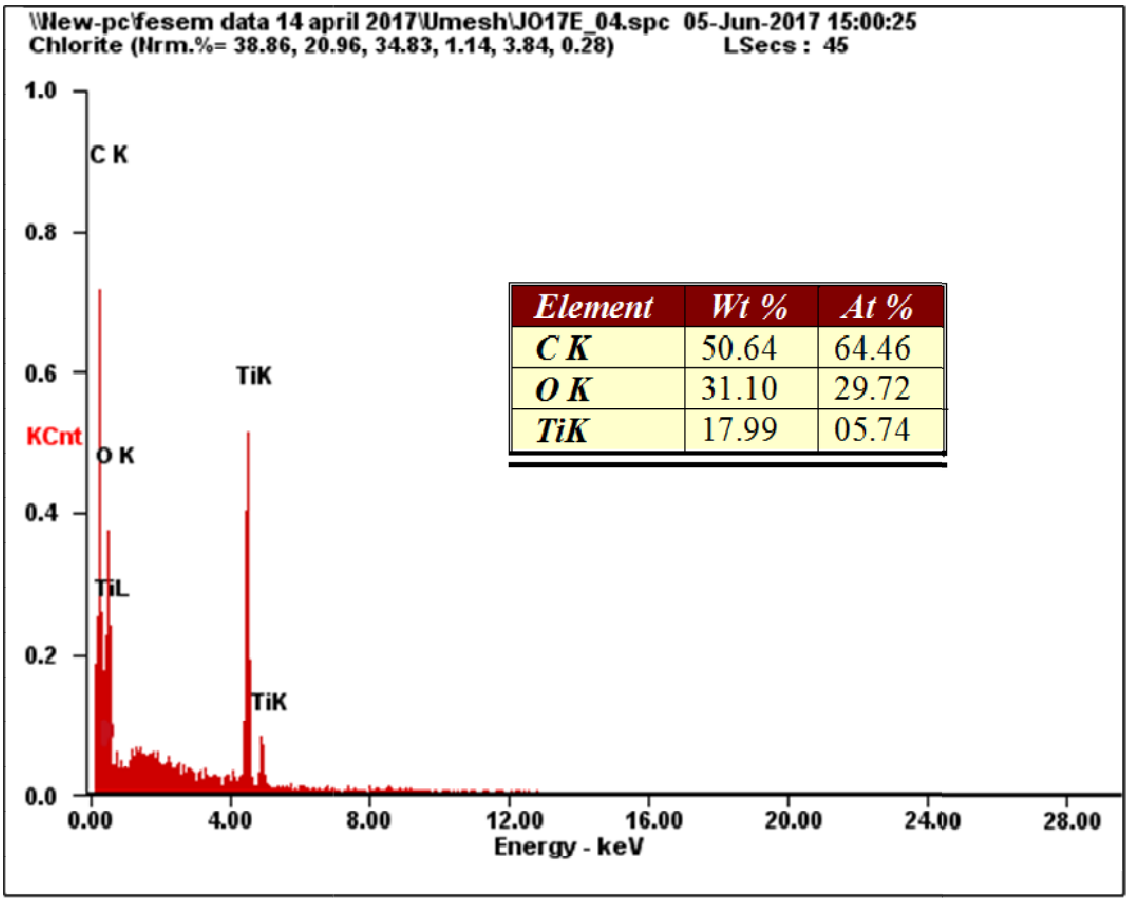

Figure 4.98 Energy-dispersive X-ray spectroscopy image of 5.0CNT-TiO_2 photocatalyst.

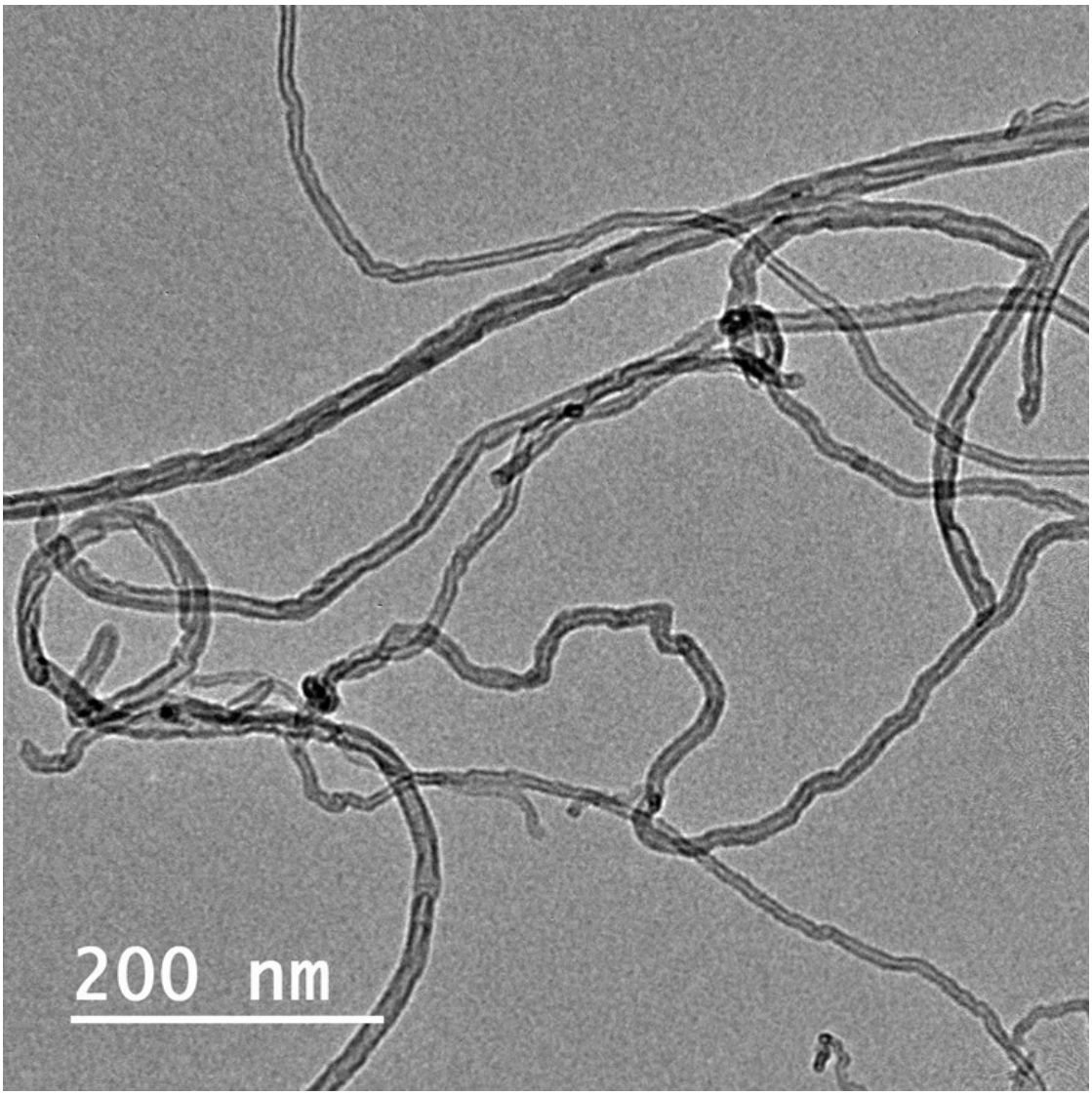

Figure 4.99 Transmission electron microscopy image of CNT sample.

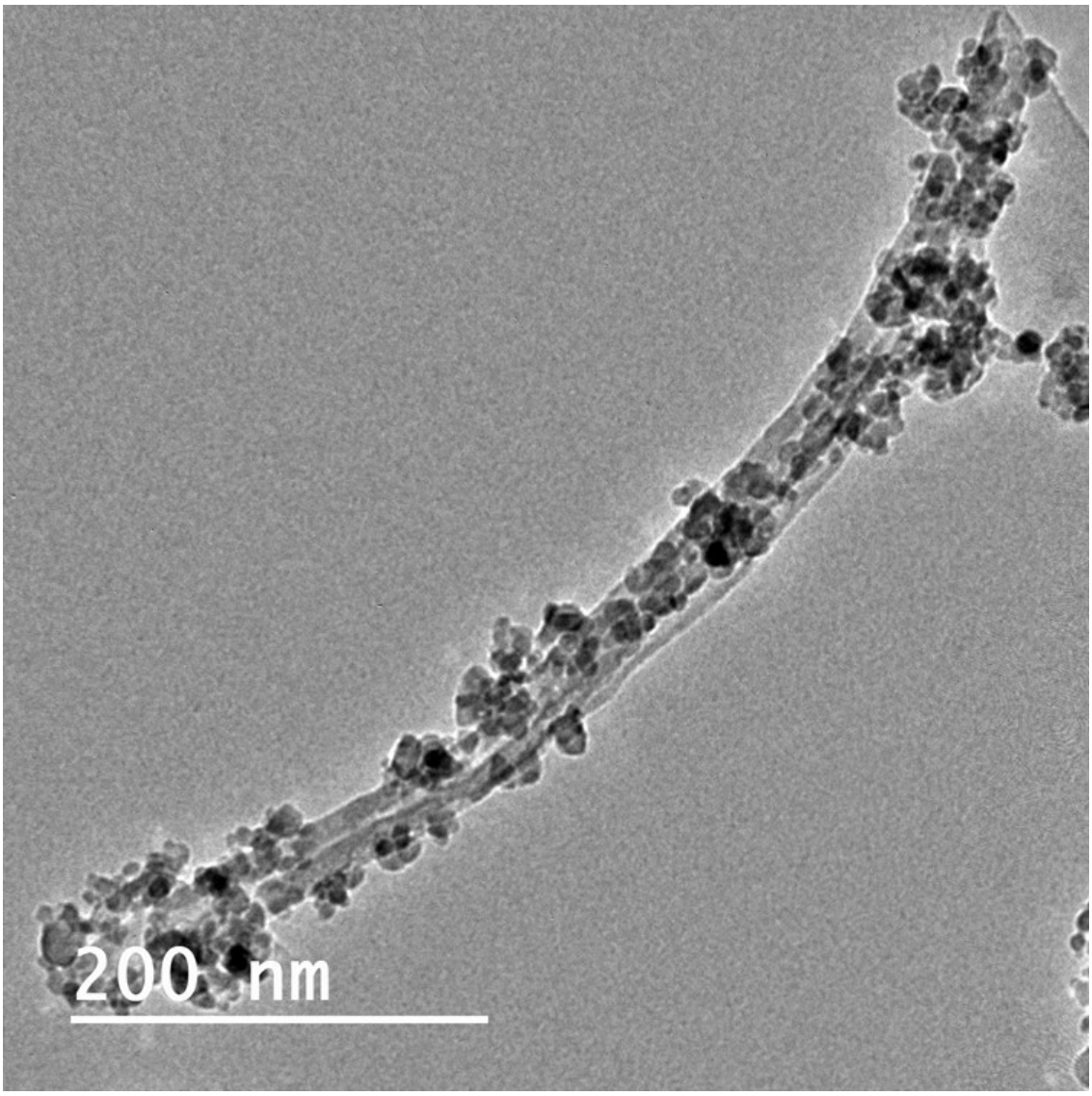

Figure 4.100. Transmission electron microscopy image of 1.0CNT-TiO_2 sample.

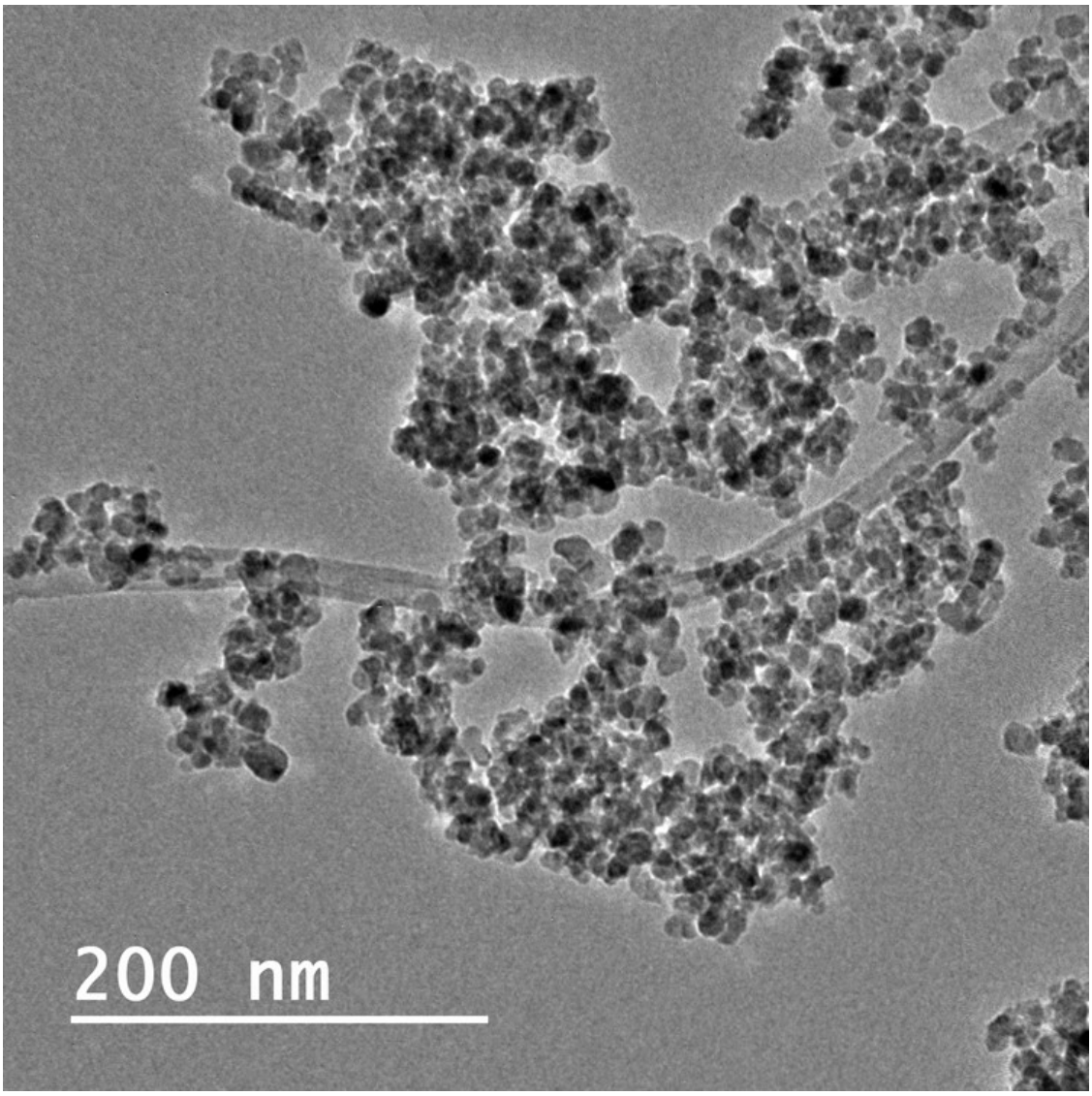

Figure 4.101 Transmission electron microscopy image of 2.0CNT-TiO_2 sample.

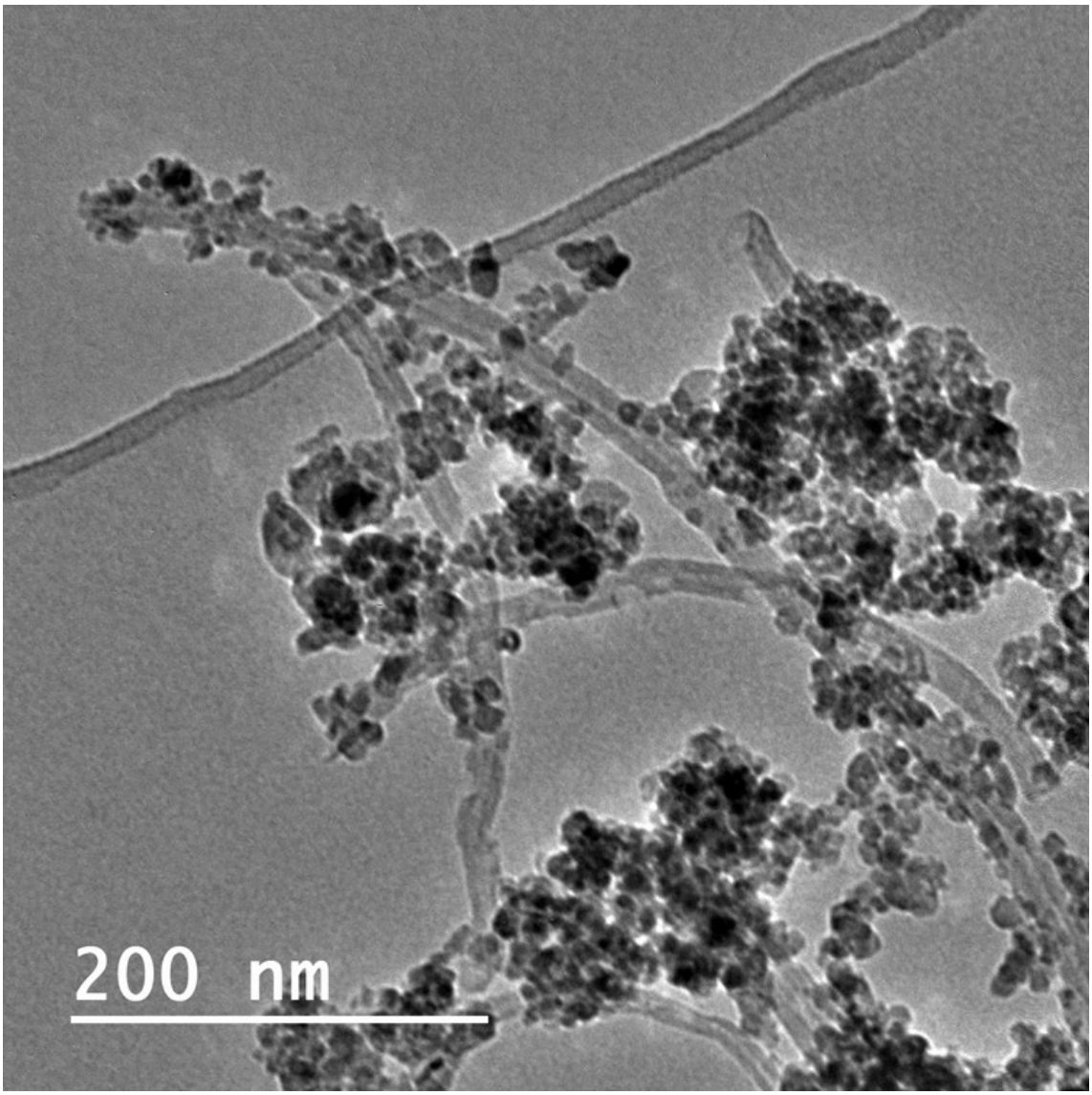

Figure 4.102. Transmission electron microscopy image of 5.0CNT-TiO_2 sample.

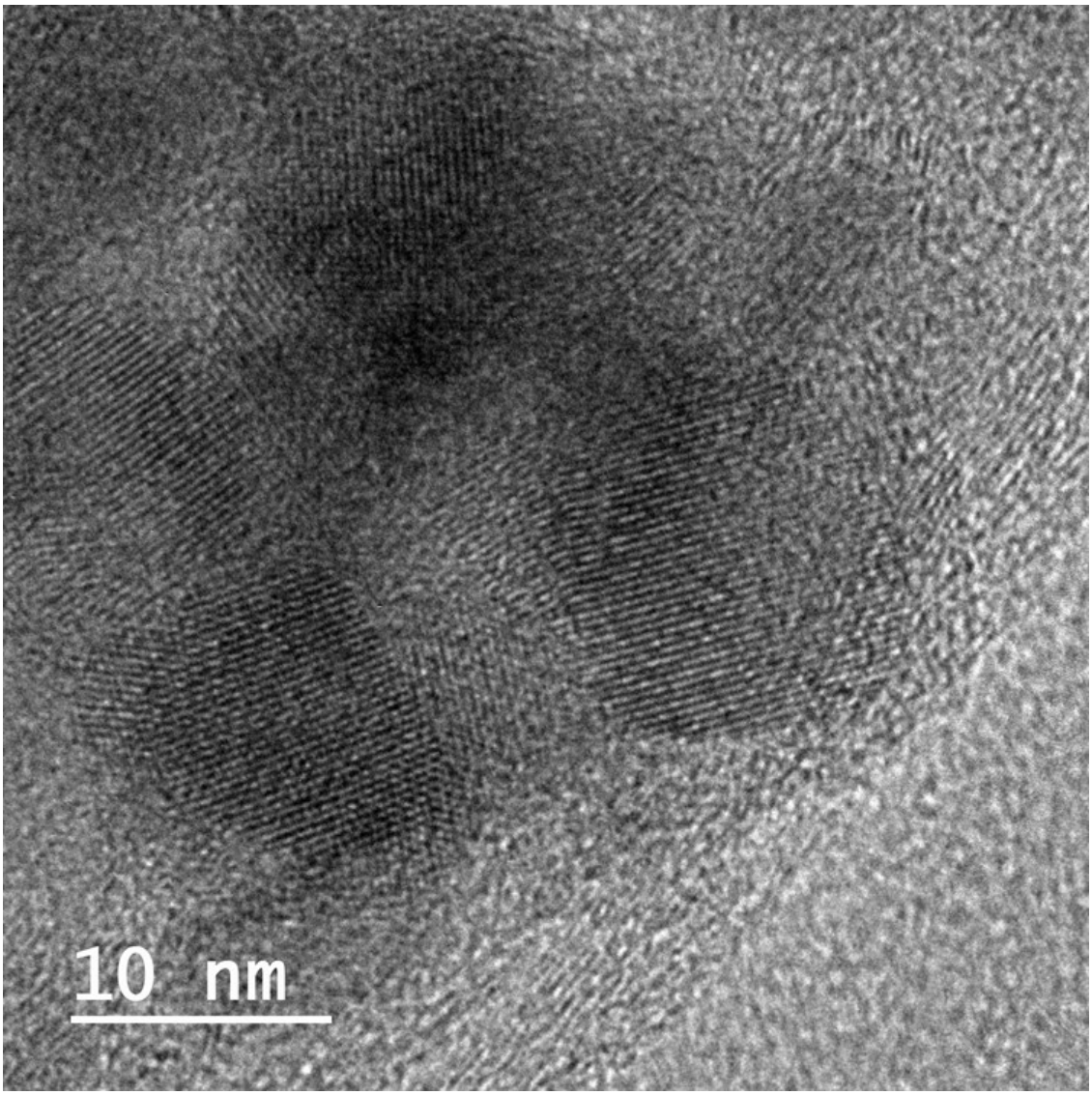

Figure 4.103 High resolution transmission electron microscopy image of 1.0CNT-TiO_2 sample.

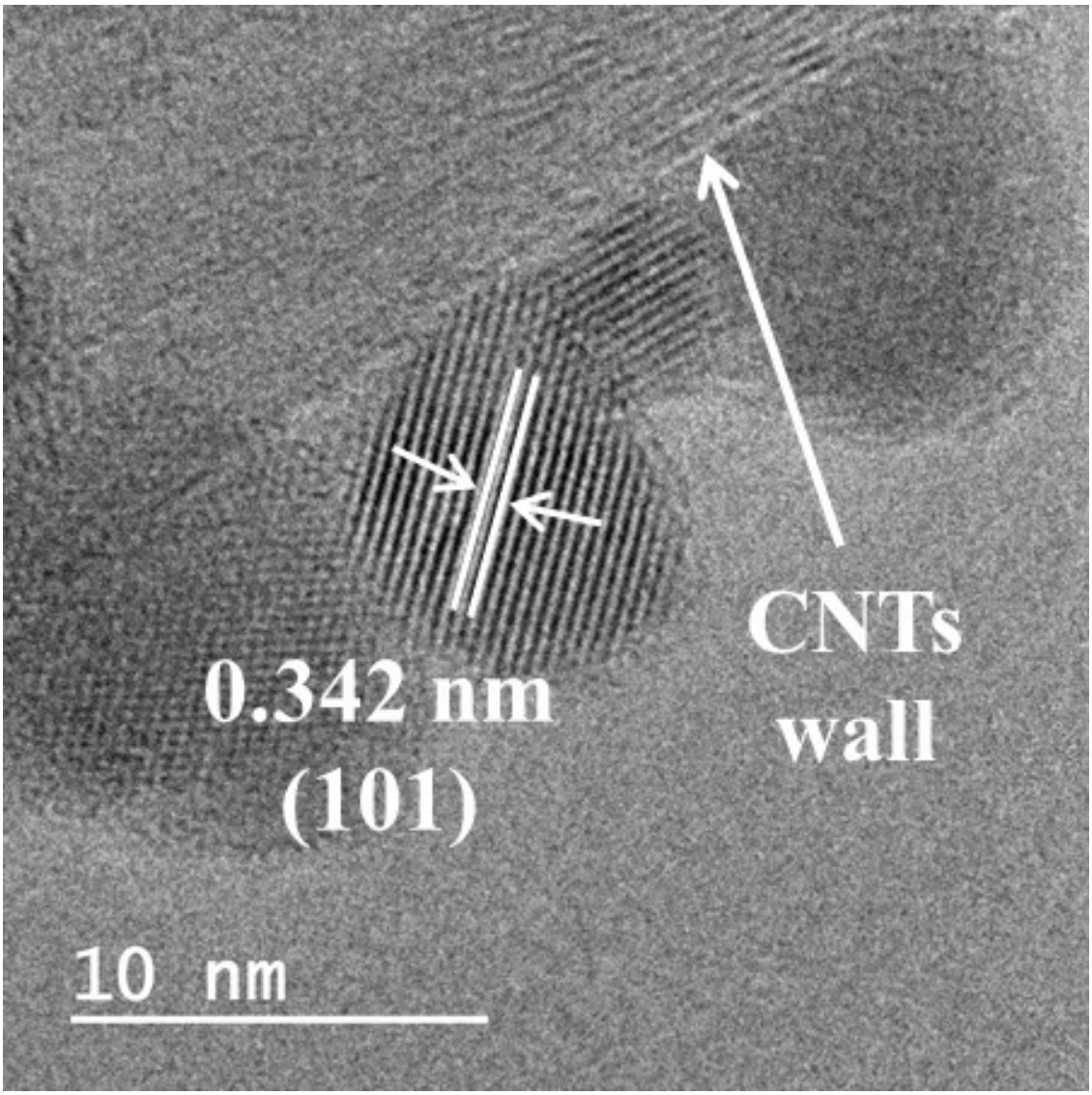

Figure 4.104 High resolution transmission electron microscopy image of 2.0CNT-TiO_2 sample.

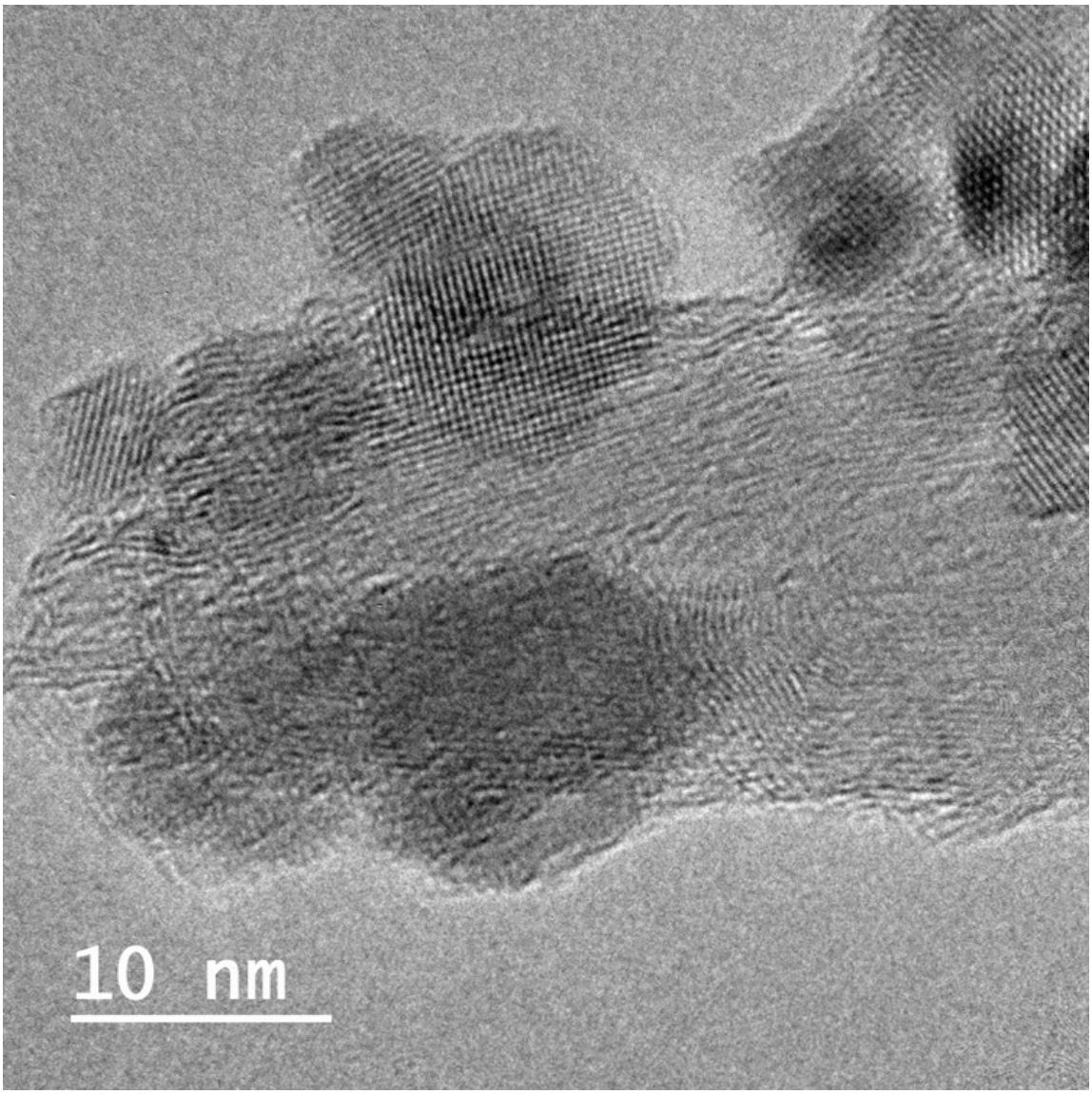

Figure 4.105 High resolution transmission electron microscopy image of 5.0CNT-TiO_2 sample.

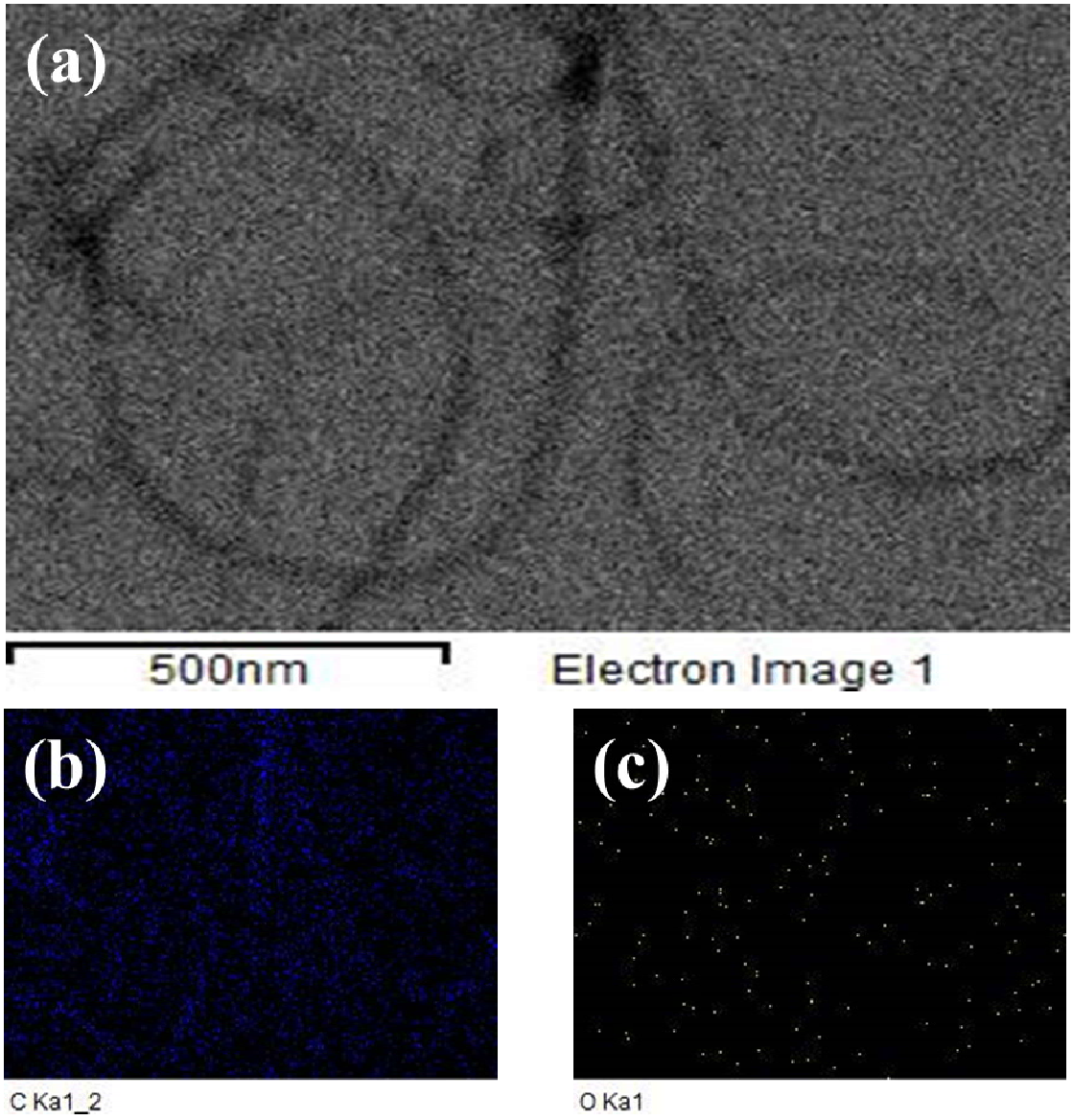

Figure 4.106 Elemental mapping of CNT sample.

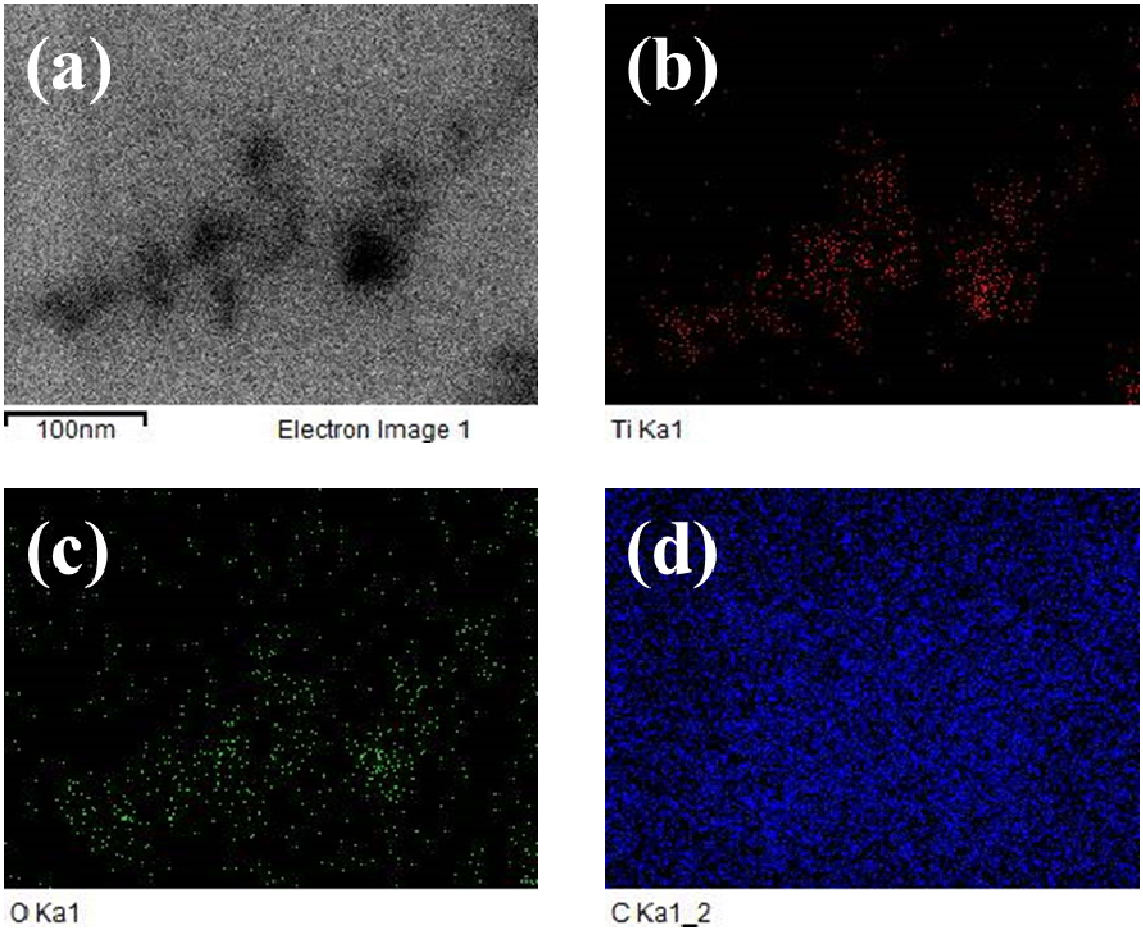

Figure 4.107 Elemental mapping of 1.0CNT-TiO_2 sample.

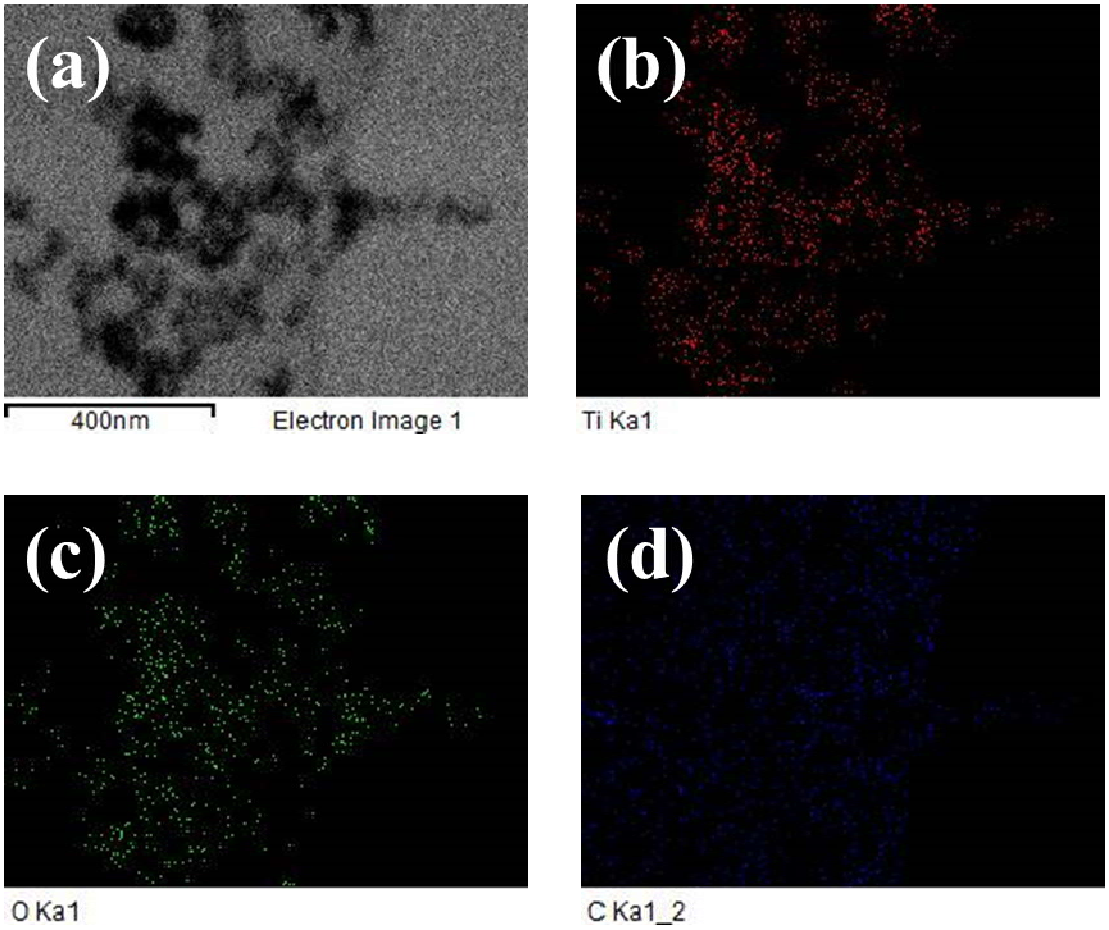

Figure 4.108 Elemental mapping of 2.0CNT-TiO_2 sample.

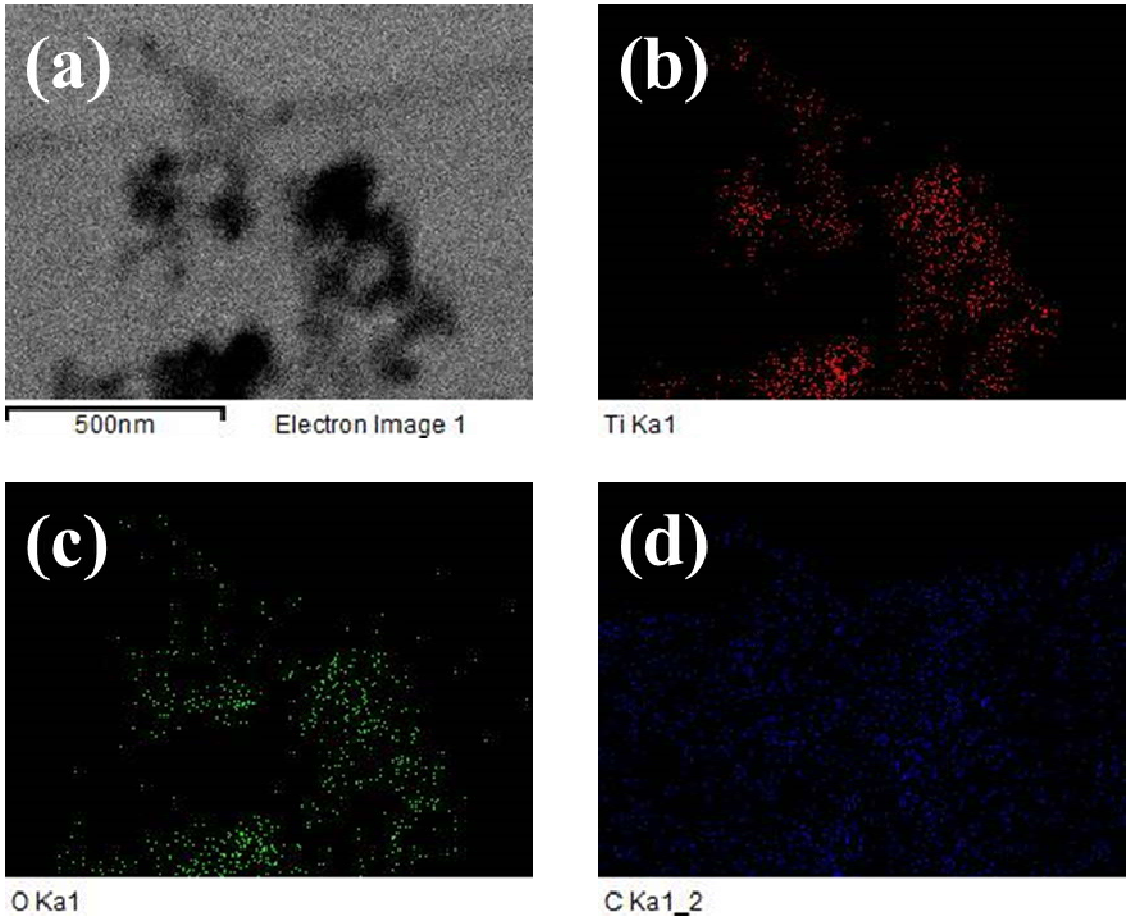

Figure 4.109 Elemental mapping of 5.0CNT-TiO_2 sample.

4.3.4 Thermogravimetric analyses and Raman spectroscopy characterisation of TiO_2 NPs and CNT-TiO_2 nanocomposites

The TGA analysis recorded under air atmosphere of CNT, TiO_2 and 2.0CNT-TiO_2 is shown in Figure 4.110. At the calcination temperature of 450 °C, the total weight loss of the pure CNT was found to be ca. 10%. This loss was a result of the removal of moisture as well as hydroxo, oxo, and carboxylic functional groups available at the surface of CNT. At the same calcination temperature, TiO_2 hada weight loss of 4% , while 2.0CNT-TiO_2 had 4.5% weight loss. The hydroxyl and moisture may be responsible for this. The TGA analysis suggests that CNT-TiO_2 nanocomposites were stable at the calcination temperature, in which the nanocomposites retained sufficient amount of CNT. Comparison of TGA curves of 2.0CNT-TiO_2 and spent 2.0CNT-TiO_2 samples is shown in Figure 4.111. The spent 2.0CNT-TiO_2 sample had 18% weight loss at the calcination temperature of 450 °C. The further weight loss by spent 2.0CNT-TiO_2 sample in comparison with the unspent 2.0CNT-TiO_2 (4.5% weight loss) can be attributed to burning out of the settled reactants and products on the surface of spent 2.0CNT-TiO_2 sample.

The Raman spectra of bare TiO_2, pure CNT and2.0CNT-TiO_2 are shown in Figure 4.112. The obtained TiO_2showedcharacteristic, strong peaks at 149.1, 397.4, 516.8 and 639.5 cm^{-1}, which were ascribed to Eg(1), B1g(1), A1g + B1g(2) and Eg(2) vibration modes of anatase TiO_2, respectively. Pure CNT exhibited two well-resolved bands at 1329.9 and 1565.0 cm^{-1}consistent to the D and Gbands, respectively. These peaks are associated with the degree of defects, thedisordered sp^2 carbon, and the existence of crystalline graphitic carbon in CNTs (Xiao *et al.,* 2016; Roy *et al.,* 2014). As expected, the peaks associated with the pure CNT were absent in bare TiO_2. The spectrum of 2.0CNT-TiO_2 nanocomposite exhibited the distinctive peaks of both CNT and TiO_2 samples. The succesful formation of the nanocomposite can also be determined from the ratio of the intensity of D and G bands (I_D/I_G). Higher I_D/I_G ratio in the nanocomposite when compared to pure CNT indicate the interaction of the nanocomposite and an increase in the average size of sp^2 domains (Vijayan *et al.,* 2012).The I_D/I_G ratio increased from 0.85 for the pure CNT to 1.08 for 2.0CNT-TiO_2 composite. Moreover, the peaks ascribed to

CNT were shifted from 1329.9 and 1565.0 $cm^{-1}$to 1340.1 and 1578.0cm^{-1} in the composite.This suggests a strong interaction between TiO_2 and CNT.

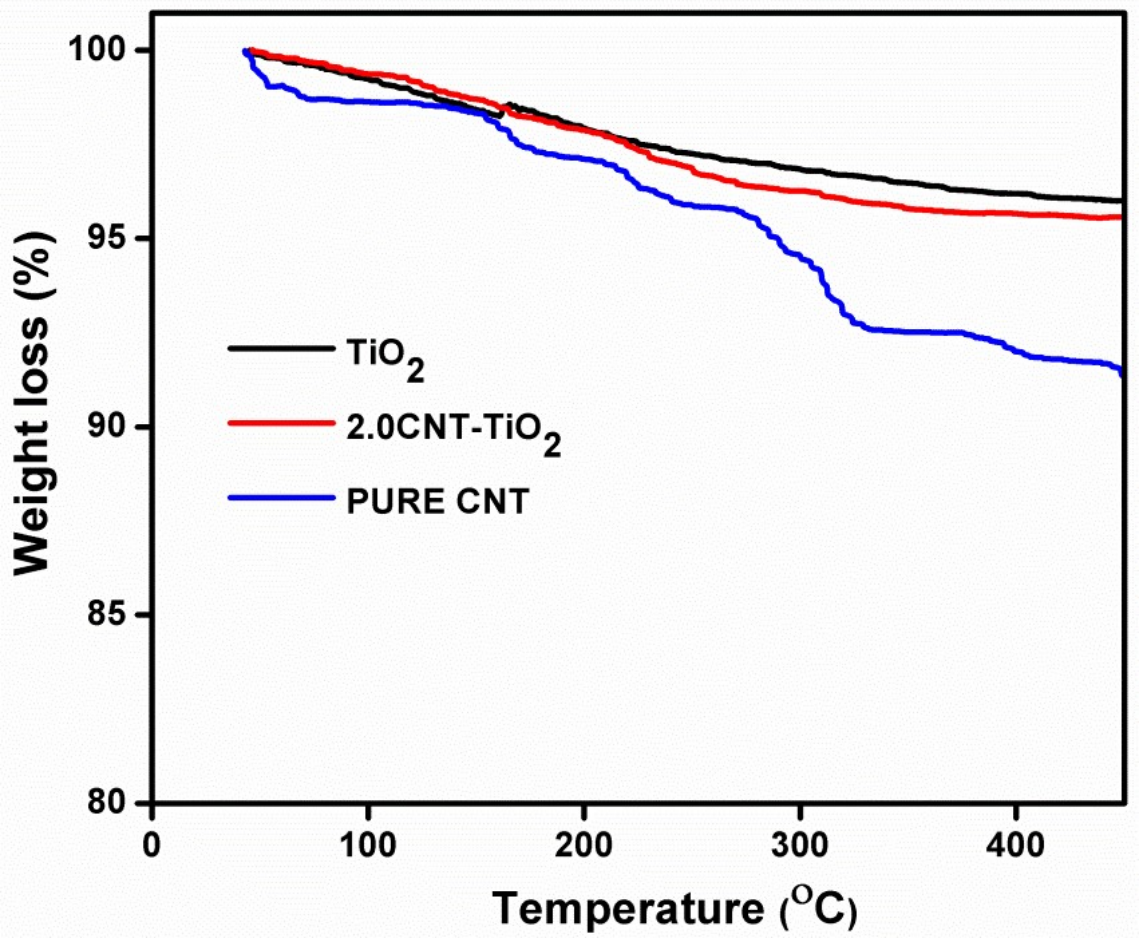

Figure 4.110 Thermogravimetric analyses curves of the prepared TiO_2, 2.0CNT-TiO_2 and pure CNT samples.

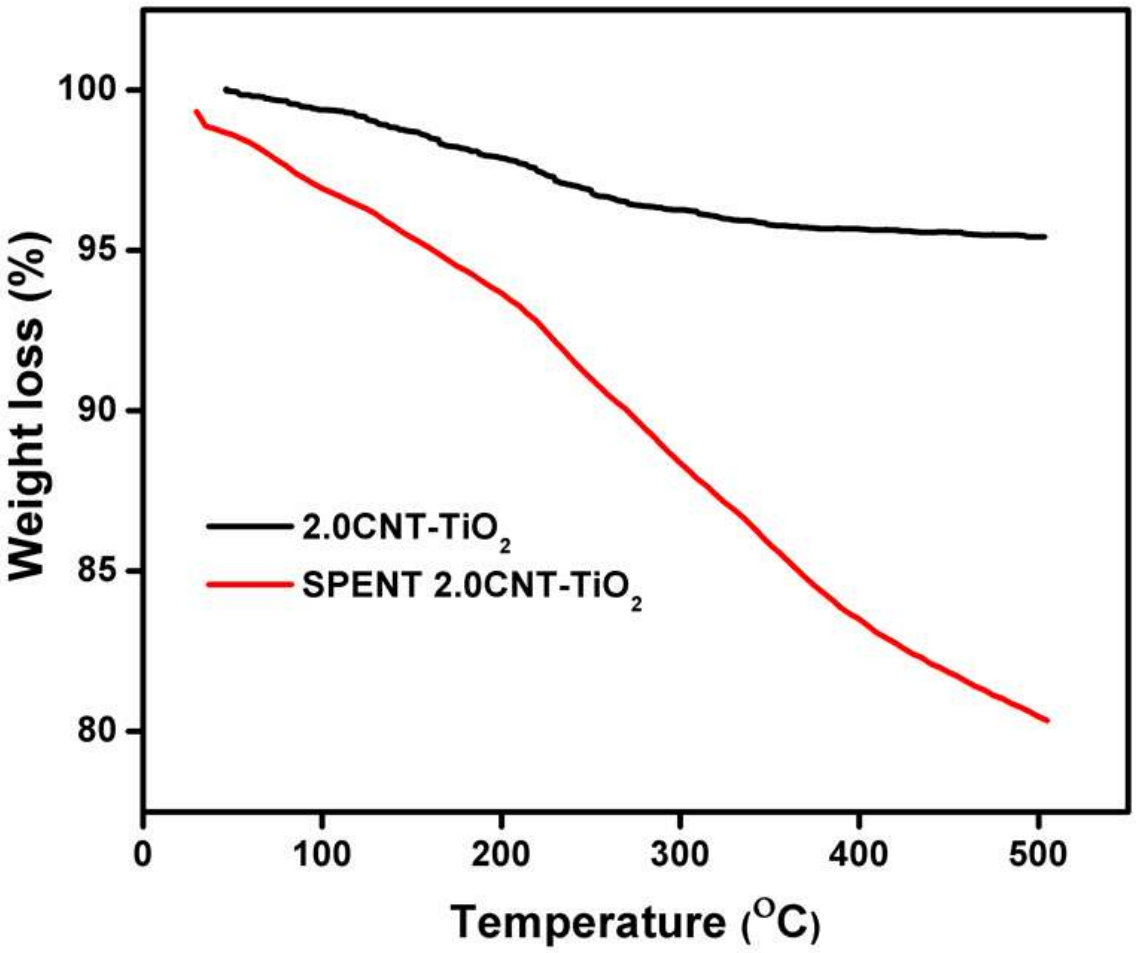

Figure 4.111 Comparison of thermogravimetric analyses curves of 2.0CNT-TiO_2 and spent 2.0CNT-TiO_2 samples.

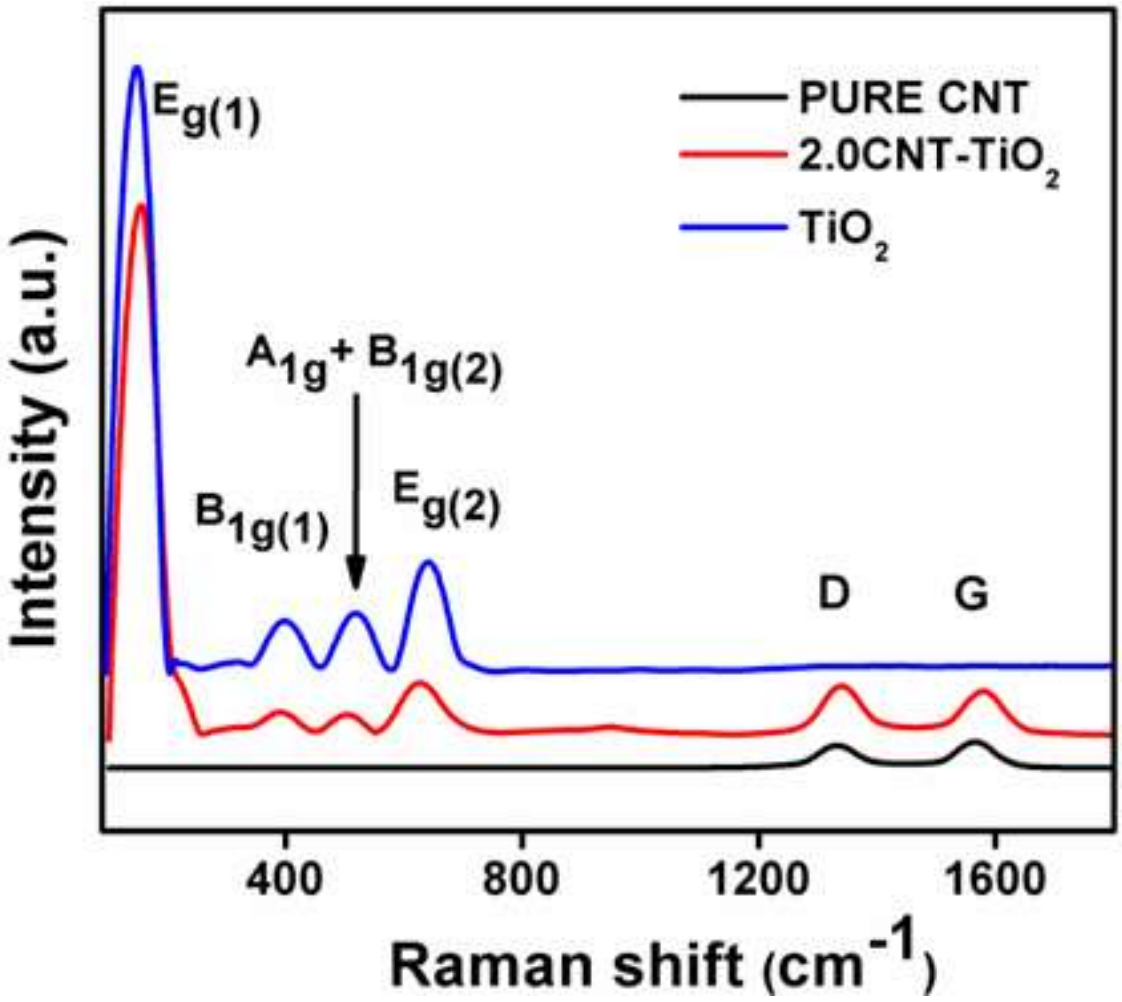

Figure 4.112 Raman spectrum of TiO_2, 2.0CNT-TiO_2 and pure CNT.

4.3.5 X-ray photoelectron spectroscopy characterisation of TiO_2 NPs and CNT-TiO_2 nanocomposites

XPS measurements were done to understand the chemical environment and the valence states of elements on the surface of the obtained TiO_2 and 2.0CNT-TiO_2 samples. The XPS survey spectra of TiO_2, 2.0CNT-TiO_2, and pure CNT are depicted in Figure 4.68, 4.113 and 4.114, respectively. The presence of Ti, O, and C on the surface of 2.0CNT-TiO_2 composite suggests the formation of CNT and TiO_2. Although, the peak ascribed to C arising on the TiO_2 surface corresponded to the reference used in the XPS instrument. It was observed that the carbon peak intensity from 2.0CNT-TiO_2 was higher in comparison with the bare TiO_2.This indicates the presence of CNT in 2.0CNT-TiO_2nanocomposite. As anticipated, pure CNT spectrum revealed the occurrence of only C and O atoms. The high-resolution XPS spectrum of Ti2p in bare TiO_2 was previously depicted in Figure 4.69. The peaks centred at 458.3 and 464.1 eV were assigned to $Ti2p_{3/2}$ and $Ti2p_{1/2}$ spin-orbital splitting photoelectrons in Ti^{4+} (Niu *etal.,* 2013).The spectrum of 2.0CNT-TiO_2 is shown inFigure 4.115.The peaks position of $Ti2p_{3/2}$ and $Ti2p_{1/2}$ were slightly shifted to 458.4 and 464.2 eV in comparison with bare TiO_2. The splitting of these peaks showed an additional two peaks at position 459.9 and 465.5 eV due to the formation of Ti-C bond arising from $Ti2p_{3/2}$ and $Ti2p_{1/2}$ peaks (Akhavan *et al.,* 2010). The formation of Ti–C bond was established from the spectra of C1s.

The high-resolution XPS spectra of C1s of pure CNT and 2.0CNT-TiO_2 are depicted in Figure 4.116 and 4.117. For pure CNT, the spectrum was fitted into three peaks. The major peak noticed at 284.3 eV was assigned to C=C and C-C bonds of the CNT. The two other peaks centred at 285.6 and 289.4 eV were assigned to C-O and C=O bonds, respectively (Akhavan *et al.,* 2010; Cong *et al.,* 2011). The spectrum for 2.0CNT-TiO_2 was deconvoluted into four peaks, showing an additional peak centred at 284.2 eV. This new peak was ascribed to Ti-C bond in the composite (Akhavan *et al.,* 2009; Akhavan *et al.,* 2010). The Ti-C bond revealed that the oxygen sites in the lattice of TiO_2 were replaced by carbon atoms, which led to the formationof a C-Ti-O structure (Huang *et al.,* 2008). Two of the three peaks (284.3 and 285.6 eV) observed with pure CNT were shifted to 285.1 and 286.2 eV, respectively. However, the peak at 289.4 eV remained

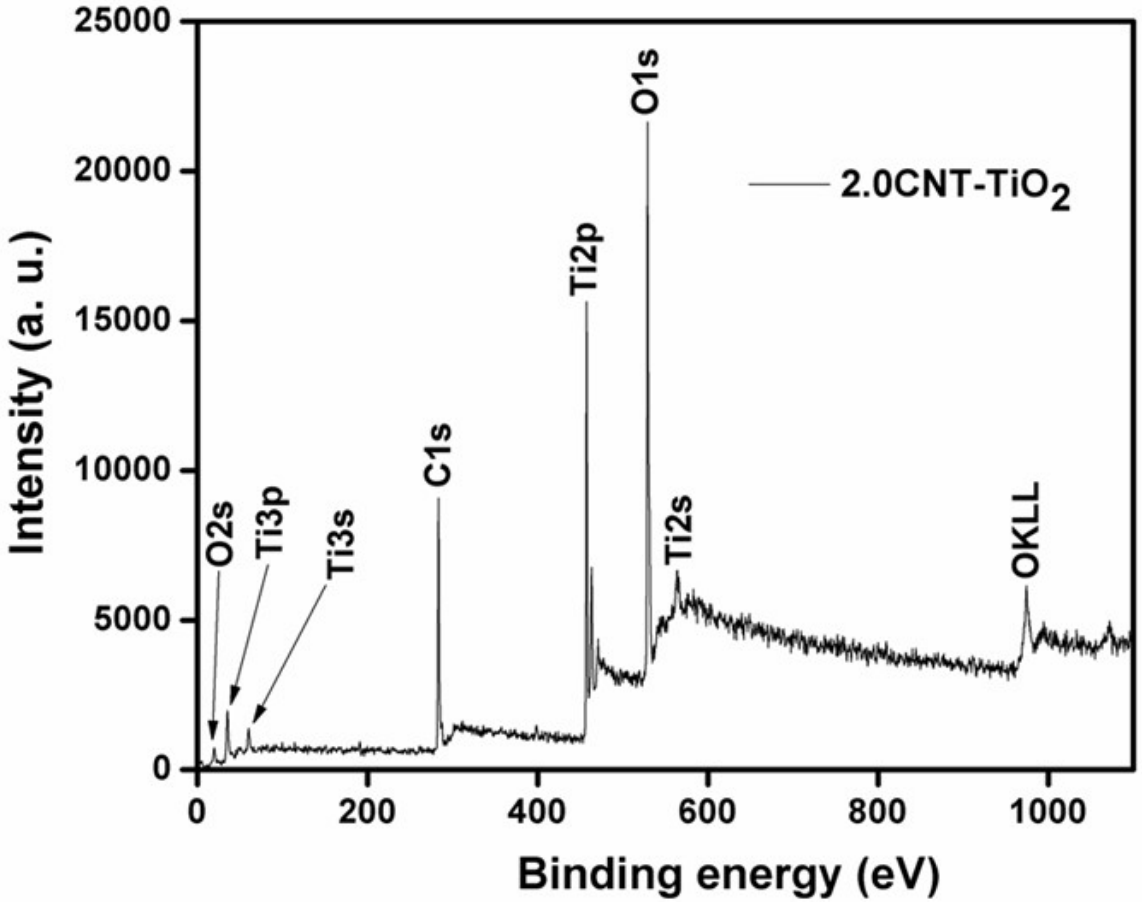

Figure 4.113 X-ray photoelectron spectroscopy survey spectrum of 2.0CNT-TiO_2.

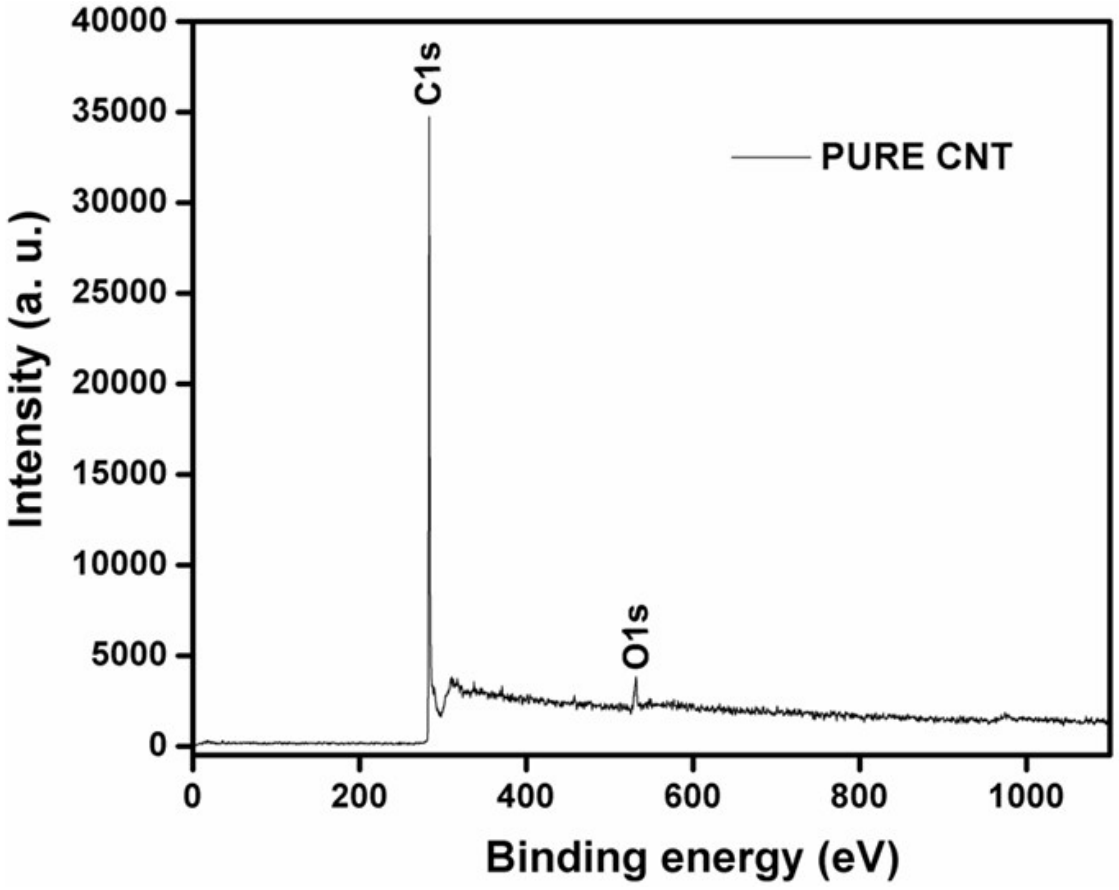

Figure 4.114 X-ray photoelectron spectroscopy survey spectrum of pure CNT.

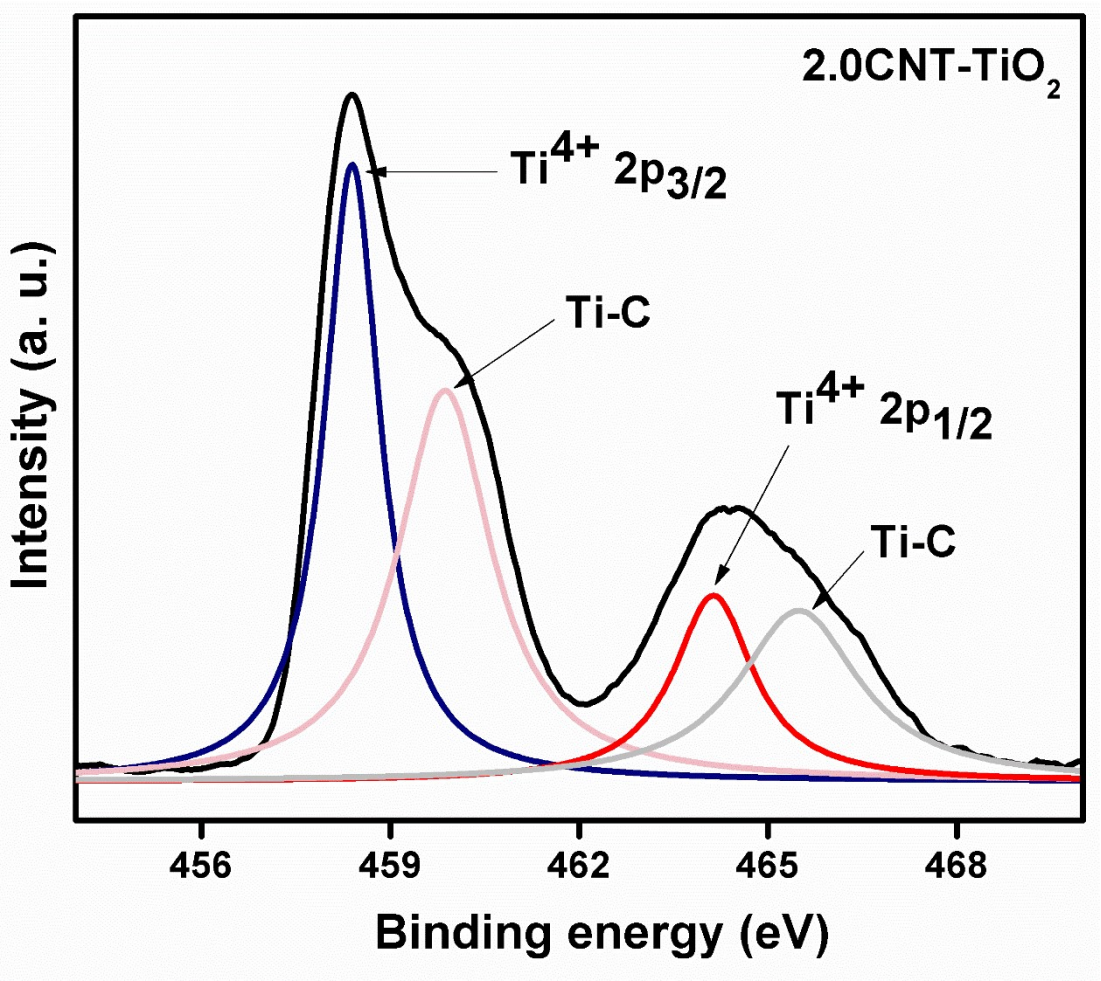

Figure 4.115 High resolution X-ray photoelectron spectroscopy spectrum of Ti2p of 2.0CNT-TiO_2.

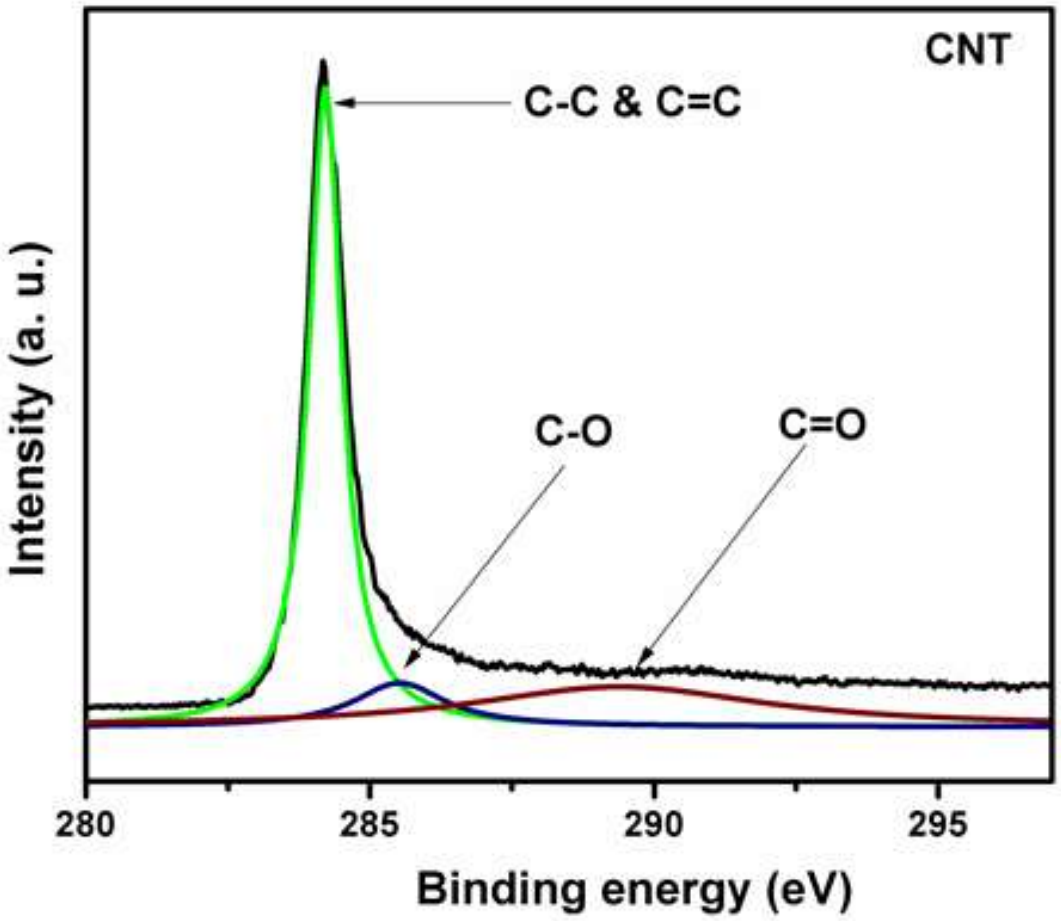

Figure 4.116 High-resolution X-ray photoelectron spectroscopy spectrum of C1s of pure CNT.

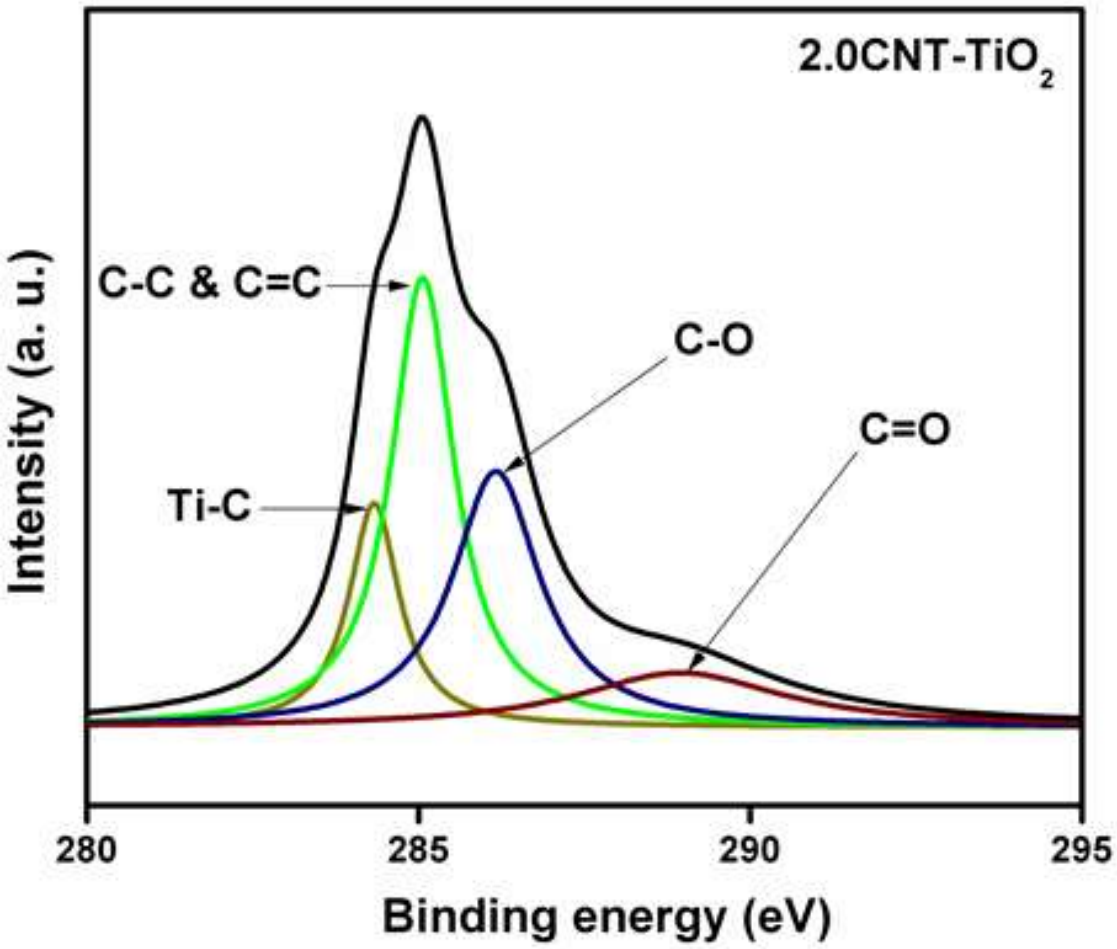

Figure 4.117 High-resolution X-ray photoelectron spectroscopy spectrum of C1s of 2.0CNT-TiO_2.

unchanged in the composite. This new peak and shifts in peaks position noticed with 2.0CNT-TiO_2 suggest strong binding of CNT and TiO_2.

The high-resolution spectra of O1s of TiO_2, 2.0CNT-TiO_2, and CNT are depicted in Figure 4.75, 4.118 and 4.119. The spectra for bare TiO_2 were fitted into two peaks. The peaks noticed at 529.5 and 531.7 eV were assigned to lattice oxygen and non-lattice oxygen (adsorbed OH group), respectively (Hafeez *et al.,* 2018). The deconvoluted O1s spectrum of 2.0CNT-TiO_2 showed an extra peak at 533.2 eV, which was assigned to C-O. The peak areanoticed at 531.7 eV with TiO_2had an increase of 38% after the addition of CNT. The increase in the area of this peak suggests that C=O and Ti-O-C bonds as well as more oxygen defects were formed (Bellamkonda *et al.,* 2017; Cong *et al.,* 2011). The above observations of O1s with 2.0CNT-TiO_2 confirmed the interaction between CNT and TiO_2 in the composite.

The XPS spectra of the spent 2.0CNT-TiO_2 catalyst are depicted in Figure 4.120 – 4.123. Similarly, the survey spectrum confirmed the presence of Ti, O and C elements in the spent 2.0CNT-TiO_2 (Figure 4.120). However, from HRXPS of the spent 2.0CNT-TiO_2 (Figure 4.121 – 4.123), the peak areas associated with Ti were reduced while the peak areas associated with C and O were increased. These observations with the peak areas were as a result of the settling of the reactants and products on the surface of the spent 2.0CNT-TiO_2.

4.3.6 Computational studies of TiO_2 NPs and CNT-TiO_2 nanocomposites

There are various possibilities of the arrangement of surface atoms in TiO_2anatase nanoparticles,which have round shape. Of all the arrangements of TiO_2 anatase nanoparticles, the most stable facet is (1 0 1). The facet (1 0 1) and facet (0 0 1) were found to be present in the synthesised materials. The possibility of having other arrangements of surface atoms in the experimentally prepared TiO_2 was not considered in the present study. The modelled TiO_2 anatase nanoparticles was denoted by Ti44r1. The nanoparticle Ti44r1 possessed facets (1 0 1) and (0 0 1) which represented a part of surface structures in the experimentally synthesised nanoparticles. CNTs were bounded to various surface arrangements of TiO_2 anatase nanoparticles. Three options of binding CNT to Ti44r1 nanoparticle were considered. They are (1) the attachment of CNT to (0 0 1) facet along the edge hydroxyl groups, (2) the attachment of CNT to(1 0 1)

facetsapproximately perpendicular to (0 0 1) facets and (3)the attachment of CNT to(1 0 1)

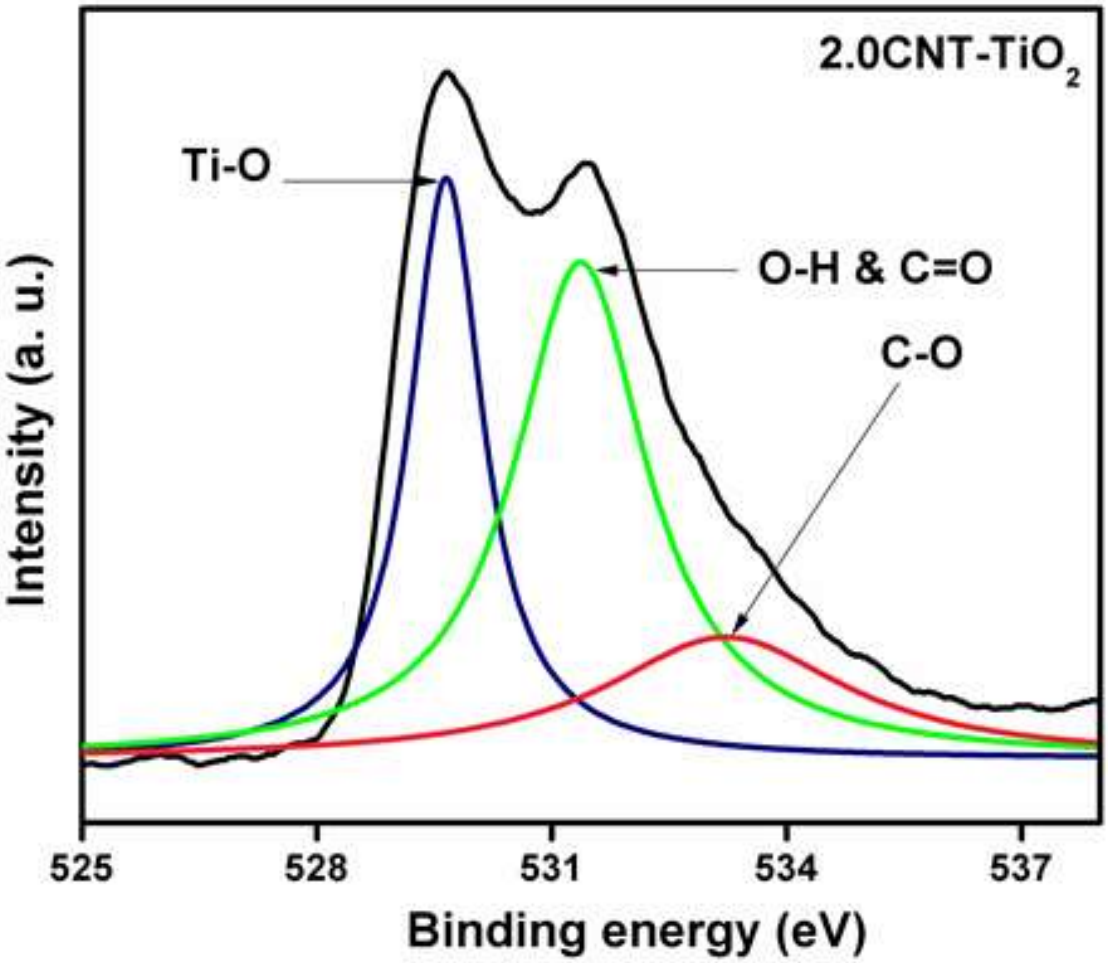

Figure 4.118 High-resolution X-ray photoelectron spectroscopy spectrum of O1s of 2.0CNT-TiO_2.

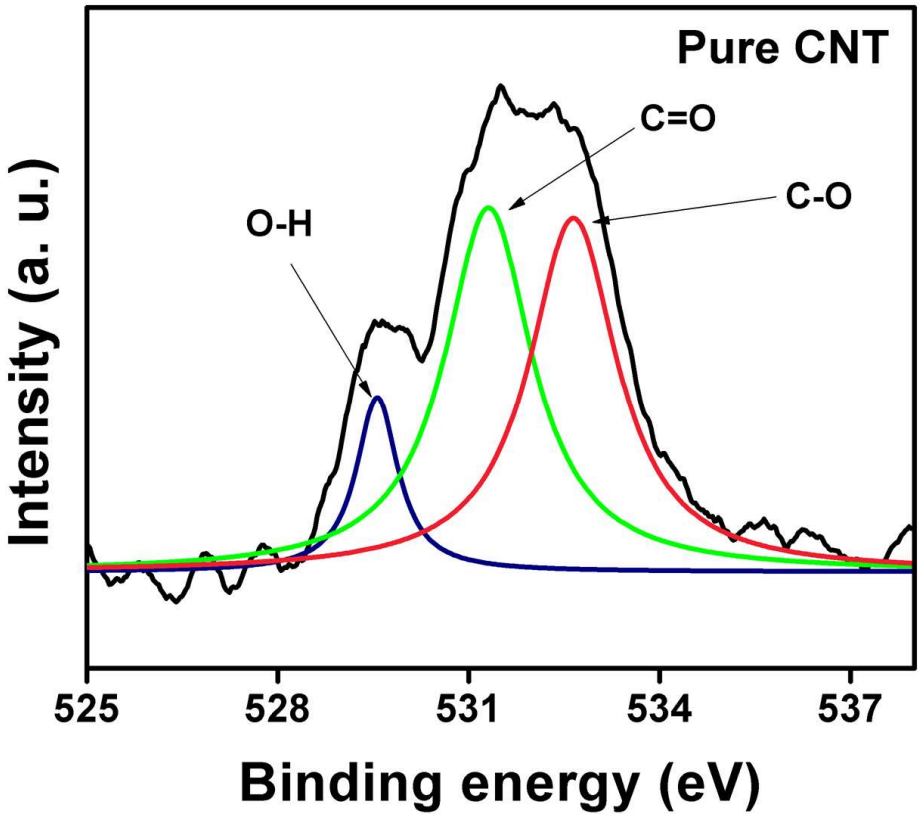

Figure 4.119 High-resolution X-ray photoelectron spectroscopy spectrum of O1s of pure CNT.

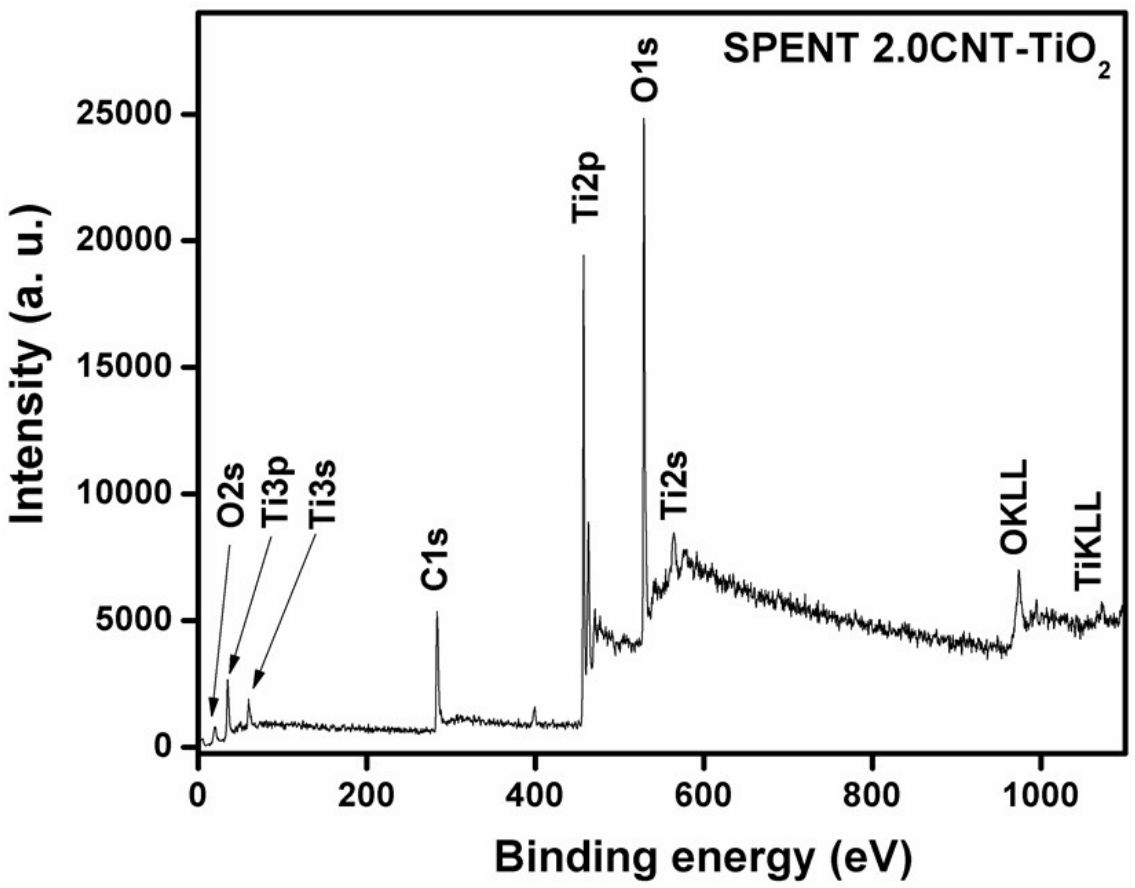

Figure 4.120 X-ray photoelectron spectroscopy survey spectrum of spent 2.0CNT-TiO_2.

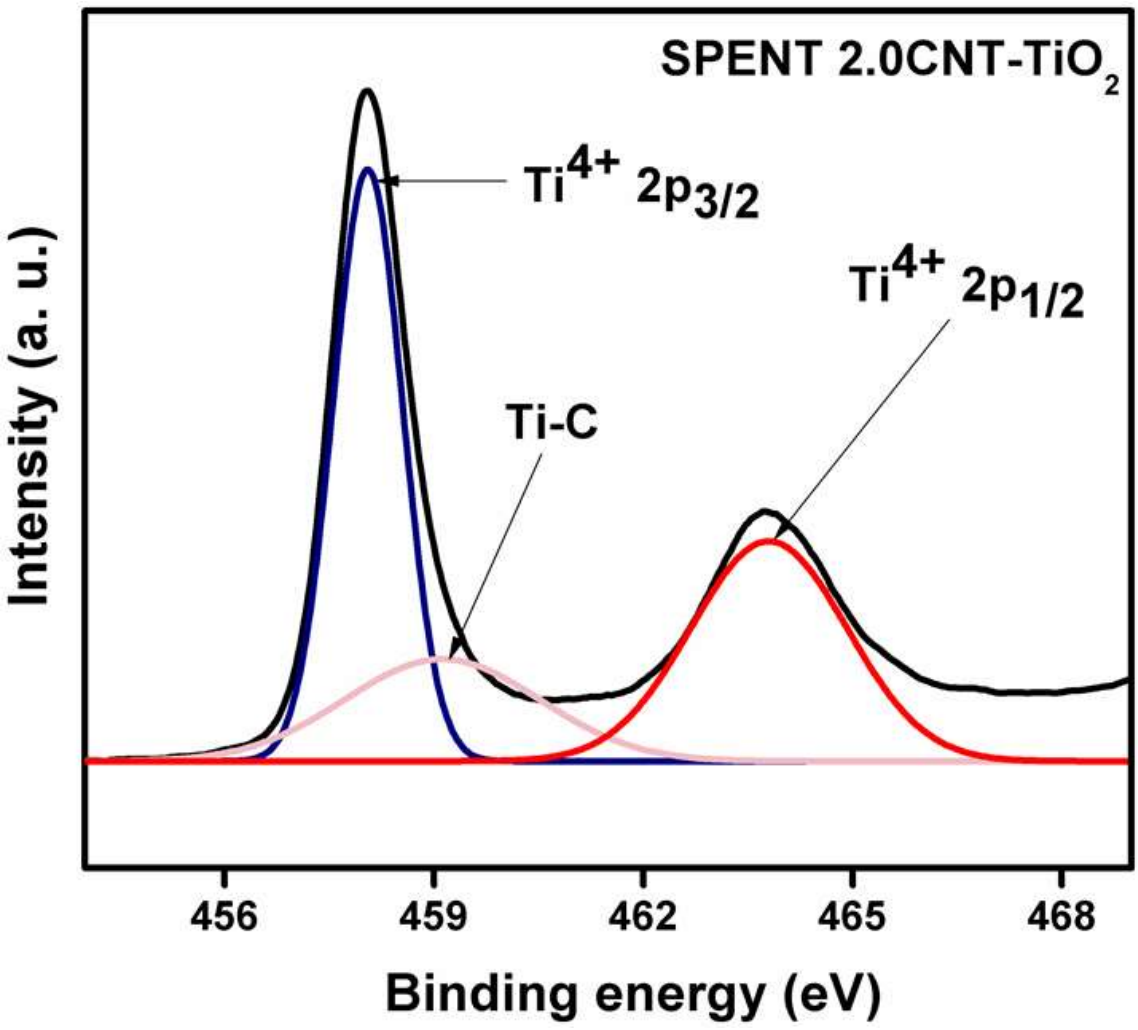

Figure 4.121 High-resolution X-ray photoelectron spectroscopy spectrum of Ti2p of spent 2.0CNT-TiO_2.

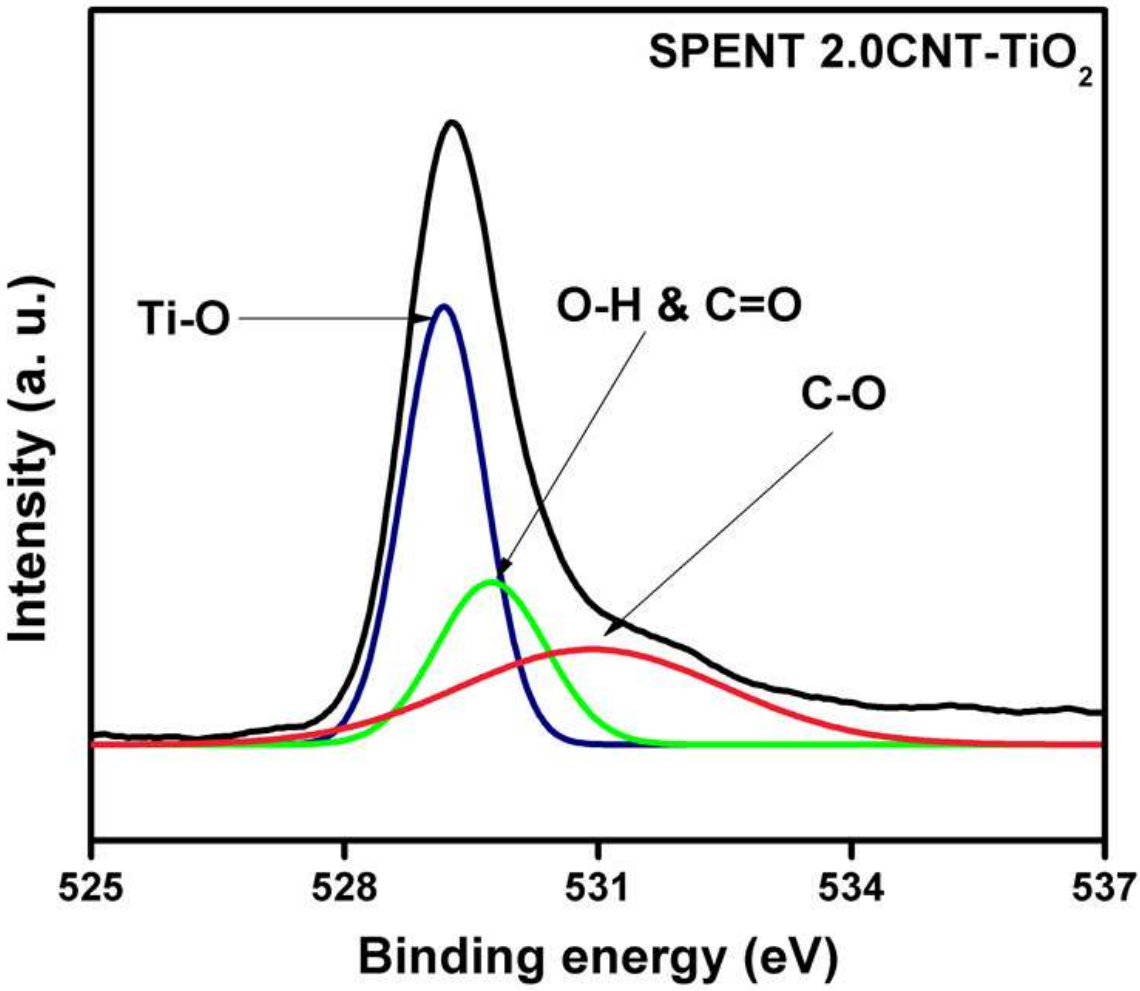

Figure 4.122 High-resolution X-ray photoelectron spectroscopy spectrum of O1s of spent 2.0CNT-TiO_2.

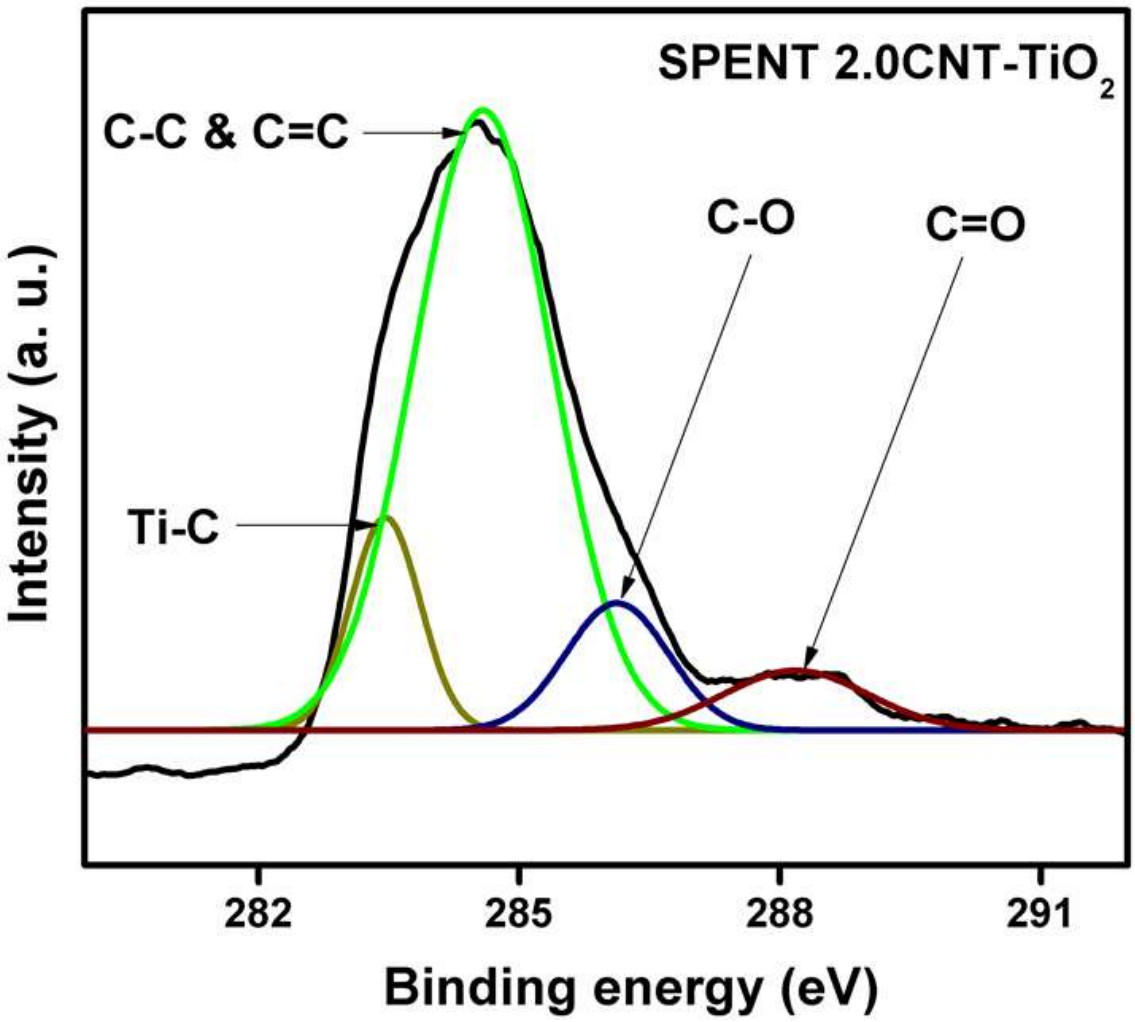

Figure 4.123 High-resolution X-ray photoelectron spectroscopy spectrum of C1s of spent 2.0CNT-TiO_2.

facetsalong (0 0 1) facets. The binding geometries of composite structure were finally obtained by the placement of CNT at the predefined locations. The structure was then optimised to obtain minimal energy.

The optimised structure of CNT attached to (0 0 1) facet of the nanoparticle is shown in Figure 4.124. The binding of CNT with this surface was weak. The adsorption energy was -5.35 kcal mol^{-1}. In addition, there was a little difference between the electronic properties of this CNT-$TiO_2$and the properties of CNT. The Fermi energy of CNT-TiO_2 was -4.39 eV, whilethat of CNT was -4.40 eV. The prevalence of CNT was due to the high amount of delocalized electrons in comparison with TiO_2 which had their electrons mostly localised. As shown in Figure 4.125, the details of CNT-TiO_2 (0 0 1) interaction was obtained by considering boundary orbitals, that is, Highest Occupied Molecular Orbital (HOMO) and Lowest Unoccupied Molecular Orbital (LUMO). The values 10^{-5} of the isosurfaces were obtained with these orbitals. It was observed that the boundary orbitals were mostly represented by electrons of CNT with a small contribution of p_O orbitals of TiO_2 (0 0 1) surface in HOMO and both p_O and d_{Ti} orbitals in LUMO.

Orbitals within the range of 1536 – 1597 were also considered. It was observed that the input of orbitals of individual CNT and TiO_2 to overall orbitals was very small. The energy for each CNT boundary was -4.56 (HOMO) and -4.24 eV (LUMO) and the band gap was 0.32 eV. For the CNT-TiO_2 (0 0 1) composite, the boundary orbitals corresponded closely to CNT, in which -4.55 (HOMO) and -4.23 eV(LUMO) values were obtained. The maininput of CNT to electronic characteristics of boundary orbitals of the CNT-TiO_2nanocomposite was confirmed by these values.

Furthermore, the inputs of orbitals at the position of energy relating to Ti44r1 cluster boundary orbitals were considered. The boundary orbitals energy was -5.47 (HOMO) and -2.53 eV (LUMO) for each cluster Ti44r1with the band gap of 2.94 eV. The boundary orbitals structure corresponded to each orbitals of Ti44r1 nanoparticle in the CNT-TiO_2 (0 0 1) nanocomposite (Vorontsov 2017). In the composite,the positions of energy of Ti44r1 orbitals were -5.45 (HOMO) and -2.49 eV (LUMO) andhad the energy band gap of 2.96 eV. This band gap value indicates that there was a slight shift in the positions of energy of the TiO_2 orbitals. This indicates that the CNT binding with TiO_2 (0 0 1) surface was too small considering both energy interaction and wavefunctions

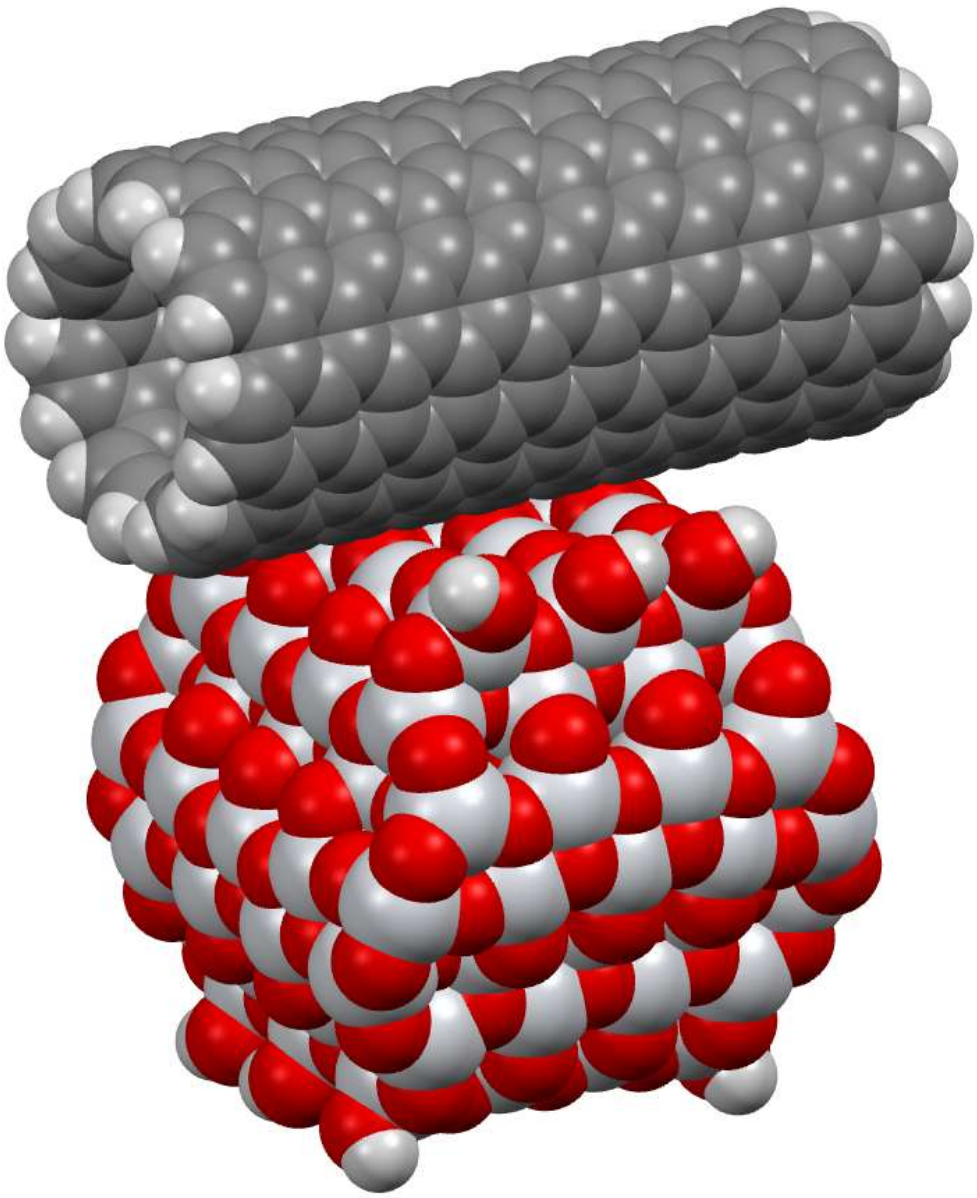

Figure 4.124 CNT-TiO_2 composite structure with CNT attachment to (001) facet.

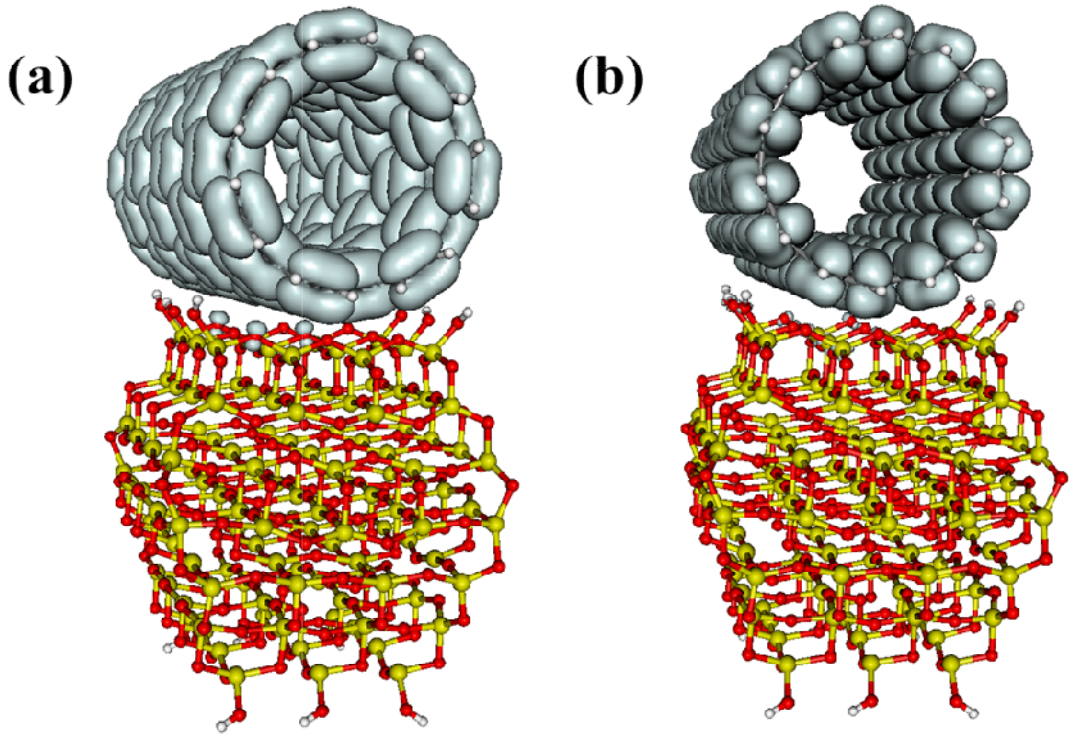

Figure 4.125 Boundary orbitals of CNT-TiO_2 (001) composite: (a) HOMO and (b) LUMO.

interpenetration.

The alternative geometry of stacking CNT and TiO_2 was CNT attachment to (1 0 1) facet of anatase, in which CNT was placed approximately perpendicular to (0 0 1) facet as shown in Figure 4.126. The Ti44r1 cluster and the nanotube were placed in a way that TiO_2 cluster interacted with the CNTat the middle part. To circumvent the effects of the short length of the CNT model used,the same placement was adopted for all other CNT-Ti44r1 composites. The binding of CNT with (1 0 1) facet was stronger than with (0 0 1) facet. The energy of adsorption of CNT with (1 0 1) facet was -6.15 kcal mol^{-1}. Nonetheless, it was a verysmall energy interaction,which was purely of van-der-Waals nature. The van-der-Waals diameters of larger distancescorresponded tothe interatomic distances.

The CNT-TiO_2 (1 0 1) complex boundary orbitals are depicted in Figure 4.127. The boundary orbitals were represented by CNT orbitals with a very small input of Ti44r1 orbitals. Partial overlapping of p_O orbitals with CNT orbitals was observed for HOMO, while partial overlappingof both p_O and d_{Ti} of (1 0 1) surface with CNT orbitalswas observed for LUMO. It was noticed that the orbitals overlap was larger than for CNT adsorbed over (0 0 1) surface. The HOMO energy was -4.57eV and the LUMO energy was -4.24 eV, which were the same as those obtained for individual CNT.

The orbitals with lower energy had inputs from both CNT and TiO_2, whereas, the CNT-TiO_2 complex boundary orbitals did not have a significant input from atomic orbitals belonging to TiO_2. These orbitals, namely, 1544 with eigenvalue -5.70 eV (Figure 4.128a) and 1561 with eigenvalue -5.45 eV (Figure 4.128b) were revealed to be linear combinations of atomic orbitals of both CNT and Ti44r1 nanoparticle.

Orbitals in the composite conduction band with the energy below the energy of Ti44r1 conduction band had a little input from the atomic orbital (AO) of TiO_2. The orbitals had a majorinput from both Ti44r1 and CNT,beginning from orbital 1588 with eigenvalue -2.48 eV. Therefore, the electron transfer from TiO_2 to CNT was as a result of the photoexcitation of CNT-Ti44r1(0 0 1) and CNT-Ti44r1(1 0 1) composites with photons of visible light range energy.The CNT-TiO_2 complex geometry that was last considered contained CNT placed over (1 0 1) facet of Ti44r1 cluster, in which CNT was directly parallel to (0 0 1) facet. The optimised complex geometry is shown in Figure

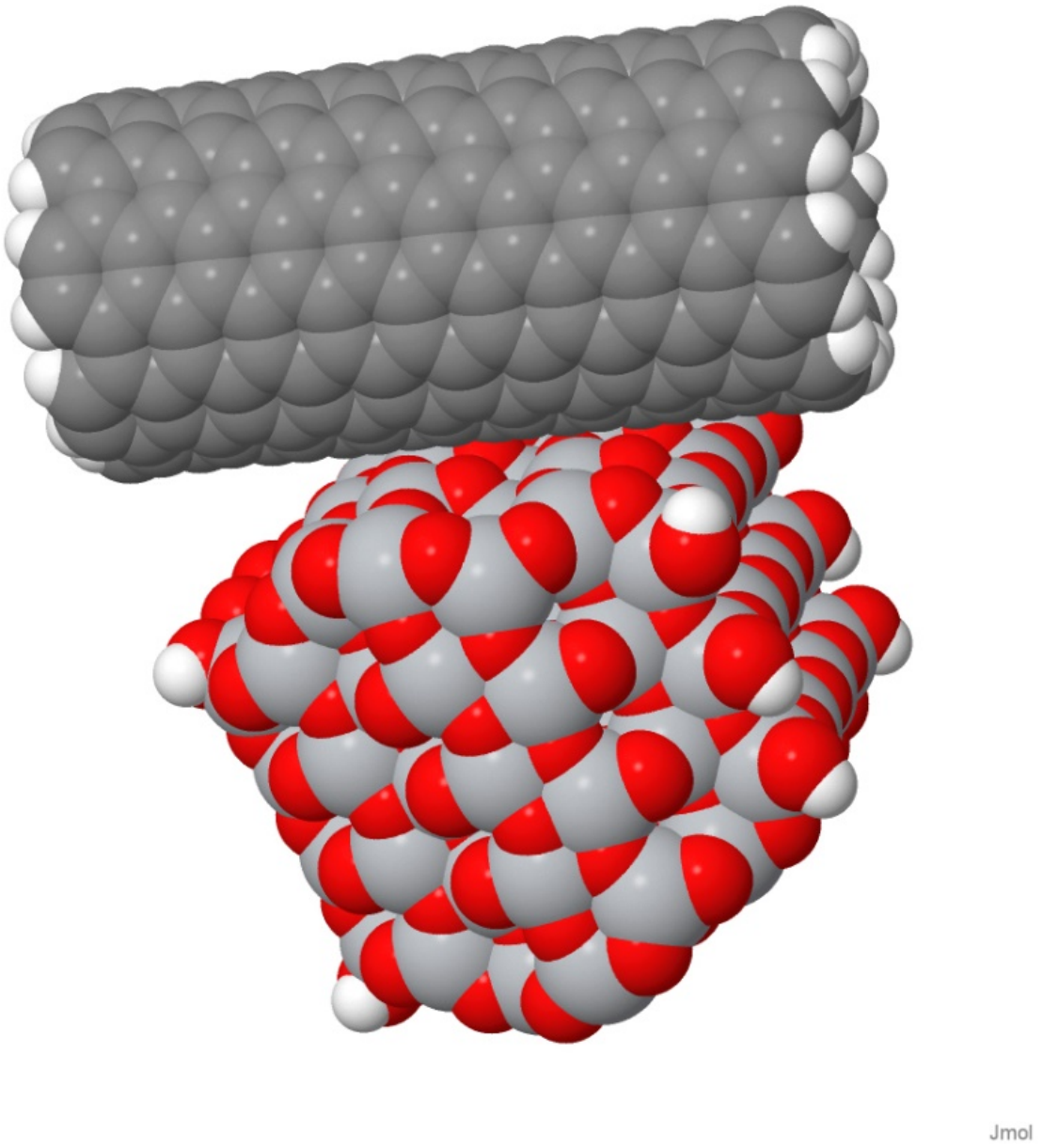

Figure 4.126 Van-der-Waals spheres representation of CNT-TiO_2 composite with CNT attached along (101) facet of TiO_2.

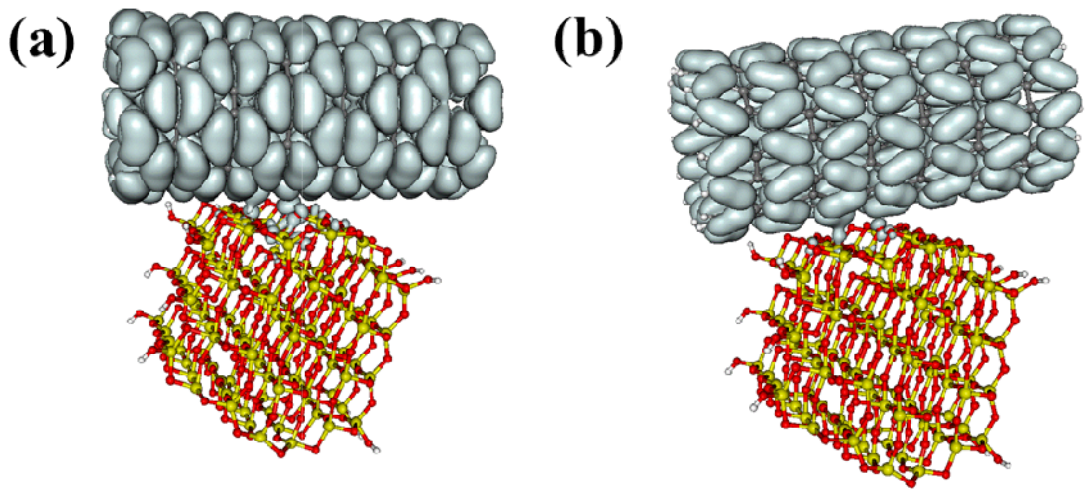

Figure 4.127 Boundary orbitals of CNT-Ti44r1 complex with CNT adsorbed over (101) facet: (a) HOMO and (b) LUMO.

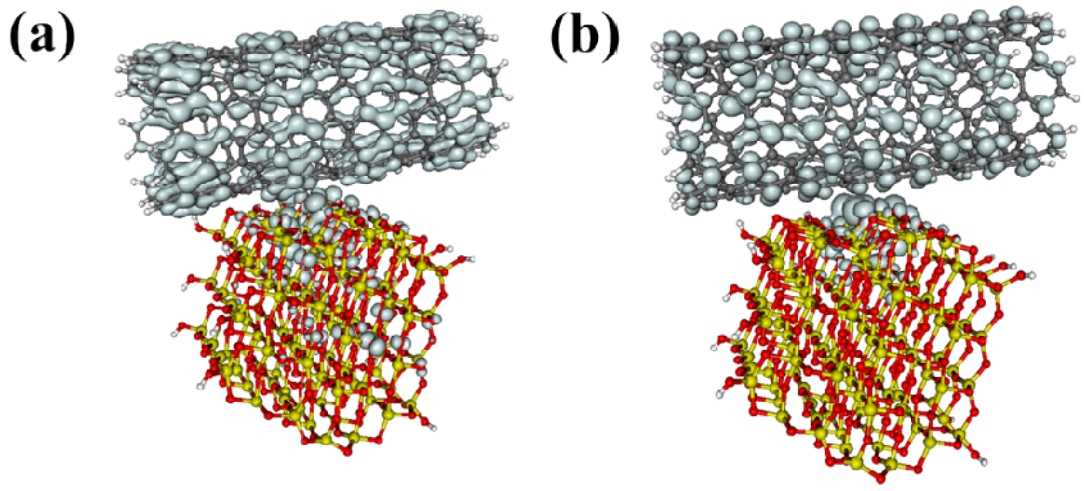

Figure 4.128 (a) Orbitals 1544 and (b) 1561 of valence band of CNT-Ti44r1 (101) composite.

4.129. CNT matched the step of the (1 0 1) surface in this composite. It was observed that a significant amount of interacting atoms caused major adsorption energy for this complex, which was equal to -20.77 kcal mol^{-1}. Figure 4.130 shows the CNT-Ti44r1 complex orbitals close to the boundary orbitals. The d_{Ti} and p_O AO in the step of (1 0 1) surface gave an input to the MO near the valence band edge of the complex. A relatively strong adsorption of CNT was observed over the step of (1 0 1) surface, which was a result of the overlapping of many AO with CNT orbitals.

4.3.7 Photocatalytic CO_2 reduction by CNT-TiO_2 nanocomposites

The photocatalytic reduction of CO_2 by TiO_2 and CNT-TiO_2 nanocomposites was performed in a reaction medium containing ACN and H_2O of ratio 16:2 v/v, with the addition of 2 mL TEOA which served as the sacrificial agent. The reaction mixture was irradiated by UVA light for a period of 24 h. As depicted in Figure 4.131, the formation of methanol was observed as the selective reaction product. The production of methanol increased with increase in time, up to 24 h. A higher amount of methanol production was observed with all the CNT-TiO_2 nanocomposites as compared with pure TiO_2, which indicate that the nanocomposites had improved photocatalytic activity. The methanol production rate of pure TiO_2 was found to be 1.44 mmol g^{-1} h^{-1}. Fast recombination of charge carriers and wider band gap could be responsible for the lower production rate by TiO_2 catalyst. The amount of CNT in the CNT-TiO_2 nanocomposite had an effect on the photocatalytic activity. The weight ratios of CNT in the nanocomposites were 1, 2 and 5% of TiO_2. It was observed that the methanol production increased up to 2% CNT loading and then decreased with 5% loading. In other words, 2% CNT loading (2.0CNT-TiO_2) was found to be the optimum, yielding a maximum methanol production rate of 2.36 mmol g^{-1} h^{-1}. This rate was found to be 1.64 times higher than pure TiO_2. Possible factors that could be responsible for the improvement of photocatalytic reduction of CO_2 by CNT nanocomposites are: (1) higher surface area as shown in Table 4.7 (Yu *et al.,* 2005b), (2) absorption of lightby the interface of CNT-TiO_2 sites and the concurrent injection of electrons in the TiO_2 conduction band (Woan *et al.,*2009), and (3) lower recombination of the photoinduced e^- - h^+ pairs (Yu *et al.,* 2007).

Higher loading of CNT did not favour photocatalytic CO_2 reduction. This could be

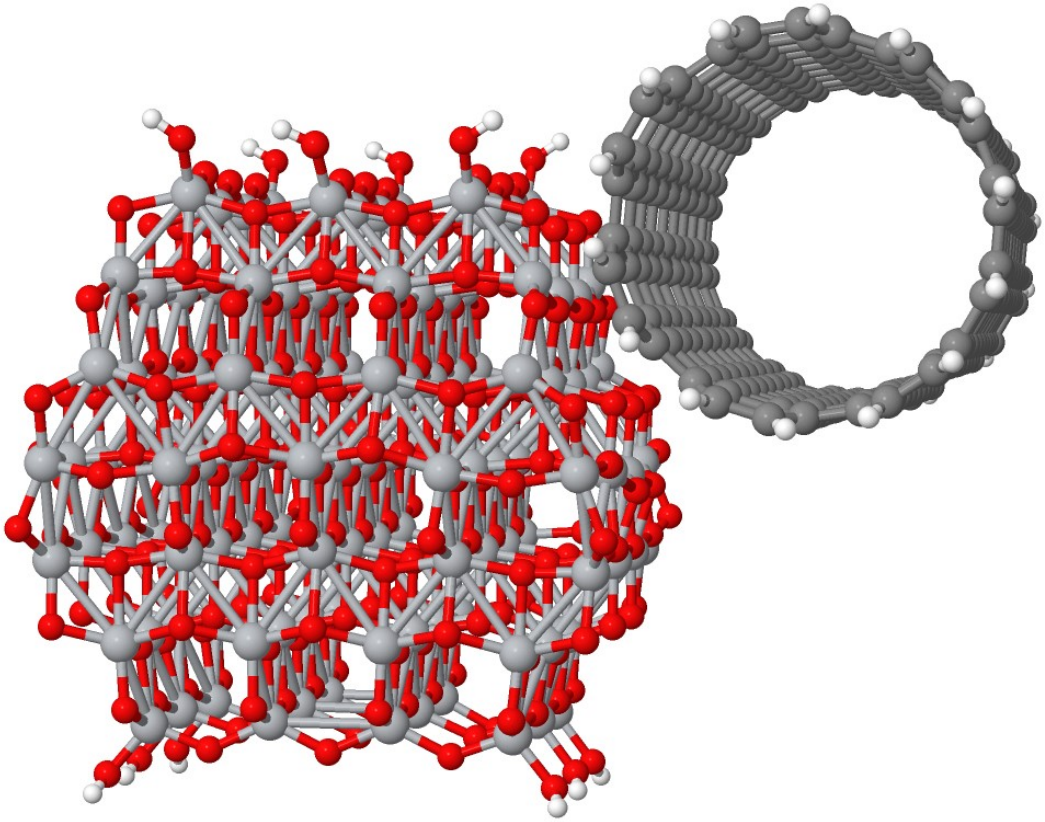

Figure 4.129 CNT-TiO_2 complex with strong interaction of CNT with (1 0 1) surface due to the matching surfaces of TiO_2 and CNT.

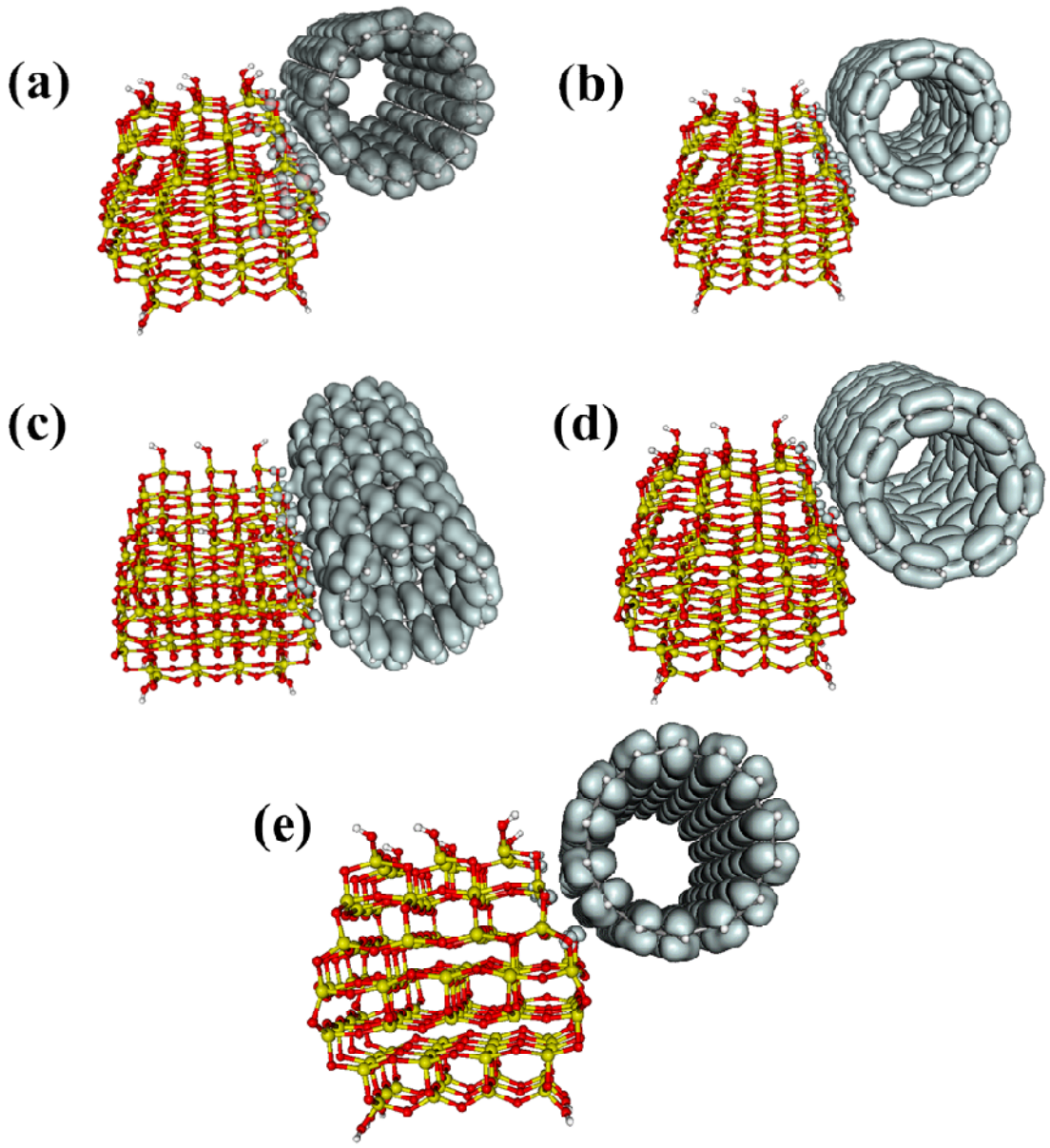

Figure4.130 (a) – 1563 (HOMO-3), (b) – 1564 (HOMO-2), (c) – 1565 (HOMO-1), (d) – 1566 (HOMO) and (e) – 1567 (LUMO)

.

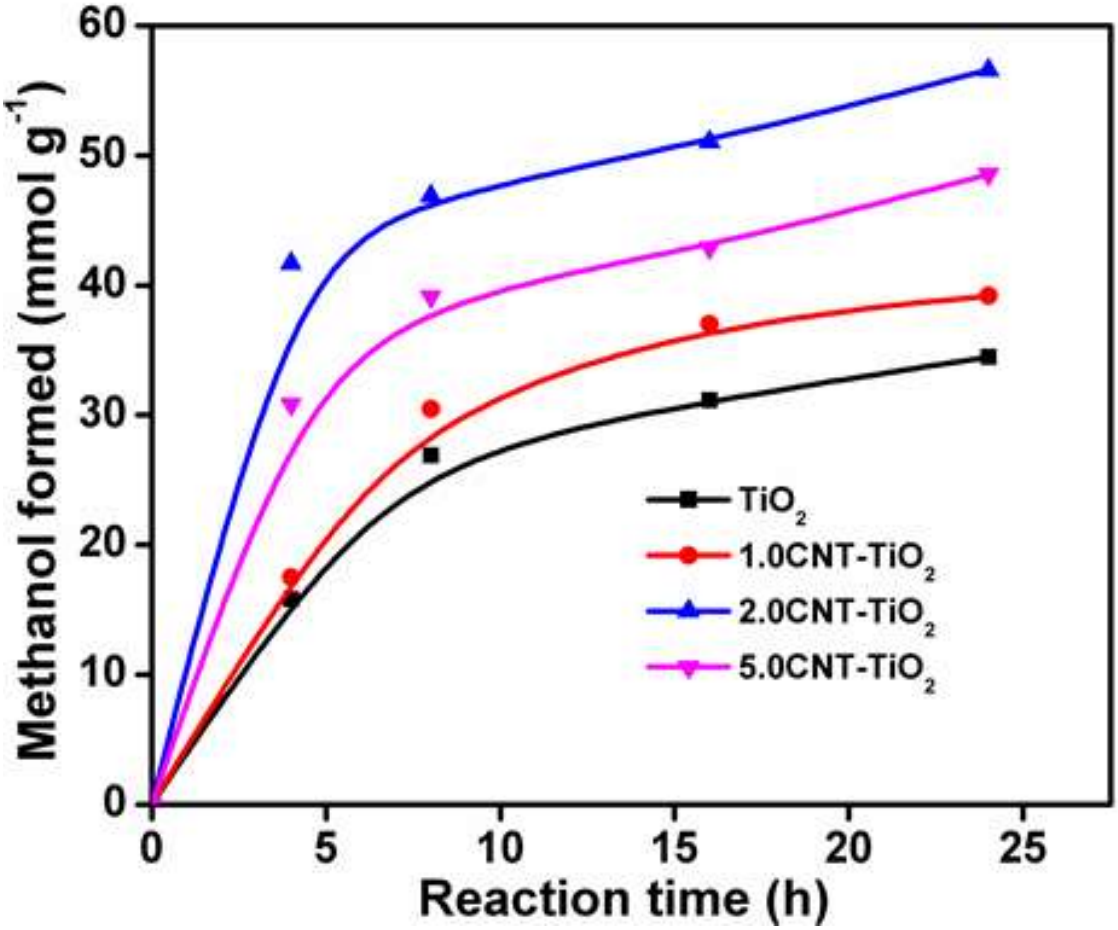

Fig 4.131 Time-dependent profiles of methanol production by pure TiO_2 and CNT-TiO_2 samples in ACN/H_2O/TEOA medium under UVA light. TEOA serves as a sacrificial agent.

due to the greatly reduced absorption of the TiO_2 of UV light. The black colour of CNT shielded the photons, and less amount of UV light was available for the photocatalytic activity of TiO_2 surface(Juang *et al.,* 2013; Yu *et al.,* 2005b).

Photocatalytic reduction of CO_2 was performed on the effect of the light wavelenght over the best-performing catalyst, 2.0CNT-TiO_2. In order to compare with the obtained methanol production under UVA, the experiment was then performed under visible light in the range of 420 to 700 nm. Other experimental conditions mentioned above were kept constant. As shown in Figure 4.132, 2.0CNT-TiO_2 was effective in the production of methanol under visible light. The methanol production rate was found to be 1.52 mmol g^{-1} h^{-1}. Factors that are responsible for the photoactivity of 2.0CNT-TiO_2 under visible light are: (1) the narrowing of the band gap (Cong *et al.,* 2011), (2) Ti-C bonds formation as established by the Raman and XPS (Vijayan *et al.,* 2012; Akhavan *et al.,* 2009; Akhavan *et al.,* 2010), and (3) photosensitization of the CNTs and the ability to utilize longer wavelength of light (Vijayan *et al.,* 2012). It was observed that the amount of methanol produced under UVA light was more than the methanol produced under visible light. The reason is possibly due tothe higher amount of TiO_2 in the composite, which could not catalyse the reaction completely under visible light. The schematic representation of the photocatalytic reduction of CO_2 to methanol by CNT-TiO_2 composites is shown in Scheme 4.3.

The recyclability and stability of 2.0CNT-TiO_2 were performed for the photocatalytic reduction of CO_2 under visible light. Other reaction conditions above were kept constant. For every 12 h till 51 h, the photoreactor was repurged with CO_2. As depicted in Figure 4.133, an increase in the amount of methanol production was observed at every 12 h interval. The yield of methanol for the first interval was 29.4 mmol g^{-1}.The reaction was stopped,and the solution was re-purged for 15 min. The reaction mixture was then kept in the dark for 1 h. A small amount of the liquid product was injected into the GC, and it was noticed that the methanol yield reduced to 25.7 mmol g^{-1} (indicating a 12% decrease in production). This reduction in production could be due to the evaporation of methanol during CO_2 purging. The process was repeated for three more intervals. A steady percentage reduction in methanol production was observed at every 12 h interval

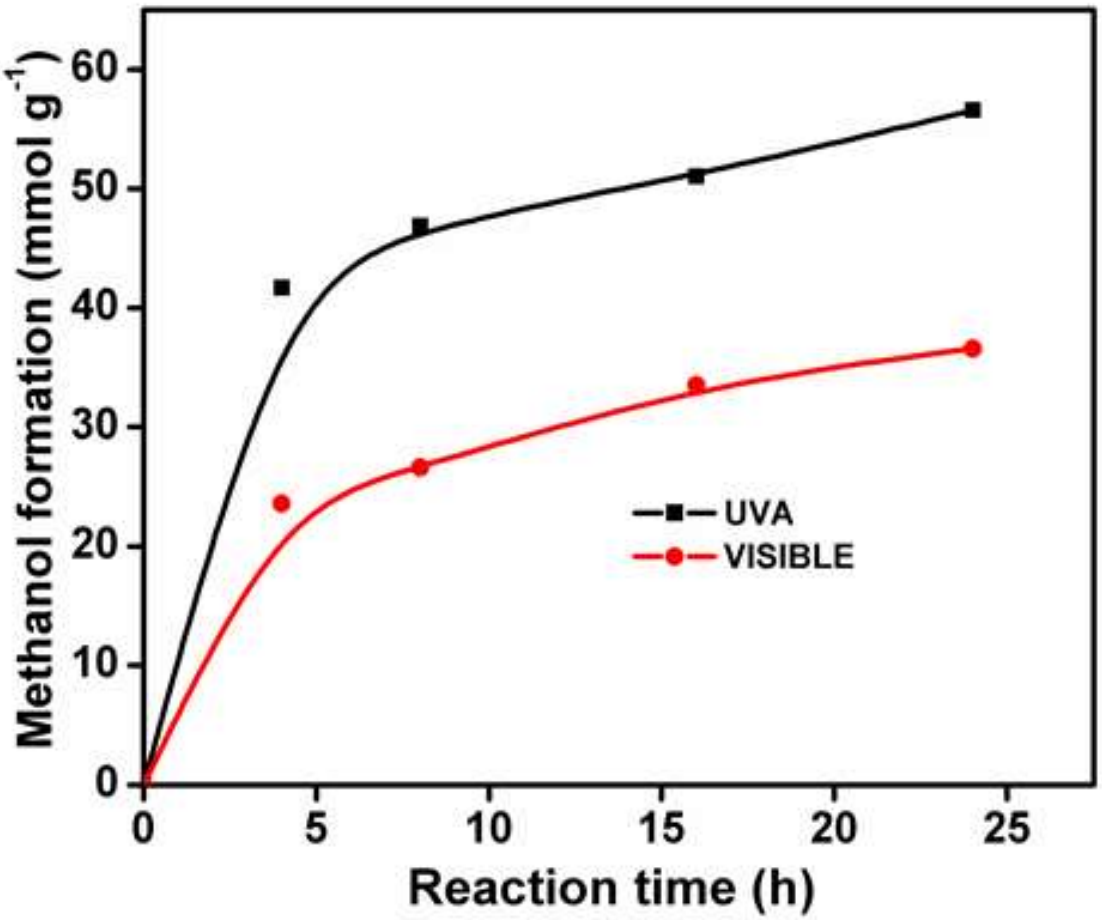

Figure 4.132 Time-dependent profiles showing the comparison of methanol production by 2.0CNT-TiO_2 under UVA and visible light in ACN/H_2O/TEOA medium.

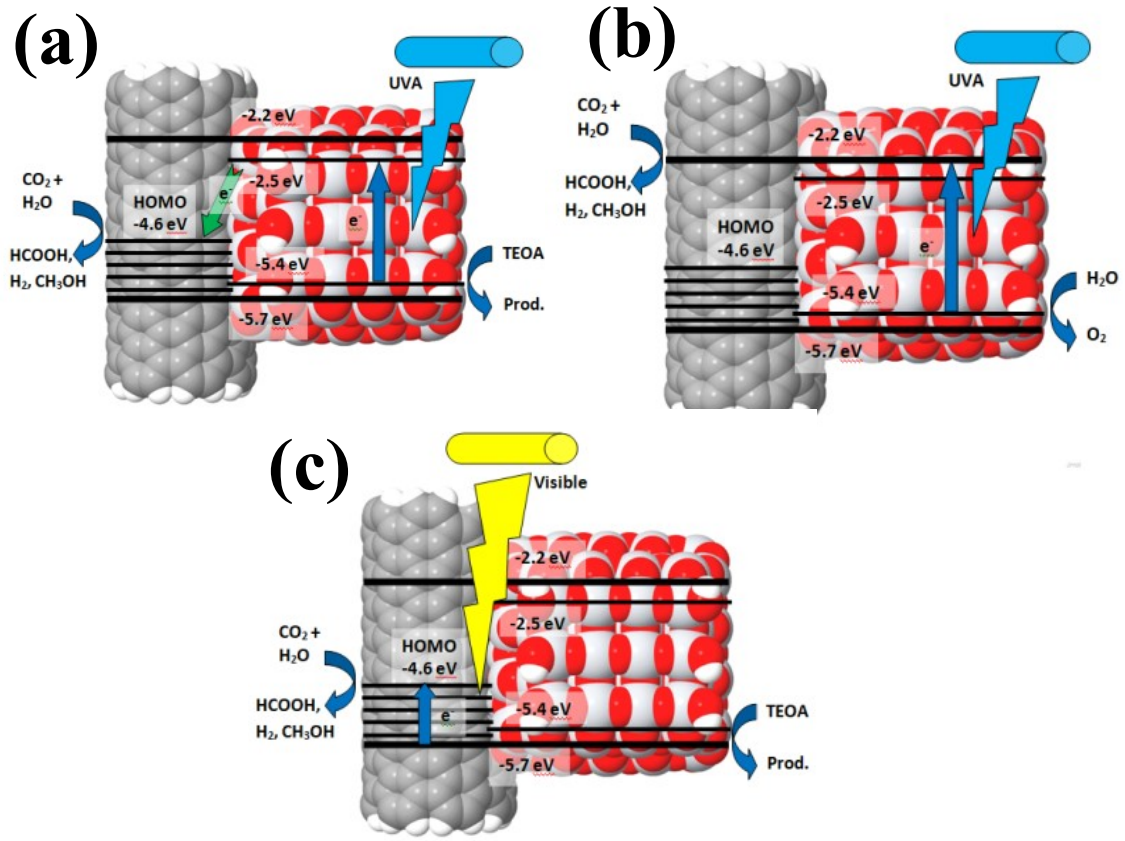

Scheme 4.3 The schematic diagram showing the product formation from CO_2 and H_2O a) under UVA irradiation in the ACN/H_2O/TEOA solvent, b) under UVA irradiation in the ACN/H_2O, and c) under visible light in ACN/H_2O/TEOA.

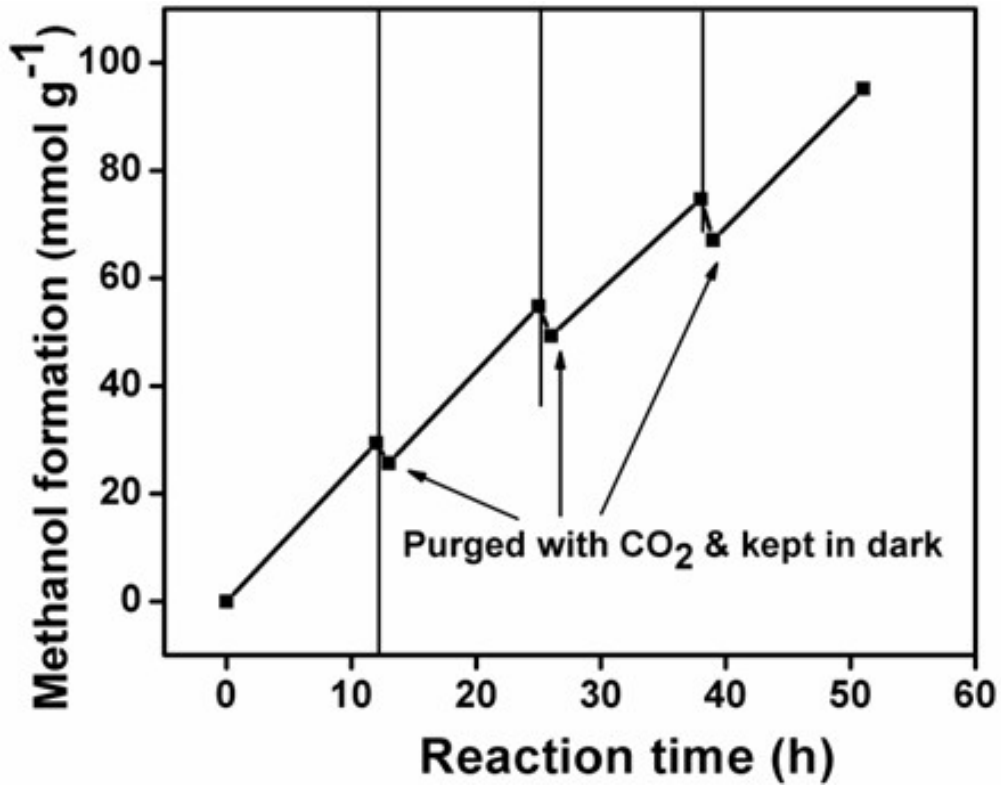

Figure 4.133 Recyclability and stability test on the production of methanol from 2.0CNT-TiO_2 under visible light for a period of 51 h.

after purging with CO_2. This steady reduction could be due to the accumulation of methanol inthe solution. Although the decrease in methanol production was observed after every purging process, the overall methanol production increased when the reaction was resumed at every stage.

4.3.8 Mechanism of photocatalytic CO_2 reduction by CNT-TiO_2 nanocomposite

To get a clear understanding of the photocatalytic reaction mechanisms, the four different regimes of photocatalytic reactions utilized were differentiated, namely (1) UV light photoexcitation in the presence of strong electron donor TEOA, (2) UV light photoexcitation in the absence of strong electron donor TEOA, (3) visible light photoexcitation in the presence of strong electron donor TEOA, and (4) visible light photoexcitation in the absence of strong electron donor TEOA. Among these four regimes, three were realised in the present study.

Under UVA light, both TiO_2 nanoparticles and CNT took part in the photoexcitation process with the dominant role of TiO_2 because of the short lifetime of charge carriers in CNT due to the absence or very small value of the band gap. Under visible light, photoexcitation proceeded with the participation of boundary orbitals of the CNT-TiO_2 composite as previously shown (Figure 4.124, 4.126 and 4.129). Common conduction and valence band orbitals of CNT-TiO_2 nanoparticles provided an effective band gap of around 1.1 eV for CNT-TiO_2 valence band to CNT charge transfer and 2.4 eV for CNT to CNT-TiO_2 conduction band charge transfer. It should be pointed out that without sacrificial electron donor, the energy level of electrons in CNT was too low (about +2.0 eV) to drive any reaction of photoreduction. However, reactions of oxidation proceeded with the formation of oxygen during CO_2 photoreduction. Under such conditions, photogenerated electrons in the CNT-TiO_2 conduction band acted as the reducing agent for CO_2 reduction (Scheme 4.3b).

In the presence of sacrificial electron donor TEOA, strongly reducing conditions were realised. Photogenerated electrons resulting from TEOA oxidation with UVA light photogenerated holes in the CNT-TiO_2 valence band were eventually transferred to CNT (Scheme 4.3a). Pumping of excessive electrons into CNT increased its redox potential to

values enough to drive diverse reduction reactions, with the production of methanol. Carbon Nanotubes (CNTs) are known to be good electrocatalysts for such reactions. Therefore, the tight contact of CNT and TiO_2 nanoparticles was the cause of the large photocatalytic activity of the CNT-TiO_2 composites of the present study. Under visible light photoexcitation, electrons from the common orbitals of the CNT-TiO_2 valence band found at -5.7 eV can be brought to the LUMO orbitals situated mostly in CNT and initiate reduction reactions over the CNT surface (Scheme 4.3c).

4.4 Synthesis of Magnesium-doped TiO_2 nanocatalysts for the photoreduction of CO_2

The TiO_2 nanoparticles and Mg-TiO_2 nanocatalystswere prepared according to Section 3.4.2. All prepared nanocatalysts were white in colour and were characterisedusing techniques as described in Section 3.2.2. In addition to the physical techniques used for the characterisation of the mixed-phase TiO_2, Inductively Coupled Plasma Atomic Emission Spectroscopy (ICP-AES) was employed for the characterisation of Mg-TiO_2 nanocatalysts.

4.4.1 Inductively coupled plasma atomic emission spectroscopy and X-ray diffraction characterisation of Mg-TiO_2 nanocatalysts

ICP-AES measurements of the nanocatalysts revealed that the amount of Mg in Mg-TiO_2 samples was in the range of 0.07 to 0.17% (Mg/(Mg + Ti)). Samples code-named Mg-TiO_2-1, Mg-TiO_2-2 and Mg-TiO_2-3 were found to contain 0.07, 0.10 and 0.17% of Mg, respectively. The XRD patterns of the prepared Mg-doped TiO_2 photocatalysts are shown in Figure 4.134. The pure TiO_2 and Mg-doped TiO_2 had major peaks at 25.5°, 38.2°, 48.3°, 55.02° and 63.02° in all the samples, which are in agreement with (1 0 1), (0 0 4), (2 0 0), (1 0 5), and (2 0 4) planes of tetragonal anatase TiO_2 (JCPDS 21-1272). The Mg^{2+} (0.72 Å) has a competitive ionic radius with Ti^{4+} (0.61 Å) and easily dope and substitute Ti^{4+} in the TiO_2 without making much distortion to the structure. No clear peak for Mg or MgO was observed in the Mg-doped TiO_2 samples. But the slight change to a lower value in the (1 0 1) peak of TiO_2 anatase reflected the doping of Mg in the TiO_2 lattice.

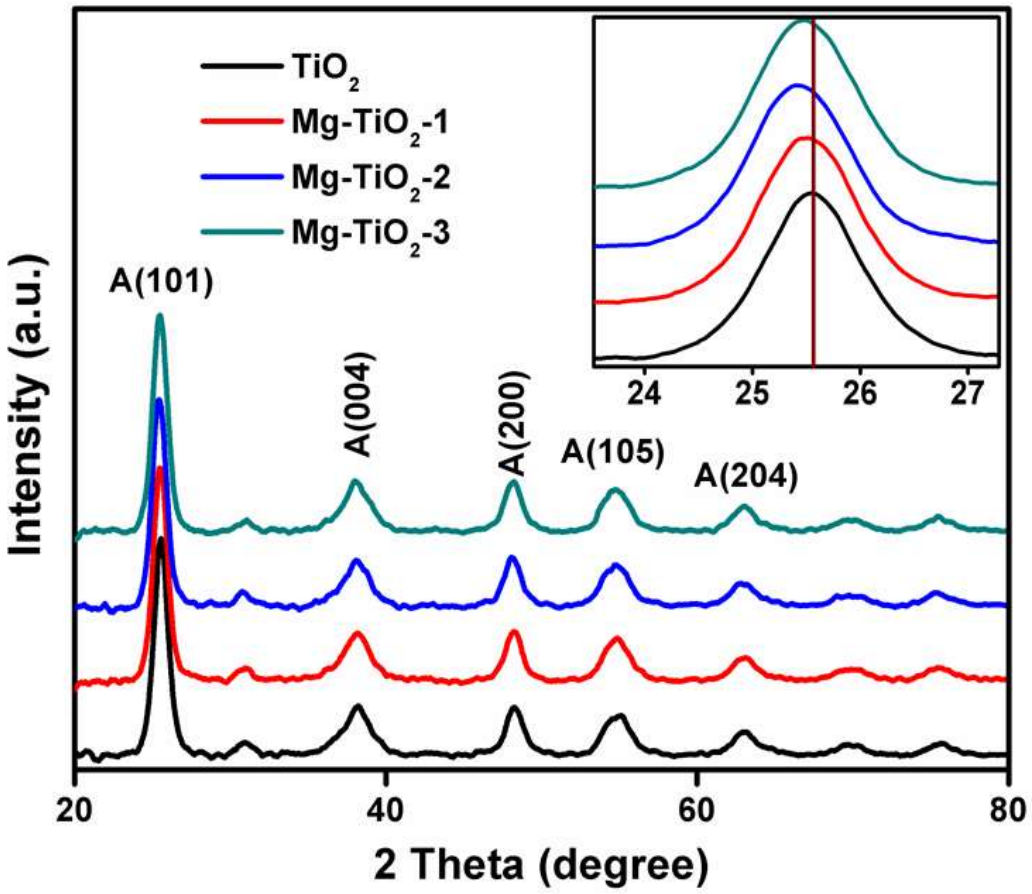

Figure 4.134 X-ray diffraction pattern of TiO_2, Mg-TiO_2-1, Mg-TiO_2-2 and Mg-TiO_2-3.

4.4.2 Surface area and UV-Vis. diffuse reflectance spectroscopycharacterisation of TiO_2 NPs and Mg-TiO_2 nanocatalysts

The surface areas of all the prepared nanocatalysts are shown in Table 4.8. The sonothermal method of TiO_2 was modified to obtain a higher surface area. The modified sonothermal method afforded the prepared TiO_2 a higher surface area of 122.8 m^3 g^{-1}; which almost double (64.5 m^2 g^{-1}) the TiO_2 previously prepared (TiO_2-S). The surface area of TiO_2 slightly decreased with the doping of Mg and was almost constant, at around 120 m^2 g^{-1}, for all doped catalysts. As shown in Figure 4.135, the nitrogen adsorption-desorption isotherms of all the nanocatalysts were of type IV (Leofanti *et al.,* 1998). The pure TiO_2 exhibited H3 type of hysteresis loop, indicating the agglomeration of particles forming slit-shaped pores. However, after doping, the hysteresis loops gradually tend towards H2 type, indicating the presence of ink-bottled pores and cylindrical-through pores. This suggests that Mg interaction with TiO_2 led to the rearrangement of pores. The total pore volume of pure TiO_2 and Mg-TiO_2-1 were almost equal, and as the amount of Mg increased the total pore volume decreased as shown in Table 4.8. This observation was also confirmed by the pore size distribution curve (Figure 4.136), in which the pore maxima shifted towards lower values with increasing Mg content. This suggests that pores became slightly narrower with Mg content. In addition, pure TiO_2 showed a higher cumulative pore volume in comparison with all Mg-doped samples (Figure 4.137). The cumulative pore volume also decreased with increasing amount of Mg.

The ultraviolet-visible absorption spectra of the prepared samples are shown in Figure 4.138. It can be noticed that the absorption edge of the pristine TiO_2 was ca. 393 nm. There was no obvious shift in the spectra after the addition of Mg dopants up to 0.1%; suggesting that the doping of Mg did not affect the band gap of TiO_2. However, the absorption edge slightly shifted to the lower wavelength (ca. 388 nm) with the maximum Mg loading. Gao and co-workers also observed a similar trend (Gao *et al.,* 2017). The band gap energies of all samples were obtained from the Tauc plot by extrapolating a tangent line to the abscissa axis. The energies of all the samples were around 3.10 eV (Figure 4.139).

Table 4.8 Physico-chemical properties of the pure TiO_2 and Mg-TiO_2 nanocatalysts.

Type of catalyst	Surface area ($m^2\ g^{-1}$)	Pore volume ($cm^3\ g^{-1}$)	Average Pore width (nm)*	Pore Maxima (nm)
TiO_2	122.76	0.26	0.71	0.67
Mg-TiO_2-1	121.60	0.25	0.64	0.77
Mg-TiO_2-2	117.40	0.24	0.63	0.72
Mg-TiO_2-3	118.45	0.23	0.63	0.72

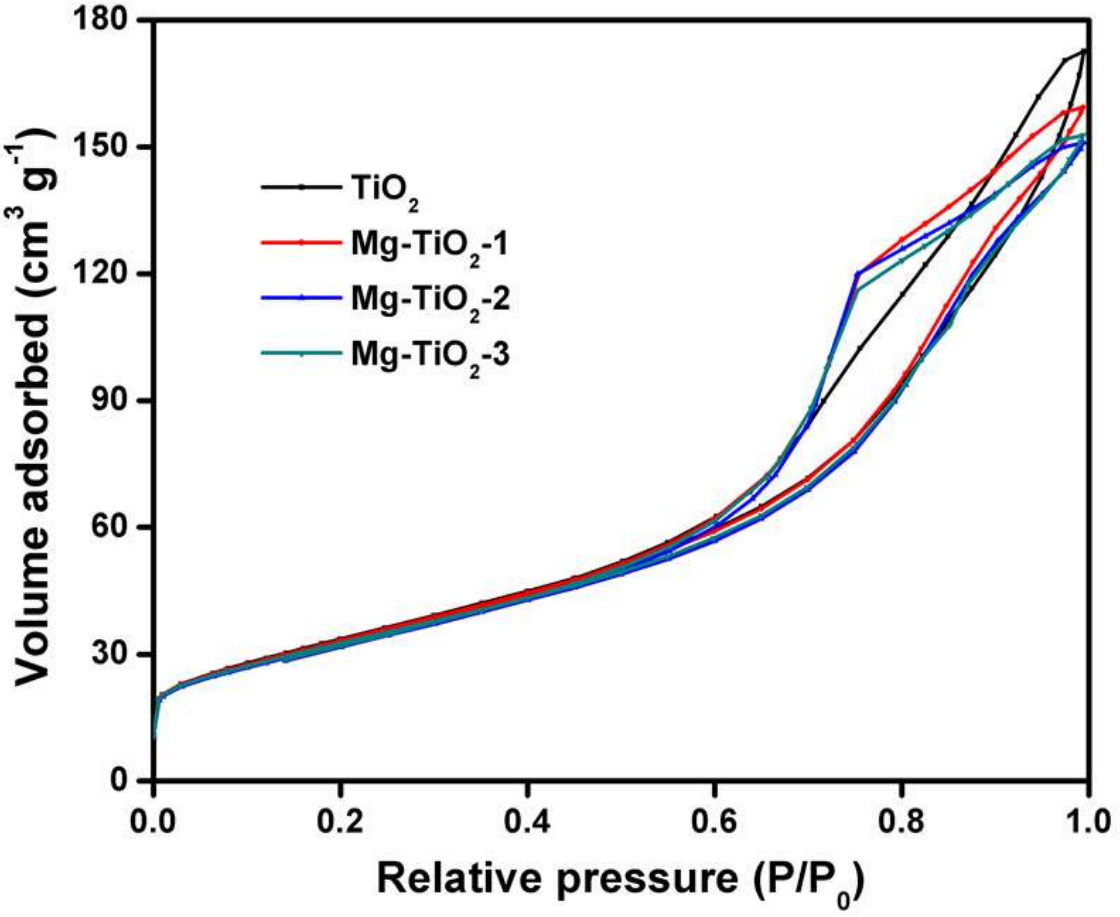

Figure 4.135 N_2 adsorption-desorption of TiO_2, Mg-TiO_2-1, Mg-TiO_2-2 and Mg-TiO_2-3.

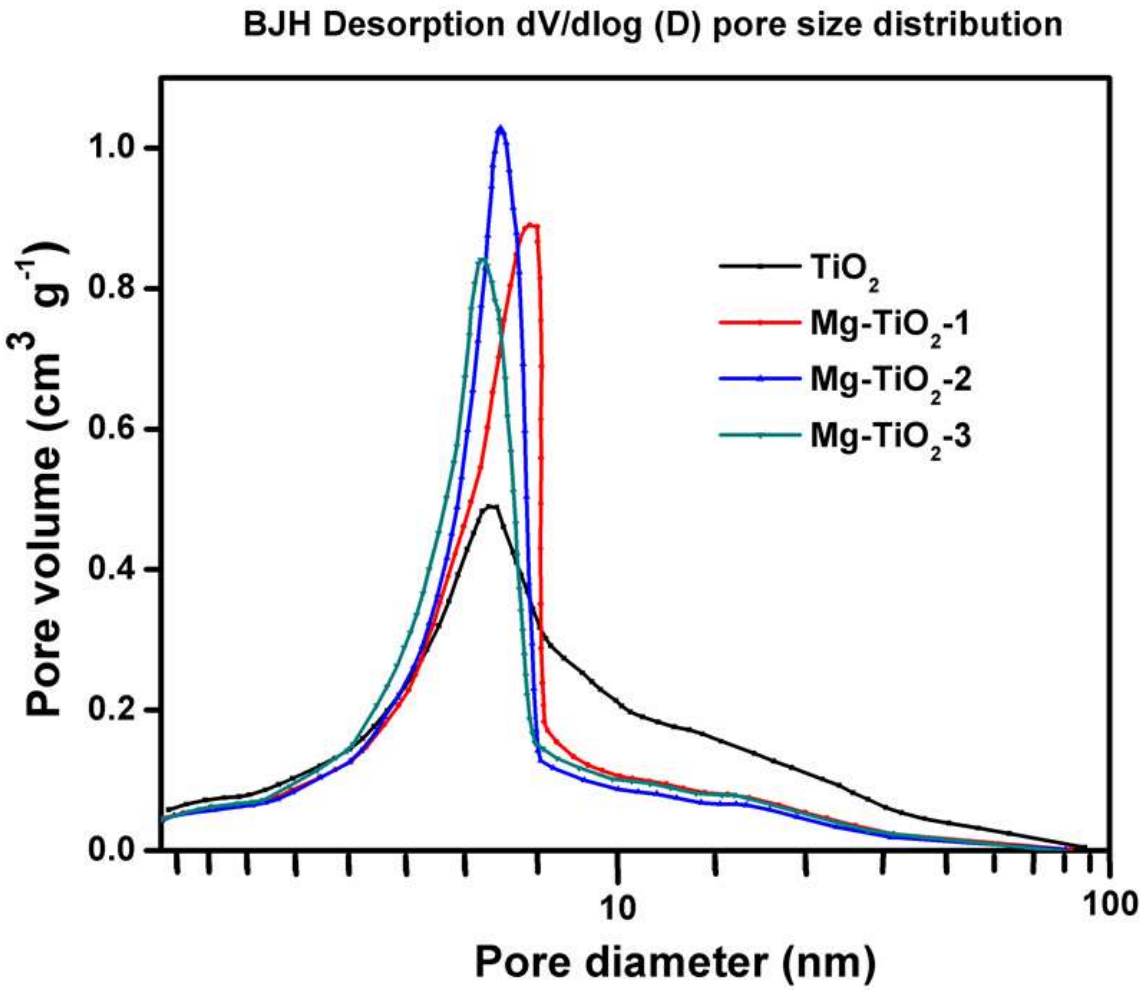

Figure 4.136 Pore size distribution of TiO_2, Mg-TiO_2-1, Mg-TiO_2-2 and Mg-TiO_2-3.

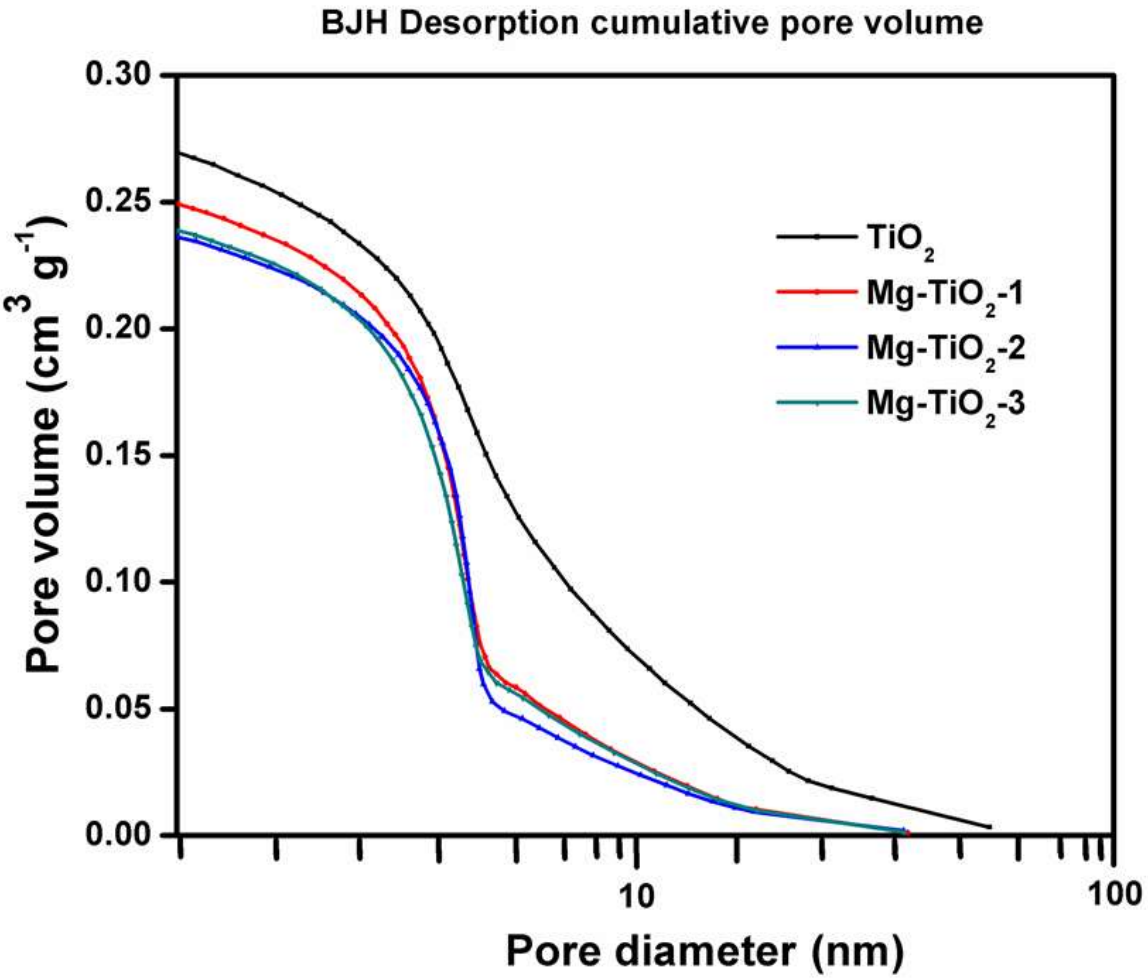

Figure4.137 Cumulative pore volume of TiO_2, Mg-TiO_2-1, Mg-TiO_2-2 and Mg-TiO_2-3.

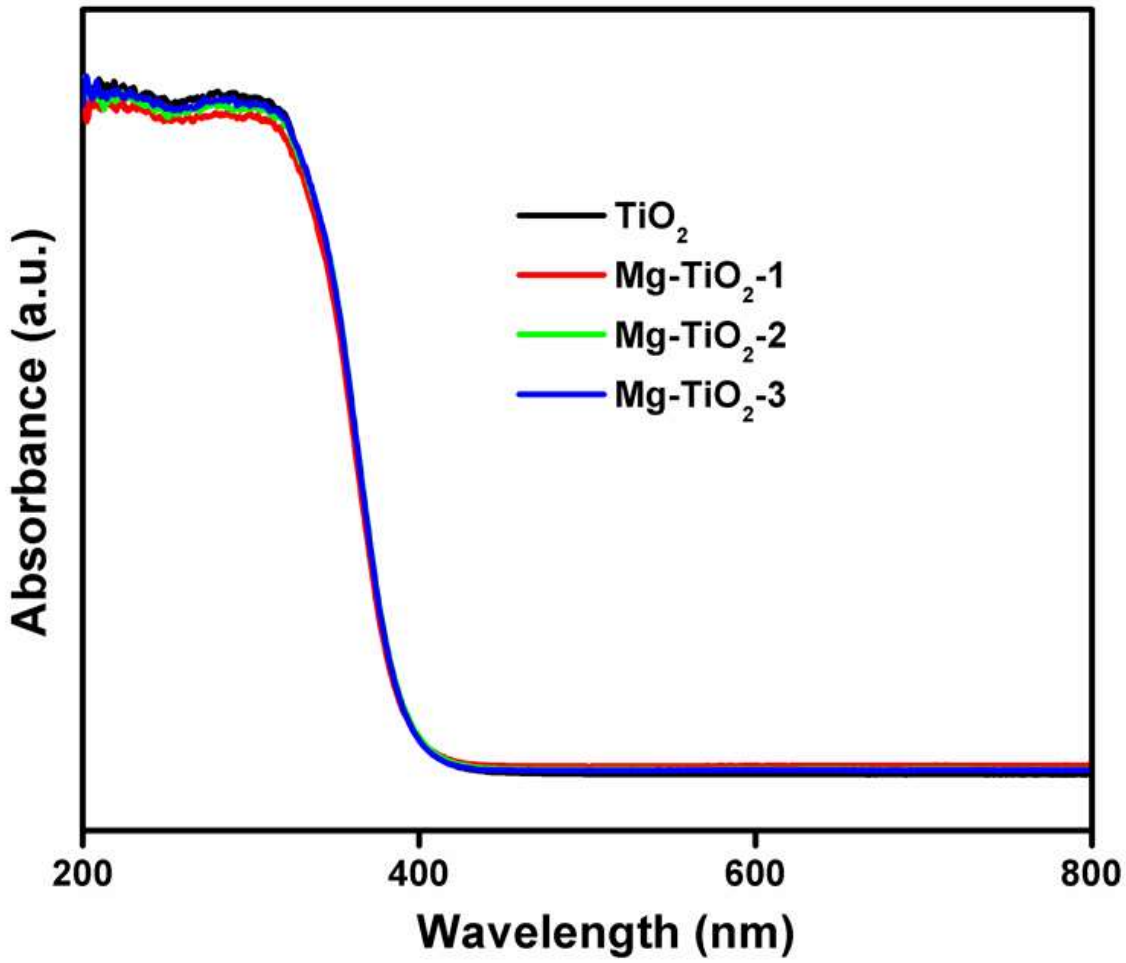

Figure 4.138 UV–vis absorbance spectra of TiO_2, Mg-TiO_2-1, Mg-TiO_2-2 and Mg-TiO_2-3.

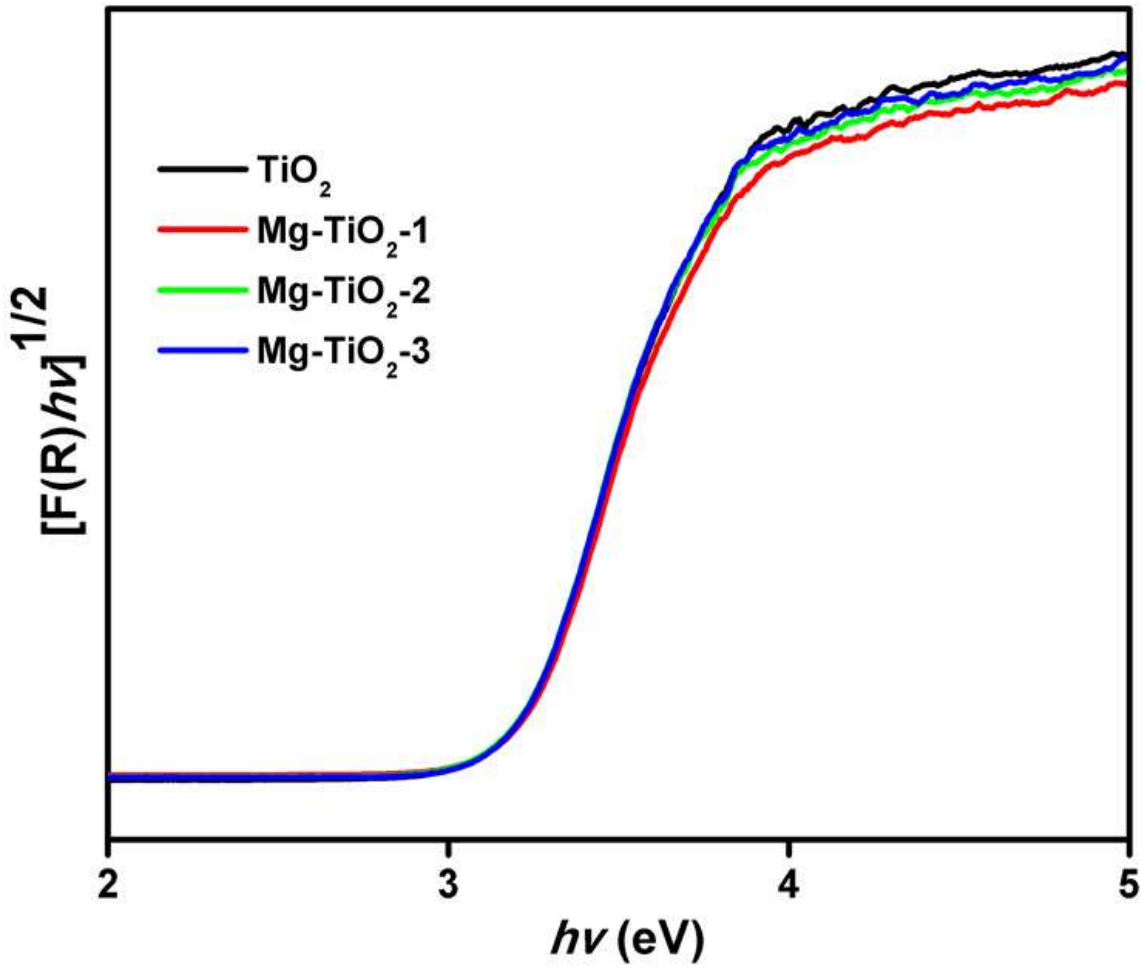

Figure 4.139 Tauc plot of TiO_2, Mg-TiO_2-1, Mg-TiO_2-2 and Mg-TiO_2-3.

4.4.3 Scanning electron microscopy and transmission electron microscopy characterisation of TiO_2 NPs and Mg-TiO_2 nanocatalysts

The SEM images of pristine TiO_2 and Mg-doped TiO_2 nanocatalysts are shown in Figure 4.140 – 4.143. The morphologies of all the catalysts were relatively similar. There was not much difference between pure TiO_2 and all Mg-doped TiO_2, suggesting that the particles were of highly homogeneous size. EDX analysis of the Mg-doped TiO_2 confirmed the presence of Mg, O, and Ti as illustrated in Figure 4.145 – 4.147. Also, for the bare TiO_2, only O and Ti were confirmed by EDX analysis (Figure 4.144).

To understand the morphology of the prepared nanocatalysts better, TEM analyses of the bare TiO_2 and Mg-doped TiO_2 catalysts were performed (4.148 – 4.151). An improvement in the homogeneity was observed for all the samples; indicating that the modified experimental procedure facilitated better dispersion of TiO_2 nanoparticles. The calculated average particle size of the pure TiO_2 was ca. 12.5 nm. However, the particle size decreased after the introduction of Mg into TiO_2. A further decrease in the particle size was observed as the amount of Mg in the Mg-TiO_2 nanocatalysts increased. The values of 9.6, 9.5 and 8.4 nm were calculated for Mg-TiO_2-1, Mg-TiO_2-2 and Mg-TiO_2-3, respectively. The d-lattice spacing of 0.35 nm was consistent with the plane (1 0 1) of anatase TiO_2 as depicted by HRTEM images (Figure 4.152). The spacing slightly reduced to 0.34 nm after the doping of Mg, indicating the interaction of Mg in the lattice of TiO_2 (Figure 4.153 – 4.155). Elemental mapping confirmed the homogenous nature of all the catalysts as shown in Figure 4.156 – 4.159.

4.4.4 X-ray photoelectron spectroscopy characterisation of TiO_2 NPs and Mg-TiO_2 nanocatalysts

To check the changes in the chemical environment, XPS measurements were performed for the prepared TiO_2 and Mg-doped TiO_2 catalysts. The XPS survey spectra of all the catalysts are shown in Figure 4.160 – 4.163. The presence of Mg2p peak observed in the spectra of all Mg-doped samples suggests the successful doping of Mg^{2+} in TiO_2. The peak of Mg2p slightly increased as the amount of Mg in TiO_2 increased.The high-resolution XPS spectrum of TiO_2 revealed two peaks at 457.7 and 463.5 eV, which were assigned to $Ti2p_{3/2}$ and $Ti2p_{1/2}$ of Ti^{4+} state (Sofianou *et al.,* 2014) asshown in Figure 4.164. An additional peak corresponding to Ti^{3+} in $Ti_2O_3$was observed with all Mg-doped

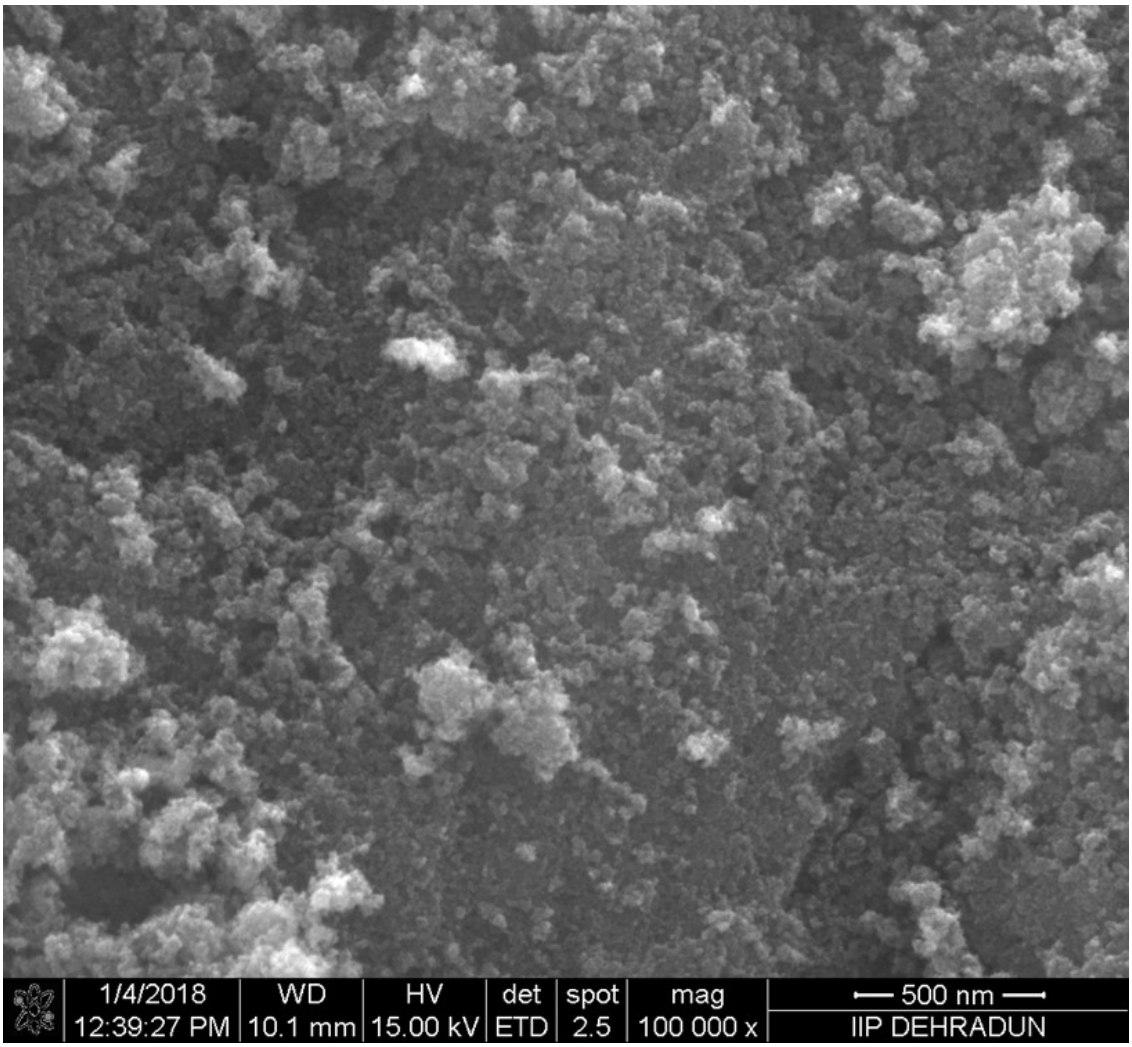

Figure 4.140 Scanning electron microscopy image of pure TiO_2 nanocatalyst.

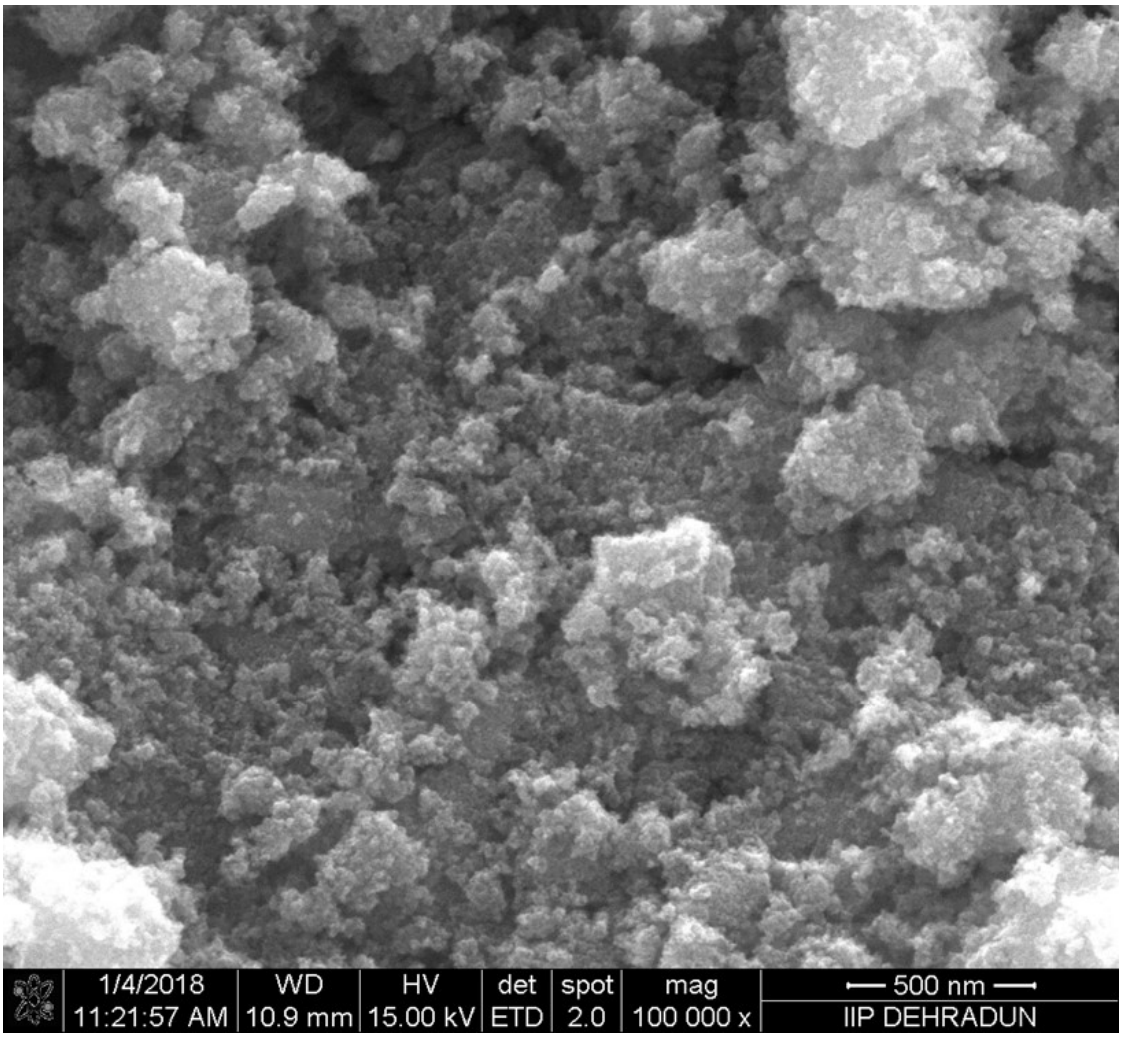

Figure 4.141 Scanning electron microscopy image of Mg-TiO_2-1 nanocatalyst.

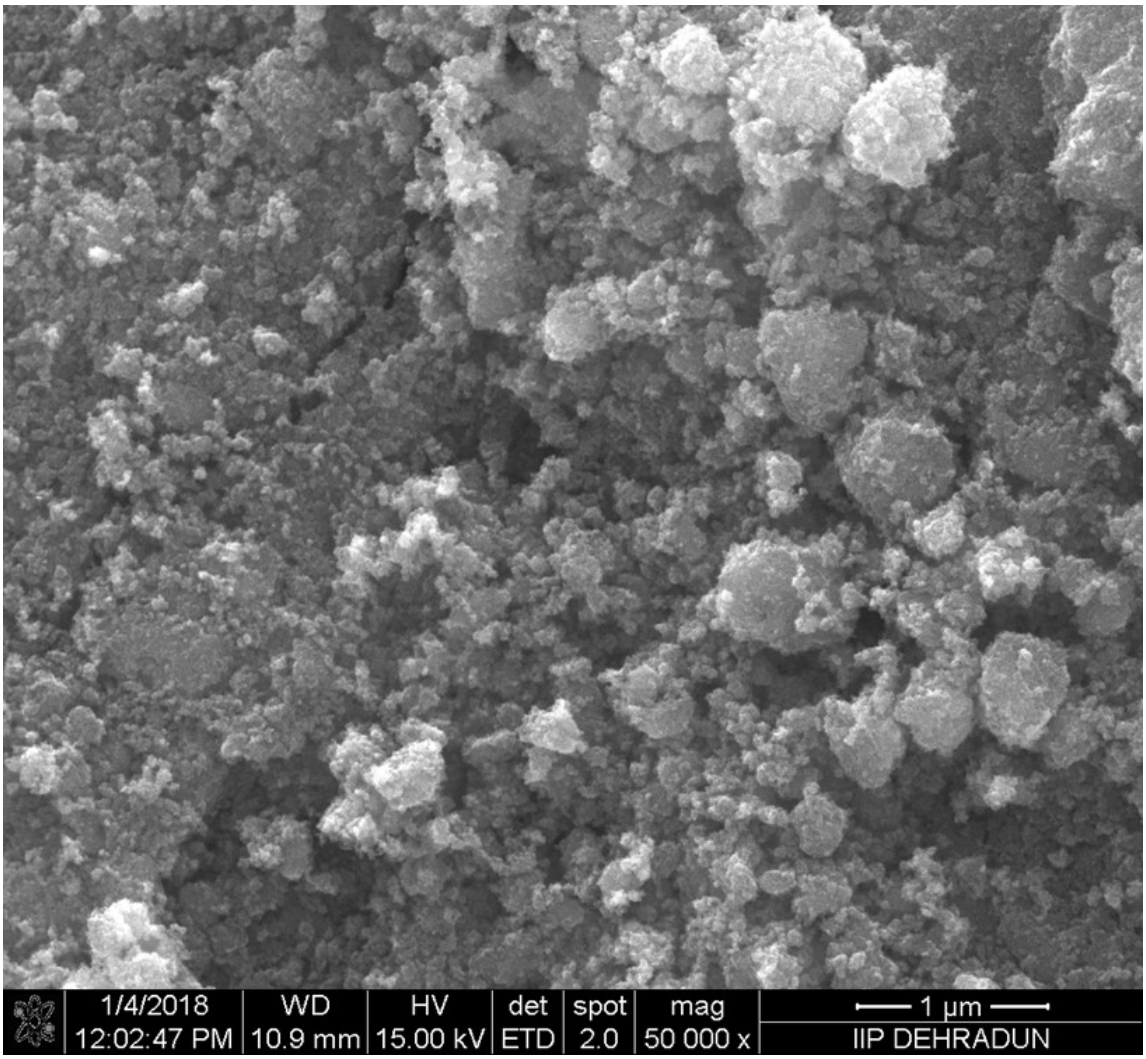

Figure 4.142 Scanning electron microscopy image of Mg-TiO_2-2 nanocatalyst.

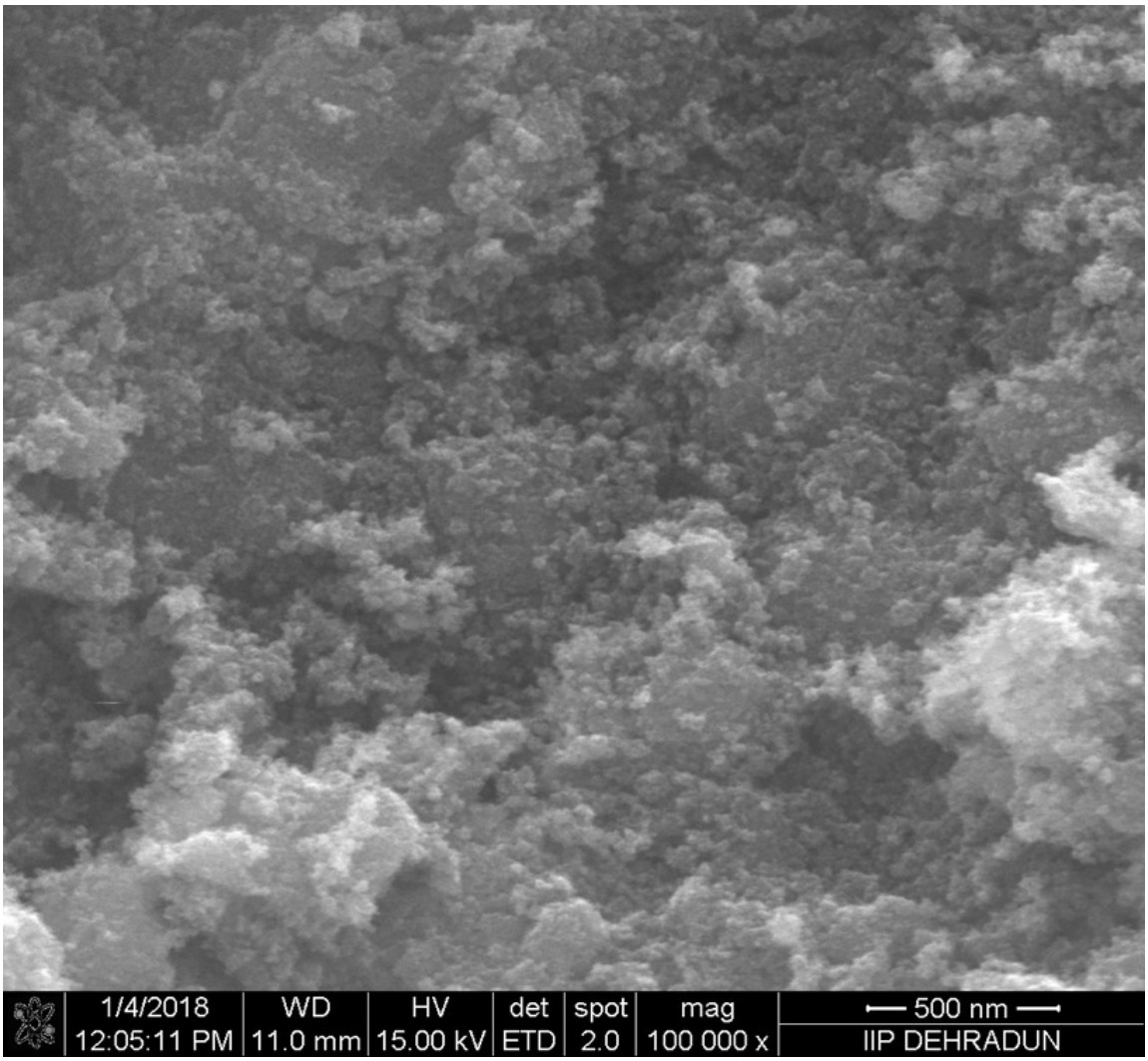

Figure 4.143 Scanning electron microscopy image of Mg-TiO_2-3 nanocatalyst.

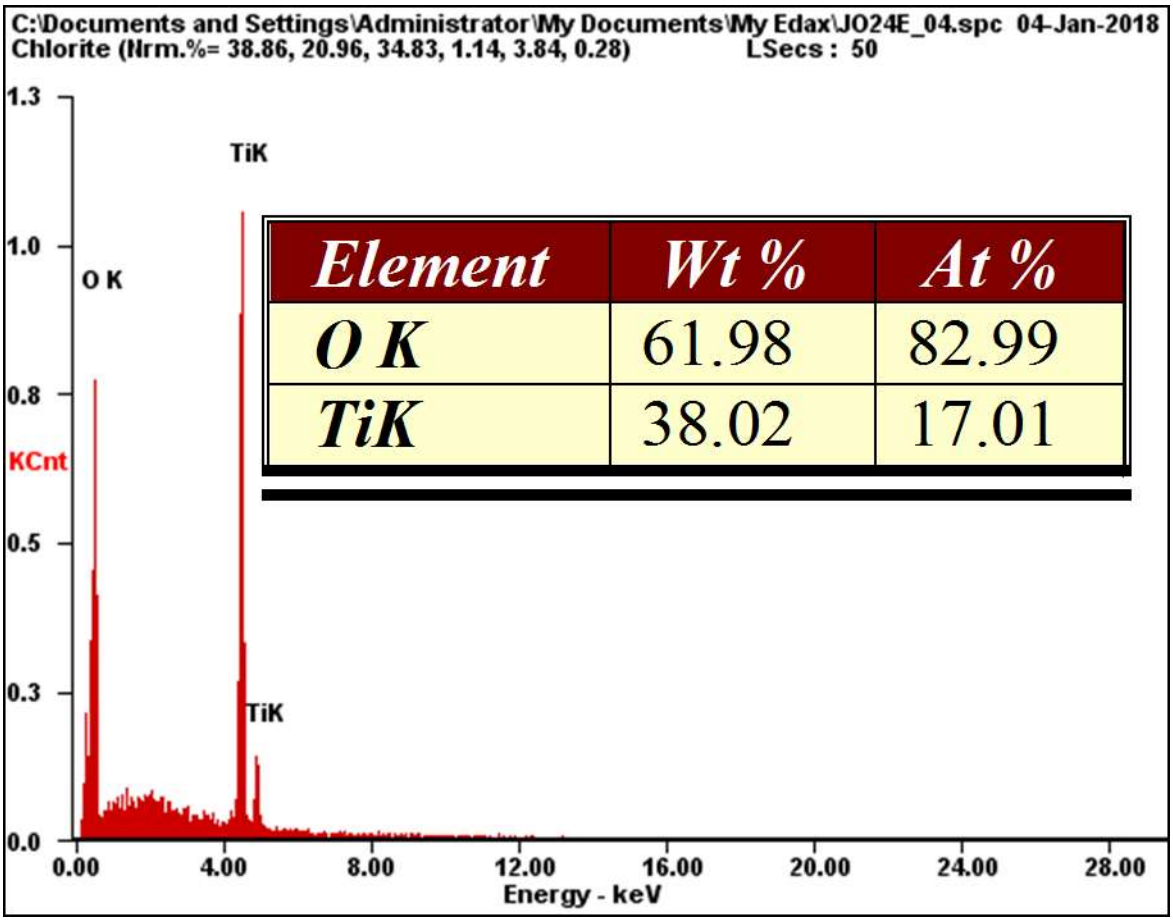

Figure 4.144 Energy-dispersive X-ray spectroscopy image of pure TiO_2 nanocatalyst.

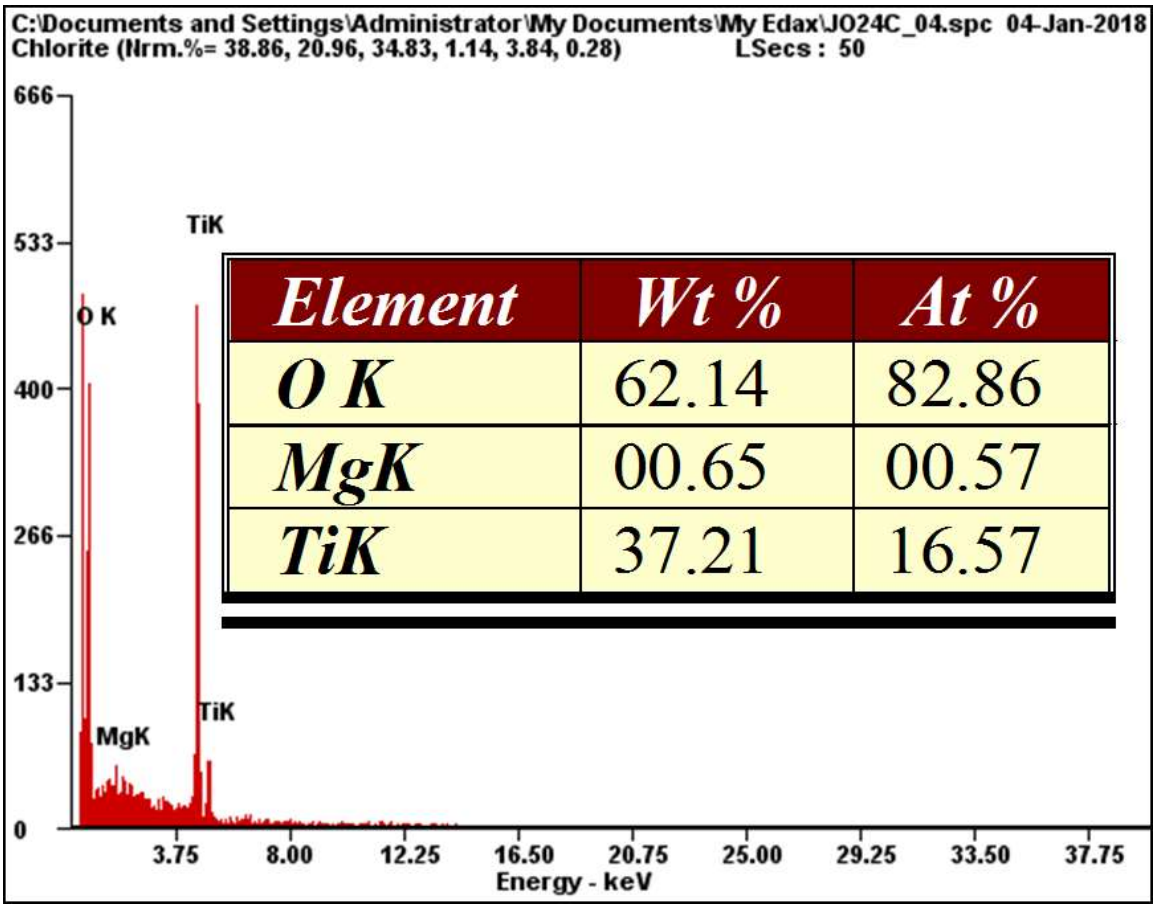

Figure 4.145 Energy-dispersive X-ray spectroscopy image of Mg-TiO_2-1 nanocatalyst.

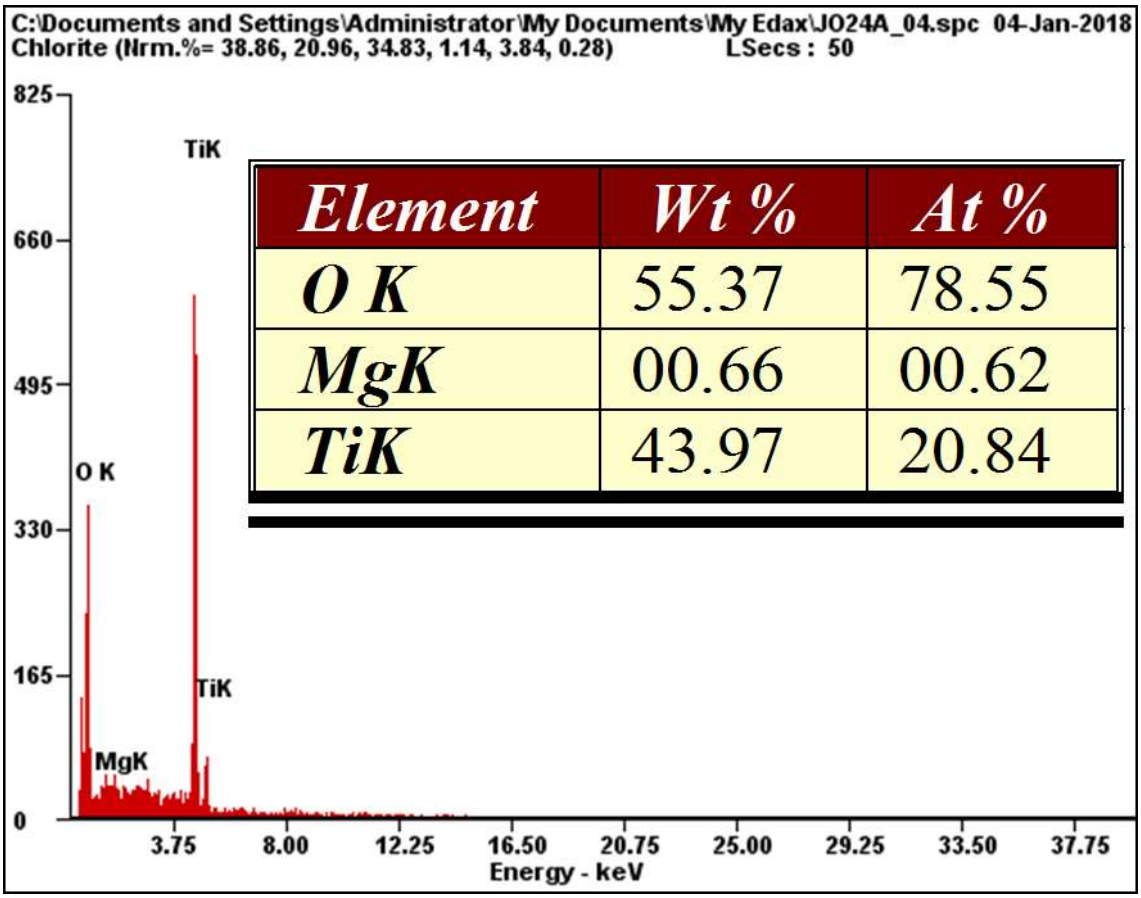

Figure 4.146 Energy-dispersive X-ray spectroscopy image of Mg-TiO_2-2 nanocatalyst.

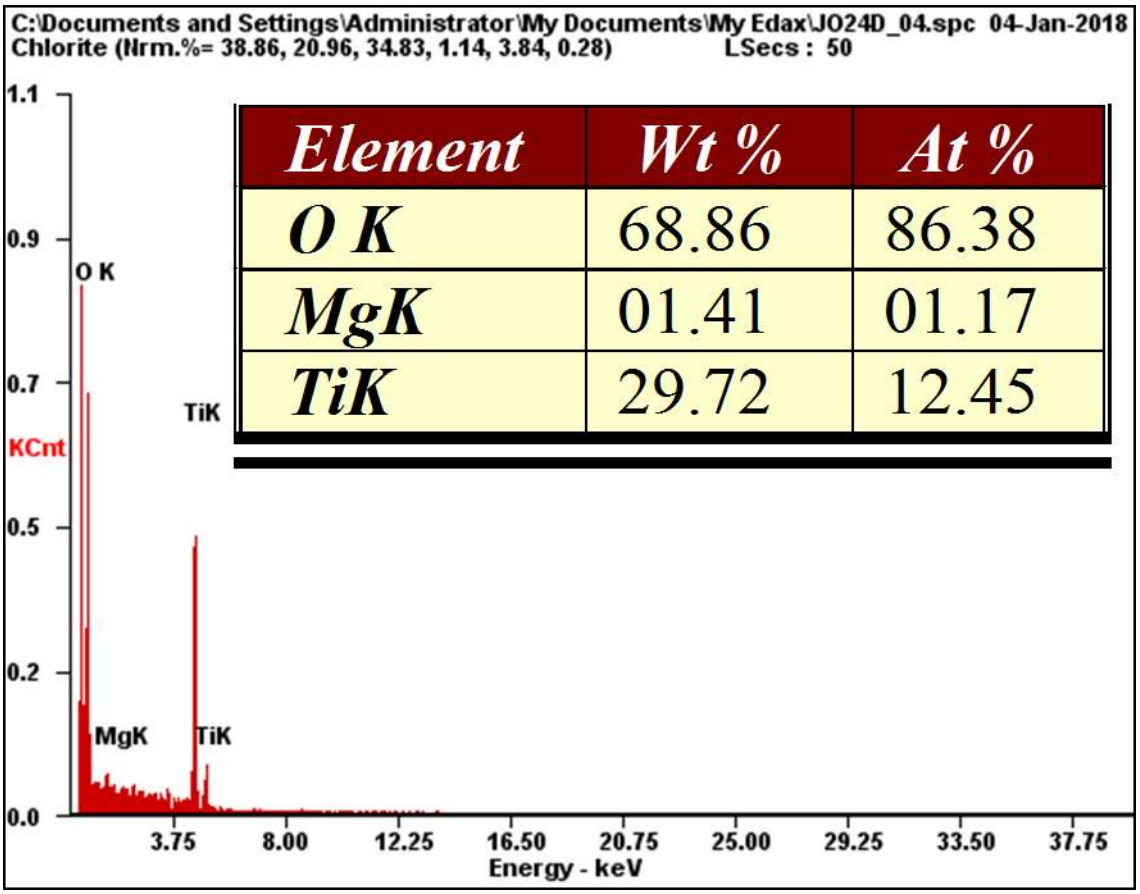

Figure 4.147 Energy-dispersive X-ray spectroscopy image of Mg-TiO_2-3 nanocatalyst.

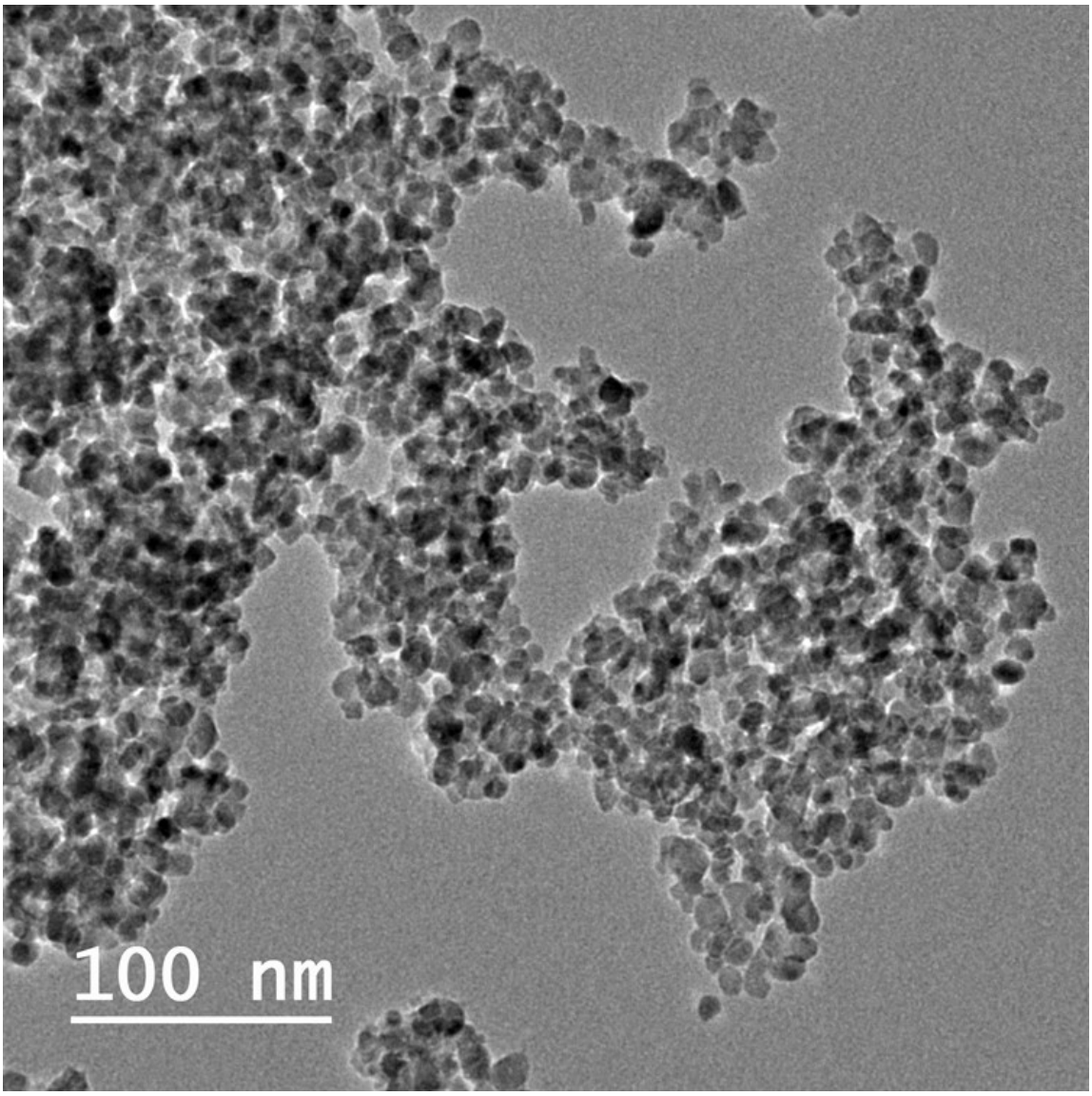

Figure 4.148 Transmission electron microscopy image of pure TiO_2 nanocatalyst.

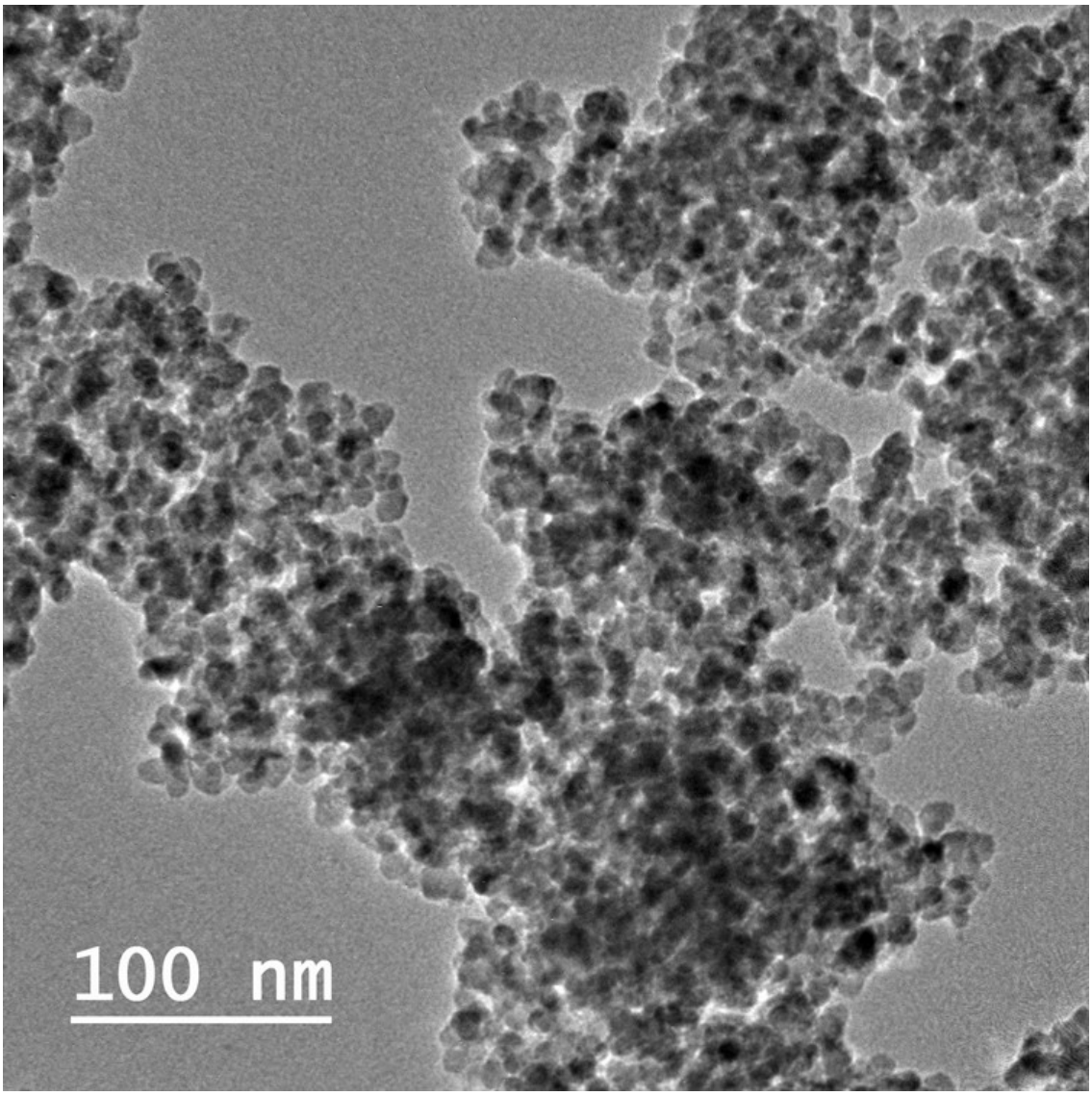

Figure 4.149 Transmission electron microscopy image of Mg-TiO_2-1 nanocatalyst.

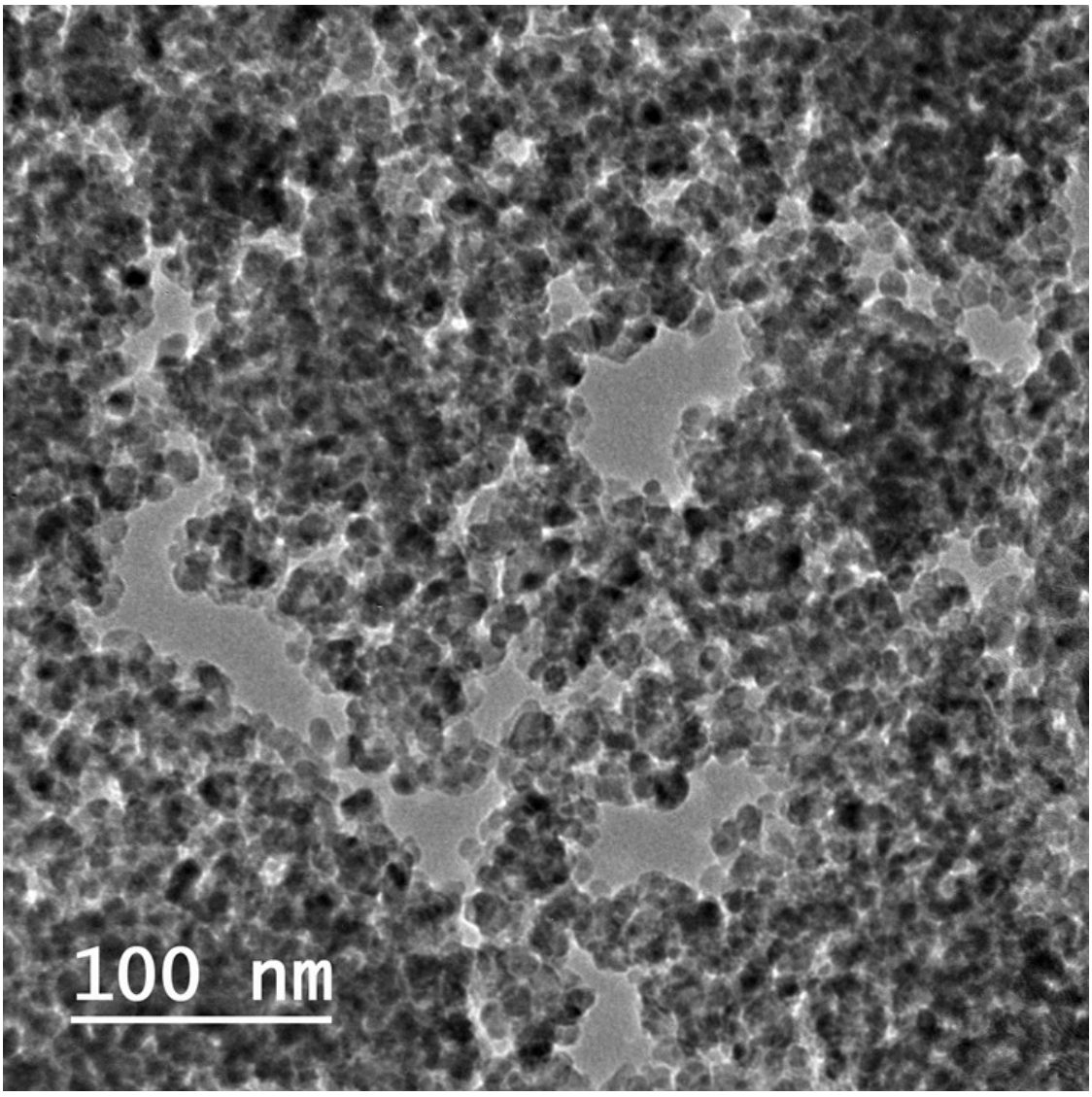

Figure 4.150 Transmission electron microscopy image of Mg-TiO_2-2 nanocatalyst.

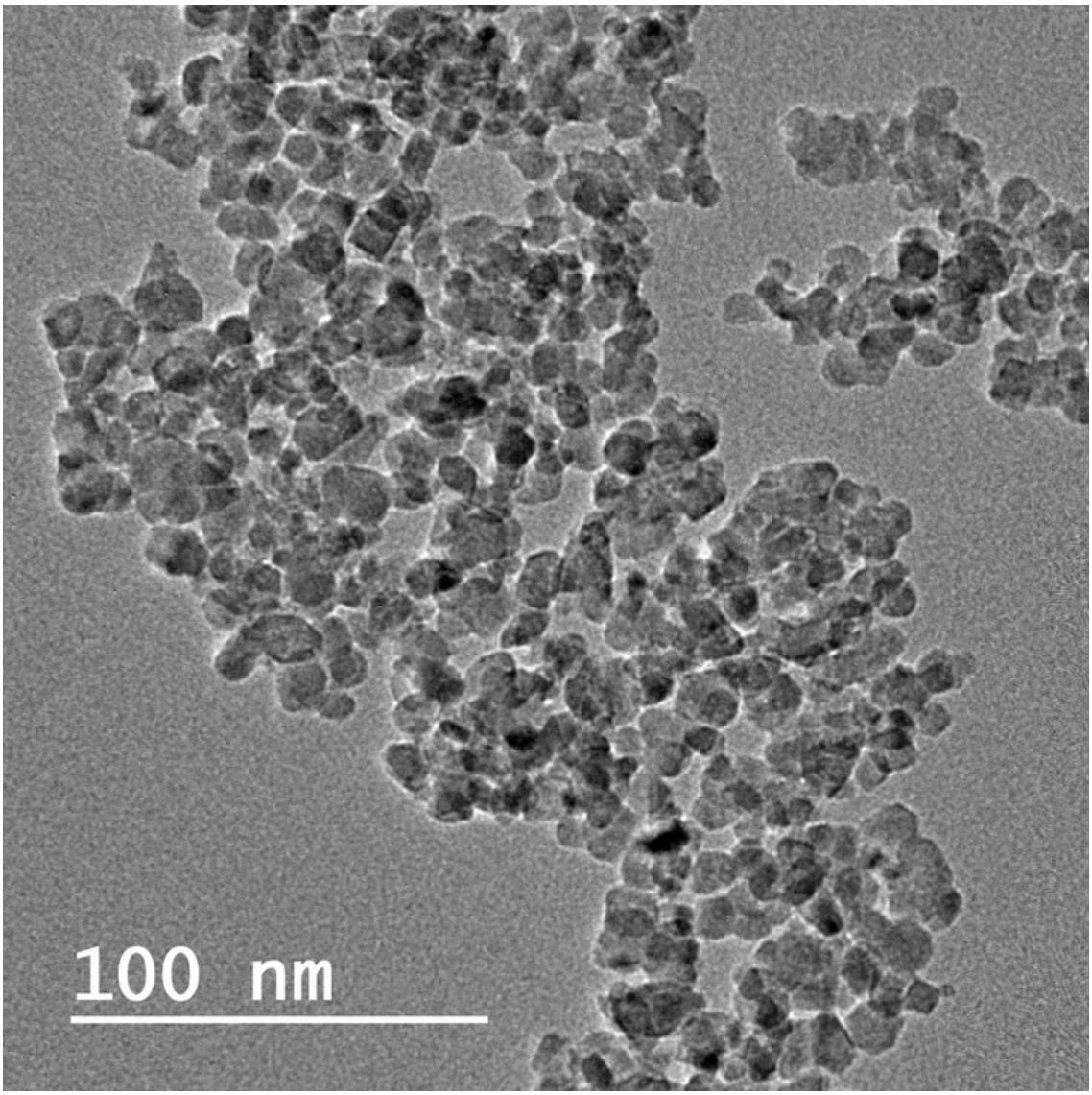

Figure 4.151 Transmission electron microscopy image of Mg-TiO_2-3 nanocatalyst.

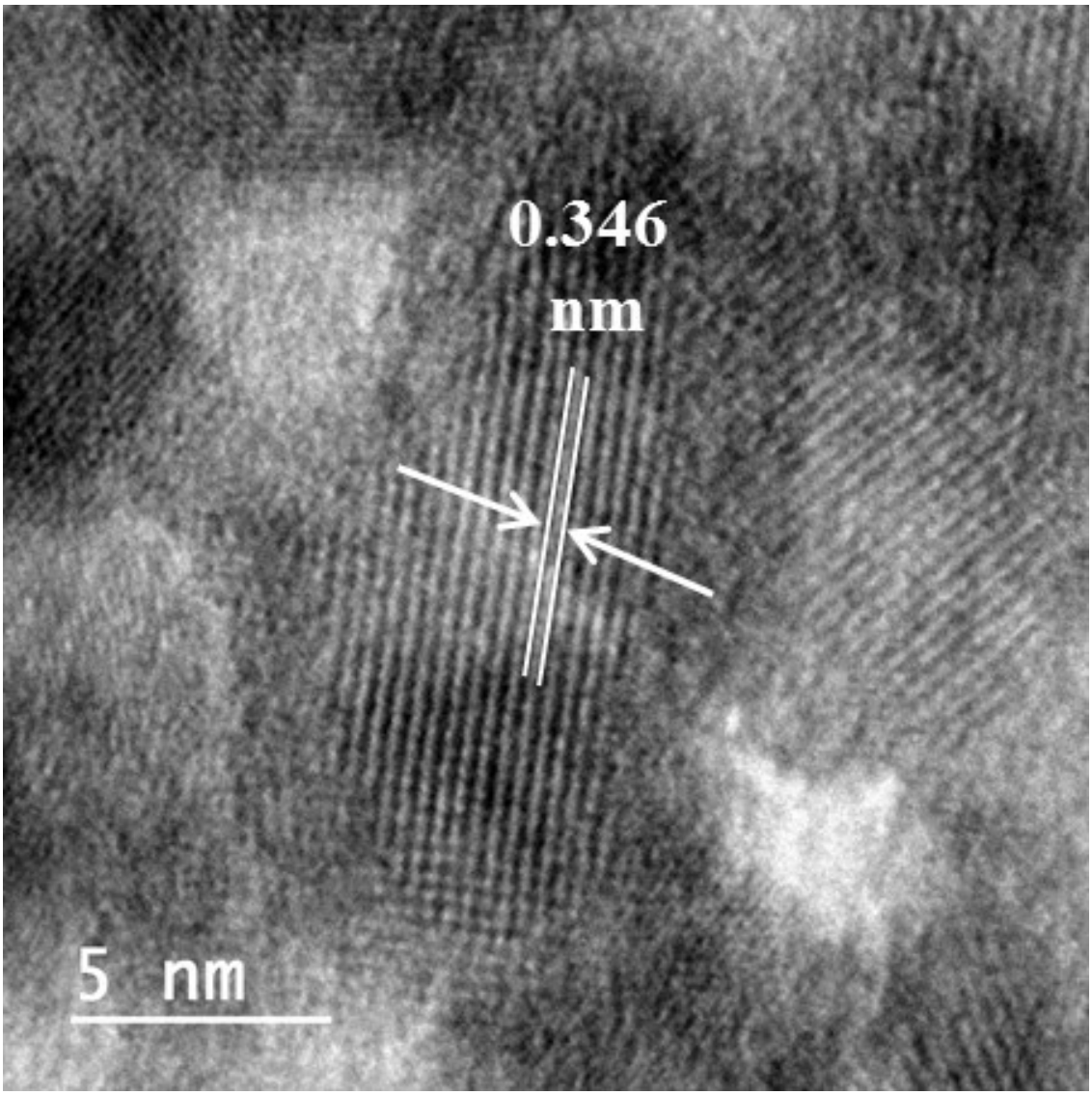

Figure 4.152 High resolution transmission electron microscopy image of TiO_2 nanocatalyst.

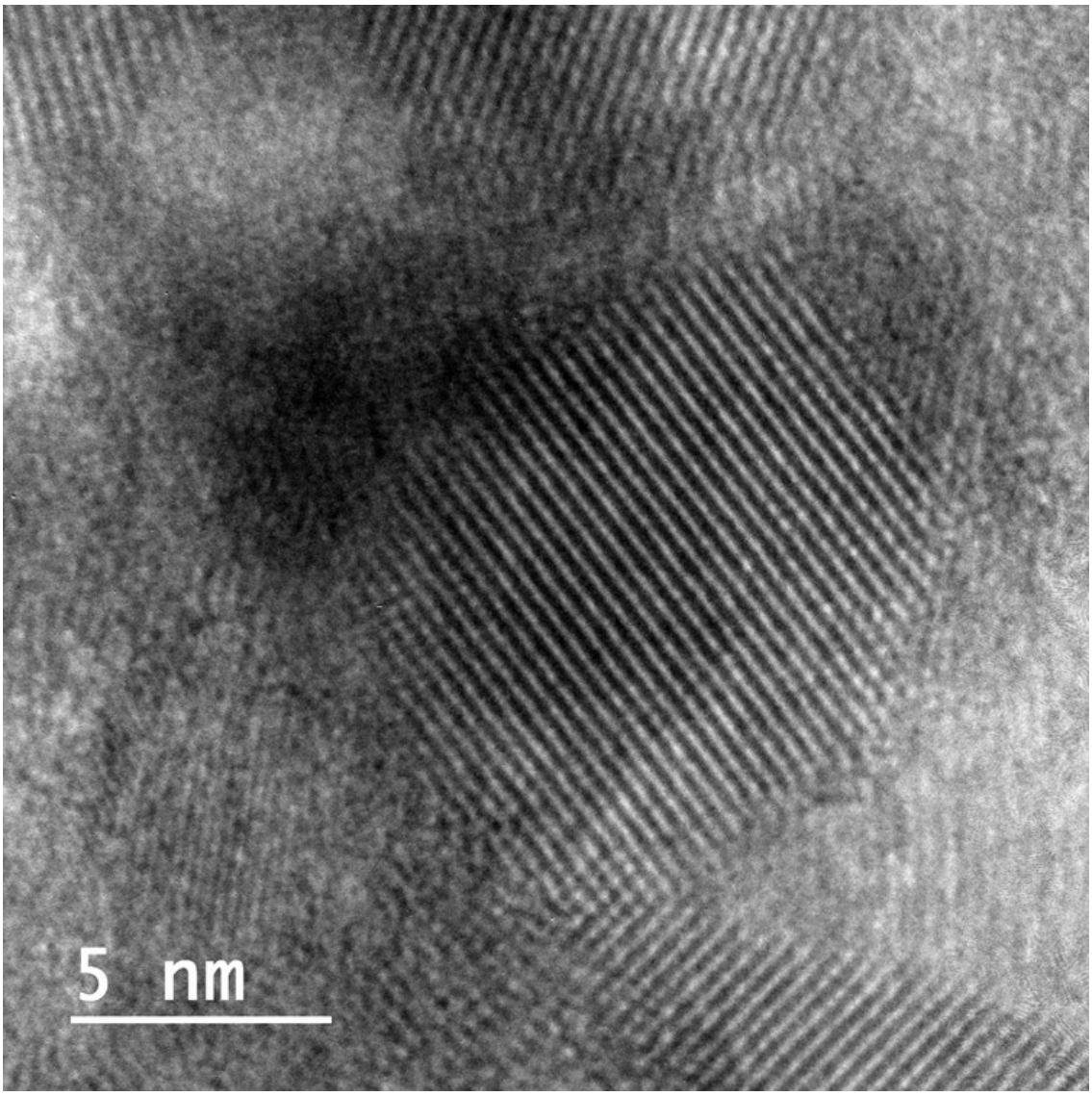

Figure4.153 High resolution transmission electron microscopy image of Mg-TiO_2-1 nanocatalyst.

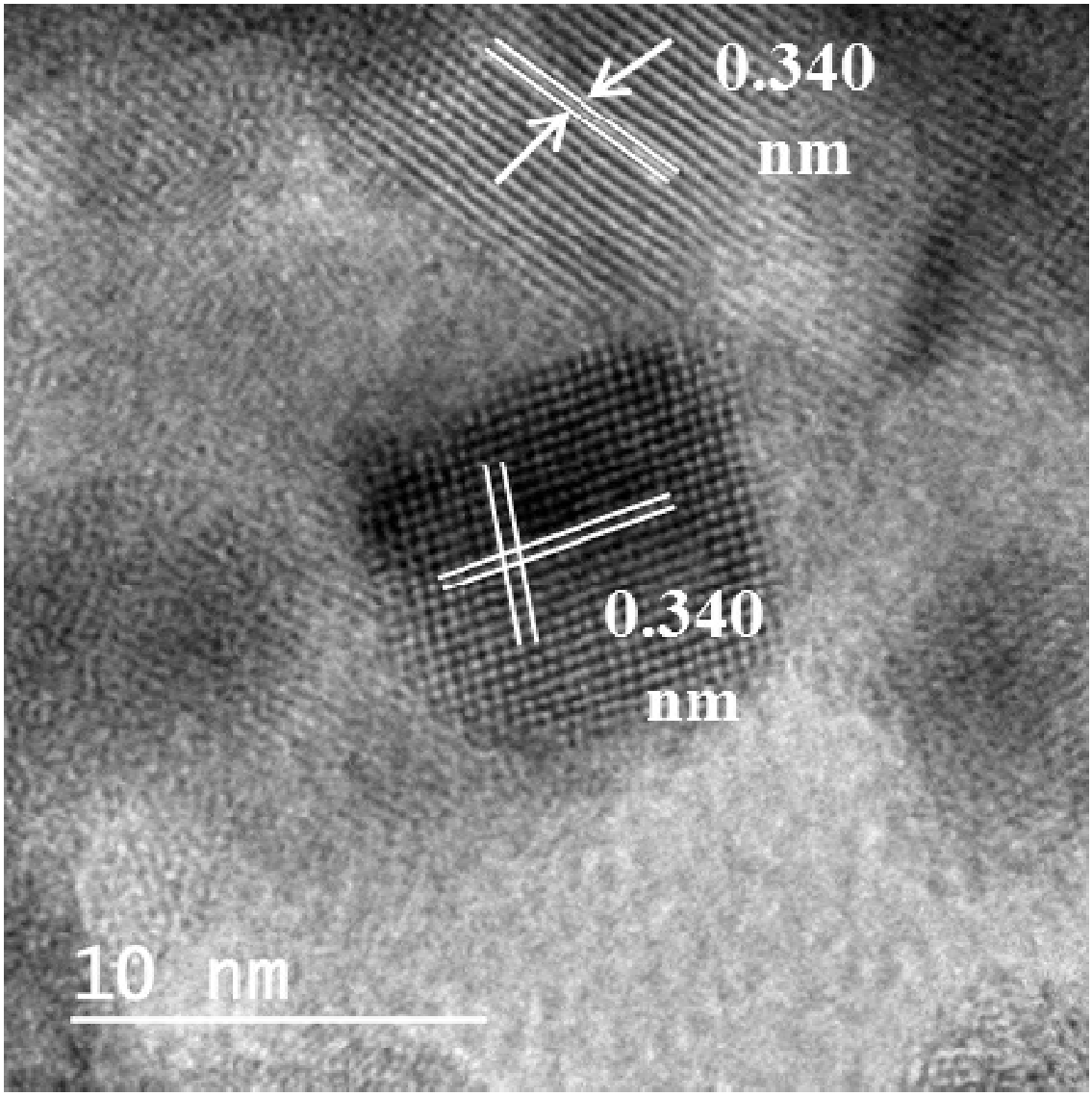

Figure 4.154 High resolution transmission electron microscopy image of Mg-TiO_2-2 nanocatalyst.

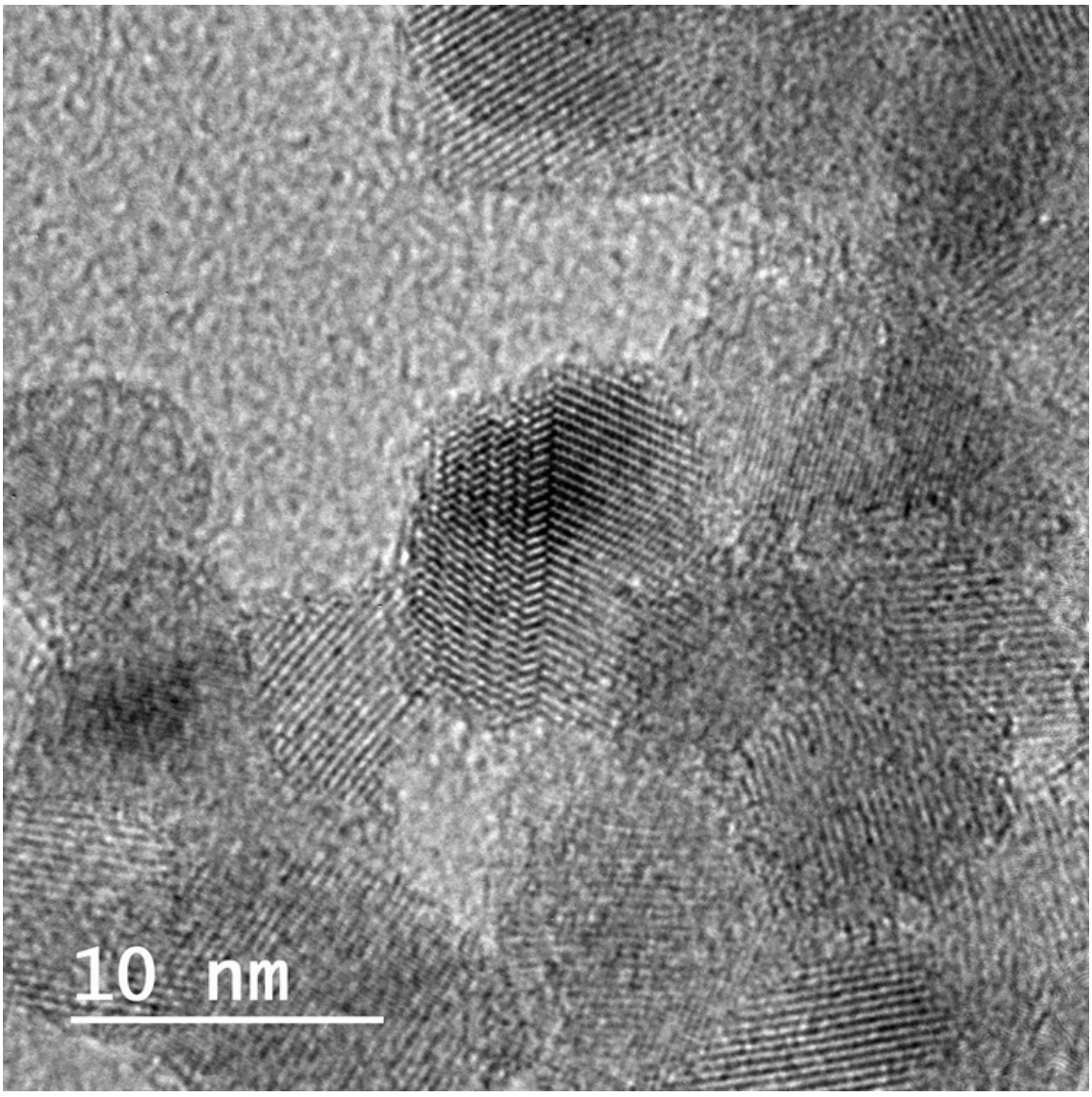

Figure 4.155 High resolution transmission electron microscopy image of Mg-TiO_2-3 nanocatalyst.

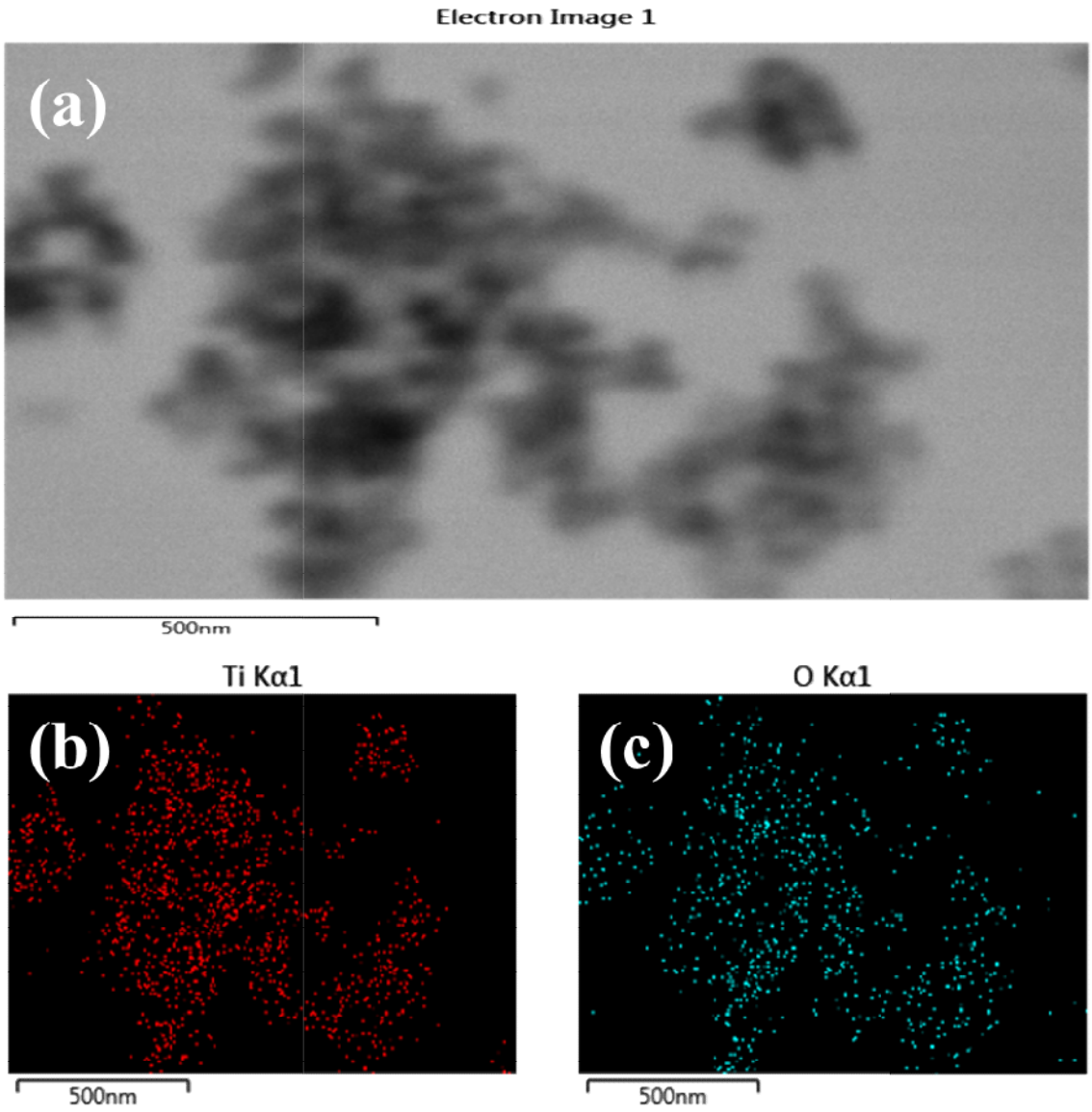

Figure 4.156 Elemental mapping of TiO_2 nanocatalyst.

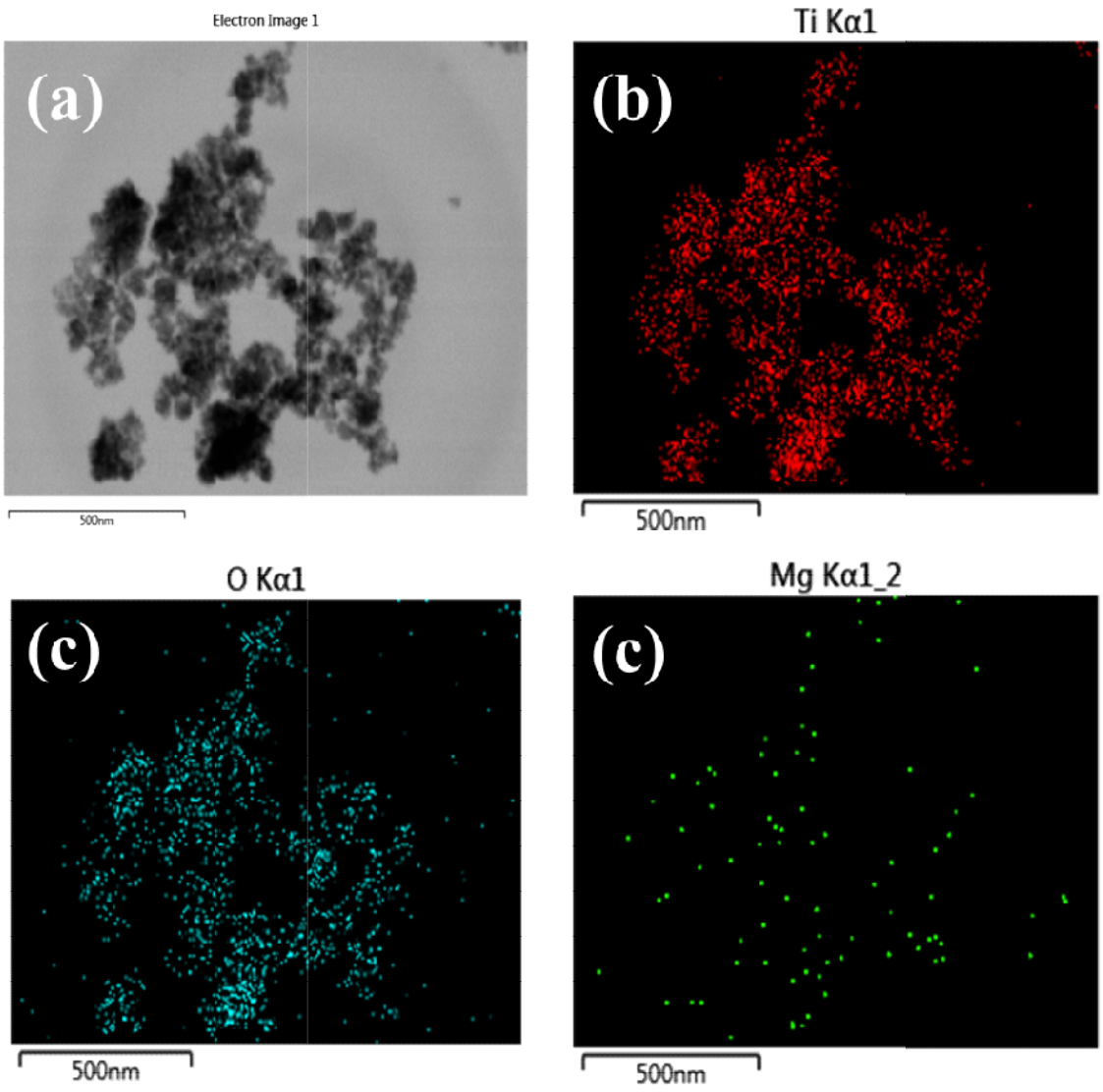

Figure 4.157 Elemental mapping of Mg-TiO_2-1 nanocatalyst.

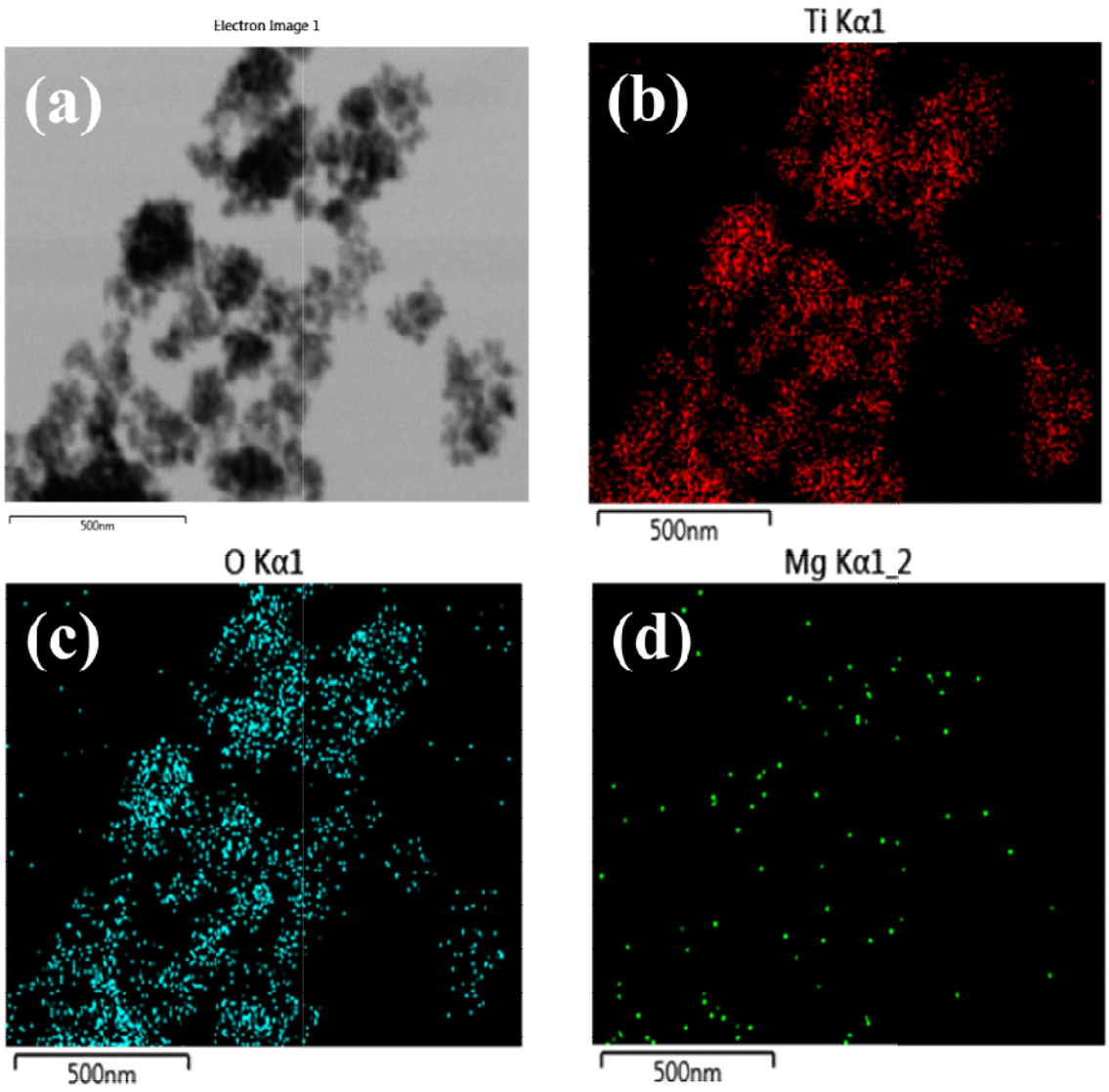

Figure 4.158 Elemental mapping of Mg-TiO_2-2 nanocatalyst.

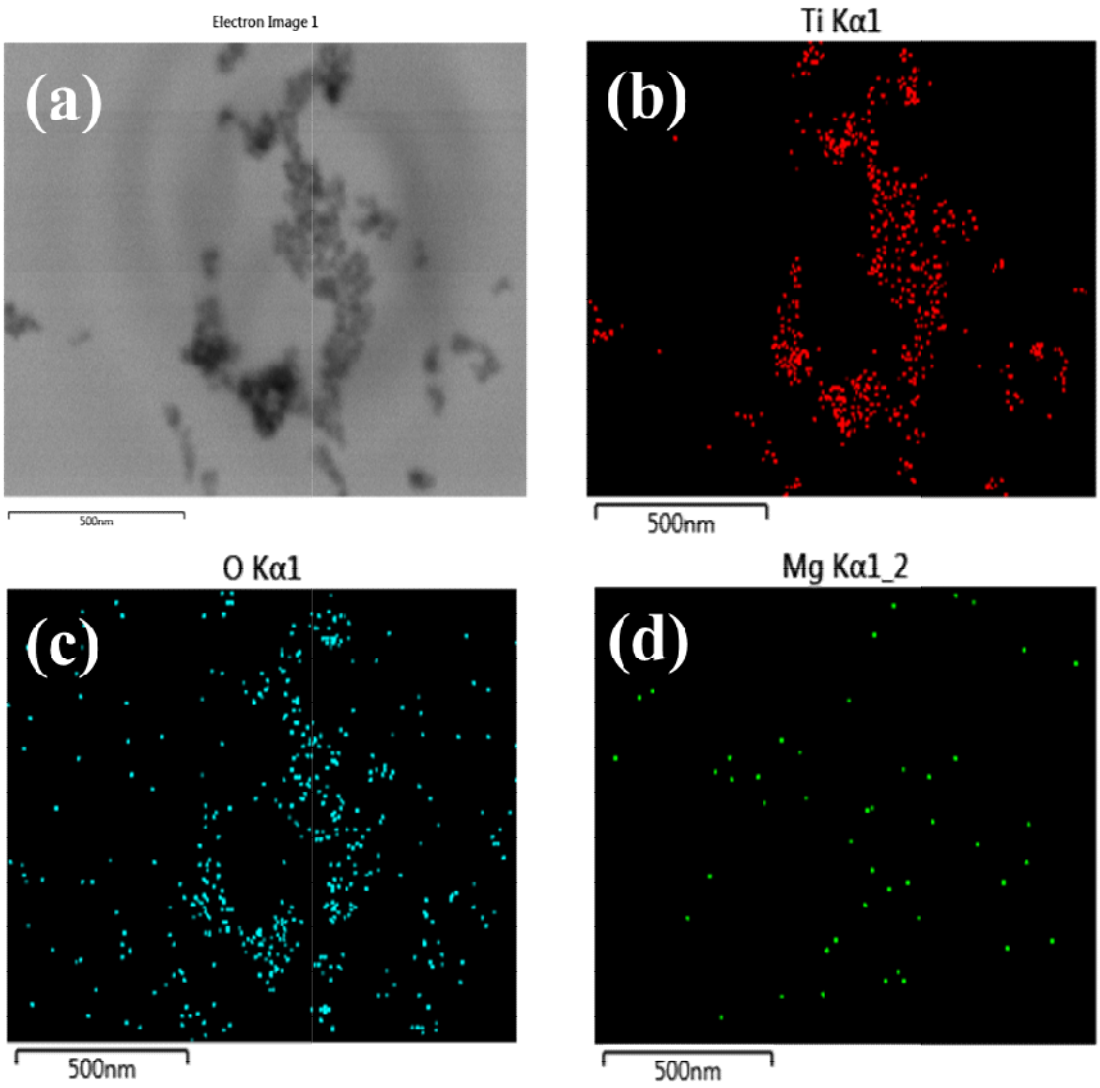

Figure 4.159 Elemental mapping of Mg-TiO_2-3 nanocatalyst.

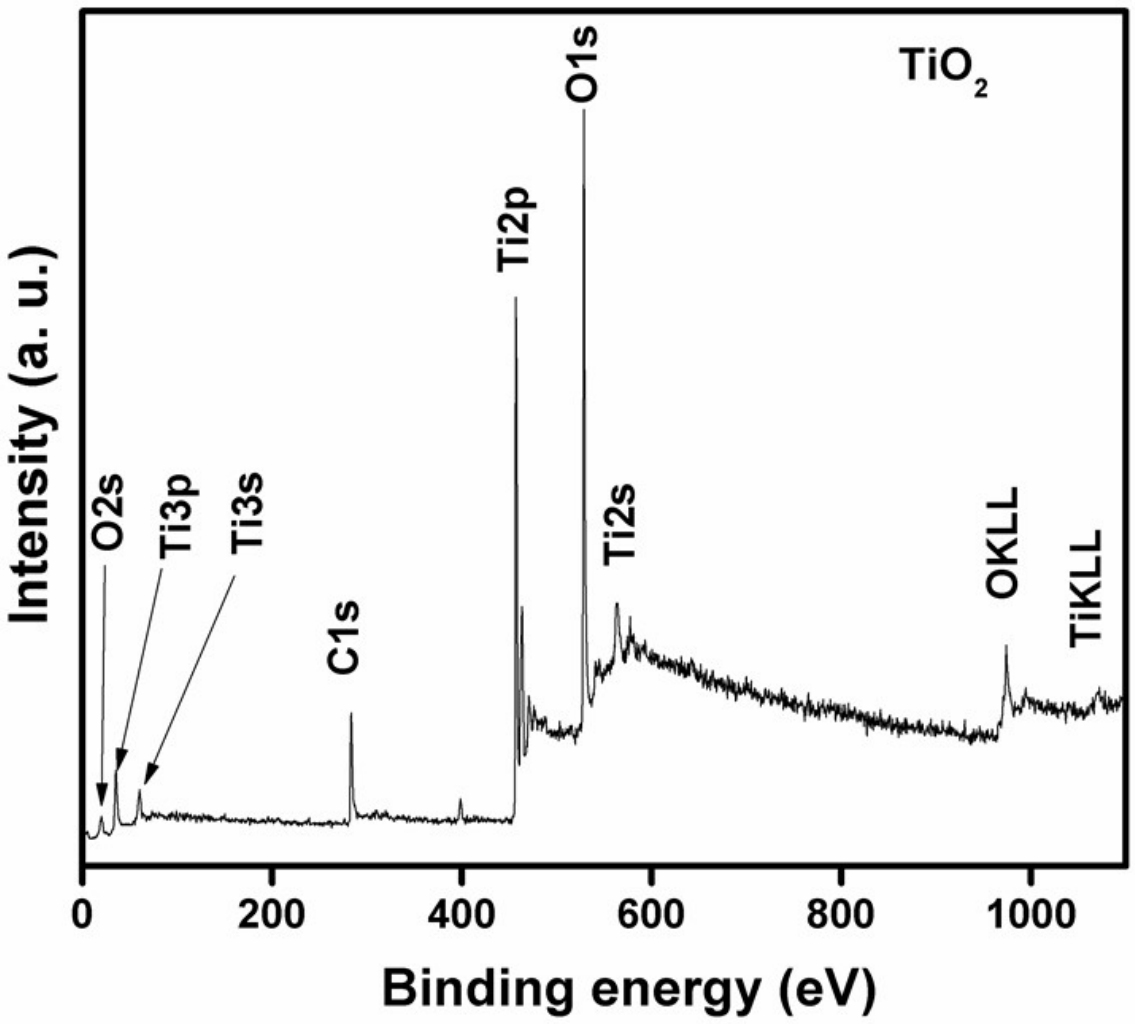

Figure 4.160 X-ray photoelectron spectroscopy survey spectrum of TiO_2.

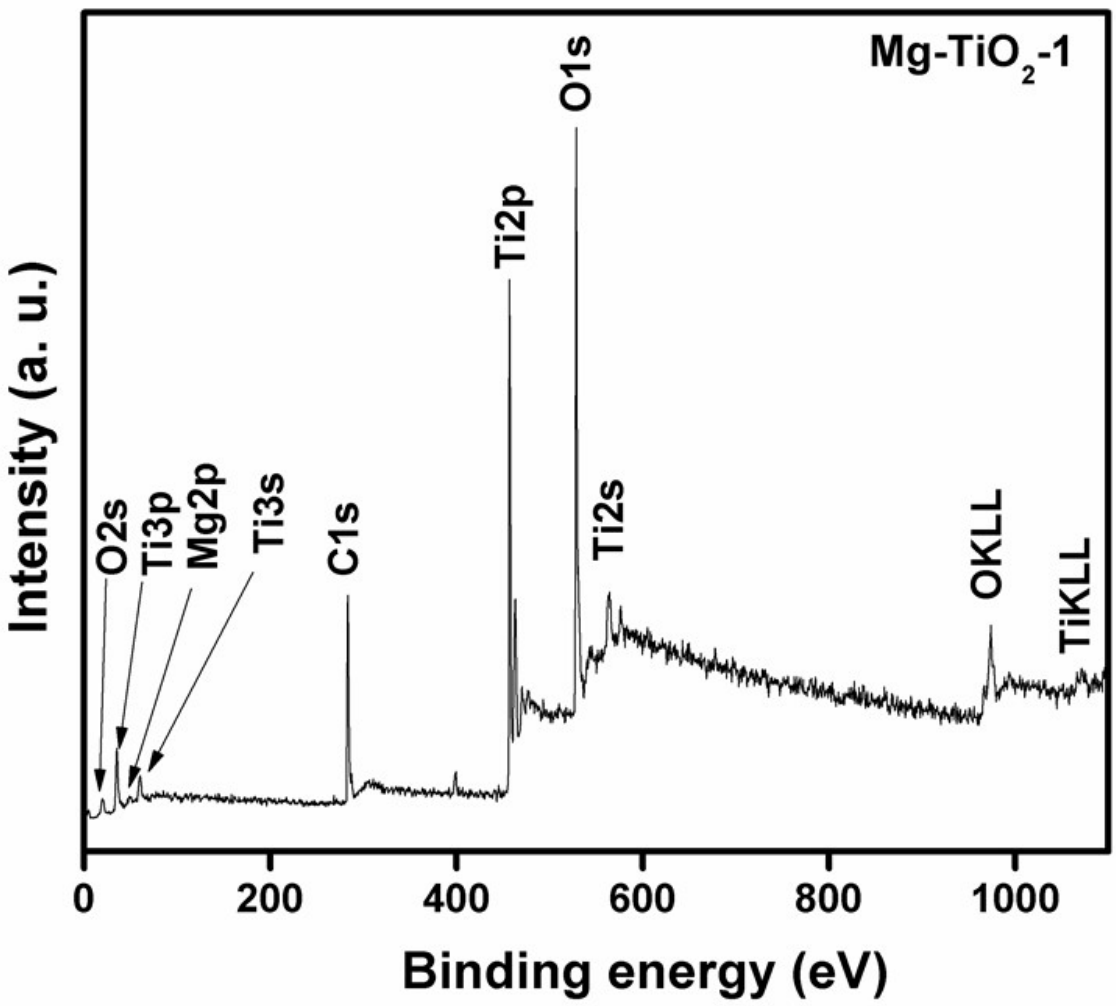

Figure 4.161 X-ray photoelectron spectroscopy survey spectrum of Mg-TiO_2-1.

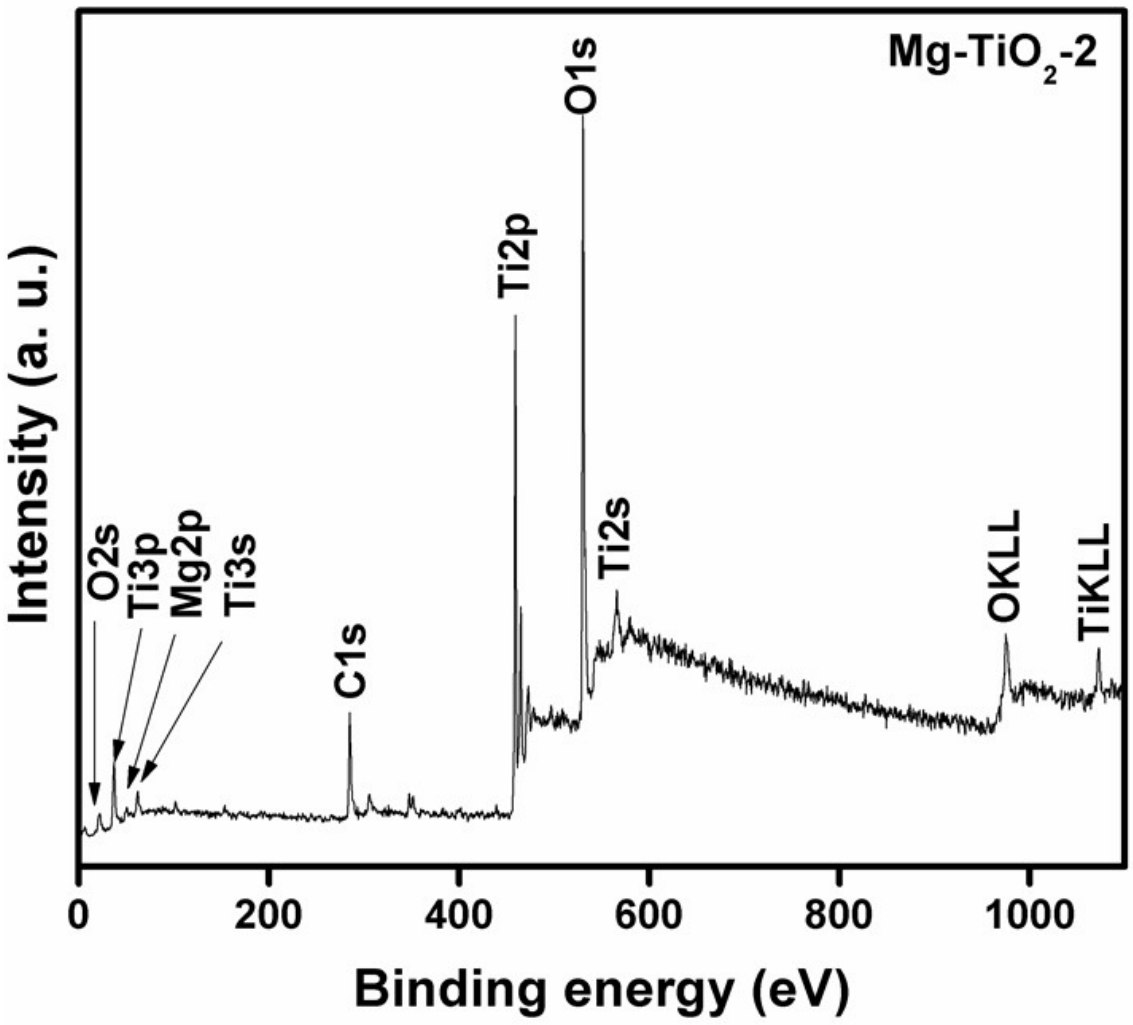

Figure 4.162 X-ray photoelectron spectroscopy survey spectrum of Mg-TiO_2-2.

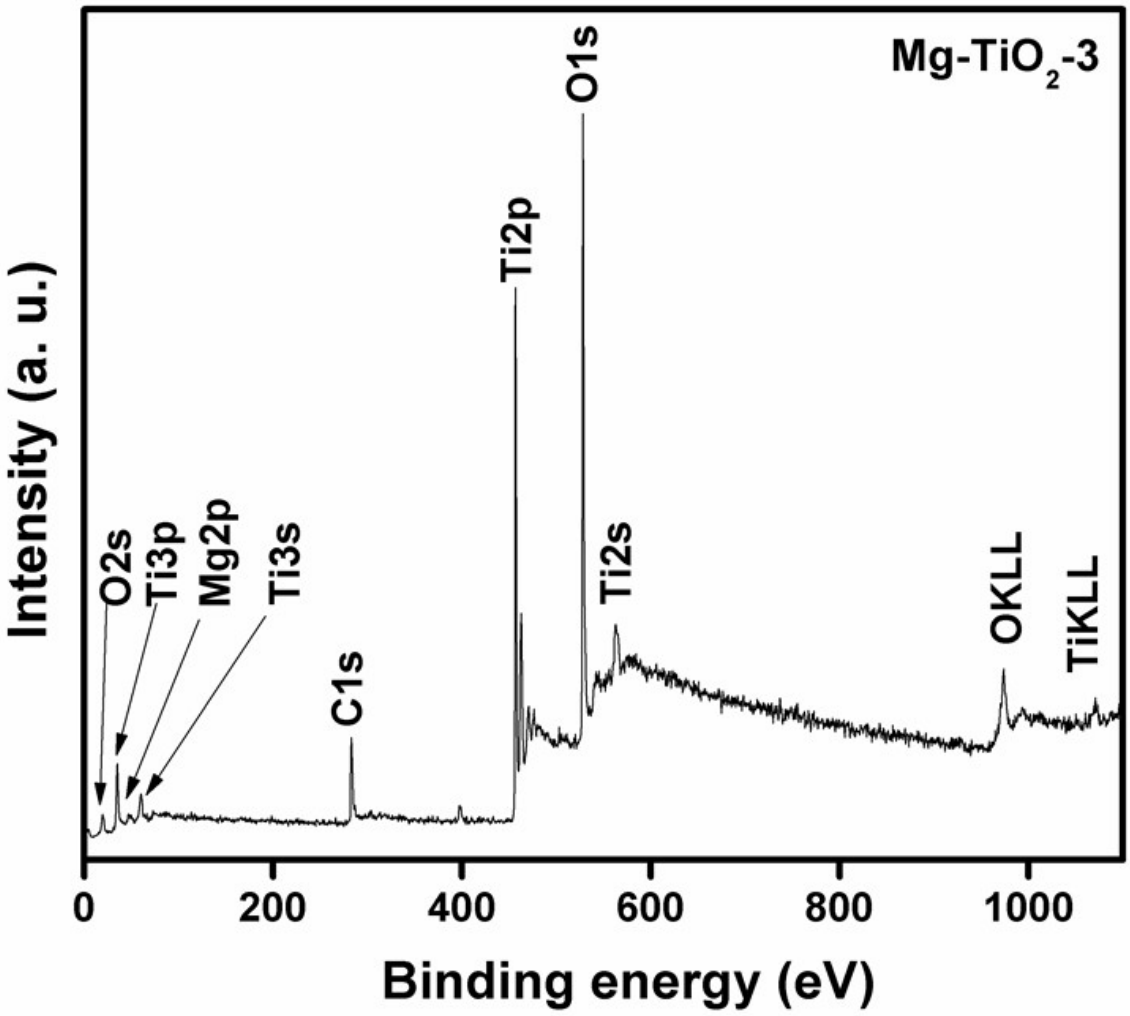

Figure 4.163 X-ray photoelectron spectroscopy survey spectrum of Mg-TiO_2-3.

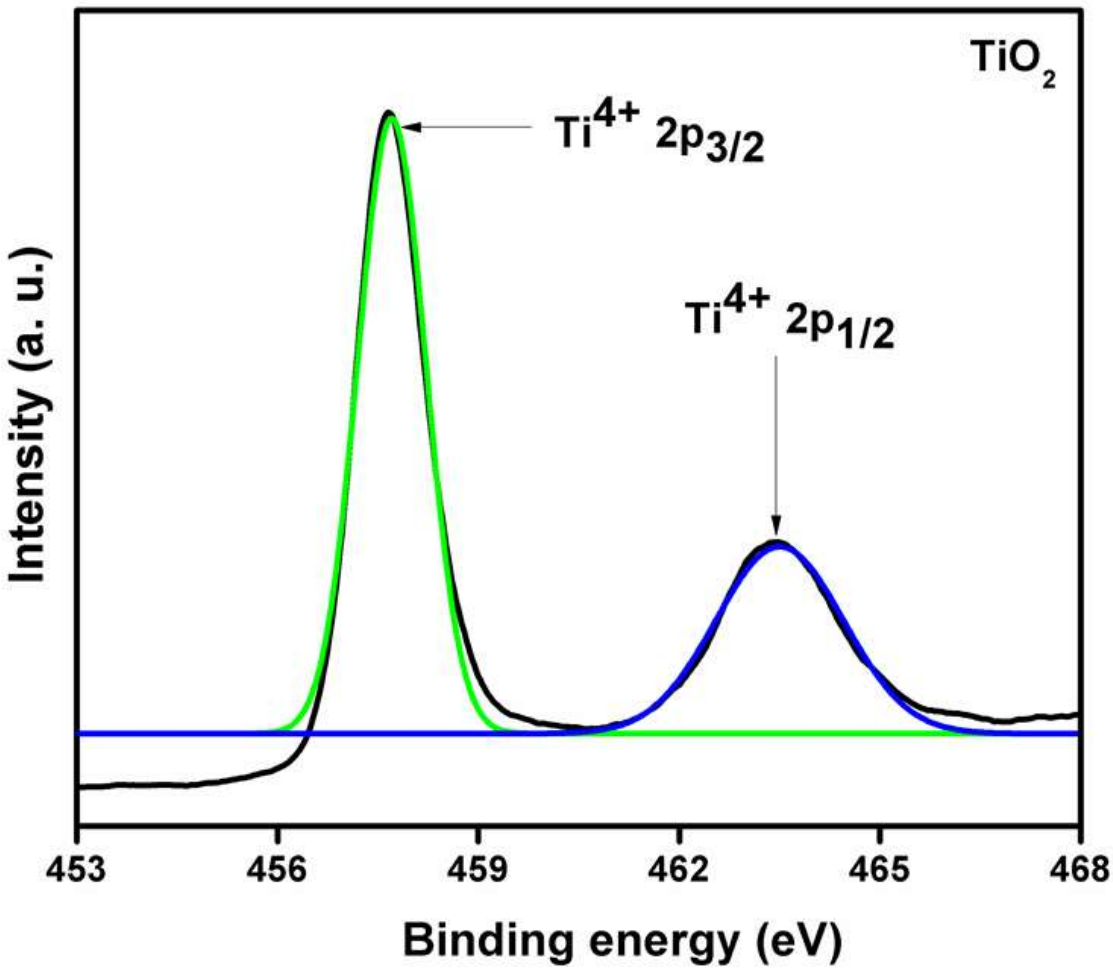

Figure 4.164 High-resolution X-ray photoelectron spectroscopy spectrum of Ti2p of TiO_2.

TiO_2 samples after deconvolution (Yang *et al.,* 2017; Li *et al.,* 2016).This indicates that both TiO_2 and Ti_2O_3were formed in all Mg-doped samples. The area of Ti^{3+} peak increased while that of Ti^{4+}peak decreased as the Mg in TiO_2 increased. Moreover, in comparison with the ordinary TiO_2, the peak positions of $Ti2p_{3/2}$ and $Ti2p_{1/2}$ in all Mg-doped TiO_2 samples were slightly shifted after the addition of Mg (Figure 4.165, 4.166 and 4.167). For instance, the peak position at 457.7 and 463.5 eV in TiO_2 respectively shifted to 457.6 and 463.4 eV for Mg-TiO_2-2 nanocatalyst (Figure 4.165). The observed additional peak and peak shifts in Mg-doped TiO_2 samples suggest that Ti ions were substituted with Mg ions in the lattices forming Ti-O-Mg bond (Sofianou *et al.,* 2014; Yang *et al.,* 2017).

The high-resolution XPS spectrum of O1s of ordinary TiO_2 was deconvoluted into two peaks as shown in Figure 4.168. In the spectrum, the peaks observed at 528.9 and 530.5 eV were attributed to lattice oxygen (Ti-O) and non-lattice oxygen (adsorbed O-H groups), respectively. However, for all Mg-doped TiO_2 samples, O1s spectrum was fitted into three peaks including an extra peak assigned to Mg-O- bond as shown in Figure 4.169, 4.170 and 4.171 (Wang *et al.,* 2016a). The area of the new peak (Mg-O-) became larger with the increase in the amount of Mg in TiO_2. Also, peaks position observed at 528.9 and 530.5 eV with ordinary TiO_2were slightly shifted for all Mg-doped TiO_2 samples. For example, the peak position slightly shifted to 528.8 and 529.4 eV in Mg-TiO_2-2 sample. The observed new peak and peak shifts in Mg-doped TiO_2 samples indicate the successful doping of Mg in TiO_2 as well as the formation of some mixed oxide and oxygen vacancies.

The high-resolution XPS spectra of Mg 2p of all Mg-doped TiO_2 samples are shown in Figure 4.172, 4.173 and 4.174. The binding energy observed was ca. 51.2 eV, which is typical of Mg^{2+} that bonds with an oxygen atom (Li *et al.,* 2014; Sofianou *et al.,* 2014).

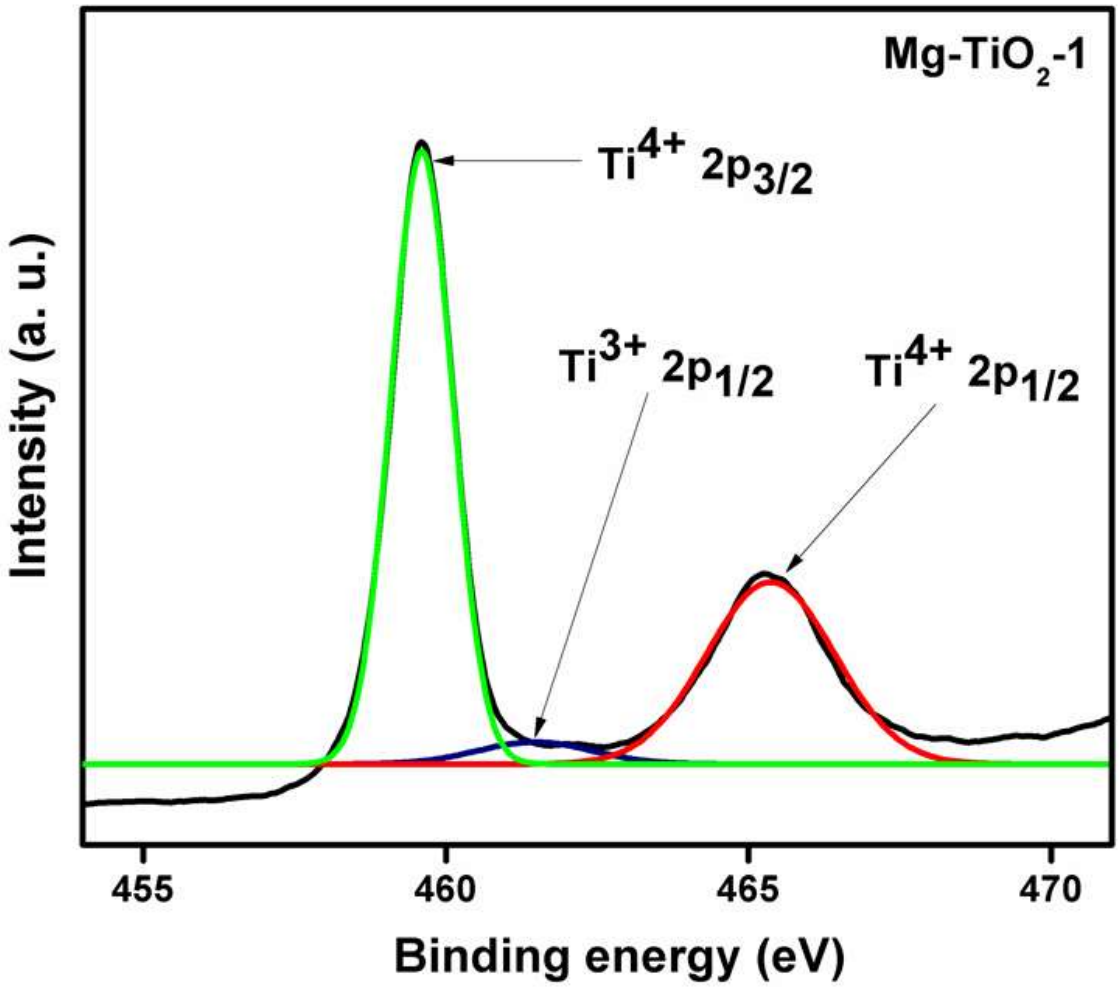

Figure 4.165 High-resolution X-ray photoelectron spectroscopy spectrum of Ti2p of Mg-TiO_2-1.

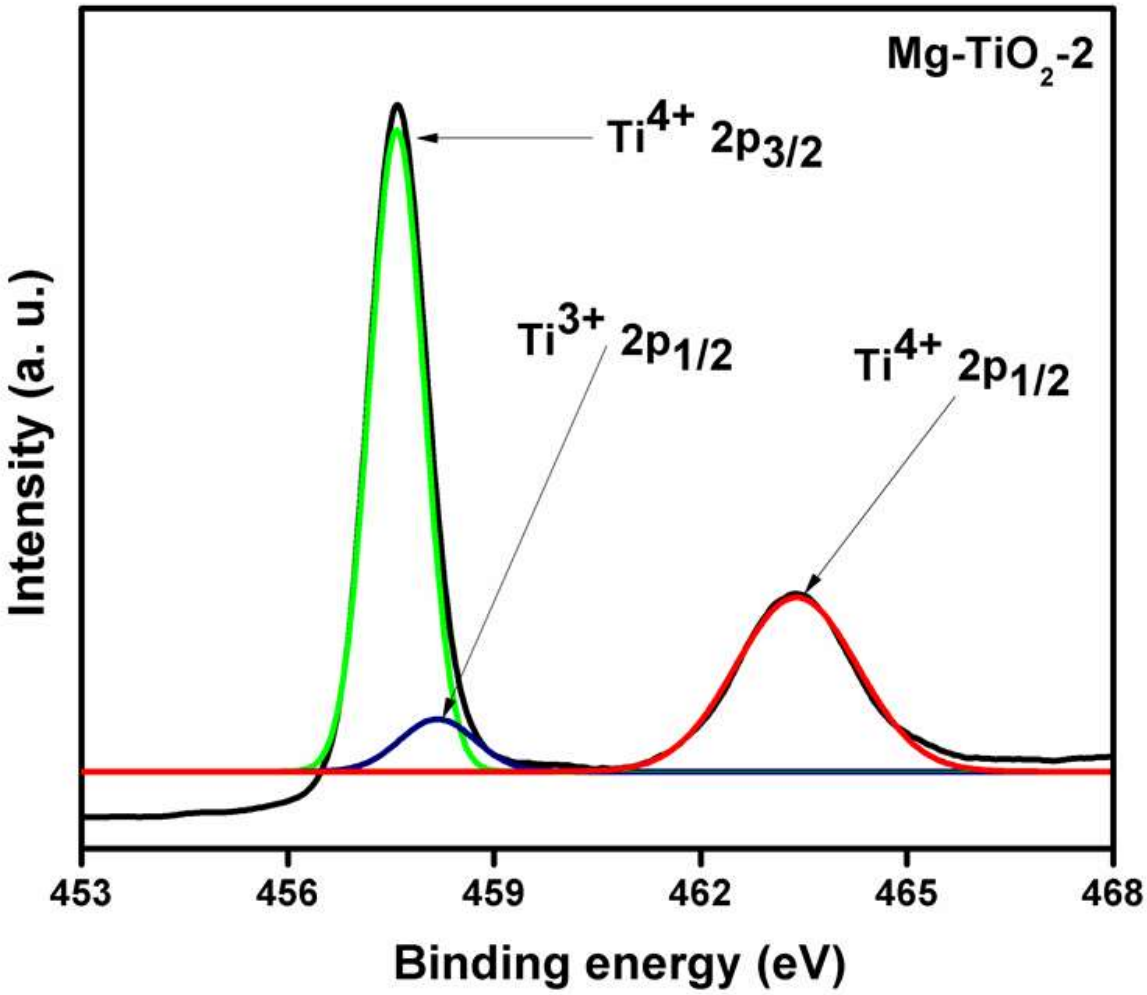

Figure 4.166 High-resolution X-ray photoelectron spectroscopy spectrum of Ti2p of Mg-TiO_2-2.

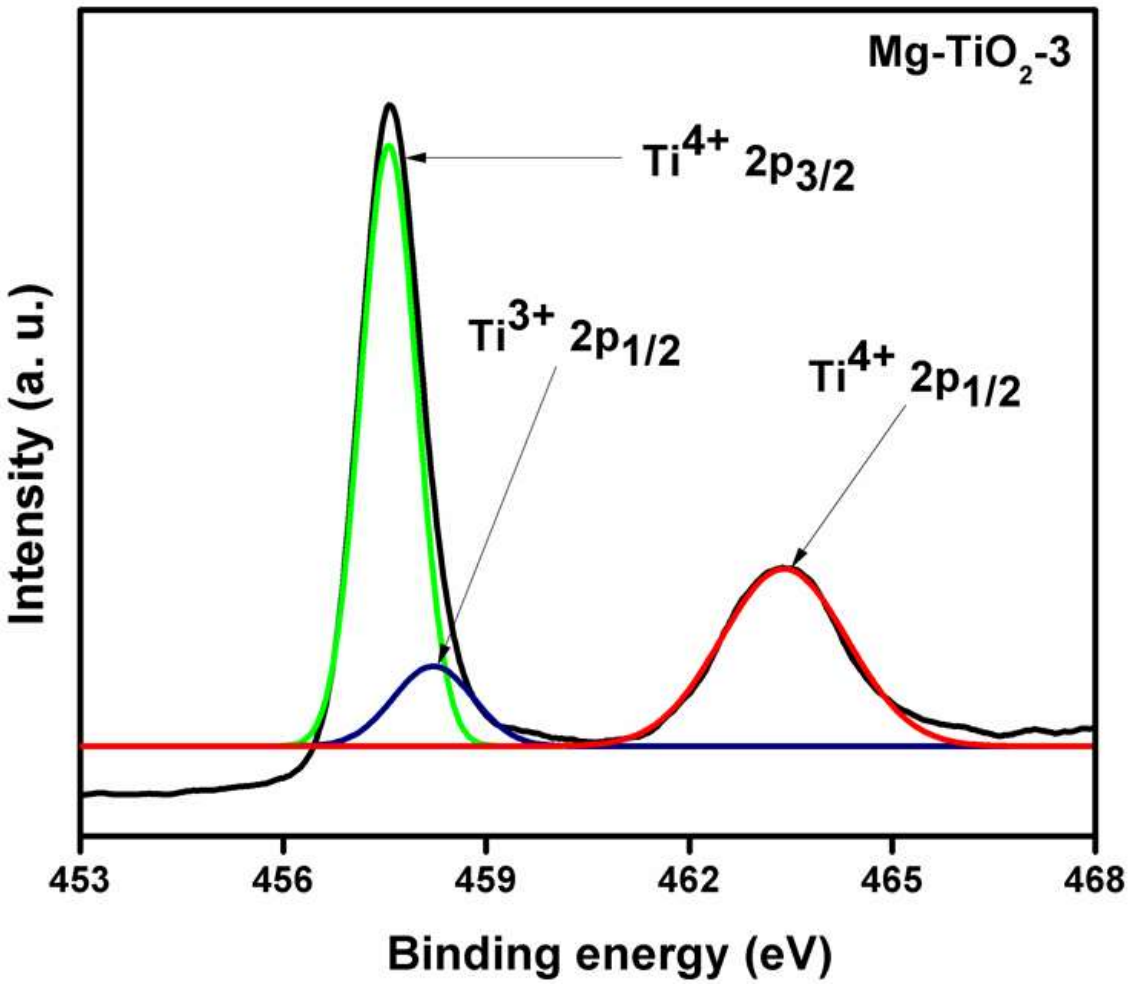

Figure 4.167 High-resolution X-ray photoelectron spectroscopy spectrum of Ti2p of Mg-TiO_2-3.

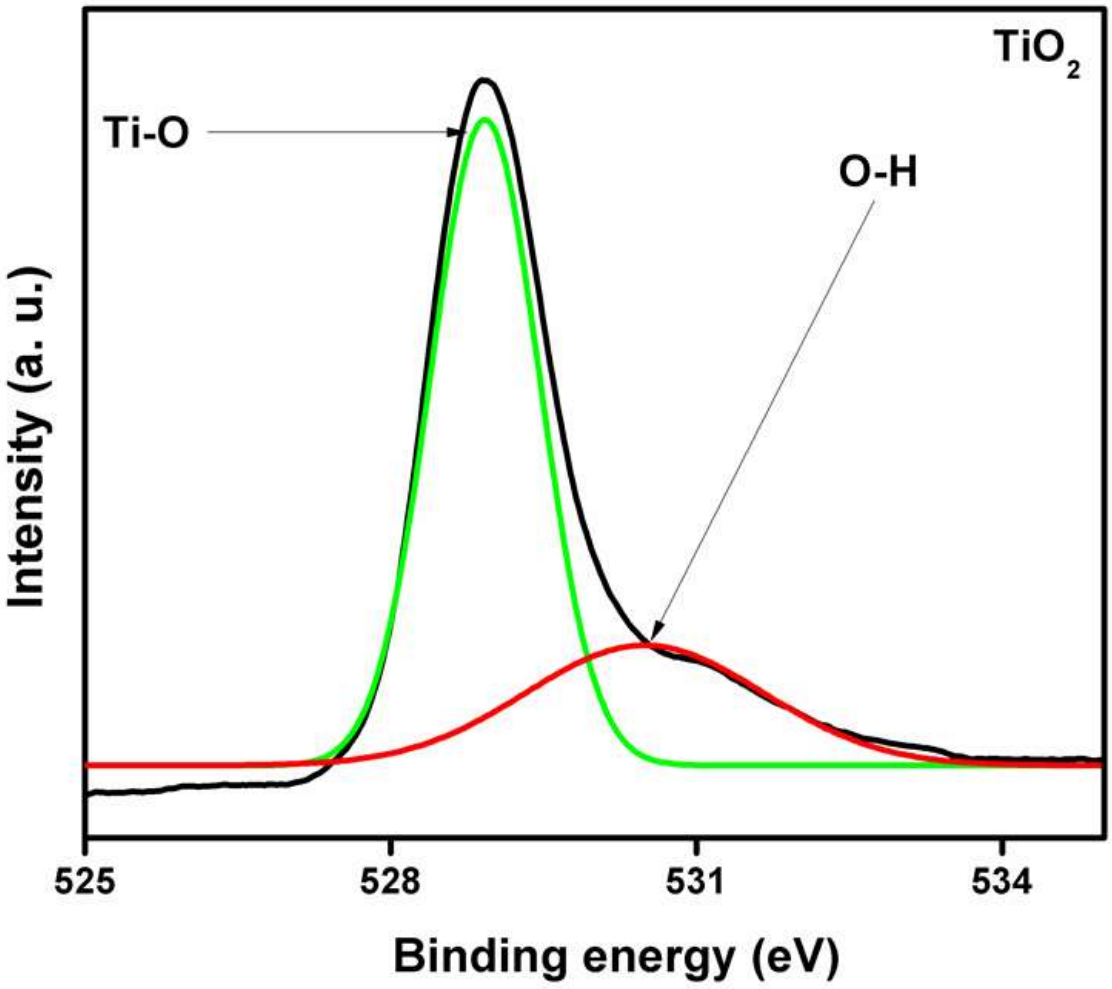

Figure 4.168 High-resolution X-ray photoelectron spectroscopy spectrum of O1s of TiO_2.

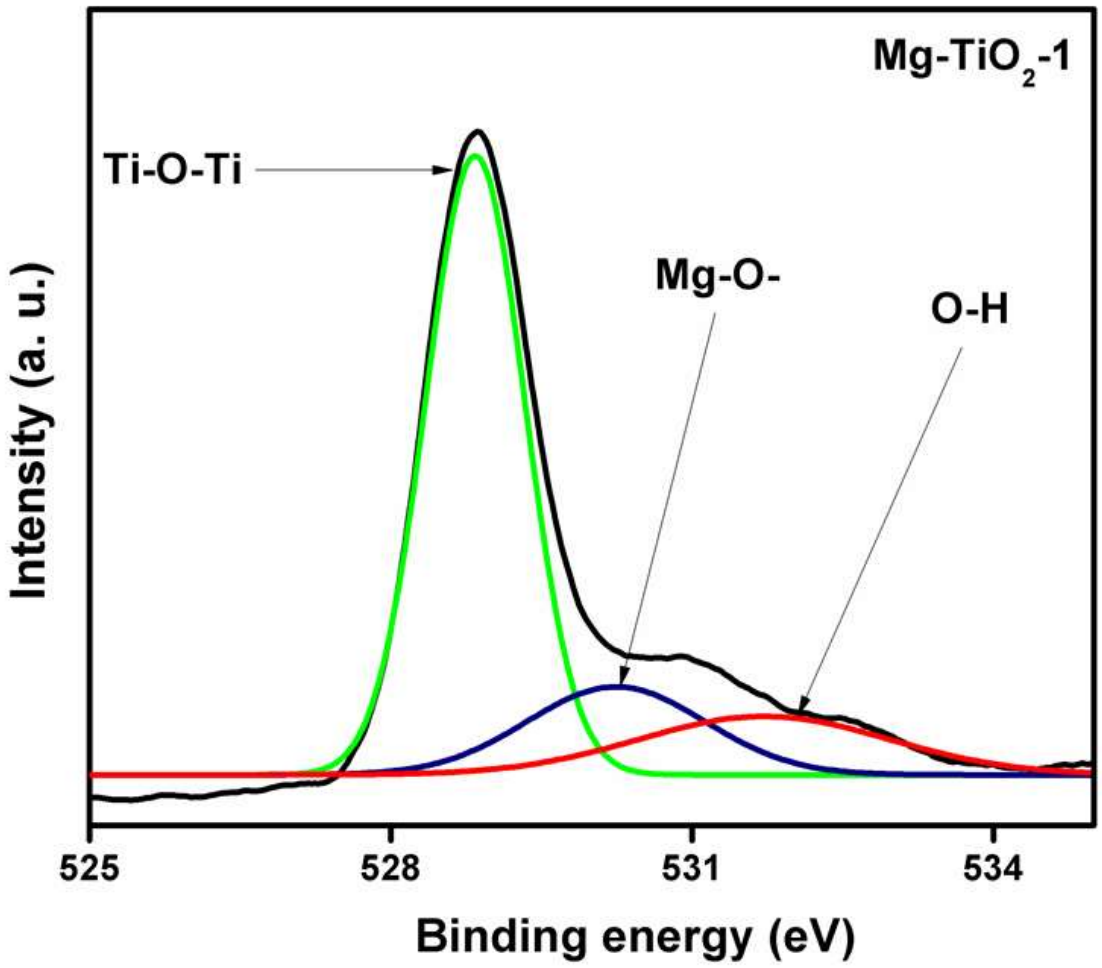

Figure 4.169 High-resolution X-ray photoelectron spectroscopy spectrum of O1s of Mg-TiO_2-1.

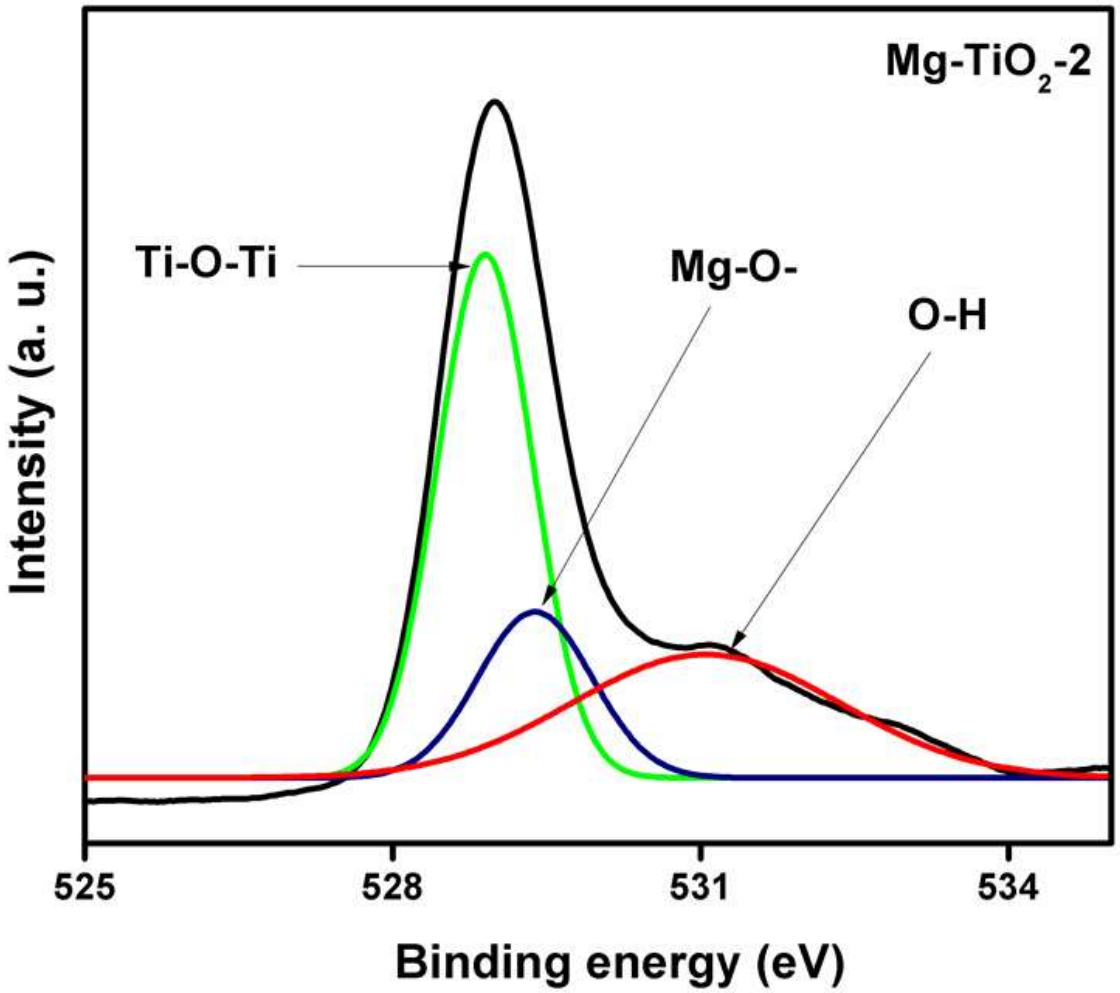

Figure 4.170 High-resolution X-ray photoelectron spectroscopy spectrum of O1s of Mg-TiO_2-2.

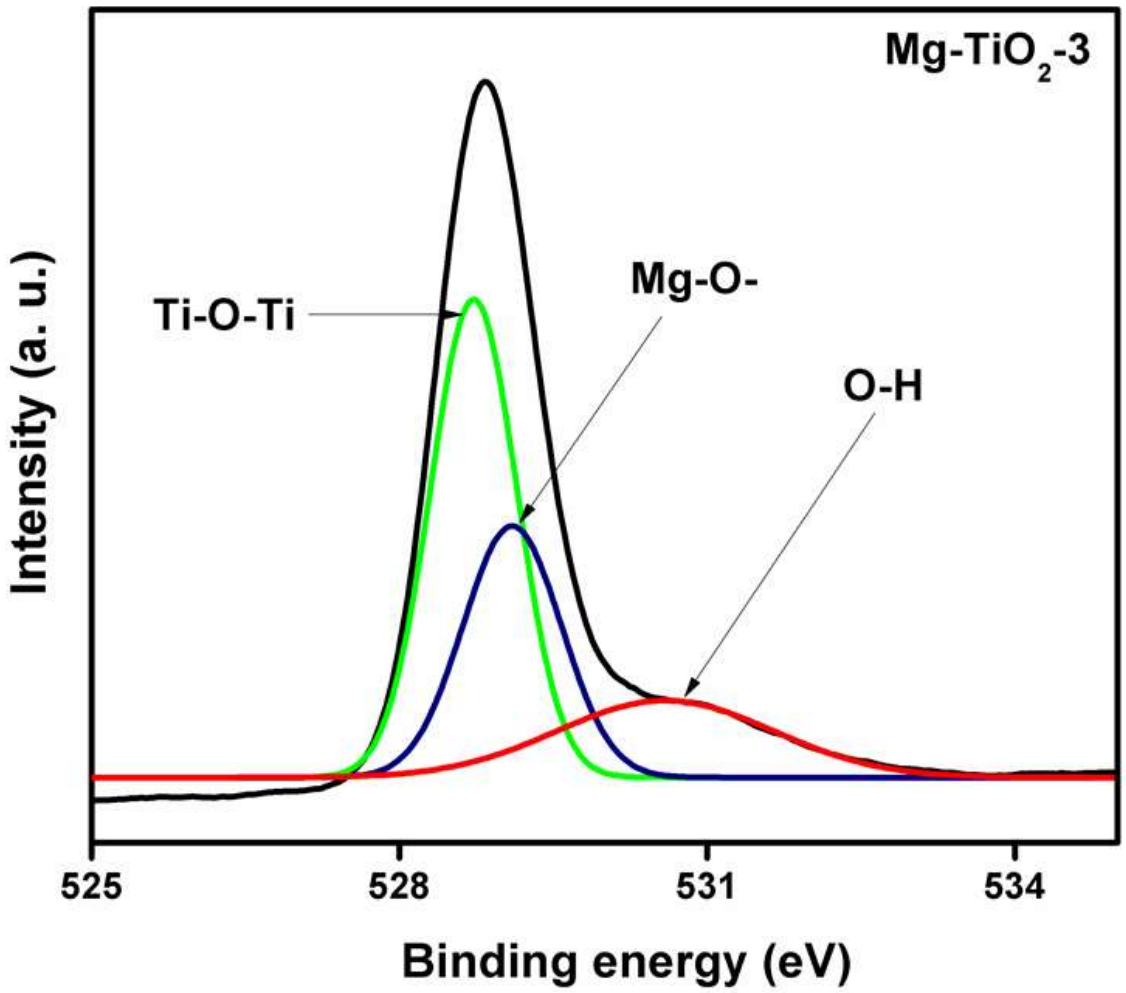

Figure 4.171 High-resolution X-ray photoelectron spectroscopy spectrum of O1s of Mg-TiO_2-3.

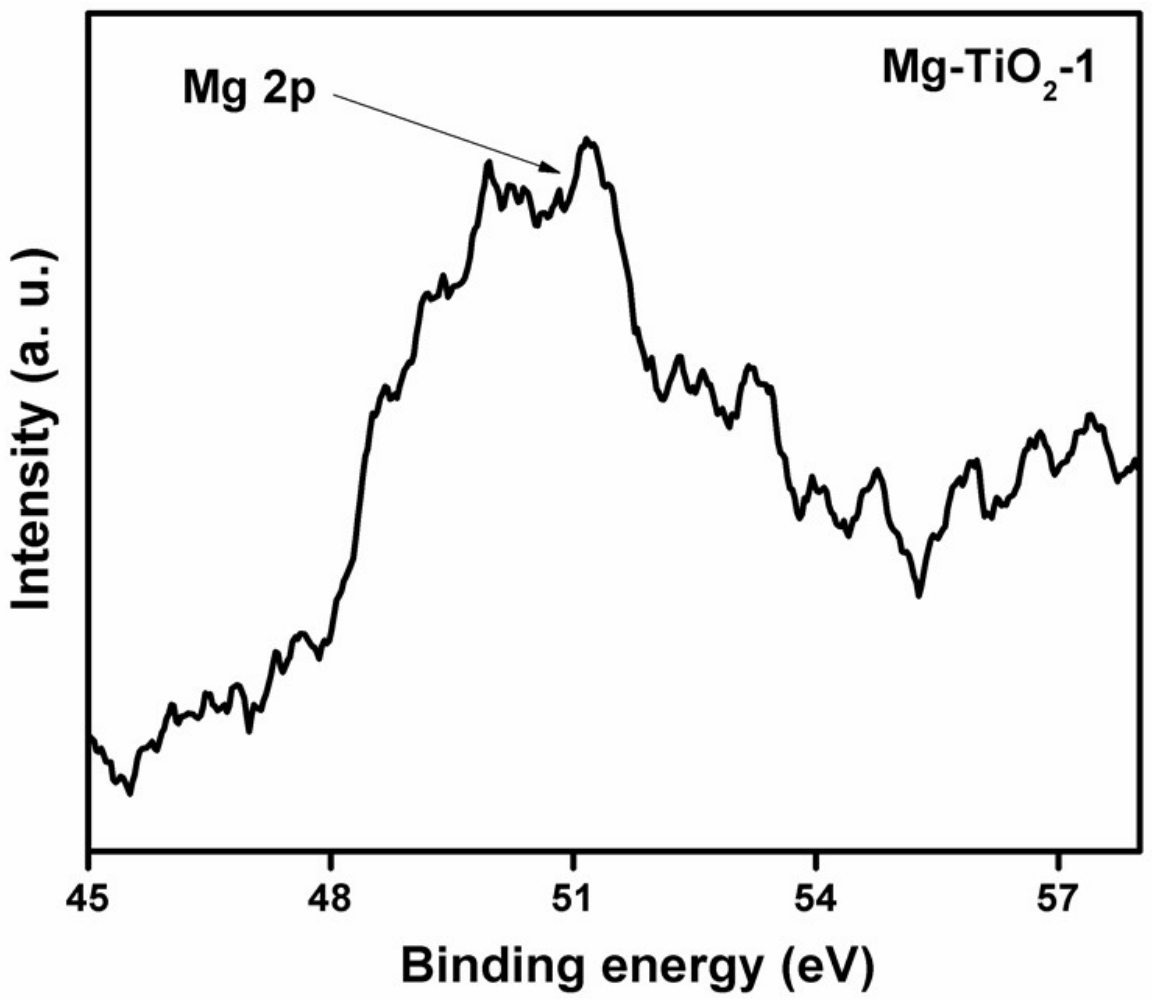

Figure 4.172 High-resolution X-ray photoelectron spectroscopy spectrum of Mg2p of Mg-TiO_2-1.

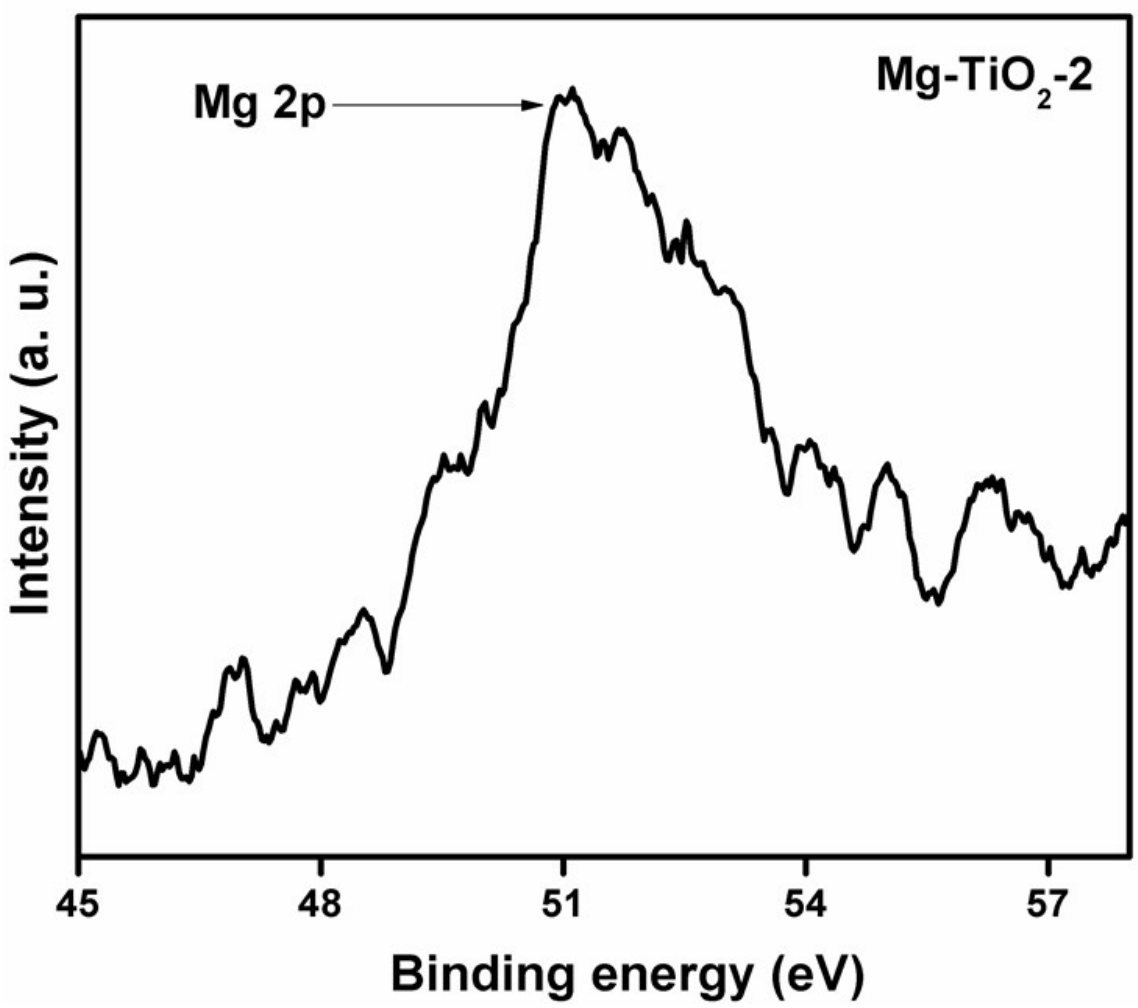

Figure 4.173 High-resolution X-ray photoelectron spectroscopy spectrum of Mg2p of Mg-TiO_2-2.

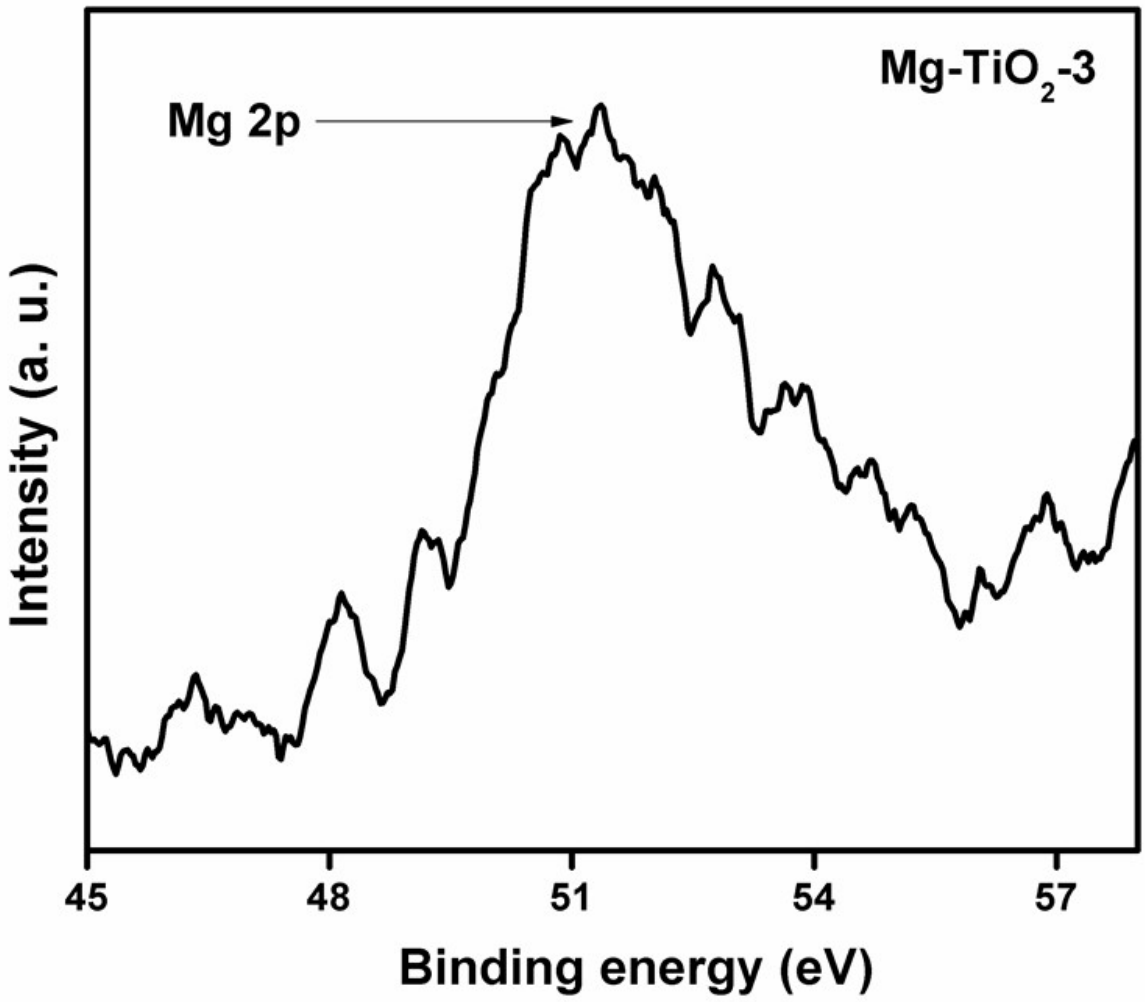

Figure 4.174 High-resolution X-ray photoelectron spectroscopy spectrum of Mg2p of Mg-TiO_2-3.

4.4.5 Computational studies of TiO_2 NPs and Mg-TiO_2 nanocatalysts

Several possibilities for the structures could be obtained when TiO_2 is doped with Mg. Large amounts of Mg could lead to the formation of separate phases of TiO_2 and MgO, meanwhile doping with a small amount could result in the isomorphic substitution of Ti because the ionic radius of Mg (0.72 Å) is close to that of Ti (0.61 Å). During the doping process, one of the nearest oxygen atoms in the surface or subsurface atomic layers was removed. This oxygen removal was to preserve the charge neutrality as a result of the difference in the formal ionic charge between Ti^{4+} and Mg^{2+}. The oxygen vacancy formed tends to be close to the doping Mg atom due to the electrostatic interaction of effective charges of Mg of -2 and of V_O of +2 in the lattice. The optimised structures of anatase nanoparticle Ti44r1 with isomorphically substituted single Ti atom in different positions are shown in Figure 4.175 – 4.177.

There were a limited number of unique Ti atoms at the surface due to the presence of symmetry planes in the Ti44r1 nanoparticle. The surface of each atom had two, three or four nearest oxygen atoms of the outer atomic layer. Since V_O in the surface layer was considered as a possible site for strong adsorption of CO_2, only surface oxygen vacancies were included in this study. Initial Ti44r1 cluster was given in Figure 4.177 to allow comparison of the structure of doped and undoped nanoparticles. Clusters 1-4, 9-10 and 12-17 demonstrated moderate structure changes as a result of doping, while clusters 5 – 8 and 11 showed strong shifts of atoms near the doping site.

The heat of formation of the doped clusters and the initial Ti44r1 nanoparticle computed with methods pm6 and pm6-d3 are listed in Table 4.9. The first of these computation methods were calibrated for obtaining correct enthalpy of formation, while the second method was developed for correctly describing interaction energies and geometries including non-covalent bonding. According to pm6 method, the most stable was cluster 7 followed by cluster 5 (+8.30 kcal mol^{-1}), 10 (+9.83 kcal mol^{-1}), 2 (+10.29 kcal mol^{-1}), 6 (+11.96 kcal mol^{-1}), 11 (+11.97 kcal mol^{-1}), 8 (+12.25 kcal mol^{-1}), 4 (+13.58 kcal mol^{-1}), and 3 (+17.3 kcal mol^{-1}). Apart from the above mentioned, other clusters were less stable by at least 30.69 kcal mol^{-1} when compared to cluster 7. Clusters 12 – 17, with oxygen vacancies at the surface (0 0 1), were all relatively unstable, although, cluster 14 showed a little level of stability among them. The obtained heat of formation indicates

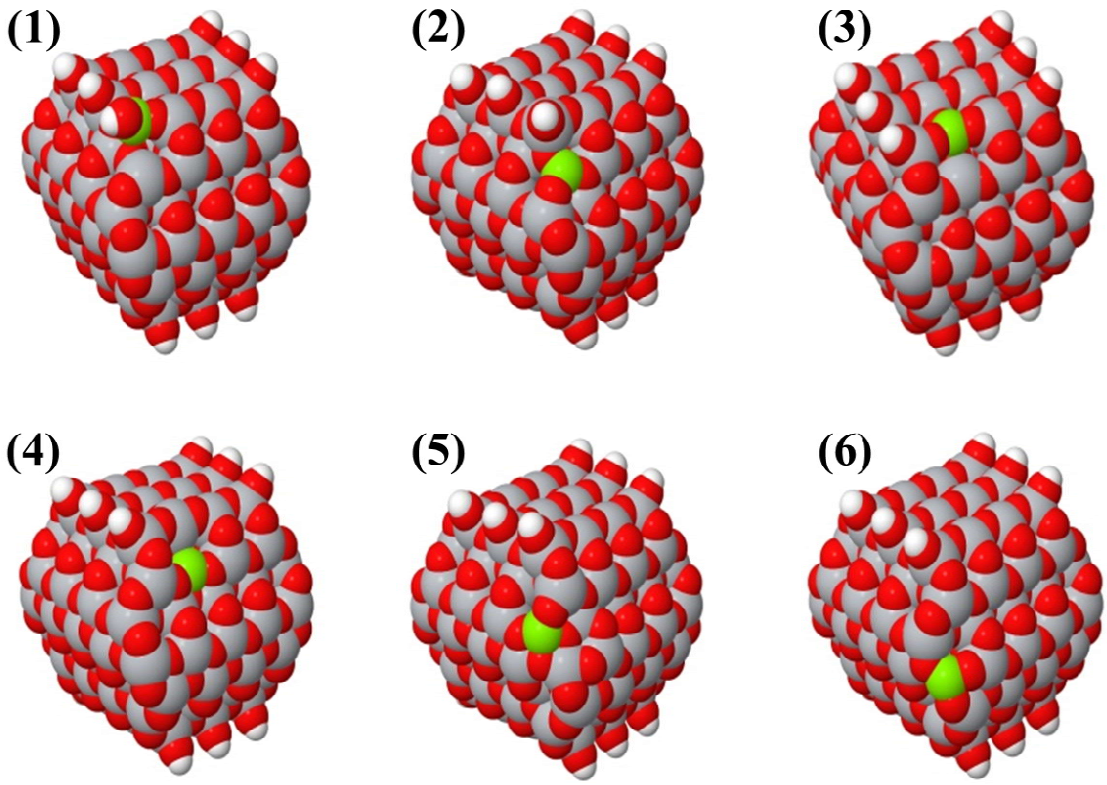

Figure 4.175 Decahedral TiO_2 anatase nanoparticle isomorphically doped with Mg in different surface positions (1 – 6). Atoms designations: green – Mg, grey – Ti, red – O, white – H.

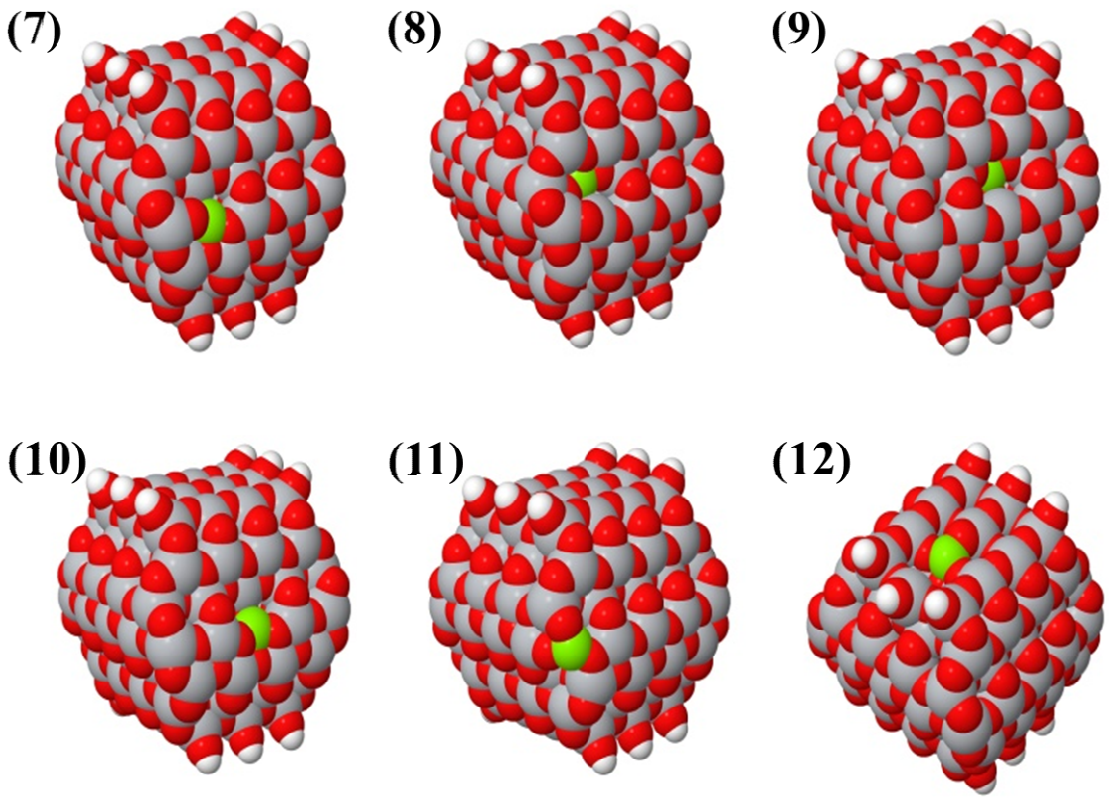

Figure 4.176 Decahedral TiO_2 anatase nanoparticle isomorphically doped with Mg in different surface positions (6 – 12). Atoms designations: green – Mg, grey – Ti, red – O, white – H.

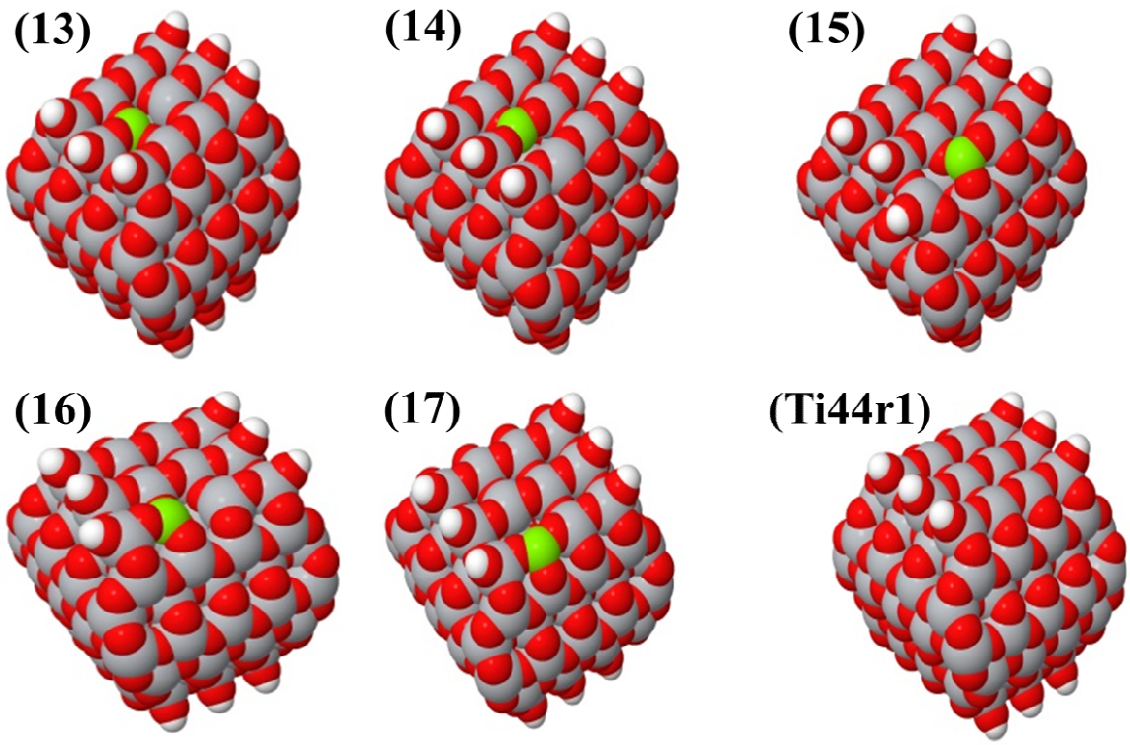

Figure4.177 Decahedral TiO_2 anatase nanoparticle isomorphically doped with Mg in different surface positions (13 – 17) and the initial nanoparticle Ti44r1. Atoms designations: green – Mg, grey – Ti, red – O, white – H.

Table 4.9 Enthalpy of formation of Mg-doped TiO_2 nanoparticles (in kcal mol^{-1}) calculated with pm6 and pm6-d3 methods.

Cluster #	Enthalpy pm6	Enthalpy pm6-d3	Cluster #	Enthalpy pm6	Enthalpy pm6-d3
1	-26291.58	-27076.14	10	-26318.81	-27102.27
2	-26318.35	-27103.22	11	-26316.67	-27102.08
3	-26311.34	-27095.76	12	-26273.50	-27055.27
4	-26315.06	-27098.67	13	-26280.05	-27062.40
5	-26320.34	-27104.57	14	-26295.46	-27078.33
6	-26316.68	-27102.05	15	-26275.65	-27058.25
7	-26328.64	-27112.53	16	-26278.53	-27061.54
8	-26316.39	-27099.11	17	-26284.21	-27066.99
9	-26297.95	-27080.59	Ti44r1	-26424.65	-27212.10

that isomorphic substitution most possibly took place over (1 0 1) facets and their junctions with facets (1 0 1) and (0 0 1).

The first stage of the heterogeneous catalytic reaction is the adsorption of reagents. CO_2 is adsorbed over photocatalyst surface which is followed by its reduction into diverse products such as CO, HCOOH and CH_3OH and the product desorption is the most energy consuming step of the reaction mechanism (Singhal *et al.,* 2016). Strongly adsorbed reagents are unfavourable for facile CO_2 reduction while too low adsorption energy would leave the photocatalyst surface unpopulated with the reagents and slow down the reaction too. Hence, some optimum condition should exist for CO_2 adsorption. Mg doping could help to attain such optimisation and also help to concentrate adsorbed CO_2 molecules at the most possible locations of photogenerated electrons. Figure 4.178 – 4.180 shows optimised structures of CO_2 adsorption complexes over different Mg-doped Ti44r1 clusters. Before adsorption, linear CO_2 molecule was placed at V_O near Mg site.

CO_2 was adsorbed in three modes, namely hydrocarbonate HCO_3 (cluster 1), as carbonate CO_3 (clusters 2, 5 – 7, 11 – 13, and 15 – 16) and as almost intact linear molecule O=C=O (clusters 3, 4, 8 – 10, 11a, 14, 17). The heat of adsorption and geometry of adsorption complexes are presented in Table 4.10. Carbonate and hydrocarbonate modes of adsorption possessed a high enthalpy of adsorption in the range of -18.22 to -38.87 kcal mol^{-1}. Adsorption in the linear form of CO_2 had a low adsorption enthalpy in the range of -4.01 to -9.53 kcal mol^{-1}.

Hydrocarbonate adsorption complex (cluster 1) had OH group connected to Mg atom and the carbonate oxygen to Ti atom. The bond lengths in Mg-OH, C-OH, C-OTi, C=O, and Ti-OC were found to be 2.05, 1.46, 1.26, 1.20 and 2.06 Å, respectively. Carbonate adsorption complexes (clusters 2, 5, 6, 11 – 13 and 15) were formed by bidentate adsorption to surface Mg and Ti atoms. Typical bond lengths were 1.91 - 2.02, 1.84 - 2.10, 1.29 - 1.32, 1.37 – 1.42 and 1.21 Å in Mg-O, Ti-O, C-OMg, C-OTi and C=O, respectively. In cluster 7, one oxygen was coordinated to surface Ti atom, while another was coordinated to both Ti and Mg atoms. This multiple coordination was observed to be beneficial for facile reduction of adsorbed CO_2 anddesorption of the reduction products, since coordination to multiple surface atoms alwaysleads to a decrease in adsorption

enthalpy. Moreover, adsorption site of complex7waslocated at the place of concentration of photogenerated electrons.

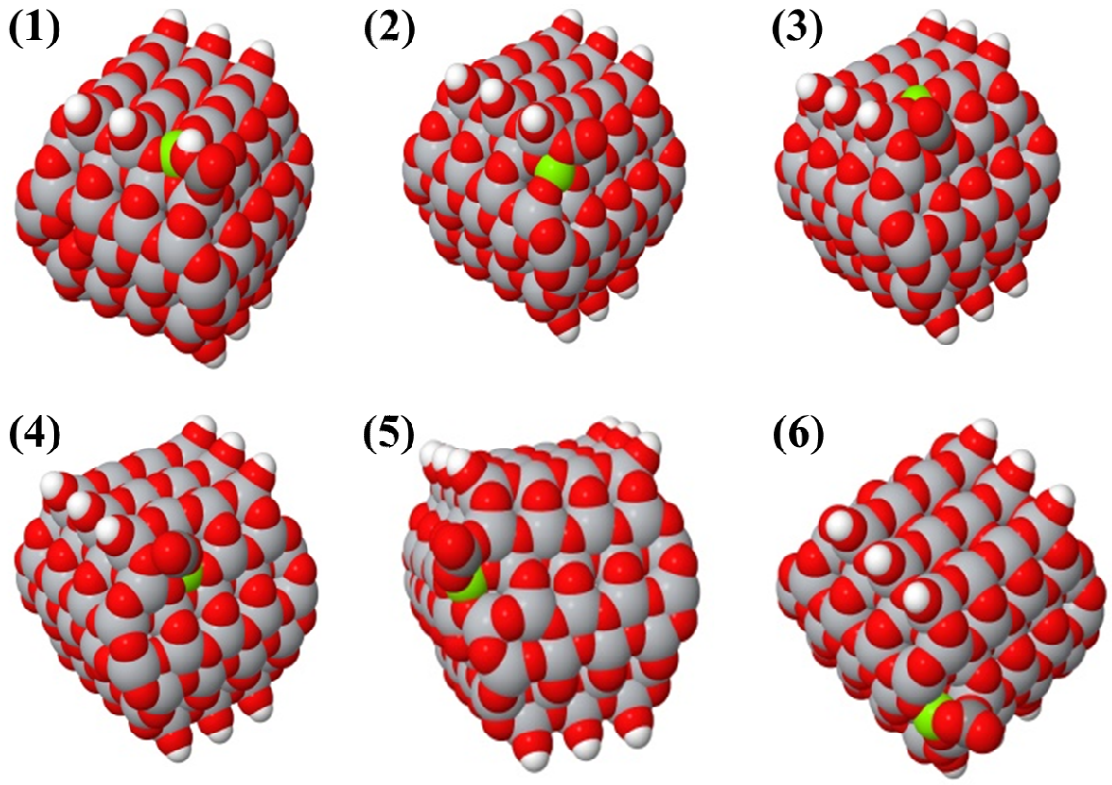

Figure 4.178 CO_2 adsorption complexes with Mg-doped Ti44r1 nanoparticles. The number of the complexes (1-6) correspond to the number of the Mg-Ti44r1 nanoparticles. Carbon atom is dark gray.

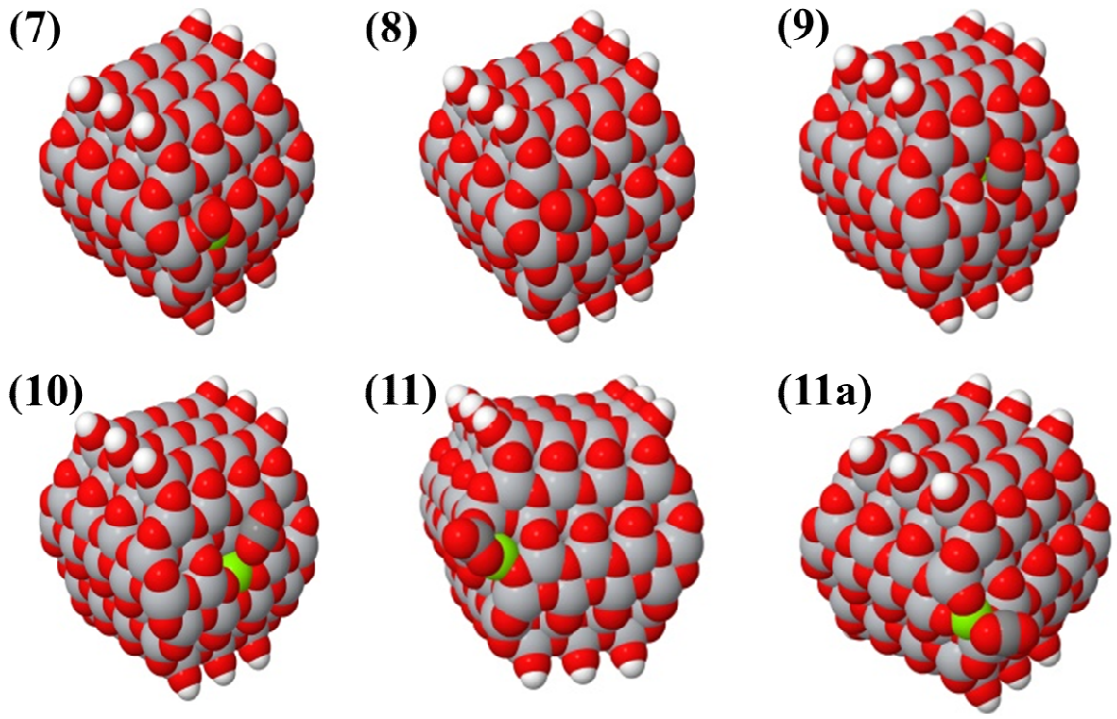

Figure 4.179 CO_2 adsorption complexes with Mg-doped Ti44r1 nanoparticles. The number of the complexes (7-11) correspond to the number of the Mg-Ti44r1 nanoparticles. The carbon atom is dark grey.

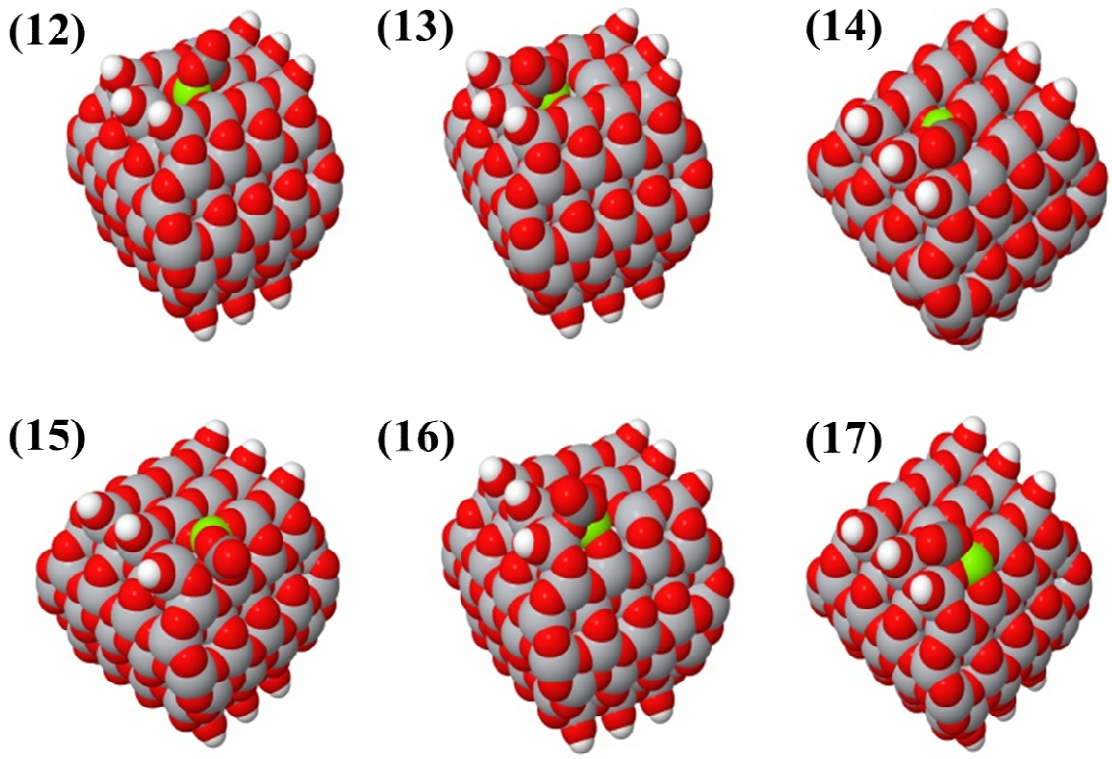

Figure 4.180 CO_2 adsorption complexes with Mg-doped Ti44r1 nanoparticles. The number of the complexes (12-17) corresponds to the number of the Mg-Ti44r1 nanoparticles. The carbon atom is dark grey.

Table 4.10 Parameters of CO_2 adsorption over different Mg-doped TiO_2 nanoparticles.

Complex #	**□ΔH_{ads}, kcal mol^{-1}**	**Geometry of CO_{2ads}**	**Complex #**	**□ΔH_{ads}, kcal mol^{-1}**	**Geometry of CO_{2ads}**
1	-38.87	HCO_3	10	-5.10	Linear
2	-25.16	CO_3	11	-38.60	CO_3
3	-7.01	Linear	11a	-5.24	Linear
4	-9.53	Linear	12	-20.73	CO_3
5	-31.86	CO_3	13	-16.97	CO_3
6	-30.17	CO_3	14	-5.39	Linear
7	-18.22	CO_3	15	-35.79	CO_3
8	-4.01	Linear	16	-24.72	CO_3
9	-5.46	Linear	17	-5.52	Linear

For linear adsorption complexes, adsorption was mostly of physical nature since the adsorption energy was low. Coordination proceeded either through one of the oxygen atoms or via a carbon atom to surface Mg or Ti atoms. The Ti-O bond length was 2.49 - 2.51 Å, while Mg-O bond length was 2.21 – 2.35 Å for respective coordination. The coordination to Mg atom (cluster 4) was stronger than to Ti atom (cluster 3). C=O bonds length in linearly adsorbed CO_2 remained almost unchanged from the free gaseous molecule of 1.17 Å. In some cases (cluster 8 and 10), adsorption was purely physical without specific interaction with any surface atom.

4.4.6 Photocatalytic CO_2 reduction by TiO_2 NPs and Mg-TiO_2 nanocatalysts

The initial screening of blank experiments confirmed the absence of any carbon-containing compounds; as a result, the obtained products (gaseous and liquid phases) originated from the photocatalytic reduction of CO_2. In the gaseous phase, CO, H_2, and CH_4 were products observed as shown in Figure 4.181 – 4.183. As expected, products yield increased after doping of Mg in TiO_2. The amount of CO production increased with Mg-doped TiO_2 up to an optimum of 0.1 wt% Mg (Mg-TiO_2-2) and then decreased significantly with further increase in Mg doping (Figure 4.181). This indicates that the production of CO was not favoured with a higher amount of Mg. The amount of CO produced was 29.2 μmol g^{-1} h^{-1} over Mg-TiO_2-2 nanocatalyst, which was higher than over pure TiO_2 (24.3 μmol g^{-1} h^{-1}). Similarly, the production rate of H_2 increased remarkably with Mg-doped TiO_2 up to an optimum of 0.1 wt% Mg (Mg-TiO_2-2) and then decreased gradually with further increase in Mg doping (Figure 4.182). The amount of H_2 produced was 28.7 μmol g^{-1} h^{-1} over 0.1 wt% (Mg-TiO_2-2), which was 21 times higher than over pure TiO_2 (1.3 μmol g^{-1} h^{-1}) (Figure 4.183). However, production of CH_4 increased up to the maximum loading of Mg in TiO_2, yielding 2.3 and 1.1 μmol g^{-1} h^{-1} with Mg-TiO_2-3 (0.17 wt%) and pure TiO_2 catalysts, respectively.

In the liquid phase, CH_3OH was the main product observed from the CO_2 reduction with H_2O on all catalysts (Figure 4.184). The production rate was increased

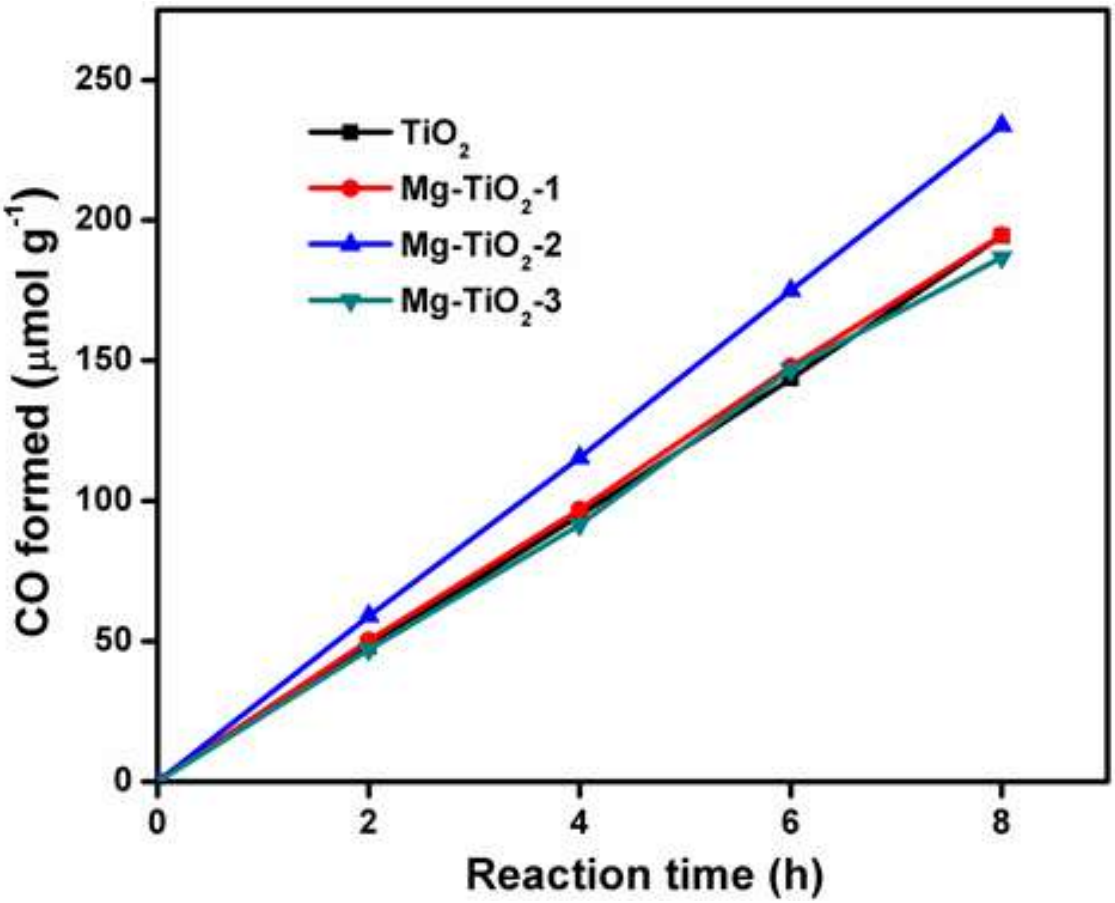

Figure 4.181 Effect of Mg-doped TiO_2 nanoparticles for the photocatalytic reduction of CO_2 with H_2O to produce CO from the gas phase at ambient conditions.

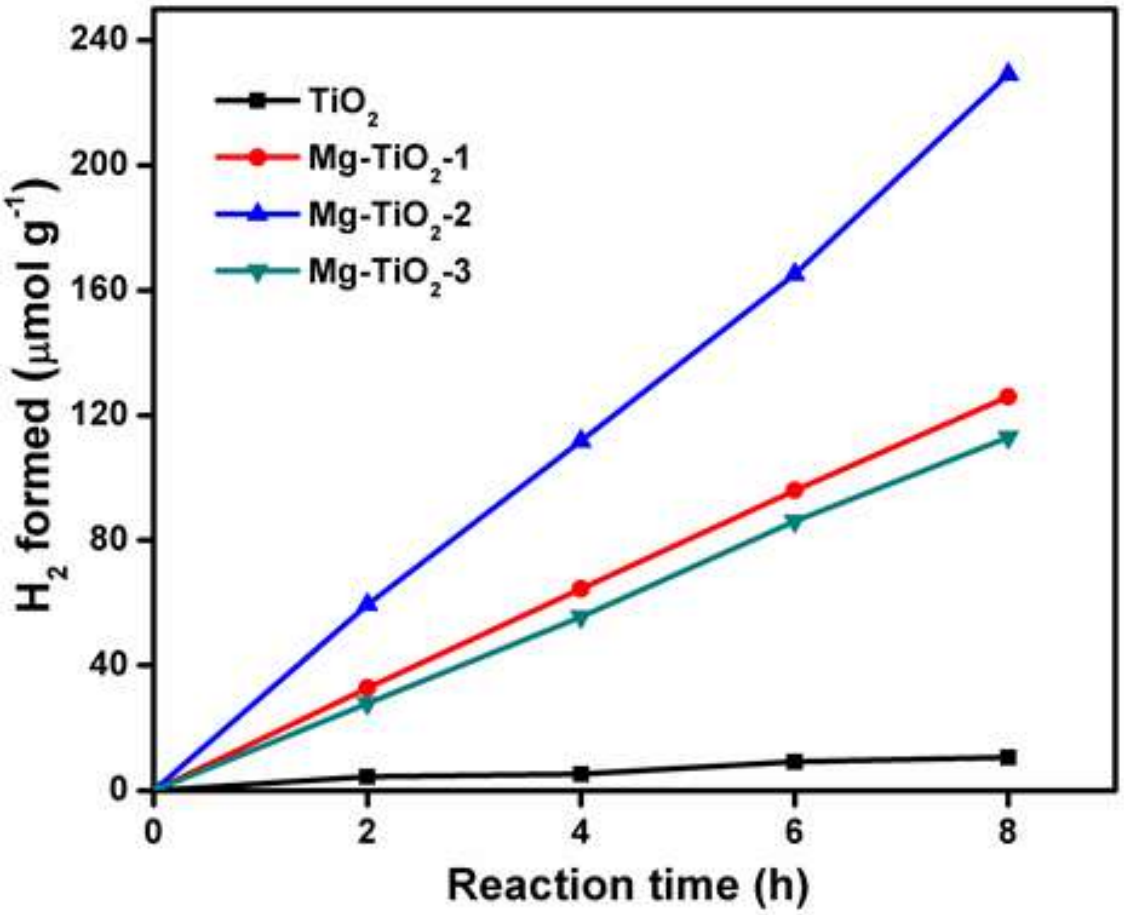

Figure 4.182 Effect of Mg-doped TiO_2 nanoparticles for the photocatalytic reduction of CO_2 with H_2O to produce H_2 from the gas phase at ambient conditions.

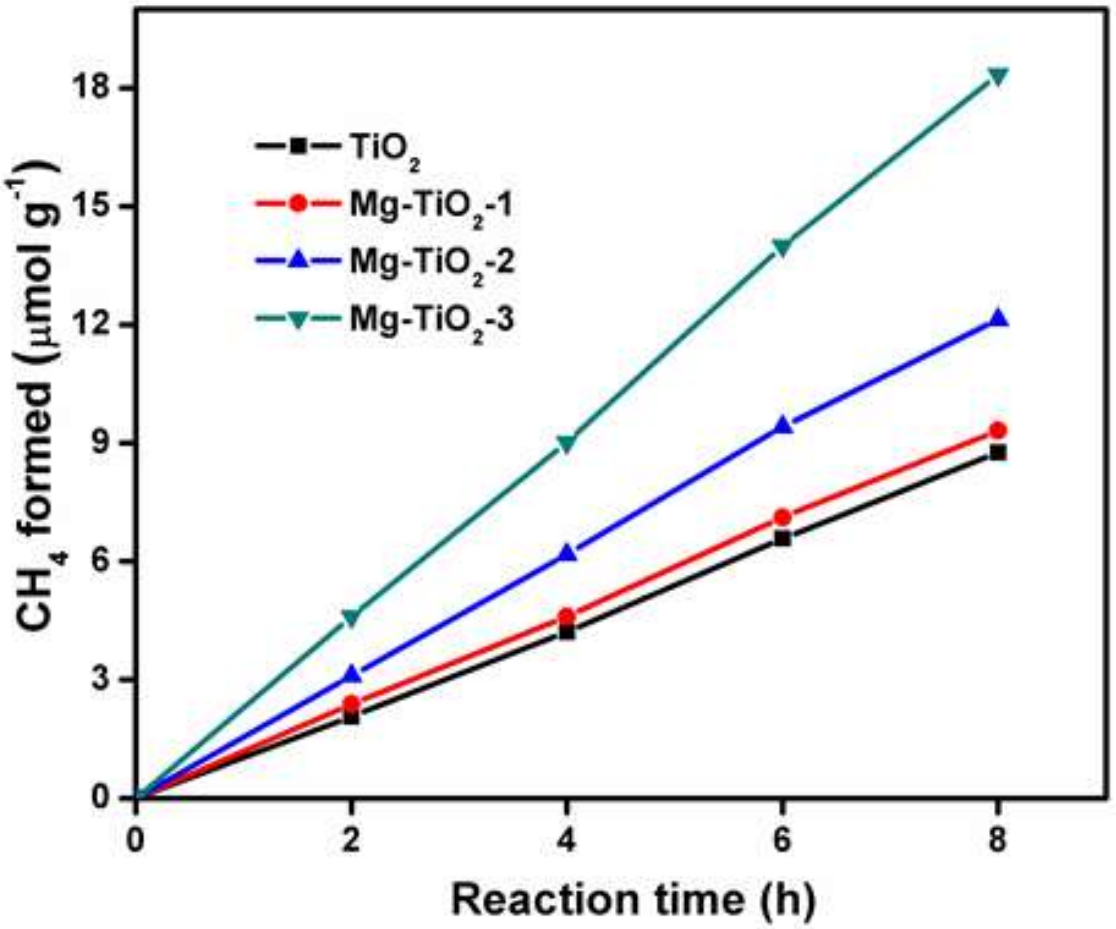

Figure 4.183 Effect of Mg-doped TiO_2 nanoparticles for the photocatalytic reduction of CO_2 with H_2O to produce CH_4 from the gas phase at ambient conditions.

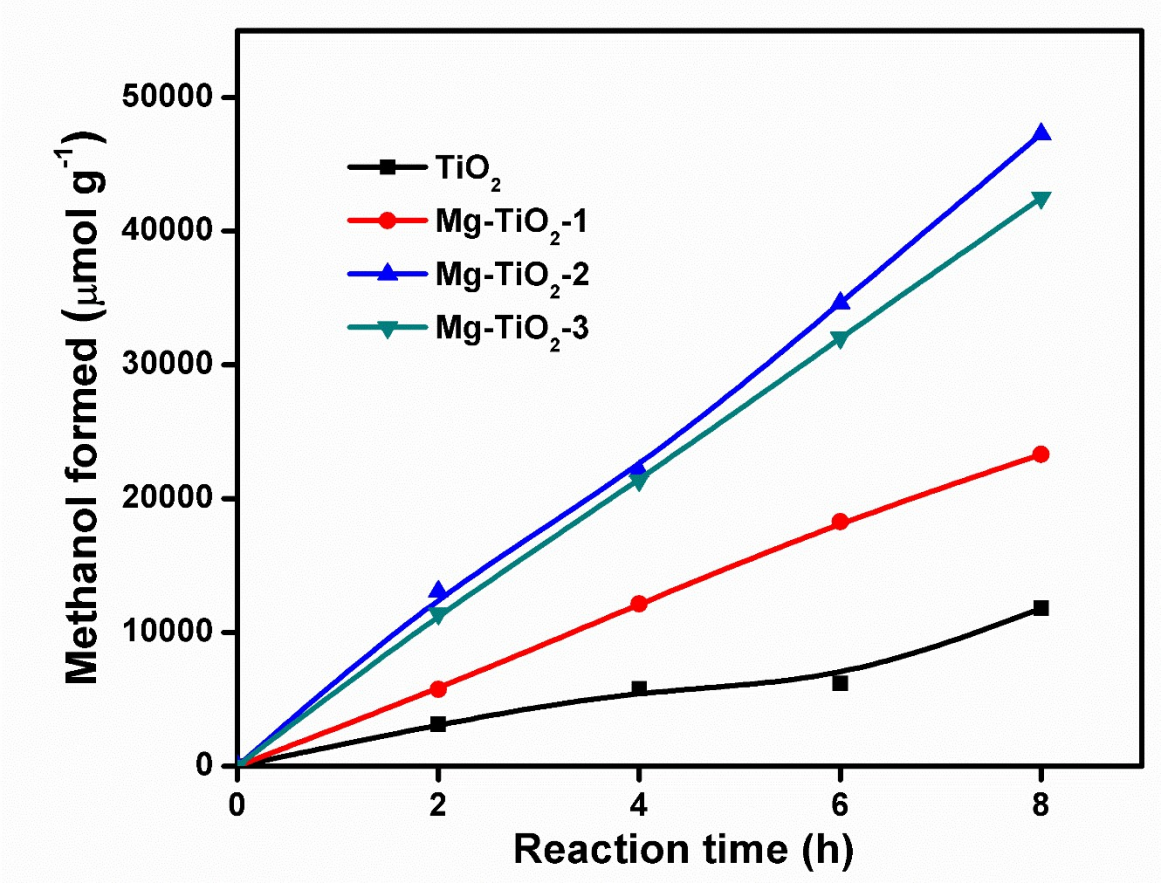

Figure 4.184 Effect of Mg-doped TiO_2 nanoparticles for the photocatalytic reduction of CO_2 with H_2O to produce CH_3OH from the liquid phase at ambient conditions.

with the doping amount of Mg in TiO_2 yielding 1470.0 and 5910.0 μmol g^{-1} h^{-1} with TiO_2 and Mg-TiO_2-2, respectively. The schematic representation of the photoreduction of CO_2 to fuels by Mg-doped-TiO_2 catalysts is shown in Scheme 4.4. As earlier stated, carbonate CO_3 mode is beneficial for the reduction of CO_2 due to its multiple coordination to the surface of the TiO_2 via both C and O atoms. The carbonate adsorption occurred at the oxygen vacancies created after the successful doping of Mg. The adsorption of CO_3 under the influence of UVA light led to the reduction of CO_2 to various products.

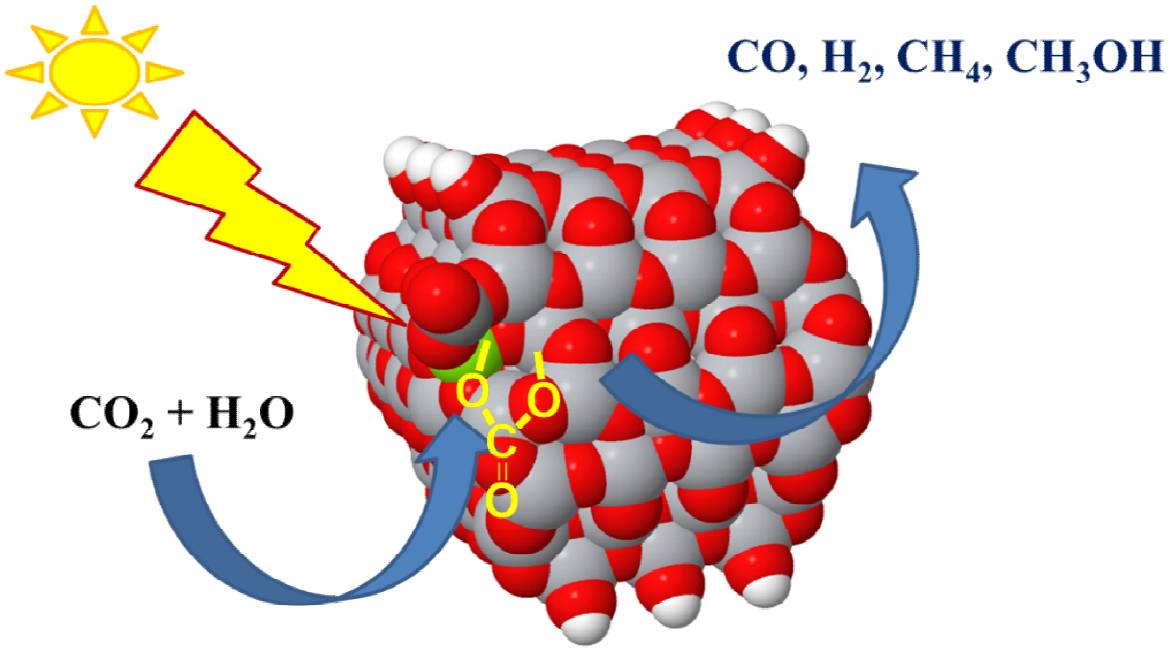

Scheme 4.4 The schematic diagram for the photoreduction of CO_2 to fuels by Mg-TiO_2 nanocatalysts.

CHAPTER FIVE
CONCLUSION AND RECOMMENDATIONS

5.1 Conclusion

Mixed phase TiO_2 photocatalysts were synthesised via sonothermal (S) and sonothermal-hydrothermal (SH) routes and applied for CO_2 reduction to produce methanol under UVA. The prepared TiO_2 catalysts had different amounts of rutile and anatase phase. The density functional calculations revealed that the anatase (1 0 1) had higher adsorption energy for the reactant molecules than the rutile (1 1 0), indicating that the anatase had a better activity for the photoreduction of CO_2 to MeOH. TiO_2-SH, with more anatase phase, exhibited better photocatalytic activity than TiO_2-S.

TiO_2 nanoparticles were further modified via a sonothermal-hydrothermal route with Reduced Graphene Oxide (RGO) to form nanocomposites. Experimental results showed that TiO_2 nanoparticles were successfully assembled on RGO sheets, forming nanocomposites. Photocatalytic studies indicated the potential use of these nanocomposites for the reduction of CO_2 under both UVA and visible light. Under the visible light, the methanol production rate was found to be 2.33 mmol g^{-1} h^{-1}. Theoretical computational results indicated that there was relatively strong adsorption of RGO on (1 0 1) surfaces of anatase. Graphene caused an upward shift of the TiO_2 bands by 0.2 eV due to the electron density contribution from RGO in the composite. The efficiency of the photocatalytic reaction greatly depended on the efficiency of electron transfer and charge transfer from TiO_2 nanoparticles to RGO. Improved tight contact between TiO_2 and RGO significantly improved the photocatalytic activity of the composite in CO_2 reduction when compared to some literature data.

TiO_2 nanoparticles modified with Carbon Nanotubes (CNT) were prepared via sonothermal-hydrothermal method. The synthesised CNT-TiO_2 photocatalysts showed improved photocatalytic activities for CO_2 reduction under both UVA and visible light at ambient temperature and pressure. The formation of Ti-C bond from the XPS results indicated the presence of strong interaction between CNT and TiO_2 nanoparticles. The computational studies revealed that decahedral anatase nanoparticles could be weakly attached to CNT with (0 0 1) surface and stronger with (1 0 1) surface. The binding with (1 0 1) surface resulted in frontier orbitals overlaps and combining of valence and

conduction band orbitals of TiO_2 and orbitals of CNT. Consequently, photoexcitation of CNT-TiO_2 composite with visible light resulted in charge transfer between TiO_2 and CNT and generation of separated charge carriers; while UV light excitation resulted in charge transfer in any direction, from CNT to TiO_2 and from TiO_2 to CNT. The latter process was more probable due to the higher density of initial states in TiO_2 compared to CNT. The unusually high photocatalytic activity of the MWCNT-TiO_2 composite resulted from the very tight contact between MWCNT and individual TiO_2 nanoparticles owing to the preparation method of the composite.

Mg-Doped TiO_2 nanoparticles were successfully prepared via a modified sonothermal method, and their photocatalytic activities were investigated for the reduction of CO_2 with H_2O. CO, H_2, CH_3OH, and CH_4 were the major products observed with a maximum production rate of 29.2, 28.7, 5910.0 and 2.3 μmol g^{-1} h^{-1}, respectively. Mg-Doped decahedral TiO_2 anatase nanoparticles were modelled and their interactions with CO_2 were studied. The most energetically profitable doping was obtained for sites at the junction of adjacent (1 0 1) facets which were also the sites of strong (ca. −30 kcal mol^{-1}) or moderately strong (−18 kcal mol^{-1}) CO_2 adsorption in carbonate form. These sites were suggested as the places for CO_2 photoreduction.

This work therefore revealed that the new synthetic routes afforded the co-existence of anatase-rutile phase in TiO_2 at 450 °C, which is below most reported phase transition temperature. This implies that more energy can be conserved via these synthetic routes. The surface areas of the prepared TiO_2 nanocatalysts were higher than those obtained from previous studies, indicating the availability of more active sites for photoactivity. For the first time, Mg-TiO_2, RGO-TiO_2 and CNT-TiO_2 nanocatalysts were applied for the photoreduction of CO_2 to methanol in the liquid phase. And when compared with other reported forms of modified TiO_2 or photocatalysts, Mg-TiO_2, RGO-TiO_2 and CNT-TiO_2 performed relatively better.

5.2 Recommendations

The success recorded in the synthesis of high surface area TiO_2 NPs with improved photocatalytic activities, via alternative routes, has opened up a wide scope for future studies on this field. Further studies could therefore be undertaken in order to explore

other new routes in the preparation of TiO_2 and/or its modified forms having higher surface area and enhanced photocatalytic efficiency.

Since the ratio of rutile phase increases with increasing calcination temperature, the effects of the temperature variation on phases of TiO_2 using the new synthetic route still need to be studied. Moreover, the effects of various proportions of phases of TiO_2 on the photocatalytic reduction of CO_2 could be studied.

The reason why the synthesised TiO_2 showed the presence of rutile at temperature as low as 450 °C could be determined by employing more characterisation techniques such as photoluminescence, electron paramagnetic resonance, photo current measurements and electrochemical impedance spectroscopy. The rate of recombination of various phases of TiO_2 is recommended to be studied by the use of electron paramagnetic resonance.

The use of hydrogen as fuel does not introduce pollution in the environment. It is therefore projected that photocatalytic hydrogen production from low cost sources such as ethanol, methanol and formic acid could serve as alternatives to fossil fuels. Hence, the production of hydrogen from water splitting and photoreforming of oxygenates could be explored by these newly prepared catalysts.

In addition, TiO_2 from the synthetic routes can open the path for the utilisation of direct sunlight. Modifications, including doping, impregnation and coupling with other semiconductors, could be explored for their photocatalytic performance.

Finally, the findings in this study will educate the public on safer and cleaner means to reduce the level of CO_2 in the atmosphere and also tap from the immense energy potential of the Sun. These findings will spur the scientific community to continue to reach its goal towards the photoconversion of the CO_2 to fuels at the industrial level. The findings will also encourage the researchers in the field of photocatalytic CO_2 reduction to further research on easier techniques to prepare TiO_2 of higher surface area.

REFERENCES

Afgan, N. 2013. Sustainable nuclear energy dilemma. *Thermal Science* 17: 305-321.

Afzal, S., Daoud, W.A. and Langford, S.J. 2013. Photostable self-cleaning cotton by a copper(II) porphyrin/TiO_2 visible-light photocatalytic system. *ACS Applied Materials & Interfaces* 5: 4753-4759.

Akhavan, O., Abdolahad, M., Abdi, Y. and Mohajerzadeh, S. 2009. Synthesis of titania/carbon nanotube heterojunction arrays for photoinactivation of E. coli in visible light irradiation. *Carbon* 47: 3280-3287.

Akhavan, O., Azimirad, R., Safa, S. and Larijani, M.M. 2010. Visible light photo-induced antibacterial activity of CNT–doped TiO_2 thin films with various CNT contents. *Journal of Materials Chemistry* 20: 7386-7387.

Akhavan, O. and Ghaderi, E. 2009. Photocatalytic reduction of graphene oxide nanosheets on TiO_2 thin film for photoinactivation of bacteria in solar light irradiation. *Journal of Physical Chemistry C* 113: 20214-20220.

Akhter, P., Hussain, M., Saracco, G. and Russo, N. 2015. Novel nanostructured-TiO_2 materials for the photocatalytic reduction of CO_2 greenhouse gas to hydrocarbons and syngas. *Fuel* 149: 55-65.

Al-Saidi, W.A., Voora, V.K. and Jordan, K.D. 2012. An Assessment of the vdW-TS method for extended systems. *Journal of Chemical Theory and Computation* 8: 1503-1513.

Albrecht, R. 1985. The role of hydrothermal synthesis in preparative chemistry. *Angewandte Chemie International Edition* 24: 1026-1040.

Aliwi, S. M. and Al-Jubori, K. F. 1989. Photoreduction of CO_2 by metal sulphide semiconductors in presence of H_2S. *Solar Energy Materials* 18: 223-229.

Allen, M. J., Tung, K.F. and Kaner, R.B. 2010. Honeycomb carbon: A review of grpahene. *Chemical Reviews* 110: 132-145.

Allen, T. 1997. *Particle Size Measurement: Surface Area and Pore Size Determination.* 5th ed. Netherlands: Springer, 252 pp.

An, T., Chen, J., Nie, X., Li, G., Zhang, H., Liu, X. and Zhao, H. 2012. Synthesis of carbon nanotube–anatase TiO_2 sub-micrometre-sized sphere composite photocatalyst for synergistic degradation of gaseous styrene. *ACS Applied Materials & Interfaces* 4: 5988-5996.

Anpo, M. and Chiba, K. 1992. Photocatalytic reduction of CO_2 on anchored titanium oxide catalysts. *Journal of Molecular Catalysis* 74: 207-212.

Aradi, B., Hourahine, B. and Frauenheim, T. 2007. DFTB+, a sparse matrix-based implementation of the DFTB Method."*The Journal of Physical Chemistry A* 111: 5678-5684.

Arakawa, H., Aresta, M., Armor, J.N., Barteau, M.A., Beckman, E.J., Bell, A.T., Bercaw, J.E., Creutz, C., Dinjus, E., Dixon, D.A., Domen, K., DuBois, D.L., Eckert, J., Fujita, E., Gibson, D.H., Goddard, W.A., Goodman, D.W., Keller, J., Kubas, G.J., Kung, H.H., Lyons, J.E., Manzer, L.E. Marks, T.J., Morokuma, K., Nicholas, K.M., Periana, R., Que, L., Rostrup-Nielson J., Sachtler, W.M.H., Schmidt, L.D., Sen, A., Somorjai, G.A., Stair, P.C., Stults, B.R. and Tumas, W. 2001. Catalysis research of relevance to carbon management: Progress, challenges, and opportunities. *Chemical Reviews* 101: 953-996.

Aruna, S.T., Tirosh, S. and Zaban, A. 2000. Nanosize rutile titania particle synthesis a hydrothermal method without mineralizers. *Journal of Materials Chemistry* 10: 2388-2391.

Balandin, A. A., Ghosh, S., Bao, W., Calizo, I., Teweldebrhan, D., Miao, F. and Lau, C.N. 2008. Superior thermal conductivity of single-layer graphene. *Nano Letters* 8: 902-907.

Baldissarelli, V.Z., de Souza, T., Andrade, L., Oliveira, L.F.C., José, H.J. and Moreira, R.F.P.M. 2015. Preparation and photocatalytic activity of TiO_2-exfoliated graphite oxide composite using an ecofriendly graphite oxidation method. *Applied Surface Science* 359: 868-874.

Bayati, M.R., Moshfegh, A.Z. and Golestani-Fard, F. 2010. On the photocatalytic activity of the sulfur-doped titania nano-porous films derived via micro-arc oxidation. *Applied Catalysis A* 389: 60-67.

Bazzo, A., and Urakawa, A. 2013. Origin of photocatalytic activity in continuous gas phase CO_2 reduction over Pt/TiO_2. *ChemSusChem* 6: 2095-2102.

Bellamkonda, S., Thangavel, N., Hafeez, H.Y., Neppolian, B. and Rao, G.R. 2017. Highly active and stable multi-walled carbon nanotubes-graphene-TiO_2 nanohybrid: An efficient non-noble metal photocatalyst for water splitting. *Catalysis Today* 321-322: 120-127.

Bensaid, S., Centi, G., Garrone, E., Perathoner, S. and Saracco, G. 2012. Towards artificial leaves for solar hydrogen and fuels from carbon dioxide. *ChemSusChem* 5: 500-521.

Blöchl, P.E. 1994. Projector augmented-wave method. *Physical Review B* 50: 17953-17979.

Blomen, E., Hendriks, C. and Neele, F. 2009. Capture technologies: Improvements and promising developments. *Energy Procedia* 1: 1505-1512.

Bolotin, K.I., Sikes, K.J., Jiang, Z., Klima, M., Fudenberg, G., Hone, J., Kim, P. and Stormer, H.L. 2008. Ultrahigh electron mobility in suspended graphene. *Solid State Communications* 146: 351-355.

Boot-Handford, M.E., Abanades, J.C., Anthony, E.J., Blunt, M.J., Brandani, S., Dowell, N.M., Fernandez, J.R., Ferrari, M., Gross, R., Hallett, J.P., Haszeldine, R.S., Heptonstall, P., Lyngfelt, A., Makuch, Z., Mangano, E., Porter, R.T.J., Pourkashanian, M., Rochelle, G.T., Shah, N., Yao, J.G. and Fennell, P.S. 2014. Carbon capture and storage update. *Energy & Environmental Science* 7: 130-189.

Bou-Orm, N., Iorgu, A., Daniele, S. and Guilhaume, N. 2013. Modification of acid-base properties of TiO_2 by Nb and Mg dopants: influence on the activity of Pd–Cu/(Mg, Nb)–TiO_2 catalysts for nitrate hydrogenation. *Applied Catalysis A* 467: 414-420.

Brinker, C.J. and Scherer, G.W. 1990. *Sol-gel science: the physics and chemistry of sol-gel processing*. 1st ed. San Diego, CA: Academic Press, Inc, 928 pp.

Calzado, C.J., Hernandez, N.C. and Sanz, J.F. 2008. Effect of on-site Coulomb repulsion term *U* on the band-gap states of the reduced rutile (110) TiO_2 surface. *Physical Review B* 77: 045118(1-10).

Cargnello, M., Gordon, T.R. and Murray, C.B. 2014. Solution-phase synthesis of titanium dioxide nanoparticles and nanocrystals. *Chemical Reviews* 114: 9319-9345.

Centi, G. and van Santen R.A. 2007. *Catalysis for renewables: from feedstock to energy production*. Weinheim: Wiley-VCH, 451 pp.

Chen, C., Hu, R., Mai, K., Ren, Z., Wang, H., Qian, G. and Wang, Z. 2011. Shape evolution of highly crystalline anatase TiO_2 nanobipyramids. *Crystal Growth & Design* 11: 5221-5226.

Chen, D.J., Zou, L.L., Li, S.X. and Zheng, F.Y. 2016. Nanospherical like reduced graphene oxide decorated TiO_2 nanoparticles: an advanced catalyst for the hydrogen evolution reaction. *Scientific Reports* 6: 20335(1-8).

Chen, W., Kuang, Q., Wang, Q. and Xie, Z. 2015. Engineering a high energy surface of anatase TiO_2 crystals towards enhanced performance for energy conversion and environmental applications. *RSC Advances* 5: 20396-20409.

Cheng, H., Ma, J., Zhao, Z. and Qi, L. 1995. Hydrothermal preparation of uniform nanosize rutile and anatase particles. *Chemistry of Materials* 7: 663-671.

Chiarello, G.L., Aguirre, M.H. and Selli, E. 2010. Hydrogen production by photocatalytic steam reforming of methanol on noble metal-modified TiO_2. *Journal of Catalysis* 273: 182-190.

Choi, W., Termin, A. and Hoffmann, M.R. 1994. The role of metal ion dopants in quantum-sized TiO_2: correlation between photoreactivity and charge carrier recombination dynamics. *The Journal of Physical Chemistry* 98: 13669-13679.

Chuan-Yu, Y., Yu-Feng, L., Chih-Hung, H., Yao-Hsuan, T., Chen-Chi, M.M., Min-Chao, C. and Hsin, S. 2008. The effects of synthesis procedures on the morphology and photocatalytic activity of multi-walled carbon nanotubes/TiO_2 nanocomposites. *Nanotechnology* 19: 045604 (1-11).

Clark, D.E., Folz, D.C. and West, J.K. 2000. Processing materials with microwave energy. *Materials Science and Engineering: A* 287: 153-158.

Cong, Y., Li, X., Qin, Y., Dong, Z., Yuan, G., Cui, Z. and Lai, X. 2011. Carbon-doped TiO_2 coating on multiwalled carbon nanotubes with higher visible light photocatalytic activity. *Applied Catalysis B* 107: 128-134.

Cook, T.R., Dogutan, D.K., Reece, S.Y., Surendranath, Y., Teets, T.S. and Nocera, D.G. 2010. Solar energy supply and storage for the legacy and nonlegacy worlds. *Chemical Reviews* 110: 6474-6502.

Cox, P.M., Betts, R.A., Jones, C.D., Spall, S.A and Totterdell, I.J. 2000. Acceleration of global warming due to carbon-cycle feedbacks in a coupled climate model. *Nature* 408: 184-187.

Cui, S.C., Sun, X.Z. and Liu, J.G. 2016. Photo-reduction of CO_2 using a rhenium complex covalently supported on a graphene/TiO_2 composite. *ChemSusChem* 9: 1698-703.

Das, S. and Daud, W.M.A.W. 2014. A review on advances in photocatalysts towards CO_2 conversion. *RSC Advances* 4: 20856-20893.

de Lasa, H. Serrano, B. and Salaices, M. 2005. *Photocatalytic Reaction Engineering*. 1st ed. New York: Springer, 193 pp.

Di-Valentin, C. and Pacchioni, G. 2013. Trends in non-metal doping of anatase TiO_2: B, C, N and F. *Catalysis Today* 206: 12-18.

Dimitrijevic, N.M., Vijayan, B.K., Poluektov, O.G., Rajh, T., Gray, K.A., He, H.Y. and Zapol, P. 2011. Role of water and carbonates in photocatalytic transformation of CO_2 to CH_4 on titania. *Journal of the American Chemical Society* 133: 3964-3971.

Dittmar, M. 2012. Nuclear energy: status and future limitations. *Energy* 37: 35-40.

Dolgonos, G., Aradi, B., Moreira, N.H. and Frauenheim, T. 2010. An improved self-consistent-charge density-functional tight-binding (SCC-DFTB) set of parameters for simulation of bulk and molecular systems involving titanium. *Journal of Chemical Theory and Computation* 6: 266-278.

Du, J., Zhang, J. and Kang, D.J. 2011. Controlled synthesis of anatase TiO_2 nano-octahedra and nanospheres: shape-dependent effects on the optical and electrochemical properties. *CrystEngComm* 13: 4270-4275.

Elstner, M., Porezag, D., Jungnickel, G., Elsner, J., Haugk, M., Frauenheim, T., Suhai, S. and Seifert, G. 1998. Self-consistent-charge density-functional tight-binding method for simulations of complex materials properties. *Physical Review B* 58: 7260-7268.

Escobedo S.S., Rosales, B.S and de Lasa, H. 2013. Quantum yield with platinum modified TiO_2 photocatalyst for hydrogen production. *Applied Catalysis B* 140-141: 523-536.

Fan, W.Q., Lai, Q.H., Zhang, Q.H. and Wang, Y. 2011. Nanocomposites of TiO_2 and reduced graphene oxide as efficient photocatalysts for hydrogen evolution. *Journal of Physical Chemistry C* 115: 10694-10701.

Fang, B., Xing, Y., Bonakdarpour, A., Zhang, S. and Wilkinson, D.P. 2015. Hierarchical CuO–TiO_2 hollow microspheres for highly efficient photodriven reduction of CO_2 to CH_4. *ACS Sustainable Chemistry & Engineering* 3: 2381-2388.

Farhadian, A. K. and Bagheri-Mohagheghi, M.M. 2013. Transition from anatase to rutile phase in titanium dioxide (TiO_2) nanoparticles synthesized by complexing sol-gel process: effect of kind of complexing agent and calcinating temperature. *Journal of Sol-Gel Science and Technology* 65: 329-335.

Freund, H. J., and Roberts, M.W. 1996. Surface chemistry of carbon dioxide. *Surface Science Reports* 25: 225-273.

Froschl, T., Hormann, U., Kubiak, P., Kucerova, G., Pfanzelt, M., Weiss, C.K., Behm, R.J., Husing, N., Kaiser, U., Landfester, K. and Wohlfahrt-Mehrensm, M. 2012. High surface area crystalline titanium dioxide: potential and limits in electrochemical energy storage and catalysis. *Chemical Society Review* 41: 5313-5360.

Gallo, A., Montini, T., Marelli, M., Minguzzi, A., Gombac, V., Psaro, R., Fornasiero, P. and Santo, V.D. 2012. H_2 production by renewables photoreforming on Pt-Au/TiO_2 catalysts activated by reduction. *Chemsuschem* 5: 1800-1811.

Gao, L., Li, Y., Ren, J., Wang, S., Wang, R., Fu, G. and Hu, Y. 2017. Passivation of defect states in anatase TiO_2 hollow spheres with Mg doping: realising efficient photocatalytic overall water splitting. *Applied Catalysis B* 202: 127-133.

Gattrell, M., Gupta, N. and Co, A. 2006. A review of the aqueous electrochemical reduction of CO_2 to hydrocarbons at copper. *Journal of Electroanalytical Chemistry* 594: 1-19.

Gedanken, A. 2004. Using sonochemistry for the fabrication of nanomaterials. *Ultrasonics Sonochemistry* 11: 47-55.

Geim, A. K., and Novoselov, K. S. 2007. The rise of graphene. *Nature Material* 6: 183-191.

Ghosh, S., Calizo, I., Teweldebrhan, D., Pokatilov, E.P., Nika, D.L., Balandin, A.A., Bao, W., Miao, F. and Lau, C.N. 2008. Extremely high thermal conductivity of graphene: prospects for thermal management applications in nanoelectronic circuits. *Applied Physics Letters* 92 15: 151911-151912.

Gopal, M., Chan, W.J.M. and De Jonghe, L.C. 1997. Room temperature synthesis of crystalline metal oxides. *Journal of Materials Science* 32: 6001-6008.

Grimme, S., Antony, J., Ehrlich, S. and Krieg, H. 2010. A consistent and accurate *ab initio* parametrisation of density functional dispersion correction (DFT-D) for the 94 elements H-Pu. *Journal of Chemical Physics* 132: 154104-18.

Gu, L.A., Wang, J.Y., Cheng, H., Zhao, Y.Z., Liu, L.F. and Han, X.J. 2013. One-Step preparation of graphene-supported anatase TiO_2 with exposed {001} facets and mechanism of enhanced photocatalytic properties. *ACS Applied Materials & Interfaces* 5: 3085-3093.

Gui, M.M., Chai, S.P., Xu, B.Q. and Mohamed, A.R. 2014. Enhanced visible light responsive MWCNT/TiO_2 core-shell nanocomposites as the potential photocatalyst for reduction of CO_2 into methane. *Solar Energy Materials and Solar Cells* 122: 183-189.

Gui, M.M., Wong, W.M.P., Chai, S. and Mohamed, A.R. 2015. One-pot synthesis of Ag-MWCNT@TiO_2 core-shell nanocomposites for photocatalytic reduction of CO_2 with water under visible light irradiation. *Chemical Engineering Journal* 278:272-278.

Gupta, S.M. and Tripathi, M. 2011. A review of TiO_2 nanoparticles. *Chinese Science Bulletin* 56 16: 1639-1657.

Habisreutinger, S.N., Schmidt-Mende, L. and Stolarczyk, J.K. 2013. Photocatalytic reduction of CO_2 on TiO_2 and other semiconductors. *Angewandte Chemie International Edition* 52: 7372-7408.

Hafeez, H.Y., Lakhera, S.K., Bellamkonda, S., Rao, G.R., Shankar, M.V., Bahnemann, D.W. and Neppolian, B. 2018. Construction of ternary hybrid layered reduced graphene oxide supported g-C_3N_4-TiO_2 nanocomposite and its photocatalytic hydrogen production activity. *International Journal of Hydrogen Energy* 43: 3892-3904.

Halmann, M. 1978. Photoelectrochemical reduction of aqueous carbon dioxide on p-type gallium phosphide in liquid junction solar cells. *Nature* 275: 115-116.

Haque, K.E. 1999. Microwave energy for mineral treatment processes—a brief review. *International Journal of Mineral Processing* 57: 1-24.

He, H., Zapol, P. and Curtiss, L.A. 2010. A theoretical study of CO_2 anions on anatase (101) surface. *The Journal of Physical Chemistry C* 114: 21474-21481.

He, J., Benkö G., Korodi, F., Polívka, T., Lomoth, R., Åkermark, B., Sun, L., Hagfeldt, A. and Sundström, V. 2002. Modified phthalocyanines for efficient near-IR sensitisation of nanostructured TiO_2 electrode. *Journal of the American Chemical Society* 124: 4922-4932.

He, Z., Yu, Y., Wang, D., Tang, J., Chen, J. and Song, S. 2016. Photocatalytic reduction of carbon dioxide using iodine-doped titanium dioxide with high exposed {001} facets under visible light. *RSC Advances* 6: 23134-23140.

Huang, Y., Ho, W., Lee, S., Zhang, L., Li, G. and Yu, J.C. 2008. Effect of carbon doping on the mesoporous structure of nanocrystalline titanium dioxide and its solar-light-driven photocatalytic degradation of NOx. *Langmuir* 24: 3510-3516.

Hummers, W.S. and Offeman, R.E. 1958. Preparation of graphitic oxide. *Journal of the American Chemical Society* 80: 1339-1339.

Ibhadon, A. and Fitzpatrick, P. 2013. Heterogeneous photocatalysis: recent advances and applications. *Catalysts* 3: 189-218.

Iijima, S. 1991. Helical microtubules of graphitic carbon. *Nature* 354: 56-58.

Ikeue, K., Nozaki, S., Ogawa, M. and Anpo, M. 2002. Characterisation of self-standing Ti-containing porous silica thin films and their reactivity for the photocatalytic reduction of CO_2 with H_2O. *Catalysis Today* 74: 241-248.

Ikeue, K., Yamashita, H., Anpo, M. and Takewaki, T. 2001. Photocatalytic reduction of CO_2 with H_2O on Ti−β zeolite photocatalysts: effect of the hydrophobic and hydrophilic properties. *The Journal of Physical Chemistry B* 105: 8350-8355.

In, S., Orlov, A., Berg, R., García, F., Pedrosa-Jimenez, S., Tikhov, M.S., Wright, D.S. and Lambert, R.M. 2007. Effective visible light-activated B-doped and B, N-codoped TiO_2 photocatalysts. *Journal of the American Chemical Society* 129: 13790-13791.

Inagaki, M. 2012. Carbon coating for enhancing the functionalities of materials. *Carbon* 50: 3247-3266.

Indrakanti, V.P., Kubicki, J.D. and Schobert, H.H. 2009. Photoinduced activation of CO_2 on Ti-based heterogeneous catalysts: current state, chemical physics-based insights and outlook. *Energy & Environmental Science* 2: 745.

Indrakanti, V. P., Kubicki, J.D. and Schobert, H.H. 2011. Photoinduced activation of CO_2 on TiO_2 surfaces: quantum chemical modelling of CO_2 adsorption on oxygen vacancies. *Fuel Processing Technology* 92: 805-811.

Inoue, T., Fujishima, A., Konishi, S. and Honda, K. 1979. Photoelectrocatalytic reduction of carbon dioxide in aqueous suspensions of semiconductor powders. *Nature* 277: 637-638.

Ismail, A.A., Geioushy, R.A., Bouzid, H., Al-Sayari, S.A., Al-Hajry, A. and Bahnemann, D.W. 2013. TiO_2 decoration of graphene layers for highly efficient photocatalyst: impact of calcination at different gas atmosphere on photocatalytic efficiency. *Applied Catalysis B* 129: 62-70.

Jaeglé, L., Steinberger, L., Martin, R.V. and Chance, K. 2005. Global partitioning of NOx sources using satellite observations: relative roles of fossil fuel combustion, biomass burning and soil emissions. *Faraday Discussions* 130: 407-423.

Jaiswal, R., Bharambe, J., Patel, N., Dashora, A., Kothari, D.C. and Miotello, A. 2015. Copper and nitrogen co-doped TiO_2 photocatalyst with enhanced optical absorption and catalytic activity. *Applied Catalysis B* 168: 333-341.

Jamel, M.S., Rahman, A.A. and Shamsuddin, A.H. 2013. Advances in the integration of solar thermal energy with conventional and non-conventional power plants. *Renewable and Sustainable Energy Reviews* 20: 71-81.

Jing, Y., Gui, C., Qu, J., Hao, S., Wang, Q. and Yu, Z. 2017. Silver silicate@carbon nanotube nanocomposites for enhanced visible light photodegradation performance. *ACS Sustainable Chemistry & Engineering* 5: 3641-3649.

Juang, L.C., Semblante, G.U., You, S.J. and Hong, S.H. 2013. Degradation of 2-chlorophenol using carbon nanotube/titanium oxide composite prepared by hydrothermal method. *Journal of the Taiwan Institute of Chemical Engineers* 44: 432-437.

Kabra, K., Chaudhary, R. and Sawhney, R.L. 2004. Treatment of hazardous organic and inorganic compounds through aqueous-phase photocatalysis: a review. *Industrial & Engineering Chemistry Research* 43: 7683-7696.

Kakiage, K., Tokutome, T., Iwamoto, S., Kyomen, T. and Hanaya, M. 2013. Fabrication of a dye-sensitised solar cell containing a Mg-doped TiO_2 electrode and a Br3(-)/Br- redox mediator with a high open-circuit photovoltage of 1.21 V. *Chemical Communication* 49: 179-80.

Kamat, P.V. 2012. Manipulation of charge transfer across semiconductor interface. A criterion that cannot be ignored in photocatalyst design. *The Journal of Physical Chemistry Letters* 3: 663-672.

Kang, Q., Wang, T., Li, P., Liu, L., Chang, K., Li, M. and Ye, J. 2015. Photocatalytic reduction of carbon dioxide by hydrous hydrazine over Au–Cu alloy nanoparticles supported on $SrTiO_3/TiO_2$ coaxial nanotube arrays. *Angewandte Chemie International Edition* 54: 841-845.

Kazuhito, H., Hiroshi, I. and Akira, F. 2005. TiO_2 photocatalysis: a historical overview and future prospects. *Japanese Journal of Applied Physics* 44: 8269-8285.

Kenarsari, S.D., Yang, D., Jiang, G., Zhang, S., Wang, J., Russell, A.G., Wei, Q. and Fan, M. 2013. Review of recent advances in carbon dioxide separation and capture. *RSC Advances* 3: 22739-22773.

Kho, Y.K., Iwase, A., Teoh, W.Y., Mädler, L., Kudo, A. and Amal, R. 2010. Photocatalytic H_2 evolution over TiO_2 nanoparticles. The synergistic effect of anatase and rutile. *The Journal of Physical Chemistry C* 114: 2821-2829.

Kim, C., Moon, B.K., Park, J., Choi, B. and Seo, H. 2003. Solvothermal synthesis of nanocrystalline TiO_2 in toluene with surfactant. *Journal of Crystal Growth* 257: 309-315.

Koci, K., Mateju, K., Obalova, L., Krejcikova, S., Lacny, Z., Placha, D., Capek, L., Hospodkova, A. and Solcova, O. 2010. Effect of silver doping on the TiO_2 for photocatalytic reduction of CO_2. *Applied Catalysis B* 96: 239-244.

Koci, K., Obalova, L. and Lacny, Z. 2008. Photocatalytic reduction of CO_2 over TiO_2 based catalysts. *Chemical Papers* 62: 1-9.

Kočí, K., Obalová, L., Matějová, L., Plachá, D., Lacný, Z., Jirkovský, J. and Šolcová, O. 2009. Effect of TiO_2 particle size on the photocatalytic reduction of CO_2. *Applied Catalysis B* 89: 494-502.

Kohno, Y., Tanaka, T., Funabiki, T. and Yoshida, S. 2000a. Photoreduction of CO_2 with H_2 over ZrO_2. A study on interaction of hydrogen with photoexcited CO_2. *Physical Chemistry Chemical Physics* 2: 2635-2639.

Kohno, Y., Tanaka, T., Funabiki, T. and Yoshida, S. 2000b. "Reaction mechanism in the photoreduction of CO_2 with CH_4 over ZrO_2. *Physical Chemistry Chemical Physics* 2: 5302-5307.

Koirala, A.R., Docao, S., Lee, S.B. and Yoon, K.B. 2015. Fate of methanol under one-pot artificial photosynthesis condition with metal-loaded TiO_2 as photocatalysts. *Catalysis Today* 243: 235-250.

Kong, M., Li, Y., Chen, X., Tian, T., Fang, P., Zheng, F. and Zhao, X. 2011. Tuning the relative concentration ratio of bulk defects to surface defects in TiO_2 nanocrystals leads to high photocatalytic efficiency. *Journal of the American Chemical Society* 133: 16414-16417.

Koppenol, W.H., and Rush, J.D. 1987. Reduction potential of the carbon dioxide/carbon dioxide radical anion: a comparison with other C1 radicals. *The Journal of Physical Chemistry* 91: 4429-4430.

Kresse, G., and Furthmüller, J. 1996a. Efficiency of ab-initio total energy calculations for metals and semiconductors using a plane-wave basis set. *Computational Materials Science* 6: 15-50.

Kresse, G., and Furthmüller, J. 1996b. Efficient iterative schemes for ab initio total-energy calculations using a plane-wave basis set. *Physical Review B* 54: 11169-11186.

Kresse, G., and Hafner, J. 1993. Abinitio molecular-dynamics for liquid-metals. *Physical Review B* 47: 558-561.

Kresse, G., and Hafner, J. 1994. Ab-initio molecular-dynamics simulation of the liquid-metal amorphous-semiconductor transition in germanium. *Physical Review B* 49: 14251-14269.

Kresse, G., and Joubert, D. 1999. From ultrasoft pseudopotentials to the projector augmented-wave method. *Physical Review B* 59: 1758-1775.

Krupa, S. V., and Kickert, R.N. 1989. The greenhouse effect: impacts of ultraviolet-B (UV-B) radiation, carbon dioxide (CO_2), and ozone (O_3) on vegetation. *Environmental Pollution* 61: 263-393.

Kuai, L., Zhou, Y., Tu, W., Li, P., Li, H., Xu, Q., Tang, L., Wang, X., Xiao, M. and Zou, Z. 2015. Rational construction of a CdS/reduced graphene oxide/TiO_2 core-shell nanostructure as an all-solid-state Z-scheme system for CO_2 photoreduction into solar fuels. *RSC Advances* 5: 88409-88413.

Kumar, P., Singh, G., Tripathi, D. and Jain, S.L. 2014. Visible light driven photocatalytic oxidation of thiols to disulfides using iron phthalocyanine immobilized on graphene oxide as a catalyst under alkali-free conditions. *RSC Advances* 4: 50331-50337.

Kumar, S.G., and Devi, L.G. 2011. Review on modified TiO_2 photocatalysis under UV/visible light: selected results and related mechanisms on interfacial charge carrier transfer dynamics *The Journal of Physical Chemistry A* 115: 13211-13241.

Kwak, B.S., Vignesh, K., Park, N., Ryu, H., Baek, J. and Kang, M. 2015. Methane formation from photoreduction of CO_2 with water using TiO_2 including Ni ingredient *Fuel* 143: 570-576.

Kwon, S., Liao, P.L., Stair, P.C. and Snurr, R.Q. 2016. Alkaline-earth metal-oxide overlayers on TiO_2: application toward CO_2 photoreduction. *Catalysis Science & Technology* 6: 7885-7895.

Lacis, A.A., Schmidt, G.A., Rind, D. and Ruedy, R.A. 2010. Atmospheric CO_2: principal control knob governing earth's temperature. *Science* 330: 356-359.

Lan, B.Y. and Shi, H.F. 2014. Review of systems for photocatalytic conversion of CO_2 to hydrocarbon fuels. *Acta Physico-Chimica Sinica* 30: 2177-2196.

Laudise, R.A. 1970. *The Growth of Single Crystals*. New Jersey: Prentice Hall Inc, 352 pp.

Leary, R. and Westwood, A. 2011. Carbonaceous nanomaterials for the enhancement of TiO_2 photocatalysis. *Carbon* 49: 741-772.

Lee, C., Wei, X., Kysar, J.W. and Hone, J. 2008. Measurement of the elastic properties and intrinsic strength of monolayer graphene. *Science* 321: 385-388.

Lee, C., Kourounioti, R.A., Wu, J.C.S., Murchie, E., Maroto-Valer, M., Jensen, O.E., Huang, C. and Ruban, A. 2014. Photocatalytic conversion of CO_2 to hydrocarbons by light-harvesting complex assisted Rh-doped TiO_2 photocatalyst. *Journal of CO_2 Utilization* 5: 33-40.

Lee, J., Back, H., Kong, J., Kang, H., Song, S., Suh, H., Kang, S. and Lee, K. 2013. Seamless polymer solar cell module architecture built upon self-aligned alternating interfacial layers. *Energy & Environmental Science* 6: 1152-1157.

Lee, S. C., Choi, B.Y., Lee, T.J., Ryu, C.K., Ahn, Y.S. and Kim, J.C. 2006. CO_2 absorption and regeneration of alkali metal-based solid sorbents. *Catalysis Today* 111: 385-390.

Leofanti, G., Padovan, M., Tozzola, G. and Venturelli, B. 1998. Surface area and pore texture of catalysts. *Catalysis Today* 41: 207-219.

Leong, K.H., Sim, L.C., Bahnemann, D., Jang, M., Ibrahim, S. and Saravanan, P. 2015. Reduced graphene oxide and Ag wrapped TiO_2 photocatalyst for enhanced visible light photocatalysis. *APL Materials* 3: 104503 (1-8).

Lewis, N.S. and Nocera, D.G. 2006. Powering the planet: chemical challenges in solar energy utilisation. *Proceedings of the National Academy of Sciences* 103: 15729-15735.

Li, G., Ciston, S., Saponjic, Z.V., Chen, L., Dimitrijevic, N.M., Rajh, T. and Gray, K.A. 2008. Synthesising mixed-phase TiO_2 nanocomposites using a hydrothermal method for photo-oxidation and photoreduction applications. *Journal of Catalysis* 253: 105-110.

Li, H., Dai, Y.J., Köhler, M. and Wang, R.Z. 2013. Simulation and parameter analysis of a two-stage desiccant cooing/heating system driven by solar air collectors. *Energy Conversion and Management* 67: 309-317.

Li, K., Lin, L., Peng, T., Guo, Y., Li, R. and Zhang, J. 2015. Asymmetric zinc porphyrin-sensitised nanosized TiO_2 for efficient visible-light-driven CO_2 photoreduction to CO/CH_4. *Chemical Communications* 51: 12443-12446.

Li, H.L., Wu, X.Y., Wang, J., Gao, Y., Li, L.Q and Shih, K.M. 2016. Enhanced activity of Ag-MgO-TiO_2 catalyst for photocatalytic conversion of CO_2 and H_2O into CH_4. *International Journal of Hydrogen Energy* 41: 8479-8488.

Li, Y.J., Li, R.Z., Li, C.W., Chen, W. and Zeng, M.X. 2012. Carbon nanotube/titania composites prepared by a micro-emulsion method exhibiting improved photocatalytic activity.*Applied Catalysis A* 427: 1-7.

Li, Q., Zong, L., Li, C. and Yang, J. 2014. Photocatalytic reduction of CO_2 on MgO/TiO_2 nanotube films. *Applied Surface Science* 319: 16-20.

Liang, Y.T., Vijayan, B.K., Gray, K.A. and Hersam, M.C. 2011. Minimising graphene defects enhances titania nanocomposite-based photocatalytic reduction of CO_2 for improved solar fuel production. *Nano Letters* 11: 2865-2870.

Liang, Y.T., Vijayan, B.K., Lyandres, O., Gray, K.A. and Hersam, M.C. 2012. Effect of dimensionality on the photocatalytic behaviour of carbon–titania nanosheet composites: charge transfer at nanomaterial interfaces. *The Journal of Physical Chemistry Letters* 3: 1760-1765.

Liao, Y., Cao, S.W., Yuan, Y., Gu, Q., Zhang, Z. and Xue, C. 2014. Efficient CO_2 capture and photoreduction by amine-functionalized TiO_2. *Chemistry* 20: 10220-10222.

Lin, C., Song, Y., Cao, L. and Chen, S. 2013. Effective photocatalysis of functional nanocomposites based on carbon and TiO_2 nanoparticles. *Nanoscale* 5: 4986-4992.

Lingampalli, S.R., Ayyub, M.M. and Rao, C.N.R. 2017. Recent progress in the photocatalytic reduction of carbon dioxide. *ACS Omega* 2: 2740-2748.

Linsebigler, A.L., Lu, G.Q. and Yates, J.T. 1995. Photocatalysis on TiO_2 surfaces: principles, mechanisms, and selected results. *Chemical Reviews* 95: 735-758.

Litter, M.I. and Navío, J.A. 1996. Photocatalytic properties of iron-doped titania semiconductors. *Journal of Photochemistry and Photobiology A: Chemistry* 98: 171-181.

Liu, G., Zhao, Y., Sun, C., Li, F., Lu, G.Q. and Cheng, H.M. 2008a. Synergistic effects of B/N doping on the visible-light photocatalytic activity of mesoporous TiO_2. *Angewandte Chemie International Edition* 47: 4516-4520.

Liu, G., Du, K., Haussener, S. and Wang, K. 2016. Charge transport in two-photon semiconducting structures for solar fuels. *ChemSusChem* 9: 2878-2904.

Liu, L., Zhao, C., Zhao, H., Pitts, D. and Li, Y. 2013. Porous microspheres of MgO-patched TiO_2 for CO_2 photoreduction with H_2O vapour: temperature-dependent activity and stability. *Chemical Communication* 49: 3664-3666.

Liu, L., Fan, W., Zhao, X., Sun, H., Li, P. and Sun, L. 2012a. Surface dependence of CO_2 adsorption on Zn_2GeO_4. *Langmuir* 28: 10415-10424.

Liu, L., Zhao, C. and Li, Y. 2012b. Spontaneous dissociation of CO_2 to CO on defective surface of Cu(I)/TiO_{2-x} nanoparticles at room temperature. *The Journal of Physical Chemistry C* 116: 7904-7912.

Liu, L., Zhao, H., Andino, J.M. and Li, Y. 2012c. Photocatalytic CO_2 reduction with H_2O on TiO_2 nanocrystals: comparison of anatase, rutile, and brookite polymorphs and exploration of surface chemistry. *ACS Catalysis* 2: 1817-1828.

Liu, L., Zhao, C., Xu, J. and Li, Y. 2015. Integrated CO_2 capture and photocatalytic conversion by a hybrid adsorbent/photocatalyst material. *Applied Catalysis B* 179: 489-499.

Liu, N., Schneider, C., Freitag, D., Hartmann, M., Venkatesan, U., Muller, J., Spiecker, E. and Schmuki, P. 2014. Black TiO_2 nanotubes: cocatalyst-free open-circuit hydrogen generation. *Nano Letters* 14: 3309-3313.

Liu, X., Lu, G.Q., Yan, Z. and Beltramini, J. 2003. Recent advances in catalysts for methanol synthesis via hydrogenation of CO and CO_2. *Industrial & Engineering Chemistry Research* 42: 6518-6530.

Liu, X., Wang, M., Zhang, S. and Pan, B. 2013. Application potential of carbon nanotubes in water treatment: a review. *Journal of Environmental Sciences* 25: 1263-1280.

Liu, Z., Robinson, J.T., Sun, X. and Dai, H. 2008b. PEGylated nanographene oxide for delivery of water-insoluble cancer drugs. *Journal of American Chemical Society* 130: 10876-10877.

Low, J., Cheng, B. and Yu, J. 2017. Surface modification and enhanced photocatalytic CO_2 reduction performance of TiO_2: a review. *Applied Surface Science* 392: 658-686.

Lowell, S. and Shields, J.E. 1991. *Powder Surface Area and Porosity*. 3rd ed. Netherlands: Springer, 252 pp.

Luo, L.J., Yang, Y., Zhang, A., Wang, M., Liu, Y.J., Bian, L.C., Jiang, F.Z. and Pan, X.J. 2015. Hydrothermal synthesis of fluorinated anatase TiO_2/reduced graphene oxide nanocomposites and their photocatalytic degradation of bisphenol A. *Applied Surface Science* 353: 469-479.

Macwan, D.P., Dave, P.N. and Chaturvedi, S. 2011. A review on nano-TiO_2 sol-gel type syntheses and its applications. *Journal of Materials Science* 46: 3669-3686.

Maginn, E.J. 2010. What to Do with CO_2. *The Journal of Physical Chemistry Letters* 1: 3478-3479.

Malato, S., Fernández-Ibáñez P., Maldonado, M.I., Blanco, J. and Gernjak, W. 2009. Decontamination and disinfection of water by solar photocatalysis: recent overview and trends. *Catalysis Today* 147: 1-59.

Manbeck, G.F. and Fujita, E. 2015. A review of iron and cobalt porphyrins, phthalocyanines and related complexes for electrochemical and photochemical reduction of carbon dioxide. *Journal of Porphyrins and Phthalocyanines* 19: 45-64.

Mao, J., Li, K. and Peng, T. 2013. Recent advances in the photocatalytic CO_2 reduction over semiconductors. *Catalysis Science & Technology* 3: 2481-2498.

Mason, T.J. 2007. Sonochemistry and the environment – providing a "green" link between chemistry, physics and engineering. *Ultrasonics Sonochemistry* 14: 476-483.

Matejova, L., Koci, K., Reli, M., Capek, L., Hospodkova, A., Peikertova, P., Matej, Z., Obalova, L., Wach, A., Kustrowski, P. and Kotarba, A. 2014. Preparation, characterisation and photocatalytic properties of cerium-doped TiO_2: on the effect of Ce loading on the photocatalytic reduction of carbon dioxide. *Applied Catalysis B* 152: 172-183.

Meagher, E.P. and Lager, G.A. 1979. Polyhedral thermal expansion in the TiO_2 polymorphs: refinement of the crystal structures of rutile and brookite at high temperature. *Canadian Mineralogist* 17: 77-85.

Meng, X., Ouyang, S., Kako, T., Li, P., Yu, Q., Wang, T. and Ye, J. 2014. Photocatalytic CO_2 conversion over alkali modified TiO_2 without loading noble metal cocatalyst. *Chemical Communications* 50: 11517-11519.

Mercer, J.H. 1978. West Antarctic ice sheet and CO_2 greenhouse effect: a threat of disaster. *Nature* 271: 321-325.

Mikkelsen, M., Jorgensen, M. and Krebs, F.C. 2010. The teraton challenge. A review of fixation and transformation of carbon dioxide. *Energy & Environmental Science* 3: 43-81.

Mitchell, J.F.B. 1989. The "Greenhouse" effect and climate change. *Reviews of Geophysics* 27: 115-139.

Mori, K., Yamashita, H. and Anpo, M. 2012. Photocatalytic reduction of CO_2 with H_2O on various titanium oxide photocatalysts. *RSC Advances* 2: 3165-3172.

Morris, A.J., Meyer, G.J. and Fujita, E. 2009. Molecular approaches to the photocatalytic reduction of carbon dioxide for solar fuels. *Accounts of Chemical Research* 42: 1983-1994.

MrGeogWagg geography. June, 2015. Retrieved on Oct. 13, 2018, from https://mrgeogwagg.wordpress.com/2015/06/24/greenhouse-effect-and-anthropogenic-warming/

Nakata, K. and Fujishima, A. 2012. TiO_2 photocatalysis: design and applications. *Journal of Photochemistry and Photobiology C: Photochemistry Reviews* 13: 169-189.

Nam, L.T.H., Vinh, T.Q., Loan, N.T.T., Tho, V.D.S., Yang, X. and Su, B. 2011. Preparation of bio-fuels by catalytic cracking reaction of vegetable oil sludge. *Fuel* 90: 1069-1075.

Narayanan, H., Viswanathan, B. and Yesodharan, S. 2006. Photocatalytic reduction of carbon dioxide: issues and prospects. *Current Catalysis* 5: 79-107.

National Aeronautics and Space Administration (NASA) and Goddard Institute for Space Studies (GISS). 2018. Retrieved on Feb. 9, 2018 from https://data.giss.nasa.gov/gistemp/.

Nguyen-Phan, T.D., Pham, V.H., Chung, J.S., Chhowalla, M., Asefa, T., Kim, W.J. and Shin, E.W. 2014. Photocatalytic performance of Sn-doped TiO_2/reduced graphene oxide composite materials. *Applied Catalysis A* 473: 21-30.

Niu, Y., Xing, M., Zhang, J. and Tian, B. 2013. Visible light activated sulfur and iron co-doped TiO_2 photocatalyst for the photocatalytic degradation of phenol. *Catalysis Today* 201: 159-166.

Nourbakhsh, A., Abbaspour, S., Masood, M., Mirsattari, S.N., Vahedi, A. and Mackenzie, K.J.D. 2016. Photocatalytic properties of mesoporous TiO_2 nanocomposites modified with carbon nanotubes and copper. *Ceramics International* 42: 11901-11906.

Novoselov, K.S., Geim, A.K., Morozov, S.V., Jiang, D., Zhang, Y., Dubonos, S.V., Grigorieva, I.V. and Firsov, A.A. 2004. Electric field effect in atomically thin carbon films. *Science* 306: 666-669.

Oh, Y. J., Yoo, J.J., Kim, Y., Yoon, J.K., Yoon, H.N., Kim, J. and Park, S.B. 2014. Oxygen functional groups and electrochemical capacitive behaviour of incompletely reduced graphene oxides as a thin-film electrode of supercapacitor. *Electrochimica Acta* 116: 118-128.

Ohno, T., Akiyoshi, M., Umebayashi, T., Asai, K., Mitsui, T. and Matsumura, M. 2004. Preparation of S-doped TiO_2 photocatalysts and their photocatalytic activities under visible light. *Applied Catalysis A* 265: 115-121.

Omidvar, H., Mirzaei, F.K., Rahimi, M.H. and Sadeghian, Z. 2012. A method for coating carbon nanotubes with titanium. *New Carbon Materials* 27: 401-408.

Ong, W., Gui, M.M., Chai, S. and Mohamed, A.R. 2013. Direct growth of carbon nanotubes on Ni/TiO_2 as next-generation catalysts for photoreduction of CO_2 to methane by water under visible light irradiation. *RSC Advances* 3: 4505-4509.

Ortega, Y., Hernandez, N.C., Menendez-Proupin, E., Graciani, J. and Sanz, J.F. 2011. Nitrogen/gold codoping of the TiO_2(101) anatase surface. A theoretical study based on DFT calculations. *Physical Chemistry Chemical Physics* 13: 11340-11350.

Ozcan, O., Yukruk, F., Akkaya, E.U. and Uner, D. 2007a. Dye-sensitized artificial photosynthesis in the gas phase over thin and thick TiO_2 films under UV and visible light irradiation. *Applied Catalysis B* 71: 291-297.

Ozcan, O., Yukruk, F., Akkaya, E.U. and Uner, D. 2007b. Dye-sensitised CO_2 reduction over pure and platinised TiO_2. *Topics in Catalysis* 44: 523-528.

Park, H., Ou, H.H., Kang, U., Choi, J. and Hoffmann, M.R. 2016. Photocatalytic conversion of carbon dioxide to methane on TiO_2/CdS in aqueous isopropanol solution. *Catalysis Today* 266: 153-159.

Pathak, P., Meziani, M.J., Castillo, L. and Sun, Y. 2005. Metal-coated nanoscale TiO_2 catalysts for enhanced CO_2 photoreduction. *Green Chemistry* 7: 667-670.

Paulino, P.N., Salim, V.M.M. and Resende, N.S. 2016. Zn-Cu promoted TiO_2 photocatalyst for CO_2 reduction with H_2O under UV light. *Applied Catalysis B* 185: 362-370.

Perdew, J.P., Burke, K. and Ernzerhof, M. 1996. Generalised gradient approximation made simple. *Physical Review Letters* 77: 3865-3868.

Perdew, J.P., Burke, K. and Ernzerhof, M. 1997. Generalised gradient approximation made simple. *Physical Review Letters* 78: 1396-1396.

Pierantozzi, R. 1993. Carbon Dioxide. In *Kirk-Othmer Encyclopedia of Chemical Technology*. 4th ed. New York: John Wiley & Sons, Inc, pp. 35-53.

Pipornpong, W., Wanbayor, R. and Ruangpornvisuti, V. 2011. Adsorption CO_2 on the perfect and oxygen vacancy defect surfaces of anatase TiO_2 and its photocatalytic mechanism of conversion to CO. *Applied Surface Science* 257: 10322-10328.

Porosoff, M.D., Yan, B. and Chen, J.G. 2016. Catalytic reduction of CO_2 by H_2 for synthesis of CO, methanol and hydrocarbons: challenges and opportunities. *Energy & Environmental Science* 9: 62-73.

Pyrgiotakis, G., Lee, S. and Sigmund, W. 2011. Advanced photocatalysis with anatase nano-coated multi-walled carbon nanotubes. *MRS Proceedings* 876: R5.7.1-R5.7.6.

Qi, K., Selvaraj, R., Al-Fahdi, T., Al-Kindy, S., Kim, Y., Wang, G., Tai, C. and Sillanpää, M. 2016. Enhanced photocatalytic activity of anatase-TiO_2 nanoparticles by fullerene modification: a theoretical and experimental study. *Applied Surface Science* 387: 750-758.

Qu, A., Xie, H., Xu, X., Zhang, Y., Wen, S. and Cui, Y. 2016. High quantum yield graphene quantum dots decorated TiO_2 nanotubes for enhancing photocatalytic activity. *Applied Surface Science* 375: 230-241.

Rajalakshmi, K, Jeyalakshmi, V., Krishnamurthy, K.R. and Viswanathan, B. 2012. Photocatalytic reduction of carbon dioxide by water on titania: role of photophysical and structural properties. *Indian Journal of Chemistry* 51A: 411-419.

Ramacharyulu, P., Kumar, J.P., Prasad, G.K. and Sreedhar, B. 2014. Sulphur doped nano TiO_2: synthesis, characterisation and photocatalytic degradation of a toxic chemical in presence of sunlight. *Materials Chemistry and Physics* 148: 692-698.

Ramimoghadam, D., Bagheri, S. and Hamid, S.B.A. 2014. Biotemplated synthesis of anatase titanium dioxide nanoparticles via lignocellulosic waste material. *BioMed Research International* 2014: 205636 (1-8).

Ran, J., Zhang, J., Yu, J., Jaroniec, M. and Qiao, S.Z. 2014. Earth-abundant cocatalysts for semiconductor-based photocatalytic water splitting. *Chemical Society Reviews* 43: 7787-7812.

Rankin, D.W.H. 2009. CRC handbook of chemistry and physics. 89th ed. Eds. Lide, D.R. *Crystallography Reviews* 15: 223-224.

Rasko, J. and Solymosi, F. 1994. Infrared spectroscopic study of the photoinduced activation of CO_2 on TiO_2 and Rh/TiO_2 catalysts. *The Journal of Physical Chemistry* 98: 7147-7152.

Razzaq, A., Grimes, C.A. and In, S.I. 2016. Facile fabrication of a noble metal-free photocatalyst: TiO_2 nanotube arrays covered with reduced graphene oxide. *Carbon* 98: 537-544.

Reñones, P., Moya, A., Fresno, F., Collado, L., Vilatela, J.J. and O'Shea, V.A. 2016. Hierarchical TiO_2 nanofibres as photocatalyst for CO_2 reduction: influence of morphology and phase composition on catalytic activity. *Journal of CO_2 Utilization* 15: 24-31.

Riedel, T., Schaub, G., Jun, K. and Lee, K. 2001. Kinetics of CO_2 hydrogenation on a K-promoted Fe catalyst. *Industrial & Engineering Chemistry Research* 40: 1355-1363.

Rodhe, H. 1990. A comparison of the contribution of various gases to the greenhouse effect. *Science* 248: 1217-1219.

Rosenzweig, C. and Hillel, D. 1998. *Climate change and the global harvest: potential impacts of the greenhouse effect on agriculture*. New York: Oxford University Press, 324 pp.

Rosseler, O., Shankar, M.V., Du, M.K., Schmidlin, L., Keller, N. and Keller, V. 2010. Solar light photocatalytic hydrogen production from water over Pt and Au/TiO_2(anatase/rutile) photocatalysts: influence of noble metal and porogen promotion. *Journal of Catalysis* 269: 179-190.

Roy, S.C., Varghese, O.K., Paulose, M. and Grimes, C.A. 2010. Toward solar fuels: photocatalytic conversion of carbon dioxide to hydrocarbons. *ACS Nano* 4: 1259-1278.

Roy, S., Das, T., Ming, Y., Chen, X., Yue, C.Y. and Hu, X. 2014. Specific functionalization and polymer grafting on multiwalled carbon nanotubes to fabricate advanced nylon 12 composites. *Journal of Materials Chemistry A* 2: 3961-3970.

Sadanandam, G., Lalitha, K., Kumari, V.D., Shankar, M.V. and Subrahmanyam, M. 2013. Cobalt-doped TiO_2: a stable and efficient photocatalyst for continuous hydrogen

production from glycerol: water mixtures under solar light irradiation. *International Journal of Hydrogen Energy* 38: 9655-9664.

Sakakura, T., Choi, J. and Yasuda, H. 2007. Transformation of carbon dioxide. *Chemical Reviews* 107: 2365-2387.

Sanz, J.F., Hernandez, N.C. and Marquez, A. 2000. A first-principles study of Pd deposition on the TiO_2(110) surface. *Theoretical Chemistry Accounts* 104: 317-322.

Sarkar, A., Gracia-Espino, E., Wagberg, T., Shchukarev, A., Mohl, M., Rautio, A.R., Pitkanen, O., Sharifi, T., Kordas, K. and Mikkola, J.P. 2016. Photocatalytic reduction of CO_2 with H_2O over modified TiO_2 nanofibers: understanding the reduction pathway. *Nano Research* 9: 1956-1968.

Schmidt, M.W., Baldridge, K.K., Boatz, J.A., Elbert, S.T., Gordon, M.S., Jensen, J.H., Koseki, S., Matsunaga, N., Nguyen, K.A., Su S., Windus, T.L., Dupuis, M. and Montgomery, J.A. 1993. General atomic and molecular electronic structure system. *Journal of Computational Chemistry* 14: 1347-1363.

Schneider, J., Matsuoka, M., Takeuchi, M., Zhang, J., Horiuchi, Y., Anpo, M. and Bahnemann, D.W. 2014. Understanding TiO_2 photocatalysis: mechanisms and materials. *Chemical Reviews* 114: 9919-9986.

Schneider, S.H. 1989. The greenhouse effect: science and policy. *Science* 243: 771-781.

Shafiullah, G.M., Amanullah, M.T.O., Ali, A.B.M.S., Jarvis, D. and Wolfs, P. 2012. Prospects of renewable energy – a feasibility study in the Australian context. *Renewable Energy* 39: 183-197.

Shah, M., Park, A.R., Zhang, K., Park, J.H. and Yoo, P.J. 2012. Green synthesis of biphasic TiO_2-reduced graphene oxide nanocomposites with highly enhanced photocatalytic activity. *ACS Applied Materials & Interfaces* 4: 3893-3901.

Shen, J.F., Yan, B., Shi, M., Ma, H.W., Li, N. and Ye, M.X. 2011. One step hydrothermal synthesis of TiO_2-reduced graphene oxide sheets. *Journal of Materials Chemistry* 21: 3415-3421.

Sher-Shah, M.S., Park, A.R., Zhang, K., Park, J.H. and Yoo, P.J. 2012. Green synthesis of biphasic TiO_2-reduced graphene oxide nanocomposites with highly enhanced photocatalytic activity. *ACS Applied Materials and Interfaces* 4: 3893-3901.

Shi, J., Jiang, Y., Jiang, Z., Wang, X., Wang, X., Zhang, S., Han, P. and Yang, C. 2015. Enzymatic conversion of carbon dioxide. *Chemical Society Reviews* 44: 5981-6000.

Singhal, N., Ali, A., Vorontsov, A., Pendem, C. and Kumar, U. 2016. Efficient approach for simultaneous CO and H_2 production via photoreduction of CO_2 with water over copper nanoparticles loaded TiO_2. *Applied Catalysis A* 523: 107-117.

Sofianou, M., Tassi, M., Boukos, N., Thanos, S., Vaimakis, T., Yu, J. and Trapalis, C. 2014. Solvothermal synthesis and photocatalytic performance of Mg^{2+}-doped anatase nanocrystals with exposed {001} facets. *Catalysis Today* 230: 125-130.

Spinner, N.S., Vega, J.A. and Mustain, W.E. 2012. Recent progress in the electrochemical conversion and utilisation of CO_2. *Catalysis Science & Technology* 2: 19-28.

Stewart, J.J. 2007. Optimisation of parameters for semiempirical methods V: modification of NDDO approximations and application to 70 elements. *Journal of Molecular Modeling* 13: 1173-1213.

Sun, M., Fu, W., Li, Q., Yin, G., Chi, K., Ma, J., Yang, L., Mu, Y., Chen, Y., Su, S., Zhang, W. and Yang, H. 2014. Embedded CdS nanorod arrays in PbS absorber layers: enhanced energy conversion efficiency in bulk heterojunction solar cells. *RSC Advances* 4: 7178-7184.

Suslick, K.S., Hyeon, T., Fang, M. and Cichowlas, A.A. 1995. Sonochemical synthesis of nanostructured catalysts. *Materials Science and Engineering: A* 204: 186-192.

Tahir, M., and Amin, N.S. 2013. Advances in visible light responsive titanium oxide-based photocatalysts for CO_2 conversion to hydrocarbon fuels. *Energy Conversion and Management* 76: 194-214.

Tahir, M., and Amin, N.S. 2015a. Indium-doped TiO_2 nanoparticles for photocatalytic CO_2 reduction with H_2O vapours to CH_4. *Applied Catalysis B* 162: 98-109.

Tahir, M., and Amin, N.S. 2015b. Photocatalytic CO_2 reduction with H_2 as reductant over copper and indium co-doped TiO_2 nanocatalysts in a monolith photoreactor. *Applied Catalysis A* 493: 90-102.

Tahir, M., Tahir, B. and Amin, N.S. 2015c. Photocatalytic CO_2 reduction by CH_4 over montmorillonite modified TiO_2 nanocomposites in a continuous monolith photoreactor." *Materials Research Bulletin* 63: 13-23.

Tahir, M., Tahir, B. and Amin, N.A. 2015d. Gold–indium modified TiO_2 nanocatalysts for photocatalytic CO_2 reduction with H_2 as reductant in a monolith photoreactor. *Applied Surface Science* 338: 1-14.

Taleshi, F. 2015. Study of morphology and band gap energy of TiO_2-carbon nanotube nanocomposite. *Journal of Materials Science-Materials in Electronics* 26: 3262-3267.

Tan, L.L., Ong, W.J., Chai, S.P. and Mohamed, A.R. 2015a. Noble metal modified reduced graphene oxide/TiO_2 ternary nanostructures for efficient visible-light-driven photoreduction of carbon dioxide into methane. *Applied Catalysis B* 166: 251-259.

Tan, L., Ong, W., Chai, S., Goh, B.T. and Mohamed, A.R. 2015b. Visible-light-active oxygen-rich TiO_2 decorated 2D graphene oxide with enhanced photocatalytic activity toward carbon dioxide reduction. *Applied Catalysis B* 179: 160-170.

Tan, L., Ong, W., Chai, S. and Mohamed, A.R. 2016. Visible-light-activated oxygen-rich TiO_2 as next-generation photocatalyst: importance of annealing temperature on the photoactivity toward reduction of carbon dioxide. *Chemical Engineering Journal* 283: 1254-1263.

Tanaka, K. and Ooyama, D. 2002. Multi-electron reduction of CO_2 via $RuCO_2$,C(O)OH, CO, CHO, and CH_2OH species. *Coordination Chemistry Reviews* 226: 211-218.

Tang, H., Hessel, C.M., Wang, J., Yang, N., Yu, R., Zhao, H. and Wang, D. 2014. Two-dimensional carbon leading to new photoconversion processes. *Chemical Society Reviews* 43: 4281-4299.

Teramura, K., Tanaka, T., Ishikawa, H., Kohno, Y. and Funabiki, T. 2004. Photocatalytic reduction of CO_2 to CO in the presence of H_2 or CH_4 as a reductant over MgO. *Journal of Physical Chemistry B* 108: 346-354.

Thampi, K.R., Kiwi, J. and Gratzel, M. 1987. Methanation and photo-methanation of carbon dioxide at room temperature and atmospheric pressure. *Nature* 327: 506-508.

The intergovernmental panel on climate change's fifth assessment report on climate change. 2014. Retrieved on Oct. 20, 2018, from https://www.ipcc.ch/report/ar5/wg3/.

The Keeling curve from the Scripps Institution of Oceanography. 2019. Retrieved on Jan. 25, 2019, from https://scripps.ucsd.edu/programs/keelingcurve/.

Thomas, A. G., Flavell, W.R., Mallick, A.K., Kumarasinghe, A.R., Tsoutsou, D., Khan, N., Chatwin, C., Rayner, S., Smith, G.C., Stockbauer, R.L., Warren, S., Johal, T.K., Patel, S., Holland, D., Taleb, A. and Wiame, F. 2007. Comparison of the electronic structure of anatase and rutile TiO_2 single-crystal surfaces using resonant photoemission and x-ray absorption spectroscopy. *Physical Review B* 75: 035105 (1-12).

Thostenson, E.T. and Chou, T.W. 1999. Microwave processing: fundamentals and applications. *Composites Part A: Applied Science and Manufacturing* 30: 1055-1071.

Thostenson, E.T., Ren, Z. and Chou, T. 2001. Advances in the science and technology of carbon nanotubes and their composites: a review. *Composites Science and Technology* 61: 1899-1912.

Tian, B., Yang, H., Liu, X., Xie, S., Yu, C., Fan, J., Tu, B. and Zhao, D. 2002. Fast preparation of highly ordered nonsiliceous mesoporous materials via mixed inorganic precursors. *Chemical Communications.* 17: 1824-1825.

Tkatchenko, A. and Scheffler, M. 2009. Accurate molecular van der waals interactions from ground-state electron density and free-atom reference data. *Physical Review Letters* 102: 073005 (1-4).

Truong, Q.D., Le, T.H., Liu, J., Chung, C. and Ling, Y. 2012. Synthesis of TiO_2 nanoparticles using novel titanium oxalate complex towards visible light-driven photocatalytic reduction of CO_2 to CH_3OH. *Applied Catalysis A* 437-438: 28-35.

Tseng, I.H. and Wu, J.C.S. 2004. Chemical states of metal-loaded titania in the photoreduction of CO_2. *Catalysis Today* 97: 113-119.

Tu, W.G., Zhou, Y., Liu, Q., Tian, Z.P., Gao, J., Chen, X.Y., Zhang, H.T., Liu, J.G. and Zou, Z.G. 2012. Robust hollow spheres consisting of alternating titania nanosheets and graphene nanosheets with high photocatalytic activity for CO_2 conversion into renewable fuels. *Advanced Functional Materials* 22: 1215-1221.

Tu, W.G., Zhou, Y. and Zou, Z.G. 2014. Photocatalytic conversion of CO_2 into renewable hydrocarbon fuels: state-of-the-art accomplishment, challenges, and prospects. *Advanced Materials* 26: 4607-4626.

Tu, W.G., Zhou, Y., Liu, Q., Yan, S., Bao, S., Wang, X., Xiao, M. and Zou, Z. 2013. An in situ simultaneous reduction-hydrolysis technique for fabrication of TiO_2-graphene 2d sandwich-like hybrid nanosheets: graphene-promoted selectivity of photocatalytic-driven hydrogenation and coupling of CO_2 into methane and ethane. *Advanced Functional Materials* 23: 1743-1749.

Vasilaki, E., Georgaki, I., Vernardou, D., Vamvakaki, M. and Katsarakis, N. 2015. Ag-loaded TiO_2/reduced graphene oxide nanocomposites for enhanced visible-light photocatalytic activity. *Applied Surface Science* 353: 865-872.

Vijayan, B.K., Dimitrijevic, N.M., Finkelstein-Shapiro, D., Wu, J. and Gray, K.A. 2012. Coupling titania nanotubes and carbon nanotubes to create photocatalytic nanocomposites. *ACS Catalysis* 2: 223-229.

Vorontsov, A.V. 2017. Structural and electronic effects in acetone adsorption over TiO_2 anatase clusters as the first stage of photocatalytic oxidation. *Journal of Nanoparticle Research* 19: 326 (1-22).

Vorontsov, A.V. and Smirniotis, P.G. 2018a. Size and surface groups effects in decahedral anatase nanoparticles for photocatalytic applications. *Journal of Photochemistry and Photobiology A: Chemistry* 363: 51-60.

Vorontsov, A.V. and Tretyakov, E.V. 2018b. Determination of graphene's edge energy using hexagonal graphene quantum dots and PM7 method. *Physical Chemistry Chemical Physics* 20: 14740-14752.

Vorontsov, A.V. and Tsybulya, S.V. 2018c. Influence of nanoparticles size on XRD patterns for small monodisperse nanoparticles of Cu0 and TiO_2 anatase. *Industrial & Engineering Chemistry Research* 57: 2526-2536.

Wang, A.J., Yu, W., Fang, Y., Song, Y.L., Jia, D., Long, L.L., Cifuentes, M.P., Humphrey, M.G. and Zhang, C. 2015. Facile hydrothermal synthesis and optical limiting properties of TiO_2-reduced graphene oxide nanocomposites. *Carbon* 89: 130-141.

Wang, C., Thompson, R.L., Ohodnicki, P., Baltrus, J. and Matranga, C. 2011a. Size-dependent photocatalytic reduction of CO_2 with PbS quantum dot sensitised TiO_2 heterostructured photocatalysts. *Journal of Materials Chemistry* 21: 13452-13457.

Wang, W., Park, J. and Biswas, P. 2011b. Rapid synthesis of nanostructured Cu-TiO_2-SiO_2 composites for CO_2 photoreduction by evaporation driven self-assembly. *Catalysis Science & Technology* 1: 593-600.

Wang, D.T., Li, X., Chen, J.F. and Tao, X. 2012. Enhanced photoelectrocatalytic activity of reduced graphene oxide/TiO_2 composite films for dye degradation. *Chemical Engineering Journal* 198: 547-554.

Wang, F., Zhou, Y., Li, P., Kuai, L.B. and Zou, Z.G. 2016a. Synthesis of bionic-macro/microporous MgO-modified TiO_2 for enhanced CO_2 photoreduction into hydrocarbon fuels. *Chinese Journal of Catalysis* 37: 863-868.

Wang, P.F., Zhan, S.H., Xia, Y.G., Ma, S.L., Zhou, Q.X. and Li, Y. 2017a. The fundamental role and mechanism of reduced graphene oxide in rGO/Pt-TiO_2 nanocomposite for high-performance photocatalytic water splitting. *Applied Catalysis B* 207: 335-346.

Wang, P., Wang, J., Wang, X.F., Yu, H.G., Yu, J.G., Lei, M. and Wang, Y.G. 2013a. One-step synthesis of easy-recycling TiO_2-rGO nanocomposite photocatalysts with enhanced photocatalytic activity. *Applied Catalysis B* 132: 452-459.

Wang, W.K., Chen, J.J., Zhang, X., Huang, Y.X., Li, W.W. and Yu, H.Q. 2016b. Self-induced synthesis of phase-junction TiO_2 with a tailored rutile to anatase ratio below phase transition temperature. *Scientific Reports* 6: 20491 (1-10).

Wang, W.L., Wang, Z.F., Liu, J.J., Luo, Z., Sui, S.L., He, P., Ding, G.Q., Zhang, Z.G. and Sun, L.Y. 2017b. Single-step one-pot synthesis of TiO_2 nanosheets doped with sulfur on reduced graphene oxide with enhanced photocatalytic activity. *Scientific Reports* 7: 46610 (1-9).

Wang, W., Serp, P., Kalck, P. and Faria, J.L. 2005. Visible light photodegradation of phenol on MWNT-TiO_2 composite catalysts prepared by a modified sol-gel method. *Journal of Molecular Catalysis A: Chemical* 235: 194-199.

Wang, X.Y., Wang, J., Dong, X.L., Zhang, F., Ma, L.G., Fei, X., Zhang, X.F. and Ma, H.C. 2016c. Synthesis and catalytic performance of hierarchical TiO_2 hollow sphere/reduced graphene oxide hybrid nanostructures. *Journal of Alloys and Compounds* 656: 181-188.

Wang, Y., Li, B., Zhang, C., Cui, L., Kang, S., Li, X. and Zhou, L. 2013b. Ordered mesoporous CeO_2-TiO_2 composites: highly efficient photocatalysts for the reduction of CO_2 with H_2O under simulated solar irradiation. *Applied Catalysis B: Environmental* 130-131: 277-284.

Woan, K., Pyrgiotakis, G. and Sigmund, W. 2009. Photocatalytic carbon-nanotube-TiO_2 composites. *Advanced Materials* 21: 2233-2239.

Wonyong, C., Andreas, T. and Michael H. R. 1994. Effects of metal-ion dopants on the photocatalytic reactivity of quantum-sized TiO_2 particles. *Angewandte Chemie International Edition* 33: 1091-1092.

Woolerton, T.W., Sheard, S., Reisner, E., Pierce, E., Ragsdale, S.W. and Armstrong, F.A. 2010. Efficient and clean photoreduction of CO_2 to CO by enzyme-modified TiO_2 nanoparticles using visible light. *Journal of the American Chemical Society* 132: 2132-2133.

Wu, H., Bai, H. and Wu, J.C.S. 2014. Photocatalytic reduction of CO_2 using Ti-MCM-41 photocatalysts in monoethanolamine solution for methane production. *Industrial & Engineering Chemistry Research* 5: 11221-11227.

Wyckoff, R.W.G. 1964. *Crystal Structures* 2nd ed.New York: John Wiley & Sons, 506 pp.

Xi, G., Ouyang, S. and Ye, J. 2011. General synthesis of hybrid TiO_2 mesoporous "french fries" toward improved photocatalytic conversion of CO_2 into hydrocarbon fuel: a case of TiO_2/ZnO. *Chemistry* 17: 9057-9061.

Xia, T., Li, N., Zhang, Y., Kruger, M.B., Murowchick, J., Selloni, A. and Chen, X. 2013. Directional heat dissipation across the interface in anatase-rutile nanocomposites. *ACS Applied Materials and Interfaces* 5: 9883-9890.

Xiang, Q.J., Cheng, B. and Yu, J.G. 2015. Graphene-based photocatalysts for solar-fuel generation. *Angewandte Chemie International Edition* 54: 11350-11366.

Xiao, S., Zhu, W., Liu, P., Liu, F., Dai, W., Zhang, D., Chen, W. and Li, H. 2016. CNTs threaded (001) exposed TiO_2 with high activity in photocatalytic NO oxidation. *Nanoscale* 8: 2899-2907.

Xie, S.J., Wang, Y., Zhang, Q.H., Deng, W.P. and Wang, Y. 2014. MgO- and Pt-promoted TiO_2 as an efficient photocatalyst for the preferential reduction of carbon dioxide in the presence of water. *ACS Catalysis* 4: 3644-3653.

Xing, M., Shen, F., Qiu, B. and Zhang, J. 2014. Highly-dispersed boron-doped graphene nanosheets loaded with TiO_2 nanoparticles for enhancing CO_2 photoreduction. *Scientific Reports* 4: 6341 (1-7).

Xiong, Z., Luo, Y., Zhao, Y., Zhang, J., Zheng, C. and Wu, J.C. 2016. Synthesis, characterisation and enhanced photocatalytic CO_2 reduction activity of graphene supported TiO_2 nanocrystals with coexposed {001} and {101} facets. *Physical Chemistry Chemical Physics* 18: 13186-13195.

Xu, H., Ouyang, S., Li, P. Kako, T. and Ye, J. 2013. High-active anatase TiO_2 nanosheets exposed with 95% {100} facets toward efficient H_2 evolution and CO_2 photoreduction. *ACS Applied Materials & Interfaces* 5: 1348-1354.

Xu, J., Li, J., Dai, W., Cao, Y., Li, H. and Fan, K. 2008. Simple fabrication of twist-like helix N, S-codoped titania photocatalyst with visible-light response. *Applied Catalysis B: Environmental* 79: 72-80.

Xu, S., Shangguan, W., Yuan, J., Chen, M. and Shi, J. 2007. Preparations and photocatalytic properties of magnetically separable nitrogen-doped TiO_2 supported on nickel ferrite. *Applied Catalysis B* 71: 177-184.

Xue, L.M., Zhang, F.H., Fan, H.J. and Bai, X.F. 2011. Preparation of C doped TiO_2 photocatalysts and their photocatalytic reduction of carbon dioxide. *Advanced Materials Research* 183-185: 18421846.

Yan, Y., Yu, Y., Cao, C., Huang, S., Yang, Y., Yang, X. and Cao, Y. 2016. Enhanced photocatalytic activity of TiO_2-Cu/C with regulation and matching of energy levels by carbon and copper for photoreduction of CO_2 into CH_4. *CrystEngComm* 18: 2956-2964.

Yang, C., Tse, M., Wei, X. and Hao, J. 2017. Colossal permittivity of (Mg + Nb) co-doped TiO_2 ceramics with low dielectric loss. *Journal of Materials Chemistry C* 5: 5170-5175.

Yang, M.Q., Zhang, N. and Xu, Y.J. 2013. Synthesis of fullerene-, carbon nanotube-, and graphene-TiO_2 nanocomposite photocatalysts for selective oxidation: a comparative study. *ACS Applied Materials & Interfaces* 5: 1156-1164.

Yao, Y., Li, G., Ciston, S., Lueptow, R.M. and Gray, K.A. 2008. Photoreactive TiO_2/carbon nanotube composites: synthesis and reactivity. *Environmental Science & Technology* 42: 4952-4957.

Yin, M., Li, Z., Kou, J. and Zou, Z. 2009. Mechanism Investigation of visible light-induced degradation in a heterogeneous TiO_2/eosin Y/rhodamine B system. *Environmental Science & Technology* 43: 8361-8366.

Yu, B., Zhou, Y., Li, P., Tu, W., Li, P., Tang, L., Ye, J. and Zou, Z. 2016. Photocatalytic reduction of CO_2 over Ag/TiO_2 nanocomposites prepared with a simple and rapid silver mirror method. *Nanoscale* 8: 11870-11874.

Yu, C., Zhou, W., Yu, J.C., Liu, H. and Wei, L. 2014. Design and fabrication of heterojunction photocatalysts for energy conversion and pollutant degradation. *Chinese Journal of Catalysis* 35: 1609-1618.

Yu, H., Quan, X., Chen, S. and Zhao, H. 2007. TiO_2−multiwalled carbon nanotube heterojunction arrays and their charge separation capability. *The Journal of Physical Chemistry C* 111: 12987-12991.

Yu, H., Quan, X., Chen, S., Zhao, H. and Zhang, Y. 2008a. TiO_2–carbon nanotube heterojunction arrays with a controllable thickness of TiO_2 layer and their first application in photocatalysis. *Journal of Photochemistry and Photobiology A: Chemistry* 200: 301-306.

Yu, K.M.K., Curcic, I., Gabriel, J. and Tsang, S.C.E. 2008b. Recent advances in CO_2 capture and utilisation. *ChemSusChem* 1: 893-899.

Yu, Y., Yu, J.C., Chan, C., Che, Y., Zhao, J., Ding, L., Ge, W. and Wong, P. 2005a. Enhancement of adsorption and photocatalytic activity of TiO_2 by using carbon nanotubes for the treatment of azo dye. *Applied Catalysis B* 61: 1-11.

Yu, Y., Yu, J.C., Yu, J., Kwok, Y., Che, Y., Zhao, J., Ding, L., Ge, W. and Wong, P. 2005b. Enhancement of photocatalytic activity of mesoporous TiO_2 by using carbon nanotubes. *Applied Catalysis A* 289: 186-196.

Yuan, L. and Xu, Y. 2015. Photocatalytic conversion of CO_2 into value-added and renewable fuels. *Applied Surface Science* 342: 154-167.

Zhang, J., Jin, X., Morales-Guzman, P.I., Yu, X., Liu, H., Zhang, H., Razzari, L. and Claverie, J.P. 2016. Engineering the absorption and field enhancement properties of Au-TiO_2 nanohybrids via whispering gallery mode resonances for photocatalytic water splitting. *ACS Nano* 10: 4496-4503.

Zhang, Q.Y., Li, Y., Ackerman, E.A., Gajdardziska-Josifovska, M. and Li, H.L. 2011a. Visible light responsive iodine-doped TiO_2 for photocatalytic reduction of CO_2 to fuels. *Applied Catalysis A* 400: 195-202.

Zhang, X., Lin, Y., He, D., Zhang, J., Fan, Z. and Xie, T. 2011b. Interface junction at anatase/rutile in mixed-phase TiO_2: formation and photo-generated charge carriers properties. *Chemical Physics Letters* 504: 71-75.

Zhang, Y.Y., Hou, X.G., Sun, T.T. and Zhao, X.L. 2017. Calcination of reduced graphene oxide decorated TiO_2 composites for recovery and reuse in photocatalytic applications. *Ceramics International* 43: 1150-1159.

Zhao, J., Li, Y., Zhu, Y., Wang, Y. and Wang, C. 2016. Enhanced CO_2 photoreduction activity of black TiO_2−coated Cu nanoparticles under visible light irradiation: role of metallic Cu. *Applied Catalysis A* 510: 34-41.

Zhen, M.M., Zhu, X.H., Zhang, X., Zhou, Z. and Liu, L. 2015. Reduced graphene oxide-supported TiO_2 fibre bundles with mesostructures as anode materials for lithium-ion batteries. *Chemistry-A European Journal* 21: 14454-14459.

Zhou, L., Zhang, X., Shen, W., Sun, S. and Li, Y. 2015. Monolayer of close-packed Pt nanocrystals on a reduced graphene oxide (RGO) nanosheet and its enhanced catalytic performance towards methanol electrooxidation. *RSC Advances* 5: 46017-46025.

.

APPENDIX I

Supplementary data for the synthesis of mixed phase TiO_2 for the photoreduction of CO_2

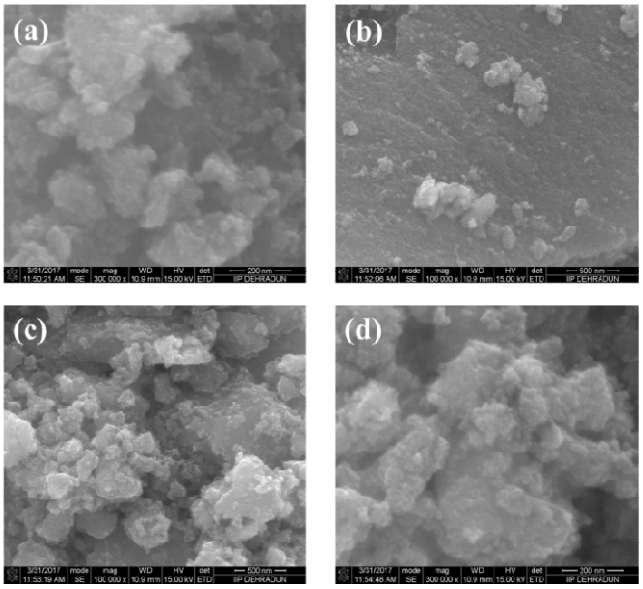

Figure A1 Scanning Electron micrographs of TiO_2-S at different magnifications (a-d).

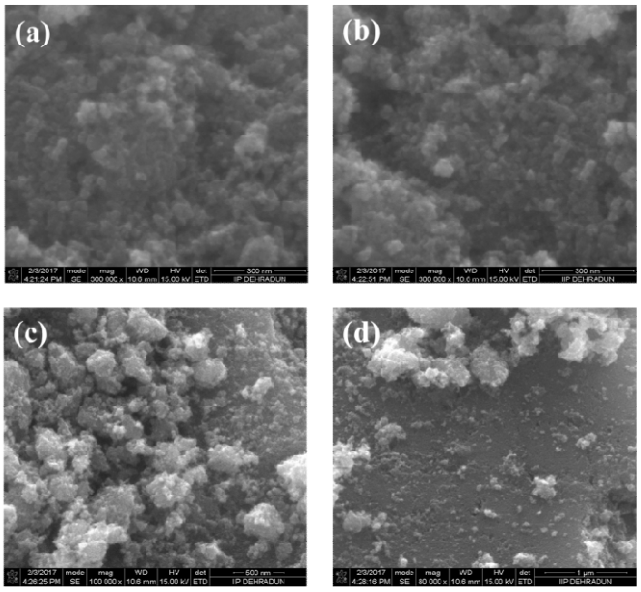

Figure A2 Scanning Electron micrographs of TiO_2-SH for different magnifications (a-d).

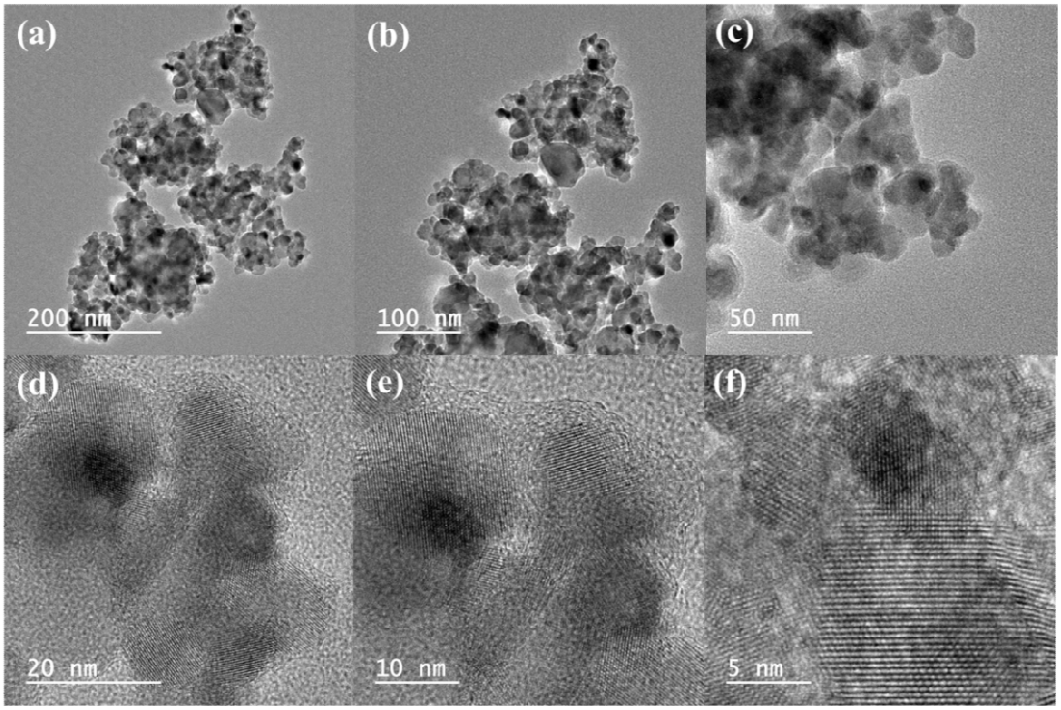

Figure A3 Transmission Electron micrographs of TiO_2-S for different magnifications (a-f).

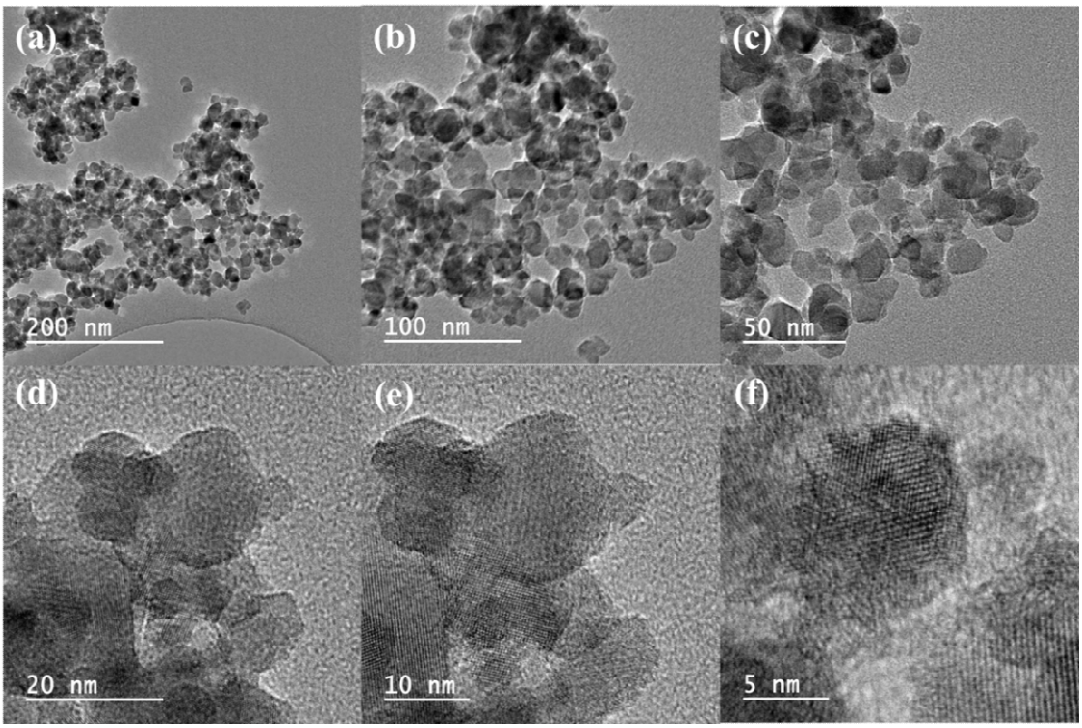

Figure A4 Transmission Electron micrographs of TiO_2-SH for different magnifications (a-f)

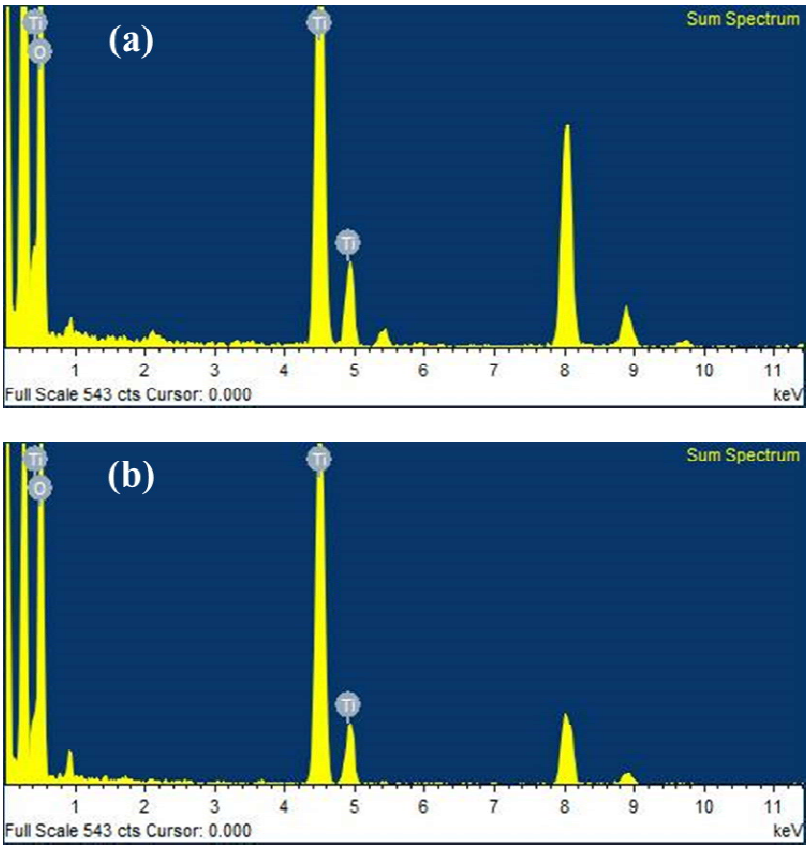

Figure A5 TEM-EDX of (a) TiO_2-S and (b) TiO_2-SH.

Table A1 Quantitative data for the production of methanol from the reduction of CO_2 on TiO_2-S catalyst

TIME (h)	GC PEAK AREA	PPM	PPM/g	µmol/g	mmol/g
8	539.97	80.347536	16069.5072	10043.442	10.043442
12	1200.89	178.692432	35738.4864	22336.554	22.336554
16	1408.81	209.630928	41926.1856	26203.866	26.203866
20	1935.33	287.977104	57595.4208	35997.138	35.997138
24	2408.01	358.311888	71662.3776	44788.986	44.788986

Table A2 Quantitative data for the production of methanol from the reduction of CO_2 on TiO_2-SH catalyst.

TIME (h)	GC PEAK AREA	PPM	PPM/g	µmol/g	mmol/g
8	710.01	105.649488	21129.8976	13206.186	13.206186
12	1291.39	192.158832	38431.7664	24019.854	24.019854
16	1492.65	222.10632	44421.264	27763.29	27.76329
20	1960.55	291.72984	58345.968	36466.23	36.46623
24	2543.47	378.468336	75693.6672	47308.542	47.308542

APPENDIX II

Supplementary data for the visible light active RGO-TiO_2 composite for selective photocatalytic reduction of CO_2 to methanol

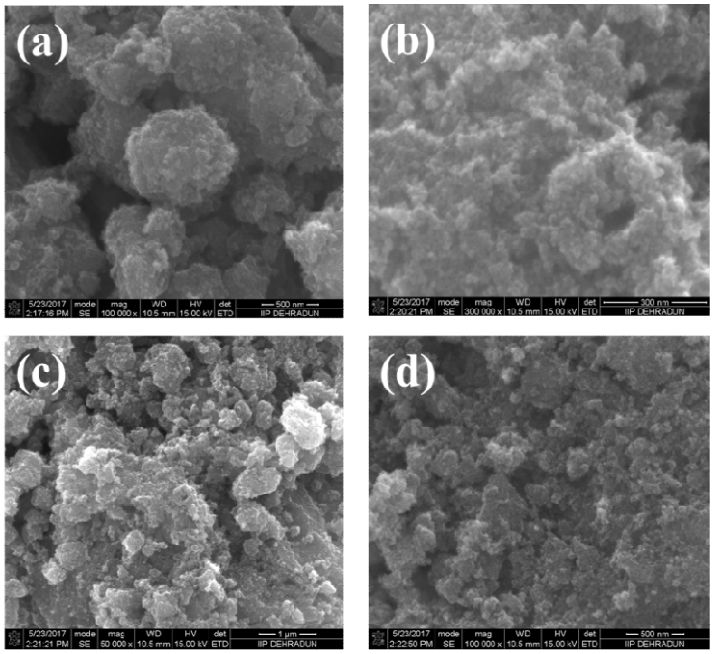

Figure B1 Scanning Electron micrographs of TiO_2 at different magnifications (a-d).

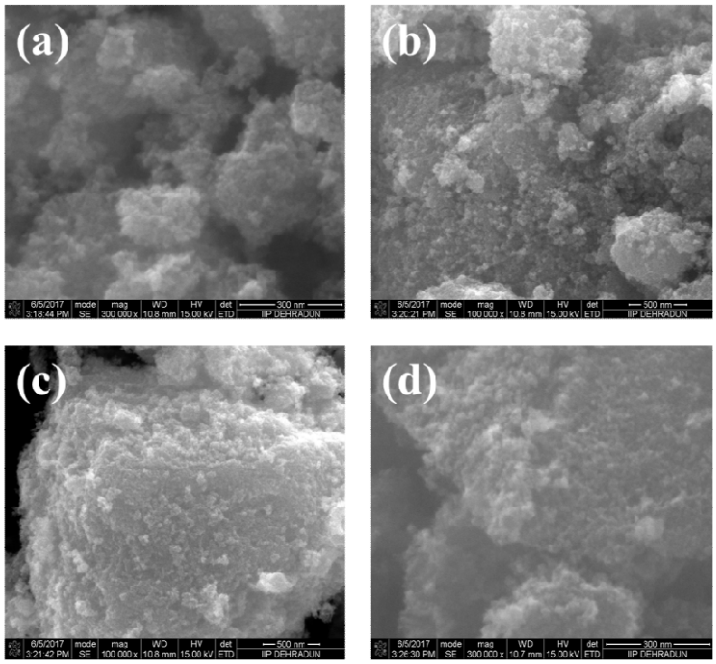

Figure B2 Scanning Electron micrographs of 1.0RGO-TiO_2 at different magnifications (a-d)

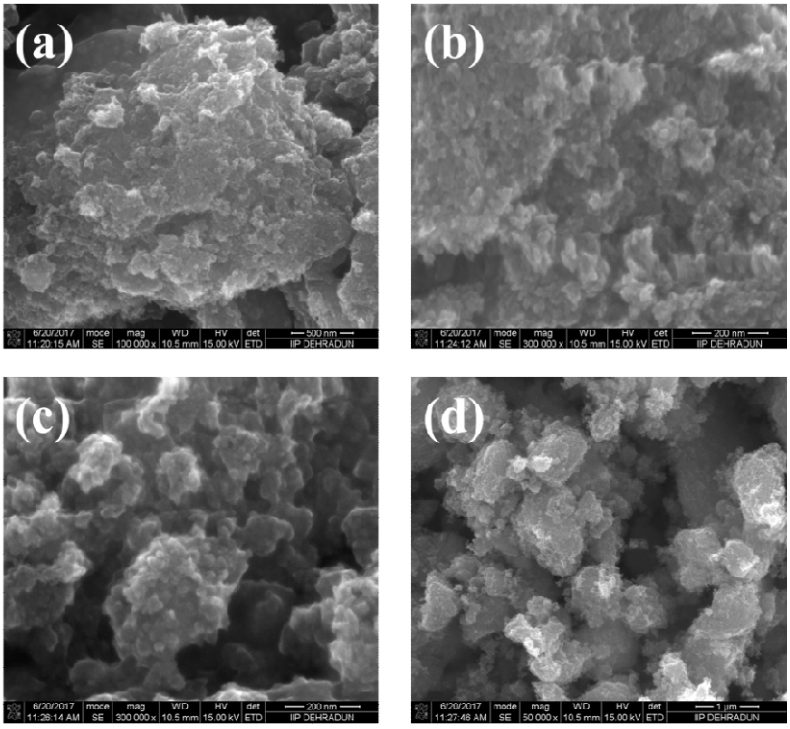

Figure B3 Scanning Electron micrographs of 2.0RGO-TiO_2 at different magnifications (a-d)

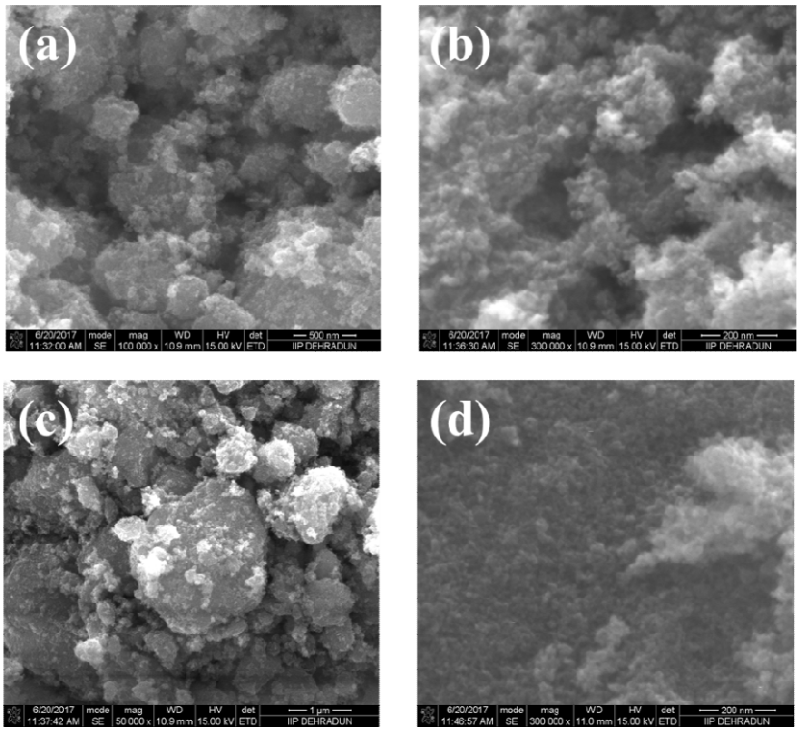

Figure B4 Scanning Electron micrographs of 5.0RGO-TiO_2 at different magnifications (a-d)

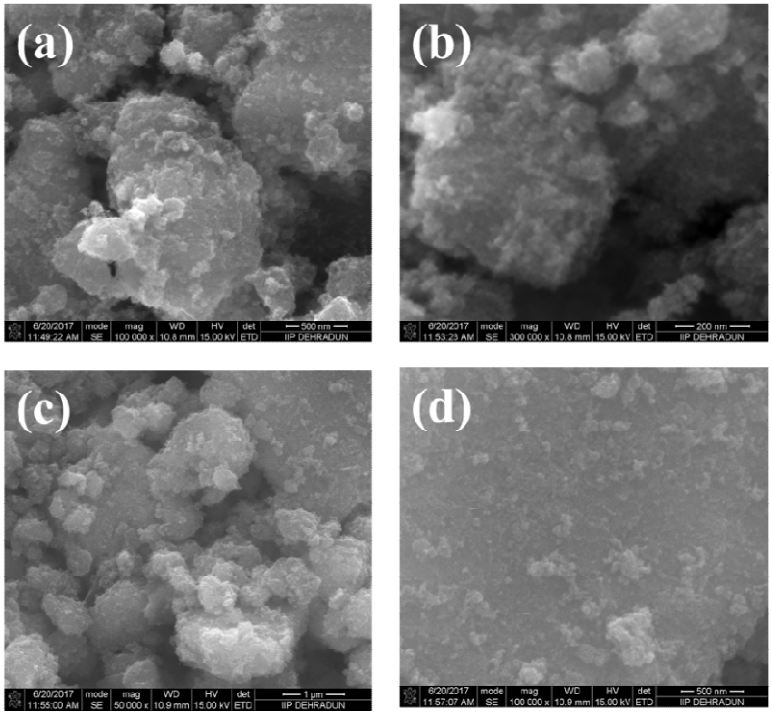

Figure B5 Scanning Electron micrographs of 10.0RGO-TiO_2 at different magnifications (a-d)

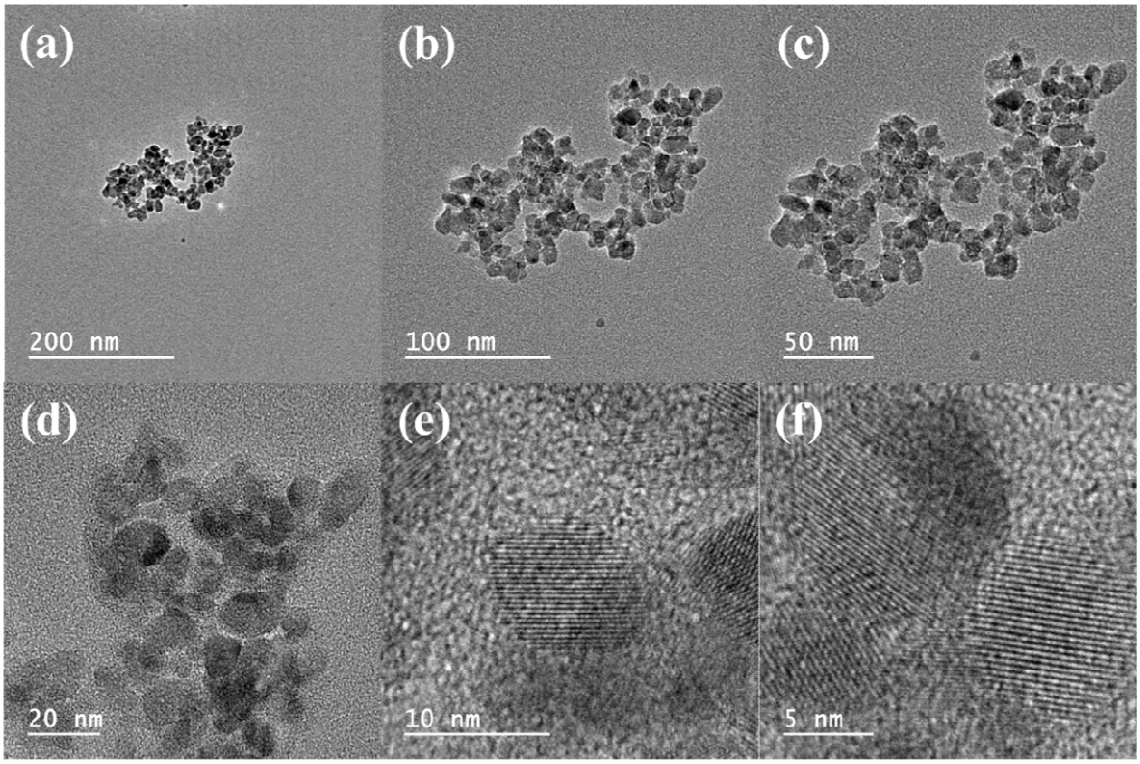

Figure B6 Transmission Electron micrographs of TiO_2 for different magnifications (a-f).

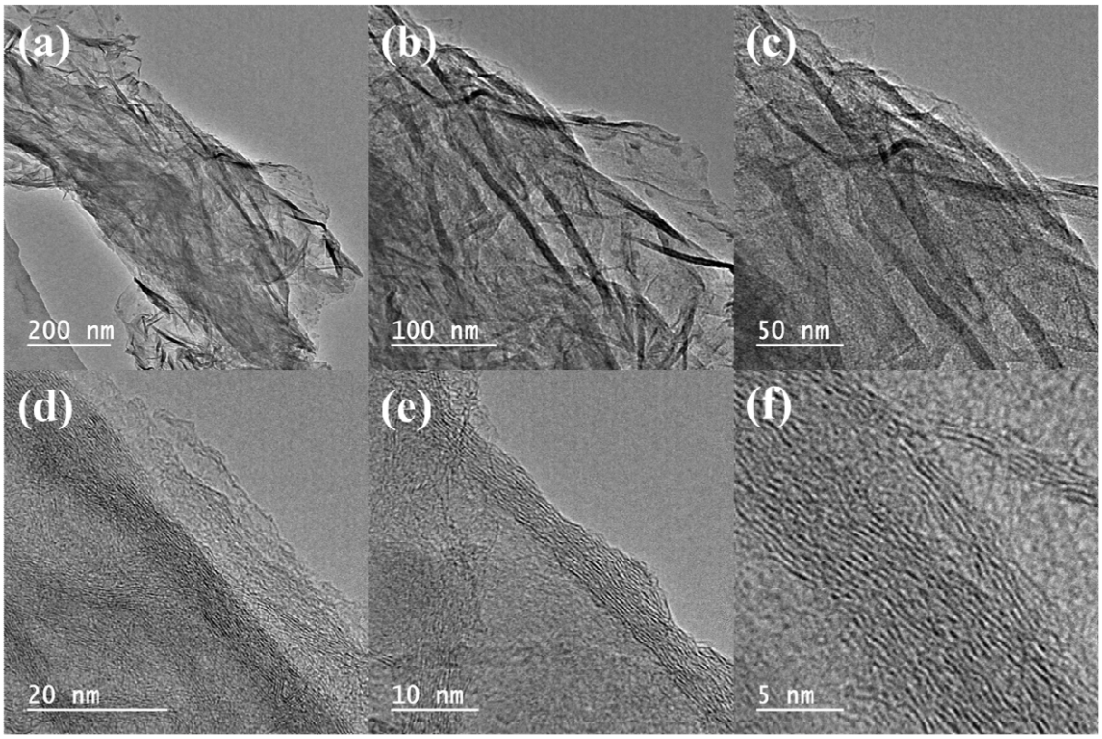

Figure B7 Transmission Electron micrographs of RGO for different magnifications (a-f).

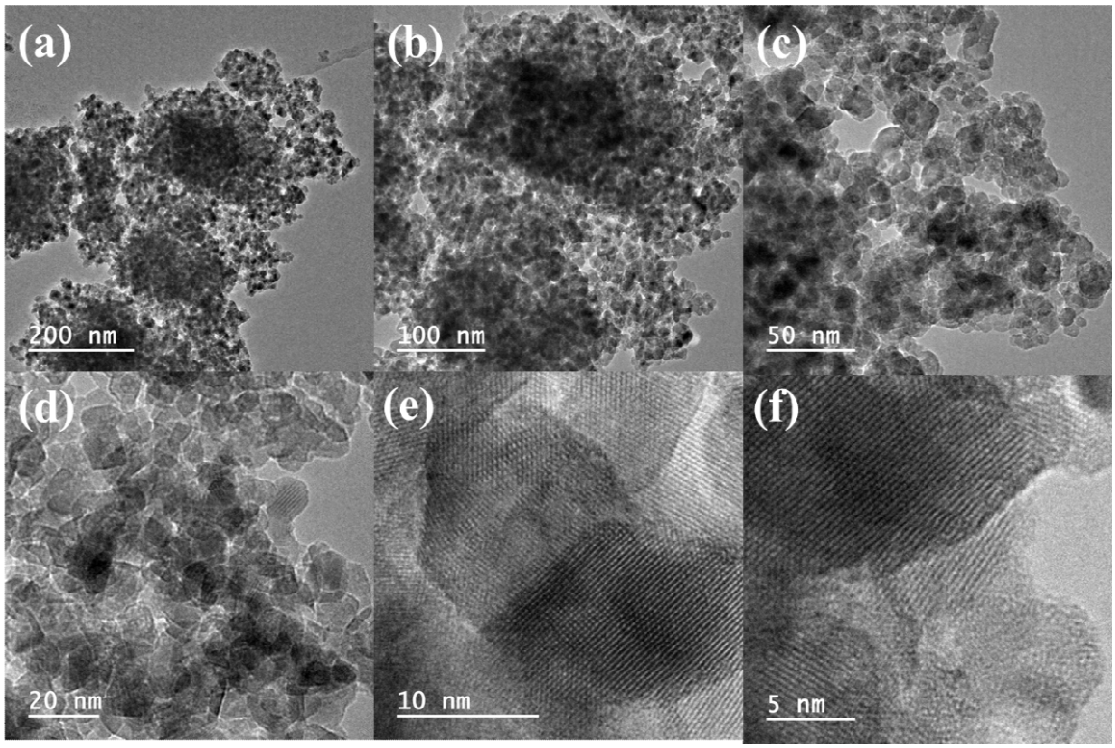

Figure B8 Transmission Electron micrographs of 1.0RGO-TiO_2 for different magnifications (a-f).

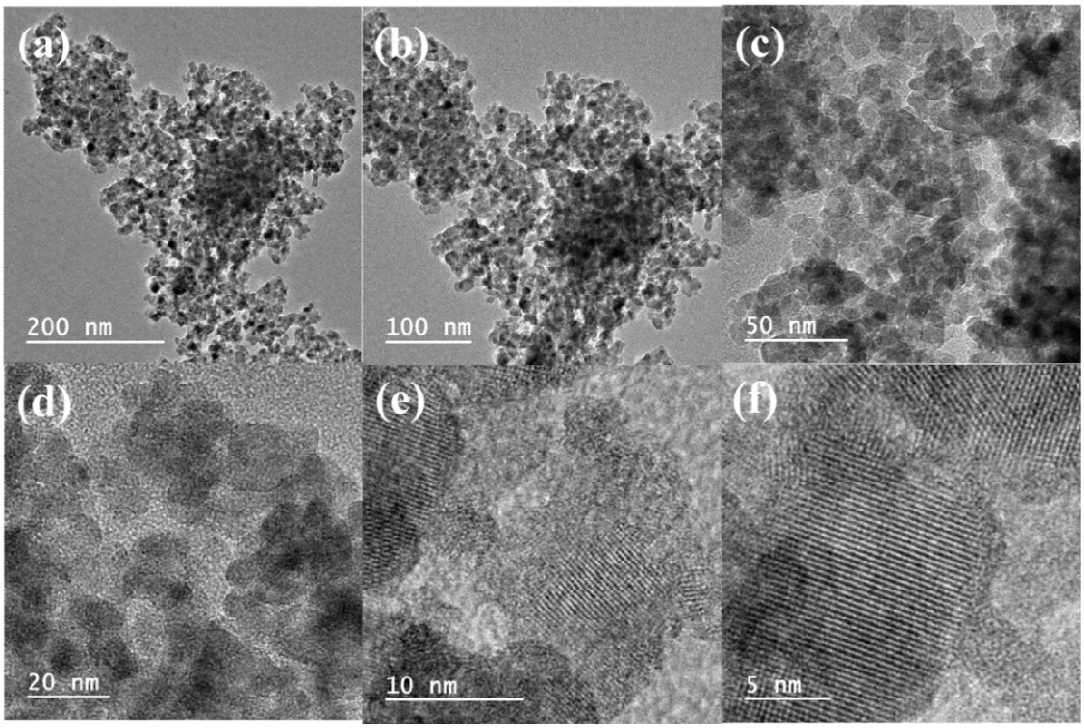

Figure B9 Transmission Electron micrographs of 2.0RGO-TiO_2 for different magnifications (a-f).

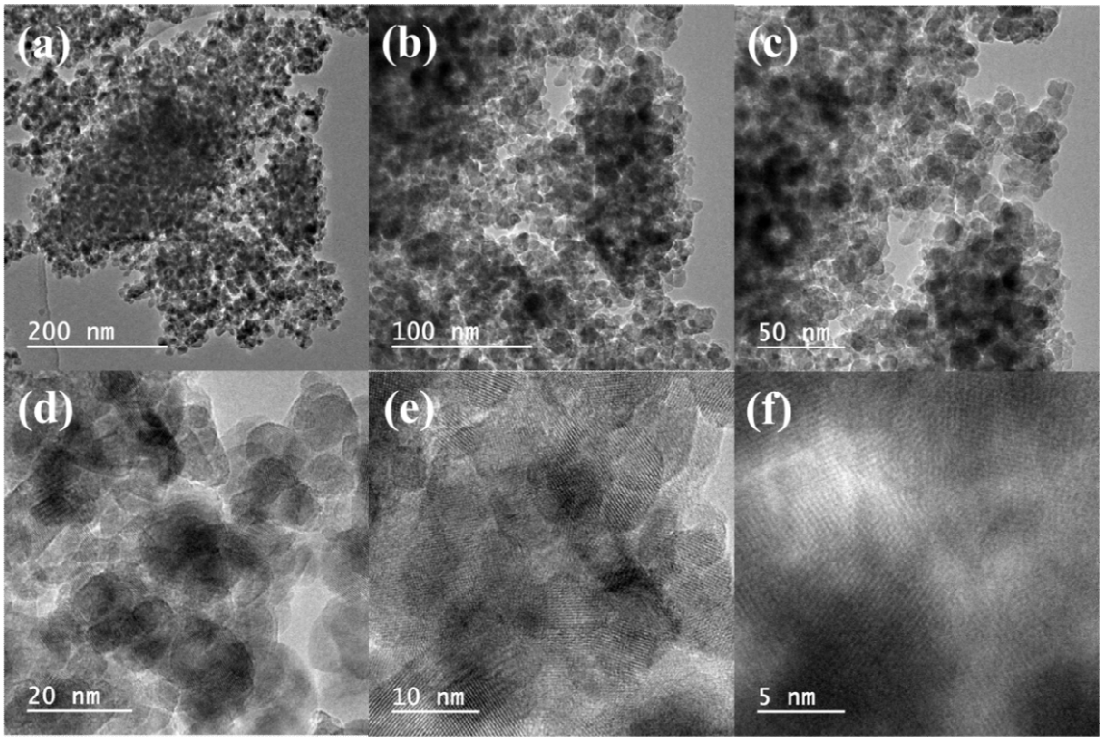

Figure B10 Transmission Electron micrographs of 5.0RGO-TiO_2 for different magnifications (a-f).

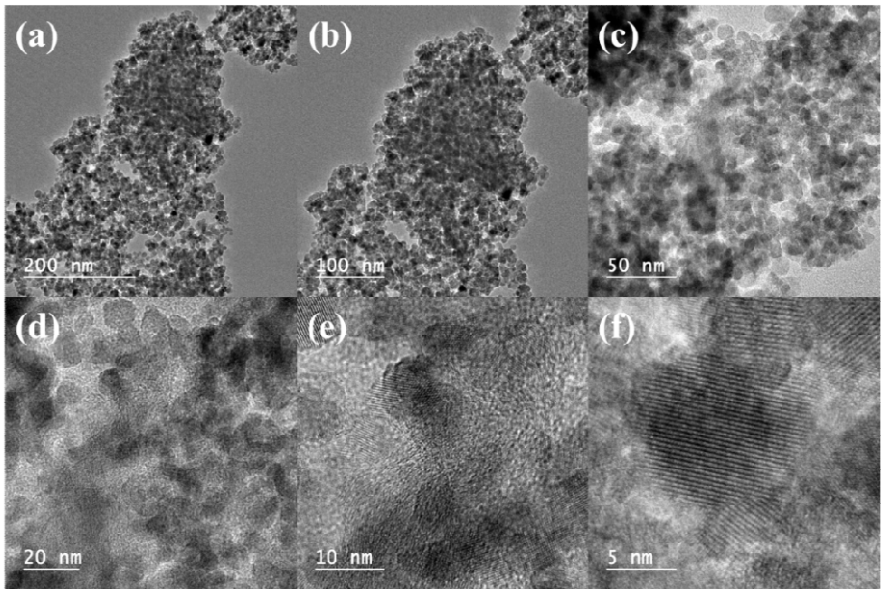

Figure B11 Transmission Electron micrographs of 10.0RGO-TiO_2 for different magnifications (a-f).

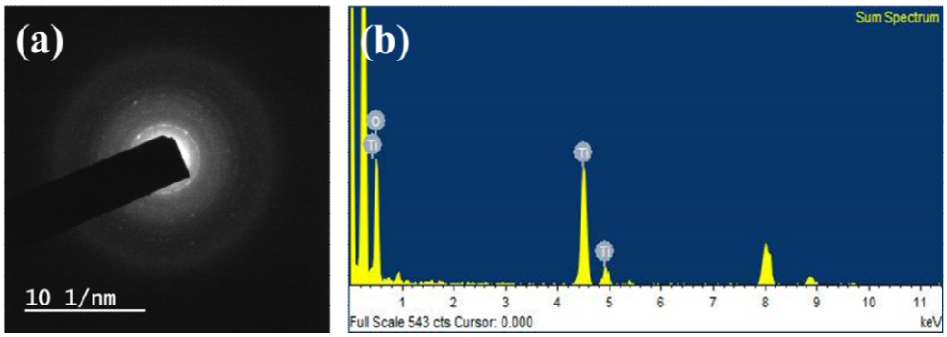

Figure B12 (a) SAED pattern and (b) TEM-EDX of TiO_2

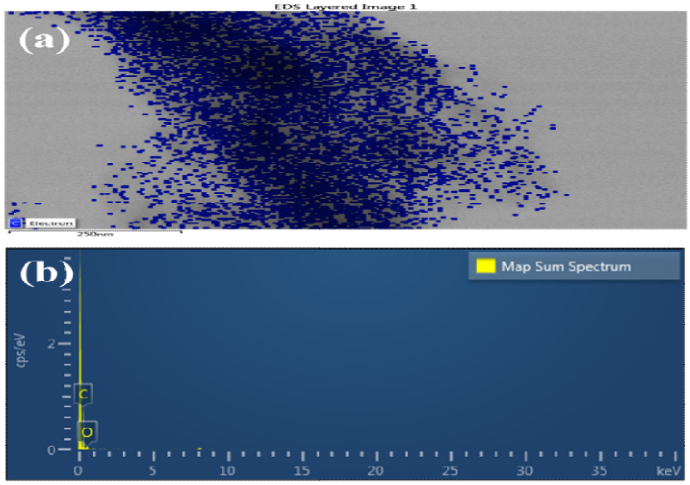

Figure B13 (a) EDS layered image and (b) TEM-EDX of RGO sample.

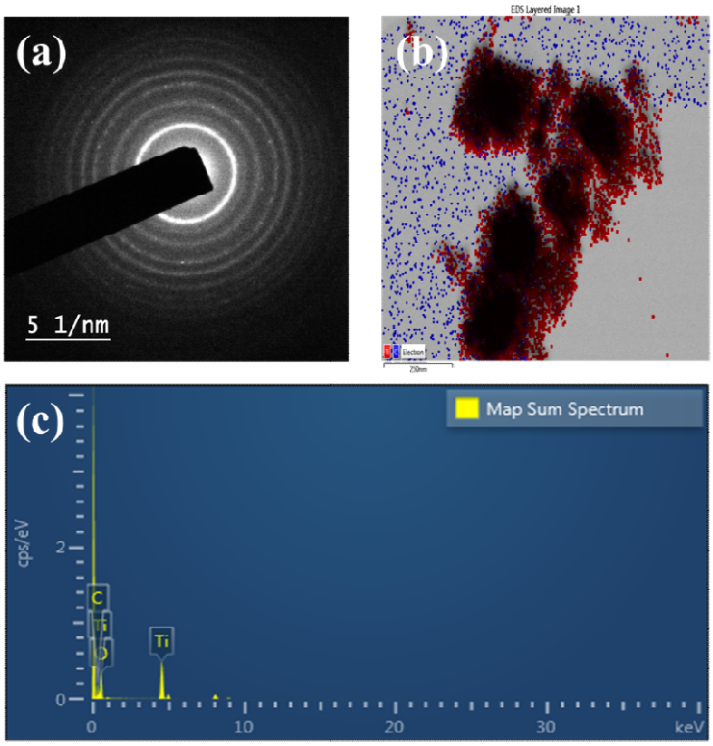

Figure B14 (a) SAED pattern (b) EDS layered image and (c) TEM-EDX of 1.0RGO-TiO_2

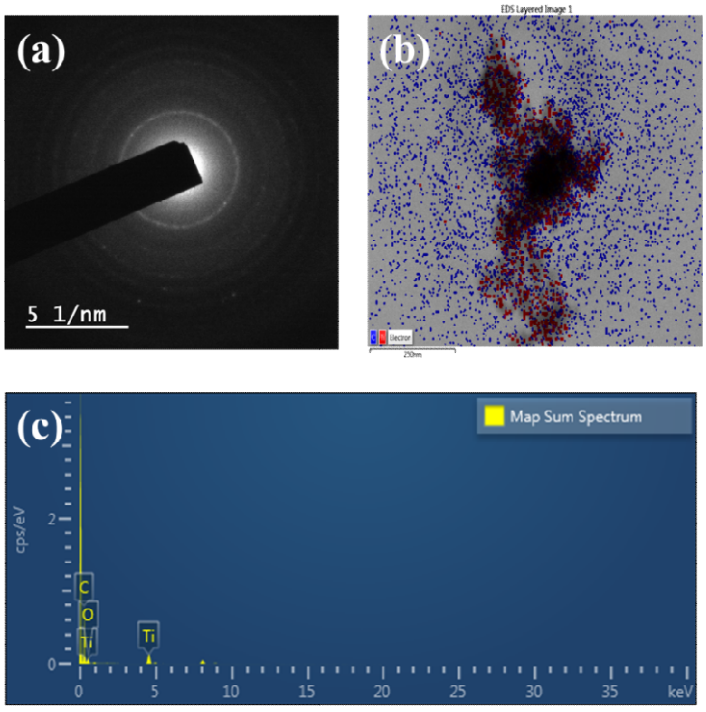

Figure B15 (a) SAED pattern (b) EDS layered image and (c) TEM-EDX of 2.0RGO-TiO_2

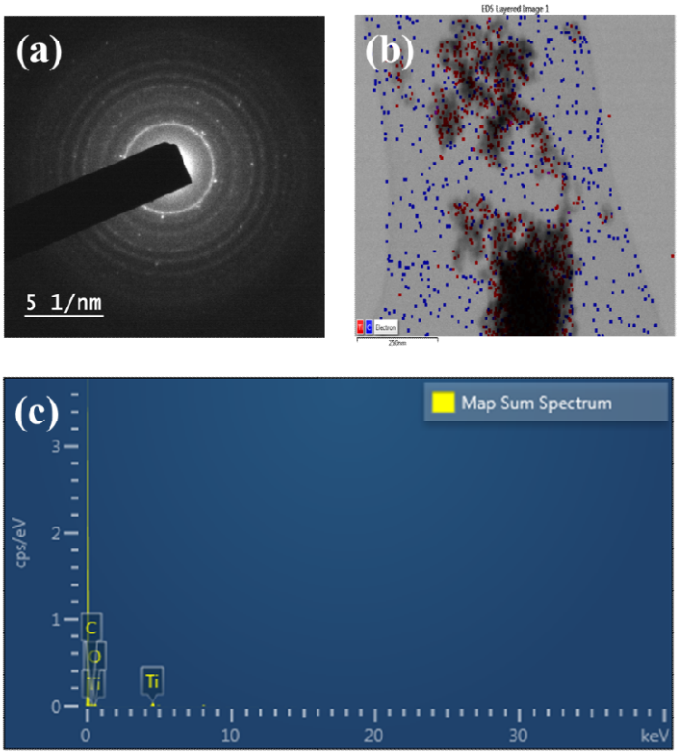

Figure B16 (a) SAED pattern (b) EDS layered image and (c) TEM-EDX of 5.0RGO-TiO_2

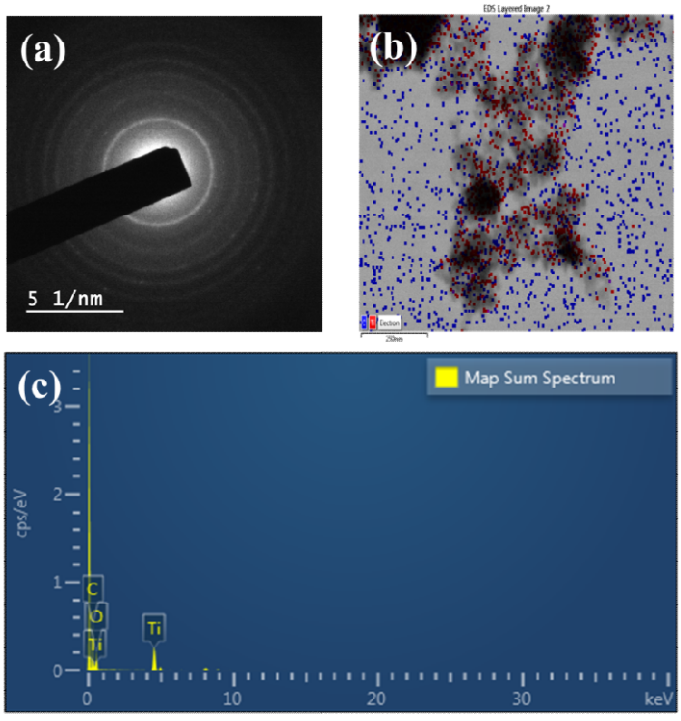

Figure B17 (a) SAED pattern (b) EDS layered image and (c) TEM-EDX of 10.0RGO-TiO_2

Table B1 Quantitative data for the production of methanol from the reduction of CO_2 on TiO_2 catalyst under UVA light

TIME (h)	GC PEAK AREA	PPM	PPM/g	µmol/g	mmol/g
4	849.23	126.3654	25273.0848	15795.678	15.7957
8	1445.71	215.1216	43024.3296	26890.206	26.8902
16	1675.26	249.2787	49855.7376	31159.836	31.1598
24	1853.33	275.7755	55155.1008	34471.938	34.4719

Table B2 Quantitative data for the production of methanol from the reduction of CO_2 on 1.0RGO-TiO_2 catalyst under UVA light

TIME (h)	GC PEAK AREA	PPM	PPM/g	µmol/g	mmol/g
4	1033.36	153.7640	30752.7936	19220.496	19.220496
8	1692.03	251.7741	50354.8128	31471.758	31.471758
16	2103.64	313.0216	62604.3264	39127.704	39.127704
24	2236.14	332.7376	66547.5264	41592.204	41.592204

Table B3 Quantitative data for the production of methanol from the reduction of CO_2 on 2.0RGO-TiO_2 catalyst under UVA

TIME (h)	GC PEAK AREA	PPM	PPM/g	µmol/g	mmol/g
4	1867.99	277.9569	55591.3824	34744.614	34.744614
8	2287.92	340.4425	68088.4992	42555.312	42.555312
16	2552.33	379.7867	75957.3408	47473.338	47.473338
24	2664.27	396.4434	79288.6752	49555.422	49.555422

Table B4 Quantitative data for the production of methanol from the reduction of CO_2 on 5.0RGO-TiO_2 catalyst under UVA light

TIME (h)	GC PEAK AREA	PPM	PPM/g	µmol/g	mmol/g
4	1951.4	290.3683	58073.664	36296.04	36.2960
8	2672.0	397.5936	79518.720	49699.2	49.6992
16	2933.26	436.4691	87293.818	54558.636	54.5586
24	3000.97	446.5443	89308.867	55818.042	55.8180

Table B5 Quantitative data for the production of methanol from the reduction of CO_2 on 10.0RGO-TiO_2 catalyst under UVA light

TIME (h)	GC PEAK AREA	PPM	PPM/g	µmol/g	mmol/g
4	1325.6	197.2493	39449.856	24656.16	24.6562
8	2065.3	307.3166	61463.328	38414.58	38.4146
16	2248.33	334.5515	66910.3008	41818.938	41.8189
24	2550.93	379.5784	75915.6768	47447.298	47.4473

Table B6 Quantitative data for the production of methanol from the reduction of CO_2 on 5.0RGO-TiO_2 catalyst under visible light

TIME (h)	GC PEAK AREA	PPM	PPM/g	µmol/g	mmol/g
4	1401.28	208.5104	41702.0928	26063.808	26.0638
8	1668.28	248.2401	49648.0128	31030.008	31.0300
16	1992.93	296.5480	59309.5968	37068.498	37.0685
24	2162.15	321.7279	64345.584	40215.99	40.2160

APPENDIX III

Supplementary data on the Insight for Enhanced Photocatalytic Activity of CNT-TiO_2 composite for storage of photon energy in chemical bonds

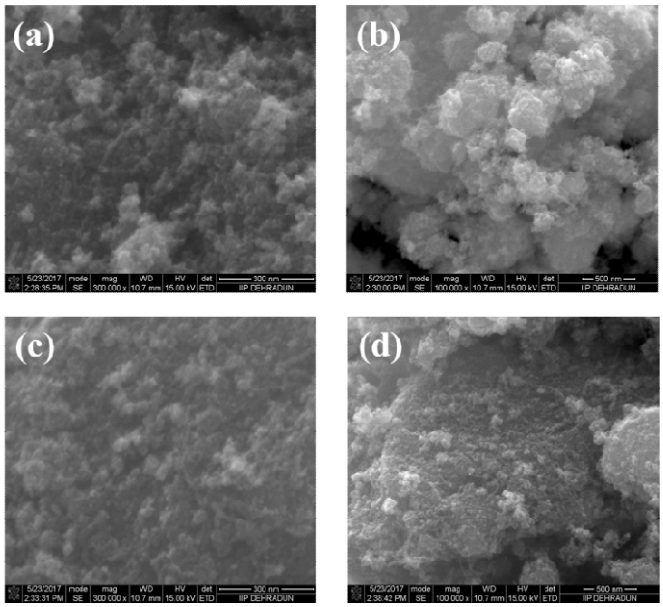

Figure C1 Scanning Electron micrographs of 1.0CNT-TiO_2 at different magnifications (a-d)

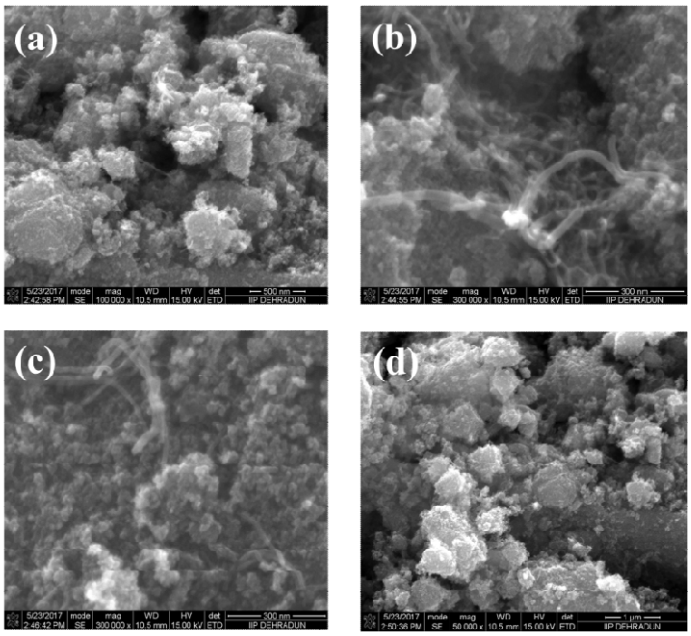

Figure C2 Scanning Electron micrographs of 2.0CNT-TiO_2 at different magnifications (a-d)

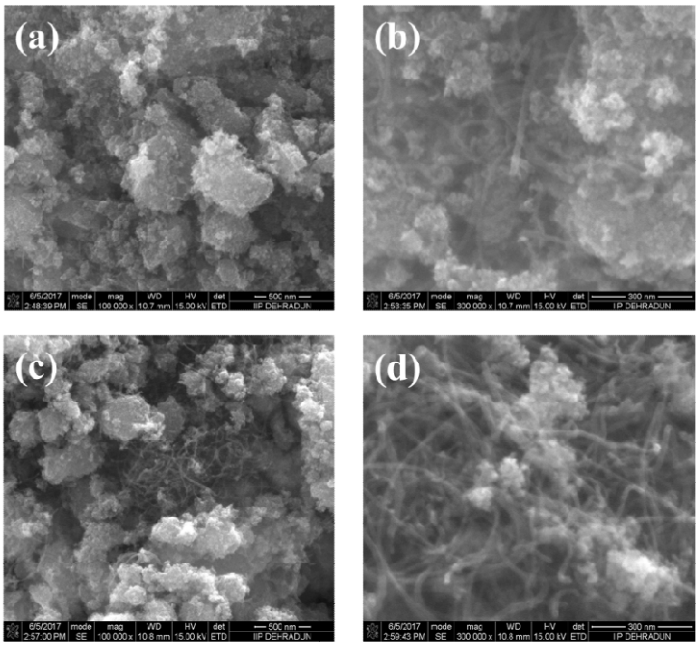

Figure C3 Scanning Electron micrographs of 5.0CNT-TiO_2 at different magnifications (a-d)

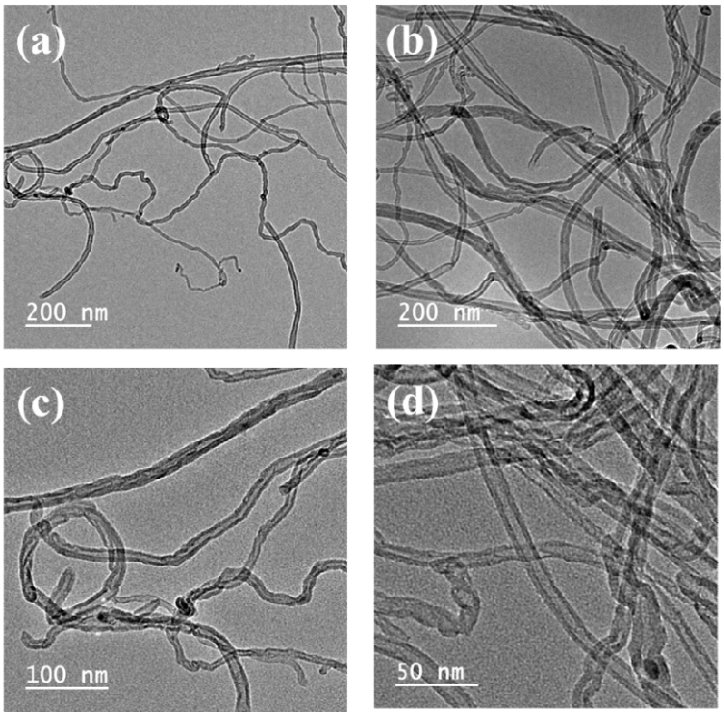

Figure C4 Transmission Electron micrographs of CNT for different magnifications (a-d).

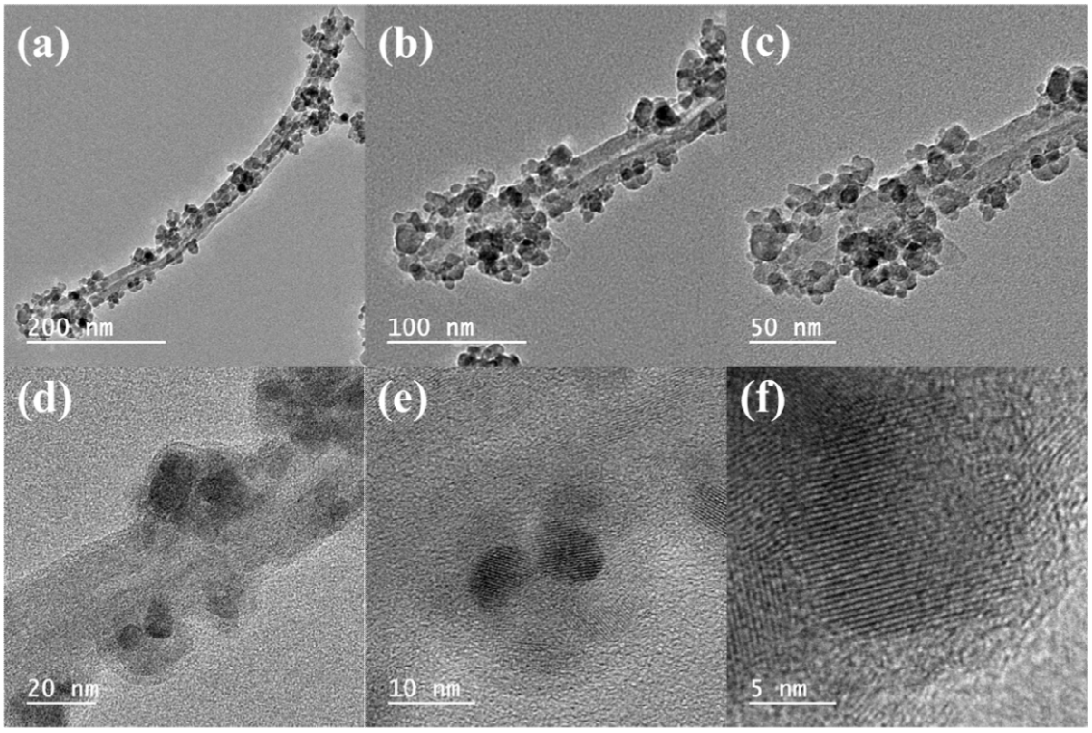

Figure C5 Transmission Electron micrographs of 1.0CNT-TiO_2 for different magnifications (a-f).

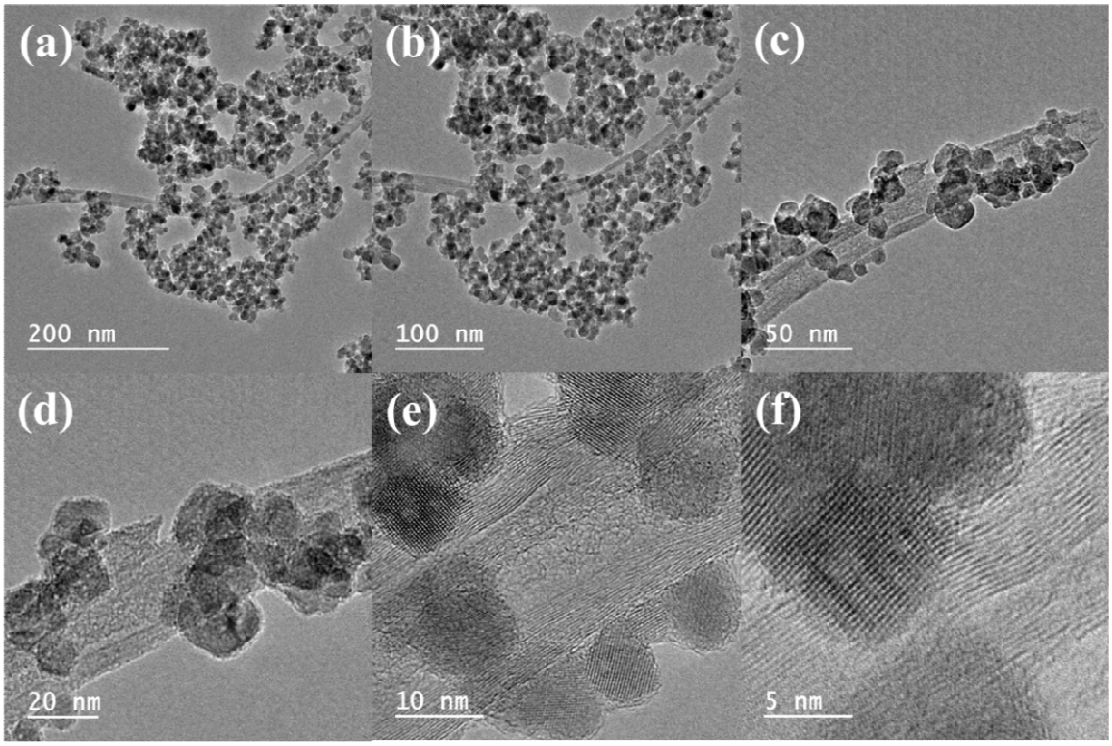

Figure C6 Transmission Electron micrographs of 2.0CNT-TiO_2 for different magnifications (a-f).

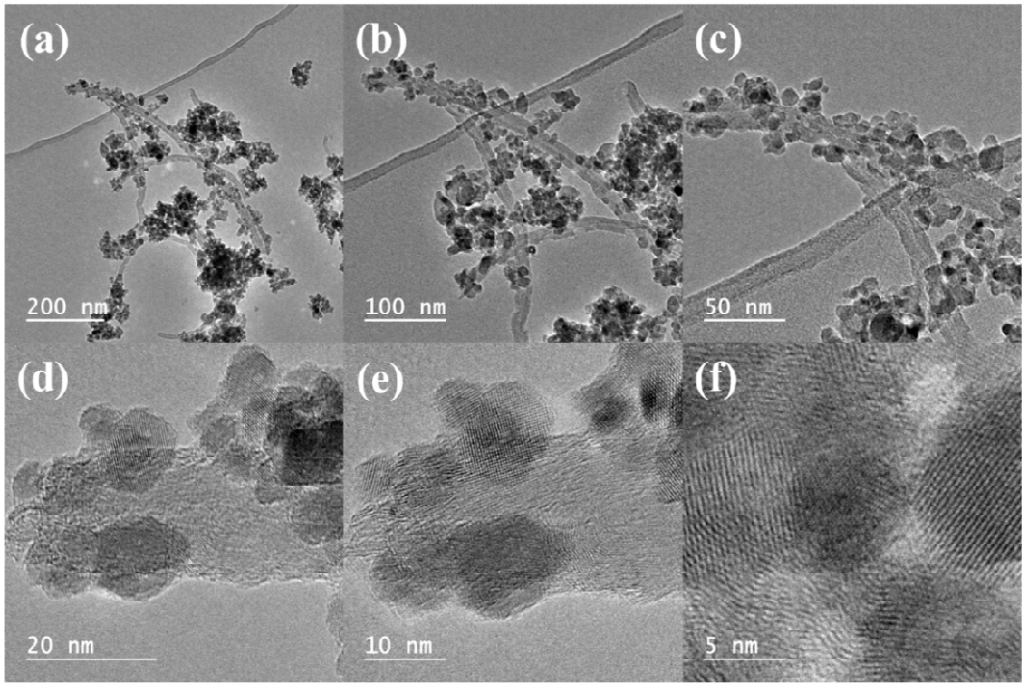

Figure C7 Transmission Electron micrographs of 5.0CNT-TiO_2 for different magnifications (a-f).

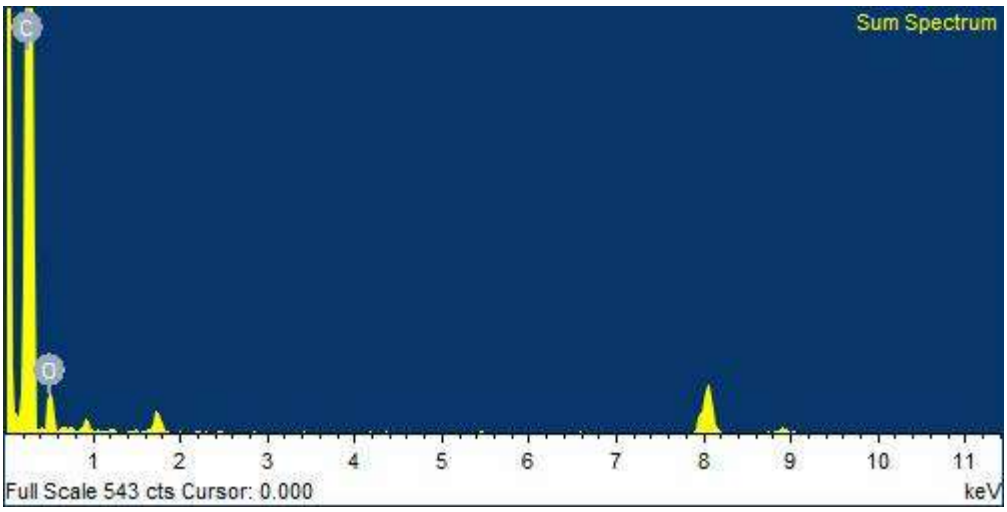

Figure C8 TEM-EDX of pure CNT

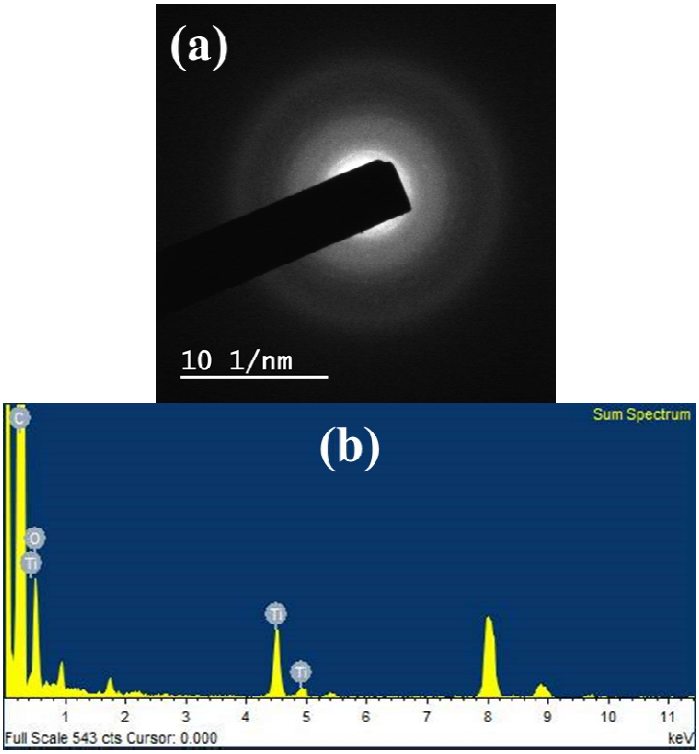

Figure C9 SAED pattern and TEM-EDX of 1.0CNT-TiO_2.

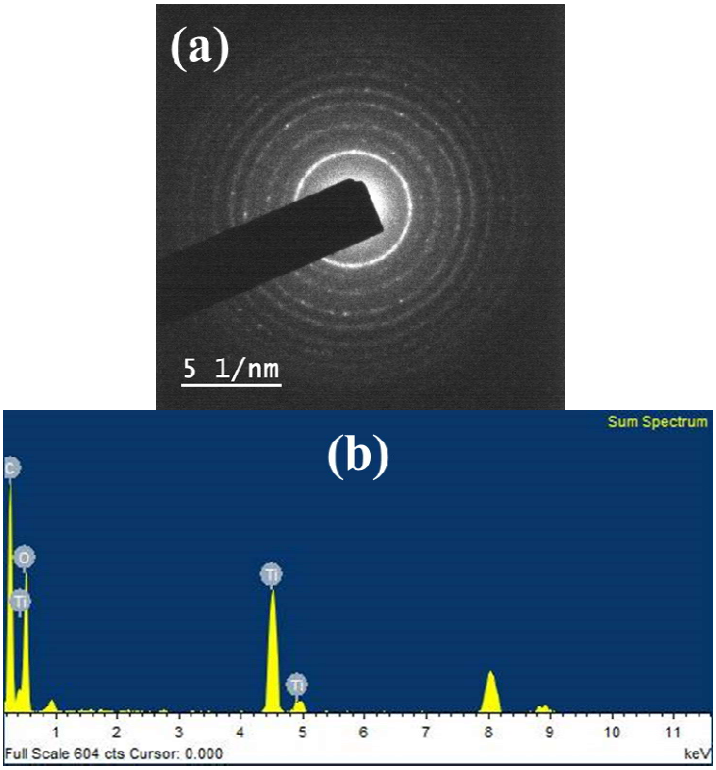

Figure C10 SAED pattern and TEM-EDX of 2.0CNT-TiO_2.

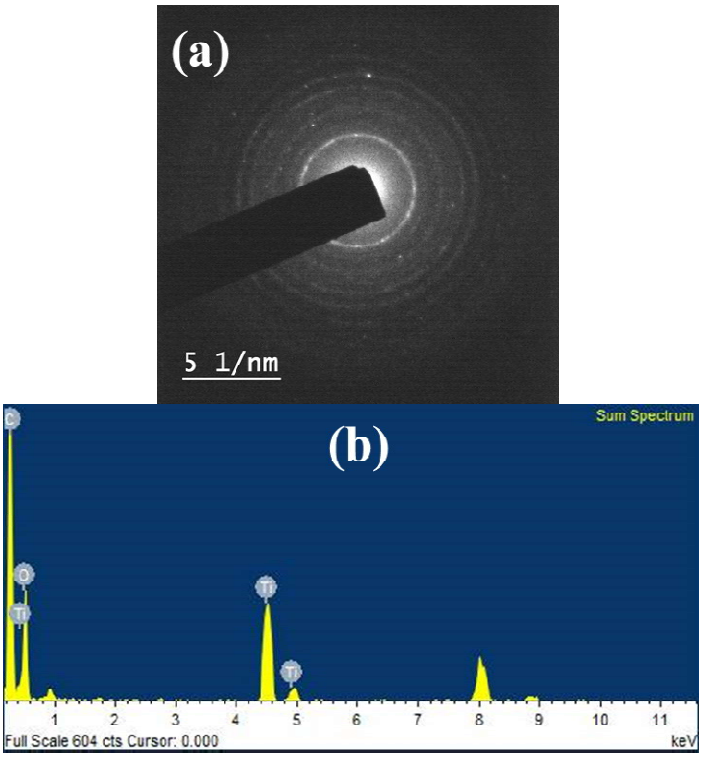

Figure C11 SAED pattern and TEM-EDX of 5.0CNT-TiO_2.

Table C1 Quantitative data for the production of methanol from the reduction of CO_2 on 1.0CNT-TiO_2 catalyst under UVA light.

TIME (h)	GC PEAK AREA	PPM	PPM/g	µmol/g	mmol/g
4	940.54	139.9523	27990.4704	17494.044	17.4940
8	1637.22	243.6183	48723.6672	30452.292	30.4523
16	1989.37	296.0182	59203.6512	37002.282	37.0023
24	2106.3	313.4174	62683.4880	39177.18	39.1772

Table C2 Quantitative data for the production of methanol from the reduction of CO_2 on 2.0CNT-TiO_2 catalyst under UVA light.

TIME (h)	GC PEAK AREA	PPM	PPM/g	µmol/g	mmol/g
4	2242.05	333.6170	66723.408	41702.13	41.7021
8	2520.05	374.9834	74996.688	46872.93	46.8729
16	2744.75	408.4188	81683.76	51052.35	51.0524
24	3042.935	452.7887	90557.7456	56598.591	56.5986

Table C3 Quantitative data for the production of methanol from the reduction of CO_2 on 5.0CNT-TiO_2 catalyst under UVA light.

TIME (h)	GC PEAK AREA	PPM	PPM/g	µmol/g	mmol/g
4	1657.56	246.6449	49328.9856	30830.616	30.8306
8	2103.04	312.9323	62586.4704	39116.544	39.1165
16	2306.05	343.1402	68628.048	42892.53	42.8925
24	2610.63	388.4617	77692.3488	48557.718	48.5577

Table C4 Quantitative data for the production of methanol from the reduction of CO_2 on 2.0CNT-TiO_2 catalyst under visible light.

TIME (h)	GC PEAK AREA	PPM	PPM/g	µmol/g	mmol/g
4	1267.5	188.604	37720.8	23575.5	23.5755
8	1430.22	212.8167	42563.3472	26602.092	26.6021
16	1801.99	268.1361	53627.2224	33517.014	33.5170
24	1966.94	292.6807	58536.1344	36585.084	36.5851

APPENDIX IV

Supplementary data on the Photocatalytic CO_2 reduction with H_2O as reductant over Magnesium-doped TiO_2 nanocatalysts

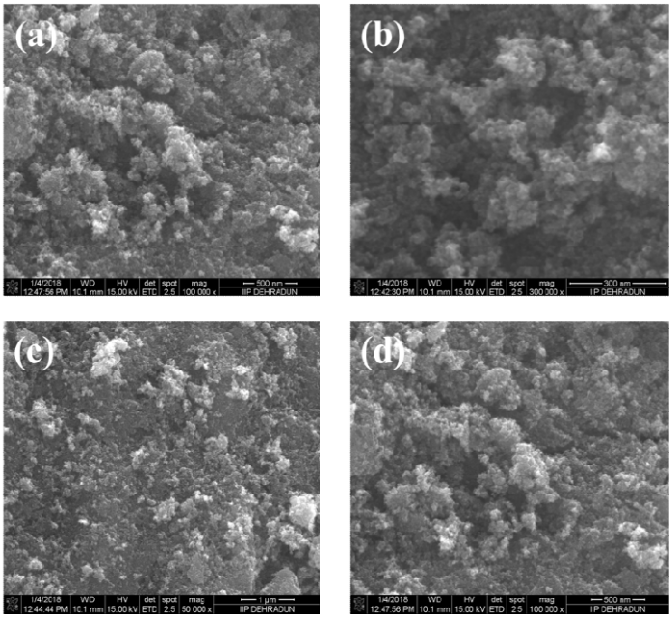

Figure D1 Scanning Electron micrographs of TiO_2 at different magnifications (a-d)

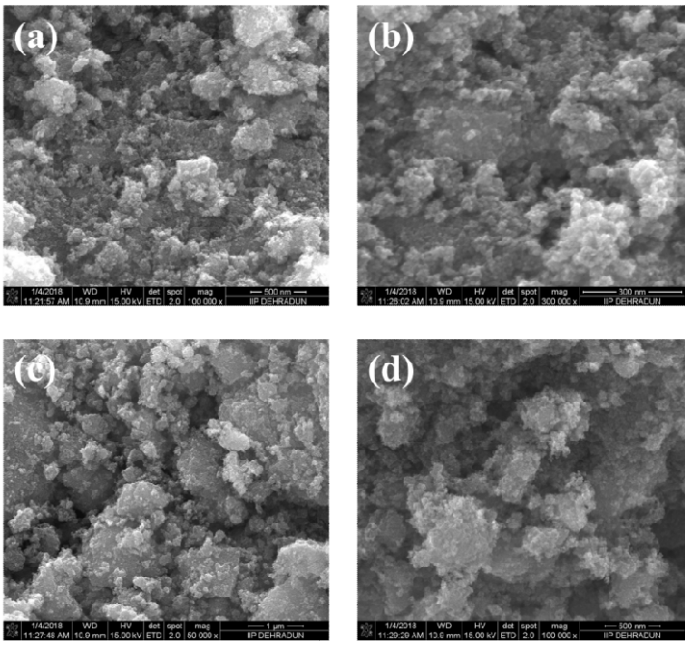

Figure D2 Scanning Electron micrographs of Mg-TiO_2-1 at different magnifications (a-d)

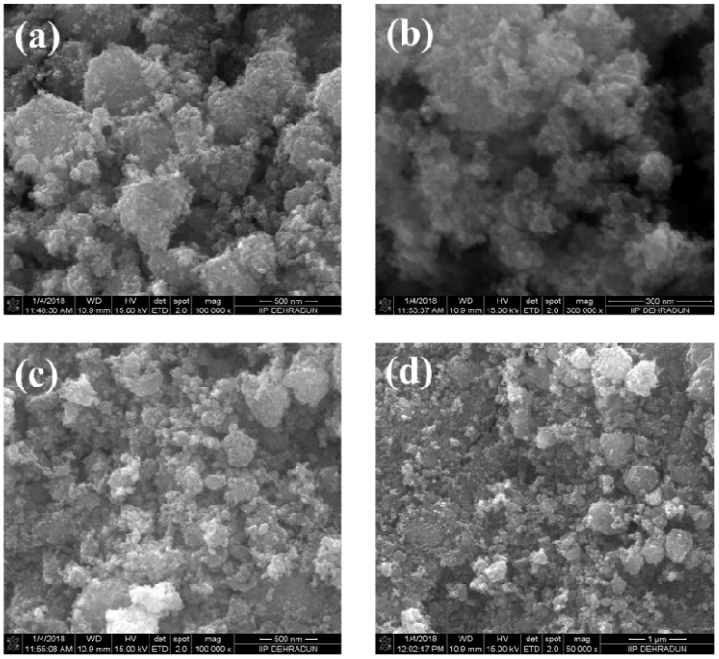

Figure D3 Scanning Electron micrographs of Mg-TiO_2-2 at different magnifications (a-d)

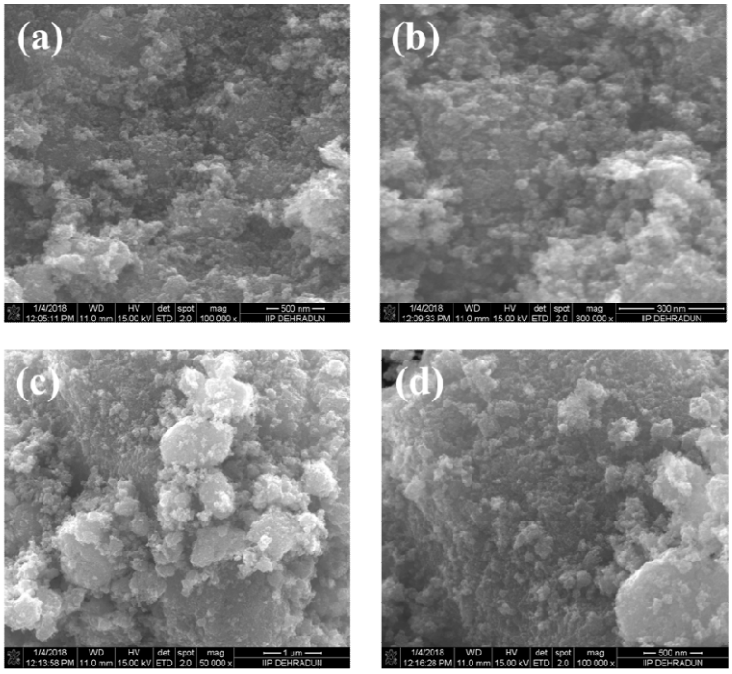

Figure D4 Scanning Electron micrographs of Mg-TiO_2-3 at different magnifications (a-d)

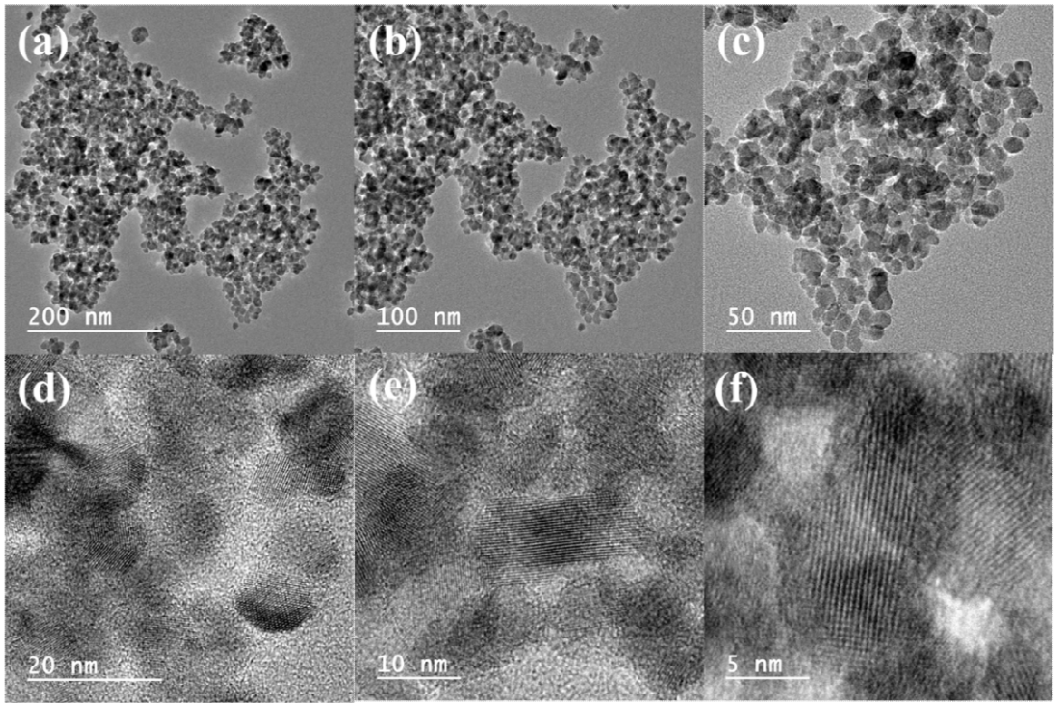

Figure D5 Transmission Electron micrographs of TiO_2 for different magnifications (a-f).

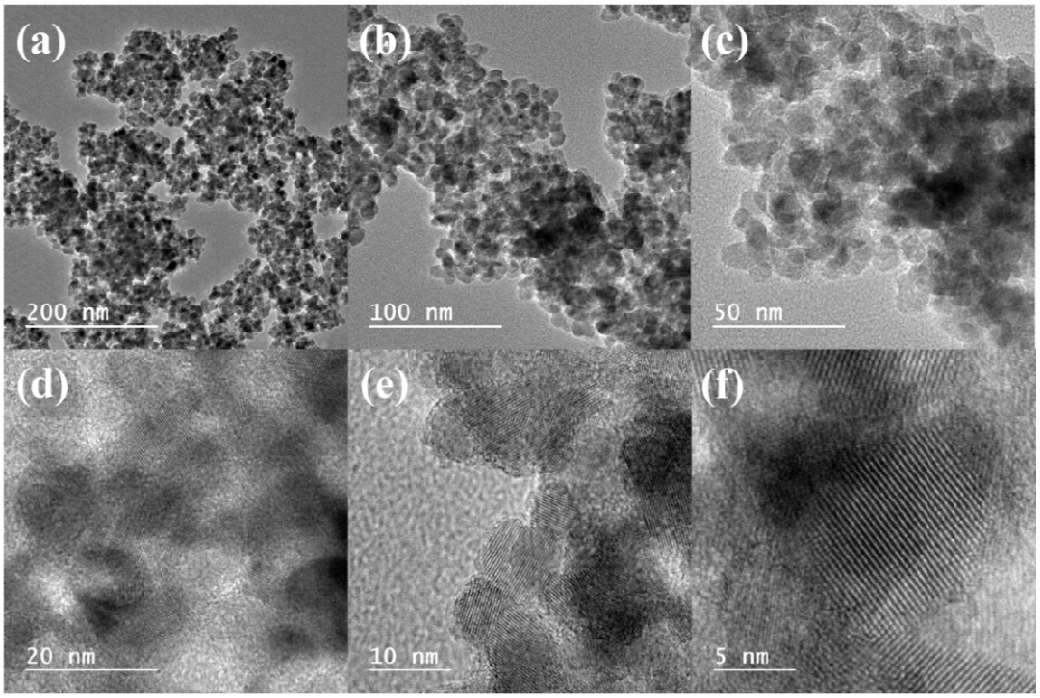

Figure D6 Transmission Electron micrographs of Mg-TiO_2-1 for different magnifications (a-f).

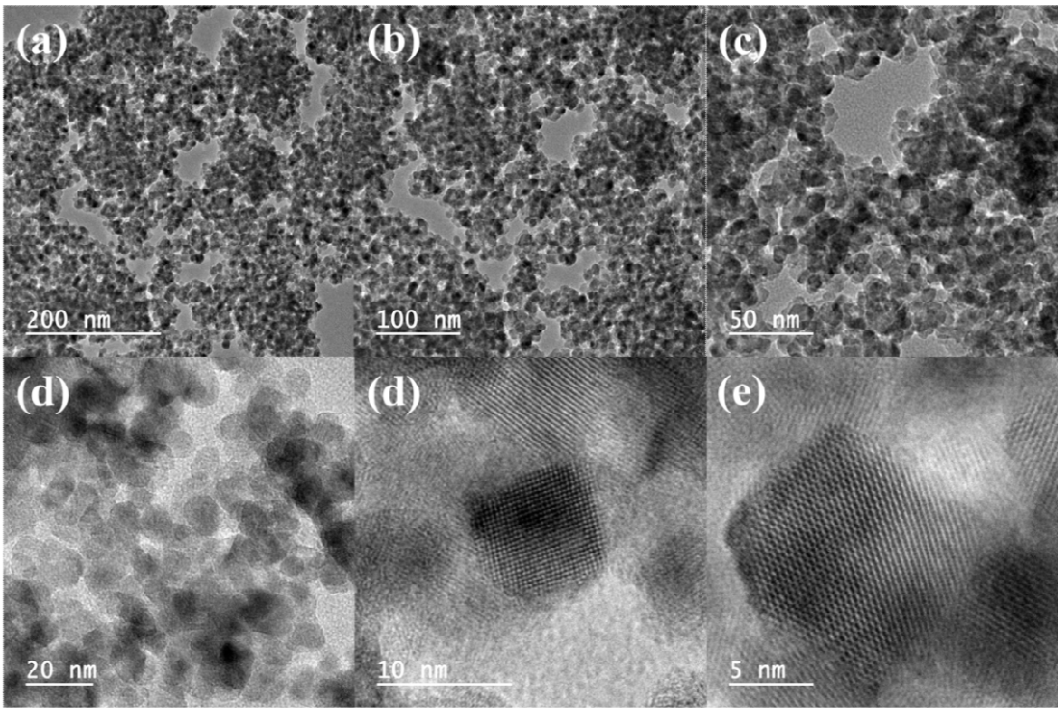

Figure D7 Transmission Electron micrographs of Mg-TiO_2-2 for different magnifications (a-f).

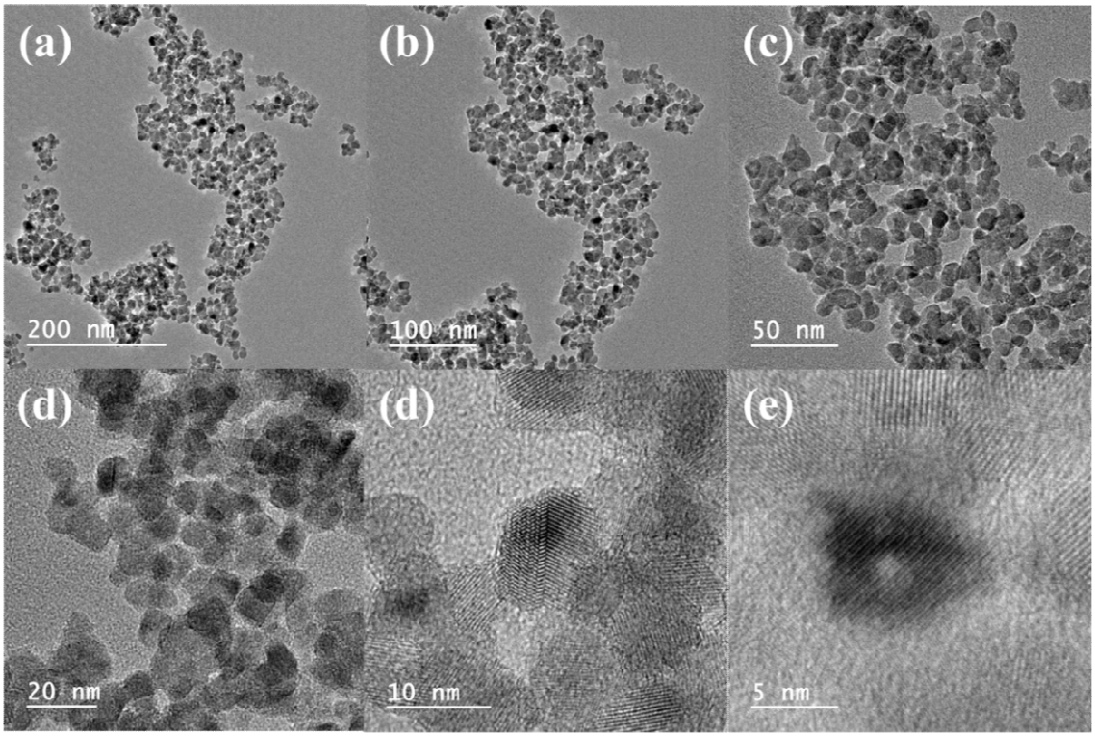

Figure D8 Transmission Electron micrographs of Mg-TiO_2-3 for different magnifications (a-f).

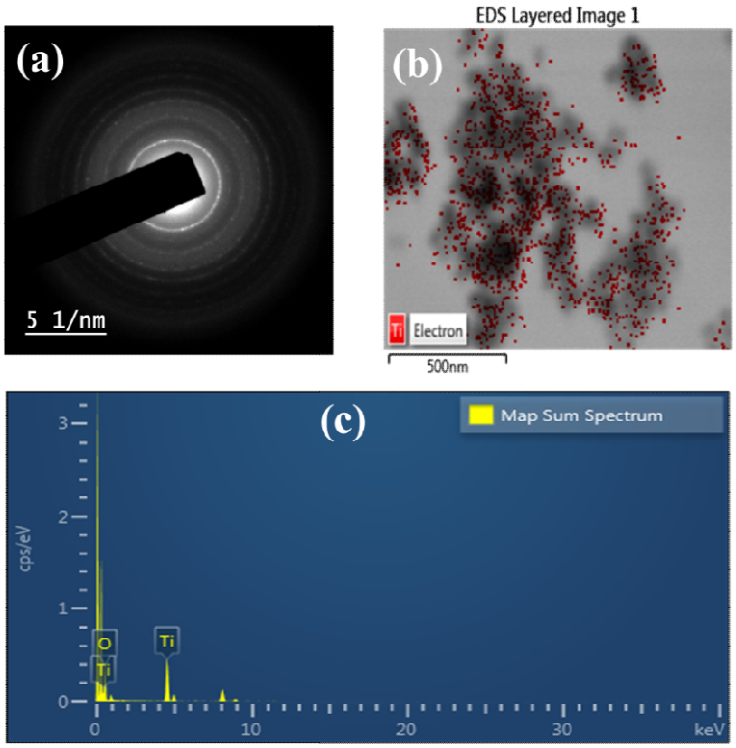

Figure D9 (a) SAED pattern (b) EDS layered image and (c) TEM-EDX of TiO_2

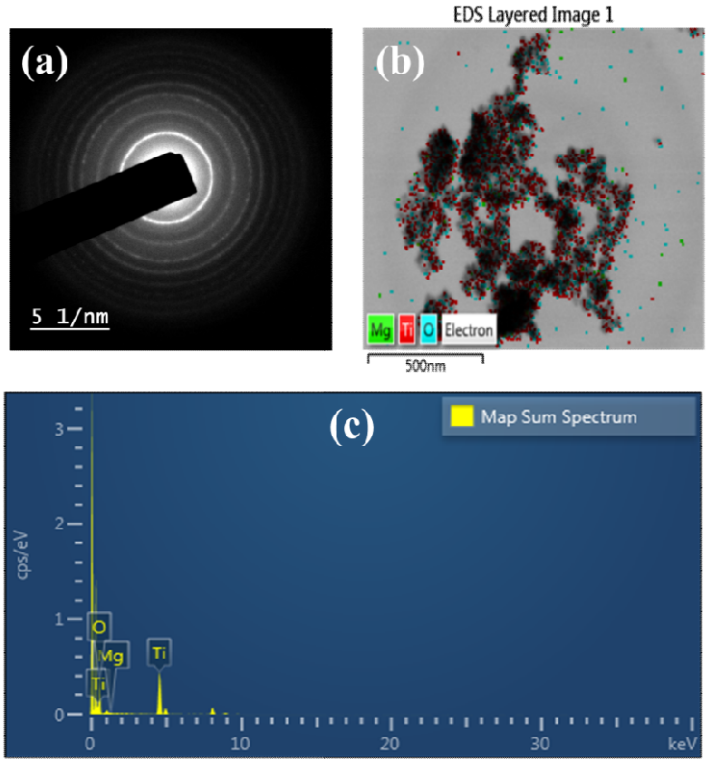

Figure D10 (a) SAED pattern (b) EDS layered image and (c) TEM-EDX of Mg-TiO_2-1

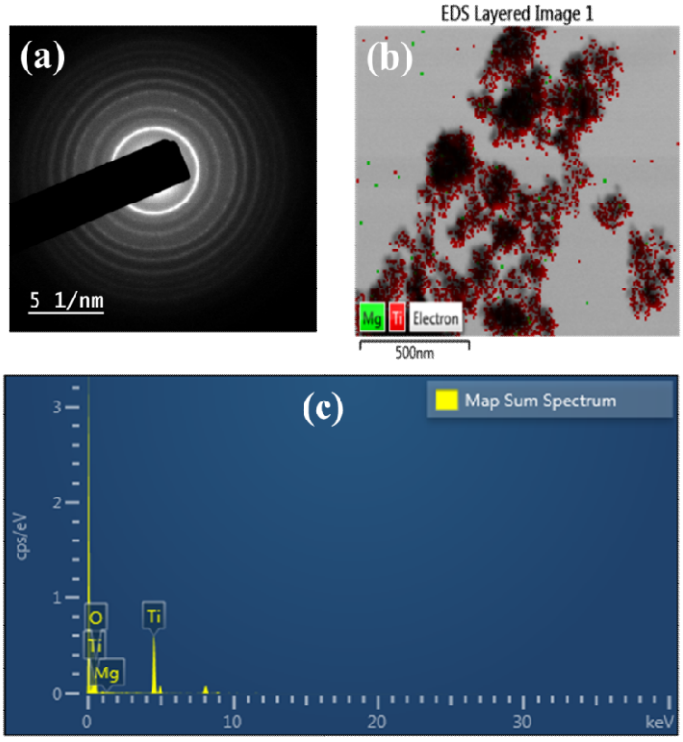

Figure D11 (a) SAED pattern (b) EDS layered image and (c) TEM-EDX of Mg-TiO_2-2

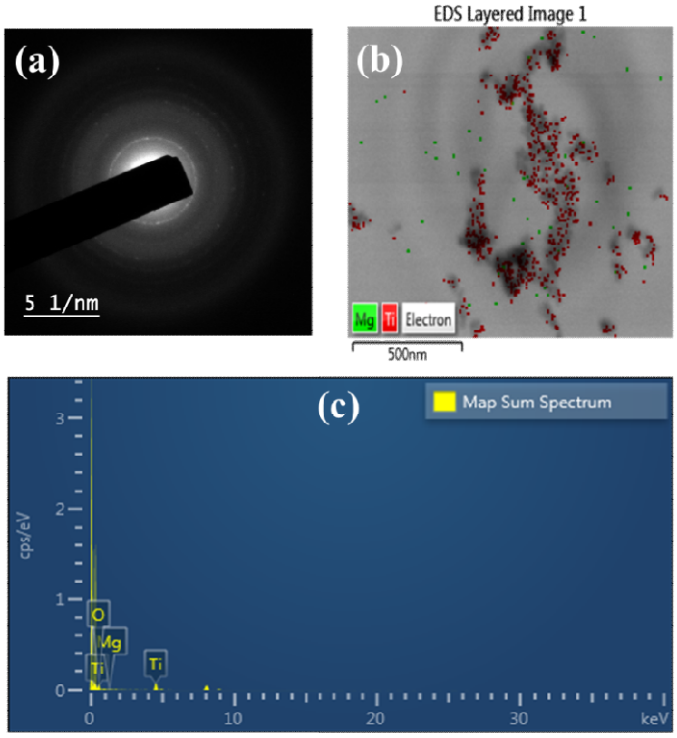

Figure D12 (a) SAED pattern (b) EDS layered image and (c) TEM-EDX of Mg-TiO_2-3

Table D1 Quantitative data for the production of methanol in mmol g^{-1} from the reduction of CO_2 on TiO_2, Mg-TiO_2-1, Mg-TiO_2-2 and Mg-TiO_2-3, under UVA light.

TIME (h)	TiO_2	Mg-TiO_2-1	Mg-TiO_2-2	Mg-TiO_2-3
2	3.12	5.734	13.06	11.4
4	6.19	12.13	22.058	21.35
6	5.79	18.272	34.612	32.01
8	11.79	23.30	47.26	42.48

Table D2 Quantitative data for the production of H_2 in µmol g^{-1} from the reduction of CO_2 on TiO_2, Mg-TiO_2-1, Mg-TiO_2-2 and Mg-TiO_2-3, under UVA light.

TIME (h)	TiO_2	Mg-TiO_2-1	Mg-TiO_2-2	Mg-TiO_2-3
2	4.37	32.85	59.47	27.93
4	5.26	64.46	111.79	55.52
6	9.15	96.01	165.1	86.11
8	10.56	125.90	229.17	112.95

Table D3 Quantitative data for the production of CH_4 in µmol g^{-1} from the reduction of CO_2 on TiO_2, Mg-TiO_2-1, Mg-TiO_2-2 and Mg-TiO_2-3, under UVA light.

TIME (h)	TiO_2	Mg-TiO_2-1	Mg-TiO_2-2	Mg-TiO_2-3
2	2.07	2.39	3.1	4.6
4	4.21	4.6	6.18	9.02
6	6.58	7.12	9.41	13.996
8	8.76	9.32	12.14	18.33

Table D4 Quantitative data for the production of CO µmol g^{-1} from the reduction of CO_2 on TiO_2, Mg-TiO_2-1, Mg-TiO_2-2 and Mg-TiO_2-3, under UVA light.

TIME (h)	TiO_2	Mg-TiO_2-1	Mg-TiO_2-2	Mg-TiO_2-3
2	48.07	50.25	58.97	47.02
4	94.72	96.9	115.37	91.49
6	143.54	147.9	175.02	146.85
8	194.46	194.60	233.78	186.75

APPENDIX V

Copy of paper published from the synthesis of mixed phase TiO_2 for the photoreduction of CO_2

ChemPubSoc Europe

DOI: 10.1002/slct.201800076

Chemistry SELECT Communications

Catalysis

Insight of Diversified Reactivity and Theoretical Study of Mixed-Phase Titanium Dioxide for the Photoactivation of Small Molecules

Joshua O. Olowoyo,[a, d] Norge Cruz Hernández,[c] Manoj Kumar,[b] Suman L. Jain,[a] Jonathan O. Babalola,[d] and Umesh Kumar*[a]

The mixed-phase titanium dioxide (TiO_2) nanoparticles were prepared by two different methods; sonothermal (S) and sonothermal followed by hydrothermal (SH). The TiO_2 prepared by SH has shown a superior hydrogen (H_2) generation via photocatalytic splitting of water (H_2O) and formic acid (FA) as well as photocatalytic reduction of carbon dioxide (CO_2) to methanol (MeOH). The H_2 production rate under UVA from H_2O and FA was 0.02 and 3.91 mmol g^{-1} h^{-1} respectively while MeOH formation rate was 1.97 mmol g^{-1} h^{-1} from CO_2. The DFT calculations of the reactants and products were also investigated.

The photocatalytic activation of small molecules such as water (H_2O), formic acid (FA) to generate hydrogen (H_2) and carbon dioxide (CO_2) to produce methanol (MeOH) could offer a great, promising alternative to the world energy needs and pollution control. Semiconductor materials play a significant role in the utilization of light-motivated reactions due to their unique versatility for energy and environmental applications.[1] The mixed-phase TiO_2 has received considerable recognition because it could delay the recombination of photogenerated e^{-1} – h^+ pair due to the charge transfer in between two phases, which ends up in better photocatalytic efficiency.[2] Till now, various synthetic methods such as ultrasonic irradiation,[3] ultrasound assisted sol-gel technique,[4] and hydrothermal process[5] have been adopted for the preparation of mixed-phase TiO_2. However, significant advancement has been made in synthesizing TiO_2-based materials with a better photocatalytic activity; it is still highly desirable to develop a simple approach for the synthesis of mixed-phase TiO_2, especially below phase transition temperature.

The photocatalysis is a surface phenomenon, and adsorption energies are required to give an insight of reaction for reactant interaction with TiO_2.[6] Higher adsorption energies of reactants lead towards better interaction with the catalyst as well as faster product formation, and lesser adsorption energies for the formed products ensure their rapid release from the catalyst's surface. It will be insufficient to solely conclude that better photocatalytic activities arise from a mixed phase of TiO_2 without considering adsorption energies. Hence, it is highly needful to calculate these energies to understand which phase is favorable for photoactivity.

Herein, we developed two kinds of mixed-phase TiO_2 using two different novel approaches; sonothermal (S) and sonothermal-hydrothermal (SH) for activation of small molecules namely for hydrogen and methanol generation. The DFT calculations in a periodic framework, as implemented in the VASP were performed for the electronic and the structural properties of reactants including H_2O, FA, and CO_2 as well as products including MeOH and H_2 present on both TiO_2: anatase (101) and rutile (110) surfaces were also investigated.

The TiO_2-S was prepared by slow addition of titanium (IV) butoxide (ethanolic solution) to the ultrasonicating water-ethanol mixture at 70 °C followed by separation, washing, drying, and calcination under air at 450 °C. Similarly, TiO_2-SH was prepared by the same method having one additional step of the hydrothermal process (180 °C, 12 h). The detailed synthetic procedures are described in the supporting information.

The prepared TiO_2 nanoparticles were characterized by XRD, SEM, TEM, solid state UV-Vis spectroscopy and BET surface area analysis. Both TiO_2 photocatalysts are crystalline, have intense XRD diffraction peaks (Figure 1a) with predominated anatase phase over rutile (TiO_2-S has 13.7% rutile, and TiO_2-SH has 8.4% rutile). The synthetic methods afford the co-existence of anatase-rutile phases below most reported phase transition temperature.[7] The calculated average crystal size of the predominant anatase phase (101) from XRD for TiO_2-S and TiO_2-SH are 15.4 and 18.1 nm respectively (Table S1). The nanoparticles are comparatively homogenous and well separated in TiO_2-SH and are in agreement with SEM (Figure S2) and TEM analysis (Figure 2a and 2c). Further, HRTEM of prepared TiO_2 reveals that the nanoparticles have both anatase and rutile

[a] J. O. Olowoyo, S. L. Jain, U. Kumar
Chemical Science Division, CSIR-Indian Institute of Petroleum, Dehradun, India
E-mail: umesh_kumar@iip.res.in
[b] M. Kumar
Catalytic Conversion Division, CSIR-Indian Institute of Petroleum, Dehradun, India
[c] N. C. Hernández
Departamento de Física Aplicada I, Escuela Politécnica Superior, Universidad de Sevilla, Sevilla, Spain
[d] J. O. Olowoyo, J. O. Babalola
Department of Chemistry, University of Ibadan, Ibadan, Nigeria

Supporting information for this article is available on the WWW under https://doi.org/10.1002/slct.201800076

© 2018 Wiley-VCH Verlag GmbH & Co. KGaA, Weinheim

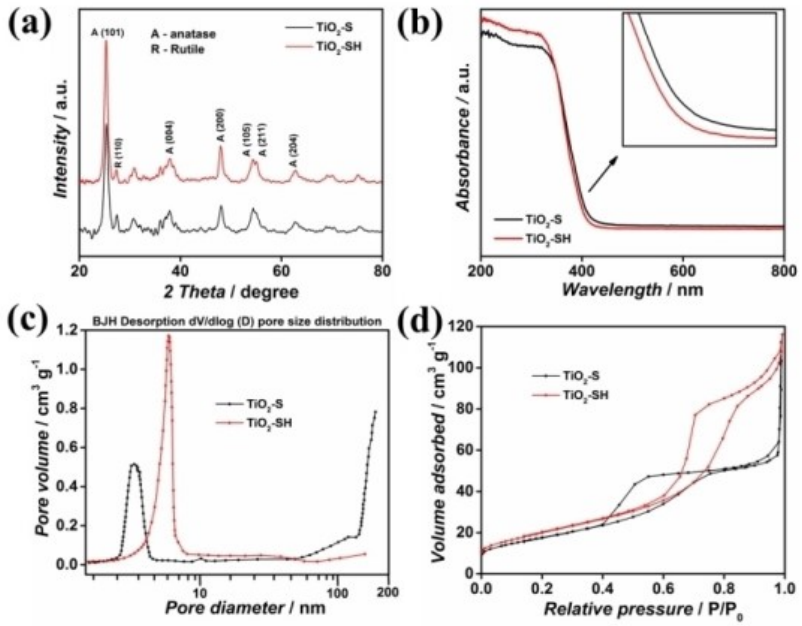

Figure 1. (a) XRD patterns (b) UV-Vis spectra (c) N_2 adsorption–desorption isotherms of TiO_2-S and TiO_2-SH samples and (d) Pore size distribution curve of TiO_2-S and TiO_2-SH samples.

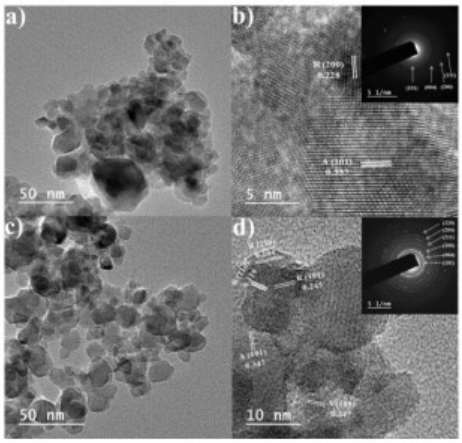

Figure 2. (a) TEM image of TiO_2-S, (b) HRTEM image of TiO_2-S, (c) TEM image of TiO_2-SH and (d) HRTEM image of TiO_2-SH.

phases with an average particle size of ca. 15 nm, and the SAED pattern indicates that TiO_2-SH is more crystalline {Figure 2b (inset) and d (inset)}. The UV–Vis DRS reveal that the TiO_2-S and TiO_2-SH have absorption band edge at 412 and 407 nm respectively. The TiO_2-SH shows a slight blue shift due to less rutile phase (Figure 1b) and the hyperchromic shift is probably due to the higher surface area. The calculated band gaps of both TiO_2 samples are found to be ca. 3.0 eV (Figure S5), which is typical of the presence of the rutile phase.[8] In addition, the TiO_2-SH (73.1 $m^2\ g^{-1}$, 0.18 $cm^3\ g^{-1}$) has better surface area and pore volume than TiO_2-S (64.5 $m^2\ g^{-1}$, 0.17 $cm^3\ g^{-1}$) (Table S2). The pore size distribution (PSD) is homogeneous in TiO_2-SH and contains a majority of mesopores with 6.1 nm pore maxima while TiO_2-S has both mesopores and more macropores (Figure 1c). Nitrogen adsorption-desorption isotherms of TiO_2-S and TiO_2-SH catalysts are of type IV according to the IUPAC classification and indicate the presence of mesopores (Figure 1d). The isotherms confirm a bimodal pore size type of distribution by exhibiting two different hysteresis loops at different P/P_0 range. A steep increasing for TiO_2-S in hysteresis loop at P/P_0 0.99 indicates the presence of macropores, as also confirmed by the curves of PSD and BJH desorption cumulative pore volume (Figure S6). It could be observed that the hysteresis loop of TiO_2-SH occurs at higher P/P_0 value in comparison with TiO_2-S, which suggests the presence of wider

© 2018 Wiley-VCH Verlag GmbH & Co. KGaA, Weinheim

mesopores and fewer macropores in TiO_2-SH (Figure 1d). In addition, wider mesopores and the higher surface area might be the factors that determine higher activities towards photocatalytic applications due to the easy access of reactant molecules to active sites in pores.

The DFT calculations in a periodic framework, as implemented in the VASP were utilized to establish the electronic, and the structural properties of H_2O, FA, CO_2, MeOH, and H_2 deposited on both TiO_2: anatase (101) and rutile (110) surfaces.[9] (Figure 3 and see full details in the supporting information)

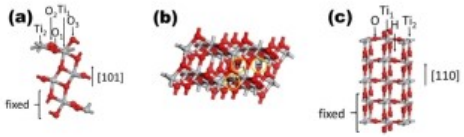

Figure 3. (a) Left and right show the side and (b) top view, respectively; of the 1 x 1 three-layer cell to describe the anatase (101) surface. (c) Side view of the 1 x 1 five-layer cell to describe the rutile (110) surface.

The adsorption energies were calculated by the expression:

$E_{ads} = E\ (molecule/surface) - E\ (surface) - E\ (molecule)$

Where the *molecule* variable can take the values of H_2O, CO_2, FA, MeOH, and H_2; and the *surface* would be anatase (101) and rutile (110). For the system *molecule/surface*, different orientations of the molecules were tested to calculate the minimum energy. The values of *E (molecule)* were obtained by performing a full geometry optimization of isolated molecules in a 10 Å x 10 Å x 10 Å supercell.

The photocatalytic activities of both TiO_2 were measured for the activation of small molecules. A series of blank experiments were performed to ascertain the formed products were the results of photocatalysis, and details are given in supporting information. The experiments were examined three times and a maximum of ca. ±5% error was observed. The error bars were included in the experimental results.

The photocatalytic H_2O splitting was performed without a sacrificial agent. In a typical experiment, 5.0 mg of catalyst was dispersed in 20 mL of HPLC grade H_2O and irradiated with UVA for 18 h (See details in supporting information). In Figure 4a, the H_2 production rate with TiO_2-SH is 19.1 μmol g^{-1} h^{-1}, 1.85 times of TiO_2-S. Chiarello et al. have utilized commercial P25 and flame spray pyrolysis-synthesized TiO_2 (FP5) for photocatalytic H_2 production (3.04 and 4.90 μmol g^{-1} h^{-1} respectively) via H_2O splitting in the absence of a sacrificial donor.[10] The TiO_2-SH has better hydrogen production, ca. 6.3 and 3.9 times than P25 and FP5 respectively. It was observed that increased performance for water splitting at TiO_2-SH is attributed to the higher adsorption energies of H_2O on its surface in comparison to TiO_2-S (Table 1 and 2). Higher adsorption of H_2O only at H hollow site in rutile in contrast with anatase is not sufficient enough for the former to split water better. Also, the

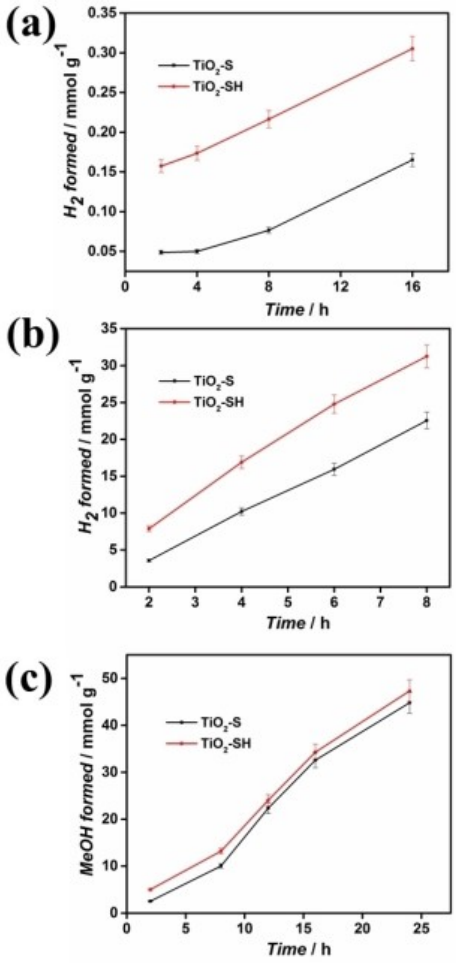

Figure 4. (a) Rate of hydrogen formation from the photocatalytic splitting of water without any sacrificial agent under UVA light (b) rate of hydrogen formation from the photocatalytic splitting of formic acid under UVA light (c) rate of methanol formation from the photoreduction of CO_2 with H_2O in the presence of TEOA under UVA light.

adsorption energy of H_2 at Ti_1 site in anatase (101) is lower than in rutile (110); this suggests that H_2 would leave faster the anatase (101) surface than rutile (110).

The photocatalytic FA splitting was performed with the 20 mL of 10% FA aqueous solution and 5 mg catalyst under UVA for 8 h (See details in supporting information). As shown in Figure 4b, TiO_2-SH performs better with H_2 production rate, i.e.,

© 2018 Wiley-VCH Verlag GmbH & Co. KGaA, Weinheim

Table 1. Adsorption energy (eV) of molecule deposited on surface anatase (101). Only the most stable case for each molecule, after deposited on the surface, are presented here.

Anatase (101) Molecule	O_1	O_2	O_3	Ti_1	Ti_2	H	H_1	H_2
H_2O	-0.92	-0.92	-0.79	-0.91	-0.91	-0.91	-0.39	-0.39
CO_2	-0.49	-0.16	-0.31	-0.37	-0.16	-0.35	-0.34	-0.35
FA	-0.80	-0.79	-1.22	-1.31	-0.79	-0.79	-1.31	-0.51
MeOH	-0.94	-0.94	-0.89	-1.01	-0.94	-0.93	-1.02	-0.48
H_2	-0.18	-0.03	-0.03	-0.03	-0.03	-0.03	-0.03	-0.03

Table 2. Adsorption energy (eV) of molecule deposited on surface rutile (110). Only the most stable case for each molecule, after deposited on the surface, are presented here.

Rutile (110) Molecule	Ti_1	Ti_2	O	H
H_2O	-0.38	-0.69	-0.53	-1.10
CO_2	-0.12	-0.15	-0.20	-0.30
FA	-1.21	-0.72	-0.72	-0.72
MeOH	-0.35	-0.83	-0.83	-0.84
H_2	-0.06	-	-	-

3.91 mmol g^{-1} h^{-1}, while TiO_2-S gives only 2.82 mmol g^{-1} h^{-1} H_2 production rate. The Table 1 and 2 suggest that (1) FA has better interaction with anatase (101), and (2) the produced H_2 has weaker. The combined effect leads to the higher activity of TiO_2-SH. The recyclability and stability of the catalyst were also checked for four consecutive cycles (further details are available in supporting information, Figure S7). The H_2 production remained almost same which confirm the catalysts are stable under acidic conditions also.

The selective methanol generation via photocatalytic reduction of CO_2 was also tested in acetonitrile (ACN), H_2O and triethanolamine (TEOA) mixture under UVA (see details in supporting information). During photocatalytic CO_2 reduction, both TiO_2-S and TiO_2-SH catalysts are equally competent and attained 1.87 and 1.97 mmol g^{-1} h^{-1} MeOH production rates respectively (Figure 4c). The adsorption energies of CO_2 are higher for most sites on anatase (101) surface than rutile, suggests that CO_2 would have better interact with anatase (101) and leads to higher activity of TiO_2-SH (Table 1 and 2).

However, the adsorption energies for MeOH are higher in anatase surface than rutile; suggesting that MeOH would leave the rutile surface faster than the anatase. Here, TiO_2-SH has the dual advantage of higher adsorption energies of CO_2 and surface area; though lesser adsorption energies of MeOH at TiO_2-S determine its closeness in the production of MeOH.

To allow the full spectrum of solar light, we experimented under the direct sunlight using filters (Lumen-Omnicure) to provide 320–390 nm and 400–500 nm. As depicted in Table 3, both TiO_2-S and TiO_2-SH are photoactive under sunlight radiation with the superiority of TiO_2-SH. It could be observed that the UV A fraction of sunlight (320 – 390 nm) is more active than the visible region (400 – 500 nm), suggesting that UVA light has the ability to excite more electrons. Hence, higher product formation was observed under UVA. It was also noticed that the complete spectrum of sunlight exhibits higher photoactivity in comparison to any single fraction of light (either UVA or visible). The higher activity in the complete spectrum is probably to the cooperative effects of the fractions of different wavelength of light within the full spectrum as previously reported in the literature.[10]

In general, the concept of adsorption energies of particular reactants and products on the different phases of TiO_2 is more crucial in tailoring which phase is more favorable for photocatalytic activities besides the known synergistic effects[11] and the built-in electric field[12] at the interface of the mixed-phase junction between anatase and rutile phases (Figure 2 and Scheme 1). From our calculated energies and experimental

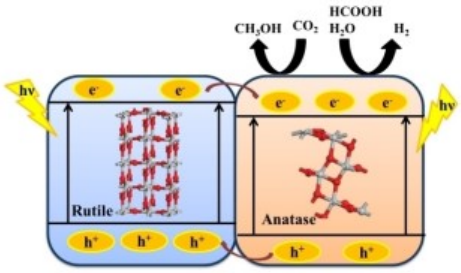

Scheme 1. Schematic presentation of activation of small molecules and products formation at the surface of TiO_2-S and TiO_2-SH catalysts.

results, the more anatase phase in TiO_2-SH is more favored for improved photocatalytic activities over TiO_2-S. Also, apart from the above-stated advantages, hydrothermal treatment plays another significant role by ensuring the better separation of

Table 3. Effect of catalysts for the activation of small molecules under UV A and sunlight irradiation.

CATALYST	UV A			Direct Sunlight (Complete Spectrum)			Sunlight (320-390 nm)			Sunlight (400-500 nm)		
	[a]H_2* (μmol g^{-1})	[b]H_2* (mmol g^{-1})	[c]CH_3OH** (mmol g^{-1})	[a]H_2* (μmol g^{-1})	[b]H_2* (mmol g^{-1})	[c]CH_3OH** (mmol g^{-1})	[a]H_2* (μmol g^{-1})	[a]H_2* (mmol g^{-1})	[c]CH_3OH** (mmol g^{-1})	[a]H_2* (μmol g^{-1})	[b]H_2* (μmol g^{-1})	[c]CH_3OH** (μmol g^{-1})
TiO_2-S	49.9	10.2	10.0	37.4	11.0	50.1	30.7	8.6	42.5	5.4	137.8	12.5
TiO_2-SH	173.6	16.9	13.2	72.3	25.8	50.3	58.9	19.8	43.2	13.4	140.0	29.4

[a]H_2 from H_2O; [b]H_2 from FA; [c]CH_3OH from CO_2; *4 h reaction time; **8 h reaction time.

© 2018 Wiley-VCH Verlag GmbH & Co. KGaA, Weinheim

various nanoparticles giving TiO_2-SH enhanced homogeneity (Figure 2c), crystallinity (Table S1), and surface area. Importantly, the synthesized photocatalysts were found to be highly reactive and selective for H_2 and methanol generation than the existing prior art.[13–14] By the use of intensity meter (UVP 97–0015-02/UVX digital Ultraviolet Meter/Radiometer), the light intensity reaching the inside of the reactor (by placing the sensor in the reactor) was measured to be ca. 0.7 and 0.9 mW/cm^2 for UVA and UV present in sunlight, respectively. Hence, the calculated quantum efficiency (QE) for TiO_2-2 under UVA was 0.012, 2.287 and 3.457% from H_2O, FA, and MeOH, respectively. Similarly, the QE for TiO_2-2 under sunlight was 0.008, 2.934 and 5.720% from H_2O, FA, and MeOH, respectively.

In summary, mixed phase TiO_2 photocatalysts were synthesized using sonothermal (S) and sonothermal-hydrothermal (SH) route and applied for the activation of small molecules, i.e., photocatalytic H_2O, FA splitting and CO_2 reduction for hydrogen and methanol generation respectively under UV–A. The prepared TiO_2 catalysts have a different amount of Rutile and Anatase phase. The DFT calculations in a periodic framework, as implemented in the VASP revealed that the anatase (101) has higher adsorption energy for the reactant molecules, so it has a better activity of activation of small molecules to produce H_2 and MeOH. Therefore, the TiO_2-SH exhibits better photocatalytic activity than TiO_2-S. The band gap of prepared catalysts may open the path for the utilization of direct sunlight for the similar application and other modifications including doping or impregnation will further help to enhance their photocatalytic performance.

Supporting Information Summary

Experimental and computational details are reported in the The Supporting Information (SI) section is attached as a separate file. The Experimental section contains explanation regarding the materials used and preparation of photocatalysts. The various characterization techniques performed on the prepared photocatlaysts well described in the characterization section. Also, the detailed information about the DFT calculations, photocatalytic experiment and quantum efficiency calculations are provided in the SI. Additional results are presented in tables and figures.

Acknowledgements

Authors are grateful to Director, IIP for his kind permission to publish the results. J. O. Olowoyo is thankful for CSIR-TWAS for research funding (22/FF/CSIR-TWAS/2015). Authors are thankful to ASD-IIP for their analytical support.

Conflict of Interest

The authors declare no conflict of interest.

Keywords: Adsorption energy · DFT Calculations · Photoactivation · Photocatalysis · TiO_2

[1] a) K. C. Christoforidis, P. Fornasiero, *Chemcatchem* **2017**, *9*, 1523–1544; b) S. M. Barrett, S. A. Slattery, A. J. M. Miller, *ACS Catal.* **2015**, *5*, 6320–6327; c) S. N. Habisreutinger, L. Schmidt-Mende, J. K. Stolarczyk, *Angew. Chem.* **2013**, *52*, 7372–7408.

[2] a) J. Zhang, Q. Xu, Z. Feng, M. Li, C. Li, *Angew. Chem.* **2008**, *47*, 1766–1769; b) S. Li, J. Chen, F. Zheng, Y. Li, F. Huang, *Nanoscale* **2013**, *5*, 12150–12155; c) M. G. Ju, G. Sun, J. Wang, Q. Meng, W. Liang, *ACS Appl. Mater. Interfaces* **2014**, *6*, 12885–12892.

[3] W. Huang, X. Tang, Y. Wang, Y. Koltypin, A. Gedanken, *Chem. Commun.* **2000**, *0*, 1415–1416.

[4] R. Kaplan, B. Erjavec, G. Drazic, J. Grdadolnik, A. Pintar, *Appl. Catal., B* **2016**, *181*, 465–474.

[5] a) R. Scotti, M. D'Arienzo, A. Testino, F. Morazzoni, *Appl. Catal., B* **2009**, *88*, 497–504; b) B. Zhao, L. Lin, D. He, *J. Mater. Chem. A* **2013**, *1*, 1659–1668.

[6] Y. Ortega, N. C. Hernandez, E. Menendez-Proupin, J. Graciani, J. F. Sanz, *Phys. Chem. Chem. Phys.* **2011**, *13*, 11340–11350.

[7] K. Farhadian Azizi, M.-M. Bagheri-Mohagheghi, *J. Sol-Gel Sci. Technol.* **2013**, *65*, 329–335.

[8] W. K. Wang, J. J. Chen, X. Zhang, Y. X. Huang, W. W. Li, H. Q. Yu, *Sci. Rep.* **2016**, *6*, 20491, DOI 10–1038/srep20491.

[9] a) G. Kresse, J. Furthmüller, *Phys. Rev. B* **1996**, *54*, 11169–11186; b) G. Kresse, J. Furthmüller, *Comput. Mater. Sci.* **1996**, *6*, 15–50; c) G. Kresse, J. Hafner, *Phys. Rev. B* **1994**, *49*, 14251–14269; d) G. Kresse, J. Hafner, *Phys. Rev. B* **1993**, *47*, 558–561; e) G. Kresse, D. Joubert, *Phys. Rev. B* **1999**, *59*, 1758–1775; f) J. P. Perdew, K. Burke, M. Ernzerhof, *Phys. Rev. Lett.* **1996**, *77*, 3865–3868.

[10] G. Mele, C. Annese, L. Accolti, A. De Riccardis, C. Fusco, L. Palmisano, A. Scarlino, G. Vasapollo, *Molecules* **2015**, *20(1)*, 396–415.

[11] Y. K. Kho, A. Iwase, W. Y. Teoh, L. Mädler, A. Kudo, R. Amal, *J. Phys. Chem. C* **2010**, *114*, 2821–2829.

[12] a) T. Xia, N. Li, Y. Zhang, M. B. Kruger, J. Murowchick, A. Selloni, X. Chen, *ACS Appl. Mater. Interfaces* **2013**, *5*, 9883–9890; b) M. G. Ju, G. Sun, J. Wang, Q. Meng, W. Liang, *ACS Appl. Mater. Interfaces* **2014**, *6*, 12885–12892; c) X. Zhang, Y. Lin, D. He, J. Zhang, Z. Fan, T. Xie, *Chem. Phys. Lett.* **2011**, *504*, 71–75.

[13] G. L. Chiarello, E. Selli, L. Forni, *Appl. Catal., B* **2008**, *84*, 332–339.

[14] a) L. Clarizia, I. Di Somma, R. Marotta, P. Minutolo, R. Villamaina, R. Andreozzi, *Appl. Catal., A* **2016**, *518*, 181–188; b) P. Kumar, N. G. Naumov, R. Boukherroub, S. L. Jain, *Appl. Catal., A* **2015**, *499*, 32–38.

Submitted: January 9, 2018
Revised: March 9, 2018
Accepted: March 22, 2018

© 2018 Wiley-VCH Verlag GmbH & Co. KGaA, Weinheim

APPENDIX VI

Copy of paper published from the Synthesis of visible light active RGO-TiO_2composites for the photoreduction of CO_2

Carbon 147 (2019) 385–397

Contents lists available at ScienceDirect

Carbon

journal homepage: www.elsevier.com/locate/carbon

Self-assembled reduced graphene oxide-TiO_2 nanocomposites: Synthesis, DFTB+ calculations, and enhanced photocatalytic reduction of CO_2 to methanol

Joshua O. Olowoyo [a, e], Manoj Kumar [b], Bhupender Singh [c], Vincent O. Oninla [d], Jonathan O. Babalola [e], Héctor Valdés [f], Alexander V. Vorontsov [g, *], Umesh Kumar [a, *]

[a] Chemical Science Division, CSIR-Indian Institute of Petroleum Dehradun, India
[b] Catalytic Conversion Division, CSIR-Indian Institute of Petroleum Dehradun, India
[c] Institute Instrumentation Centre, Indian Institute of Technology Roorkee, India
[d] Department of Chemistry, Obafemi Awolowo University, Ile-Ife, Osun State, Nigeria
[e] Department of Chemistry, University of Ibadan, Ibadan, Nigeria
[f] Laboratorio de Tecnologías Limpias, Facultad de Ingeniería, Universidad Católica de la Santísima Concepción, Alonso de Ribera 2850, Concepción, Chile
[g] Altai State University, pr. Lenina 61, Barnaul 656049, Russia

ARTICLE INFO

Article history:
Received 2 December 2018
Received in revised form
20 February 2019
Accepted 8 March 2019
Available online 12 March 2019

Keywords:
CO_2 reduction
DFTB+ calculations
Photocatalysis
Sonothermal-hydrothermal

ABSTRACT

A facile combined method, namely sonothermal-hydrothermal, was adopted to assemble titanium dioxide (TiO_2) nanoparticles on the surface of reduced graphene oxide (RGO) to form nanocomposites. Characterization techniques confirm that RGO-TiO_2 composite is well constituted. Enhanced photocatalytic CO_2 reduction to methanol by the composites under UVA and visible irradiation suggests the modification in the band gap of the composite and promotion of the separation of photogenerated carriers, yielding methanol production rate of 2.33 mmol g^{-1} h^{-1}. Theoretical investigation demonstrated that combining RGO with TiO_2 resulted in an upward shift of TiO_2 bands by 0.2 V due to the contribution of RGO electrons. Relatively strong adsorption of RGO over the (101) anatase surface with the binding energy of approximately 0.4 kcal mol^{-1} per carbon atom was observed. Consideration of orbitals of TiO_2, RGO and RGO-TiO_2 composite led to a conclusion that UVA photoreaction proceeds *via* the traditional mechanism of photogenerated electron transfer to RGO while visible light CO_2 reduction proceeds as a result of charge transfer photoexcitation that directly produces electrons in RGO and holes in TiO_2. Superior photocatalytic activity of RGO-TiO_2 composite in the present study is attributed to the formation of tight contact between its constituents, which is required for efficient electron and charge transfer.

© 2019 Published by Elsevier Ltd.

1. Introduction

Since the discovery of graphene [1] and specifically reduced graphene oxide (RGO), which is an analog of graphene with a two-dimensional sp^2-hybridized carbon nanosheet, has immense attraction within the scientific community due to its unique properties such as high chemical stability [2], excellent mechanical strength [3], high thermal conductivity (~5000 W m^{-1} K^{-1}) [4], flexible structure [5], excellent mobility of charge carriers (20,000 cm^2 V^{-1} s^{-1}) [6,7], and relatively good optical transparency [8]. Aside from the application of RGO alone, there have been successful attempts to hybridize RGO with semiconductor nanoparticles to form nanocomposites.

So far, among the known semiconductors adopted in various applications such as photocatalysis, supercapacitors, and energy conversion devices; titanium dioxide nanoparticles (TiO_2-NPs) have been the most researched and promising due to their extraordinary performance in photocatalysis, high stability, non-toxicity and low price [9,10]. With the uniqueness of TiO_2 in diverse applications such as water splitting, organic dye degradation, CO_2 reduction and so on, it is not without its flaws such as (i) large band gap, (ii) fast recombination of photogenerated electron-hole pairs, (iii) inefficient interaction with reagents and (iv) low selectivity towards desired products. Till now, various efforts

* Corresponding authors.
E-mail addresses: a-voronts@yandex.ru (A.V. Vorontsov), umesh_kumar@iip.res.in (U. Kumar).

https://doi.org/10.1016/j.carbon.2019.03.019
0008-6223/© 2019 Published by Elsevier Ltd.

including metal/non-metal doping, metal impregnation, noble metal loading, composites, sensitization by dyes and heterojunction fabrication have been made to solve these problems. Among these, fabricating nanocomposites allowed the significant advancements in obtaining high-performance photocatalysts.

The improved performance of TiO_2-NPs photocatalyts could be achieved by coupling with carbon-based materials such as RGO to obtain nanocomposites (RGO-TiO_2). The presence of RGO in the nanocomposites helps extend the photon absorption of TiO_2 into the visible region; since RGO is known for its high optical transparency in both visible and near-infrared regions. Moreover, RGO acts a sink for electrons as well as an effective charge transporting bridge due to its high electron mobility and extended π-electron conjugation. Therefore, the heterojunction formed at the interface of RGO and TiO_2 separates the photoexcited electron–hole pairs and retards the recombination process. The incorporation of RGO also helps to increase the surface area of TiO_2 [11–14].

Various synthetic approaches have been used to fabricate RGO-TiO_2. Fan and co-workers have made the efforts to prepare nanocomposites of titanium dioxide (P25) and RGO by several techniques; including UV – assisted photocatalytic reduction, hydrazine reduction, and hydrothermal method and used them as photocatalysts for hydrogen generation from alcohol solution under UV-Vis irradiation. The P25-RGO composite prepared by the hydrothermal method performed best due to stronger interaction between P25 and graphene [15]. Among the various applications of RGO-TiO_2 such as photocatalytic CO_2 reduction [16], water splitting [17], dye and organic pollutant degradation [18,19], lithium-ion batteries [20], and antibacterial activity [21]; photocatalytic CO_2 reduction to valuable hydrocarbons *via* solar irradiation could serve as a solution to the total dependence on fossil fuels with its concomitant global warming. Till date, the majority of all reported studies on CO_2 reduction in the gas phase to valuable fuel with RGO-TiO_2 observed methane as the product [16,22–27]; however, reports on products like methanol from the liquid phase are rare. The fine structure of RGO-TiO_2 interactions and reasons for improved photocatalytic activity has been previously studied computationally using periodic and cluster models. A significant interaction was found; and strong visible light absorption with charge transfer between the two was suggested. However, these computational results are partially dealing with experimental study. Herein, in this work, a facile combined method, namely sonothermal and hydrothermal to assemble titanium dioxide nanoparticles (TiO_2-NPs) on the surface of RGO was applied to form nanocomposites, by varying the amount of RGO. As compared to the pure TiO_2-NPs, RGO-TiO_2 nanocomposites have significantly enhanced photocatalytic activity under UVA and visible-light. The influence of reaction media, ACN/H_2O, DMF/H_2O, and DMSO/H_2O, was also investigated. Properties of the RGO-TiO_2 interface were assessed by cluster DFTB calculations, and they revealed only moderate interaction and limited visible light charge transfer. To obtain more relevant explanations on the RGO-TiO_2 interface properties, a computational model with TiO_2 nanoparticle size of around 2 nm was used in the present study. More realistic size of the TiO_2 nanoparticle resulted in a better agreement of computational and experimental results.

2. Experimental

2.1. Materials

Graphite powder; sodium nitrate ($NaNO_3$), hydrazine monohydrate ($H_4N_2 \cdot H_2O$, 64–65%), potassium permanganate ($KMnO_4$), and titanium (IV) butoxide ($Ti(OBu)_4$) were purchased from Sigma Aldrich; hydrochloric acid (HCl), hydrogen peroxide (H_2O_2), methanol (CH_3OH), nitric acid (HNO_3), triethanolamine (TEOA) and *N,N*-dimethyl formamide (DMF) from Merck; dimethyl sulphoxide (DMSO) from BDH laboratory; ethanol (C_2H_5OH) from Fischer Chemicals; acetonitrile (ACN) for HPLC spectroscopy from Sd finechem limited; sulfuric acid (H_2SO_4) from Loba Chemie; CO_2 (>99.9995%) from Sigma gases; and HPLC grade water (H_2O). All chemicals were of analytical grade and used without further purification.

2.2. Synthesis of graphene oxide

Graphene oxide (GO) was prepared from graphite powder using a modified Hummer's method [28,29]. Briefly, 450 mL of H_2SO_4 was placed in a 2000 mL beaker in an ice water bath under stirring. 12 g of $NaNO_3$ was added very slowly followed by the addition of 10 g of graphite powder and kept under stirring for 30 min. Then 50 g of $KMnO_4$ was slowly added and stirred for additional 3 h. 700 mL of distilled water was slowly added to the mixture and stirred vigorously overnight at room temperature. After that, 40 mL H_2O_2 (50 wt %) was added to the mixture and stirred for a further 4 h, yielding a yellow-brown suspension. The obtained suspension was centrifuged and washed with 500 mL of 10% HCl. Additional washing was performed by dispersing the suspension in 1000 mL of H_2O under vigorous stirring followed by bath sonication to obtain a single layer sheet of GO. The acquired GO was centrifuged to remove the unexfoliated precipitation. Finally, the brown dispersion of exfoliated GO was dried in an oven at 80 °C.

2.3. Preparation of RGO

RGO was prepared as follows. 2 g of GO was suspended in 30 mL of toluene, and 2 mL of hydrazine monohydrate was added to the mixture followed by refluxing at 80 °C for 12 h. After cooling to room temperature, the mixture was centrifuged, washed with toluene and subsequently dried in an oven at 80 °C to obtain black RGO powders.

2.4. Synthesis of the RGO-TiO_2 photocatalysts

RGO-TiO_2 nanocomposites were prepared by the sonothermal and hydrothermal methods [30]. In a typical experiment, 10 mg of the prepared RGO was dispersed in 30 mL of water: ethanol solution (2:1 v/v) in a 100 mL beaker and sonicated at 70 °C for 15 min to get a homogenized suspension. Then, 10 g of $Ti(OBu)_4$ dissolved in 30 mL ethanol was added dropwise to the RGO suspension under ultrasonication at 70 °C followed by the addition of few drops of HNO_3. The sonication of the mixture further continued for an additional 45 min. After that, the sonicated mixture was transferred into a 100 mL Teflon-lined stainless steel autoclave. The autoclave was sealed and heated at 180 °C for 12 h, and then cooled to room temperature. After hydrothermal treatment, the obtained precipitate was separated by centrifugation (6000 rpm), and dried overnight in an air oven at 80 °C. The collected sample was ground; and calcined in a furnace at a temperature of 400 °C for 2 h with a heating rate of 2 °C min^{-1} to finally get 1%RGO-TiO_2 (w/w ratio), code-named 1.0RGO-TiO_2. Other mass ratios including 2, 5 and 10 wt% were also synthesized to obtain 2.0RGO-TiO_2, 5.0RGO-TiO_2 and 10.0RGO-TiO_2, respectively. The same procedure was adopted for the synthesis of pure TiO_2 as a reference.

2.5. Characterization of TiO_2, pure RGO, and synthesized RGO-TiO_2 nanocomposites

The obtained samples were characterized by various spectroscopic and analytical techniques. Thermal stability of the fresh

catalysts was performed by thermogravimetric analysis (TGA) with Perkin Elmer TGA4000. For this analysis, 10 mg of the sample was placed in a platinum crucible and heated from ambient temperature to 450 °C at a rate of 10 °C min^{-1} under air atmosphere. The Raman analysis of the prepared catalyst was done with STR 500 Airix.

The crystal structures of the bare TiO_2 and RGO- containing samples were identified by X-ray diffraction (XRD) on a Bruker D8 Advance X-ray diffractometer using monochromatic Cu Kα (λ = 1.5418 Å) radiation in the 2θ range from 2° to 80° with a step size 0.02° s^{-1}.

Textural characterization such as surface area, pore size, and pore volume of the TiO_2 and RGO-containing samples was analyzed with a Micromeritics ASAP 2010. The N_2 adsorption-desorption properties at 77 K were examined with Brunauer–Emmett–Teller (BET) method. The pore size distribution was measured from the desorption branch of the isotherm using the Barrett–Joyner–Halenda method.

The solid-state UV–visible diffuse reflectance spectra were recorded with Shimadzu 2600 UV/Vis-NIR spectrophotometer, equipped with an integrated sphere in the wavelength range of 200–800 nm, using $BaSO_4$ as the total reflecting standard.

Transmission electron microscopy (TEM) and high-resolution transmission electron microscopy (HRTEM) images were obtained with a JEM-2100 instrument (JEOL, Japan) with a LaB_6 filament, an accelerating voltage of 200 kV and resolution of 1.4 Å. The catalyst particles were loaded on the carbon coated copper grid *via* dispersion in ethyl alcohol using the ultrasonic processor.

Chemical composition determined from X-ray photoelectron spectroscopy (XPS) analysis of materials was carried out using ESCA+, (Omicron nanotechnology, Oxford Instrument Germany) equipped with a monochromator Aluminum Source (Al kα radiation hν = 1486.7 eV).

The steady state emission and fluorescence lifetime decay spectra were recorded on Horiba Jobin Yvon, Fluorocube Model. The powder sample was shone with the excitation source of Nano LED 375 nm at 45° for recording these spectra.

2.6. Photocatalytic CO_2 reduction

The photocatalytic reduction of CO_2 was performed according to our previous studies [30,31]. Briefly, 5 mg of the catalyst was suspended in a closed gas-recirculation quartz reactor containing 20 mL HPLC grade water: ACN mixture (4: 16 v/v) in the presence of TEOA as the sacrificial agent. The photocatalytic system was illuminated by an 8 W, UV-A lamp (PEN-RAY lamp, 350 nm, 2.13″, Cole-Parmer, 120 μW cm^{-2}) located at a distance of 0.2 cm from the reactor. A small aliquot liquid sample was taken out at a regular time interval and analyzed by a gas chromatograph Perkin Elmer Clarus 680 equipped with FID and TCD, plot-Q and shin carbon columns. A series of blank experiments were performed under the following conditions: (a) in the dark without CO_2 in the presence of catalyst, (b) in the dark with CO_2 in the presence of catalyst, (c) UV-illuminated in the absence of both CO_2 and catalyst, (d) UV-illuminated in the presence of CO_2 and absence of catalyst, (e) UV-illuminated in absence of CO_2 and the presence of the catalyst. No carbonaceous product was detected in the above blank tests, only traces of hydrogen were observed in (e) conditions.

2.7. Computational study on RGO-TiO_2 composite

For purposes of quantum chemical modelling, RGO nanosheet was represented by a rectangular graphene quantum dot (GQD) having hydrogen passivated zigzag and armchair edges. This GQD has 10 benzene rings along the zigzag edge, and six benzene rings in the outer armchair edge. Atomic structure of this $C_{252}H_{44}$ GQD after full geometry relaxation is shown in Fig. 1. The advantage of using finite size cluster graphene models as opposed to infinite periodic boundary condition models consists of the full presence of rotational degrees of freedom in geometry relaxation of TiO_2-RGO composite. Thus, not only the distance between RGO and TiO_2 but also tilting angles can be adjusted.

Anatase titanium dioxide nanoparticles were represented by one of the most stable isomers of anatase decahedral cluster models denoted Ti44r1. This nanoparticle with the molecular formula $(TiO_2)_{121}(H_2O)_6$ contained (001) and (101) facets, hydroxyl groups at (001)/(101) edges and was considered in details in previous studies [32–34].

Quantum chemical treatment of the models included complete geometry optimization of the GQD and GQD-Ti44r1 composite. Previously, it has been found that interaction of a carbon nanotube with the Ti44r1 nanoparticle is much stronger on (101) facet than on (001) facet of this TiO_2 anatase nanoparticle [35]. Due to the structural analogy of carbon nanotubes and graphene nanosheets, it was reasonable to suppose much stronger interaction of RGO with the (101) facet compared to the (001) facet. Hence, the only interaction of RGO with the (101) facet was considered. Dftb+ program was used for all computations [36]. The scc-dftb method was utilized for obtaining energy [37] with Slater-Koster files tiorg-0-1 [38], and mio-1-1 [37]. Geometry optimization was performed until the maximal force component becomes smaller than 0.05 kcal $(mol Å)^{-1}$. Molecular orbitals were plotted using the 0.0005 isovalue surface of charge density.

3. Results and discussion

3.1. Characterization of nanocomposites

The thermal behavior of TiO_2, 5.0RGO-TiO_2, and pure RGO was examined by TGA analysis recorded under air atmosphere. As shown in Fig. 2a, two obvious weight losses were observed with pure RGO. First, the loss (*ca.* 10%) noticed in the range *ca.* 30–125 °C was due to the evaporation of the adsorbed moisture while other loss (15%) observed in the range 125–330 °C was attributed to the burning of remaining organic solvents and oxygen-containing

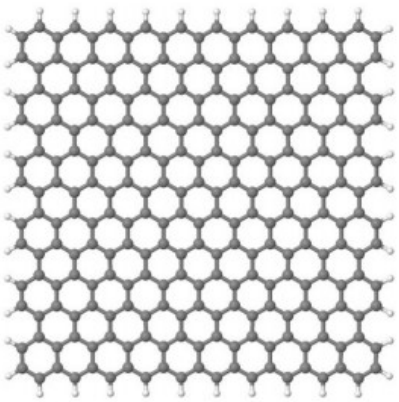

Fig. 1. Rectangular graphene quantum dot with hydrogen passivated edges used as an RGO model in the present study.

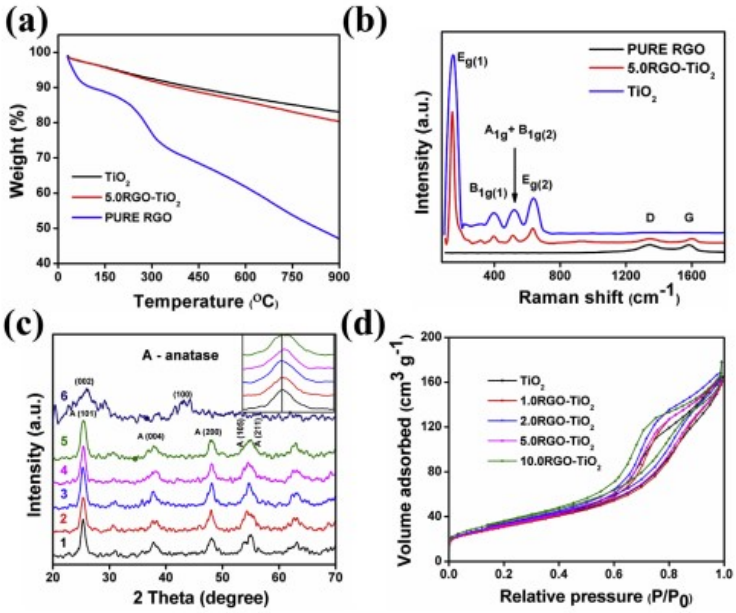

Fig. 2. (a) TGA curves; (b) Raman spectra of TiO_2, 5.0RGO-TiO_2 and pure RGO; (c) XRD peaks of (1) TiO_2, (2) 1.0RGO-TiO_2, (3) 2.0RGO-TiO_2, (4) 5.0RGO-TiO_2, (5) 10.0RGO-TiO_2, and (6) RGO. (d) N_2 adsorption-desorption isotherms of pure TiO_2 and RGO-TiO_2 samples.

functional groups of RGO [39,40]. Beyond 330 °C, the gradual reduction in weight till 900 °C (*ca.* 50% total loss) was from the burning of the carbon skeleton [39]. The TGA curve for the pure TiO_2 had a weight loss of 9.4% at 400 °C and total weight loss of 17% at 900 °C, as a result of the loss of inter lattice moisture and adsorbed water. However, the curve for 5.0RGO-TiO_2 nanocomposite did not reveal the two significant mass losses of RGO. This is due to the strong attachment of RGO with TiO_2 during the calcination process and the small loading amount of RGO in the composite. The weight losses of 10.4% and 20% were observed in the nanocomposite at the calcination temperature 400 and 900 °C, respectively. This indicates that there was no significant weight loss of RGO in the nanocomposite, confirming the stability of the nanocomposite at calcination temperature.

To evaluate the interaction between RGO and TiO_2, Raman spectra were obtained for TiO_2, 5.0RGO-TiO_2, and pure RGO samples. As shown in Fig. 2b, there were two characteristic peaks at 1340.8 and 1580.3 cm^{-1}, which were assigned to D and G bands of RGO sample. The bands correspond to the first-order scattering of the E_2g mode for sp^2 carbon domain as well as the structural defects, amorphous carbon, or edges that break the symmetry and selection rule [41,42]. The bare TiO_2 showed strong peaks at 149.2, 397.4, 516.8 and 639.5 cm^{-1}, which were attributed to Eg(1), B1g(1), A1g + B1g(2) and Eg(2) vibration modes of anatase TiO_2, respectively. The characteristic peaks for both RGO and TiO_2 were retained in the spectra of the 5.0RGO-TiO_2 nanocomposite. In comparison to RGO, the G band was shifted to 1598.8 cm^{-1} with a red shift in the composite, confirming the formation of the nanocomposite, while, a slight red shift was observed with the D-band. A similar phenomenon was observed by Shah and co-workers [43].

The XRD patterns of the prepared RGO and RGO-TiO_2 catalysts are shown in Fig. 2c. The peaks at $2\theta = 25.9°$ and 43.2° were assigned to planes (002) and (100) of the RGO sample. All other catalysts, including TiO_2 and RGO-TiO_2, depicted similar XRD peaks, which agree well with the tetragonal anatase TiO_2 (JCPDS 21-1272). Since no characteristic peak of RGO was observed, there was no noticeable difference in the peaks of TiO_2 as the loading amount of RGO increases in the RGO-TiO_2 composite. It was reasoned that peaks of TiO_2 overlapped the peaks of RGO. Notably, from Fig. 2c (inset), the width of the major peak (101) in TiO_2 was widened with the increasing amount of RGO in RGO-TiO_2 composites. This widening changed the crystallite size of TiO_2 in the nanocomposites. The crystallite size of pure TiO_2 and RGO-TiO_2 nanocomposite for TiO_2 was calculated by using the Scherrer's formula. The size of the pure TiO_2 was 16 nm; however, that of TiO_2 in the nanocomposites decreased gradually from 14 nm to 12 nm with increasing RGO content (Table 1). This suggests that presence of RGO helped to control the crystal size of TiO_2 [44].

The BET surface area of pure TiO_2 was found to be 108.3 $m^2 g^{-1}$; however, an increase in surface area was observed for all samples with RGO (Table 1). The adsorption-desorption isotherms of the prepared catalysts are shown in Fig. 2d. In comparison with pure TiO_2, the hysteresis loop was increased and widened after the incorporation of RGOs, suggesting an increase in the porosity in all RGO-TiO_2 samples. Sample with maximum RGO content showed the presence of macropores, as observed by a steep rise in hysteresis at $P/P_o = 0.99$. Fig. S2 with pore size distribution curve showed that the mesopore size maxima shifted from 7.5 nm in pure TiO_2 to 6.4 nm after the addition of RGO. With higher RGO content, the pore size distribution was in the narrower range of mesopores, as shown in Fig. 2d and Fig. S2. Cumulative pore volume also showed higher volume with increasing RGO content (Fig. S3). Higher pore

Table 1
Physico-chemical properties of the pure TiO_2 and RGO-TiO_2 samples.

Type of catalyst	Crystalline size (nm)	Surface area ($m^2\ g^{-1}$)	Pore volume ($cm^3\ g^{-1}$)	Pore maxima (nm)
TiO_2	16.0	108.3	0.25	7.5
1.0RGO-TiO_2	14.3	111.2	0.25	6.9
2.0RGO-TiO_2	14.1	119.9	0.28	7.0
5.0RGO-TiO_2	14.9	115.2	0.25	7.5
10.0RGO-TiO_2	11.9	128.62	0.27	6.7

volume may help in the smooth diffusion of molecules of CO_2 reduction reaction.

The UV-visible diffuse reflectance spectra of prepared TiO_2 and RGO-TiO_2 were obtained to investigate the change in absorption properties of the prepared catalysts (see Fig. 3a). The absorption edge of TiO_2, which was determined by the extrapolation of the linear part of the plot to the absorption background in the visible light, was found to be around 392 nm, which did not change significantly in RGO-TiO_2 composites. The introduction of RGO into TiO_2 did not significantly cause a redshift to a longer wavelength in the absorption edge of TiO_2, and this phenomenon is discussed and further confirmed in the section devoted to the results of the theoretical study. The optical band gap energies of the prepared catalysts were also determined from the Tauc plot of $[F(R)hv]^{1/2}$ versus the photon energy *via* the intercept of the tangent to the x-axis [45]. As shown in Fig. S5, the band gap of TiO_2 was found to be 3.2 eV, which gradually decreased to about 2.9 eV with 10.0RGO-TiO_2. The observed decrease in the TiO_2 band gap was small and may be due to the formation of Ti—O—C bonds in the composite [41–43,46].

The morphologies and crystal characteristics of TiO_2 and 5.0RGO-TiO_2 catalysts were revealed by TEM and HRTEM (Fig. 4). Fig. 4d shows that the TiO_2 nanoparticles were embedded in the sheets of RGO. The thickness of the monolayer of the RGO was calculated to be 0.35 nm. The calculated average particle size gradually decreased from *ca.* 11.44 nm in TiO_2 to 11.39, 10.83, 10.46 and 9.38 nm in 1.0RGO-TiO_2, 2.0RGO-TiO_2, 5.0RGO-TiO_2 and 10.0RGO-TiO_2, respectively (Fig. 4a and b and S4). The addition of RGO, which served as the support, ensured more dispersion and suppressed the further growth of TiO_2 nanoparticles [47]. The d-spacing of 0.342 nm were consistent with anatase (101) plane of TiO_2 in both samples (Fig. 4b and d), suggesting that RGO had little influence on the crystal phase of TiO_2. In Fig. S8, the selected area electron diffraction patterns confirmed that the ordinary TiO_2 and all RGO-containing composites exhibited polycrystalline structure, which was in agreement with the result of XRD analysis.

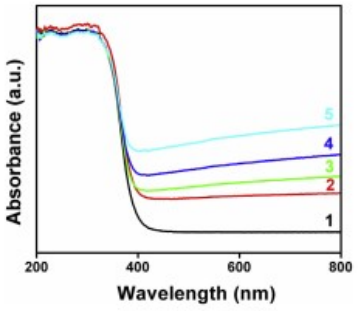

Fig. 3. UV-Vis diffuse reflectance s spectra of samples: (1) pure TiO_2, (2) 1.0RGO-TiO_2, (3) 2.0RGO-TiO_2, (4) 5.0RGO-TiO_2 and (5) 10.0RGO-TiO_2.

XPS spectra were employed to study the surface state and the interaction of the prepared TiO_2 with RGO. The full-scale spectra of TiO_2, 5.0RGO-TiO_2, and pure RGO are shown in Fig. S9 - S11. The spectrum of 5.0RGO-TiO_2 showed the existence of Ti, O and C peaks. Also, C and O peaks were consistent with pure RGO. However, C peak observed in the spectrum of TiO_2 was a result of the instrument reference standard, and the peak was lower in intensity in comparison with 5.0RGO-TiO_2. The high-resolution XPS spectrum of Ti2p for TiO_2 is shown in Fig. 5a. The peaks centered at 458.3 and 464.0 eV were attributed to $Ti2p_{3/2}$ and $Ti2p_{1/2}$ respectively, which were in good agreement with the binding energy values of Ti^{4+} in pure anatase. For 5.0RGO-TiO_2 composite, these two peaks were shifted to 459.9 and 465.6 eV, as shown in Fig. 5b. This shift is due to the highly electronegative O, which withdraws the electron density from Ti of 5.0TiO_2-RGO [43].

The high-resolution XPS spectra of C1s from pure RGO and 5.0RGO-TiO_2 are shown in Fig. 5c and d. For pure RGO, the core-level spectrum was deconvoluted into three components. The main peak centered at about 284.2 eV was attributed to the non-oxygenated ring C including C—C, C═C and C—H bonds. The other two peaks centered at 284.9 and 287.8 eV were assigned to carbon atoms connecting with oxygenate groups, C—O and C═O bonds, respectively [42,48]. Accordingly, these three peaks also were present in 5.0RGO-TiO_2 and were shifted to 284.8, 285.5 and 288.7 eV. The areas of the peaks assigned to C—O and C═O bonds significantly reduced by 35.2 and 83.8%, respectively (Table S1); indicating the elimination of considerable fraction of oxygen-containing group during the hydrothermal process. The observed peak shift and reduction of the peak areas with 5.0RGO-TiO_2 indicate the interaction of RGO and TiO_2 in the composite [49].

The narrow scan spectra of O1s for the pure RGO, 5.0RGO-TiO_2 and TiO_2 samples are shown in Fig. 5e, f and S12. The deconvolution of the spectrum for the pure RGO showed three main peaks centered at 530.3, 531.2 and 532.8 eV which were assigned to carbonyl oxygen from O—C═O, C═O and hydroxyl oxygen from C—O—H. The fourth peak centered at 534.9 eV was the adsorbed O—H group [50,51]. For 5.0RGO-TiO_2 (Fig. 5f), similar peaks were observed. However, the presence of Ti—O—Ti was observed at peak position 533.5 eV. This peak overlapped with O—C═O peak, which increased in area by 51.8% in comparison with pure RGO [52]. The increased peak area at 533.5 eV indicated that there was an interaction between RGO and TiO_2. As expected for the pure TiO_2, the peaks observed at 529.5 and 531.3 eV were attributed to lattice oxygen and non-lattice oxygen (adsorbed OH group), respectively (Fig. S12).

Photoluminescence (PL) spectroscopy has been employed to study the emission mechanism and charge transfer efficiencies in semiconductors. In order to confirm the electron transfer from the conduction band of TiO_2 to RGO, PL and PL lifetime decay traces of bare TiO_2 and TiO_2-RGO nanocomposites were recorded. Since, the absorption edge of these materials was observed around 390 nm (from Tauc's Plot), Nano LED with an excitation energy of about 3.2 eV (375 nm) was used as excitation source for recording the steady state emission spectra (Fig. 6a) in the wavelength range of 390—500 nm and emission maxima was observed at about 428 nm.

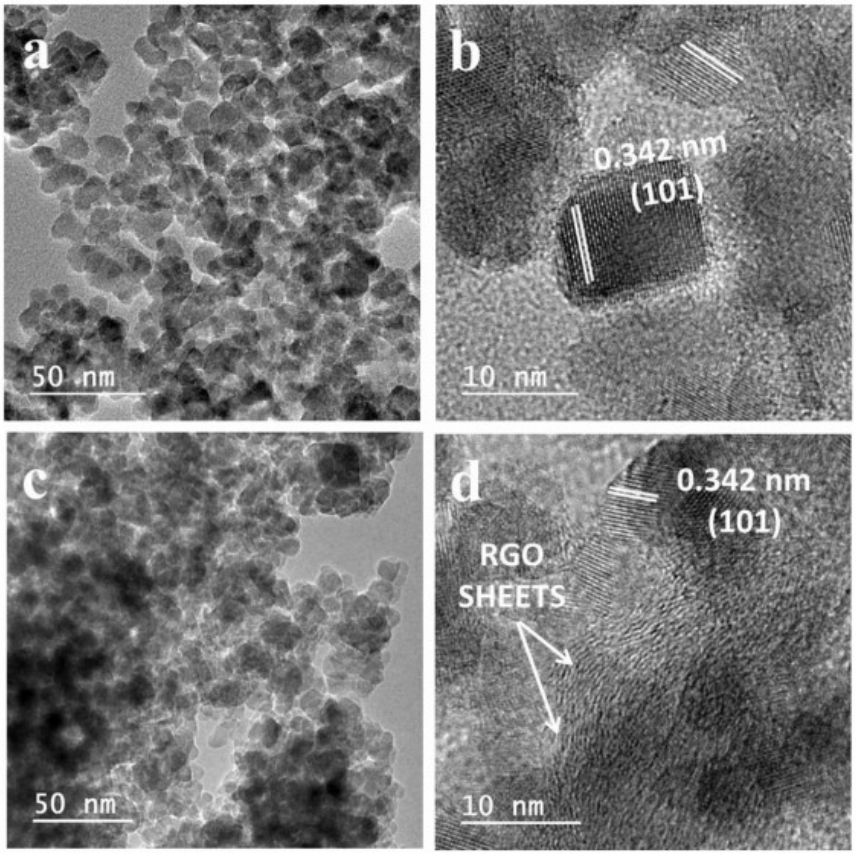

Fig. 4. (a) TEM image of pure TiO_2, (b) HRTEM of pure TiO_2, (c) TEM image of 5.0RGO-TiO_2, (d) HRTEM of 5.0RGO-TiO_2.

The intensity of TiO_2 was found to decrease when its composites were formed with RGO, which confirms the interaction between the TiO_2 and RGO and demonstrates electronic transitions between TiO_2 and RGO. The formation of interface between TiO_2 and RGO possibly affecting the pathway of excitons recombination due to narrowing down of the band gap associated with intermixing of density of states of the two moieties. Noteworthy, increased intensity by 10.0RGO in comparison with all RGO-TiO_2 samples could have been as a result of excessive doping. Similar observations have also been reported in literature [26,53,54].

Further investigation was performed by recording the time resolved fluorescence decay curve (Fig. 6b) of TiO_2 and its composites with RGO using Nano LED as excitation source having wavelength of 375 nm and fluorescence decay was monitored at 428 nm. The fluorescence decay curves were fitted using three-exponential decay. The average lifetimes were found to be 45.57, 37.80, 36.24, 33.98 and 38.02 ns for TiO_2, 1.0RGO-TiO_2, 2.0RGO-TiO_2, 5.0RGO-TiO_2 and 10.0RGO-TiO_2, respectively. The lifetime data observed was also in line with the steady state emission behavior. This might be possibly due to formation of non-radiative sites at the interface of TiO_2 and RGO, which provided the surfaces for the photo-catalytic conversion of CO_2. Though, the exact proportion of TiO_2 and RGO needs to be explored further in order to optimize the photo – physical parameters and to attain the optimum conversion efficiency. At this stage, it was associated with the narrowing of the band gap which provides surface for the photoconversion of CO_2.

3.2. Evaluation of the photocatalytic activity of RGO-TiO_2 nanocomposites

The photocatalytic activity of the prepared series of catalysts RGO–TiO_2 was assessed for the reduction of CO_2 under UVA light for 16 h with 5 mg and benchmarked against TiO_2 using the same experimental conditions. In Fig. 7a, all prepared catalysts showed considerable activity for selective photocatalytic CO_2 reduction to methanol in water: ACN medium (16:2 v/v in mL) using TEOA (2 mL) as the sacrificial electron donor. Measurements were conducted initially for the 8 h at 4 h intervals for the first day; then the reaction was stopped, stored in the dark for few hours and resumed almost midnight and allowed to run overnight for the next 8 h till

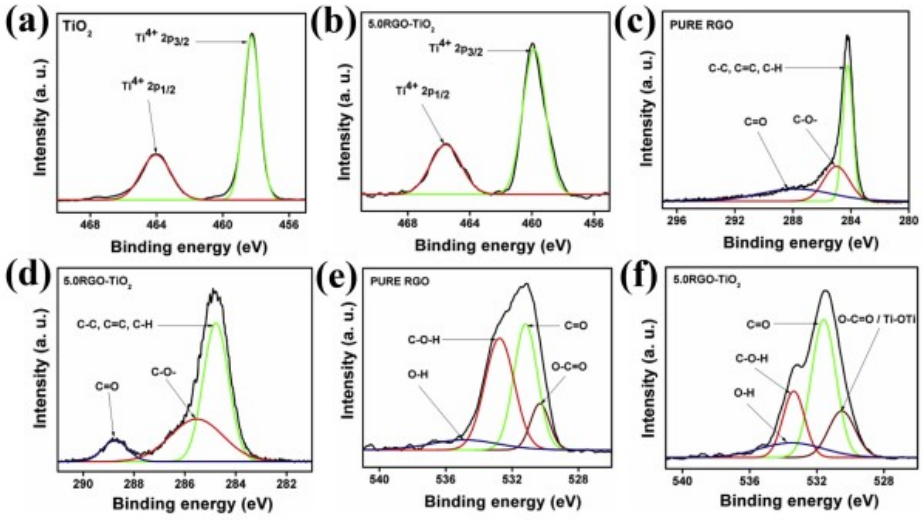

Fig. 5. High-resolution XPS spectra: (a) Ti2p of bare TiO_2, (b) Ti2p of 5.0RGO-TiO_2, (c) C1s of pure RGO, (d) C1s of 5.0RGO-TiO_2, (e) O1s of pure RGO, and (f) O1s of 5.0RGO-TiO_2.

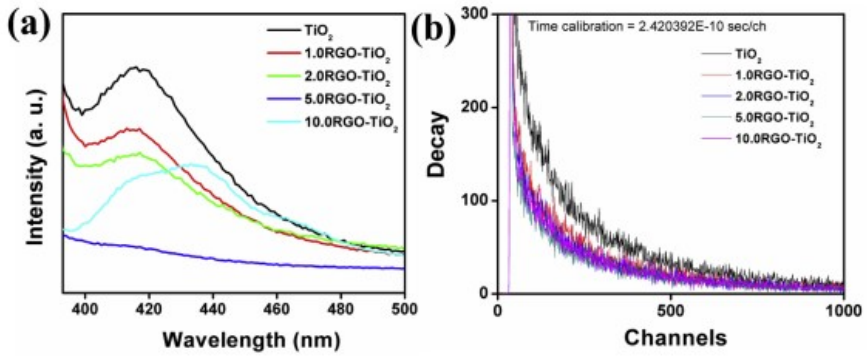

Fig. 6. (a) Steady state emission spectra and (b) Time-resolved fluorescence decay curve of pure TiO_2 and RGO-TiO_2 composites.

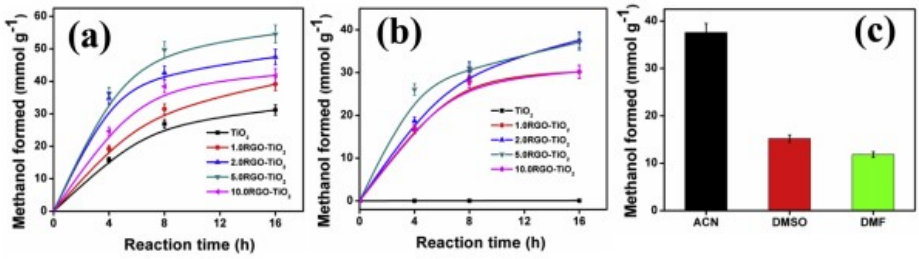

Fig. 7. (a) Rate of the formation of methanol from the reduction of CO_2 under UVA light irradiation (8 W UVA PEN-RAY lamp, 350 nm, 2.13", Cole-Parmer, 120 mW cm^{-2}) of pure TiO_2 and all RGO-TiO_2 samples (b) rate of the production of methanol from the reduction of CO_2 under visible light irradiation (20 W white cold LED lamp, 400–800 nm Siska LED, 20 mW cm^{-2}) by all RGO-TiO_2 composites (c) influence of the reaction medium for the production of methanol from CO_2 reduction under visible light by 5.0RGO-TiO_2 for a period of 16 h.

16 h (next day). For all samples, the production of methanol increased with time. TiO_2, as the control sample, exhibited a methanol production rate of *ca.* 1.95 mmol g^{-1} h^{-1}; this rate was lower than for all RGO-containing samples. The explanation of this observation could be that the large band gap and fast recombination of e^- - h^+ pairs in TiO_2 [40,55]. The wrapping of RGO on TiO_2 exhibited a significant influence on the photocatalytic activity. Factors such as: (1) synergistic effect between TiO_2 and RGO as a result of hydrothermal reaction, which allows the formation of chemical bond [14,15] and reduced recombination of e^- $^-$ h^+ pair [55], and (2) higher surface area which provides more active adsorption sites, and photocatalytic reaction centers [40]. Increase in photocatalytic activity was observed with a higher dosage of RGO from 1% to 5% weight ratio in the RGO–TiO_2 composites. However, a decreasing trend was found with the further addition of RGO, suggesting that excess RGO might work as a competitor with TiO_2. An excess amount of RGO could increase the unproductive consumption of photons in the photocatalytic system, thus shielding the light reaching the surface of the TiO_2 photocatalysts [14]. Hence, it was critical to get the optimum loading amount of RGO in the RGO–TiO_2 composites. Here, 5% RGO was the optimum as in 5.0RGO–TiO_2 with the methanol production rate of 3.41 mmol g^{-1} h^{-1}, almost double the pure TiO_2.

For comparison and to further probe the effect of optical properties with all RGO-TiO_2 composites, photocatalytic reduction of CO_2 to methanol was performed under visible light by maintaining the above experimental conditions. Fig. 7b reveals that all the composites were photocatalytically active under visible light with 2.0RGO-TiO_2 and 5.0RGO-TiO_2 performed almost equally, with the methanol production rate of *ca.* 2.33 mmol g^{-1} h^{-1}. However, as expected, TiO_2 showed little activity under visible light. These results suggest that RGO acted as a sensitizer for TiO_2 in a way to enhance its visible light activity. It is noteworthy that 5.0RGO–TiO_2 exhibited lower photocatalytic activities under the visible light when compared to UVA light. This might be because TiO_2, which was in higher amount in comparison with RGO, cannot effectively catalyze the reaction under visible light. Hence, the reaction rate was mainly determined by the amount of TiO_2 catalyst present [55,56]. To check whether pure RGO alone was active for CO_2 reduction under UV and visible light, the equivalent weight of its calcined form was used. At similar conditions, it was observed that 13.48 and 31.61 μmol g^{-1} h^{-1} of methanol were produced. These values were so insignificant in comparison to ones obtained with bare TiO_2 and RGO-TiO_2 nanocomposites. These observations were further explained by DFT calculation section 3.3 and 3.4.

The influence of reaction medium on the photocatalytic reduction of CO_2 was performed with 5.0RGO–TiO_2 in the presence of DMF, ACN, and DMSO by keeping other parameters constant under the visible light, as shown in Fig. 7c. The trend in the photoreduction activity was found to be ACN > DMSO > DMF yielding 2.33, 0.95 and 0.74 mmol g^{-1} h^{-1}, respectively. CO_2 has a higher solubility in ACN medium, and this might play a crucial role in product formation. The photocatalytic activities of all the reported work on the use of graphene-TiO_2 composite for CO_2 reduction were measured in the presence of CO_2 and water vapor [16,22–27]. Also, the majority of the observed products reported for the reduction of CO_2 using these composite is CH_4 [22–26]; other products like CO [16] and C_2H_4 [27] were also reported as shown in Table S2. In the present work, the reaction was performed in the liquid phase either in ACN or DMSO or DMF reaction media; providing the higher possibilities for the formation of methanol. Remarkably, our prepared composites were able to attain a specific surface area of 128.6 m^2 g^{-1}; higher than the reported surface area (114.9 m^2 g^{-1}) of these composites for CO_2 reduction [27].

3.3. Quantum chemistry view on RGO-TiO_2 interaction

It was surprising to observe significant visible light methanol production over RGO-TiO_2 while TiO_2 component absorption edge remained unchanged. Density functional theory based semi-empirical quantum chemistry computations were employed to get a better understanding of the RGO-TiO_2 composite photocatalytic properties. Cluster models of RGO and the decahedral cluster of anatase TiO_2 were used for this part of our investigation.

In order to study the interaction of RGO and TiO_2 anatase, the rectangular GQD and TiO_2 nanoparticle cluster Ti44r1 were initially placed to ensure the contact of a (101) facet of the nanoparticle, which was then approximately situated in the center of the GQD. Also, (001) facet of the TiO_2 nanoparticle was initially placed parallel to the armchair edges of the GQD.

Fig. 8 shows the atomic structure of the composite GQDTi44r1 after its full geometry relaxation performed using a conjugate gradient method. It was observed that atoms of carbon of GQD and atoms of (101) facet were moved to a distance closer than the sum of the van der Waals radii (Fig. 8a). Typical interatomic C–O distances were 2.7–3.0 Å. In comparison to the initial configuration in which the armchair edge was parallel to the (001) surface, some rotation of GQD was observed during the geometry optimization (Fig. 8b).

According to the results of computations, the adsorption energy of RGO over (101) facet of the TiO_2 nanoparticle Ti44r1 was −27.38 kcal mol^{-1}. Approximately 63 carbon atoms of the GQD took part in the GQD-Ti44r1 van der Waals complex, that is, the interaction energy was 0.43 kcal mol^{-1} of carbon atoms. This is about twice lower than the average reported in the literature interaction energy between graphene sheets of 0.804 kcal mol^{-1} C [57]. The difference may be partially due to the non-flat character of the (101) surface, in which many atoms were not close enough. The formation of the composite resulted in charge transfer from RGO to TiO_2 nanoparticle to result in accumulation of −0.195 electrons charge in Ti44r1 and +0.195 electrons charge in RGO nanosheet.

Fig. 9 shows the density of states of the separate Ti44r1, GQD, and the GQD-Ti44r1 complex in the range of energy eigenvalues of −10 to 0 eV. Fermi level energies of these nano-objects at 298.15 K were −4.00, −4.48, and −4.49 eV, correspondingly. Thus, the Fermi level position in the composite was determined by RGO due to the higher density of its conducting electrons. Tables S3–S5 list energy, electron population at 298.15 K and spatial properties of orbitals within 0.5 eV from the frontier orbitals of the TiO_2 nanoparticle. Ti44r1 exhibited the band gap of 2.94 eV which was close to that of bulk anatase, while GQD did not show any band gap with a smearing of orbitals population among eigenvalues of −4.55 to −4.37 eV (Table S4). A significant number of states, which was equal to 20 residing inside the band gap of Ti44r1 stretching from −5.47 to −2.52 eV, was possessed by GQD. Moreover, a significant change in DOS distribution and appearance of new energy levels inside the Ti44r1 band gap were observed with the formation of GQD-Ti44r1 (Table S5). This led to the number of states inside the band gap as 28.

The presence of states in the band gap for the GQD-Ti44r1 composite means that this composite can be excited under visible light irradiation, and produced electrons and holes can reside in different sides of the GQD-TiO_2 heterojunction. Since the number of states within the band gap is small relative to bands of TiO_2, the contribution of RGO to absorption of TiO_2 is small (Fig. 3). A real advantage of the composite in comparison to separate components can be obtained if photoexcitation (1) proceeds under visible light, (2) creates electrons and holes with energy enough to drive the reactions, and (3) produces photogenerated charges with a lifetime long enough for their reaction to complete. There are three

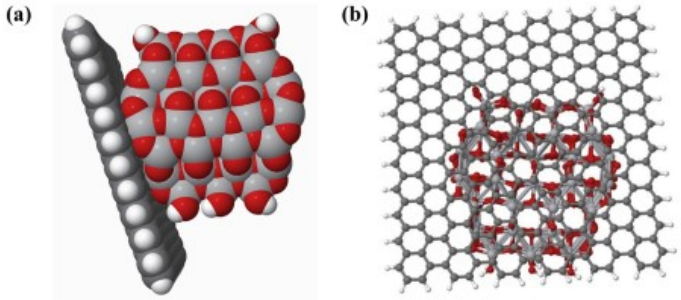

Fig. 8. Structure of the fully optimized RGO-Ti44r1 composite in (a) van der Waals spheres, and (b) ball-and-stick representations. Atom designations: H - white, C – dark gray, O – red, Ti – gray balls.

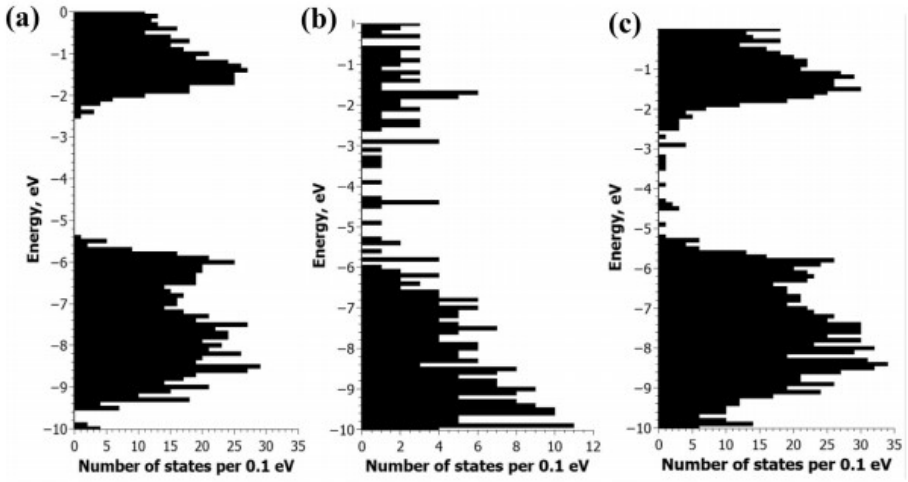

Fig. 9. Density of states for (a) optimized TiO_2 nanoparticle, (b) graphene quantum dot, and (c) GQD-Ti44r1 composite.

different possibilities of photoexcitation with visible light: (1) photoexcitation of graphene component with the creation of electron and hole in graphene; (2) excitation with charge transfer from the valence band of TiO_2 to graphene; and (3) excitation with charge transfer from graphene to the conduction band of TiO_2. It can be logically deduced that only route (2) is productive for visible light photocatalytic reduction of CO_2 in the presence of a sacrificial electron donor.

It is often suggested that photogenerated charges are quickly thermalized before taking part in electron transfer reactions [58]. For graphene, this means quick recombination of photogenerated charges since there is no band gap in it. Thus, electrons for photocatalytic reduction under ultraviolet light can be produced either in TiO_2 by bandgap excitation or by charge transfer excitation from the valence band of TiO_2 to RGO.

Taking the TiO_2 conduction band edge potential as −0.1 V vs. NHE, GQD Fermi level potential was calculated using data in Tables S3 and S4 as about +1.9 V which is too much positive to drive any reaction of reduction of CO_2. In the presence of sacrificial electron donors, however, excess electrons are accumulated in RGO that causes a strong rise of its reduction potential while photogenerated holes are quickly scavenged by the sacrificial electron donor. Such an excess of electrons should provide potential negative enough to carry out the reactions of hydrogen production ($E^0 = 0$ V at pH 0) or CO_2 reduction ($E^0 = -0.24$ V for methane product, −0.38 V for methanol, and −0.53 V for CO at pH 7).

Frontier orbitals are known to be the first approximation to the localization of photogenerated electrons and holes. At room temperature, thermal energy contribution makes available for the thermalized charge carriers not only the frontier orbitals but also orbitals within approximately $3k_BT \approx 0.077$ eV. Therefore, it is important to know the shape of orbitals within $3k_BT$ of frontier orbitals to get an idea where reduction and oxidation reactions proceed.

Spatial distribution of other orbitals in the TiO_2 nanoparticle, GQD and GQD-TiO_2 composite is important to know as well. This

allows building correlations between TiO_2, GQD, and GQD-TiO_2 orbitals to obtain the understanding of orbitals energy shifts and shape changes as a result of the formation of the composite. Tables S3–S5 give a description of orbitals with energy within 0.5 eV of Ti44r1 nanoparticle band gap and Fig. 10 shows most interesting molecular orbitals of the GQD-Ti44r1 composite.

Concerning the nanoparticulate TiO_2, it is of high interest to trace surface states since surface gives a large contribution to nanoparticles properties. Table S3 demonstrates that single surface states with high electronic density were distributed in the whole region of energies considered (e.g., orbitals # 969, 971, 973, 976 etc.). However, closer to the band gap, surface states were in a

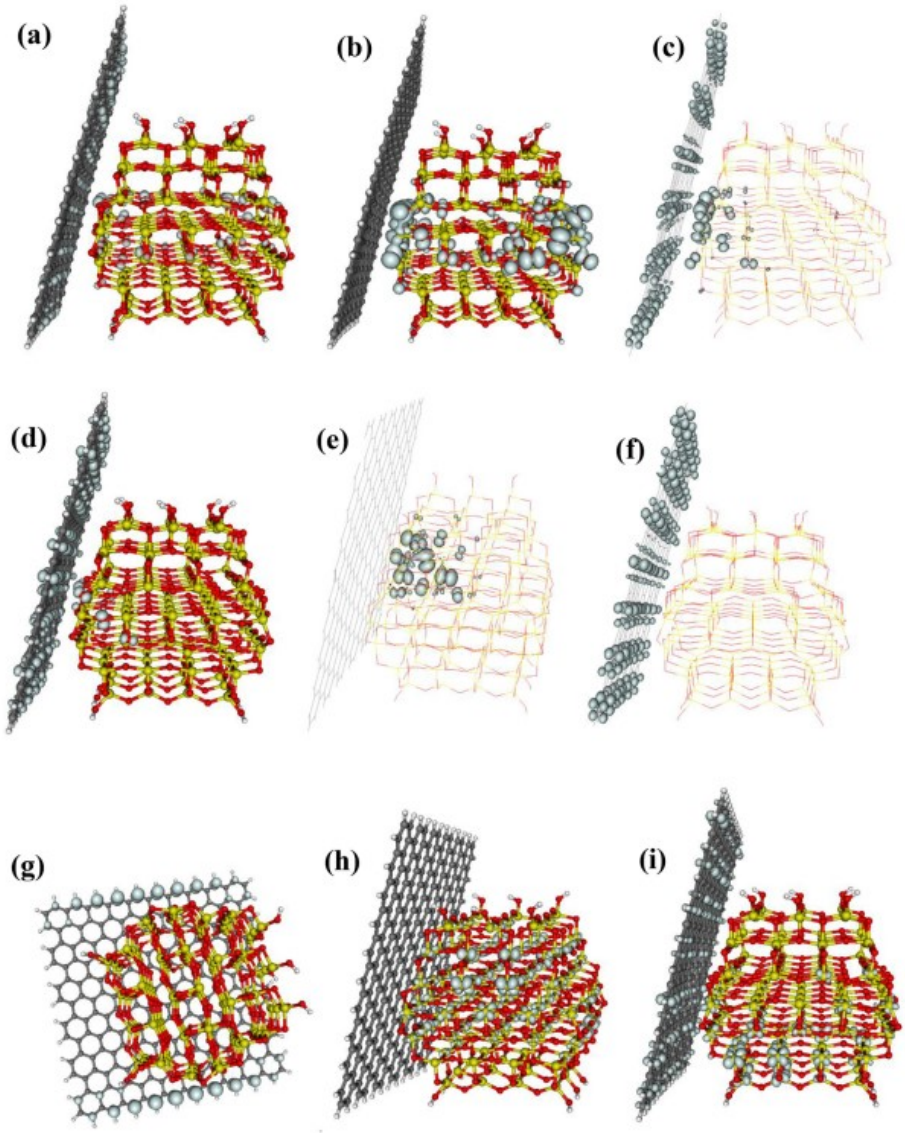

Fig. 10. Selected molecular orbitals in the GQD-TiO_2 composite. Occupied orbitals: (a) 1492, (b) 1505–1509 except 1507, (c) 1507, (d) 1513, (e) 1514, (f) 1515, (g) 1517; vacant orbitals: (h) 1538, (i) 1552–1553.

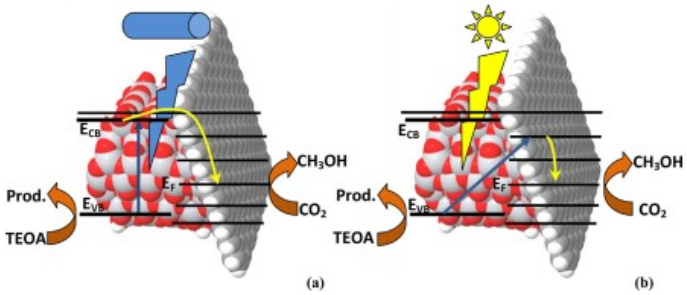

Fig. 11. Schematic representation of electronic excitations and electron transfer processes in the graphene-anatase composite during CO_2 photoreduction, according to the results of computational studies: (a) under UV light irradiation; (b) with visible light photoexcitation.

continuous array: orbitals 980–992 (E = −5.75 to −5.47 eV) were concentrated in corners of the nanoparticle formed by four adjacent (101) surfaces. For conduction band, surface states array were inside the band away from its bottom with orbitals 999–1002 (E = −2.22 to −2.20 eV) corresponding to them. Excluding the surface states, one could estimate the "true" electronic band gap of the Ti44r1 nanoparticle to be 3.23 eV.

For the graphene nanoparticle, the appearance of states with electronic density concentrated close to these edges was caused by the presence of the zigzag and armchair edges.

For the GQD-TiO_2 composite, as a result of the presence of GQD, asymmetry of orbitals was observed, which tend to distribute over layers of atoms far from GQD. States 1502 to 1514 (E = −5.55 to −5.27 eV) had orbitals localized closer to one of the corners formed by four adjacent (101) facets. Comparison with the original Ti44r1 nanoparticle, these same 12 states were shifted upwards by 0.2 eV in the composite. Therefore, the valence band ceiling of Ti44r1 was shifted by +0.2 eV in the composite. This shift was caused by the partial injection of electronic density from GQD to the Ti44r1 nanoparticle as charge analysis demonstrated.

States within the shifted band gap of Ti44r1 nanoparticle 1515 to 1537 were represented exclusively by orbitals of GQD. Starting from orbital 1538 (E = −2.38 eV) were states corresponding to the valence band of TiO_2.

A number of states within the bands of Ti44r1 correspond to orbitals of exclusively GQD and linear combinations of orbitals of GQD and Ti44r1. Fig. 10 shows several examples of such orbitals. State # 1518 (E = −4.50 eV) corresponds to HOMO of the GQD-Ti44r1 conjugate at 0 K. Energy levels 1516 to 1521 were partially filled with electrons at 298.15 K.

3.4. Photophysical and photochemical events in RGO-TiO_2 nanocomposite

According to the results of the experimental and the theoretical studies, the mechanism of CO_2 photoreduction using RGO-TiO_2 nanocomposite could be represented by the scheme shown in Fig. 11. Under UV light photoexcitation, electrons and holes are produced in TiO_2 nanoparticles, and electrons are transferred into RGO. Under visible light photoexcitation, charge transfer results in holes in TiO_2 and electrons in RGO. The positive effect of the presence of graphene on the reduction of CO_2 is associated with a high electrocatalytic activity of carbon electrodes in reduction reactions. The sacrificial electron donor is oxidized on the surface of TiO_2 nanoparticles under UV and visible light irradiation. Since the density of states in RGO-TiO_2 composite is low in the energy limits of TiO_2 band gap, visible light absorption with charge transfer has a low contribution, and this causes a lower photocatalytic activity compared to UV light excitation. Excitation could also proceed in graphene. However, its direct contribution to the photoreaction is much lower than that of TiO_2 because only moderate amounts of graphene (5%) are beneficial for the photoreduction.

4. Conclusions

Experimental results showed successfully assembled TiO_2 nanoparticles on RGO sheets, forming nanocomposites. Photocatalytic studies indicated the potential use of these nanocomposites for the reduction of CO_2 under both UVA and visible light. Under the visible light, the methanol production rate was found to be 2.33 mmol g^{-1} h^{-1}. Theoretical computational results indicated that there is relatively strong adsorption of RGO on (101) surfaces of anatase. Graphene causes the upward shift of the TiO_2 bands by 0.2 eV due to the electron density contribution from RGO in the composite. The efficiency of the photocatalytic reaction depends greatly on the efficiency of electron transfer and charge transfer from TiO_2 nanoparticles to RGO. Improved tight contact between TiO_2 and RGO induced significantly improved the photocatalytic activity of the composite in CO_2 reduction in the present study compared to some literature data. This phenomenon could open doors to explore the production of new active materials to visible light based on the synthesis of graphene-TiO_2 composites.

Acknowledgments

Authors are grateful to Director, IIP for his kind permission to publish the results. J. O. Olowoyo is thankful to CSIR-TWAS for the funding of the research work (22/FF/CSIR-TWAS/2015). Authors are also thankful to ASD-IIP for their analytical support.

Appendix A. Supplementary data

Supplementary data to this article can be found online at https://doi.org/10.1016/j.carbon.2019.03.019.

References

[1] K.S. Novoselov, A.K. Geim, S.V. Morozov, D. Jiang, Y. Zhang, et al., Electric field effect in atomically thin carbon films, Science 306 (2004) 666–669.
[2] A.K. Geim, K.S. Novoselov, The rise of graphene, Nat. Mater. 6 (2007) 183–191.
[3] E.T. Thostenson, Z. Ren, T.-W. Chou, Advances in the science and technology of carbon nanotubes and their composites: a review, Compos. Sci. Technol. 61 (2001) 1899–1912.
[4] S. Ghosh, I. Calizo, D. Teweldebrhan, E.P. Pokatilov, D.L. Nika, et al., Extremely high thermal conductivity of graphene: prospects for thermal management applications in nanoelectronic circuits, Appl. Phys. Lett. 92 (2008) 151911.
[5] C. Lee, X. Wei, J.W. Kysar, J. Hone, Measurement of the elastic properties and intrinsic strength of monolayer graphene, Science 321 (2008) 385–388.
[6] K.I. Bolotin, K.J. Sikes, Z. Jiang, M. Klima, G. Fudenberg, et al., Ultrahigh electron mobility in suspended graphene, Solid State Commun. 146 (2008) 351–355.
[7] M.J. Allen, V.C. Tung, R.B. Kaner, Honeycomb Carbon: a review of graphene, Chem. Rev. 110 (2010) 132–145.
[8] K.P. Loh, Q. Bao, P.K. Ang, J. Yang, The chemistry of graphene, J. Mater. Chem. 20 (2010) 2277–2289.
[9] S.N. Habisreutinger, L. Schmidt-Mende, J.K. Stolarczyk, Photocatalytic reduction of CO_2 on TiO_2 and other semiconductors, Angew. Chem. 52 (2013) 7372–7408.
[10] Y.L. Pang, S. Lim, H.C. Ong, W.T. Chong, A critical review on the recent progress of synthesizing techniques and fabrication of TiO_2-based nanotubes photocatalysts, Appl. Catal., A 481 (2014) 127–142.
[11] G. Zerjav, M.S. Arshad, P. Djinovic, I. Junkar, J. Kovac, et al., Improved electron-hole separation and migration in anatase TiO_2 nanorod/reduced graphene oxide composites and their influence on photocatalytic performance, Nanoscale 9 (2017) 4578–4592.
[12] P.N.O. Gillespie, N. Martsinovich, Electronic structure and charge transfer in the TiO_2 rutile (110)/graphene composite using hybrid DFT calculations, J. Phys. Chem. C 121 (2017) 4158–4171.
[13] A.W. Morawskia, E. Kusiak-Nejman, A. Wanag, J. Kapica-Kozar, R.J. Wrobel, et al., Photocatalytic degradation of acetic acid in the presence of visible light-active TiO_2-reduced graphene oxide photocatalysts, Catal. Today 280 (2017) 108–113.
[14] Y.Y. Zhang, X.G. Hou, T.T. Sun, X.L. Zhao, Calcination of reduced graphene oxide decorated TiO_2 composites for recovery and reuse in photocatalytic applications, Ceram. Int. 43 (2017) 1150–1159.
[15] W.Q. Fan, Q.H. Lai, Q.H. Zhang, Y. Wang, Nanocomposites of TiO_2 and reduced graphene oxide as efficient photocatalysts for hydrogen evolution, J. Phys. Chem. C 115 (2011) 10694–10701.
[16] W. Tu, Y. Zhou, Q. Liu, Z. Tian, J. Gao, et al., Robust hollow spheres consisting of alternating titania nanosheets and graphene nanosheets with high photocatalytic activity for CO_2 conversion into renewable fuels, Adv. Funct. Mater. 22 (2012) 1215–1221.
[17] P.F. Wang, S.H. Zhan, Y.G. Xia, S.L. Ma, Q.X. Zhou, Y. Li, The fundamental role and mechanism of reduced graphene oxide in rGO/Pt-TiO_2 nanocomposite for high-performance photocatalytic water splitting, Appl. Catal., B 207 (2017) 335–346.
[18] C. Wang, D.L. Meng, J.H. Sun, J. Memon, Y. Huang, J.X. Geng, Graphene wrapped TiO_2 based catalysts with enhanced photocatalytic activity, Adv Mater Interfaces 1 (2014) 1300150.
[19] X.Y. Wang, J. Wang, X.L. Dong, F. Zhang, L.G. Ma, et al., Synthesis and catalytic performance of hierarchical TiO_2 hollow sphere/reduced graphene oxide hybrid nanostructures, J. Alloy. Comp. 656 (2016) 181–188.
[20] M.M. Zhen, X.H. Zhu, X. Zhang, Z. Zhou, L. Liu, Reduced graphene oxide-supported TiO_2 fiber bundles with mesostructures as anode materials for lithium-ion batteries, Chem. Eur J. 21 (2015) 14454–14459.
[21] O. Akhavan, E. Ghaderi, Photocatalytic reduction of graphene oxide nanosheets on TiO_2 thin film for photoinactivation of bacteria in solar light irradiation, J. Phys. Chem. C 113 (2009) 20214–20220.
[22] L.L. Tan, W.J. Ong, S.P. Chai, A.R. Mohamed, Noble metal modified reduced graphene oxide/TiO_2 ternary nanostructures for efficient visible-light-driven photoreduction of carbon dioxide into methane, Appl. Catal., B 166 (2015) 251–259.
[23] L.C. Sim, K.H. Leong, P. Saravanan, S. Ibrahim, Rapid thermal reduced graphene oxide/Pt-TiO_2 nanotube arrays for enhanced visible-light-driven photocatalytic reduction of CO_2, Appl. Surf. Sci. 358 (2015) 122–129.
[24] A. Razzaq, C.A. Grimes, S.I. In, Facile fabrication of a noble metal-free photocatalyst: TiO_2 nanotube arrays covered with reduced graphene oxide, Carbon 98 (2016) 537–544.
[25] Y.T. Liang, B.K. Vijayan, K.A. Gray, M.C. Hersam, Minimizing graphene defects enhances titania nanocomposite-based photocatalytic reduction of CO_2 for improved solar fuel production, Nano Lett. 11 (2011) 2865–2870.
[26] L.-L. Tan, W.-J. Ong, S.-P. Chai, B.T. Goh, A.R. Mohamed, Visible-light-active oxygen-rich TiO_2 decorated 2D graphene oxide with enhanced photocatalytic activity toward carbon dioxide reduction, Appl. Catal., B 179 (2015) 160–170.
[27] W. Tu, Y. Zhou, Q. Liu, S. Yan, S. Bao, et al., An in Situ Simultaneous reduction-hydrolysis technique for fabrication of TiO_2-graphene 2D sandwich-like hybrid nanosheets: graphene-promoted selectivity of photocatalytic-driven hydrogenation and coupling of CO_2 into methane and ethane, Adv. Funct. Mater. 23 (2013) 1743–1749.
[28] P. Kumar, G. Singh, D. Tripathi, S.L. Jain, Visible light driven photocatalytic oxidation of thiols to disulfides using iron phthalocyanine immobilized on graphene oxide as a catalyst under alkali free conditions, RSC Adv. 4 (2014) 50331–50337.
[29] W.S. Hummers, R.E. Offeman, Preparation of graphitic oxide, J. Am. Chem. Soc. 80 (1958) 1339.
[30] J.O. Olowoyo, N.C. Hernández, M. Kumar, S.L. Jain, J.O. Babalola, U. Kumar, Insight of diversified reactivity and theoretical study of mixed-phase titanium dioxide for the photoactivation of small molecules, ChemistrySelect 3 (2018) 3659–3663.
[31] J.O. Olowoyo, M. Kumar, N. Singhal, S.L. Jain, J.O. Babalola, et al., Engineering and modeling the effect of Mg doping in TiO_2 for enhanced photocatalytic reduction of CO_2 to fuels, Catal Sci Technol 8 (2018) 3686–3694.
[32] A.V. Vorontsov, S.V. Tsybulya, Influence of nanoparticles size on XRD patterns for small monodisperse nanoparticles of Cu0 and TiO_2 anatase, Ind. Eng. Chem. Res. 57 (2018) 2526–2536.
[33] A.V. Vorontsov, P.G. Smirniotis, Size and surface groups effects in decahedral anatase nanoparticles for photocatalytic applications, J. Photochem. Photobiol., A 363 (2018) 51–60.
[34] A.V. Vorontsov, Structural and electronic effects in acetone adsorption over TiO_2 anatase clusters as the first stage of photocatalytic oxidation, J. Nanoparticle Res. 19 (2017) 326.
[35] J.O. Olowoyo, M. Kumar, S.L. Jain, J.O. Babalola, A.V. Vorontsov, U. Kumar, Insight into enhanced photocatalytic activity of CNT-TiO_2 composite for storage of photon energy in chemical bonds: CO_2 reduction and water splitting, J. Phys. Chem. C 123 (2019) 367–378.
[36] B. Aradi, B. Hourahine, T. Frauenheim, DFTB+, a sparse matrix-based implementation of the DFTB method, J. Phys. Chem. A 111 (2007) 5678–5684.
[37] M. Elstner, D. Porezag, G. Jungnickel, J. Elsner, M. Haugk, et al., Self-consistent-charge density-functional tight-binding method for simulations of complex materials properties, Phys. Rev. B 58 (1998) 7260–7268.
[38] G. Dolgonos, B. Aradi, N.H. Moreira, T. Frauenheim, An improved self-consistent-charge density-functional tight-binding (SCC-DFTB) set of parameters for simulation of bulk and molecular systems involving titanium, J. Chem. Theory Comput. 6 (2010) 266–278.
[39] J.F. Shen, B. Yan, M. Shi, H.W. Ma, N. Li, M.X. Ye, One step hydrothermal synthesis of TiO_2-reduced graphene oxide sheets, J. Mater. Chem. 21 (2011) 3415–3421.
[40] D.J. Chen, L.L. Zou, S.X. Li, F.Y. Zheng, Nanospherical like reduced graphene oxide decorated TiO_2 nanoparticles: an advanced catalyst for the hydrogen evolution reaction, Sci. Rep. 6 (2016) 20335.
[41] T.D. Nguyen-Phan, V.H. Pham, J.S. Chung, M. Chhowalla, T. Asefa, et al., Photocatalytic performance of Sn-doped TiO_2/reduced graphene oxide composite materials, Appl. Catal., A 473 (2014) 21–30.
[42] P. Wang, J. Wang, X.F. Wang, H.G. Yu, J.G. Yu, et al., One-step synthesis of easy-recycling TiO_2-rGO nanocomposite photocatalysts with enhanced photocatalytic activity, Appl. Catal., B 132 (2013) 452–459.
[43] M. Shah, A.R. Park, K. Zhang, J.H. Park, P.J. Yoo, Green synthesis of biphasic TiO_2-reduced graphene oxide nanocomposites with highly enhanced photocatalytic activity, ACS Appl. Mater. Interfaces 4 (2012) 3893–3901.
[44] T. An, J. Chen, X. Nie, G. Li, H. Zhang, et al., Synthesis of carbon nanotube–anatase TiO_2 sub-micrometer-sized sphere composite photocatalyst for synergistic degradation of gaseous styrene, ACS Appl. Mater. Interfaces 4 (2012) 5988–5996.
[45] R. Jaiswal, J. Bharambe, N. Patel, A. Dashora, D.C. Kothari, A. Miotello, Copper and nitrogen co-doped TiO_2 photocatalyst with enhanced optical absorption and catalytic activity, Appl. Catal., B 168 (2015) 333–341.
[46] A.J. Wang, W. Yu, Y. Fang, Y.L. Song, D. Jia, et al., Facile hydrothermal synthesis and optical limiting properties of TiO_2-reduced graphene oxide nanocomposites, Carbon 89 (2015) 130–141.
[47] L.A. Gu, J.Y. Wang, H. Cheng, Y.Z. Zhao, L.F. Liu, X.J. Han, One-step preparation of graphene-supported anatase TiO_2 with exposed {001} facets and mechanism of enhanced photocatalytic properties, ACS Appl. Mater. Interfaces 5 (2013) 3085–3093.
[48] A.A. Ismail, R.A. Geioushy, H. Bouzid, S.A. Al-Sayari, A. Al-Hajry, D.W. Bahnemann, TiO_2 decoration of graphene layers for highly efficient photocatalyst: impact of calcination at different gas atmosphere on photocatalytic efficiency, Appl. Catal., B 129 (2013) 62–70.
[49] K.H. Leong, L.C. Sim, D. Bahnemann, M. Jang, S. Ibrahim, P. Saravanan, Reduced graphene oxide and Ag wrapped TiO_2 photocatalyst for enhanced visible light photocatalysis, Apl. Mater. 3 (2015) 104503.
[50] L.-N. Zhou, X.-T. Zhang, W.-J. Shen, S.-G. Sun, Y.-J. Li, Monolayer of close-packed Pt nanocrystals on a reduced graphene oxide (RGO) nanosheet and its enhanced catalytic performance towards methanol electrooxidation, RSC Adv. 5 (2015) 46017–46025.
[51] Y.J. Oh, J.J. Yoo, Y.I. Kim, J.K. Yoon, H.N. Yoon, et al., Oxygen functional groups and electrochemical capacitive behavior of incompletely reduced graphene oxides as a thin-film electrode of supercapacitor, Electrochim. Acta 116 (2014) 118–128.
[52] L.J. Luo, Y. Yang, A. Zhang, M. Wang, Y.J. Liu, et al., Hydrothermal synthesis of fluorinated anatase TiO_2/reduced graphene oxide nanocomposites and their photocatalytic degradation of bisphenol A, Appl. Surf. Sci. 353 (2015) 469–479.
[53] S.P. Zhang, J. Xu, J. Hu, C.Z. Cui, H.L. Liu, Interfacial growth of TiO2-rGO composite by Pickering emulsion for photocatalytic degradation, Langmuir: the ACS journal of surfaces and colloids 33 (2017) 5015–5024.

[54] R. Raja, M. Govindaraj, M.D. Antony, K. Krishnan, E. Velusamy, et al., Effect of TiO2/reduced graphene oxide composite thin film as a blocking layer on the efficiency of dye-sensitized solar cells, J. Solid State Electrochem. 21 (2017) 891–903.
[55] W.L. Wang, Z.F. Wang, J.J. Liu, Z. Luo, S.L. Sui, et al., Single-step one-pot synthesis of TiO_2 nanosheets doped with sulfur on reduced graphene oxide with enhanced photocatalytic activity, Sci. Rep. 7 (2017) 46610.
[56] Y.J. Li, L.Y. Li, C.W. Li, W. Chen, M.X. Zeng, Carbon nanotube/titania composites prepared by a micro-emulsion method exhibiting improved photocatalytic activity, Appl. Catal., A 427 (2012) 1–7.
[57] A.V. Vorontsov, E.V. Tretyakov, Determination of graphene's edge energy using hexagonal graphene quantum dots and PM7 method, Phys. Chem. Chem. Phys. 20 (2018) 14740–14752.
[58] Y.-K. Peng, S.C.E. Tsang, Facet-dependent photocatalysis of nanosize semiconductive metal oxides and progress of their characterization, Nano Today 18 (2018) 15–34.

APPENDIX VII

Copy of paper published from the Insight for Enhanced Photocatalytic Activity of CNT-TiO_2 composite for storage of photon energy in chemical bonds

THE JOURNAL OF PHYSICAL CHEMISTRY C

Article

pubs.acs.org/JPCC

Insights into Reinforced Photocatalytic Activity of the CNT–TiO_2 Nanocomposite for CO_2 Reduction and Water Splitting

Joshua O. Olowoyo,[†,§] Manoj Kumar,[‡] Suman L. Jain,[†] Jonathan O. Babalola,[§] Alexander V. Vorontsov,[*,∥] and Umesh Kumar[*,†]

[†]Chemical Science Division and [‡]Catalytic Conversion Division, CSIR-Indian Institute of Petroleum, Dehradun 248005, India

[§]Department of Chemistry, University of Ibadan, Ibadan 200284, Nigeria

[∥]Altai State University, pr. Lenina 61, Barnaul 656049, Russia

Supporting Information

ABSTRACT: Using titanium dioxide (TiO_2) and its modified forms for the photocatalytic reduction of CO_2 reduction and production of hydrogen is a promising route for providing solutions to the world energy demand in the foreseeable future. Here, we report the synthesis of a series of efficient stable TiO_2 nanoparticles modified with multiwalled carbon nanotubes (CNTs) via a simple combined sonothermal method, followed by a hydrothermal treatment. In comparison to bare TiO_2, the synthesized CNT–TiO_2 photocatalysts showed improved photocatalytic activities for CO_2 reduction under UVA as well as under visible light and water (H_2O) splitting under visible light at ambient temperature and pressure. The 2.0CNT–TiO_2 has performed the best for methanol, hydrogen, and formic acid production from the reduction of CO_2 with yield rates of 2360.0, 3246.1, and 68.5 μmol g^{-1} h^{-1} under UVA, respectively. Its potential was further tested under visible light for methanol production, 1520.0 μmol g^{-1} h^{-1}. Also, the highest rate of hydrogen yield from water splitting was 69.41 μmol g^{-1} h^{-1} with 2.0CNT–TiO_2 under visible light at pH 2. The primary photocatalytic reactions of CNT–TiO_2 composites and their intimate structure were studied computationally. It was demonstrated that the binding of CNT to TiO_2 nanoparticles is preferable at (101) surfaces than at (001) facets. Interaction of CNT with TiO_2 results in common orbitals within the TiO_2 band gap that enables visible light excitation of the CNT–TiO_2 composites can lead to charge transfer between TiO_2 and CNT, whereas UV light excitation can result in charge transfer in any direction from CNT to TiO_2 and from TiO_2 to CNT. The latter process is operative in the presence of a sacrificial electron donor triethanolamine.

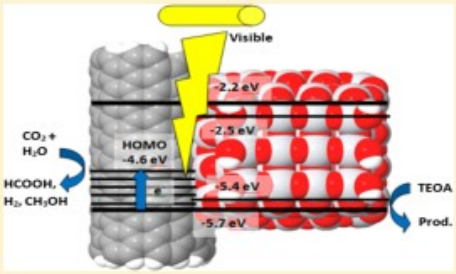

1. INTRODUCTION

The exploitation of fossil fuel-based energy is mainly responsible for a continuous increment of CO_2 level in the atmospheric environment. It is now of great necessity to control the increase of CO_2 rise because of inherent global warming and climate change concern. However, high cost and storage limitations of CO_2 among other challenges have so far doused the interest in reductive transformation of this C1 carbon source.[1,2] TiO_2 is a well-known active material for CO_2 photoreduction into hydrocarbons.[3] The modifications of TiO_2 such as (1) doping with cations, anions, and noble metals and (2) coupling with narrow band gap semiconductors assist in obtaining the visible light active material ($h\nu$ < 3.2 eV) with decreased charge recombination rate.[4,5] The unique charge transfer and electron-conducting properties as well as high mechanical strength, hollow, layered structure and large surface area of carbon nanotubes (CNTs) are well-known and made them promising candidates as dopants and supports for photocatalysts.[6−9] CNTs are also known to provide landing sites for coatings with nanoparticles of different sizes.[8]

The coupling of CNTs with TiO_2 can offer an advanced nanocomposite with improved quantum efficiency because it (1) forms a heterojunction that hinders e^-–h^+ pair recombination; (2) creates e^-–h^+ pairs when excited by light, thereby providing more electrons that are easily transferred to the conduction band of TiO_2; or (3) acts as an impurity by forming Ti–O–C or Ti–C defect sites that enable visible light absorption.[8,10,11] TiO_2–CNT nanocomposites have been reported in the literature to have enhanced activities including photocatalytic degradation of pollutants in water and air,[7,12] photo-oxidation,[11,13] bacterial degradation,[14,15] hydrogen storage,[16] hydrogen production,[17] CO_2 photoreduction,[18,19] sensors,[20] and solar cells.[21]

Received: August 14, 2018
Revised: December 6, 2018
Published: December 7, 2018

ACS Publications © XXXX American Chemical Society

DOI: 10.1021/acs.jpcc.8b07894
J. Phys. Chem. C XXXX, XXX, XXX−XXX

Several methods such as hydrothermal method,[7] sol−gel,[13] hydration−dehydration processes,[11,22] sonochemical,[23] microemulsion,[24] chemical vapor deposition,[25] electrospinning,[26] and mechanical mixing of TiO_2 and CNTs[27] have been adopted for the synthesis of CNT−TiO_2. Depending on the synthetic method, CNT−TiO_2 composites with varying physicochemical properties and structural forms have been prepared. There have been cases of uniform coating (complete or partial) of TiO_2 on the surface of the CNT.

The activation of small molecules including CO_2 and H_2O by the synergistic effect in CNT−TiO_2 has not been fully explored. Ong and co-workers synthesized CNT@Ni/TiO_2 nanocomposites by coprecipitation and used for the photoreduction of CO_2 to methane (CH_4, 0.145 μmol g^{-1} h^{-1}) under visible light irradiation.[19] The Ag-doped multiwalled CNT (MWCNT)@TiO_2 core−shell nanocomposites with various Ag loadings were also reported for continuous CO_2 photoreduction under visible light. Products such as methane (0.91 μmol g^{-1} h^{-1}) and ethylene (0.048 μmol g^{-1} h^{-1}) were obtained.[28] Only a few works related to the CNT−TiO_2 composite demonstrated methane, ethylene, and CO formation upon photoreduction of CO_2, but all have the lower rate of product formation.[18,19,28] Also reports on CNT−TiO_2 nanocomposites and their metal modified of Pt and Ni and so forth, for water splitting for hydrogen production under UV and visible light. However, most of the reported studies require an excess amount of sacrificial electron donors such as alcohols, organic acids, and sulfide/sulfide, which make the process costly and impractical.[29−32] Combinations of TiO_2 and CNT have been studied computationally in many works.[33−39] However, intimate details of CNT−TiO_2 interactions and mechanism of photocatalytic action remained elusive. It is of great importance to develop more efficient nanocomposites of TiO_2 with CNT for a higher rate of CO_2 reduction and water splitting (without a sacrificial agent) as well as to have a profound insight into the interaction between TiO_2 and CNT. The CO_2 reduction to methanol and formic acid with simultaneous hydrogen production is not well explored. Hydrogen production on water splitting without a sacrificial donor has also not been reported using CNT−TiO_2.

In continuation of our previous work on exploring photocatalytic CO_2 reduction and water splitting,[40,41] herein, we have prepared a series of CNT−TiO_2 composites by a simple combined sonothermal−hydrothermal method and tested for the photocatalytic CO_2 reduction and water splitting. The synthesized CNT−TiO_2 photocatalysts have shown improved photocatalytic activities under visible light at ambient temperature and pressure. We have also examined the effect of reaction medium and pH. The interaction of CNT and TiO_2 nanoparticles and improved photogenerated charge separation is computationally investigated using a complete anatase nanoparticle. The results shed light on the details of the photocatalytic action of the CNT−TiO_2 composite and reasons for its superiority over individual CNT and TiO_2.

2. EXPERIMENTAL SECTION

2.1. Materials. The chemicals used are as follows: CNTs with a diameter of 8−15 nm and a length of 10−30 μm from Sisco Research Laboratories Pvt. Ltd; titanium(IV) butoxide ($Ti(OBu)_4$) and formic acid from Aldrich; methanol (CH_3OH), nitric acid (HNO_3), triethanolamine (TEOA), hydrochloric acid (HCl), potassium hydroxide (KOH), and sodium hydroxide (NaOH) from Merck; ethanol (C_2H_5OH) from Fischer Chemicals; acetonitrile (ACN) HPLC grade from Sd fine-chem limited; sodium carbonate anhydrous (Na_2CO_3) from HiMedia; potassium carbonate (K_2CO_3) from Loba Chemie; CO_2 (99.9995%) from Sigma gases; methane, ethylene, and hydrogen standard gases (99.9995%) from Sigma gases; and deionized HPLC grade water (H_2O). All chemicals were used as received.

2.2. Synthesis of Catalysts. A series of CNT/TiO_2 nanocomposites containing different CNT/TiO_2 weight ratios were prepared by the combination of the sonothermal−hydrothermal method. The significance of this combined method was explored in our previous work for the synthesis of TiO_2 nanoparticles.[40] In a typical experiment, 10 mg of MWCNTs was dispersed in 30 mL of H_2O/ethanol solution (2:1 v/v), and few drops of HNO_3 were introduced, followed by sonication at 70 °C for 15 min to get a homogenized suspension as well as activation of the CNT surface. The presence of HNO_3 provides carboxyl (−COOH) and hydroxyl (−OH) groups at the surface of CNTs and hence improves their dispersion in the mixture.[42] Then, 7.33 g of $Ti(OBu)_4$ dissolved in 30 mL ethanol was added dropwise to the CNT suspension under ultrasonication at 70 °C. The mixture was further sonicated for 45 min and then transferred to a 100 mL Teflon-lined stainless steel autoclave, sealed, and heated at 180 °C for 12 h with the ramp rate of 2 °C min^{-1}, and then it was cooled to room temperature. The obtained precipitate was centrifuged (6000 rpm, 10 min) and dried overnight in an air oven at 80 °C; it was well ground, followed by calcination at 400 °C for 2 h with the heating rate of 2 °C to get 1% CNT−TiO_2 (w/w ratio), code-named 1.0CNT−TiO_2. Other weight ratios including 2 and 5 wt % were also synthesized by a similar procedure to obtain 2.0CNT−TiO_2, 5.0CNT−TiO_2, and bare TiO_2, respectively.

2.3. Characterization. Thermal stability of the fresh catalysts was evaluated by thermogravimetric analysis (TGA) with PerkinElmer TGA4000. The crystalline phases in the samples were revealed by X-ray diffraction (XRD) patterns obtained on a Bruker D8 ADVANCE X-ray diffractometer. Textural characterization of the samples was done with a Micromeritics ASAP 2010. The morphologies of the samples were observed by transmission electron microscopy (TEM) and high-resolution TEM (HRTEM) using a JEM-2010 instrument (JEOL, Japan). The solid-state UV−vis diffuse reflectance spectra (DRS) were recorded on a Shimadzu 2600 UV−vis−NIR spectrophotometer. X-ray photoelectron microscopy using ESCA+ (omicron nanotechnology, Oxford Instrument Germany) was equipped with monochromator aluminum source (Al Kα radiation $h\nu$ = 1486.7 eV). Raman analysis of the prepared catalyst was done with STR 500 Airix.

2.4. Photocatalytic CO_2 Reduction. The photocatalytic reduction of carbon dioxide was carried out in a closed gas-recirculation quartz reactor of 50 cm^3 internal volume. The reaction setup included a gas inlet and an outlet, a gas sampling port, and a liquid sampling facility. The catalyst (5.0 mg) was suspended in the ACN/H_2O/TEOA (16:2:2 mL) solution and ultrasonicated for 10 min for homogeneous dispersion. The reaction mixture was preconditioned by repeated evacuation and purging with nitrogen to remove any dissolved gases, followed by CO_2 inflow for 30 min to get a CO_2-saturated reaction mixture. The photocatalytic system was illuminated by a 8 W UV-A lamp (PEN-RAY lamp, 350 nm, 2.13″, Cole-Parmer, 120 μW cm^{-2}) or 20 W visible light white cold light-emitting diode (LED) lamp (Siska LED 20 μW cm^{-2}) to drive

DOI: 10.1021/acs.jpcc.8b07894
J. Phys. Chem. C XXXX, XXX, XXX−XXX

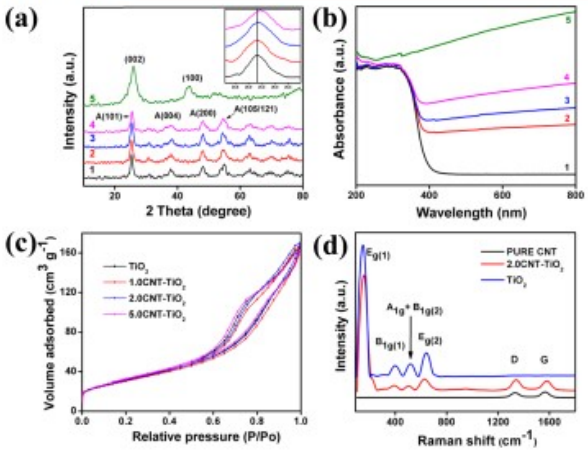

Figure 1. (a) XRD pattern; (b) UV−vis spectra of (1) TiO_2, (2) 1.0CNT−TiO_2, (3) 2.0CNT−TiO_2, (4) 5.0CNT−TiO_2, and (5) pure CNT; (c) N_2 adsorption−desorption of TiO_2 and CNT containing TiO_2 samples; and (d) Raman spectra of TiO_2, 2.0CNT−TiO_2, and pure CNT.

the reaction. A small aliquot of gas and liquid samples was taken out at a regular time interval, and the reaction progress was monitored on a gas chromatograph PerkinElmer Clarus 680 equipped with a flame ionization detector and a thermal conductivity detector (TCD), plot-Q (30 m × 0.53 mm), and shin carbon (1.8 m × 1/8" OD × 80/100 mesh) columns. Analysis of formic acid was performed on high-performance liquid chromatography (HPLC) using a Shimadzu UFLC instrument equipped with a ELSD (SOFTA) detector and a Unibond C18 250 × 4.6 mm column under isocratic conditions. ACN and H_2O (80:20 mL) were used as the mobile phase with a flow rate of 0.8 mL min^{-1}.

To ascertain that the formed products originated from the photoreduction of CO_2, a series of blank experiments were performed in a preconditioned reactor under following conditions: (a) in dark without CO_2 in the presence of the catalyst, (b) in dark with CO_2 in the presence of the catalyst, (c) UV-illuminated in the absence of both CO_2 and catalyst, (d) UV-illuminated in the presence of CO_2 but in the absence of the catalyst. (e) UV-illuminated in the presence of the catalyst but in the absence of CO_2. No carbonaceous product was detected in the above blank tests. Only in condition (e), 6.5 μmol g^{-1} h^{-1} of hydrogen production was observed. Every sampling was repeated three times to get the error in quantification. The error bars were also included in the photocatalytic plots.

2.5. Photocatalytic Hydrogen Production. Photocatalytic experiments were conducted under batch conditions at different pH ranges. Typically, 5 mg of the catalyst was loaded into a 50 mL quartz reactor. A 20 mL of HPLC grade deionized water, with required pH adjusted by either HCl or NaOH, was added to a closed gas circulation and evacuation reactor. The reactor was then purged with Ar for 30 min under ultrasonication to remove all dissolved gases. The reaction was irradiated with visible light (20 W Sisca white LED) under continuous stirring. The reaction progress was monitored by sampling a small aliquot every 2 h. Gas products were analyzed using gas chromatography (GC) equipped with a TCD and shin carbon packed column with Ar as the carrier gas. The experimental setup for all the experiment is shown in Figure S1.

2.6. Computational Details. Construction and properties of the TiO_2 anatase cluster representing a complete anatase nanoparticle have been reported previously.[43−45] In brief, the cluster designated Ti44r1 has four by four anatase elementary cells in directions *a* and *b* and 1.5 elementary cells in direction *c*. The zero charge of the cluster was ensured by attaching 12 hydroxyl groups at the four edges between facets (001) and (101). A CNT model, simulating real much larger MWCNT, was created by folding a graphene nanosheet to result in an object of diameter 0.95 nm and a length of about 2.34 nm. The carbon atoms at the ends of the nanotube formed armchair edges and were passivated by attaching hydrogen atoms. The model nanotube contains 7 benzene rings in each of two armchair hydrogenated edges and 9.5 fused benzene rings along its length. The molecular formula of the nanotube is $C_{280}H_{28}$. All computations were carried out using dftb+[46] and Gamess[47] software using tiorg-0-1[48] and mio-1-1[49] Slater−Koster parameter files.

3. RESULTS AND DISCUSSION

3.1. Characterization. The TGA recorded under air atmosphere of the samples is shown in Figure S2. The weight loss (ca. 1.9%) of pure (uncalcined) CNT in the range of ca. 40−150 °C could be attributed to the loss of moisture. The further loss (ca. 6.8%) observed in the range of 150−450 °C is due to the removal of oxo, hydroxo, and carboxylic functional groups present at the surface of the CNT. Therefore, the total weight loss observed with CNT at 450 °C is ca. 9%. On the other hand, a steady decrease in weight losses is observed with both pure TiO_2 and 2.0CNT−TiO_2. The pure TiO_2 has 4% of weight loss, and 2.0CNT−TiO_2 has 4.5% weight loss at 450 °C. The hydroxyl groups and moisture may be responsible for this. Also, the calcination process helps in the strong attachment of the CNT with TiO_2 in 2.0CNT−TiO_2 samples, resulting in decreased weight (total) loss in comparison with

DOI: 10.1021/acs.jpcc.8b07894
J. Phys. Chem. C XXXX, XXX, XXX−XXX

pure CNT. The TGA indicates that the catalysts are stable at elevated temperature and during the synthesis procedure, in which the catalyst has retained a sufficient amount of CNTs.

The XRD patterns of the CNT, synthesized TiO_2, and CNT−TiO_2 are shown in Figure 1. The two peaks located at 25.9° and 43.5° can be indexed to (002) and (100) planes of the CNT, respectively. All diffraction peaks observed in pure TiO_2 and CNT−TiO_2 correspond to tetragonal anatase TiO_2 (JCPDS 21-1272). However, no significant peak of the CNT at 2θ = 25.9° was observed in all CNT−TiO_2 samples. The nonappearance of CNT suggests that the peak of the CNT at 2θ = 25.9° has been overshadowed by the significant peak of TiO_2 at 2θ = 25.3°. In Figure 1a (inset), we can see the broadening of the TiO_2 peak (101) at 2θ = 25.3° as the amount of the CNT in the CNT−TiO_2 composite was increased, indicating that the addition of the CNT also decreases the crystallinity of TiO_2. Using Scherrer's formula, the crystalline size of TiO_2 was found to reduce from 16.0 to 13.2 nm in the composites (Table S1). This decreasing trend suggests that the CNT reduces the crystal growth of TiO_2 in the calcination stage. Yen and co-workers have also reported a similar phenomenon.[12] Also, a shift in the peak (101) was visibly observed with 2.0CNT−TiO_2 and 5.0CNT−TiO_2 catalysts. The observation is because of the titania doping with carbon as confirmed by X-ray photoelectron spectroscopy (XPS), which shows the formation of the Ti−C bond. In other words, C replaces O in the TiO_2 lattice. On the other hand, it is difficult to observe the presence of a peak (100) in all CNT−TiO_2 because of the lower content of CNT as well as the reduced intensity of the peak (100) in comparison to the peak (002). However, when the amounts of CNT were increased in the composites from 5 to 10% (10.0CNT−TiO_2), a broadening with the peak (200) was observed as a result of its overlapping with the peak (100) as shown in Figure S3.

The UV−vis DRS are shown in Figure 1b. Pure TiO_2 catalyst exhibited the characteristic absorption edge at about 392 nm, confirming its absorption in the UV region. Apparently, the continuous absorption in the visible light (400−800 nm) increases with an increase in the CNT amount in the composite. Also, the red shift to higher wavelength by CNT−TiO_2 is due to the electronic interaction between CNT and TiO_2.[7,50,51] However, excessive addition of CNT could hinder the illumination intensity for TiO_2 as a result of the shielding effect of CNT, which creates excessive light absorption by CNT with an insufficient amount for TiO_2.[24,35] The band gap energy of pure TiO_2 was found to be 3.2 eV, whereas energies of 1.0CNT−TiO_2, 2.0CNT−TiO_2, and 5.0CNT−TiO_2 were found to be 3.0, 2.9, and 2.8 eV, respectively, by using the Tauc plot (Figure S4). It could be noticed that the band gap of TiO_2 decreases with the increasing CNT content, suggesting that CNT−TiO_2 composites can efficiently absorb visible light.[15,52,53]

The adsorption−desorption isotherms of all samples are shown in Figure 1c. All samples exhibited type IV isotherm, which is characteristic of a mesoporous material. This type of isotherm is further classified as type H3 hysteresis loop, which occurs by the agglomeration of particles forming slit-shaped pores (plates or edged particles such as cubes)[54] According to the pore size distribution curve (Figure S5), it is noticed that as we increase the percentage of CNT in the composite, the pore maxima were shifted to the lower side. The pore size decreases as a function of increasing CNT content in TiO_2, whereas the total pore volume remains almost the same for all samples (Table S1). The reducing pore size at similar constant total pore volume will contribute to the higher surface area according to Wheeler's eq 1 shown below.

$$\text{Surface area} = \frac{4 \times \text{pore volume}}{\text{pore width (size)}} \quad (1)$$

If the pore volume is constant, the surface area is inversely proportional to the pore width. Noteworthy, the Brunauer−Emmett−Teller surface area of bare TiO_2 was 108.3 $m^2\ g^{-1}$; which increases with an increase in the amount of CNT in the composite up to 117.1 $m^2\ g^{-1}$ (Table S1).

The Raman spectra of TiO_2, 2.0CNT−TiO_2, and pure CNT are shown in Figure 1d. The prepared TiO_2 exhibited distinctive strong peaks at 149.1, 397.4, 516.8, and 639.5 cm^{-1}, which are assigned to $E_g^{(1)}$, $B_{1g}^{(1)}$, A_{1g} + $B_{1g}^{(2)}$, and $E_g^{(2)}$ vibration modes of anatase TiO_2, respectively. Meanwhile, pure CNT displayed two well-resolved bands at 1329.9 and 1565.0 cm^{-1} and an additional peak at 2667.8 cm^{-1} corresponding to the D, G, and 2D bands, respectively. These peaks are related to the disordered sp^2 carbon, degree of defects, and the presence of crystalline graphitic carbon in the CNTs.[55,56] As expected, the peaks were absent in bare TiO_2. Unsurprisingly, the spectra of the 2.0CNT−TiO_2 composite possessed the characteristic peaks of both TiO_2 and pure CNT samples. The I_D/I_G ratio increased from 0.85 for the pure CNT to 1.08 for the 2.0CNT−TiO_2 composite, indicating either an increase in the average size of sp^2 domains or an interaction between TiO_2 and CNT. Also, the peaks related to CNT were shifted to 1340.1, 1578.0, and 2682.6 cm^{-1} in the composite, indicating a strong interaction between TiO_2 and CNT.[11]

Figure 2 shows the TEM image of pure TiO_2 and 2.0CNT−TiO_2 to understand the microstructure of the prepared

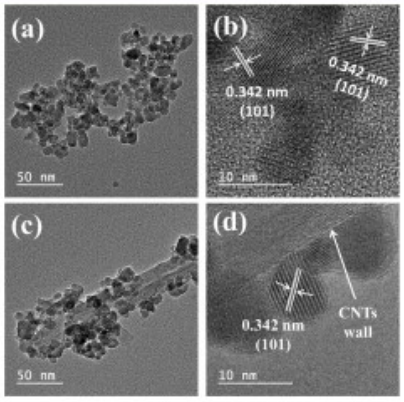

Figure 2. TEM and HRTEM images of the synthesized (a,b) TiO_2 and (c,d) 2.0CNT−TiO_2.

catalysts further and explore the influence of CNT on TiO_2 morphology. As shown in Figure S7, the addition of CNT to TiO_2 does have a slight impact on the morphology of TiO_2. Noticeably, the TiO_2 nanoparticles are spherical with an average particle size calculated to be around 12 nm, which decreased steadily to 7 nm with an increase in the CNT contents, confirming the inhibitory role of CNT on the growth of TiO_2 particles.[7] This trend is in agreement with the XRD

DOI: 10.1021/acs.jpcc.8b07894
J. Phys. Chem. C XXXX, XXX, XXX−XXX

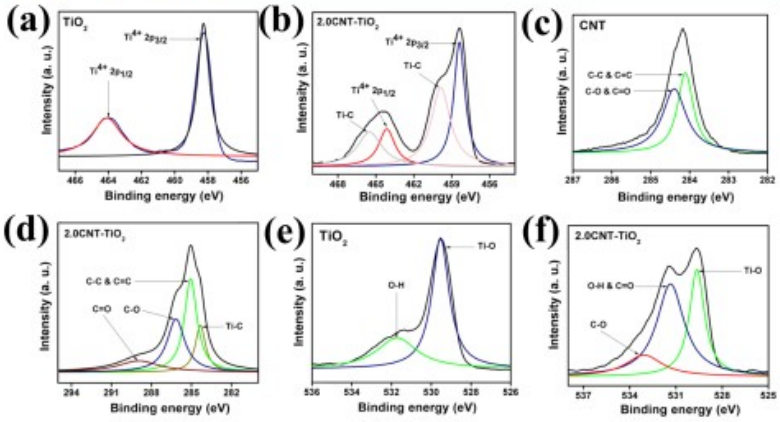

Figure 3. HR XPS spectra of (a) Ti 2p of bare TiO_2; (b) Ti 2p of 2.0CNT−TiO_2; (c) C 1s of pure CNT; (d) C 1s of 2.0CNT−TiO_2; (e) O 1s of pure CNT; and (f) O 1s of 2.0CNT−TiO_2.

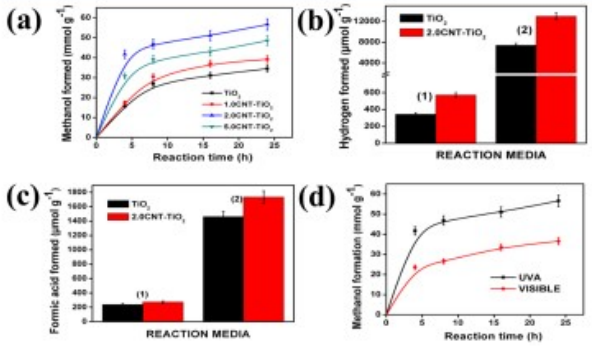

Figure 4. (a) Time-dependent profiles of methanol production by pure TiO_2 and CNT−TiO_2 samples in the ACN/H_2O/TEOA medium under UVA light. TEOA serves as a sacrificial agent. (b) Comparison of hydrogen evolution performance on photocatalytic CO_2 reduction with pure TiO_2 and 2.0CNT−TiO_2 in a different reaction medium including (1) ACN/H_2O and (2) ACN/H_2O/TEOA under UVA for 4 h. (c) Comparison of formic acid production performance with pure TiO_2 and 2.0CNT−TiO_2 in a different reaction medium including (1) ACN/H_2O and (2) ACN/H_2O/TEOA under UVA for 4 h. (d) Time-dependent profiles showing the comparison of methanol production by 2.0CNT−TiO_2 under UVA and visible light in the ACN/H_2O/TEOA medium.

results. Figure 2c exhibits the attachment of spherical TiO_2 on the wall of CNT. As the amount of CNT increases, more chance is available for TiO_2 to be attached on CNT to yield a structure resembling a branch-like tree (Figure S7). The appearance of the composites suggests the physical and chemical interactions between TiO_2 and varying amount of CNT in a way to improve the electron and ion transport properties at the interfaces.[57] The lattice fringe spacing of 0.342 nm is assigned to the (101) plane of anatase TiO_2 as confirmed by HRTEM images (Figure 2b,d). Energy-dispersive X-ray (EDX) confirms the presence of Ti, O, and C in the samples (Figure S9).

XPS measurements were performed to understand the valence states and the chemical environment of elements on the surface of prepared TiO_2 and 2.0CNT−TiO_2. The XPS survey spectra of TiO_2, 2.0CNT−TiO_2, and pure CNT are shown in Figures S10−S12. The presence of Ti, O, and C on the surface of the 2.0CNT−TiO_2 composite indicates the interaction of CNT and TiO_2. However, the peak assigned to C arising on the TiO_2 surface corresponds to the reference in the XPS instrument. The intensity of the carbon peak from 2.0CNT−TiO_2 is higher in comparison with that of TiO_2, confirming the presence of CNT in the composite. As expected, the pure CNT spectrum reveals the presence of only C and O atoms. The high-resolution (HR) XPS spectrum of bare TiO_2 is shown in Figure 3a. The peaks centered at 458.3 and 464.1 eV were attributed to Ti $2p_{3/2}$ and Ti $2p_{1/2}$ spin-orbital splitting photoelectrons in Ti^{4+}, respectively.[58] Figure 3b shows the spectrum of 2.0CNT−TiO_2. As compared to bare TiO_2, the peak positions of Ti $2p_{3/2}$ and Ti $2p_{1/2}$ were slightly shifted to 458.4 and 464.1 eV, respectively. The deconvolution of these peaks revealed additional two peaks at

DOI: 10.1021/acs.jpcc.8b07894
J. Phys. Chem. C XXXX, XXX, XXX−XXX

positions 459.9 and 465.49 eV because of the formation of the Ti−C bond arising from Ti $2p_{3/2}$ and Ti $2p_{1/2}$ peaks.[15] The formation of the Ti−C bond can also be confirmed from the spectra of C 1s.

The HR XPS spectra of C 1s of pure CNT and 2.0CNT−TiO_2 are shown in Figure 3c,d. For pure CNT, the spectrum was deconvoluted into two peaks. The peak observed at 284.1 eV is attributed to C═C and C−C bonds of the CNT, whereas the peak centered at 284.4 eV is ascribed to C−O and C═O bonds.[15,59] However, the spectrum for 2.0CNT−TiO_2 was fitted into four peaks, revealing an additional peak centered at 284.3 eV. The new peak is assigned to the Ti−C bond in the composite.[14,15] The Ti−C bond reveals that the oxygen sites in the TiO_2 lattice were substituted by carbon atoms and formed a C−Ti−O structure.[60] This new peak observed with 2.0CNT−TiO_2 indicates a strong interaction of CNT and TiO_2.

The HR XPS spectra of O 1s of the bare TiO_2, 2.0CNT−TiO_2, and pure CNT are shown in Figure 3e,f, which were deconvoluted into two peaks. The peaks observed at 529.5 and 531.7 eV are attributed to lattice oxygen and nonlattice oxygen (adsorbed OH group), respectively.[61] The deconvoluted O 1s spectrum of 2.0CNT−TiO_2 displays an additional peak at 533.2 eV, which is assigned to the C−O bond. The area of the peak observed at 531.7 eV with bare TiO_2 increased by 38% after the incorporation of CNT. This increased peak area indicates the formation of C═O as well as the generation of more oxygen defects.[59,62] The above observations of O 1s with 2.0CNT−TiO_2 confirm the interaction between CNT and TiO_2 in the composite.

3.2. Photocatalytic CO_2 Reduction. The photocatalytic activity of the prepared catalysts was evaluated for the CO_2 reduction under UVA using ACN/H_2O (16:2 v/v) as the reaction medium and in the presence of a sacrificial reagent TEOA (2 mL). As shown in Figure 4a, all prepared catalysts exhibited selectivity toward methanol formation, which increased up to 24 h reaction time. In comparison to the bare sample TiO_2, the significant improvement in photocatalytic activity with all CNT−TiO_2 composites was observed. In 24 h, relative to the composites, the lower activity by TiO_2 with a methanol production rate of 1.44 mmol g^{-1} h^{-1} may be due to rapid recombination of charge carriers and absence of a reduction reaction cocatalyst. In the range from 1 to 5% of CNT and TiO_2 weight ratio, the 2% CNT loading amount was observed to be optimal, and a gradual decrease in activity was observed with higher CNT loadings. These decreasing trends in activity with the increase of the CNT content could be due to the shielding effect of CNT.[24,35] The light absorption is one of the most critical factors for the photocatalysts.[63] The methanol production rate at 24 h with the 2.0CNT−TiO_2 (2.36 mmol g^{-1} h^{-1}) was found to be 1.64 times higher than bare TiO_2. The enhancement in activity of the CNT−TiO_2 nanocomposites in comparison with that of bare TiO_2 can be ascribed to several possible factors: (1) the higher surface area of the composites (Table S1) could offer higher active adsorption sites;[64] (2) retardation in the recombination of the photogenerated electron/hole pairs by easy transfer of photoelectrons to CNT;[8] and (3) the CNT−TiO_2 interface acting as sites for the absorption of photons with simultaneous injection of electrons in the TiO_2 conduction band.[10] To understand better the synergistic role of both CNT and TiO_2, we prepared CNT−TiO_2 by mixing 20.0 mg of CNT and 1.0 g of pure TiO_2 using a mechanical grinder to get 2.0CNT−TiO_2−MIX. By maintaining the above experimental conditions, 2.0CNT−TiO_2−MIX was able to generate 1.54 mmol g^{-1} h^{-1} (Figure S17), which was 1.53 times less than 2.0CNT−TiO_2. Hence, the suitable preparation method including calcination is required to get the proper interaction between CNT and TiO_2.

The simultaneous hydrogen and formic acid production with photoreduction of CO_2 was also observed, and the reaction progress was monitored for 4 h under UVA light in two different mixtures, namely, ACN/H_2O (18:2 v/v) and ACN/H_2O/TEOA (16:2:2 v/v). As shown in Figure 4b, 86.0 and 142.9 μmol g^{-1} h^{-1} of hydrogen were formed in the ACN/H_2O mixture for TiO_2 and 2.0CNT−TiO_2, respectively. However, in the presence of TEOA as a sacrificial electron donor, hydrogen production rates were 22 (1853.2 μmol g^{-1} h^{-1}) and 23 (3246.1 μmol g^{-1} h^{-1}) times higher with TiO_2 and 2.0CNT−TiO_2, respectively. As expected, there was a trace amount of hydrogen evolution in ACN only, which confirms that H_2 production from ACN/H_2O and ACN/H_2O/TEOA media was due to water splitting or formic acid splitting formed during the photoreduction of CO_2. The production rates of formic acid in the ACN/H_2O mixture were found to be 59.9 and 68.5 μmol g^{-1} h^{-1} for TiO_2 and 2.0CNT−TiO_2, respectively, under UVA. Unsurprisingly, in the presence of TEOA, the amount of formic acid increased by 6 times because of the vast availability of electrons from this excellent electron donor. Similar observations were observed in our previous studies, in which formic acid worked as an intermediate to produce hydrogen during the photocatalytic reduction of CO_2.[65]

To compare the effect of light wavelength, Figure 4d shows the yields of methanol in the photoconversion of CO_2 over 2.0CNT−TiO_2 under visible light (420−700 nm) by keeping the above experimental conditions constant. 2.0CNT−TiO_2 exhibited significant methanol production under visible light. The methanol production rate was observed to be 1.52 mmol g^{-1} h^{-1}, which indicates that 2.0CNT−TiO_2 is also active in the visible light. Factors such as (1) band gap narrowing of the composites,[59] (2) formation of Ti−C bonds, as confirmed by the XPS and Raman, by the CNT−TiO_2 coupling, leading to the visible light activity,[11,14,15] and (3) CNTs acting as a photosensitizer or cocatalyst for the catalytic reaction lead to utilization of longer wavelength photons.[11] It is interesting to note that 2.0CNT−TiO_2 performed reasonably good under visible light. However, methanol production is significantly higher under UV light. The reason might be the higher content of TiO_2 in the composite, which is unable to catalyze the reaction under visible light completely. The experimental results are in agreement with our theoretical investigation described in Section 3.4. The fact that hydrogen production was only marginally improved by the introduction of CNT into TiO_2 signifies that CNT did not act as an efficient hydrogen evolution cocatalyst. Indeed, the Fermi level of the CNT lies too low for the electrons transferred into CNT to possess enough reductive power. Instead, electrons are transferred from CNT into TiO_2 nanoparticles under UV and visible light excitation. Admixture energy levels correspond to overlapping orbitals of TiO_2 and CNT inside the TiO_2 band gap. Therefore, CNT serves as an electron donor and oxidation electrocatalyst for TEOA.

Table S2 shows a comparison of CNT−TiO_2 composites studied in the literature to the photocatalysts of the present study in CO_2 photoreduction and hydrogen production. The

DOI: 10.1021/acs.jpcc.8b07894
J. Phys. Chem. C XXXX, XXX, XXX−XXX

comparison demonstrates the advantages of the composites of the present study that obviously result from the application of the sonothermal−hydrothermal preparation method. The formation of tight binding of CNTs to the surface of TiO_2 is responsible for efficient catalyst photoexcitation and electron transfer to CNT to provide a high rate of photoreactions.

Additional experiments were performed to check the stability and recyclability of 2.0CNT−TiO_2. For CO_2 reduction, the reactor was recharged with CO_2 after every 12 h up to 51 h under visible light by maintaining other conditions mentioned above. It was observed that an incremental amount of methanol was produced at every 12 h interval as shown in Figure 5. For the first interval, the

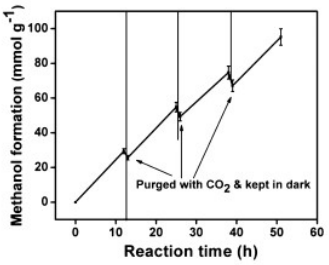

Figure 5. Recyclability and stability test on the production of methanol from 2.0CNT−TiO_2 under visible light for a period of 51 h.

methanol yield was 29.4 mmol g^{-1}, and then the solution was repurged for at least 15 min and kept in the dark for almost 1 h. After a small aliquot of the liquid is injected into the GC, we observed that the methanol production reduced to 25.7 mmol g^{-1} (−12%). Some amount of methanol was evaporated out during CO_2 purge. The reaction was resumed for another 12 h, and production reached 54.8 mmol g^{-1}. The percent reduction steadily increased because of the accumulation of methanol in the solution, whereas the percent increase steadily improved as each interval progressed.

3.3. Photocatalytic Hydrogen Production. Figure 6a presents H_2 production rates from H_2O at different pHs (2, 4, 6, 7, 8, 10, and 12) over 2.0CNT−TiO_2 catalysts in the absence of a sacrificial agent under visible light illumination during a time course of 8 h. The pH was adjusted by either HCl or NaOH. These results indicate that the lower pH range is favorable for the evolution of H_2 from H_2O. The H_2 yield rate observed was 69.41, 40.05, 26.35, 24.90, 23.85, 15.75, and 7.66 μmol g^{-1} h^{-1} at pH 2, 4, 6, 7, 8, 10, and 12, respectively. The reason behind the higher performance of 2.0CNT−TiO_2 for H_2 evolution in the acidic medium may be due to the higher concentration of H^+ ions in the acidic solution, which serves as the reactant, and this increases the reaction rate. The protons adsorbed on the photocatalyst can easily interact with generated and stored electrons, leading to molecular hydrogen formation.[66,67] Comparison of the rate of hydrogen production obtained in our present study with literature data in Table S2 demonstrates a very competitive performance of the composite photocatalyst in this study. Possible reasons for this high performance are elucidated using quantum chemical modeling of the CNT−TiO_2 composite in the next section, followed by mechanistic considerations in Section 3.5.

Further, we tested for the recyclability of H_2 from H_2O over 2.0CNT−TiO_2 catalysts at pH 2 under visible light illumination. As shown in Figure 6b, these results clearly indicate that 2.0CNT−TiO_2 is a stable photocatalyst for H_2 production as they were tested for three cycles in 3 days. After analyzing the product for the first cycle in 8 h, the reaction was stopped and reactor was in the dark till the second day and then the reactor was degassed using a mechanical pump. Thereafter, the reaction was resumed for the second cycle; the same procedure was performed for the third cycle.

3.4. Nature of Anatase Nanoparticle Interaction with CNT. Quantum chemical computations were undertaken in the present study to elucidate types of possible interaction between CNT and TiO_2 nanoparticles. Anatase nanoparticles of round shape (Figure 2) have a variety of possible surface atoms arrangements. The most stable facet of anatase is, however, (101). This facet and facet (001) are undoubtedly present in the synthesized materials. Other arrangements of surface atoms are also possible in the experimentally obtained TiO_2, but they are not considered in the present study for the sake of clearness. The nanoparticle Ti44r1, which is a model for the TiO_2 nanoparticles of the present study, possesses facets (101) and (001) representing a part of surface structures in experimentally synthesized nanoparticles. CNTs can be attached to different surface arrangements of TiO_2 anatase nanoparticles. We consider here three alternatives of attaching CNT to a Ti44r1 nanoparticle—one variant for connecting to the (001) facet along the edge hydroxyl groups and two variants for attaching to (101) facets—approximately perpendicular to (001) facets and along (001) facets. To obtain the final attachment geometries, CNT was placed at the predefined locations, and the structure was optimized to achieve minimal energy.

Figure 7a demonstrates the optimized structures of CNT attached to the (001) facet as well as two variants of

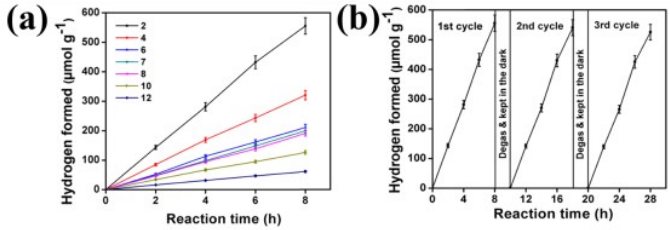

Figure 6. (a) Typical time course of hydrogen evolution from H_2O by 2.0CNT−TiO_2 in the absence of a sacrificial agent under different pHs using visible light irradiation. (b) Recyclability test on the evolution of H_2 from H_2O by 2.0CNT−TiO_2 at pH 2.

DOI: 10.1021/acs.jpcc.8b07894
J. Phys. Chem. C XXXX, XXX, XXX−XXX

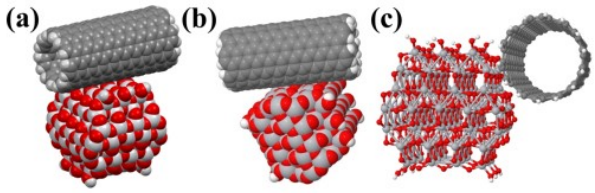

Figure 7. CNT−TiO_2 composite structure with CNT attachment to the (001) facet (a) and to the (101) facet (b,c).

attachment to the (101) facet of the anatase model nanoparticle (Figure 7b,c). The interaction of CNT with the (001) surface is rather weak: the adsorption energy is −5.35 kcal mol^{-1}. The electronic properties of this CNT−TiO_2 composite structure are not much different from the properties of CNT: Fermi energy of the CNT−TiO_2 composite is −4.39 eV, and Fermi energy of CNT is −4.40 eV. The predominance of the CNT properties in the composite is due to the high number of delocalized electrons in it in contrast to TiO_2 that has their electrons mostly localized in oxygen atoms. The details of the CNT−TiO_2 (001) interaction can be obtained by considering frontier orbitals—highest occupied molecular orbital (HOMO) and lowest unoccupied molecular orbital (LUMO). Figure S18 shows these orbitals with the isosurfaces 10^{-5} for the CNT location close to the (001) surface. We can see that electrons of CNT mostly represent the boundary orbitals with a minimal contribution of p_O orbitals of the TiO_2 (001) surface in HOMO and both p_O and d_{Ti} orbitals in LUMO.

The minimal contribution of orbitals of CNT and TiO_2 to overall orbitals is also valid for other considered orbitals in the range of orbitals 1536−1597. For individual CNT, the boundary orbital energy is −4.56 (HOMO) and −4.24 eV (LUMO) with the band gap of 0.32 eV. In the CNT−TiO_2 (001) composite, the boundary orbitals correspond closely to CNT: −4.55 (HOMO) and −4.23 eV (LUMO). It confirms the predominant contribution of CNT to the electronic properties of boundary orbitals of the CNT−TiO_2 composite. It is interesting to consider the contributions of orbitals at the energy position corresponding to Ti44r1 cluster boundary orbitals. For individual cluster Ti44r1, the boundary orbital energies are −5.47 (HOMO) and −2.53 eV (LUMO) with the band gap of 2.94 eV. This value of the electronic band gap is in excellent agreement with the experimental value of optical band gap 3.2 eV. In the CNT−TiO_2 (001) composite, the structure of the boundary orbitals corresponds to that of individual orbitals of the Ti44r1 nanoparticle.[43] The energy positions of Ti44r1 orbitals in the composite are −5.45 (HOMO) and −2.49 eV (LUMO). There is a minimal shift in the energy positions of the TiO_2 orbitals, which signifies that the interaction of CNT with the (001) surface of TiO_2 is too small regarding both interaction energy and wave functions interpenetration.

Figure 7b,c shows the variant of CNT and TiO_2 nanoparticle interposition in which CNT is located along the (101) facet and approximately perpendicular to the (001) facet. The nanotube and the Ti44r1 cluster are positioned in such a way that the TiO_2 cluster interacts with the middle part of the CNT. This positioning was used to avoid the effects of the limited length of the CNT model used. The interaction of CNT with the (101) facet is stronger than with the (001) facet: the adsorption energy is −6.15 kcal mol^{-1} for the geometry as shown in Figure 7b. However, it is still minimal interaction energy, and the interaction is mainly of the van der Waals nature. The interatomic distances correspond to van der Waals diameters or larger distances.

Figure 8 demonstrates the boundary orbitals of the CNT−TiO_2 (101) complex of the geometry shown in Figure 8b.

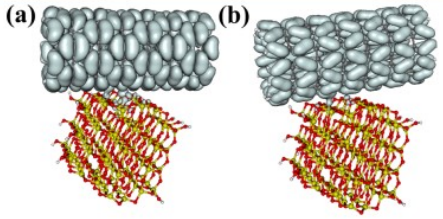

Figure 8. Boundary orbitals of the CNT-Ti44r1 complex with CNT adsorbed over the (101) facet: (a) HOMO and (b) LUMO.

CNT orbitals represent the boundary orbitals with a tiny contribution of Ti44r1 orbitals. For HOMO, p_O orbitals partially overlap with CNT orbitals, whereas for LUMO, both p_O and d_{Ti} of the (101) surface partially overlap with some of the CNT orbitals. The orbitals overlap stronger than for CNT adsorbed over the (001) surface. The energy of HOMO is −4.57 and that of LUMO is −4.24 eV, which is the same as for individual CNTs.

While boundary orbitals of the CNT−TiO_2 complex do not have a significant contribution from atomic orbitals (AOs) belonging to TiO_2, orbitals with lower energy do have contributions from both CNT and TiO_2. Figure S19 illustrates this and reveals that orbital 1544 (Figure S19a) with an eigenvalue of −5.70 eV and orbital 1561 (Figure S19b) with an eigenvalue of −5.45 eV are linear combinations of AOs of both CNT and Ti44r1 nanoparticles. There are other orbitals in the energy range between these molecular orbitals (MOs) that have significant contributions from both CNT and TiO_2.

Orbitals in the conduction band of the composite with the energy below the energy of the conduction band of Ti44r1 have a little contribution from the AO of TiO_2. Starting from orbital 1588 with an eigenvalue of −2.48 eV, orbitals can have a significant contribution from both Ti44r1 and CNT. Thus, photoexcitation of CNT−Ti44r1 (001) and CNT−Ti44r1 (101) composites considered above with photons of visible light range energy can result in electron transfer from TiO_2 to CNT.

The last considered geometry of the CNT−TiO_2 complex contains CNT adsorbed over the (101) facet of the Ti44r1 cluster and directed parallel to the (001) facet. Figure 7c shows

DOI: 10.1021/acs.jpcc.8b07894
J. Phys. Chem. C XXXX, XXX, XXX−XXX

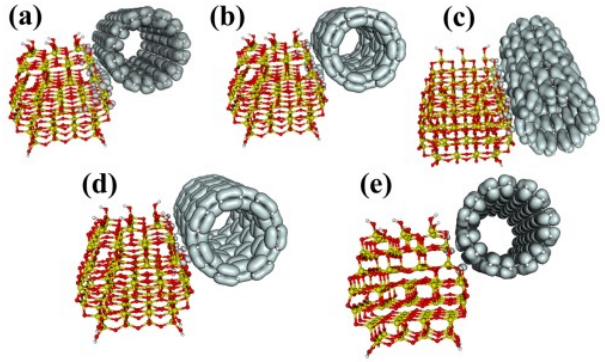

Figure 9. Orbitals of the CNT−TiO_2 adsorption complex shown in Figure 7c. (a) 1563 (HOMO − 3), (b) 1564 (HOMO − 2), (c) 1565 (HOMO − 1), (d) 1566 (HOMO), and (e) 1567 (LUMO).

Scheme 1. Schematic Diagram Showing the Product Formation from CO_2 and H_2O (a) under UVA Irradiation in the ACN/H_2O/TEOA Solvent, (b) under UVA Irradiation in ACN/H_2O, and (c) under Visible Light in ACN/H_2O/TEOA

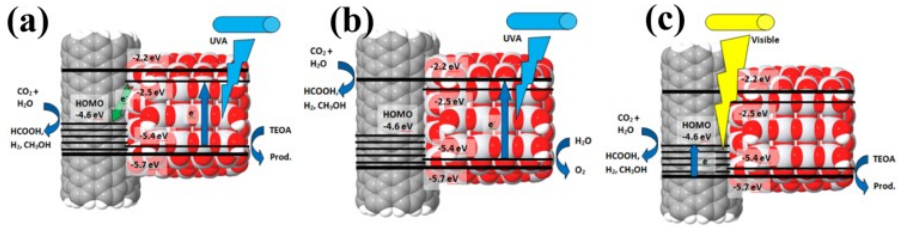

the optimized geometry of this adsorption complex. CNT matches the step of the (101) surface in this complex. A large number of interacting atoms cause significant adsorption energy for this adsorption complex that is equal to −20.77 kcal mol^{-1}. This strong interaction is supported by the formation of Ti−C bonds earlier discussed from the XPS results.

Figure 9 shows orbitals of the CNT−Ti44r1 complex close to the frontier orbitals. The d_{Ti} and p_O AO in step in the (101) surface give a contribution to the MO near the edge of the valence band of the complex. Overlap of many AOs of TiO_2 with orbitals of the CNT results in relatively strong adsorption of CNT over the step of the (101) surface.

3.5. Mechanism of Enhancement of TiO_2 Photocatalytic Reactions with CNT. It has been demonstrated in the previous section that CNTs can form heterojunctions with (101) surfaces of anatase nanoparticles of comparable size with significant orbital overlap if the nanotube is parallel to the (001) surface of the anatase nanoparticle. TEM images in Figures 2 and S6 demonstrate that the diameter of MWCNT and size of TiO_2 anatase nanoparticles are of comparable value to confirm the validity of the system used in quantum chemical modeling. The HRTEM images also reveal the tight contact of individual TiO_2 nanoparticles and agglomerates of TiO_2 nanoparticles with the CNT surface. Under the conditions of such tight contacts, orbitals of TiO_2 nanoparticles and CNT overlap as it was demonstrated in Figures 7 and 8. The fact that TiO_2 and CNT orbitals form linear combinations with significant contribution from both parts makes it possible for these common orbitals to participate in the process of photoexcitation and efficient electron transfer between TiO_2 and CNT.

Scheme 1 illustrates photophysical and photochemical processes that are suggested to take place during photocatalytic hydrogen production and CO_2 photoreduction in the present study. To get a clear comprehension of the photocatalytic reaction mechanisms, we need to distinguish the four different regimes of photocatalytic reactions utilized, namely, UV and visible light photoexcitation in the presence and absence of a strong electron donor TEOA. Of these four regimes, three were realized in the present study.

Under UVA light, both TiO_2 nanoparticles and MWCNT can take part in the photoexcitation process with the dominant role of TiO_2 because of the short lifetime of charge carriers in CNT because of the absence or very small value of the band gap. Under visible light, photoexcitation can proceed with the participation of boundary orbitals of the CNT−TiO_2 composite shown in Figures 7 and 8, which are common conduction and valence band orbitals of CNT−TiO_2 nanoparticles, which provide an effective band gap of around 1.1 eV for CNT−TiO_2 valence band to CNT charge transfer and 2.4 eV for CNT to CNT−TiO_2 conduction band charge transfer. It should be pointed out that without a sacrificial electron donor, the energy level of electrons in CNT is too low (about +2.0 eV) to drive any reaction of photoreduction. However, reactions of oxidation can proceed with the formation of oxygen during CO_2 photoreduction and water splitting. Under such conditions, photogenerated electrons in the CNT−TiO_2

DOI: 10.1021/acs.jpcc.8b07894
J. Phys. Chem. C XXXX, XXX, XXX−XXX

conduction band act as the reducing agent for CO_2 reduction and H_2 formation from H_2O (Scheme 1b).

In the presence of a sacrificial electron donor TEOA, strongly reducing conditions are realized. Photogenerated electrons resulting from TEOA oxidation with UVA light photogenerated holes in the CNT−TiO_2 valence band eventually are transferred to CNT (Scheme 1a). Pumping of excessive electrons into CNT increases its redox potential to values enough to drive diverse reactions of reduction with the production of hydrogen, formic acid, and methanol. CNTs are known to be a good electrocatalyst for such reactions. Therefore, the tight contact of MWCNT and TiO_2 nanoparticles is the cause of the large photocatalytic activity of the MWCNT−TiO_2 composites of the present study. Under visible light photoexcitation, electrons from the common orbitals of the CNT−TiO_2 valence band found at −5.7 eV can be brought to the LUMO orbitals situated mostly in CNTs and initiate reduction reactions over the CNT surface (Scheme 1c).

4. CONCLUSIONS

We have reported the synthesis of a series of efficient stable TiO_2 nanoparticles modified with CNTs via a simple sonothermal method, followed by a hydrothermal treatment. The synthesized CNT−TiO_2 photocatalysts have shown improved photocatalytic activities for CO_2 reduction under both UVA and visible light at ambient temperature and pressure. Hydrogen production from water splitting was significantly enhanced under UVA irradiation. The effect of pH was also considered, and the highest hydrogen production rate was observed at the lowest pH 2.0. The formation of the Ti−C bond from the XPS results indicated the presence of a strong interaction between CNT and TiO_2 nanoparticles. The computational studies revealed that decahedral anatase nanoparticles could be weakly attached to CNT with the (001) surface and strongly attached to CNT with the (101) surface. The binding with (101) results in frontier orbital overlap and combination of valence and conduction band orbitals of TiO_2 and orbitals of CNT. Consequently, photoexcitation of the CNT−TiO_2 composite with visible light can result in charge transfer between TiO_2 and CNT and generation of separated charge carriers, whereas UV light excitation can result in charge transfer in any direction from CNT to TiO_2 and from TiO_2 to CNT, the latter process being more probable because of the higher density of initial states in TiO_2 compared to CNT. The unusually high photocatalytic activity of the MWCNT−TiO_2 composite in the present study was found to result from the realization of very tight contact between MWCNT and individual TiO_2 nanoparticles owing to the preparation method of the composite.

■ ASSOCIATED CONTENT

Supporting Information

The Supporting Information is available free of charge on the ACS Publications website at DOI: 10.1021/acs.jpcc.8b07894.

TGA and Tauc plots; physicochemical properties of the pure TiO_2 and CNT−TiO_2 samples; TEM and EDX images; XPS spectra; comparison of the photocatalytic results with previous studies; orbitals of CNT−TiO_2 nanocomposites; and details of methanol quantification (PDF)

■ AUTHOR INFORMATION

Corresponding Authors

*E-mail: a-voronts@yandex.ru. Phone: +79537855528 (A.V.V.).

*E-mail: umesh_kumar@iip.res.in. Phone: +91-135-2525-795 (U.K.).

ORCID

Alexander V. Vorontsov: 0000-0002-2791-3278

Umesh Kumar: 0000-0002-6226-0305

Notes

The authors declare no competing financial interest.

■ ACKNOWLEDGMENTS

The authors are grateful to Director, IIP for his kind permission to publish the results. J. O. Olowoyo is thankful to CSIR-TWAS for the funding of the research work (22/FF/CSIR-TWAS/2015). The authors are thankful to ASD-IIP for their analytical support.

■ REFERENCES

(1) Lingampalli, S. R.; Ayyub, M. M.; Rao, C. N. R. Recent Progress in the Photocatalytic Reduction of Carbon Dioxide. *ACS Omega* **2017**, *2*, 2740−2748.

(2) Bai, S.; Wang, L.; Li, Z.; Xiong, Y. Facet-Engineered Surface and Interface Design of Photocatalytic Materials. *Adv. Sci.* **2016**, *4*, 1600216.

(3) Zhang, T.; Low, J.; Koh, K.; Yu, J.; Asefa, T. Mesoporous TiO_2 Comprising Small, Highly Crystalline Nanoparticles for Efficient CO_2 Reduction by H_2O. *ACS Sustainable Chem. Eng.* **2017**, *6*, 531−540.

(4) Low, J.; Cheng, B.; Yu, J. Surface Modification and Enhanced Photocatalytic CO_2 Reduction Performance of TiO_2: a Review. *Appl. Surf. Sci.* **2017**, *392*, 658−686.

(5) Cai, Y.; Feng, Y. P. Review on Charge Transfer and Chemical Activity of TiO_2: Mechanism and Applications. *Prog. Surf. Sci.* **2016**, *91*, 183−202.

(6) Fraser, A.; Zhang, Z.; Merle, G.; Gbureck, U.; Ye, S.; Gostick, J.; Barralet, J. Composite Carbon Nanotube Microsphere Coatings for Use as Electrode Supports. *Adv. Funct. Mater.* **2018**, *28*, 1803713.

(7) An, T.; Chen, J.; Nie, X.; Li, G.; Zhang, H.; Liu, X.; Zhao, H. Synthesis of Carbon Nanotube−Anatase TiO_2 Sub-Micrometer-Sized Sphere Composite Photocatalyst for Synergistic Degradation of Gaseous Styrene. *ACS Sustain. Chem. Eng* **2012**, *4*, 5988−5996.

(8) Yu, H.; Quan, X.; Chen, S.; Zhao, H. TiO_2−Multiwalled Carbon Nanotube Heterojunction Arrays and Their Charge Separation Capability. *J. Phys. Chem. C* **2007**, *111*, 12987−12991.

(9) Thostenson, E. T.; Ren, Z.; Chou, T.-W. Advances in the Science and Technology of Carbon Nanotubes and Their Composites: A Review. *Compos. Sci. Technol.* **2001**, *61*, 1899−1912.

(10) Woan, K.; Pyrgiotakis, G.; Sigmund, W. Photocatalytic Carbon-Nanotube-TiO_2 Composites. *Adv. Mater.* **2009**, *21*, 2233−2239.

(11) Vijayan, B. K.; Dimitrijevic, N. M.; Finkelstein-Shapiro, D.; Wu, J.; Gray, K. A. Coupling Titania Nanotubes and Carbon Nanotubes to Create Photocatalytic Nanocomposites. *ACS Catal.* **2012**, *2*, 223−229.

(12) Yen, C.-Y.; Lin, Y.-F.; Hung, C.-H.; Tseng, Y.-H.; Ma, C.-C. M.; Chang, M.-C.; Shao, H. The Effects of Synthesis Procedures on the Morphology and Photocatalytic Activity of Multiwalled Carbon Nanotubes/TiO_2 Nanocomposites. *Nanotechnology* **2008**, *19*, 045604.

(13) Yang, M.-Q.; Zhang, N.; Xu, Y.-J. Synthesis of Fullerene-, Carbon Nanotube-, and Graphene-TiO_2 Nanocomposite Photocatalysts for Selective Oxidation: A Comparative Study. *ACS Appl. Mater. Interfaces* **2013**, *5*, 1156−1164.

(14) Akhavan, O.; Abdolahad, M.; Abdi, Y.; Mohajerzadeh, S. Synthesis of Titania/Carbon Nanotube Heterojunction Arrays for Photoinactivation of E. coli in Visible Light Irradiation. *Carbon* **2009**, *47*, 3280−3287.

(15) Akhavan, O.; Azimirad, R.; Safa, S.; Larijani, M. M. Visible Light Photo-Induced Antibacterial Activity of CNT–doped TiO_2 Thin Films with Various CNT Contents. *J. Mater. Chem.* **2010**, *20*, 7386.

(16) Lavanya, R.; Surya, V. J.; Lakshmi, I.; Iyakutti, K.; Vasu, V.; Mizuseki, H.; Kawazoe, Y. Hydrogen Storage in TiO_2 Functionalized (10,10) Single Walled Carbon Nanotube (SWCNT) - First Principles Study. *Int. J. Hydrogen Energy* **2014**, *39*, 4973–4980.

(17) Dai, K.; Peng, T.; Ke, D.; Wei, B. Photocatalytic Hydrogen Generation Using a Nanocomposite of Multi-Walled Carbon Nanotubes and TiO_2 Nanoparticles Under Visible Light Irradiation. *Nanotechnology* **2009**, *20*, 125603.

(18) Lee, K.-Y.; Rahman Mohamed, A.; Sato, K. Enhanced Photocatalytic Activity of TiO_2–CNT Composites for Photoreduction of CO_2. *Sens. Mater.* **2015**, *27*, 993–1001.

(19) Ong, W.-J.; Gui, M. M.; Chai, S.-P.; Mohamed, A. R. Direct Growth of Carbon Nanotubes on Ni/TiO_2 as Next Generation Catalysts for Photoreduction of CO_2 to Methane by Water Under Visible Light Irradiation. *RSC Adv.* **2013**, *3*, 4505–4509.

(20) Khalilian, M.; Abdi, Y.; Arzi, E. Formation of Well-Packed TiO_2 Nanoparticles on Multiwall Carbon Nanotubes Using CVD Method to Fabricate High Sensitive Gas Sensors. *J. Nanoparticle Res.* **2011**, *13*, 5257–5264.

(21) Charinpanitkul, T.; Lorturn, P.; Ratismith, W.; Viriya-empikul, N.; Tumcharern, G.; Wilcox, J. Hydrothermal Synthesis of Titanate Nanoparticle/Carbon Nanotube Hybridized Material for Dye Sensitized Solar Cell Application. *Mater. Res. Bull.* **2011**, *46*, 1604–1609.

(22) Miranda, S. M.; Romanos, G. E.; Likodimos, V.; Marques, R. R. N.; Favvas, E. P.; Katsaros, F. K.; Stefanopoulos, K. L.; Vilar, V. J. P.; Faria, J. L.; Falaras, P.; et al. Pore Structure, Interface Properties and Photocatalytic Efficiency of Hydration/Dehydration Derived TiO_2/CNT Composites. *Appl. Catal., B* **2014**, *147*, 65–81.

(23) Abdulrazzak, F. H.; Hussein, F. H.; Alkaim, A. F.; Ivanova, I.; Emeline, A. V.; Bahnemann, D. W. Sonochemical/Hydration-Dehydration Synthesis of Pt-TiO_2 NPs/Decorated Carbon Nanotubes with Enhanced Photocatalytic Hydrogen Production Activity. *Photochem. Photobiol. Sci.* **2016**, *15*, 1347–1357.

(24) Li, Y.; Li, L.; Li, C.; Chen, W.; Zeng, M. Carbon Nanotube/Titania Composites Prepared by a Micro-Emulsion Method Exhibiting Improved Photocatalytic Activity. *Appl. Catal., A* **2012**, *427–428*, 1–7.

(25) Yu, H.; Quan, X.; Chen, S.; Zhao, H.; Zhang, Y. TiO_2–Carbon Nanotube Heterojunction Arrays with a Controllable Thickness of TiO_2 Layer and Their First Application in Photocatalysis. *J. Photochem. Photobiol., A* **2008**, *200*, 301–306.

(26) Aryal, S.; Kim, C. K.; Kim, K.-W.; Khil, M. S.; Kim, H. Y. Multi-Walled Carbon Nanotubes/TiO_2 Composite Nanofiber by Electrospinning. *Mater. Sci. Eng., C* **2008**, *28*, 75–79.

(27) Ahmmad, B.; Kusumoto, Y.; Somekawa, S.; Ikeda, M. Carbon Nanotubes Synergistically Enhance Photocatalytic Activity of TiO_2. *Catal. Commun.* **2008**, *9*, 1410–1413.

(28) Gui, M. M.; Wong, W. M. P.; Chai, S.-P.; Mohamed, A. R. One-Pot Synthesis of Ag-MWCNT@TiO_2 Core–Shell Nanocomposites for Photocatalytic Reduction of CO_2 with Water Under Visible Light Irradiation. *Chem. Eng. J.* **2015**, *278*, 272–278.

(29) Kim, J.; Monllor-Satoca, D.; Choi, W. Simultaneous Production of Hydrogen with the Degradation of Organic Pollutants Using TiO_2 Photocatalyst Modified with Dual Surface Components. *Energy Environ. Sci.* **2012**, *5*, 7647.

(30) Christoforidis, K. C.; Fornasiero, P. Photocatalytic Hydrogen Production: A Rift into the Future Energy Supply. *ChemCatChem* **2017**, *9*, 1523–1544.

(31) Zhang, X.-Y.; Li, H.-P.; Cui, X.-L.; Lin, Y. Graphene/TiO_2 Nanocomposites: Synthesis, Characterization and Application in Hydrogen Evolution from Water Photocatalytic Splitting. *J. Mater. Chem.* **2010**, *20*, 2801.

(32) Zielinska, B.; Borowiakpalen, E.; Kalenczuk, R. Photocatalytic Hydrogen Generation Over Alkaline-Earth Titanates in the Presence of Electron Donors. *Int. J. Hydrogen Energy* **2008**, *33*, 1797–1802.

(33) Duong, T.-T.; Nguyen, Q.-D.; Hong, S.-K.; Kim, D.; Yoon, S.-G.; Pham, T.-H. Enhanced Photoelectrochemical Activity of the TiO_2/ITO Nanocomposites Grown onto Single-Walled Carbon Nanotubes at a Low Temperature by Nanocluster Deposition. *Adv. Mater.* **2011**, *23*, 5557–5562.

(34) Nguyen, M. T.; Nguyen, C. K.; Vu, T. M. P.; Duong, Q. V.; Pham, T. L.; Nguyen, T. C. A Study on Carbon Nanotube Titanium Dioxide Hybrids: Experiment and Calculation. *Adv. Nat. Sci.: Nanosci. Nanotechnol.* **2014**, *5*, 045018.

(35) Yao, Y.; Li, G.; Ciston, S.; Lueptow, R. M.; Gray, K. A. Photoreactive TiO_2/Carbon Nanotube Composites: Synthesis and Reactivity. *Environ. Sci. Technol.* **2008**, *42*, 4952–4957.

(36) Duong, T.-T.; Kim, D.-J.; Kim, C.-S.; Yoon, S.-G. Ultraviolet Response and Photoelectrochemical Properties of a Rutile and Anatase Mixture Grown onto Single-Wall Carbon Nanotubes at a Low Temperature Using Nano-Cluster Deposition. *J. Mater. Chem.* **2011**, *21*, 16473–16479.

(37) Gialampouki, M. A.; Lekka, C. E. Early Stages of Ti-O Cluster Growth on Carbon Nanotubes by Ab Initio Calculations. *J. Phys. Chem. A* **2013**, *117*, 10397–10406.

(38) Ayissi, S.; Charpentier, P. A.; Palotás, K.; Farhangi, N.; Schwarz, F.; Hofer, W. A. Preferential Adsorption of TiO_2 Nanostructures on Functionalized Single-Walled Carbon Nanotubes: A DFT Study. *J. Phys. Chem. C* **2015**, *119*, 15085–15093.

(39) Geng, W.; Liu, H.; Yao, X. Enhanced Photocatalytic Properties of Titania-Graphene Nanocomposites: A Density Functional Theory Study. *Phys. Chem. Chem. Phys.* **2013**, *15*, 6025–6033.

(40) Olowoyo, J. O.; Hernández, N. C.; Kumar, M.; Jain, S. L.; Babalola, J. O.; Kumar, U. Insight of Diversified Reactivity and Theoretical Study of Mixed-Phase Titanium Dioxide for the Photoactivation of Small Molecules. *ChemistrySelect* **2018**, *3*, 3659–3663.

(41) Olowoyo, J. O.; Kumar, M.; Singhal, N.; Jain, S. L.; Babalola, J. O.; Vorontsov, A. V.; Kumar, U. Engineering and Modeling the Effect of Mg Doping in TiO_2 for Enhanced Photocatalytic Reduction of CO_2 to Fuels. *Catal. Sci. Technol.* **2018**, *8*, 3686–3694.

(42) Omidvar, H.; Mirzaei, F. K.; Rahimi, M. H.; Sadeghian, Z. A Method for Coating Carbon Nanotubes with Titanium. *New Carbon Mater.* **2012**, *27*, 401–408.

(43) Vorontsov, A. V. Structural and Electronic Effects in Acetone Adsorption over TiO_2 Anatase Clusters as the First Stage of Photocatalytic Oxidation. *ýJ. Nanoparticle Res.* **2017**, *19*, 326.

(44) Vorontsov, A. V.; Tsybulya, S. V. Influence of Nanoparticles Size on XRD Patterns for Small Monodisperse Nanoparticles of Cu^0 and TiO_2 Anatase. *Ind. Eng. Chem. Res.* **2018**, *57*, 2526–2536.

(45) Vorontsov, A. V.; Smirniotis, P. G. Size and Surface Groups Effects in Decahedral Anatase Nanoparticles for Photocatalytic Applications. *J. Photochem. Photobiol., A* **2018**, *363*, 51–60.

(46) Aradi, B.; Hourahine, B.; Frauenheim, T. DFTB+, a Sparse Matrix-Based Implementation of the DFTB Method. *J. Phys. Chem. A* **2007**, *111*, 5678–5684.

(47) Schmidt, M. W.; Baldridge, K. K.; Boatz, J. A.; Elbert, S. T.; Gordon, M. S.; Jensen, J. H.; Koseki, S.; Matsunaga, N.; Nguyen, K. A.; Su, S.; et al. General Atomic and Molecular Electronic Structure System. *J. Comput. Chem.* **1993**, *14*, 1347–1363.

(48) Dolgonos, G.; Aradi, B.; Moreira, N. H.; Frauenheim, T. An Improved Self-Consistent-Charge Density-Functional Tight-Binding (SCC-DFTB) Set of Parameters for Simulation of Bulk and Molecular Systems Involving Titanium. *J. Chem. Theory Comput.* **2010**, *6*, 266–278.

(49) Elstner, M.; Porezag, D.; Jungnickel, G.; Elsner, J.; Haugk, M.; Frauenheim, T.; Suhai, S.; Seifert, G. Self-Consistent-Charge Density-Functional Tight-Binding Method for Simulations of Complex Materials Properties. *Phys. Rev. B: Condens. Matter Mater. Phys.* **1998**, *58*, 7260–7268.

DOI: 10.1021/acs.jpcc.8b07894
J. Phys. Chem. C XXXX, XXX, XXX–XXX

(50) Yang, M.-Q.; Zhang, N.; Xu, Y.-J. Synthesis of Fullerene−, Carbon Nanotube−, and Graphene−TiO_2 Nanocomposite Photocatalysts for Selective Oxidation: A Comparative Study. *ACS Appl. Mater. Interfaces* **2013**, *5*, 1156−1164.
(51) Zhang, Y.; Tang, Z.-R.; Fu, X.; Xu, Y.-J. Engineering the Unique 2D Mat of Graphene to Achieve Graphene-TiO_2 Nanocomposite for Photocatalytic Selective Transformation: What Advantage does Graphene have over its Forebear Carbon Nanotube? *ACS Nano* **2011**, *5*, 7426−7435.
(52) Taleshi, F. Study of Morphology and Band Gap Energy of TiO_2-Carbon Nanotube Nanocomposite. *J. Mater. Sci.: Mater. Electron.* **2015**, *26*, 3262−3267.
(53) Nourbakhsh, A.; Abbaspour, S.; Masood, M.; Mirsattari, S. N.; Vahedi, A.; Mackenzie, K. J. D. Photocatalytic Properties of Mesoporous TiO_2 Nanocomposites Modified with Carbon Nanotubes and Copper. *Ceram. Int.* **2016**, *42*, 11901−11906.
(54) Leofanti, G.; Padovan, M.; Tozzola, G.; Venturelli, B. Surface Area and Pore Texture of Catalysts. *Catal. Today* **1998**, *41*, 207−219.
(55) Xiao, S.; Zhu, W.; Liu, P.; Liu, F.; Dai, W.; Zhang, D.; Chen, W.; Li, H. CNTs Threaded (001) Exposed TiO_2 with High Activity in Photocatalytic NO Oxidation. *Nanoscale* **2016**, *8*, 2899−2907.
(56) Roy, S.; Das, T.; Ming, Y.; Chen, X.; Yue, C. Y.; Hu, X. Specific Functionalization and Polymer Grafting on Multiwalled Carbon Nanotubes to Fabricate Advanced Nylon 12 Composites. *J. Mater. Chem. A* **2014**, *2*, 3961−3970.
(57) Jing, Y.-Q.; Gui, C.-X.; Qu, J.; Hao, S.-M.; Wang, Q.-Q.; Yu, Z.-Z. Silver Silicate@Carbon Nanotube Nanocomposites for Enhanced Visible Light Photodegradation Performance. *ACS Sustainable Chem. Eng.* **2017**, *5*, 3641−3649.
(58) Niu, Y.; Xing, M.; Zhang, J.; Tian, B. Visible Light Activated Sulfur and Iron Co-Doped TiO_2 Photocatalyst for the Photocatalytic Degradation of Phenol. *Catal. Today* **2013**, *201*, 159−166.
(59) Cong, Y.; Li, X.; Qin, Y.; Dong, Z.; Yuan, G.; Cui, Z.; Lai, X. Carbon-Doped TiO_2 Coating on Multiwalled Carbon Nanotubes with Higher Visible Light Photocatalytic Activity. *Appl. Catal., B* **2011**, *107*, 128−134.
(60) Huang, Y.; Ho, W.; Lee, S.; Zhang, L.; Li, G.; Yu, J. C. Effect of Carbon Doping on the Mesoporous Structure of Nanocrystalline Titanium Dioxide and its Solar-Light-Driven Photocatalytic Degradation of NOx. *Langmuir* **2008**, *24*, 3510−3516.
(61) Hafeez, H. Y.; Lakhera, S. K.; Bellamkonda, S.; Rao, G. R.; Shankar, M. V.; Bahnemann, D. W.; Neppolian, B. Construction of Ternary Hybrid Layered Reduced Graphene Oxide Supported g-C_3N_4-TiO_2 Nanocomposite and its Photocatalytic Hydrogen Production Activity. *Int. J. Hydrogen Energy* **2018**, *43*, 3892−3904.
(62) Bellamkonda, S.; Thangavel, N.; Hafeez, H. Y.; Neppolian, B.; Rao, G. R. Highly Active and Stable Multi-Walled Carbon Nanotubes-Graphene-TiO_2 Nanohybrid: An Efficient Non-noble Metal Photocatalyst for Water Splitting. *Catal. Today* **2019**, *321*−*322*, 120−127.
(63) Juang, L.-C.; Semblante, G. U.; You, S.-J.; Hong, S.-H. Degradation of 2-Chlorophenol using Carbon Nanotube/Titanium Oxide Composite Prepared by Hydrothermal Method. *J. Taiwan Inst. Chem. Eng.* **2013**, *44*, 432−437.
(64) Yu, Y.; Yu, J. C.; Chan, C.-Y.; Che, Y.-K.; Zhao, J.-C.; Ding, L.; Ge, W.-K.; Wong, P.-K. Enhancement of Adsorption and Photocatalytic Activity of TiO_2 by using Carbon Nanotubes for the Treatment of Azo Dye. *Appl. Catal., B* **2005**, *61*, 1−11.
(65) Singhal, N.; Ali, A.; Vorontsov, A.; Pendem, C.; Kumar, U. Efficient Approach for Simultaneous CO and H_2 Production via Photoreduction of CO_2 with Water over Copper Nanoparticles Loaded TiO_2. *Appl. Catal., A* **2016**, *523*, 107−117.
(66) Salas, S. E.; Rosales, B. S.; de Lasa, H. Quantum Yield with Platinum Modified TiO_2 Photocatalyst for Hydrogen Production. *Appl. Catal., B* **2013**, *140*−*141*, 523−536.
(67) Sadeghi, I.; Arbab, P.; Fathizadeh, M.; Fakhraee, H.; Amrollahi, M. Optimization of Nano- Photocatalytic Reactor for Organophosphorus Degradation. *Adv. Mater. Sci. Eng.* **2012**, *2012*, 1−5.

DOI: 10.1021/acs.jpcc.8b07894
J. Phys. Chem. C XXXX, XXX, XXX−XXX

APPENDIX VIII

Copy of paper published from the Photocatalytic CO_2 reduction with H_2O as reductant over Magnesium-doped TiO_2 nanocatalysts

Catalysis Science & Technology

PAPER

View Article Online
View Journal | View Issue

Published on 25 June 2018. Downloaded by Indian Institute of Petroleum on 7/17/2018 10:36:33 AM.

Check for updates

Cite this: *Catal. Sci. Technol.*, 2018, 8, 3686

Engineering and modeling the effect of Mg doping in TiO_2 for enhanced photocatalytic reduction of CO_2 to fuels†

Joshua O. Olowoyo,[ac] Manoj Kumar,[b] Nikita Singhal,[a] Suman L. Jain,[a] Jonathan O. Babalola,[c] Alexander V. Vorontsov *[d] and Umesh Kumar *[a]

Received 16th May 2018,
Accepted 25th June 2018

DOI: 10.1039/c8cy00987b

rsc.li/catalysis

Mg-Doped TiO_2 nanoparticles were prepared *via* a modified sonothermal method, and their photocatalytic activities were investigated for the reduction of CO_2 with H_2O. The structural properties of the prepared catalysts with varying Mg doping levels were studied by UV-vis spectroscopy, N_2 adsorption–desorption, XRD, SEM, TEM, and XPS. CO, H_2, CH_3OH, and CH_4 were the major products observed with a maximum production rate of 29.2, 28.7, 5910.0 and 2.3 μmol g^{-1} h^{-1}, respectively. Preferable Mg doping sites in TiO_2 nanoparticles and interaction of CO_2 with Mg-doped TiO_2 were studied computationally. Modeling revealed that (101) facets and junctions of (101)/(101) and (001)/(101) facets are the preferred locations of surface Mg atoms. Adsorption of CO_2 proceeds in the bent carbonate and hydrocarbonate forms. The increased activity of Mg-doped TiO_2 is explained by the close proximity of surface Mg reaction sites to the positions of photogenerated electrons on (101) facets.

Introduction

Over the years, the major cause of global warming has been the increasing energy demand and continuous combustion of fossil fuels, which has generated an imbalance between the amount of CO_2 produced and consumed by green plants. At the same time, exploring alternative pathways for the generation of the depleting fossil-originated organic fuels and green fuel H_2 has been the subject of long-time research interests. One of the promising solutions is to convert CO_2 into valuable compounds by utilizing solar energy in the presence of a semiconductor, leading to a dual advantage of reducing CO_2 emission as well conversion/storage of solar energy.[1]

Of all the known semiconductors, TiO_2 has been the most investigated photocatalyst for CO_2 conversion. Although, fast recombination of electron–hole (e^- – h^+) pairs in anatase titania and a wide band gap of 3.2 eV restricts its effectiveness for the photocatalytic reduction of CO_2 using solar light.[2] Till now, anion doping has shown huge potential by introducing trapping states in the lattice of TiO_2, eventually delaying e^- – h^+ recombination.[3] The use of transition metals as dopants is well known because the electrons in their d orbitals have high energy levels, which could cause visible light absorption upon doping but also increased recombination rates.[4]

Mg doping has received attention recently due to the ionic radius of Mg being similar to that of Ti. Other advantages of Mg-containing TiO_2 have been reported as (1) promotion of the energy position of the conduction band minimum of TiO_2[5] and (2) the increase in the amount of CO_2 chemisorption in the presence of water leading to an enhancement in the efficiency of the catalyst.[6] Enhancement of photogenerated charge separation is possible in isomorphically substituted Mg-doped TiO_2 since the difference in the formal charge of Mg^{2+} and Ti^{4+} obliges the creation of oxygen vacancies, and these vacancies can serve as traps for photogenerated electrons on the photocatalyst surface.

The stability of CO_2 has been a big challenge for its activation and conversion into organic compounds since the dissociation energy of a C=O bond in CO_2 is ~750 kJ mol^{-1}, higher than that for many other chemical bonds such as C–H (~430 kJ mol^{-1}) and C–C (~336 kJ mol^{-1}).[6b] Hence, the total efficiency of the CO_2 reduction process depends critically on the type of reductant, nature of the photocatalyst and its surface area. Various reductants for the photoreduction of CO_2 have been reported to include H_2O,[7] H_2,[8] H_2S (ref. 9) and CH_4.[10] In comparison with most of the organic sacrificial electron donors used for the reduction of CO_2, water is the most abundant and low-cost reagent.[2a,11] Also, H_2O serves as a source of H_2 to produce hydrogenated products such as

[a] *Chemical Science Division, CSIR-Indian Institute of Petroleum, Dehradun, India. E-mail: umesh_kumar@iip.res.in*
[b] *Catalytic Conversion Division, CSIR-Indian Institute of Petroleum, Dehradun, India*
[c] *Department of Chemistry, University of Ibadan, Ibadan, Nigeria*
[d] *Altai State University, pr. Lenina 61, Barnaul 656049, Russia. E-mail: a-voronts@yandex.ru*

† Electronic supplementary information (ESI) available. See DOI: 10.1039/c8cy00987b

This journal is © The Royal Society of Chemistry 2018

methanol and methane.[7] High surface area has been considered to be critical for the number of surface-adsorbed reactants, and determines the photocatalytic activity.[12] Therefore, photocatalysts with a higher surface area are beneficial for the conversion of CO_2. The adsorption constant of CO_2 also plays a vital role in the reaction rate as the Langmuir–Hinshelwood equation depends on it.

Many of the previous works reported Mg as either MgO or MgO coated on TiO_2 for the photoreduction of CO_2.[6b,7,13] Manzanares *et al.*[14] demonstrated clearly that Mg is concentrated in the surface layer of Mg-doped TiO_2. Hence, it is essential to determine the most probable location of the Mg dopant on the TiO_2 nanoparticle surface. Adsorption is the first step of CO_2 photoreduction, and we investigate the adsorption strength and adsorption modes of CO_2 over Mg dopant surface sites. The knowledge of this kind will help to develop future generations of active photocatalysts with finely engineered surface and crystals. In continuation of our previous studies, we have developed a scarcely reported series of Mg-doped TiO_2 with a higher surface area and explored their photocatalytic potential for CO_2 reduction using H_2O as the reductant. Quantum chemical computations were performed using MOPAC2016 software to fully understand the role of Mg doping in the lattice of TiO_2 at various sites and interaction of the doped TiO_2 with CO_2.

Experimental

Materials

Titanium(IV) butoxide ($Ti(OBu)_4$) was purchased from Aldrich; magnesium nitrate hexahydrate ($Mg(NO_3)_2{\cdot}6H_2O$) from Sisco Research Laboratories; ethanol (C_2H_5OH) from Fischer Chemicals; acetonitrile (ACN) for HPLC spectroscopy from SD Fine-Chem Limited; methanol (CH_3OH) from Merck; CO_2, argon and hydrogen (99.9995%) from Sigma Gases; CO, methane and hydrogen standard gases (99.9995%) from Sigma Gases; and deionized HPLC grade water (H_2O) were used as chemicals. All chemicals were of analytical grade and used without further purification.

Synthesis of catalysts

A series of Mg-doped TiO_2 catalysts were synthesized using a modified sonothermal method from our previously reported work.[15] Briefly, 50 mL ethanolic solution of $Ti(OBu)_4$ (8.76 g) was mixed with 50 mL ethanolic solution of $Mg(NO_3)_2{\cdot}6H_2O$ (0.11 g). The resulting mixture was then dropwise added under ultrasonication to 200 mL of ethanol–water (150 : 50 v/v) mixture at 70 °C. Mg-Doped TiO_2 nanoparticles immediately formed from the dropping solution and the resulting reaction mixture was ultrasonicated at the same temperature further for 1 h to obtain Mg–TiO_2-1. The similar method was applied by using 0.21 and 0.42 g of $Mg(NO_3)_3{\cdot}6H_2O$ to obtain Mg–TiO_2-2, and Mg–TiO_2-3, respectively. The Mg–TiO_2 catalysts were separated by centrifugation, washed thoroughly with water and calcined in air at 400 °C for 4 h with a heating ramp rate of 1 °C min^{-1}. The pure TiO_2 sample was also prepared for catalytic comparison by the same procedure.

Characterization of catalysts

The actual amount of Mg-doped in Mg–TiO_2 samples was analyzed by inductively coupled plasma atomic emission spectroscopy (ICP-AES) from M/s Leeman Labs Inc, USA, equipped with a DRE PS 3000 UV (simultaneous plus sequential system) Echelle spectrometer. The various samples were mixed with HNO_3 for the digestion of Mg followed by the addition of deionized HPLC grade water.

Solid-state UV-vis diffuse reflectance spectra were obtained from a Shimadzu 2600 UV/Vis-NIR spectrophotometer, equipped with an integrated sphere in the wavelength range of 200–800 nm, using $BaSO_4$ as a reflecting standard. Both absorbance and reflectance values were obtained. The reflectance values were then transformed using the Tauc plot, which shows the relation $(F(R_\infty)h\nu)^{1/2}$ *vs.* $(h\nu - \varepsilon_0)$ with the assumption of an indirect optical transition, where ε_0 is the energy of the absorption edge to be determined from the plots obtained, h is the Planck constant and ν is the frequency.[16]

The crystalline phases in the samples were determined using X-ray diffraction (XRD) patterns taken on a Bruker D8 Advance X-ray diffractometer using monochromatic Cu Kα (λ = 1.5418 Å) radiation in the 2θ range from 2° to 80° with a scan rate of 0.02° s^{-1}.

N_2 adsorption–desorption properties were examined at −196 °C. The specific surface area of monolayer coverage was determined using the Brunauer–Emmett–Teller (BET) method. The pore size distribution was measured from the desorption branch of the isotherm using the Barrett–Joyner–Halenda (BJH) method. The total pore volume was taken at the saturation of pores around P/P_0 = 0.99.

Morphological information and elemental mapping of the catalysts were obtained using a FEI Quanta 200F scanning electron microscope (SEM) system equipped with energy-dispersive X-ray (EDX) spectroscopy. Transmission electron microscopy (TEM) and high-resolution transmission electron microscopy (HRTEM) analyses were performed using a JEM-2010 instrument (JEOL, Japan). The accelerating voltage was 200 kV, and the resolution was 1.4 Å. The samples were loaded on a carbon coated copper grid *via* dispersion in ethyl alcohol using an ultrasonic processor. The local elemental composition in HR-TEM was measured using an energy-dispersive spectrometer (EDX) produced by Phoenix using a Si (Li) detector with an energy resolution of 130 eV.

X-ray photoelectron spectroscopy study was done using ESCA+, (Omicron Nanotechnology, Oxford Instrument Germany) equipped with a monochromator aluminum source (Al Kα radiation $h\nu$ = 1486.7 eV). The instrument was operated at 15 kV and 20 mA. The pass energy for the short scan pass energy is 20 eV, and in the case of a survey, 50 eV. Samples (powder or pellet form) were deposited on Cu tape and degassed overnight in an XPSFEL chamber to minimize air contamination at the sample surface as well as degassing in

Published on 25 June 2018. Downloaded by Indian Institute of Petroleum on 7/17/2018 10:36:33 AM.

the main chamber. To overcome the charging problem, a charge neutralizer of 2 keV is applied, and the binding energy of the C1s core (284.6 eV) was taken as reference. The analyzer is from Argus with a mean radius of 124 mm, an inner radius of 120.8 mm, and an outer radius of 127.2 mm and the angle between the analyzer and the source was 90°. The resolution was confirmed by FWHM of about 0.60 eV.

Photocatalytic CO_2 reduction

The photocatalytic reduction of CO_2 using H_2O as the reductant was performed in a closed gas-recirculation quartz reactor of 50 cm^3 internal volume. The experimental setup was equipped with a gas inlet, outlet, gas sampling port, and a liquid sampling facility (Fig. S1†). 5 mg of the catalyst was suspended in 20 mL HPLC grade water : ACN mixture (4 : 16 v/v) and ultrasonicated for 10 min to ensure homogeneous dispersion. The reaction mixture was preconditioned by repeated evacuation. The mixture was then purged with argon to remove any dissolved gases followed by CO_2 purging for the required time to obtain the CO_2 saturated reaction mixture. The photocatalytic system was illuminated by a 8 W UV-A lamp (PEN-RAY lamp, 350 nm, 2.13″, Cole-Parmer, 120 μW cm^{-2}). A small aliquot of gas and liquid sample was taken out at a regular time interval and analyzed using a gas chromatograph, Perkin Elmer Clarus 680, equipped with a FID and a TCD and plot-Q and shin carbon columns.

To ascertain that the formed products originated from the photoreduction of CO_2, a series of blank experiments were performed in a preconditioned reactor under the following conditions: a) in the dark without CO_2 in the presence of the catalyst, b) in the dark with CO_2 in the presence of the catalyst, c) UV-illuminated in the absence of both CO_2 and the catalyst, and d) UV-illuminated in the presence of CO_2 and absence of the catalyst. No carbonaceous product was detected in the above blank tests.

Computational details

Quantum chemical computations were carried out using the MOPAC2016 software. Methods pm6-d3 and pm6 (ref. 17) were used for obtaining the enthalpy of formation of Mg-doped TiO_2 nanoparticles while method pm6-d3 which implement Grimme dispersion correction[18] was used to investigate the interaction of CO_2 with photocatalyst nanoparticles. The decahedral TiO_2 anatase nanoparticle designated Ti44r1 was used for doping and CO_2 interaction studies. The properties of this nanoparticle and its interaction with an acetone molecule were investigated previously.[19] Using the scc-dftb method, it was found that photogenerated holes are located on oxygen atoms at the corners between four adjacent (101) facets, while photogenerated electrons are distributed among Ti atoms around the edges between adjacent (101) facets away from (001) facets.

Doping of the Ti44r1 nanoparticle was performed by substitution of a surface Ti atom with the Mg atom and removal of an adjacent oxygen atom to preserve charge neutrality according to the following equation:

$$(TiO_2)_{121}(H_2O)_6 + Mg = (MgO)(TiO_2)_{120}(H_2O)_6 + TiO.$$

Interaction of the CO_2 molecule with the doped Ti44r1 cluster was studied by placing the CO_2 molecule at the oxygen vacancy formed during doping and full optimization of the structure. The heat of adsorption was calculated by subtracting the enthalpy of formation of CO_2 and Mg/Ti44r1 from the enthalpy of formation of the CO_2–Mg/Ti44r1 adsorption complex.

Results and discussion

Catalyst characterization

ICP-AES measurements reveal that the amount of Mg in Mg-TiO_2 samples are in the range of 0.07 to 0.17% (Mg/(Mg + Ti)) and gradually increases with increasing Mg content in precursors. Here, Mg–TiO_2-1, Mg–TiO_2-2, and Mg–TiO_2-3 have 0.07, 0.10 and 0.17 wt% Mg, respectively.

The ultraviolet-visible (UV-vis) absorption spectra of the obtained samples are depicted in Fig. 1a. It can be observed that the absorption edge of the pristine TiO_2 was *ca.* 393 nm. There was no noticeable shift in the spectra after the addition of Mg dopants up to 0.1% suggesting that Mg doping does not influence the band gap of TiO_2. However, the absorption edge is slightly shifted to a lower wavelength (*ca.* 388 nm) with maximum Mg loadings (Fig. 1a and S2†). Hu and co-workers observed a similar trend.[4] The band gap energies of all samples were obtained from the Tauc plot by extrapolating a tangent line to the abscissa axis. The energies of all samples were around 3.10 eV (Fig. S3†).

The XRD patterns of the series of Mg-doped TiO_2 photocatalysts are shown in Fig. 1b. The pure TiO_2 and Mg-doped TiO_2 photocatalysts have major peaks at 25.5°, 38.2°, 48.3°,

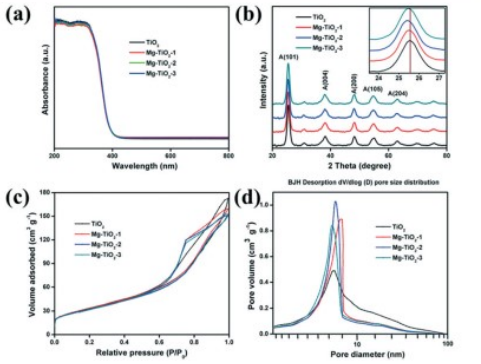

Fig. 1 (a) UV-vis absorbance spectra, (b) XRD patterns, (c) N_2 adsorption–desorption and (d) pore size distribution of TiO_2, Mg–TiO_2-1, Mg–TiO_2-2 and Mg–TiO_2-3.

This journal is © The Royal Society of Chemistry 2018

Published on 25 June 2018. Downloaded by Indian Institute of Petroleum on 7/17/2018 10:36:33 AM.

55.02° and 63.02° in all samples which is consistent with (1 0 1), (0 0 4), (2 0 0), (1 0 5), and (2 0 4) planes of tetragonal anatase TiO_2 (JCPDS 21-1272). Mg^{2+} (0.72 Å) has a comparable ionic radius with that of Ti^{4+} (0.61 Å), is easily doped and substitutes Ti^{4+} in TiO_2 without much distortion to the structure. Therefore, no clear peak for Mg or MgO was observed in the Mg-doped TiO_2 samples, but the slight change to a lower value in the (1 0 1) peak of TiO_2 anatase reflects the doping of Mg in the TiO_2 lattice. For instance, the anatase (1 0 1) peak positions of all the prepared catalysts are located at 25.55°, 25.50°, 25.42° and 25.41° for TiO_2, Mg–TiO_2-1, Mg–TiO_2-2 and Mg–TiO_2-3, respectively. Also, these slight shifts indicate that the structure of the anatase is preserved.

The surface areas (SAs) of all samples are shown in Table 1. The modified sonothermal method affords the prepared TiO_2 a higher surface area of 122.8 $m^2\ g^{-1}$, which is almost double (64.5 $m^2\ g^{-1}$) that of TiO_2 from our previous report.[15] Interestingly, the SA nearly remains constant, around 120 $m^2\ g^{-1}$, with all Mg-doped catalysts of the present study and higher than most reported Mg-doped TiO_2 as shown in Table 2.[15,20] As shown in Fig. 1c, N_2 adsorption–desorption isotherms of all samples are of type IV.[21] Pure TiO_2 exhibited an H3 type of hysteresis loop, indicating the agglomeration of particles forming slit-shaped pores. However, after doping, the hysteresis loop gradually tends towards the H2 type, showing the presence of ink-bottled pores and cylindrical-through pores. The presence of these pores in Mg-doped TiO_2 samples confirms that Mg interaction with TiO_2 leads to the rearrangement of pores. The total pore volume of pure TiO_2 and Mg–TiO_2-1 are almost equal; as the amount of Mg increases, the total pore volume decreases as shown in Table 1. The decreasing trend is also confirmed by the pore size distribution curve (Fig. 1d), in which the pore maxima shifted towards lower values with increasing Mg content. This suggests that the pores are becoming slightly narrower as the Mg content increases. Also, pure TiO_2 has shown a higher cumulative pore volume in comparison with all Mg-doped samples (Fig. S4†). Also, the decreasing trend was observed in the cumulative pore volume with increasing amount of Mg.

The SEM images of pristine TiO_2 and Mg-doped TiO_2 samples are shown in Fig. S5.† The morphologies of all samples are relatively similar. There was not much difference between pure TiO_2 and all Mg-doped TiO_2, indicating that particles are of highly homogeneous size. EDX analysis of Mg-doped TiO_2 samples confirmed the presence of Mg, O, and Ti as illustrated in Fig. S5,† while for bare TiO_2, only O and Ti were confirmed by EDX analysis.

To understand the morphology of prepared photocatalysts better, the TEM images of pristine TiO_2 and Mg-doped TiO_2 samples are depicted in Fig. 2 and S6–S9.† An improvement in the homogeneity was observed for all samples; indicating that the modified experimental procedure facilitates better dispersion of TiO_2 nanoparticles. The calculated average particle size of pure TiO_2 was *ca.* 12.5 nm. A gradual decrease in particle size was observed with an increase of Mg doping in TiO_2. The values of 9.6, 9.5 and 8.4 nm were calculated for Mg–TiO_2-1, Mg–TiO_2-2, and Mg–TiO_2-3, respectively. The *d*-lattice spacing of 0.35 nm is consistent with the (101) plane of anatase TiO_2 as depicted by HRTEM images (Fig. 2b and d). Notably, the spacing was slightly reduced to 0.34 nm after doping of Mg, suggesting the interaction of Mg in the lattice of TiO_2. Elemental mapping confirms the homogenous nature of all catalysts (Fig. S10–S13†).

To check the changes in the chemical environment, XPS measurements were performed on the prepared TiO_2 and Mg-doped TiO_2 catalysts. The XPS survey spectra of all catalysts are shown in Fig. S14–S17.† The presence of the Mg 2p peak only in the spectra of all Mg-doped samples indicates the successful doping of Mg^{2+} in TiO_2. The Mg 2p peak slightly increases as the amount of Mg in TiO_2 increases. The high-resolution XPS spectrum of TiO_2 reveals two peaks at 457.7 and 463.5 eV, which are assigned to Ti $2p_{3/2}$ and Ti $2p_{1/2}$ of the Ti^{4+} state[22] as shown in Fig. S18.† Also, the peak positions of Ti $2p_{3/2}$ and Ti $2p_{1/2}$ in all Mg-doped TiO_2 samples were slightly shifted after the addition of Mg (Fig. 3a, S19 and S20†) in comparison with ordinary TiO_2. For instance, the peak position at 457.7 and 463.5 eV with TiO_2 shifted to 457.4 and 463.2 eV in Mg–TiO_2-2, respectively (Fig. 3a). The peak shifts in Mg-doped TiO_2 samples suggest that Ti ions were substituted with Mg ions in the lattices forming the Ti–O–Mg bond.[22,23]

The high-resolution XPS spectrum of O1s of TiO_2 was deconvoluted into two peaks as shown in Fig. 3b. In the spectrum, the peaks observed at 528.9 and 530.5 eV are attributed to lattice oxygen (Ti–O) and non-lattice oxygen (adsorbed O–H groups), respectively. However, for all Mg-doped TiO_2 samples, the O1s spectrum was fitted into three peaks including an additional peak assigned to the Mg–O– bond (Fig. 3c, S21 and S22†).[13b] The area of the new peak (Mg–O–) becomes larger with an increase in the amount of Mg in TiO_2. Also, the peak positions observed at 528.9 and 530.5 eV with TiO_2 are slightly shifted for all Mg-doped TiO_2 samples. For example, the peak position slightly shifted to 528.8 and 529.4 eV in the Mg–TiO_2-2 sample. The observed new peak and peak

Table 1 Physico-chemical properties of the prepared TiO_2 and Mg-doped TiO_2 catalysts

Type of catalyst	Surface area ($m^2\ g^{-1}$)	Pore volume ($cm^3\ g^{-1}$)	Average pore width[a] (nm)	Pore maxima (nm)
TiO_2	122.76	0.26	0.71	0.67
Mg–TiO_2-1	121.60	0.25	0.64	0.77
Mg–TiO_2-2	117.40	0.24	0.63	0.72
Mg–TiO_2-3	118.45	0.23	0.63	0.72

[a] BJH desorption average pore diameter.

Published on 25 June 2018. Downloaded by Indian Institute of Petroleum on 7/17/2018 10:36:33 AM.

Table 2 Comparison of the prepared Mg-doped TiO_2 catalysts with previous studies

Catalyst	Synthetic method	Surface area ($m^2\ g^{-1}$)	Photocatalytic activity	Ref.
Mg-Doped TiO_2	Co-hydrolysis	58	Hydrogenation of nitrates	20*a*
Magnesium doped TiO_2 nanoparticles	Sol–gel technique	112	Degradation of bisphenol-A	20*b*
Mg-Doped TiO_2	Sol–gel method	112	Degradation of 4-chlorophenol	20*c*
Mg-Doped TiO_2 nanoparticles	Sol–gel method	48.5	Degradation of acid red 27	20*d*
Mg-Doped TiO_2 nanoparticles	Sol–gel method	65.8	Degradation of C. I. acid red 27	20*e*
Mg-Doped TiO_2 nanoparticles	Modified sonothermal–hydrothermal	121.6	Photocatalytic CO_2 reduction	This paper

shift in Mg-doped TiO_2 samples indicate successful doping of Mg in TiO_2 as well as the formation of some mixed oxide and oxygen vacancies.

The high-resolution XPS spectra of Mg 2p of all Mg-doped TiO_2 samples are shown in Fig. 3d, S23 and S24.† The binding energy observed was *ca.* 51.2 eV, which is typical of Mg^{2+} that bonds with an oxygen atom.[22,24]

Photocatalytic experiments

The initial screening of blank experiments confirmed the absence of any carbon-containing compounds; as a result, the obtained products (gaseous and liquid phases) originated from the photocatalytic reduction of CO_2. In the gaseous phase, CO, H_2, and CH_4 were the products observed as shown in Fig. 4. As expected, the product yields increase after doping of Mg in TiO_2. The amount of CO production increased with Mg-doped TiO_2 up to an optimum of 0.1 wt% Mg (Mg–TiO_2-2) and then decreased significantly with further increase in Mg doping (Fig. 4a). This suggests that the production of CO is not favored with a higher amount of Mg. The amount of CO produced was 29.2 μmol g^{-1} h^{-1} over 0.1 wt% (Mg–TiO_2-2), which was higher than that over pure TiO_2 (24.3 μmol g^{-1} h^{-1}). Similarly, the production rate of H_2 increased remarkably with Mg-doped TiO_2 up to an optimum of 0.1 wt% Mg (Mg–TiO_2-2) and then decreased gradually with further increase in Mg doping (Fig. 4b). The amount of H_2 produced was 28.7 μmol g^{-1} h^{-1} over 0.1 wt% (Mg–TiO_2-2), which was 21 times higher than that over pure TiO_2 (1.3 μmol g^{-1} h^{-1}) (Fig. 4c). However, the production of CH_4 increased up to the maximum loading of Mg in TiO_2, yielding 2.3 and 1.1 μmol g^{-1} h^{-1} with Mg–TiO_2-3 (0.17 wt%) and pure TiO_2 catalysts, respectively.

In the liquid phase, CH_3OH was the main product observed from the CO_2 reduction with H_2O on all catalysts (Fig. 4d). The production rate was increased with the doping amount of Mg in TiO_2 yielding 1470.0 and 5910.0 μmol g^{-1} h^{-1} with TiO_2 and Mg–TiO_2-2, respectively. It is worthy to note that the formation of Ti^{3+} in all Mg-doped TiO_2 samples could be responsible for their higher activities in comparison with ordinary TiO_2 since Ti^{3+} can help delay the recombination of the $e^- - h^+$ pair.[25]

The Mg doping alters the acid–base properties of TiO_2 and enhances more basic character in TiO_2. Hence, the properties favor better adsorption of CO_2 at the surface of TiO_2.[6b,7,13,14] The reaction phase can directly affect the product selectivity.[6b,20a] The enhanced CO_2 adsorption was also

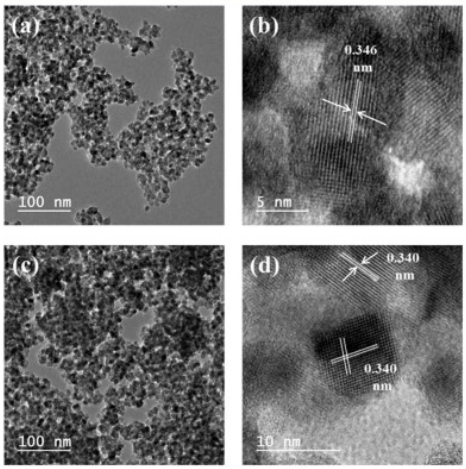

Fig. 2 TEM and HRTEM images of (a and b) TiO_2 and (c and d) Mg–TiO_2-2.

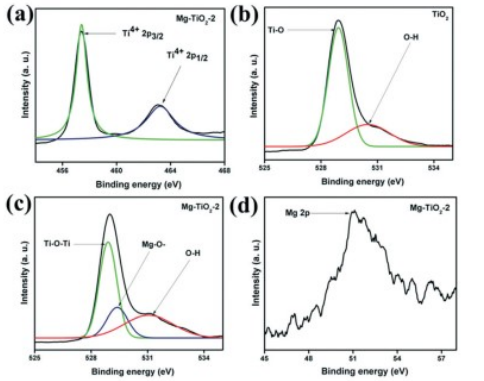

Fig. 3 High resolution XPS spectra of (a) Ti 2p of Mg–TiO_2-2; (b) O 1s of TiO_2; (c) O 1s of Mg–TiO_2-2 and (d) Mg 2p of Mg–TiO_2-2.

This journal is © The Royal Society of Chemistry 2018

Published on 25 June 2018. Downloaded by Indian Institute of Petroleum on 7/17/2018 10:36:33 AM.

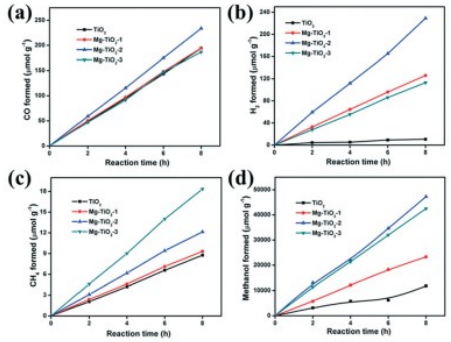

Fig. 4 Effect of Mg-doped TiO_2 nanoparticles for the photocatalytic reduction of CO_2 with H_2O to produce (a) CO, (b) H_2 and (c) CH_4 from the gas phase, and (d) CH_3OH from the liquid phase under ambient conditions.

observed for CPO-27-Mg/TiO_2 leading to enhanced photocatalytic CO_2 reduction under UVA.[26] In the gas phase, the product selectivity moves towards CH_4, CO and H_2 formation due to the probable low amount of H_2O as the reducing agent. The vapor or gas phase processes are majorly continuous flow processes where the formed products separate quickly from the catalyst site. However, in the liquid phase reaction, an excess of reactant (H_2O) present at the surface and the possibility to reconnect with intermediates species will favor the formation of CH_3OH.[1b,15]

Computational studies

There are several possibilities for the structures of the composite obtained when doping TiO_2 with magnesium. Using large amounts of Mg can result in the formation of separate phases of TiO_2 and MgO while doping with small amounts can result in the isomorphic substitution of Ti because the ionic radius of Mg (0.72 Å) is close to that of Ti (0.61 Å). Our experimental method affords the doping of small amounts of Mg in TiO_2. Of particular interest for the CO_2 photoreduction are surface Mg atoms that can serve as reaction sites and here we consider surface doping of a decahedral TiO_2 nanoparticle. Due to the different formal ionic charge of Ti^{4+} and Mg^{2+}, one of the nearest oxygen atoms on the surface or subsurface atomic layers is removed during doping to preserve charge neutrality. The oxygen vacancy formed tends to be close to the doping Mg atom due to electrostatic interaction of effective charges of Mg of −2 and of V_O of +2 in the TiO_2 lattice. Fig. 5 shows

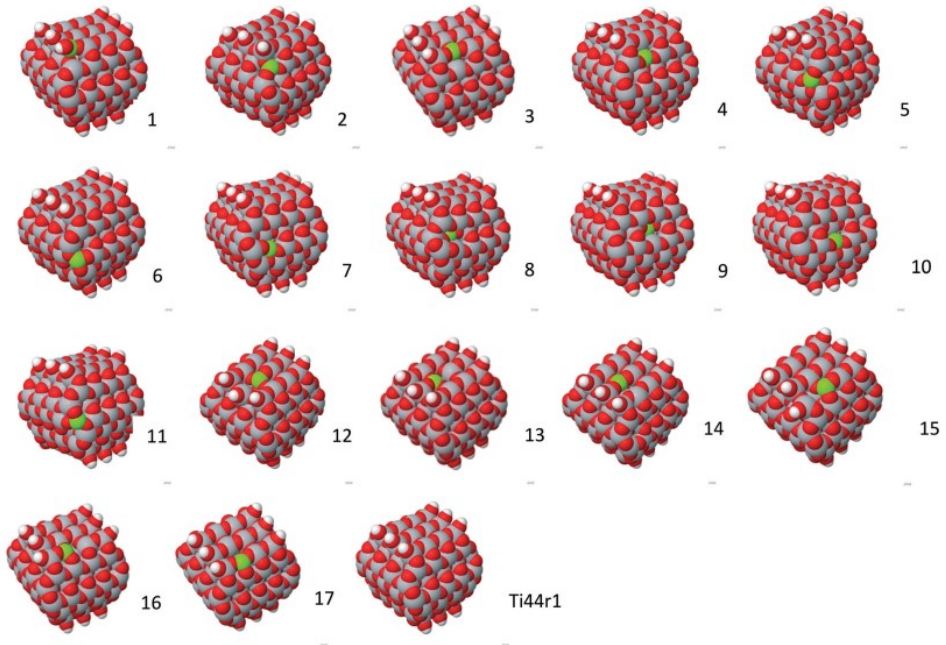

Fig. 5 Decahedral TiO_2 anatase nanoparticle was isomorphically doped with Mg in different surface positions (1–17) and the initial nanoparticle Ti44r1. Atom designations: green – Mg, gray – Ti, red – O, and white – H.

Published on 25 June 2018. Downloaded by Indian Institute of Petroleum on 7/17/2018 10:36:33 AM.

Table 3 Enthalpy of formation of Mg-doped TiO_2 nanoparticles (in kcal mol^{-1}) calculated with pm6 and pm6-d3 methods

Cluster #	Enthalpy pm6	Enthalpy pm6-d3	Cluster #	Enthalpy pm6	Enthalpy pm6-d3
1	−26 291.58	−27 076.14	10	−26 318.81	−27 102.27
2	−26 318.35	−27 103.22	11	−26 316.67	−27 102.08
3	−26 311.34	−27 095.76	12	−26 273.50	−27 055.27
4	−26 315.06	−27 098.67	13	−26 280.05	−27 062.40
5	−26 320.34	−27 104.57	14	−26 295.46	−27 078.33
6	−26 316.68	−27 102.05	15	−26 275.65	−27 058.25
7	−26 328.64	−27 112.53	16	−26 278.53	−27 061.54
8	−26 316.39	−27 099.11	17	−26 284.21	−27 066.99
9	−26 297.95	−27 080.59	Ti44r1	−26 424.65	−27 212.10

the optimized structures of anatase nanoparticle Ti44r1 with the isomorphically substituted single Ti atom in different surface positions.

Due to the presence of symmetry planes in the Ti44r1 nanoparticle, there are a limited number of unique Ti atoms on the surface, and all of them are considered in Fig. 5. Each titanium atom has four or five nearest oxygen atoms of the outer atomic layer. Since V_O in the surface layer is regarded as a possible site for strong adsorption of CO_2, only surface oxygen vacancies are included in this study. The initial Ti44r1 cluster is given in Fig. 5 to allow comparison of the structure of doped and undoped nanoparticles. Clusters 1–4, 9–10 and 12–17 demonstrate moderate structure changes as a result of doping, while clusters 5–8 and 11 show strong shifts of atoms near the doping site.

Table 3 lists the heat of formation of the doped clusters and the initial Ti44r1 nanoparticle computed with methods pm6 and pm6-d3. The first of these computation methods was calibrated to obtain the correct enthalpy of formation, while the second method was developed to correctly describe interaction energies and geometries including non-covalent bonding. According to the pm6 method, the most stable is cluster 7 followed by cluster 5 (+8.30 kcal mol^{-1}), 10 (+9.83 kcal mol^{-1}), 2 (+10.29 kcal mol^{-1}), 6 (+11.96 kcal mol^{-1}), 11 (+11.97 kcal mol^{-1}), 8 (+12.25 kcal mol^{-1}), 4 (+13.58 kcal mol^{-1}), and 3 (+17.3 kcal mol^{-1}). Other clusters are less stable by at least 30.69 kcal mol^{-1} (cluster 9) as compared to cluster 7. Clusters 12–17 with oxygen vacancies at the surface (001) are all relatively unstable with cluster 14 being most stable among them. Thus, most possibly isomorphic substitution takes place on (101) facets and their junctions with facets (101) and (001).

Adsorption of reagents is the first stage of the vast majority of heterogeneous catalytic reactions. CO_2 is adsorbed on

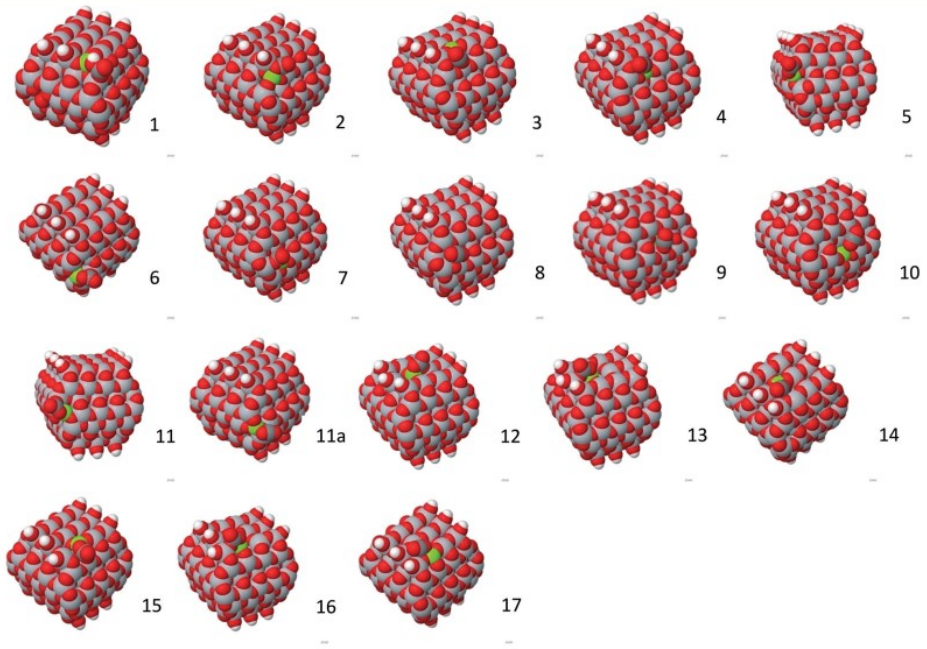

Fig. 6 CO_2 adsorption complexes with Mg-doped Ti44r1 nanoparticles. The numbers of the complexes correspond to the number of the Mg-Ti44r1 nanoparticles. The carbon atom is dark gray.

 This journal is © The Royal Society of Chemistry 2018

Published on 25 June 2018. Downloaded by Indian Institute of Petroleum on 7/17/2018 10:36:33 AM.

the photocatalyst surface which is followed by its reduction in diverse products such as CO, CH_4, and CH_3OH. Previously, we investigated the photocatalytic reduction of CO_2 to CO over the Cu/TiO_2 photocatalyst[1b] and suggested that product desorption is the most energy consuming step of the reaction mechanism. This means that strongly adsorbed reagents are unfavorable for facile CO_2 reduction while too low adsorption energy would leave the photocatalyst surface unpopulated with the reagents and slow down the reaction.[15] Some optimum should exist for CO_2 adsorption. Mg doping could help attain such optimization and also help concentrate adsorbed CO_2 molecules at the most probable locations of photogenerated electrons. Fig. 6 shows optimized structures of CO_2 adsorption complexes over different Mg- doped Ti44r1 clusters. Before adsorption, the linear CO_2 molecule was placed at V_O near Mg sites.

We can see that CO_2 is adsorbed in three modes (Fig. 6), as hydrocarbonate HCO_3 (complex 1), as carbonate CO_3 (complexes 2, 5–7, 11–13, and 15–16) and as an almost intact linear molecule O═C═O (complexes 3, 4, 8–10, 11a, 14, 17). Table 4 presents the heat of adsorption and geometry of adsorption complexes. Carbonate and hydrocarbonate modes of adsorption exhibit a high enthalpy of adsorption in the range of −18.22 to −38.87 kcal mol^{-1}. Adsorption in the linear form of CO_2 has a low adsorption enthalpy in the range of −4.01 to −9.53 kcal mol^{-1}.

The hydrocarbonate adsorption complex (complex 1) has OH group connected to the Mg atom and another carbonate oxygen to the Ti atom. The bond lengths for Mg–OH is 2.05 Å, C–OH is 1.46 Å, C–OTi is 1.26 Å, C═O is 1.20 Å, and Ti–OC is 2.06 Å. Carbonate adsorption complexes 2, 5, 6, 11–13, and 15 are formed by bidentate adsorption to surface Mg and Ti atoms. Typical bond lengths are Mg–O 1.91–2.02 Å, Ti–O 1.84–2.10 Å, C–OMg 1.29–1.32 Å, C–OTi 1.37–1.42 Å and C═O 1.21 Å. In complex 7, one oxygen atom is coordinated to the surface Ti atom, while another to both Ti and Mg atoms. Coordination to multiple surface atoms decreases adsorption enthalpy which is beneficial for facile reduction of adsorbed CO_2 and desorption of reduction products. Moreover, the adsorption site of complex 7 is located at the place of concentration of photogenerated electrons.

For linear adsorption complexes, adsorption is mostly of physical nature since the adsorption energy is low. Coordination proceeds either through one of the oxygen atoms or *via* a carbon atom to surface Mg or Ti atoms. The Ti–O bond length is 2.49–2.51 Å, while the Mg–O bond length is 2.21–2.35 Å for respective coordination. The coordination to the Mg atom (complexes 4) is stronger than to the Ti atom (complexes 3,). The C═O bond length of 1.17 Å in linearly adsorbed CO_2 remains almost unchanged from the free gaseous molecule. In some cases (complexes 8, 10), adsorption is purely physical without specific interaction with any surface atom.

Since the adsorption energy for a linear form of CO_2 adsorbate is low, its existence under the typical conditions of photocatalytic reduction in a humid atmosphere or aqueous solution is hardly possible due to the strong competitive adsorption of water molecules. Complexes 5–7 are most possible candidates of photogenerated reduction sites since they are closely located to photogenerated electrons and exhibit enough stability to exist under the conditions of photocatalytic reduction.

Table 4 Parameters of CO_2 adsorption over different Mg-doped TiO_2 nanoparticles

Complex #	ΔH_{ads}, kcal mol^{-1}	Geometry of CO_{2ads}	Complex #	ΔH_{ads}, kcal mol^{-1}	Geometry of CO_{2ads}
1	−38.87	HCO_3	10	−5.10	Linear
2	−25.16	CO_3	11	−38.60	CO_3
3	−7.01	Linear	11a	−5.24	Linear
4	−9.53	Linear	12	−20.73	CO_3
5	−31.86	CO_3	13	−16.97	CO_3
6	−30.17	CO_3	14	−5.39	Linear
7	−18.22	CO_3	15	−35.79	CO_3
8	−4.01	Linear	16	−24.72	CO_3
9	−5.46	Linear	17	−5.52	Linear

Conclusions

Mg-Doped TiO_2 nanoparticles have been successfully prepared *via* a modified sonothermal method, and their photocatalytic activities were investigated for the reduction of CO_2 with H_2O. CO, H_2, CH_3OH, and CH_4 were the major products observed with a maximum production rate of 29.2, 28.7, 5910.0 and 2.3 μmol g^{-1} h^{-1}, respectively. Mg-Doped decahedral TiO_2 anatase nanoparticles are modeled using the modern semi-empirical method, and their interaction with CO_2 is studied. The most energetically profitable doping is obtained for sites at the junction of adjacent (101) facets which are also the sites of strong (*ca.* −30 kcal mol^{-1}) or moderately strong (−18 kcal mol^{-1}) CO_2 adsorption in carbonate form. These sites are suggested as the places for CO_2 photoreduction.

Conflicts of interest

There are no conflicts to declare.

Acknowledgements

The authors are grateful to the Director of IIP for his kind permission to publish the results. J. O. Olowoyo is thankful to CSIR-TWAS for the funding of the research work (22/FF/CSIR-TWAS/2015). The authors are thankful to ASD-IIP for their analytical support.

Notes and references

1 (*a*) H. Wang, L. Zhang, Z. Chen, J. Hu, S. Li, Z. Wang, J. Liu and X. Wang, *Chem. Soc. Rev.*, 2014, **43**, 5234–5244; (*b*) N. Singhal, A. Ali, A. Vorontsov, C. Pendem and U. Kumar, *Appl. Catal., A*, 2016, **523**, 107–117.

2 (*a*) S. N. Habisreutinger, L. Schmidt-Mende and J. K. Stolarczyk, *Angew. Chem., Int. Ed.*, 2013, **52**, 7372–7408; (*b*) G. Liu, Y. Zhao, C. Sun, F. Li, G. Q. Lu and H. M. Cheng, *Angew. Chem., Int. Ed.*, 2008, **47**, 4516–4520.

Published on 25 June 2018. Downloaded by Indian Institute of Petroleum on 7/17/2018 10:36:33 AM.

3 S. R. Lingampalli, M. M. Ayyub and C. N. R. Rao, *ACS Omega*, 2017, **2**, 2740–2748.
4 L. Gao, Y. Li, J. Ren, S. Wang, R. Wang, G. Fu and Y. Hu, *Appl. Catal., B*, 2017, **202**, 127–133.
5 (*a*) K. Kakiage, T. Tokutome, S. Iwamoto, T. Kyomen and M. Hanaya, *Chem. Commun.*, 2013, **49**, 179–180; (*b*) S. Iwamoto, Y. Sazanami, M. Inoue, T. Inoue, T. Hoshi, K. Shigaki, M. Kaneko and A. Maenosono, *ChemSusChem*, 2008, **1**, 401–403.
6 (*a*) K. Teramura, T. Tanaka, H. Ishikawa, Y. Kohno and T. Funabiki, *J. Phys. Chem. B*, 2004, **108**, 346–354; (*b*) S. J. Xie, Y. Wang, Q. H. Zhang, W. P. Deng and Y. Wang, *ACS Catal.*, 2014, **4**, 3644–3653.
7 S. Kwon, P. L. Liao, P. C. Stair and R. Q. Snurr, *Catal. Sci. Technol.*, 2016, **6**, 7885–7895.
8 Y. Kohno, T. Tanaka, T. Funabiki and S. Yoshida, *Phys. Chem. Chem. Phys.*, 2000, **2**, 2635–2639.
9 S. M. Aliwi and K. F. Al-Jubori, *Sol. Energy Mater. Sol. Cells*, 1989, **18**, 223–229.
10 Y. Kohno, T. Tanaka, T. Funabiki and S. Yoshida, *Phys. Chem. Chem. Phys.*, 2000, **2**, 5302–5307.
11 F. Sastre, A. V. Puga, L. Liu, A. Corma and H. Garcia, *J. Am. Chem. Soc.*, 2014, **136**, 6798–6801.
12 (*a*) F. Amano, K. Nogami, M. Tanaka and B. Ohtani, *Langmuir*, 2010, **26**, 7174–7180; (*b*) H. Kominami, S.-y. Murakami, J.-i. Kato, Y. Kera and B. Ohtani, *J. Phys. Chem. B*, 2002, **106**, 10501–10507.
13 (*a*) B. Selvaratnam and R. T. Koodali, *Catal. Today*, 2018, **300**, 39–49; (*b*) F. Wang, Y. Zhou, P. Li, L. B. Kuai and Z. G. Zou, *Chin. J. Catal.*, 2016, **37**, 863–868; (*c*) Q. Y. Li, L. L. Zong, C. Li and J. J. Yang, *Appl. Surf. Sci.*, 2014, **319**, 16–20.
14 M. Manzanares, C. Fàbrega, J. Oriol Ossó, L. F. Vega, T. Andreu and J. R. Morante, *Appl. Catal., B*, 2014, **150-151**, 57–62.
15 J. O. Olowoyo, N. C. Hernández, M. Kumar, S. L. Jain, J. O. Babalola and U. Kumar, *ChemistrySelect*, 2018, **3**, 3659–3663.
16 (*a*) H. Park, H. H. Ou, U. Kang, J. Choi and M. R. Hoffmann, *Catal. Today*, 2016, **266**, 153–159; (*b*) L. Matejova, K. Koci, M. Reli, L. Capek, A. Hospodkova, P. Peikertova, Z. Matej, L. Obalova, A. Wach, P. Kustrowski and A. Kotarba, *Appl. Catal., B*, 2014, **152**, 172–183; (*c*) K. Koci, L. Obalova, L. Matejova, D. Placha, Z. Lacny, J. Jirkovsky and O. Solcova, *Appl. Catal., B*, 2009, **89**, 494–502.
17 J. J. Stewart, *J. Mol. Model.*, 2007, **13**, 1173–1213.
18 S. Grimme, J. Antony, S. Ehrlich and H. Krieg, *J. Chem. Phys.*, 2010, **132**, 154104–154119.
19 (*a*) A. V. Vorontsov and S. V. Tsybulya, *Ind. Eng. Chem. Res.*, 2018, **57**, 2526–2536; (*b*) A. V. Vorontsov, *J. Nanopart. Res.*, 2017, **19**, 326.
20 (*a*) N. Bou-Orm, A. Iorgu, S. Daniele and N. Guilhaume, *Appl. Catal., A*, 2013, **467**, 414–420; (*b*) N. Venkatachalam, M. Palanichamy, B. Arabindoo and V. Murugesan, *Catal. Commun.*, 2007, **8**, 1088–1093; (*c*) N. Venkatachalam, M. Palanichamy and V. Murugesan, *J. Mol. Catal. A: Chem.*, 2007, **273**, 177–185; (*d*) M. A. Behnajady, B. Alizade and N. Modirshahla, *Photochem. Photobiol.*, 2011, **87**, 1308–1314; (*e*) J. Talat-Mehrabad, M. Khosravi, N. Modirshahla and M. A. Behnajady, *Res. Chem. Intermed.*, 2015, **42**, 595–609.
21 G. Leofanti, M. Padovan, G. Tozzola and B. Venturelli, *Catal. Today*, 1998, **41**, 207–219.
22 M.-V. Sofianou, M. Tassi, N. Boukos, S. Thanos, T. Vaimakis, J. Yu and C. Trapalis, *Catal. Today*, 2014, **230**, 125–130.
23 (*a*) C. Yang, M.-Y. Tse, X. Wei and J. Hao, *J. Mater. Chem. C*, 2017, **5**, 5170–5175; (*b*) H. L. Li, X. Y. Wu, J. Wang, Y. Gao, L. Q. Li and K. M. Shih, *Int. J. Hydrogen Energy*, 2016, **41**, 8479–8488.
24 Q. Li, L. Zong, C. Li and J. Yang, *Appl. Surf. Sci.*, 2014, **319**, 16–20.
25 Y. Xu, S. Wu, P. Wan, J. Sun and Z. D. Hood, *RSC Adv.*, 2017, **7**, 32461–32467.
26 M. T. Wang, D. K. Wang and Z. H. Li, *Appl. Catal., B*, 2016, **183**, 47–52.

 This journal is © The Royal Society of Chemistry 2018